UNIVERSITAT POLITÈCNICA DE CATALUNYA BARCELONATECH

Particle model for crushable aggregates which includes size, time and relative humidity effects

by

Mauricio Alberto Tapias Camacho

PARTICLE MODEL FOR CRUSHABLE AGGREGATES WHICH INCLUDES SIZE, TIME AND RELATIVE HUMIDITY EFFECTS

By

MAURICIO ALBERTO TAPIAS CAMACHO

PhD Thesis

A thesis submitted in partial fulfillment of the requirements for the degree of Doctor of Philosophy

Division of Geotechnical Engineering and Geosciences
Department of Civil and Environmental Engineering
E.T.S.E.C.C.P.B., L'Escola Tècnica Superior d'Enginyers de Camins, Canals i Ports
UPC, Universitat Politècnica de Catalunya, BARCELONATECH

Supervisors:
Prof. Eduardo Alonso Pérez de Agreda
Prof. Josep A. Gili Ripoll

Barcelona, Spain
November 2016

UNIVERSITAT POLITÈCNICA DE CATALUNYA
BARCELONATECH
Escola de Doctorat

Assessment results for the doctoral thesis | **Academic year: 2016**

Full name	MAURICIO ALBERTO TAPIAS CAMACHO
Doctoral programme	INGENIERÍA DEL TERRENO
Structural unit in charge of the programme	DEPARTAMENTO DE INGENIERÍA CIVIL Y AMBIENTAL

Decision of the committee

In a meeting with the examination committee convened for this purpose, the doctoral candidate presented the topic of his/her doctoral thesis entitled PARTICLE MODEL FOR CRUSHABLE AGGREGATES WHICH INCLUDES SIZE, TIME AND RELATIVE HUMIDITY EFFECTS.

Once the candidate had defended the thesis and answered the questions put to him/her, the examiners decided to award a mark of:

☐ FAIL ☐ SATISFACTORY ☐ VERY GOOD ☐ EXCELLENT

(Full name and signature) Chairperson	(Full name and signature) Secretary	
(Full name and signature) Member	(Full name and signature) Member	(Full name and signature) Member

_____, _____

The votes of the members of the examination committee were counted by the Standing Committee of the Doctoral School, and the result is to award the CUM LAUDE DISTINCTION:

☐ YES ☐ NO

(Full name and signature) Chair of the Standing Committee of the Doctoral School	(Full name and signature) Secretary of the Standing Committee of the Doctoral Schoo

Barcelona, _____

International doctorate certification in the doctoral degree

- As the secretary of the examination committee, I hereby state that the thesis was partly (at least the summary and conclusions) written and presented in one of the languages commonly used for science communication in the relevant field of knowledge, which must not be an official language of Spain. This rule does not apply to stays, reports and experts from Spanish-speaking countries.

(Full name and signature) Secretary of the Examination Committee

To Mary, Seat of Wisdom

A la virgen María, Madre de la Sabiduría

AGRADECIMIENTOS

En primer lugar quiero agradecer a mis directores, profesores Eduardo Alonso y Josep Gili, por su orientación, supervisión y consejos en el desarrollo de la tesis. Sin duda, este proyecto de investigación no hubiera llegado a feliz término sin su valioso aporte.

Al profesor Eduardo Alonso quiero manifestar mi más profunda gratitud: para mí ha sido un honor trabajar a su lado. Admiro su visión de conjunto, su conocimiento extraordinario de la ingeniería geotécnica entre otras muchas cosas, su prestigio, su habilidad para enfrentar y resolver los problemas, y sus consejos. Agradezco también su orientación, y su confianza al permitirme explorar y emprender con libertad caminos novedosos para mí durante esta investigación. Gracias también por permitirme trabajar en sus proyectos de investigación en esta etapa de conclusión de la tesis y contribuir de esta forma también con su financiamiento.

Al profesor Josep Gili quiero también agradecerle por su dirección, sus consejos, y por animarme en el avance de la investigación. De forma especial, quiero agradecerle por su apoyo en la revisión del inglés.

Agradezco a todo el personal del laboratorio de Geotecnia de la UPC por su colaboración y soporte en la realización de los diferentes ensayos: A José Álvarez, Víctor Lozano, Rodrigo Gómez y Tomás Pérez. Especialmente quiero manifestar mi gratitud a José y a Víctor por su valiosa ayuda en el laboratorio y por su amistad.

Agradezco al profesor Enrique Romero, director del laboratorio de Geotecnia, por haber sido mi tutor para la beca del programa Alβan en el inicio de mi doctorado.

Agradezco a los señores de la cantera FOJ de Vallirana (Barcelona) por donar el material, fragmentos de roca caliza, para la realización de los ensayos de laboratorio.

Agradezco a las entidades que colaboraron con el financiamiento de mi doctorado: Al inicio de la investigación, Programa Alβan “Programa de la Unión Europea de Becas de Alto Nivel para América Latina”; y al final de la investigación, la Agencia de Gestión de Ayudas Universitarias y de Investigación (FI-AGAUR) de la Generalitat de Catalunya.

Agradezco a los profesores del departamento de Ingeniería del Terreno que estuvieron en la etapa de docencia dentro de mi formación de doctorado.

Agradezco a todos mis amigos y compañeros de la UPC que han estado durante esta etapa de mi vida, especialmente a Nubia, Pablo, Rodrigo, Clara, Tere, Dani, Enrique, Josbel, Alba, Joanna, Prashanth, Nuria y Anna. Indudablemente, además de su amistad y compañerismo, he contado con su apoyo, ánimo y solidaridad.

Extiendo mis agradecimientos a los profesores y amigos de la Universidad de

Roma Tor Vergata donde hice la estancia internacional durante algunos meses del doctorado. En particular quiero manifestar mi gratitud a la profesora Francesca Casini por su orientación y haber sido mi tutora durante la estancia. También agradezco a los profesores Giulia Viggiani, Nunzio Losacco y Ricardo Conti; y a los chicos del doctorado Marco, Alberto, Giulia y Manuel. Realmente Roma fue una temporada muy fructífera en el avance de la escritura de la tesis bajo una calidez humana y fraterna de este valioso equipo de trabajo.

Agradezco a mi familia, a mis padres, hermanas y hermanos, sobrinos y sobrinas, por su infinito amor y apoyo incondicional.

Finalmente, el agradecimiento más importante es para Dios, ese ser supremo que siempre ha estado conmigo, ahí presente, siendo mi soporte y mi fortaleza, desbordando y compartiendo su Sabiduría, presente en este camino, camino emprendido en un medio distinto, discreto, pero en contacto siempre con el otro, interactuando en medio de su todo.

ABSTRACT

This thesis presents a study of the mechanical behaviour of coarse-crushable aggregates, using the discrete element method (DEM). A novel DEM model has been developed taking into account particle breakage, the influence of the relative humidity, time-dependent behaviour and the effect of particle size.

A criterion of particle breakage has been proposed based in fracture mechanics and the theory of subcritical crack propagation. Three theoretical models for the crack propagation are proposed taking into account the relative humidity.

Pyramidal macroparticles, which behave like clumps and can break, were selected for the DEM model, in view of the results of the analysis performed on the effect of particle shape. The model has been implemented using the commercial software PFC3D, through the incorporation of functions programmed in FISH language.

The proposed DEM model is mainly based on three parameters: the inter-granular contact stiffness (k_n), the inter-particle friction (μ) and the fracture toughness of the material (K_c). It also takes into account the surface roughness of the particles through the solid angle describing contact stresses (θ_0) and the yield stress of the aggregates (σ_y).

In order to calibrate the parameters of the model, some laboratory tests were performed. The basic (ϕ_b) and mineral (ϕ_m) friction angles were determined by means of shear tests using Tilt table test and a Direct shear cell. Contact stiffness tests in one-directional compression on prismatic specimens allowed the determination of k_n. θ_0 was found by means of an estimation of mean roughness (R_a) and by microscope examination of grain surfaces.

The calibration of the DEM parameters was also carried out by means of a back analysis oedometer tests and experimental data. Compressibility, the evolution of grain size distribution curves and the calculation of breakage indices helped to perform the calibration.

Additionally, several oedometer tests were performed on a brittle-crushable material -sugar cubes- in order to investigate the mechanisms of breakage. Two types of arrangements were used to obtain two very different initial void ratios: 0.80 and 0.20. Two mechanisms of breakage were determined: Comminution crushing and particle splitting. An analysis of time-dependent behaviour was also carried out. These considerations were taken into account in the DEM model.

Blind numerical triaxial tests were also performed using parameters previously calibrated in the back analysis of oedometer tests. The prediction was quite accurate and it shows the capability of the DEM model developed to reproduce the constitutive behaviour of crushable aggregates compared with experimental results from the literature.

The DEM simulations of the oedometer and triaxial tests were consistent and accurate. The influence of the relative humidity on the mechanical behaviour, particle size effects, time-dependent behaviour and the evolution of the grain size distribution were well reproduced.

RESUMEN

Esta tesis presenta un estudio del comportamiento mecánico de los agregados gruesos a partir de la modelación numérica utilizando el método de Elementos Discretos (DEM). Se ha desarrollado un novedoso modelo DEM que tiene en cuenta la rotura de las partículas, la humedad relativa, la influencia del tiempo y el efecto del tamaño de las partículas.

Se propone un criterio de rotura de partículas con base en la mecánica de fracturas y la teoría de propagación subcrítica de grietas. Tres modelos teóricos para la propagación de grietas se proponen teniendo en cuenta la influencia de la humedad relativa.

Después de realizar un análisis de sensibilidad de formas de las partículas, para el modelo DEM se seleccionaron macropartículas con formas piramidales que se comportan como clumps (totalmente rígidas) y pueden romper. El modelo ha sido implementado utilizando el software comercial PFC3D, mediante la incorporación de funciones programadas en lenguaje FISH.

El modelo DEM propuesto trabaja principalmente con tres parámetros: la rigidez de los contactos (k_n), la fricción entre las partículas (μ) y la tenacidad de Fractura del material (K_c). También tiene en cuenta la rugosidad superficial de las partículas a través del parámetro θ_0 (ángulo sólido-solid angle) y la tensión de fluencia de los agregados σ_y.

Con el fin de calibrar los parámetros del modelo se realizaron algunos ensayos de laboratorio. Para la estimación de μ: ensayos para determinar el ángulo de fricción básico (ϕ_b) y mineral (ϕ_m) de los agregados a partir de ensayos de corte utilizando la Mesa Inclinada y el Corte Directo. Para la determinación de k_n: ensayos de Rigidez de Contactos a partir de compresión uni-direccional sobre muestras prismáticas con uno de sus extremos de forma piramidal apoyado sobre una superficie plana. Para la determinación de θ_0: estimación de la Rugosidad media (R_a) medida a partir de observaciones con el microscopio.

La calibración de los parámetros del modelo DEM también se llevó a cabo a partir de un análisis retrospectivo (back analysis) de los ensayos numéricos edométricos comparados con datos experimentales –realizando un análisis de sensibilidad de diferentes parámetros-. Se tuvieron en cuenta la compresibilidad, la evolución de las curvas granulométricas y el cálculo de índices de rotura.

Adicionalmente, con el fin de investigar sobre los mecanismos de rotura, se realizaron ensayos edométricos sobre un material frágil: cubos de azúcar. Se utilizaron dos tipos de arreglos de los cubos obteniéndose dos relaciones de vacíos iniciales muy diferentes: 0.80 y 0.20. Se determinaron dos mecanismos de rotura: Rotura local (comminution crushing) y divisiones en dos partes que se aproximaron a mitades (particle splitting). Así mismo se realizó un análisis del comportamiento en el tiempo. Estas consideraciones fueron tenidas en cuenta en el modelo DEM.

También se ejecutaron ensayos triaxiales numéricos con los parámetros calibrados previamente en los ensayos edométricos y se compararon con resultados experimentales de la literatura. La predicción del comportamiento fue bastante acertada mostrando de esta forma la fiabilidad del modelo desarrollado.

Las simulaciones DEM de los ensayos edométricos y triaxiales fueron consistentes y bastante ajustadas con los resultados experimentales. La influencia de la humedad relativa en el comportamiento mecánico, el efecto del tamaño de las partículas, el comportamiento dependiente del tiempo y la evolución de la curvas de distribución granulométrica fueron bien reproducidas.

PUBLICATIONS

Some major contributions of this thesis have been published in the following publications:

Journal papers:

Tapias, M., Alonso, E.E. & Gili, J. (2016). *Compressibility, grain breakage and time dependent behaviour of gap graded aggregates of sugar cubes*. Soils and Foundations, Vol.56 (5), No.5, 805-817.

Tapias, M., Alonso, E.E. & Gili, J. (2015). *A particle model for rockfill behaviour*. Géotechnique 65 (12), 975–994. (http://dx.doi.org/10.1680/jgeot.14.P.170)

Alonso, E.E., Tapias, M. & Gili, J. (2012). *Scale effects in rockfill behaviour*. Géotechnique Letters, 2: 155-160. (http://dx.doi.org/10.1680/geolett.12.00025)

Congress and Technical Meetings:

Alonso, E.E. & Tapias, M. (2015). *Rockfill Mechanics. Experimental Observations and DEM Modelling*. Proceedings of the 15th Pan-American Conference on Soil Mechanics and Geotechnical Engineering. Buenos Aires (Argentina), November 15th - 18th, 2015.

Alonso, E.E., Tapias, M., & Gili, J. (2015). *Avances en la modelización de escolleras mediante DEM*. (Written in Spanish. In English: "*Advances in modeling rockfills using DEM*").Proceedings of the 10th Spanish Conference on Dams "X Jornadas Españolas de Presas". Spanish Committee on Large Dams – SPANCOLD (Comité Nacional Español de Grandes Presas). Sevilla (Spain), February 18th -20th 2015.

Tapias, M., Alonso, E.E. & Gili, J. (2014). *Compressibility and grain breakage of a gap graded material*. Proceedings of the International Symposium "Geomechanics from Micro to Macro IS_Cambridge". University of Cambridge, Cambridge (U.K.), September 1st-3rd, 2014.

Tapias, M., Alonso, E.E. & Gili, J. (2013). *DEM modeling of unsaturated rockfill. Scale effects*. Proceedings of the 1st Pan-American Conference on Unsaturated Soils. Cartagena de Indias (Colombia), February 20th–22nd, 2013.

Tapias, M., Alonso, E.E. & Gili, J.A. (2011). *Analysis of Micro-properties for Triaxial Behaviour on Coarse Aggregates using DEM*. Proceedings of the 2nd International Conference on Particle-Based Methods: Fundamentals and Applications. Barcelona (Spain), October 26th-28th, 2011.

Alonso, E.E., Tapias, M. & Gili, J.A. (2011). *Simulating Particle Breakage and Relative Humidity Effects in Rockfill Behaviour*. Proceedings of the 2nd International Symposium on Computational Geomechanics: ComGeo II. Cavtat-Dubrovnik (Croatia), April 29th, 2011.

CONTENTS

LIST OF TABLES

Appendix 1

Appendix 2

Appendix 3

Appendix 4

LIST OF FIGURES

Chapter 2

Chapter 3

Chapter 4

Chapter 5

Chapter 6

Chapter 7

Appendix 1

Appendix 2

Appendix 3

Appendix 4

Appendix 5

Chapter 1

Introduction

The motivation for this research, the main objective, methodology and outline of the thesis are presented below.

1.1 Motivation for the research

This thesis has been developed within a particular line of research at the Division of Geotechnical Engineering and Geosciences, UPC Department of Civil and Environmental Engineering, which focuses on the behaviour of rockfill and coarse aggregates. The following doctoral theses have been developed in this research line:

- Oldecop (2000): A large oedometer equipment with controlled suction for testing samples of 0.30m in diameter and 0.20m in height was built. Slate gravels of a maximum size of about 0.04m were tested and a constitutive model for rockfill compressibility was proposed in a continuum media.
- Chávez (2003): A large triaxial equipment with controlled suction for testing samples of 0.25m in diameter and 0.50m in height was built. Slate fragments of the same material used by Oldecop (2000) were tested and a constitutive model for triaxial behaviour was proposed in a continuum media.
- Ortega (2008): Several laboratory tests using the large oedometer and triaxial equipment with controlled suction were performed on limestone fragments of a maximum size of 0.04m.
- Alvarado (In progress): This research is in progress and is related to the study of hydro-mechanical and chemical behaviour of coarse aggregates. The focus is on the effect of the activity of porous liquid on the mechanical behaviour.

Furthermore, some other master theses and final bachelor projects have also been produced in order to study features of the rockfill behaviour, e.g. (Cañavate, 2011; Hueso, 2003; Montobbio, 2001; Ramon, 2006).

The sizes of rock fragments in coarse aggregates are in general greater than coarse sands size. Rockfill includes sizes greater than 0.50m. Coarse aggregates and rockfill are commonly found in large civil engineering structures such as rockfill

dams and railway embankments, or in mining installations such as tailing heaps.

Considerable deformations have been observed in these civil structures and time-dependent behaviour has also been recorded. This time-dependent behaviour is controlled by stress and the Relative Humidity. On the other hand, breakage of rock fragments is the main cause of the deformation of the rockfill and coarse aggregates.

Deformability, strength and long-term behaviour of rockfill and coarse aggregates as well as the effect of water/Relative Humidity have been investigated by testing programs involving heavy equipment that allow working with large specimens. However, generally the size of the prototype rock fragments should be decreased in order to perform the tests: the grain size tested is much smaller than the prototype dimensions.

Research on rockfill behaviour has demonstrated that the grain size affects the stress-strain-time behaviour.

Some elastoplastic models have been developed (Bauer, 2009; Chávez and Alonso, 2003; Indraratna et al., 2011; Naylor et al., 1997, 1986; Oldecop and Alonso, 2001; Salim and Indraratna, 2004) to reproduce some features of the rockfill behaviour. However, a comprehensive “continuum” model has not yet been proposed and scale effects have not yet received a comprehensive modelling approach.

A modelling alternative is to study the rockfill and coarse aggregate behaviour using the Distinct Element Method, DEM (Cundall and Strack, 1979). DEM allows the simulation of the assembly of rock fragments as an arrangement of distinct particles which interact at their contacts. A DEM model could allow simulating real conditions of a granular mass. In fact, there have been some DEM models used to simulate the behaviour of granular soils in both 2D and 3D conditions, and the breakage of particles has been taken into account using different techniques:

(1) Considering the breakage of contact bonds between particles (Cheng et al., 2003; Deluzarche and Cambou, 2006; Kafui and Thornton, 2000; Lim and McDowell, 2005; Lu and McDowell, 2006; McDowell and Harireche, 2002; Robertson and Bolton, 2001; Robertson, 2000; Thornton and Liu, 2004). This technique requires some problems to be solved: ensuring the rigidity of the whole cluster that should behave as a rigid macroparticle, and, on the other hand, avoiding a rolling effect caused by the use of contact bonds, which allows the rolling of one ball relative to another even without breakage;
(2) Replacing broken particles by smaller particles (Astrom and Herrmann, 1998; Ben-Nun and Einav, 2010, 2008; Bruchmüller et al., 2011; Ciantia et al., 2015; Lobo-Guerrero and Vallejo, 2005; Marketos and Bolton, 2009; Marketos, 2007; McDowell and De Bono, 2013; Tsoungui et al., 1999). Models based on this technique generally do not obey the law of mass conservation;

(3) Removing particles from clusters (Couroyer et al., 2000), but there is also mass loss;
(4) Reducing stiffness at contacts (Marketos and Bolton, 2009); however, this procedure does not consider the evolution of the grain size distribution.

The previous DEM models do not consider the influence of the relative humidity or the time-dependent behaviour.

On the other hand, there are DEM models which take into account the action of water in saturated conditions calculating forces from the fluid phase and applying them to the solid particles at contacts but which do not consider particle breakage; for instance research on the consolidation process of saturated samples by Catalano et al. (2011). Unsaturated conditions using DEM models have been treated considering capillary forces from the suction acting on the contacts (Chareyre and Scholtès, 2011; Chareyre et al., 2009; Gili and Alonso, 2002); for instance Gili and Alonso (2002) presented a 2D model for unsaturated granular media that takes into account the interaction of particles, pores and water menisci.

However, the effect of capillary forces between contacts is not relevant in the rockfill behaviour.

This thesis presents a novel DEM model for rockfill and coarse aggregates in a 3D condition. The model takes into account particle breakage, the influence of the relative humidity, time-dependent behaviour and the particle size. The DEM model simulates the rock fragments as rigid macroparticles or clumps that can break. Macroparticles are composed of an assembly of spheres. A proposal to calibrate the parameters of the DEM model using experimental data from laboratory oedometer tests is made. Furthermore, some laboratory tests are proposed and performed to calculate some of these DEM parameters, e.g. friction coefficient (μ) using basic friction angle (ϕ_b) obtained from tilting table tests and direct shear tests, normal contact stiffness (k_n) using contact stiffness tests, and the solid angle (θ_0) using mean roughness measurement (R_a).

The DEM model is applied in simulations of oedometer and triaxial tests using experimental data from Ortega (2008) on limestone gravels.

Breakage mechanisms and time-dependent behaviour are studied through an experimental stage involving brittle sugar cubes in widely different geometrical arrangements.

1.2 Objective and methodology

1.2.1 General objective

The main objective of this research is to simulate the mechanical behaviour of

rockfill and gravels by developing a discrete model (DEM model). This model should take into account the effect of the relative humidity around the particles and the size effects of the particles, and reproduce the time-dependent behaviour of the granular mass.

1.2.2 Methodology

In order to achieve the main objective, the thesis has been organized following the tasks listed below:

- Developing a DEM model, for 3D conditions, using the PFC3D code of the ITASCA Group as a base code. The thesis required a very substantial effort of additional program coding.
- Defining the numerical shape of the particles (macroparticles) using assemblies of spheres (microparticles).
- Incorporating the breakage of particles in loading processes and defining a failure criterion of the particles. Analysis of breakage mechanisms in brittle particles which proved to be useful to comprehend the rupture of particles so these will be taken into account to divide the macroparticles in the DEM model.
- Applying the DEM model to the numerical simulation of oedometer and triaxial laboratory tests. The experimental data will be taken from the literature. Likewise, implementing a protocol to estimate the parameters of the DEM model.
- Using the DEM model as a virtual tool to simulate laboratory tests and study, for instance, the size effects of macroparticles.
- Incorporating the effect of the relative humidity (RH) in the DEM model.
- Studying the time-dependent behaviour in the numerical simulation of the oedometer test.

1.3 Thesis layout

Many of the aspects treated in this thesis are already published in journals and conference proceedings listed previously in the Publication list. However, the chapters of the thesis have been re-written as a self-contained manuscript, incorporating the main facts and results of the papers, along other new information.

Thus, this thesis is written in eight chapters and six appendices. A summary of the content of each chapter is as follows:

Chapter 1 introduces the thesis and presents the motivation for the research, the objective, methodology and outline of the thesis.

Chapter 2 presents a background of the relevant aspects of the mechanical behaviour of rockfill and coarse aggregates and a compendium of some constitutive models that have been developed.

Chapter 3 presents the basic aspects of the distinct element method (DEM). Furthermore, a compendium of DEM models that take into account particle breakage is described. The main characteristics of the PFC3D code, which is the software used in the thesis, is also presented.

Chapter 4 presents the results of an experimental investigation about the behaviour of a crushable and brittle granular material: sugar cubes. Compressibility and the evolution of the grain size at the end of the loading process in one-dimensional compression tests is studied for two different initial arrangements of particles with different void ratios. Two breakage mechanisms, comminution and splitting, are identified and related with the compressibility and the evolution of grain sizes during loading. Time-dependent behaviour is also studied.

Chapter 5 presents a DEM model for rockfill and crushable coarse aggregates that includes particle crushing. The discrete model presents a novel approach which combines a closed-form solution for stress distribution inside particles and a crack propagation criterion derived from fracture mechanics concepts. The DEM model considers the two breakage mechanisms studied in the previous chapter. The model simulates a rock fragment as a macroparticle or clump which consists of an assembly of spheres in a pyramidal shape. The main parameters of the model are the contact stiffness (k_n), friction coefficient (μ) and the particle toughness (K_c). A proposal to calibrate these parameters is made by a sensitivity analysis based on experimental data of oedometer tests taking into account compressibility and the evolution of grain size distribution. Furthermore, an additional proposal to obtain these parameters by experimental tests is made. The contact stiffness, friction, and the solid angle which is another parameter of the model are determined by experiments. A large diameter oedometer test on hard limestone gravel is simulated. Using the same parameters obtained for the oedometer test, a large scale triaxial test on the same material is also simulated.

Chapter 6 corresponds to the study of the size effects in rockfill behaviour under dry conditions and presents numerical simulations of oedometer tests in the range of 2.8-560 mm of initial particle size using the proposed DEM model. Compressibility and creep are partially validated by comparing calculations with test results covering a reduced range of particles. Furthermore, numerical simulations of large scale triaxial tests are performed varying the initial particle sizes. Results are compared with the experimental data obtained by Ortega (2008) on limestone gravels.

Chapter 7 includes the relative humidity and the time effect in the DEM model. Three models of subcritical crack propagation are proposed that take into account the relative humidity based on a compilation of experimental data of crack propagation tests performed by different authors. Numerical simulations of oedometer and triaxial tests which consider different relative humidity conditions are performed. Size effects are also studied through the performance of some numerical triaxial tests taking into account the relative humidity. Furthermore, time-

dependent behaviour is analyzed from a numerical oedometer test. The DEM results are compared with the experimental data from Ortega (2008).

Chapter 8 presents the conclusions of the thesis, a summary of the innovative contributions of this research, and recommendations for future work.

Appendix 1 presents a sensitivity analysis of the numerical simulations of oedometer tests that considers different probability distributions of initial crack lengths inside macroparticles.

Appendix 2 presents an analysis of micro-properties for triaxial behaviour on coarse aggregates using DEM.

Appendix 3 presents an analysis of micro-properties for oedometer behaviour on coarse aggregates using DEM

Appendix 4 presents a summary of the experimental data of the laboratory tests performed on sugar cubes: Simple compression tests; oedometer tests on ordered and disordered arrangements with granulometry tests using sieving technique; time effect in oedometer tests on disordered arrangements and granulometry tests using sieving technique.

Appendix 5 presents a summary of the experimental data of the laboratory tests performed on limestone fragments: Mineral and basic friction angle using the tilt table and direct shear tests; Mean roughness; and Contact stiffness tests.

Appendix 6 presents the proposed DEM code.

1.4 References

Alvarado, C., (In Progress). Chemical loading effects on rockfill behaviour. PhD Thesis. Universitat Politècnica de Catalunya, Barcelona, Spain.

Astrom, J.A., Herrmann, H.J., 1998. Fragmentation of grains in a two-dimensional packing. Eur. Phys. J. B 5, 551–554.

Bauer, E., 2009. Hypoplastic modelling of moisture-sensitive weathered rockfill materials. Acta Geotech. 4, 261–272. doi:10.1007/s11440-009-0099-y

Ben-Nun, O., Einav, I., 2010. The role of self-organization during confined comminution of granular materials. Philos. Trans. R. Soc. London A 231–247.

Ben-Nun, O., Einav, I., 2008. A refined DEM study of grain size reduction in uniaxial compression, in: Proocedings of the 12th International Conference of the International Association for Computer Methods and Advances in Geomechanics (IACMAG). Goa, India, pp. 702–708.

Bruchmüller, J., Van Wachem, B.G.M., Gu, S., Luo, K.H., 2011. Modelling discrete fragmentation of brittle particles. Powder Technol. 208, 731–739. doi:10.1016/j.powtec.2011.01.017

Cañavate, A., 2011. Influencia de la forma de las partículas en la compresibilidad de las escolleras. Master Thesis. Universitat Politècnica de Catalunya, Barcelona, Spain.

Catalano, E., Chareyre, B., Cortis, A., Barthelemy, E., 2011. A pore-scale hydro-mechanical coupled model for geomaterials, in: Oñate, E., Owen, D.R.J. (Eds.), II International Conference on Particle-Based Methods. Fundamentals and Applications. Barcelona (Spain), pp. 1–12.

Chareyre, B., Scholtès, L., 2011. Discrete Models of Wet Granular Media, in: Radjai, F., Dubois, F. (Eds.), Discrete-Element Modeling of Granular Materials. ISTE Ltd; John Wiley & Sons, Inc., London, UK, pp. 367–392.

Chareyre, B., Scholtès, L., Darve, F., 2009. Micro-statics and micro-kinematics of capillary phenomena in dense granular materials. Powders Grains 2009 (Golden, USA) 1145, 927–930. doi:10.1063/1.3180083

Chávez, C., 2003. Estudio del comportamiento triaxial de materiales granulares de tamaño medio con énfasis en la influencia de la succión. PhD. Thesis. Technical University of Catalonia. UPC, Barcelona, Spain (in Spanish).

Chávez, C., Alonso, E.E., 2003. A constitutive model for crushed granular aggregates which includes suction effects. Soils Found. 43, 215–227.

Cheng, Y.., Nakata, Y., Bolton, M.D., 2003. Discrete element simulation of crushable soil. Géotechnique 53, 633–641. doi:10.1680/geot.2003.53.7.633

Ciantia, M.O., Arroyo, M., Calvetti, F., Gens, A., 2015. An approach to enhance efficiency of DEM modelling of soils with crushable grains. Géotechnique 65, 91–110.

Couroyer, C., Ning, Z., Ghadiri, M., 2000. Distinct element analysis of bulk crushing: effect of particle propertiesand loading rate. Powder Technol. 109, 241–254. doi:10.1016/S0032-5910(99)00240-5

Cundall, P.A., Strack, O.D.L., 1979. A discrete numerical model for granular assemblies. Géotechnique 29, 47–65.

Deluzarche, R., Cambou, B., 2006. Discrete numerical modelling of rockfill dams. Int. J. Numer. Anal. Methods Geomech. 30, 1075–1096. doi:10.1002/nag

Gili, J.A., Alonso, E.E., 2002. Microstructural deformation mechanisms of unsaturated granular soils. Int. J. Numer. Anal. Methods Geomech. 26, 433–468. doi:10.1002/nag.206

Hueso, O., 2003. Compresibilidad de escolleras : Influencia de la humedad relativa. (Final work of undergraduated course). Universitat Politècnica de Catalunya, Escola Tècnica Superior d'Enginyers de Camins Canals i Ports; Universitat de Barcelona, Facultat de Geologia.

Indraratna, B., Salim, W., Rujikiatkamjorn, C., 2011. Advanced rail geotechnology – ballasted track. Balkema, CRC Press, Taylor & Francis Group, London, UK.

Kafui, K., Thornton, C., 2000. Numerical simulations of impact breakage of a spherical crystalline agglomerate. Powder Technol. 109, 113–132.

Lim, W.L., McDowell, G.R., 2005. Discrete element modelling of railway ballast. Granul. Matter 7, 19–29. doi:10.1007/s10035-004-0189-3

Lobo-Guerrero, S., Vallejo, L.E., 2005. Discrete Element Method Evaluation of Granular Crushing Under Direct Shear Test Conditions. J. Geotech. Geoenvironmental Eng. ASCE 131, 1295–1300.

Lu, M., McDowell, G.R., 2006. Discrete element modelling of ballast abrasion. Géotechnique 56, 651–655.

Marketos, G., 2007. An investigation of crushing and compaction bands in granular material. PhD. Thesis. Cambridge University, U.K.

Marketos, G., Bolton, M.D., 2009. Compaction bands simulated in discrete element methods. J. Struct. Geol. 31, 479–490.

McDowell, G.R., De Bono, J.P., 2013. On the micro mechanics of one-dimensional normal compression. Géotechnique 63, 895–908. doi:10.1680/geot.12.P.041

McDowell, G.R., Harireche, O., 2002. Discrete element modelling of soil particle fracture. Géotechnique 52, 131–135.

Montobbio, D., 2001. Efecto de la granulometría en la compresibilidad de escolleras. (Final work of undergraduated course). Universitat de Barcelona, Facultat de Geologia; Universitat Politècnica de Catalunya, Escola Tècnica Superior d'Enginyers de Camins, Canals i Ports de Barcelona.

Naylor, D.J., Maranha Das Neves, E., Mattar, D., Veiga Pinto, A.A., 1986. Prediction of construction performance of Beliche Dam. Géotechnique 36, 359–376.

Naylor, D.J., Maranha, J.R., Maranha das Neves, E., Veiga Pinto, A.A., 1997. A back-analysis of Beliche Dam. Géotechnique 47, 221–233.

Oldecop, L.A., 2000. Compresibilidad de escolleras. Influencia de la humedad. PhD. Thesis. Technical University of Catalonia. UPC, Barcelona, Spain (in Spanish).

Oldecop, L.A., Alonso, E.E., 2001. A model for rockfill compressibility. Géotechnique 51, 127–139.

Ortega, E., 2008. Comportamiento de materiales granulares gruesos - Efecto de la succión. PhD. Thesis. Technical University of Catalonia. UPC, Barcelona, Spain (in Spanish).

Ramon, A., 2006. Efecte de la granulometria en el comportament d'esculleres. (Final work of undergraduated course). Universitat Politècnica de Catalunya, Barcelona, Spain.

Robertson, D., 2000. Computer simulations of crushable aggregates. PhD. Thesis. Cambridge University.

Robertson, D., Bolton, M.D., 2001. DEM simulations of crushable grains and soils, in: Proceedings of the 4th International Conference on Micromechanics of Powders and Grains. Sendai, Japan, pp. 623–626.

Salim, W., Indraratna, B., 2004. A new elastoplastic constitutive model for coarse granular aggregates incorporating particle breakage. Can. Geotech. J. 41, 657–671. doi:10.1139/t04-025

Thornton, C., Liu, L., 2004. How do agglomerates break? Powder Technol. 143-144, 110–116.

Tsoungui, O., Vallet, D., Charmet, J.C., 1999. Numerical model of crushing of grains inside two-dimensional granular materials. Powder Technol. 105, 190–198. doi:10.1016/S0032-5910(99)00137-0

Chapter 2

Mechanical behaviour of rockfill and gravels: Background

This chapter presents the main features of the mechanical behaviour of rockfill and gravels and some constitutive models which can be found in the literature.

Rockfill behaviour is presented considering four relevant aspects: (1) particle breakage, which is the main deformation mechanism of the aggregates because after these ruptures a rearrangement of the particles occurs; (2) time-dependent behaviour; (3) influence of the environmental humidity conditions and (4) size or scale effects. Some other aspects are also presented.

Finally, a compendium of some constitutive models is presented. The first two constitutive models presented here are based on the experimental research done at the Universitat Politècnica de Catalunya (UPC) about compressibility and triaxial behaviour, respectively. All the models are based on the continuum media.

2.1 Introduction

Coarse granular aggregates may include rock fragments with sizes greater than coarse sands.

The following particle sizes are commonly used mainly by the Unified Soil Classification System (USCS), (Holtz and Kovacs, 1981), British Soil Classification System (BSCS), (Craig, 2004), and others:

- Coarse sands: 2-4.75mm (USCS); 0.6-2mm (BSCS)
- Fine gravels: 4.75-19mm (USCS); 2-6mm(BSCS)
- Coarse gravels: 19 – 75mm (USCS)
- Medium and coarse gravels: 6-60mm (BSCS);
- Cobbles: 75-300mm (USCS); 60-200mm (BSCS);
- Boulders: >300mm (USCS); > 200mm (BSCS);
- Ballasts: 10-60mm (Indraratna et al., 2011);
- Rockfill: 500-1500mm (Oldecop, 2000).

The larger coarse aggregates (ballast and rockfill) are usually from quarries and used in large civil engineering structures such as embankments and dams. They are laid loosely as well as in compacted layers. Rock fragments from quarries have

angular and rough forms.

Generally, rockfill has uniform size distributions (poorly-graded). **Figure 2-1** shows pictures of a mining operation in the FOJ quarry (Vallirana, Spain) on hard limestone. Different sizes of these coarse limestone aggregates and their angular shapes can be seen. Fragments of this hard limestone were tested in this research (basic and mineral friction angle tests; compression tests in order to obtain the contact stiffness and roughness surface tests) and its mechanical behaviour was simulated using the DEM model proposed in this research (chapter 5). Ortega's tests were also performed on these materials and are described below in the present chapter.

Figure 2-2 presents pictures of two rockfill dams: Lechago dam in Spain (**Figure 2-2** a-d) and Calanda dam in Spain (**Figure 2-2** e and f). **Figure 2-2**d shows a crack in the crest due to settlements.

In order to study the mechanical response of these aggregates, the compressibility and strength behaviour have been studied using rock fragments with smaller sizes to reduce costs because of the inconvenience of handling larger sizes and the availability of equipment.

Table 2-1 shows some of the performed oedometer and triaxial tests over the last five decades using rock fragments larger than 0.01m.

2.2 Deformation Mechanisms in rockfill

The deformation of the coarse granular aggregates, especially rockfill, is mainly caused by two mechanisms: rupture of particles and rearrangement of the granular mass (because particle breakage leads to the instability in the granular mass structure).

These mechanisms are influenced by the environmental humidity conditions and the particle sizes, among others. The deformation process also evolves in time.

2.2.1 Particle breakage

Granular aggregates subject to certain high stresses can exhibit significant breakage of their particles. Some breakages can even occur at low confining pressures. These ruptures can occur due to different factors: The magnitude of the load, cyclic loading, density of the aggregates, particle shape, confinement pressure, saturation degree, and grain size distribution (gsd), among others. The fracture toughness of the particles is a key factor that governs the breakage. A particle breaks when the supported load exceeds its strength.

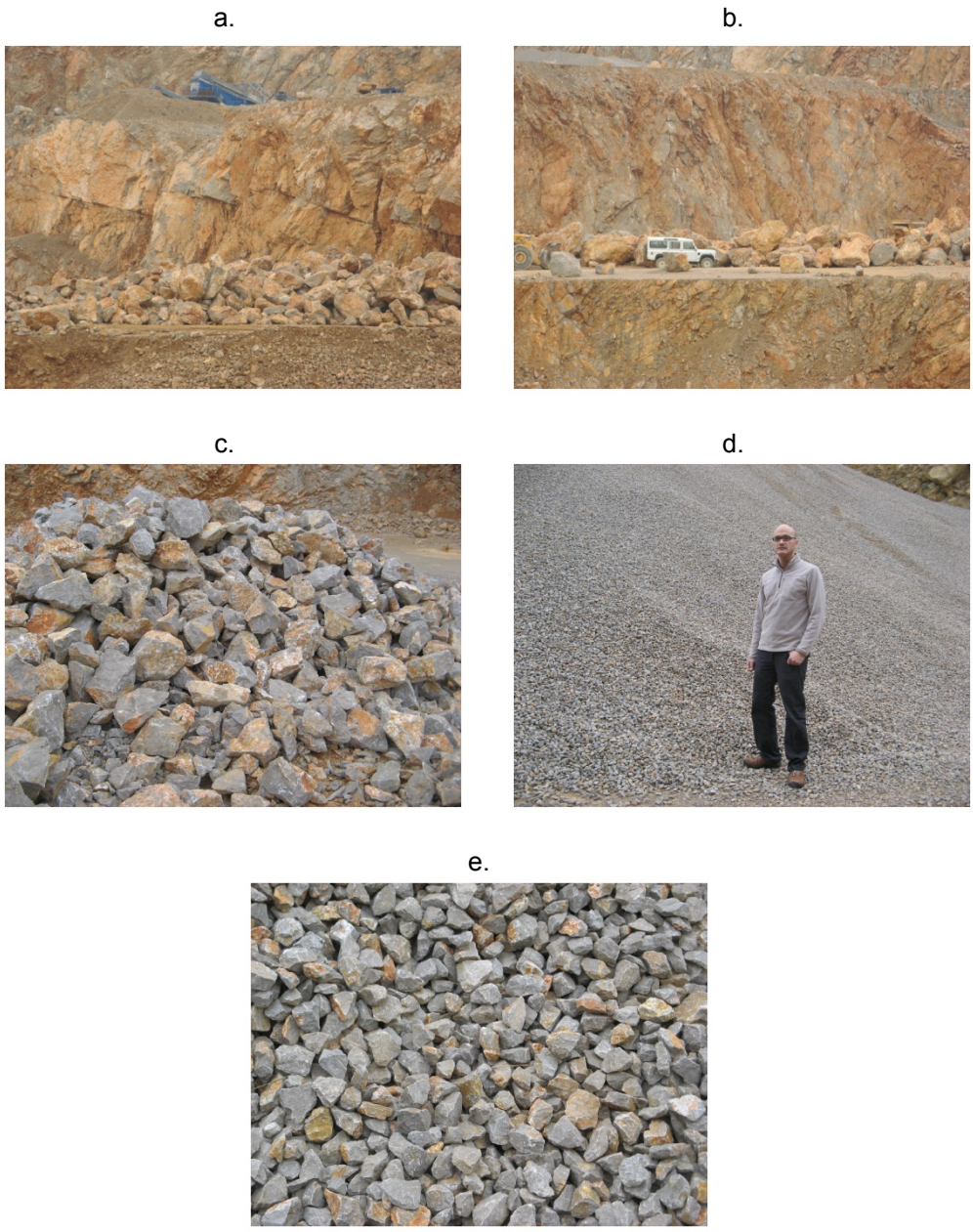

Figure 2-1 Hard limestone gravels and rockfill from quarry FOJ S.A., Vallirana (Barcelona, Spain): (a) Mining operation: Particle size > 1m; (b) Particle size > 1m; (c) Particle size: 0.1 – 0.5m; (d) Mean particle size: 0.03m; (e) Detail of rock fragments.

a.

b.

c.

d.

e.

f.

Figure 2-2 Rockfill dams: (a)-(d) Construction of Lechago Dam in 2008 (Spain): (a) Detail of rockfill in the shoulder upstream; (b) Detail of shoulder upstream and the crest of the dam; (c) Detail of rockfill; (d) Detail of slate rockfill. (e)-(f) Calanda dam in 1983 (Spain): (e) Detail of rockfill; (f) Detail of crack in the crest due to settlements (Photos are courtesy of the Professor E.E. Alonso).

Table 2-1 Triaxial and oedometer tests on gravels and rock fragments (Modified and updated from Oldecop, 2000).

Test	Reference	Sample Dimension		Maximum grain size (m)
		Diameter (m)	Height (m)	
Triaxial	UNAM – CFE (Mexico): Marsal (1973, 1967)	1.13	2.5	0.18
	ISMES (Italy): Fumagalli (1969)	0.35	0.70	-
	Univ. California – Berkeley (USA): Marachi et al. (1972, 1969)	0.07; 0.31; 0.91	0.15; 0.68; 2.29	0.152
	Monash U. (Australia): Parkin and Adikari (1981)	0.38; 0.57	-	-
	LNEC (Portugal): Naylor et al. (1997); Veiga Pinto, (1983)	0.30	0.76	0.10 – 0.05
	AIT (Bangkok): Indraratna et al. (1993)	0.30	0.60	0.0381
	Indraratna et al. (1998)	0.30	0.60	0.053
	Japan: Yasuda and Matsumoto (1994); Yasuda et al. (1997)	0.30	0.60	0.0635
	UPC (Spain): Chávez and Alonso (2003)	0.25	0.50	0.04
	UPC (Spain): Ortega (2008)	0.25	0.50	0.04
Oedometer	Norwegian Geotechnical Institute (Norway): Kjaernsli and Sande (1963)	0.50	0.25	0.064
	Georgia Inst. of Technoloy (USA): Sowers et al. (1965)	0.19	0.10	0.038
	UNAM – CFE (Mexico): Marsal (1973, 1967)	1.13	1.13	0.20
	ISMES (Italy): Fumagalli (1969)	0.10; 0.50; 1.30	0.20; 1.00; 2.00	0.26
	Build. Research Establishment (UK):Penman and Charles (1976)	0.60; 1.00	0.50	0.125
	Build. Research Establishment (UK): Clements (1981)	0.45	0.225	0.076
	Monash U. (Australia): Parkin and Adikari (1981)	0.635	0.61	0.09
	LNEC (Portugal): Naylor et al. (1986); Veiga Pinto (1983)	0.50	0.50	0.10
	Brasil: Caproni and Armelin (1998)	1.00	1.00	0.20
	UPC (Spain): Oldecop and Alonso (2001)	0.30	0.20	0.04
	UPC (Spain): Ortega (2008)	0.30	0.20	0.04

Inside the granular mass, the loads are transmitted through the contacts between particles: normal and shear contact loads. Generally, normal contact loads are compression loads which generate high shear and compression stresses close to the point where the load is applied, and tensile stresses inside the particle near the center (Russell and Muir Wood, 2009; Tsoungui et al., 1999). Each of these stresses may cause particle breakage. Details about the particle breakage mechanisms can be found in chapters 4 and 5.

There is experimental evidence of breakage of rock fragments due to an increasing load: this can be appreciated in the evolution of the gsd curves in unidirectional compression tests (e.g. see **Figure 2-3**a) (Nakata et al., 2001; Oldecop, 2000; Ortega, 2008) and triaxial tests (e.g. see **Figure 2-3**b) (Chávez and Alonso, 2003; Indraratna et al., 1998, 1993; Ortega, 2008). During the tests, the proportion of the largest particles decreases and finer material appears.

Figure 2-3a shows the gsd curves at the end of two oedometer tests on slate gravels of a maximum size of 40mm (Oldecop, 2000). Before the tests, the two specimens 9-I and 3-II were compacted at energy compaction of 597J/l and 593J/l, respectively. Initial Relative Humidity (RH) was about 50% for the two specimens. After the compaction, they were flooded and then subjected to a vertical load (**Figure 2-4**). Maximum vertical stresses were 1 MPa and 2.8 MPa for 9-I and 3-II specimens, respectively. The initial and post-compaction gsd curves are also presented. Particle breakage increases when the load is increased.

Figure 2-3b shows the gsd curve at the end of a triaxial test on limestone gravels of a maximum size of 40mm (Ortega, 2008) with RH=50% maintained during the test. The gsd curve at the beginning of the test is also shown. The evolution of the gsd curves evidences particle breakage during the test.

On the other hand, regarding triaxial tests and according to Indraratna et al. (1998), the peak friction angle decreases when the breakage increases. Similarly, Marsal (1967) found that the shear strength decreases with increasing particle breakage.

Particle breakage is a major cause of the deformation of the coarse aggregates, because after the breakage a subsequent rearrangement of the granular mass occurs. The particle breakage can be influenced by the humidity conditions and the particle size. Furthermore, it can be delayed in time. Details about these aspects can be found in chapters 6 -7.

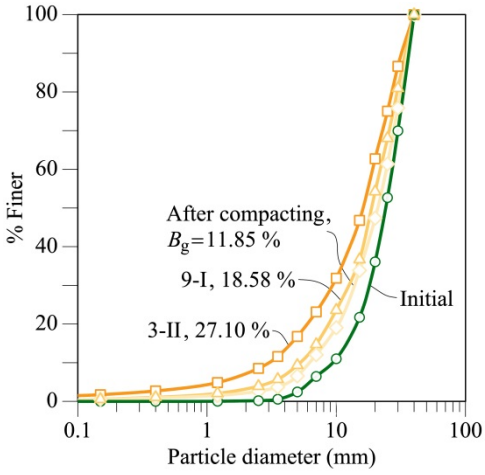

a. Oedometer tests on slate gravels (From Oldecop (2000)). Initial and after compaction gsd with RH=50%; specimens were flooded after compaction.

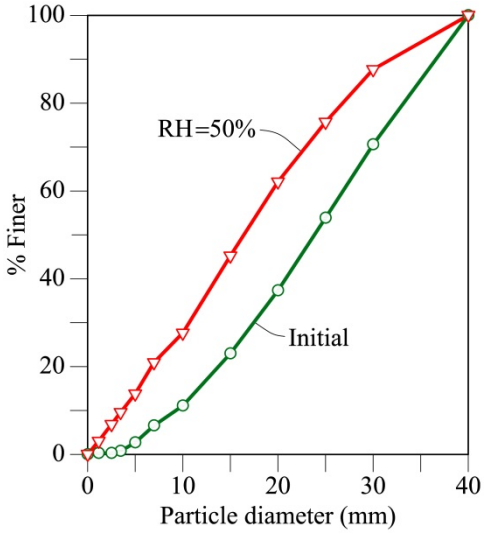

b. Triaxial tests on limestone gravels (From Ortega (2008)). Initial and final test with RH=50%.

Figure 2-3 Evolution of grain size distribution (gsd) curves during oedometer and triaxial tests.

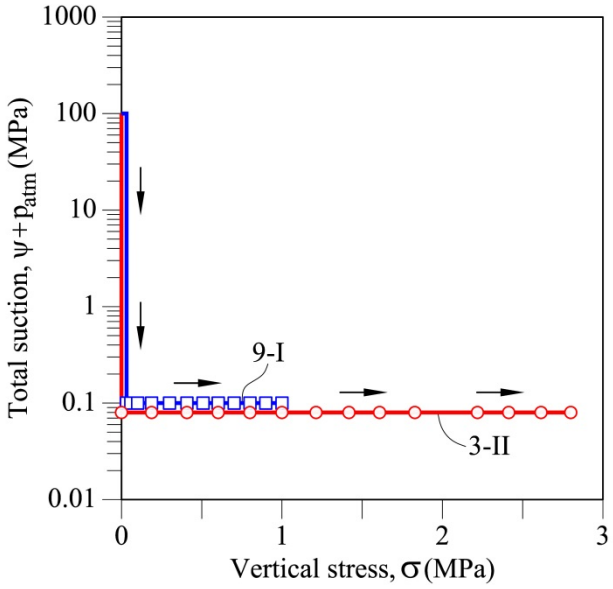

Figure 2-4 Stress path related to applied suction for oedometer tests of **Figure 2-3**a: Specimens 3-II and 9-I (From Oldecop (2000)). Open circles and squares indicate the saturation of the specimen.

2.3 Time-dependent behaviour

This phenomenon can be seen in the settlements delayed in time of rockfill dams (**Figure 2-5**). These dams present settlements with considerable magnitudes: deformations begin at the early stage of building and continue for many years after the end of the construction.

The creeping behaviour can be explained by the fact that the particle breakage may occur instantaneously after applying the loads or it may be delayed in time. As a result, deformations in the granular mass are also delayed in time. This time effect has been treated by Oldecop and Alonso (2007) and Takei et al. (2001), among others. Details about these aspects can be found in chapters 4 and 7.

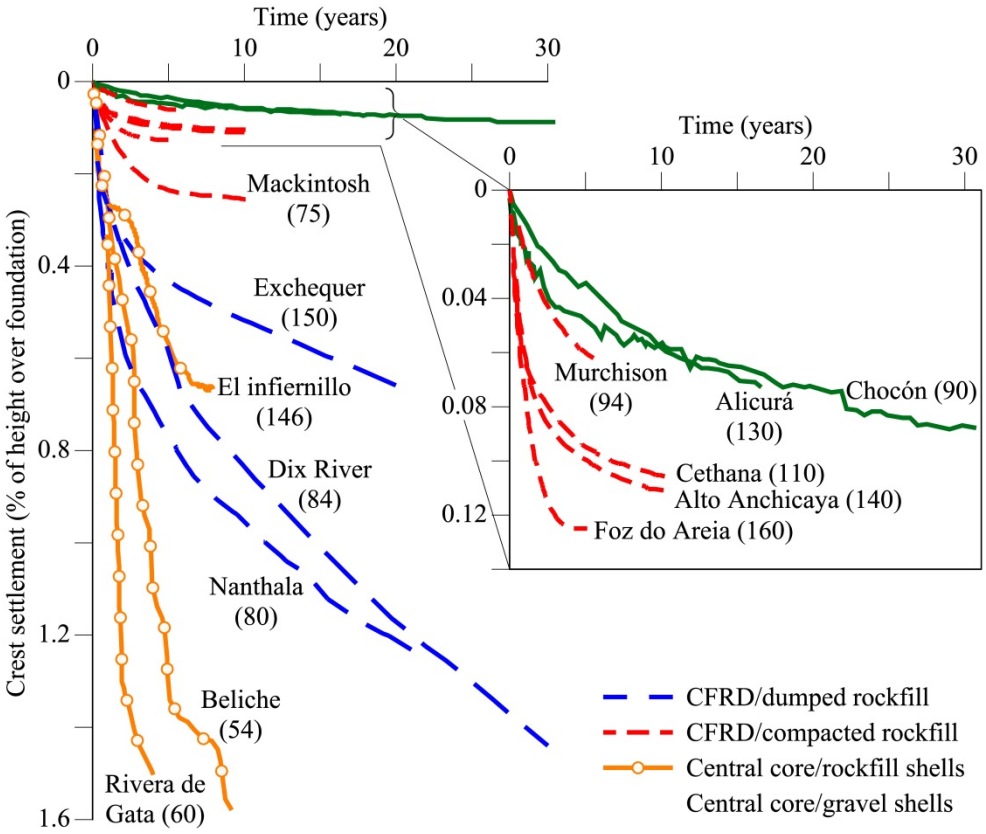

Figure 2-5 Settlements in time for several rockfill dams: CFRD, Concrete face rockfill dams – Dumped and Compacted rockfill; Central clay core dams with rockfill shells and Central clay core dams with gravel shells (From Oldecop and Alonso (2007).

2.4 Influence of environmental humidity conditions

Environmental humidity conditions are a key aspect to take into account in the analysis of the mechanical behaviour of rockfill. Details about the influence of the water inside the granular mass can be found in chapter 7. Some features of this aspect are presented below.

2.4.1 Collapse in deformations due to wetting in large civil structures

Rockfill structures such as embankments and dams can present deformation collapse when they are immersed in water, a phenomenon that occurs during the reservoir impoundment, and also when there is an increase in humidity caused by rainfall. **Figure 2-6** illustrates crest settlement records in three control points (A, B, and C) located in the crest of the Dix River Dam (USA). The collapse due to the flooding of the lower third of the dam during a flood can be observed. **Figure 2-7** shows the record of settlements in time for J40 control point located downstream from the Beliche Dam (Portugal): Records of the reservoir level and monthly rainfall from the same period are also shown. The collapses related to both the filling of the reservoir and rains are visible.

Another example of the influence of the environmental humidity conditions can be appreciated in **Figure 2-8**. This figure shows a settlement record in time for an embankment of the Madrid-Seville High Speed railway (AVE trains, Spain). The settlements have been related to the rainfall record. Collapse deformations occur after rains.

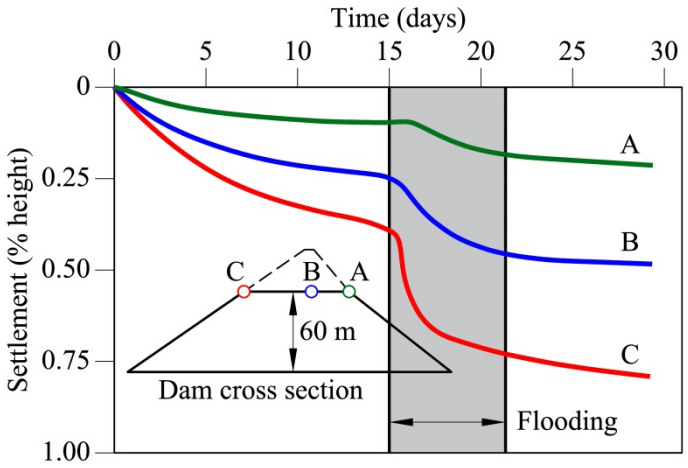

Figure 2-6 Settlement record for Dix River Dam (From Nobari and Duncan (1972) Nobari and Duncan (1972), cited by Oldecop (2000)). Collapse in settlements due to flooding.

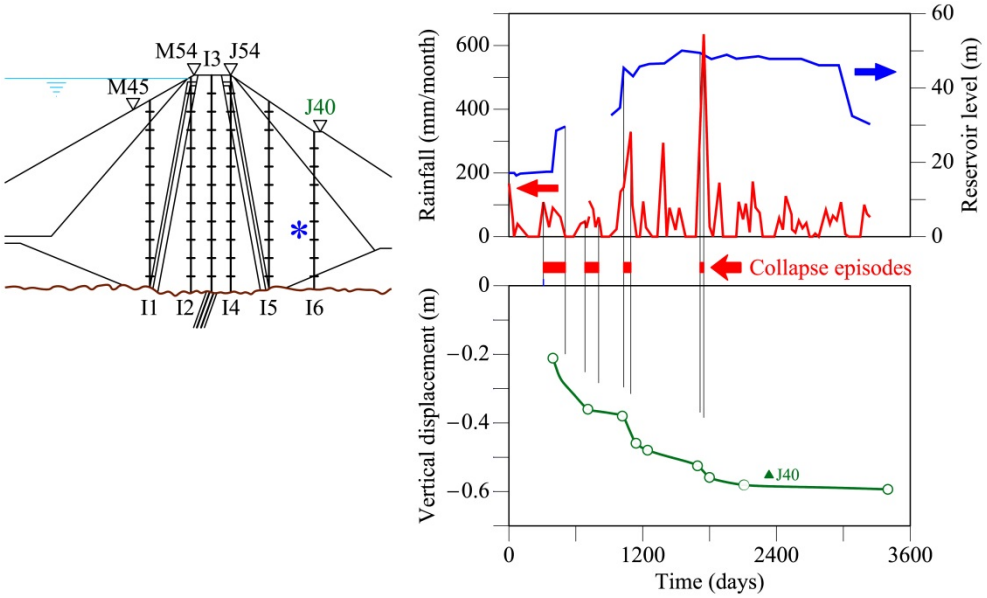

Figure 2-7 Settlements in time for Beliche Dam (Portugal) (Modified from Alonso et al. (2005)). Records of monthly rainfall and reservoir level.

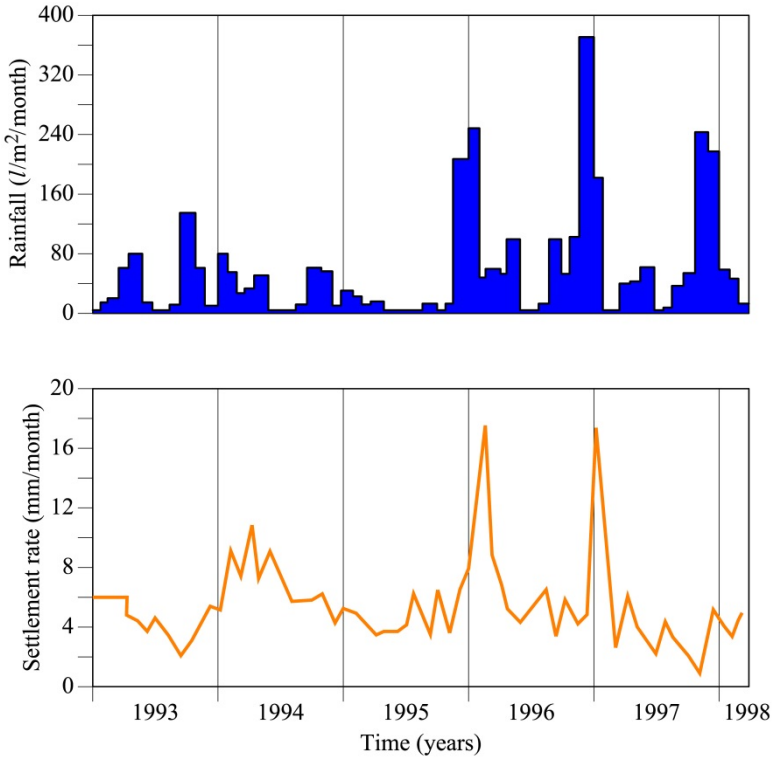

Figure 2-8 Settlements over time on the crest of 40m railway rockfill embankment composed of schist and shale fragments. Madrid-Seville High Speed Railway (AVE railway, Spain). (From Soriano and Sánchez (1999), cited by Oldecop (2000)).

2.4.2 Suction effect in experimental testing

The environmental humidity condition is a key aspect in the rockfill behaviour. It is related to the presence of liquid water and/or water vapour around the rock fragments. It can be measured by the Relative Humidity inside the granular mass. This relative humidity can be related to the suction by the psychrometric law.

In order to study the influence of the relative humidity (or the suction) on the triaxial and compressibility behaviour of rockfill, experimental investigations have been performed at the UPC using large triaxial and oedometer equipment with suction control: Regarding the triaxial behaviour, higher strength was obtained for lower relative humidity specimens (Chávez, 2003; Chávez and Alonso, 2003; Ortega, 2008). According to the oedometer tests, aggregates with higher relative humidity are more compressible, and, furthermore, the saturation of dried specimens generates collapses in the volumetric strain (Oldecop, 2000; Oldecop and Alonso, 2004, 2001; Ortega, 2008). Some phenomenological models have been proposed. They are explained below (sections 2.7.1 and 2.7.2) and include the influence of the suction/RH.

2.4.3 Phenomenological explanation

The influence of the environmental humidity conditions is a relevant aspect of the mechanical behaviour of the coarse aggregates (Chávez and Alonso, 2003; Clements, 1981; Nobari and Duncan, 1972; Oldecop and Alonso, 2001; Ortega, 2008). Liquid water and water vapour present in the voids between grains facilitate the rupture of particles.

The rupture of particles is associated with crack propagation inside particles. These ruptures can occur instantaneously in a catastrophic way when the stress state exceeds the strength of the particle. The stress state and the strength are associated with the stress intensity factor (K) and the fracture toughness (K_c), respectively. Rupture models based on fracture mechanics can explain this phenomenon.

However, crack propagation can occur for $K \leq K_c$. This condition is called subcritical crack propagation.

The subcritical crack propagation for ceramic and glass materials has been studied by several researchers (Atkinson, 1979; Evans, 1972; Wiederhorn, 1978, 1974; Wiederhorn and Boltz, 1970). Subcritical crack growth depends on the stress intensity factor and the amount of water in the environment; the water can be present in liquid or vapour state.

Subcritical crack propagation is caused by different mechanisms, some of which depend on certain environmental chemical conditions. These mechanisms include stress corrosion (Atkinson, 1984, 1979, Charles, 1958a, 1958b; Wiederhorn and Boltz, 1970), dissolution, diffusion, ion exchange, and microplasticity. All of them are influenced by the chemical effects of pore water (Atkinson, 1984; Wiederhorn et al., 1982). The stress corrosion is the main mechanism of the subcritical

propagation because strong molecular bonds caused by the presence of water and the action of hydrolysis processes can lead to weak bonds in hydroxyl groups (Atkinson, 1984).

The chemical reactions occur mainly at the tip of the crack where the stresses are high. This corrosion reaction involves the chemical potential of the reactive species of rock (e.g. Si-O bonds), chemical potential of water, and temperature, among others.

This chemical reaction between the corrosive agent and the material of the tip causes a change in the chemical composition of the tip material. This is known as the activated complex: the atomic bonds are weaker than the intact material and so the fracture toughness is reduced locally at the tip of the crack. For this reason, the crack is propagated for $K \leq K_c$.

Freiman (1984) proposed the following expression for H_2O reacting with a Si-O bond on the stress corrosion for silica glasses and polycrystalline ceramics:

$$\left[Si-O-Si\right]+H_2O \rightleftharpoons \chi \rightarrow 2\left[SiOH\right] \qquad (2:1)$$

where χ is the activated complex. Michalske and Freiman (1982), (cited in Freiman, 1984; Oldecop, 2000), have described a chemical mechanism by strained Si-O bonds in vitreous silica reaction with H_2O molecule of gas or liquid. This model can be appreciated in **Figure 2-9** and occurs in three steps: (1) One of the hydrogen atoms of the H_2O molecule is bonded to the oxygen of the Silica molecule - this reaction is favoured by the high deformation of the Si-O bond; (2) two new bonds are formed: Si-O_{water} and H-O_{silica}; (3) the weak bond between the O_{water} and H is broken by the mechanical action of the stress state.

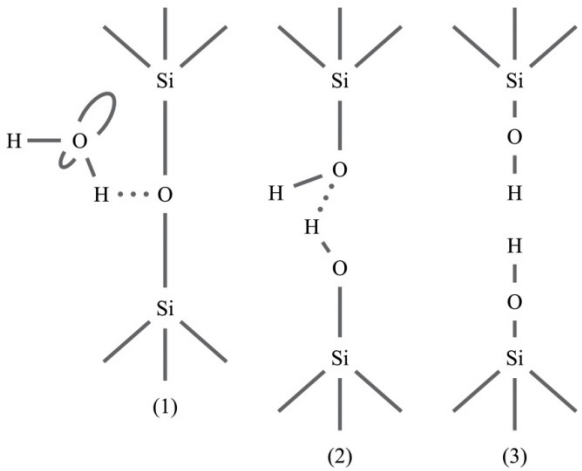

Figure 2-9 Model for the stress-induced chemical reaction of H_2O with amorphous silica: (1) One of the hydrogen atoms of the H_2O molecule is bonded to the oxygen of the Silica molecule. This reaction is favoured by the high deformation of the Si-O bond; (2) Two new bonds are formed: Si-O_{water} and H-O_{silica}; (3) The weak bond between the O_{water} and H is broken by the mechanical action of the stress state (From Freiman (1984), after Michalske and Freiman (1982); Oldecop (2000)).

On the other hand, it can be expected that the velocity of crack propagation is controlled by the velocity of the propagation of the corrosion reaction under a given stress. The corrosive agent would be water vapour (Wiederhorn et al., 1982). Thus, the action of the corrosive agent can be related to the action of the relative humidity RH in the environment.

The relative humidity of the air is defined as "*the ratio of the partial pressure of the water vapor present at a given temperature and barometric pressure, to the partial pressure of the water present at saturation for the given temperature and pressure*" (Parish and Putnam, 1977). The partial pressure of the water present at saturation or saturation vapor pressure can be found on the free water surface.

The involvement of RH in the crack propagation has been treated by (Atkinson, 1984, 1979; Atkinson and Meredith, 1987; Freiman, 1984; Oldecop, 2000; Wiederhorn et al., 1982) based on the approaches of (Charles, 1958a, 1958b; Charles and Hilling, 1962; Wiederhorn and Boltz, 1970).

Some expressions that have been used to describe the subcritical crack propagation are listed below:

(a) Charles's law (Charles, 1958a, 1958b):

The following expression was obtained (Charles, 1958b) for the penetration velocity of the crack tip in the x direction (v_x) based on **Figure 2-10**:

$$\mathrm{v}_x = C\left(\frac{x}{x_{cr}}\right)^{n/2} \exp\left[\frac{-H}{RT}\right] \tag{2:2}$$

where C is a constant (reference velocity); x is the crack depth; x_{cr} is the crack depth for spontaneous rupture; n is the stress corrosion or subcritical crack growth index (constant); H=Activation Enthalpy; R=Gas constant; T=Absolute temperature;

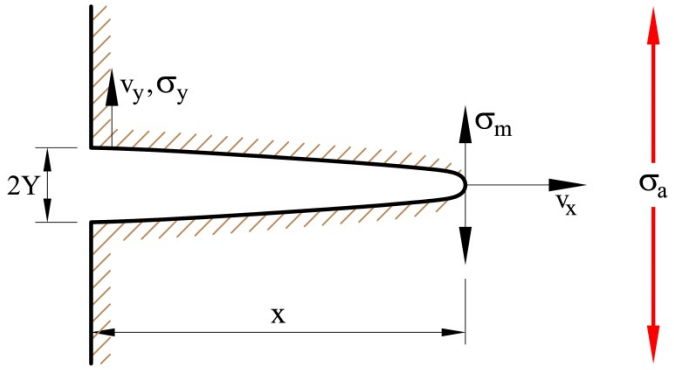

Figure 2-10 Scheme for a surface crack propagation on glass (From (Charles, 1958a)). v_x, v_y: growth velocities in x and y directions; σ_a, σ_m, σ_y : applied, tip and surface stresses near the crack.

The last equation can be expressed as:

$$v_x = C\left(\frac{\sigma_m}{\sigma_{cr}}\right)^n \exp\left[\frac{-H}{RT}\right] \tag{2:3}$$

where σ_m and σ_{cr} are the tip stress and the rupture strength.

(b) Expression of Wiederhorn and Boltz (1970):

$$v = v_0 \exp\left[\frac{\left[-H + (2V^* K_I)/(\pi r_c)^{1/2}\right]}{RT}\right] \tag{2:4}$$

where v=crack velocity; v_0=reference velocity (constant); H=Activation Enthalpy; K_I= Stress intensity factor (Mode I); R=Gas constant; T=Absolute temperature; V^*=Activation volume; r_c=radius of curvature of the crack tip.

This expression can be simplified as follows (Atkinson, 1984):

$$v = v_0 \exp\left[\frac{\left[-H + bK_I\right]}{RT}\right] \tag{2:5}$$

where b=experimentally determined constant. These equations are the same when $V^*=(b/2)(\pi r_c)^{1/2}$.

(c) Expression obtained by Freiman (1984):

$$v = v_0 \left[a(H_2O)\right] \exp\left[\frac{\left(-E + bK\right)}{RT}\right] \tag{2:6}$$

where v=crack velocity; v_0=reference velocity; $a(H_2O)$=Activity of the water; E=Activation Energy (non-stress dependent term); b=Material constant; K= Stress intensity factor; R=Gas constant; T=Temperature.

$a(H_2O)$ is related to the Relative Humidity. For higher humidity, higher velocities of propagation are obtained.

(d) Expression of Oldecop and Alonso (2007): Normalized version of Charles's law (Charles, 1958b) with regard to fracture toughness K_c.

$$v = v_0 * \left(\frac{K}{K_c} \right)^n \quad (2:7)$$

where v_0 = Reference velocity (constant); K= Stress intensity factor (Mode I); K_c= Fracture toughness; n=Stress corrosion or Subcritical crack growth index.

In summary, the water action is associated with stress corrosion phenomenon: the water action brings on the crack propagation in the particles. The effect of water vapour and liquid water has been related with the Relative Humidity, and this may also be correlated with the suction.

2.5 Influence of the grain size

Factors such as larger particle sizes, angular shapes of the particles and uniform aggregates can increase the particle breakage (Lee and Farhoomand, 1967). Larger particles can contain more inner defects so they may be more likely to disintegrate (Lade et al., 1996). In order to show some particle size effects on the particle breakage and aggregate behaviour, some results of experimental tests on aggregates and singular rock fragments varying the particle sizes are described below.

2.5.1 Coarse aggregates behaviour based on experimental tests

The rockfill particle size (0.4-1.5m) is a limitation for experimental research in laboratory. Usually, smaller particles sizes (<0.05m) are tested in order to study the mechanical behaviour of larger particles. In the literature, there are a few examples that have used large-scale triaxial and oedometer equipment: For instance, **Table 2-1** shows that some researchers (Marachi et al., 1972, 1969, Marsal, 1973, 1967, Naylor et al., 1997, 1986; Veiga Pinto, 1983) tested particle sizes 0.10-0.20m.

Some conclusions can be found in the literature about the size effect based on experimental tests. According to Indraratna et al. (2011), there is controversy in some studies: For Kolbuszewski and Frederick (1963), the angle of shear strength increases with larger particle sizes because the dilatancy component also increases -Islam et al. (2011) also present experimental results of direct shear tests on sands where the maximum shear strength and the angle of internal friction increase when particle sizes increase-, while for Marachi et al. (1972), the internal friction angle decreases with increasing particle size. From large-scale triaxial tests, Indraratna et al. (1998) conclude that the peak friction angle decreases slightly with larger sizes at a low confining pressure (<300 kPa), while this size effect is negligible at high confining stresses (>400kPa).

Moreover, there is also the size effect on the tensile strength of a particle, which decreases as the size increases (Lee, 1992; McDowell and Bolton, 1998). Details of the particle size effect are found in the next section.

On the other hand, the particle size also influences the compressibility of the

aggregates: higher plastic strain occurs for larger particle sizes (Ortega, 2008).

Finally, some constitutive models of compressibility and resistance for rockfill behaviour have been applied in dam engineering (Alonso et al., 2005; Frossard et al., 2012) with the size effect taken into account. Frossard et al. (2012) propose some rules to scale up some properties such as strength.

Details about the grain size effect on the rockfill behaviour can be found in chapter 6.

2.5.2 Particle size effect based on tests on singular rock fragments

Some researchers (Lee, 1992; Marsal, 1973; Marsal and Resendiz, 1975) have studied the effect of the particle size through one-directional compression tests of singular rock fragments (and other materials), placing the material between two steel plates and applying loads until the failure of particles was reached (**Figure 2-11**a and b). Marsal (1973) did several tests for different rocks: Pinzandarán gravel, Las Piedras tuff, La Angostura limestone, Mica granitic gneiss, El Infiernillo diorite, San Francisco basalt, Chivor phyllite, and La Angostura gravel. He defined the "*rupture load (P_a)*" as the load that causes the diametrical rupture of the particle and related it to the average size in the failure plane (d_m) as follows (Oldecop, 2000):

$$P_a = \eta \, d_m^{\lambda} \tag{2:8}$$

where P_a is given in kg, d_m is given in cm, η and λ are constants. λ values are between 1.2 and 1.8. η values depend on the rock.

In a similar way, Lee (1992) performed compression tests on individual rock fragments of Leighton Buzzard sand, oolitic limestone and carboniferous limestone (cited by McDowell and Bolton, 1998) and calculated the tensile strength of grains (σ_f) as:

$$\sigma_f = \frac{F_f}{d^2} \tag{2:9}$$

where d is the diameter of the grain and F_f is the maximum load that causes the catastrophic failure when the grain splits. After this failure the load drops dramatically. This expression is in accordance with Jaeger (1967) and Shipway and Hutchings (1993) and it is consistent with the definition of tensile strength of concrete in the Brazilian test.

Therefore, the tensile strength (σ_f) and the particle size (d) are related as follows (McDowell and Bolton, 1998):

$$\sigma_f \propto d^b \tag{2:10}$$

where σ_f is given in MPa and d is given in mm. Typical values of b are given by -

0.357, -0.343 and -0.420 for Leighton Buzzard sand, oolitic limestone and carboniferous limestone, respectively.

Figure 2-12 shows the results of Lee (1992), Marsal (1973) and others (Oldecop and Alonso, 2013). The curves follow a similar tendency. Tensile strength decreases when particle size increases.

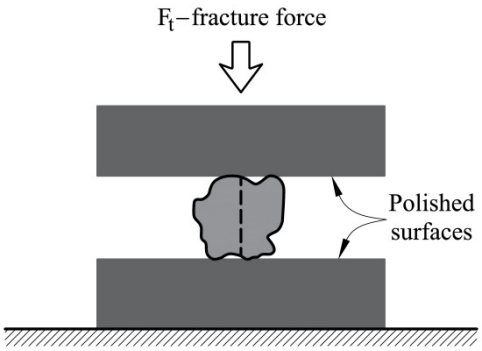

a. Scheme of the tests followed by Lee (1992). (From McDowell and Bolton (1998)).

b. Brazilian test on limestone particle (From Ortega (2008)).

Figure 2-11 Particle tensile strength on rock fragment.

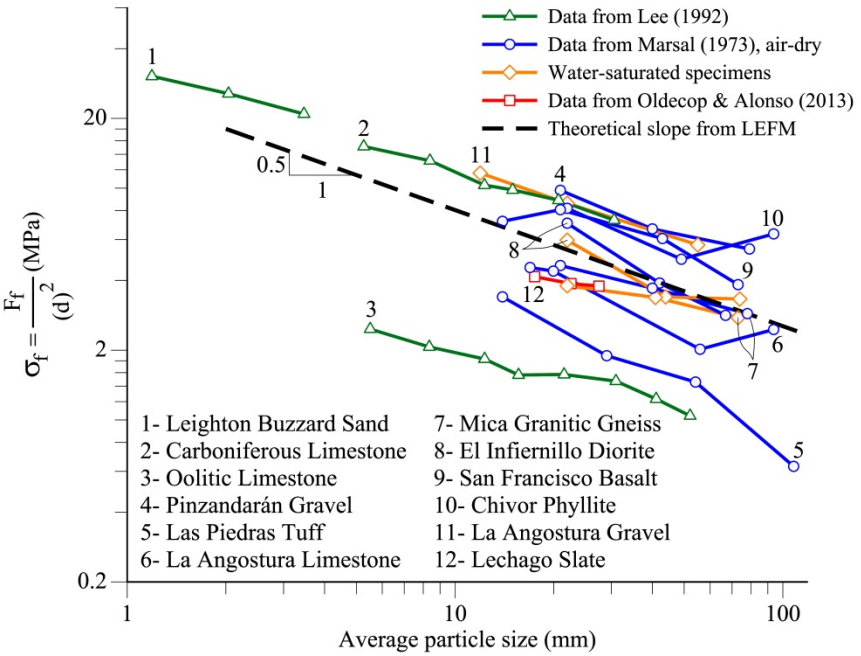

Figure 2-12 Compilation of results of Tensile strength tests on different rocks obtained by different authors: Tensile strength vs. particle size. (From Oldecop and Alonso (2013)).

2.5.3 Statistical approach

Weibull statistics of fracture can explain the tensile strength and its relation with particle size found by Lee (1992) and Marsal (1973). McDowell and Bolton (1998) present this explanation based on the data results of Lee (1992).

Weibull (1951, 1939) studied the tensile strength behaviour of brittle ceramics and proposed a statistical approach to determine the survival probability $P_{survival}(V,\sigma)$ of a block of V volume under an applied tensile stress σ as follows:

$$P_{survival}(V,\sigma) = \exp\left[-\left(\frac{V}{V_0}\right)\left(\frac{\sigma}{\sigma_0}\right)^m\right] \quad (2:11)$$

where V_0 is a reference volume of a material such as:

$$P_{survival}(V_0,\sigma) = \exp\left[-\left(\frac{\sigma}{\sigma_0}\right)^m\right] \quad (2:12)$$

σ_0 is the value of tensile stress σ so that 36.7879% of the total number of tested blocks survives (see **Figure 2-13**), and m is the Weibull modulus: $m\approx10$ for ceramic materials; $m\approx5$ for chalk, stone, pottery and cement; $5<m<10$ for soils.

For a block material of volume V_1 under tensile stress σ_1 and $P_{survival}(V_1, \sigma_1)$=0.367879, the tensile strength can be calculated as:

$$\sigma_1 = \sigma_0\left(\frac{V_0}{V_1}\right)^{1/m} \quad (2:13)$$

McDowell and Bolton (1998) applied the Weibull statistics to data results of the particle tensile strength tests done by Lee (1992). For particles with similar geometry, the Eq.(2:11) can be applied to determine the survival probability of a particle size d under diametrical compression as follows:

$$P_{survival}(d,\sigma) = \exp\left[-\left(\frac{d}{d_0}\right)^{n_d}\left(\frac{\sigma}{\sigma_0}\right)^m\right] \quad (2:14)$$

where σ is the tensile stress induced in the particle calculated as F/d^2, (F is the diametrical compression load over a particle size d) and σ_0 is the value of F/d^2 at which 36.7879% of the particles survive, approximately equal to the mean tensile strength of particles of size d_0. n_d is equal to 1, 2 or 3 for uni-, two- or three-dimensional similarity (Bazant, 1999).

According to Eq.(2:13) and (2:14), the mean tensile strength can be calculated as:

$$\sigma_1 = \sigma_0 \left(\frac{d_0}{d_1} \right)^{n_d/m} \tag{2:15}$$

If the mean tensile strength is named as σ_f for a particle of size d, σ_f can be scaled with the particle size as follows:

$$\sigma_f = C d^{-n_d/m} \tag{2:16}$$

where:

$$C = \sigma_0 \left(d_0 \right)^{n_d/m} \tag{2:17}$$

Eq.(2:16) is similar to Eq.(2:10).

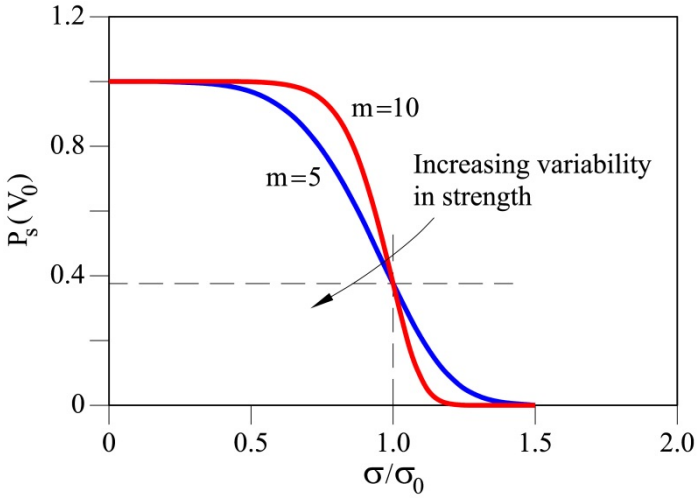

Figure 2-13 Weibull distribution of tensile strengths. (From McDowell and Bolton (1998)).

2.5.4 Fracture mechanics model

The *linear elastic fracture mechanics* (LEFM), whose model will be detailed later in chapter 5, can also explain the size effect on the tensile strength of materials.

For a particle with a crack of length $2a$ inside which is subjected to tensile stresses σ as shown in **Figure 2-14** (Mode I), the stress intensity factor (K) is defined as:

$$K = \beta \sigma \sqrt{(\pi a)} \tag{2:18}$$

where β is a dimensionless coefficient, explained in chapter 5, and a is the half-length of the crack.

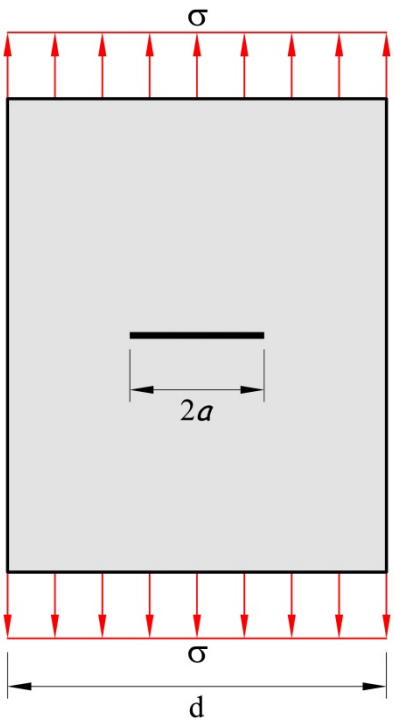

Figure 2-14 Middle Tension Panel: Crack of 2*a* length inside a plate subjected to a uniform tensile stress. (Modified from Saouma (2007)).

One of the principles of fracture mechanics is that unstable fracture occurs when *K* reaches a critical value K_c. This value is known as the fracture toughness. K_c represents the inherent ability of a material to withstand a given stress field intensity at the crack tip and to resist progressive tensile crack extension (Saouma, 2007).

If the tensile strength σ_f is associated with the tensile stress σ when K_c is reached, then Eq.(2:18) can be modified as

$$\sigma_f = \frac{K_c}{\beta\sqrt{(\pi a)}} \tag{2:19}$$

Half-length *a* is related to the particle size *d* because it is inside the particle. Moreover, if S_1 is a proportion of *d,* then half-length can be expressed as

$$a = S_1 d \tag{2:20}$$

Therefore, tensile strength σ_f can be calculated as follows:

$$\sigma_f = C_{FM}\, d^{-1/2} \tag{2:21}$$

where:

$$C_{FM} = \frac{K_c}{\beta\sqrt{(\pi\, S_1)}} \tag{2:22}$$

Eq. (2:10), (2:16) and (2:21) are similar. For LEFM, the slope which relate σ_f to the particle size is -0.5. It is also drawn in **Figure 2-12** . LEFM model provides a good fit.

On the other hand, (Bazant, 1984) related the size effect on the nominal stress at the failure to some strength criteria (**Figure 2-15**): this figure shows some results of the size effect on concrete structures (structures of different sizes but geometrically similar shapes, for instance beams of the same span-to-depth ratio and the same crack length-to-depth ratio) subjected to various elementary situations, such as beam bending, shear and torsion. This behaviour can be extended to rock fragments because of the similarities of the fracture mechanism. The LEFM fits well for large sizes.

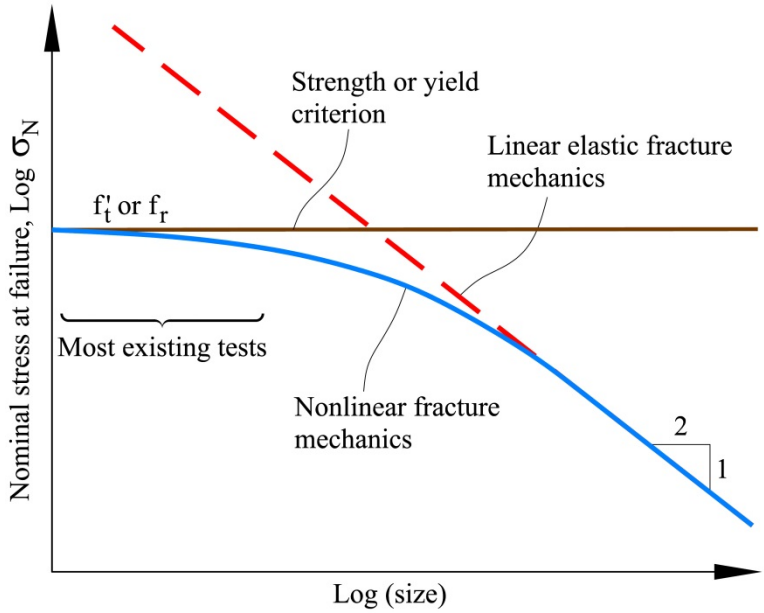

Figure 2-15 Size effect according to strength criteria and linear or nonlinear Fracture Mechanics (From Bazant (1984)): f_t' is direct tensile strength (concrete); fr is the failure state according to any kind of yield criterion.

2.6 Other aspects

Although the previous aspects are considered fundamental in the rockfill behavior, there are other aspects to be taken into account in order to have a comprehensive knowledge of their mechanical behaviour. Some of these are described below.

Particle shape: Interlocking between the rock fragments is affected by their shape

and therefore the shear strength of the granular mass is also influenced: The friction angle is higher for angular shapes than for subrounded rock fragments (Holtz and Gibbs, 1956; Indraratna et al., 2011; Vallerga et al., 1957). Likewise, dilatancy is required in order to move angular shape fragments and causes shear strength to increase (Chrismer, 1985).

Surface roughness: The surface roughness is one of the key factors that govern the internal friction angle and therefore the resistance of the aggregates. Friction and frictional forces depend on the roughness of the loaded surface. The resistance to plastic strain accumulation increases with increasing apparent surface roughness (Indraratna et al., 2011; Thom and Brown, 1989). However, this surface roughness deteriorates with time under cyclic loading.

The roughness effect is analyzed in chapter 5 and taken into account in the DEM model presented in this research.

Strength effect of the parent rock: Rock fragments with low strength break more easily and cause higher plastic strain.

Initial porosity effect of the granular mass: Density and strength increase with lower porosities. On the other hand, plastic strain of the granular mass decreases with lower porosities.

Particle size distribution: According to results of several triaxial tests by Thom and Brown (1988) on crushed dolomite with similar maximum particle size of about 10mm but varying the grain size distribution (gsd) from uniform to well-graded and for different compaction effort, the density and friction angle decrease with the uniform gsd (the higher internal friction angle was obtained for well-graded aggregates). However, the authors also note that the gsd did not significantly influence the internal friction angle for uncompacted specimens (Indraratna et al., 2011).

Effect of the confining pressure: the peak friction angle decreases with the increasing confining pressure (Charles and Watts, 1980; Indraratna et al., 1998, 1993; Marsal, 1967; Vesic and Clough, 1968). At a low confining stress, high values of apparent friction angle occur due to the dilatancy component. At a high confining stress, particle rupture and simple slips occur more significantly (Vesic and Clough, 1968).

2.7 Constitutive models for rockfill behaviour

During the last 20 years, several investigations about the mechanical behaviour of rockfill have been performed by the UPC in Barcelona, Spain. These studies have been carried out based on scaled material testing: rock fragments of 1-4cm in size. A summary of the experimental results and the constitutive model are presented below: (Oldecop, 2000; Oldecop and Alonso, 2007, 2004, 2003, 2001; Ortega, 2008) have researched the compressibility behaviour; and (Chávez, 2003; Chávez and Alonso, 2003; Ortega, 2008) have studied the triaxial behaviour. Furthermore, other constitutive models are also presented.

2.7.1 Compressibility of rockfill: Experimental results and constitutive model - UPC research

2.7.1.1 Experimental oedometer tests

UPC research: Oldecop and Alonso (2001; 2003)

In order to study rockfill compressibility under the influence of humidity, Oldecop and Alonso (2004, 2003, 2001) reported the results of several one-dimensional compression tests using a Rowe oedometer with standard procedures and relative humidity control (or suction-controlled) (**Figure 2-16**a). These tests were performed on crushed slate gravels from a quarry near Pancrudo river (Teruel, Spain) between sizes 0.4 and 40 mm (see initial gsd curve in **Figure 2-3**a). Gravels were compacted into four layers using a standard Proctor compaction energy of 600 J/l.

To control the humidity of the specimen, a mixed technique was used: the suction was controlled by saline solution and measurements of the relative humidity using a hygrometer (**Figure 2-16**b). The suction was controlled by using salt solutions to create a relative humidity gradient between the specimen and the solution container. The process was divided into wetting/drying stages using the saline solutions and a stabilization stage. In this stabilization stage, the saline solution container is removed and the hygrometer measurements are recorded until they reach a stable value of the relative humidity (RH).

The flow of water vapour between the saline solution container and the rockfill voids (space between particles) is advective and the flow between these voids and the porous rock particles occurs by molecular diffusion (see **Figure 2-16**b).

Figure 2-17 illustrates the compressibility curves of five performed oedometer tests. All specimens were loaded up to a maximum vertical stress of 2.8 MPa for different relative humidity (RH) conditions. **Figure 2-17**a shows the vertical stress (horizontal axis) in a natural scale while **Figure 2-17**b is in logarithmic scale.

Saturation of the rock particle pores when RH=100% produces the same collapse strain as the collapse strain due to the flooding of the specimen under the same vertical stress. These results are compatible with collapse deformations due to rainfall at rockfill dams and embankments (**Figure 2-7** and **Figure 2-8**).

From a macroscopic and phenomenological point of view, rockfill behaviour presents similar aspects to unsaturated soils. The compressibility curves are defined for constant suction values. The slope of these curves (compressibility of the material) changes with the total suction. When the suction decreases, the compressibility of the material increases.

The compressibility curves coincide for suction values (ψ) close to 0 (saturation of the rock particle pores) for different stress-suction paths. On the other hand, rockfill behaviour does not depend on the water effect for $\sigma<\sigma_y$. σ_y is the clastic yield stress.

a.

b.

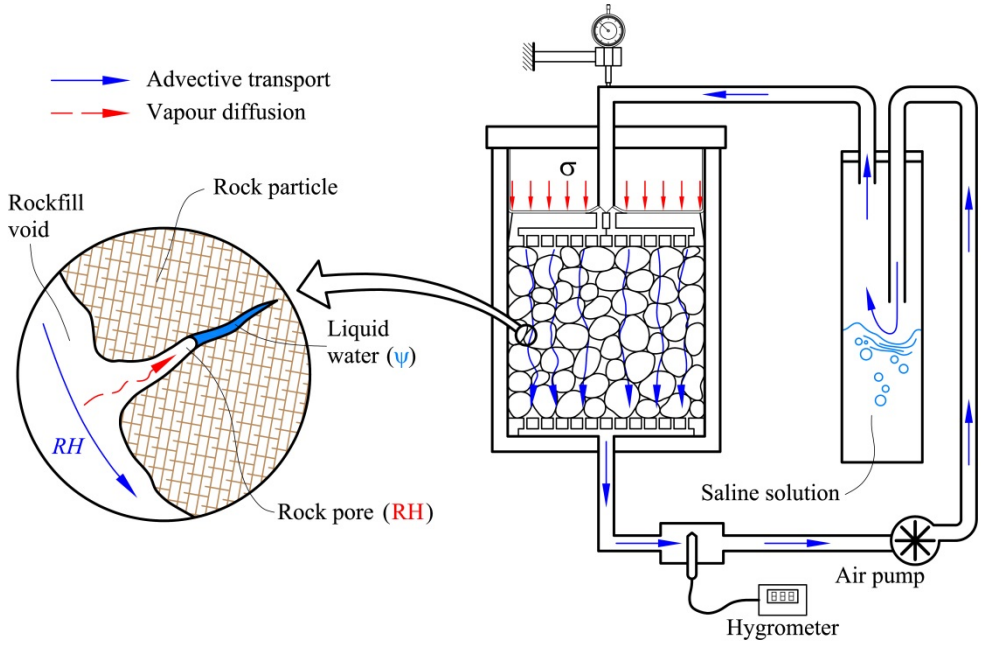

Figure 2-16 Oedometer test equipment used by (Oldecop and Alonso, 2004, 2001; Ortega, 2008): (a) Rowe oedometer with control of Relative Humidity: diameter of specimen = 300 mm, Height of specimen = 200 mm; (b) Operating scheme.

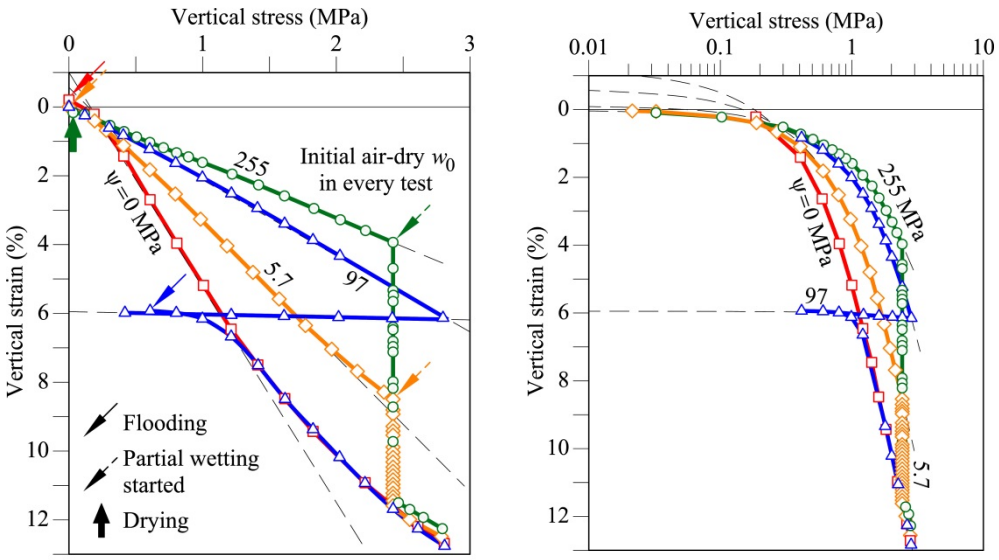

Figure 2-17 Compressibility curves - Results of oedometer tests on Pancrudo slate gravels: (a) vertical stresses in "*natural*" arithmetic scale; (b) vertical stresses in logarithmic scale. (From Oldecop (2000)) .

Collapse strain occurs in a "*small*" range of gravimetric humidity values (w<4% for the tested material). Additional increments of humidity beyond this range have no effect on the mechanical behavior of the aggregates (**Figure 2-18**). This feature distinguishes the rockfill behaviour: collapse strain occurs when the total suction is reduced to zero (when the rock particle pores are saturated and RH=100%), and this may happen without flooding the specimen.

The records of the axial strain in time under constant total suction and vertical stress display a time-dependent behaviour. **Figure 2-19** shows the records for two specimens with different relative humidity values. The time-dependent behaviour is influenced by both the vertical stress applied and the total suction imposed.

The strain behavior in time of the material under constant stress-suction condition can be divided into two stages (**Figure 2-19**). The first stage occurs at the beginning during a certain initial elapsed time and it is between 0.1 and 100 minutes after the application of the load for this tested material. The behavior in this stage depends on both the stress and suction applied as well as the load-suction history. Instantaneous deformation and sudden collapse deformations are observed in this stage. In the second stage, the behaviour may approach to a linear ε-ln(t) ratio. The long-term compressibility index λ_t may be calculated as this slope value ($\lambda_t=d\varepsilon/d(\ln t)$). **Figure 2-20** shows λ_t behaviour in relation to the vertical stress applied and the total suction for the different tests.

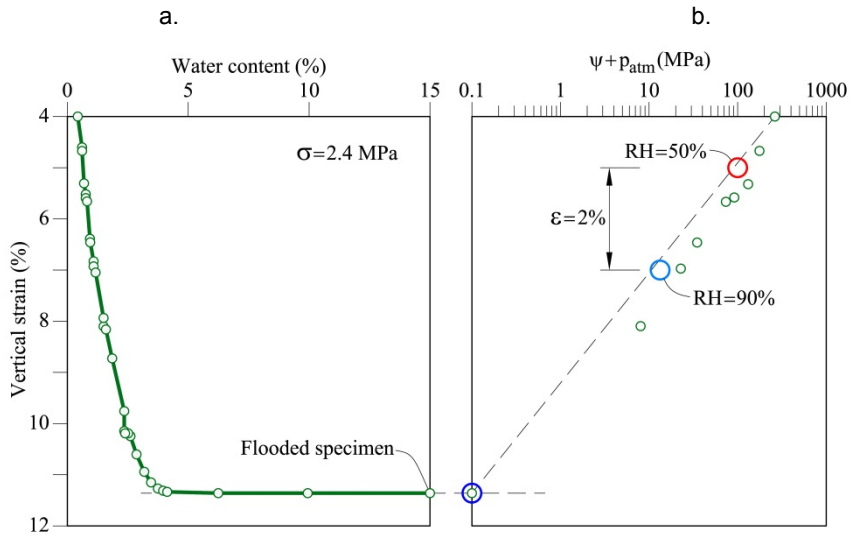

Figure 2-18 Wetting effect under constant vertical stress: (a) vertical strain-humidity curve; (b) vertical strain-total suction curve. (From Oldecop (2000)) .

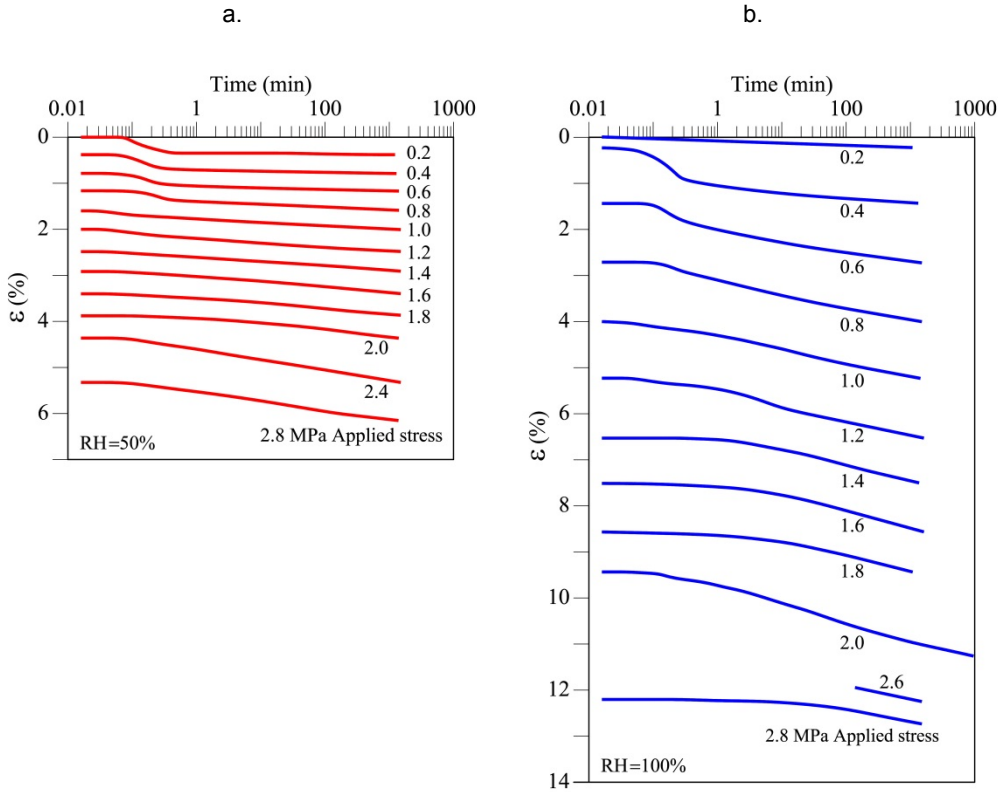

Figure 2-19 Records of vertical strain in time for constant vertical stresses and relative humidity-Results of oedometer tests on Pancrudo slate gravels: (a) RH=50%; (b) RH=100%. (From Oldecop (2000)).

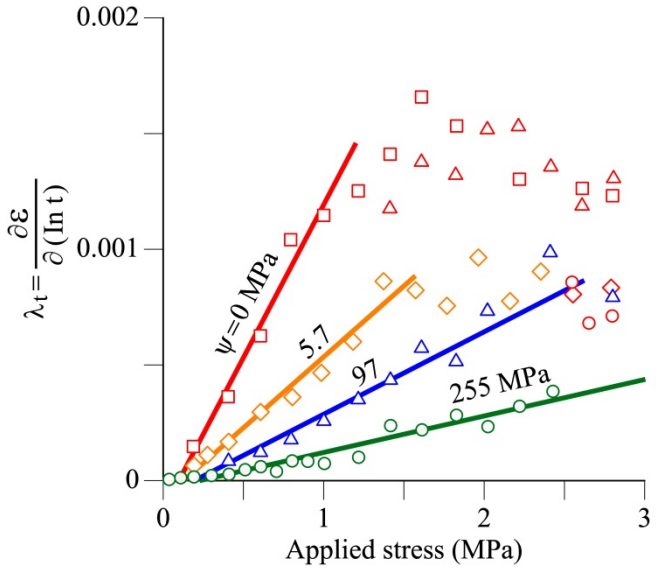

Figure 2-20 Long term compressibility index λ_t behaviour in relation to vertical stress applied for different values of total suction. Results of oedometer tests on Pancrudo slate gravels. (From Oldecop (2000)).

UPC research: Ortega and Alonso (2008)

Ortega (2008) tested limestone ballast, a material significantly harder than the Pancrudo slate using the same Rowe equipment as Oldecop and Alonso (2004, 2003, 2001). Some of these experimental observations were used to calibrate the DEM proposed in this thesis and described in later chapters.

Despite the hard nature of limestone gravels, a significant grain breakage was observed in oedometer (and also triaxial) loading at stresses of engineering significance (e.g. dams). This is shown in **Figure 2-21** for oedometer tests on four uniform samples of different initial sizes. Compression was carried out in an oedometer cell under a high suction (ψ = 320 MPa). The samples were loaded to σ_v = 2.8 MPa. They were fully wetted at this confining stress and unloaded. The figure shows the significant development of sandy particles in all cases.

Time effects were also recorded in all the oedometer tests performed.

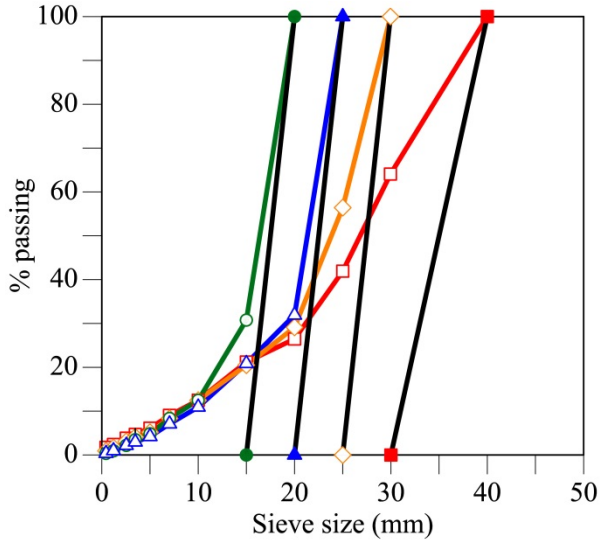

Figure 2-21 Grain size distribution curves after oedometer tests of uniform samples of Garraf hard limestone gravels having different initial particle sizes. Black lines indicate initial gsds before testing (From Ortega (2008)).

2.7.1.2 Compressibility constitutive model for rockfill: Model of Oldecop and Alonso (2001;2003)

Based on the results of the experimental oedometer tests, an elastoplastic constitutive model for rockfill under compression loads that takes into account the influence of humidity was proposed. This influence is introduced in two alternative ways: by the gravimetric water content (w) or by the total suction (ψ). The two formulations are equal if the uniqueness of the retention curve is assumed. The formulation with total suction is considered here. Because the formulation is based on observations and experimental data, this constitutive model can be considered a phenomenological model.

On the basis of the deformation mechanism for rockfill (rupture particle due to subcritical crack propagation), a thermodynamic justification for the use of the total suction as a fundamental variable in the formulation of the constitutive model was obtained. The total suction is a direct measure of the chemical potential of water and has a direct influence on the rate of crack propagation.

This model considers two deformation mechanisms producing plastic strains: the instantaneous deformation mechanism (IDM) and the time-dependent deformation mechanism (TDM). The IDM is present at any stress level and stress increment, and does not depend on the water action. The TDM is active above a threshold total stress value σ_y, and depends on the water action. This σ_y is the clastic yield stress, the stress threshold value that marks the onset of particle breakage.

Total strain-stress relationships

Assuming a linear relation between an increase in strains (ε) and applied stress (σ), these expressions are obtained (**Figure 2-22**):

For $\sigma_0 < \sigma_y$ (particle rearrangement stage):

$$d\varepsilon = d\varepsilon^i = \underline{\lambda}^r d\sigma \tag{2:23}$$

where $d\varepsilon$ is the total strain increment (elastic plus plastic components), $d\sigma$ is the vertical stress increment and $\underline{\lambda}$ is the slope of the curve ε – ln σ. $\underline{\lambda}$ represents the compressibility index of rockfill. $\underline{\lambda}^r$ is the compressibility index for $\sigma_0 < \sigma_y$ (particle rearrangement stage) and does not depend on the water action.

For $\sigma_0 \geq \sigma_y$ (clastic yielding stage):

$$d\varepsilon = \underline{\lambda}(\psi) d\sigma \tag{2:24}$$

where the compressibility index ($\underline{\lambda}$) depends on the relative humidity or the total suction (ψ). It is defined as:

$$\underline{\lambda}(\psi) = \underline{\lambda}_0 - \alpha_\psi \ln\left[\frac{(\psi + p_{atm})}{p_{atm}}\right] \tag{2:25}$$

And,

$$\underline{\lambda}(\psi) \geq \underline{\lambda}^i \tag{2:26}$$

where $\underline{\lambda}_0$, $\underline{\lambda}^i$ and α_ψ are model parameters; ψ is the total suction and p_{atm} is the atmospheric pressure. $\underline{\lambda}_0$ is the maximum compressibility index corresponding to the saturated material (ψ=0). $\underline{\lambda}^i$ is a minimum compressibility index which corresponds to a very dry state. α_ψ is a coefficient that depends on two variables: χ_ψ (relationship between suction and collapse strain), and κ_ψ (relationship between suction and elastic strain):

$$\alpha_\psi = \frac{\kappa_\psi + \chi_\psi}{\sigma_0 - \sigma_y} \tag{2:27}$$

Elastic behaviour

Elastic strain increments can occur as a result of changes in stress or in suction and can be calculated as:

a. Elastic strain due to stress increment:

$$d\varepsilon^e = \underline{\kappa} d\sigma \tag{2:28}$$

where $\underline{\kappa}$ is the elastic stress-related compressibility index and is assumed to be independent of the water action.

b. Elastic strain due to suction changes:

$$d\varepsilon^{\psi} = \kappa_{\psi} \frac{d\psi}{(\psi + p_{atm})} \tag{2:29}$$

where κ_{ψ}, which was defined previously, is the elastic suction-related swelling/retraction index. It is assumed to be independent of the stress level.

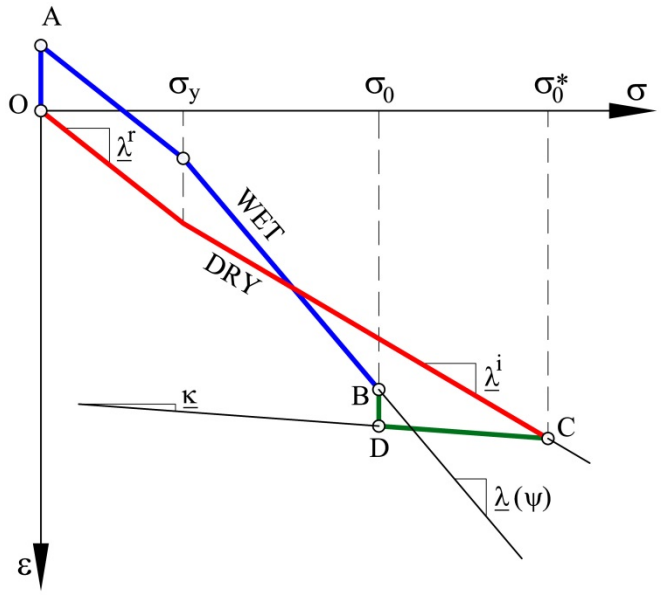

Figure 2-22 Compressibility model for rockfill (From Oldecop (2000); modified from Oldecop and Alonso (2001)).

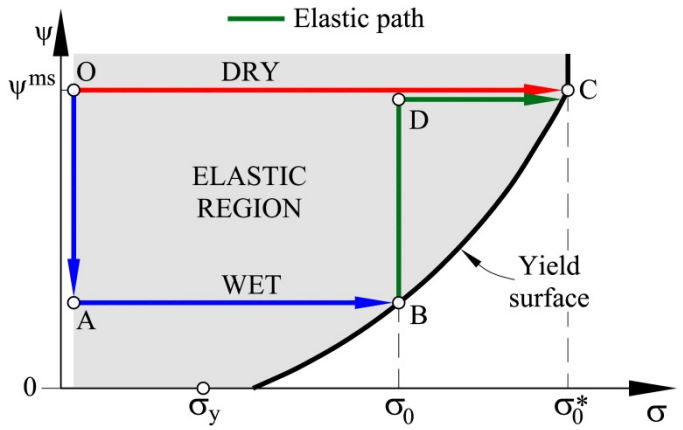

Figure 2-23 Yield surface: Stress paths considered to derive the yield surface (From Oldecop (2000); modified from Oldecop and Alonso (2001)).

Yield Surface, hardening law and flow rule

The yield surface is formulated in the following stress space: vertical stress – gravimetric water content (σ,w) or vertical stress – total suction (σ,ψ) (Figure 2-23). Only formulation with total suction is considered here.

The elastic region is limited by the Load-Collapse curve (LC) or yield surface in the stress space (σ,ψ). This surface allows the prediction of volumetric strains (unrecoverable strain) for any stress path: for an increase in stress σ, and/or a decrease in suction ψ.

In order to obtain the equation of the yield surface, the behavior of two specimens of identical aggregates in an initial dry condition was considered (see the stress-suction paths in **Figure 2-23** and stress-strain paths in **Figure 2-22**):

a. **Specimen 1:** This specimen is loaded to a vertical stress σ_0^* greater than σ_0 maintaining the initial dry condition (OC path).

b. **Specimen 2:** At the beginning, water is added (before loading) until humidity less than saturation humidity is reached. As observed in experiments, increasing the humidity (or decreasing total suction) causes swelling (OA path). Then, the load of the wet specimen is increased until a vertical stress σ_0 greater than σ_y (AB path) is achieved. If points B and C belong to the same yield surface, then it must be possible to lead the wet specimen in stage B until it reaches stage C, following a stress-humidity (or stress-suction) path in a completely elastic range. One of the possible paths is shown in **Figure 2-22** and **Figure 2-23**. It involves drying at constant stress (BD path) and then an increasing stress at constant humidity (DC path).

Therefore, each member of the following equation expresses the deformation in point C, considering the paths OABDC for specimen 2 (left part of the equation) and OC for specimen 1 (right part of the equation):

$$-\kappa_\psi \psi + \underline{\lambda}^{\mathrm{r}} \sigma_{\mathrm{y}} + \left(\sigma_0 - \sigma_{\mathrm{y}}\right) \underline{\lambda}(\psi) + \kappa_\psi \psi + \left(\sigma_0^* - \sigma_0\right) \underline{\kappa} = \underline{\lambda}^{\mathrm{r}} \sigma_{\mathrm{y}} + \left(\sigma_0^* - \sigma_{\mathrm{y}}\right) \underline{\lambda}^{\mathrm{i}} \qquad (2:30)$$

After grouping the variables, the yield surface in the σ-ψ space is expressed as:

$$\mathrm{F}(\sigma, \psi) = 0 \qquad (2:31)$$

$$\sigma_0 \left[\underline{\lambda}(\psi) - \underline{\kappa}\right] - \sigma_{\mathrm{y}} \left[\underline{\lambda}(\psi) - \underline{\lambda}^{i}\right] - \sigma_0^* \left[\underline{\lambda}^{i} - \underline{\kappa}\right] = 0 \qquad (2:32)$$

where σ_0^* is the yield stress of the dry state rockfill and is appropriately selected as the hardening parameter. Equation (2:32) is the yield surface for $\sigma > \sigma_y$.

During particle rearrangement (for $\sigma < \sigma_y$), suction changes do not produce plastic strains and the yield surface is a vertical line (in the stress-total suction space) and it is simply defined as:

$$F(\sigma,\psi)=\sigma_0-\sigma_0^*=0 \tag{2:33}$$

Hardening Law

Figure 2-24 illustrates the compressibility curve taking into account the clastic hardening stage. For this model, an additional hardening parameter σ_0^{ch} is introduced, which is defined as the value of the threshold stress where the clastic hardening stage starts.

For $\sigma_0^* < \sigma_y$, the model considers the following hardening rule:

$$d\sigma_0^*=\left[\frac{d\varepsilon^p}{\left(\underline{\lambda}^r-\underline{\kappa}\right)}\right] \tag{2:34}$$

In clastic yielding stage, for $\sigma_y < \sigma_0^* < \sigma_0^{ch}$, a simple plastic volumetric strain hardening law is considered:

$$d\sigma_0^*=\left[\frac{d\varepsilon^p}{\left(\underline{\lambda}^i-\underline{\kappa}\right)}\right] \tag{2:35}$$

The ratio between stresses and plastic strain in the hardening stage is logarithmic. This expression was proposed for the hardening law in the hardening stage:

For $\sigma_0^* > \sigma_0^{ch}$:

$$d\sigma_0^*=\left[\frac{\left(\sigma_0^*-\sigma_y\right)}{\left(\sigma_0^{ch}-\sigma_y\right)}\right]\left[\frac{d\varepsilon^p}{\left(\underline{\lambda}^i-\underline{\kappa}\right)}\right] \tag{2:36}$$

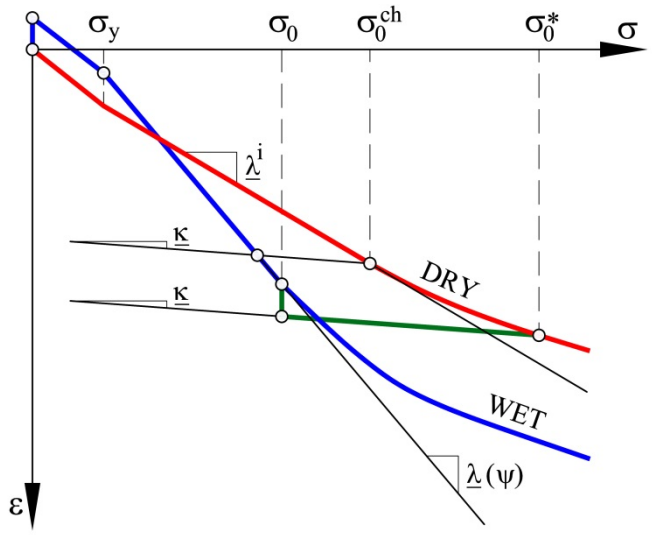

Figure 2-24 Compressibility model for rockfill considering clastic hardening (From Oldecop (2000); modified from Oldecop and Alonso (2001)).

In summary, the model uses 9 parameters that are evaluated from oedometer tests: $\underline{\lambda}^{r}$; $\underline{\lambda}^{i}$; $\underline{\lambda}_0$; $\underline{\kappa}$; κ_ψ ; α_ψ ; σ_y ; σ_0^{ch} ; χ_ψ. The model also includes a value for the atmospheric pressure p_{atm}.

2.7.2 Triaxial behaviour of rockfill (Deviatoric stress state): Experimental results and constitutive model - UPC research

2.7.2.1 Experimental triaxial tests

UPC research: Chavez and Alonso (2003)

In order to study the triaxial behaviour for rockfill under suction-controlled conditions, Chávez and Alonso (2003) reported results of several triaxial tests on the same material studied by Oldecop and Alonso (2001) for the compressibility behaviour: crushed slate gravels (crushed Cambric slate) from a quarry near Pancrudo river (Teruel, Spain) between sizes 0.4 and 40 mm (see initial gsd curve in **Figure 2-3**a). Triaxial equipment used is shown in **Figure 2-25**. The aggregate specimens were 25 cm in diameter and 50 cm in height. The specimens were compacted over the triaxial cell base inside a thick membrane of neoprene placed into a split mould (**Figure 2-25**b). Gravels were compacted into six layers using a standard Proctor compaction energy between 600 and 700 J/l. The mean initial void ratio (e_0) was 0.628 ± 0.03 at the beginning of the tests. The mould was removed after compaction and the membrane provided a small confinement to maintain the sample geometry.

a.

b.

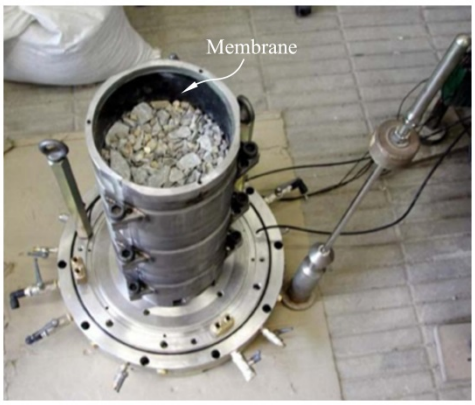

c.

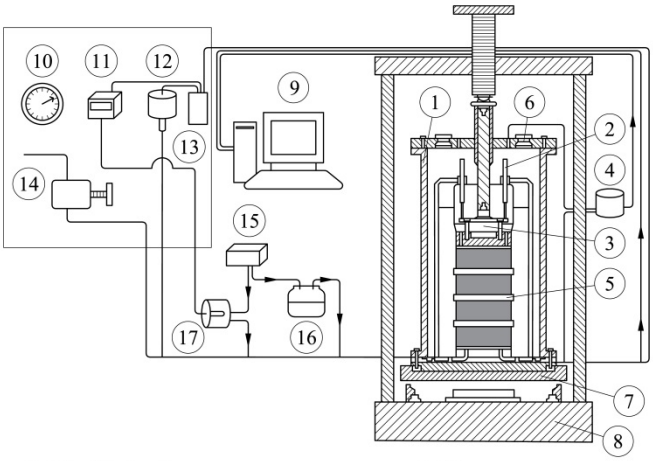

1. Triaxial chamber
2. LVDT for axial measure
3. Load cell
4. DPT
5. Diametral Measure Transducer (DTM)
6. Window
7. Car to move to cell
8. Load frame
9. Data acquisition system
10. Vacuum gauge
11. Hydrometer
12. Pressure transducer
13. Power supply
14. Pressure regulator
15. Air bomb
16. Pot with salt solution
17. Hygrometer sensor

Figure 2-25 Triaxial test equipment used by (Chávez and Alonso, 2003; Ortega, 2008): (a) Triaxial with control of Relative Humidity: diameter of specimen = 250mm, Height of specimen = 500mm (From Ortega (2008)); (b) Upper view of the specimen inside a split mould with a thick membrane of neoprene during compaction (From Ortega (2008)); (c) Operating scheme (From Chávez and Alonso (2003)).

Chávez and Alonso (2003) reported two series of strain control triaxial tests: The first series was performed under fully saturated conditions: Saturated tests S1, S3, S5 and S8. In the second series a constant relative humidity RH of 36% (equivalent to a total suction of ψ=142 MPa) was imposed: Dry tests D1, D3, D5 and D8. The two series of tests followed the same procedure: After compaction, the aggregate specimens were maintained under constant humidity conditions (fully saturated and RH=36% for the first and second series, respectively); each specimen was subjected to a confining pressure (the following pressures were applied: σ_3 = 0.1, 0.3, 0.5 and 0.8 MPa); and finally, deviatoric stresses were applied under these constant lateral stresses (confining pressure). In the curves of **Figure 2-26**, the number of the test name (1,3,5 and 8) refers to σ_3, and the letters D and S stand for 'dry' (RH=36%) and 'saturated' (RH=100%) conditions.

Figure 2-26 shows the results of the tests for the saturated (**Figure 2-26**a and **Figure 2-26**c) and dry (**Figure 2-26**b and **Figure 2-26**d) conditions: deviatoric stress (q) vs. axial strain (ε_a) curves are shown in **Figure 2-26**a and **Figure 2-26**b; volumetric strain (ε_p) vs. axial strain (ε_a) are shown in **Figure 2-26**c and **Figure 2-26**d. These curves conclude that dry samples reach higher strength than saturated specimens, and dilation behaviour is observed mainly in dry conditions for samples with $\sigma_3 \leq 0.5$ MPa. Unloading-reloading cycles were imposed at certain strain levels to estimate the elastic stiffness of the aggregates.

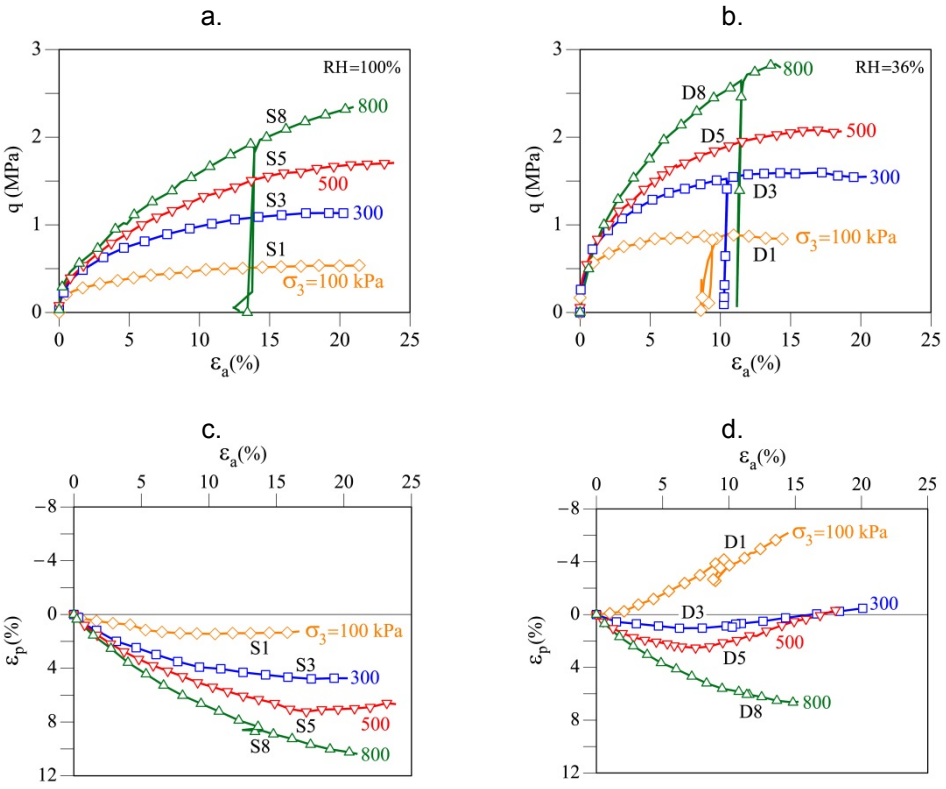

Figure 2-26 Triaxial behaviour of rockfill - Results of strain control triaxial tests on Pancrudo crushed (Cambric) slate gravels: (a) q-ε_a curves for saturated conditions (RH=100%); (b) q-ε_a curves for dry conditions (RH=36%); (c) ε_p- ε_a curves for saturated conditions (RH=100%); (d) ε_p- ε_a curves for dry conditions (RH=36%). (From Chávez (2003)).

Figure 2-27 shows the evolution of the gsd curves for the tests: At the beginning, after compaction and at the end of the tests. **Figure 2-27**a presents the curves for saturated conditions (RH=100%) and **Figure 2-27**b for dry conditions (RH=36%). This evolution of the gsd curve evidences the particle rupture process during the triaxial tests. Particle breakage can be estimated by calculating the Hardin B_r (Hardin, 1985) and Marsal B_g (Marsal, 1967) breakage indexes. The evolution of B_r and B_g indexes is shown in **Figure 2-27**c. Both B_r and B_g increase with increasing σ_3 and are higher for saturated conditions than dry conditions: for instance, in the triaxial tests at σ_3=0.8MPa, B_r is 0.2 for RH=100% and 0.075 for RH=36%. This figure further shows that particle breakage also occurs in the compaction stage: B_r is close to 0.05 at the end of compaction.

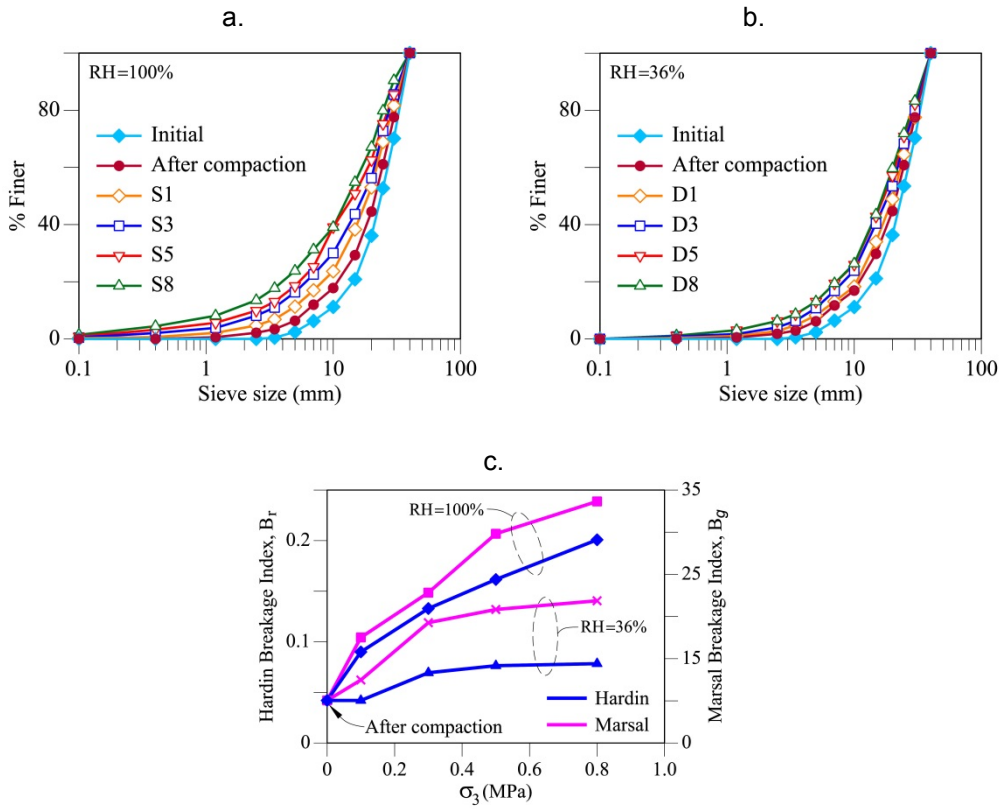

Figure 2-27 Evolution of gsd curves and Breaking index - Results of strain control triaxial tests on Pancrudo crushed (Cambric) slate gravels: (a) gsd curves for saturated conditions (RH=100%); (b) gsd curves for dry conditions (RH=36%); (c) Hardin and Marsal breakage indexes for saturated and dry conditions. (From Chávez and Alonso (2003) and Chávez (2003)).

Figure 2-27 also shows that there is a threshold value of confining stress (σ_3) that accelerates the breakage of the particle, a result that is consistent with Yamamuro and Lade (1996), who have also shown that particle breakage in sands subjected to triaxial loading does not start until beyond a given confining stress. A threshold vertical stress (σ_y) was also identified in oedometer tests which marked the beginning of the particle breakage (Oldecop and Alonso, 2001) and was

commented above in the description of the constitutive model for rockfill compressibility. Although oedometer and triaxial tests are different regarding particle breakage, these experimental results will be taken into account for the DEM model.

For the dry condition, **Figure 2-27**b shows that the curve for σ_3=0.1 MPa (curve D1) is almost the same as the after-compaction curve. The gsd curves evolve for σ_3 > 0.1 MPa. This value σ_3=0.1 MPa can be considered the threshold value. For the saturated condition, **Figure 2-27**a, all the curves (S1, S3, S5, S8) evolve and it can be assumed that the threshold value of σ_3 is between 0 and 0.1 MPa.

UPC research: Ortega and Alonso (2008)

Ortega (2008) also tested well-graded and poorly-graded ballast samples in a suction-controlled triaxial cell: the same hard limestone ballast used for his oedometer tests. Significant grain breakage was observed. Some of these experimental observations were simulated using the DEM proposed in this thesis and described in later chapters.

Figure 2-28 shows a characteristic result. In this case, a well-graded sample (in the range coarse sand – medium gravel) was initially confined to a cell pressure of 0.3 MPa and then sheared by increasing the vertical stress. Three levels of humidity are compared: RH=10%, 50% and 100%.

The figure shows that the effect of RH on strength is quite moderate. The sample shows a ductile behaviour despite the relatively high density (e_0=0.54). In fact, none of the samples tested, irrespective of their initial density and grading, exhibited peak behaviour.

For a wide range of applied vertical strains (0-10%) the behaviour is contractant. The effect of RH to control volume change is relevant, especially when the dilatant behaviour manifests. Also shown in the figure is the effect of wetting the sample loaded under RH=10% at a particular value of deformation, when the limiting strength was reached. The test was performed at a constant rate of vertical deformation. Wetting the dry sample results in a rapid reduction of measured deviatoric stress (this is a consequence of an internal collapse of the granular structure) and the reactivation of a compressive volumetric strain, even if dilatancy (expansion) was already under way. It will be shown below that all of these features are reproduced by the particulate model developed.

Figure 2-29 shows the approximate shape of the yield locus determined by means of stress paths, at decreasing confining stress, performed in a triaxial cell. The figure compares the yield locus for two RH's: 50% and 100%. This figure also shows the incremental plastic strain vectors which are calculated at certain values of the total deviatoric strain applied. The figure shows the irreversible compressive strains on the wet side of the yield locus and the dilatancy observed on the "dry" side. The effect of RH is also clear: increasing RH reinforces the compressive strains. Critical state conditions could not be found in the tests performed. Dilatancy increased at a significant rate even if deviatoric strains reached 20%. These observations also stress the difficulty of building 'continuum' constitutive models.

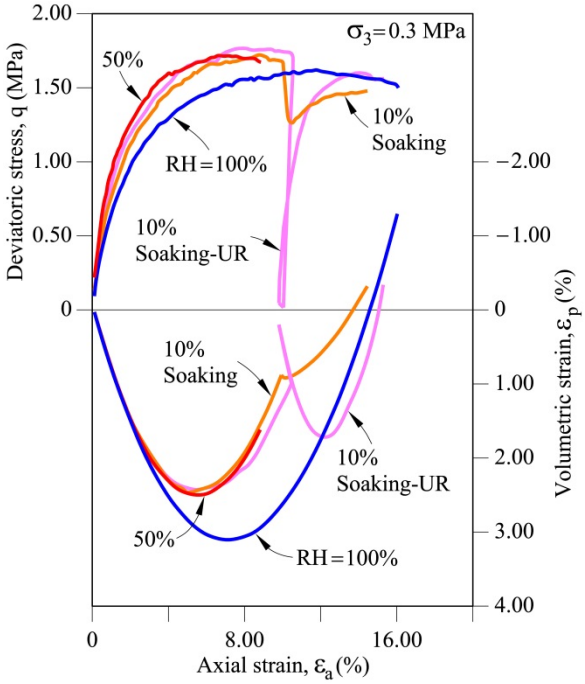

Figure 2-28 Deviatoric behaviour for well-graded aggregates of Garraf limestone gravels (Diameter size: 1.4-40mm). Results of suction-controlled triaxial tests for σ_3=0.3MPa and different Relative Humidity conditions: 10%, 50% and 100%. One of the samples at RH=10% was flooded at ε_a ≈12% (10%-Soaking curve) and the other one was unloaded at ε_a ≈ 11% and then flooded, before resuming the test (10%-Soaking-UR curve). (From Ortega (2008)) .

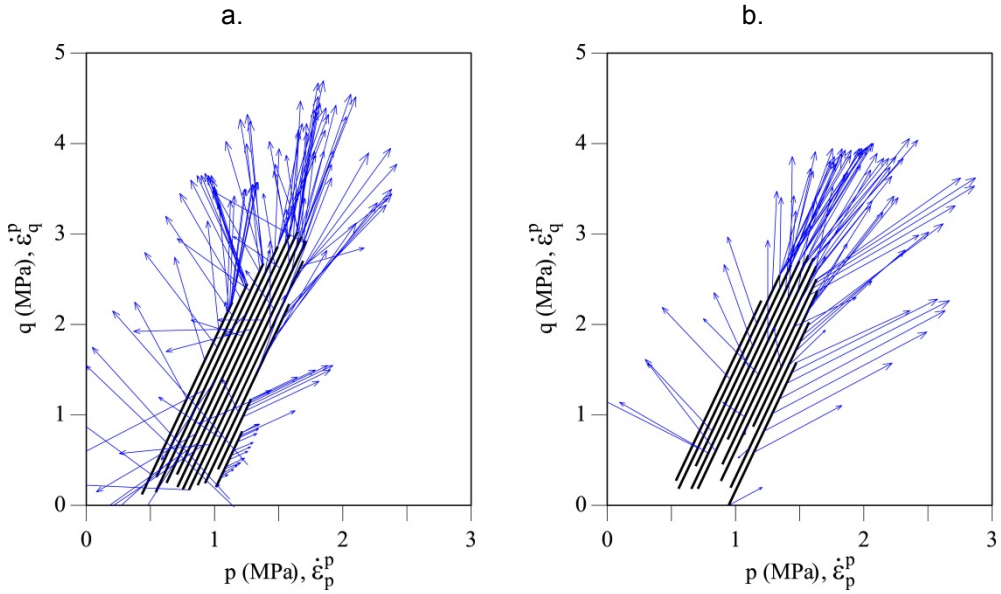

Figure 2-29 Yield locus and Incremental plastic strain vectors. Results of suction-controlled triaxial tests on well-graded aggregates of Garraf limestone gravels (Diameter size: 1.4-40mm): (a) RH=100%; (b) RH=50%. (From Ortega (2008)).

2.7.2.2 *Constitutive model for triaxial behaviour: Model of Chávez and Alonso (2003)*

The model assumes that rockfill material tends toward a critical state when it is subjected to shear stresses and work-hardening dependence is introduced in some model parameters to take into account the effect of particle breakage.

Figure 2-30 shows the yield surfaces considered by the model. This model follows the proposal of Wan and Guo (1998) for the saturated materials and modifies it considering unsaturated conditions. Two yield surfaces are considered for the saturated conditions: A shear and a cap yield surface. Yield is activated at the initial unloaded state (i.e. compacted state). For instance, point A in the figure represents the current state of a sample loaded along the indicated stress path.

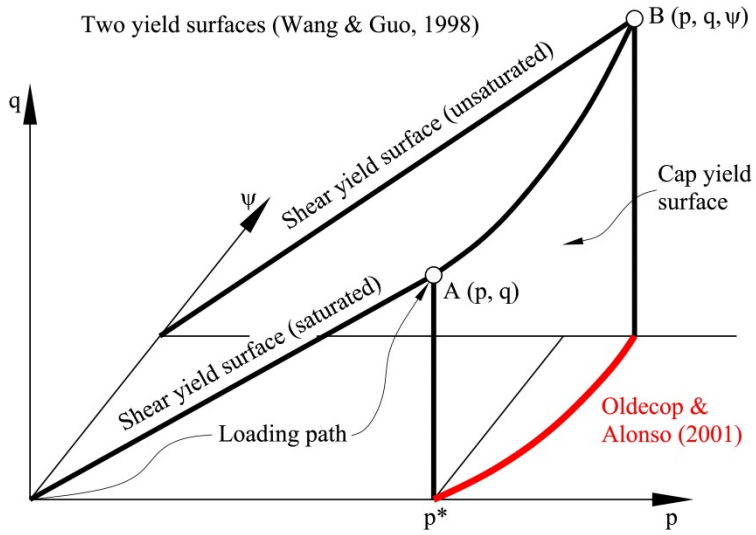

Figure 2-30 Yield surfaces of the model. (From Chávez and Alonso (2003)).

Shear yield surface

The following expression represents the shear yield surface:

$$f_q\left(q,p,\psi,W^P,\varepsilon_q^p\right)=\frac{q}{p}-\eta_s=0 \qquad (2:37)$$

where q=(σ_1–σ_3) represents the deviatoric stress; p=[(1/3)*(σ_1+2 σ_3)] represents the mean stress; ψ=suction; W^P=plastic work; ε_q^p =[(2/3)*(ε_1^p-ε_3^p)] is the deviatoric plastic strain; and η_s is the stress ratio. σ_1 and ε_1^p are the vertical stress and plastic axial (vertical) strain, respectively. σ_3 and ε_3^p are the (constant) confining lateral stress and plastic lateral strain, respectively. The plastic strains are derived from the total strains by subtracting the calculated elastic strains (elastic parameters are obtained from the loading/unloading path).

η_s can be obtained from this hardening rule following Muir Wood et al. (1994) and

relating some parameter to the plastic work W^P:

$$\frac{\eta_s}{r\, M_c(W_E^P,\psi)} = \frac{\varepsilon_q^p}{b(W_T^P)+\varepsilon_q^p} \tag{2:38}$$

where $M_c(W_E^P,\psi)$ is the critical state stress ratio and is given in relation to the "effective" plastic work W_E^P and suction ψ; and b is a parameter linked to the initial stiffness of the soil and it is given in relation to the total plastic work W_T^P. b is assumed not to depend on the relative humidity or suction. r is a parameter that depends on the distance between the critical state specific volume ν_{cr} and the current value ν (Been and Jefferies, 1985). It is calculated as follows:

$$r = 1 - \mathrm{k}\left(\nu - \nu_{cr}\right) \tag{2:39}$$

where k is a constant, and the critical state specific volume ν_{cr} depends on the suction and is calculated as follows in a ν-p space (ν=specific volume; p=mean stress) (**Figure 2-31**):

$$v_{cr} = y(\psi) - m_{cr}\, p \tag{2:40}$$

$$y(\psi) = y_0 + \alpha_y \ln\left(\frac{\psi + p_{atm}}{p_{atm}}\right) \tag{2:41}$$

m_{cr}, y_0, and α_y are constants. p_{atm} is the atmospheric pressure and is introduced to recover saturated conditions when ψ=0. $y(\psi)$ represents the specific volume in relation to the suction and is derived from the results of Oldecop and Alonso (2001) for the compressibility behaviour explained above.

Critical state stress ratio $M_c(W_E^P,\psi)$ decreases when the "effective" plastic work W_E^P increases (and confining stress also increases), and increases when suction increases. The evolution of $M_c(W_E^P,\psi)$ can be observed in **Figure 2-32**. This effective plastic work is calculated as:

$$W_E^P = W_T^P - W_R^P \tag{2:42}$$

where W_T^P is the total plastic work and W_R^P is the plastic work associated with particle rearrangement. W_R^P is a threshold work below which there is no particle breakage. The total plastic work can be calculated from the following expression:

$$\delta W_T^P = p\,\delta\varepsilon_p^p + q\,\delta\varepsilon_q^p \tag{2:43}$$

where $\varepsilon_q^p = [(2/3)*(\varepsilon_1^p - \varepsilon_3^p)]$; and $\varepsilon_p^p = (\varepsilon_1^p + 2\varepsilon_3^p)$.

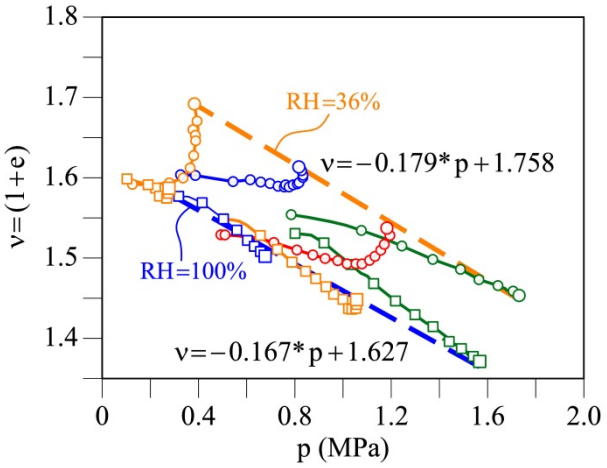

Figure 2-31 Evolution of specific volume ν during the tests ((ν-mean stress *p*) path) and estimated position of critical state lines for unsaturated (RH=36%) and saturated conditions (RH=100%). (From Chávez (2003)).

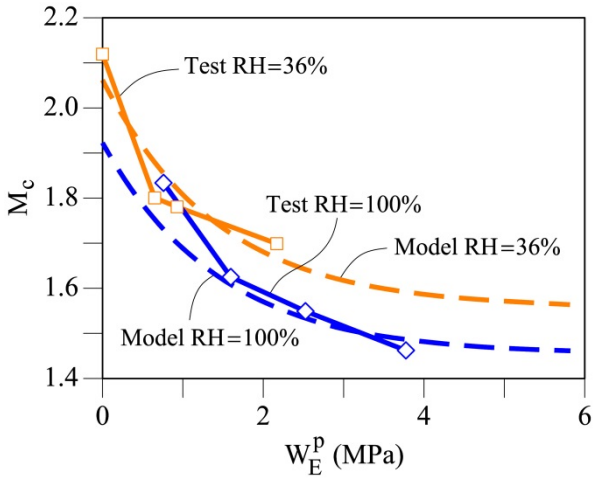

Figure 2-32 Evolution of M_c during the tests. Comparison between experimental data and model for unsaturated (RH=36%) and saturated conditions (RH=100%). (From Chávez and Alonso (2003)).

$M_c(W_E^P, \psi)$ is calculated as follows:

$$M_c\left(W_E^P,\psi\right)=M_{cr}\left(W_E^P\right)\left(1+k_s\ln\left(\frac{\psi+p_{atm}}{p_{atm}}\right)\right) \tag{2:44}$$

$$M_{cr}\left(W_E^P\right)=M_{cres}+\left(M_{c0}-M_{cres}\right)e^{-\left(aW_E^P\right)} \tag{2:45}$$

where M_{cres}, M_{c0} and k_s are constants. k_s describes the gain of strength induced by suction. M_{cres} is a residual stress ratio for unsaturated conditions and corresponds theoretically to the limiting stress ratio as the effective plastic work accumulates. a is a model parameter. The adjusted curves of $M_c(W_E^P, \psi)$ which were obtained by

the model are also shown in **Figure 2-32**.

Finally, parameter *b,* which is proportional to the inverse of the normalized initial tangent stiffness of rockfill, is assumed to depend on the total plastic work W_T^P. It is calculated as:

$$b = B\left(\frac{W_T^P}{c + W_T^P}\right) \tag{2:46}$$

where *B* is the maximum value of parameter *b* as W_T^P increases; and *c* is a constant. **Figure 2-33** shows the experimental data and the adjusted curve of the model obtained by Chávez (2003).

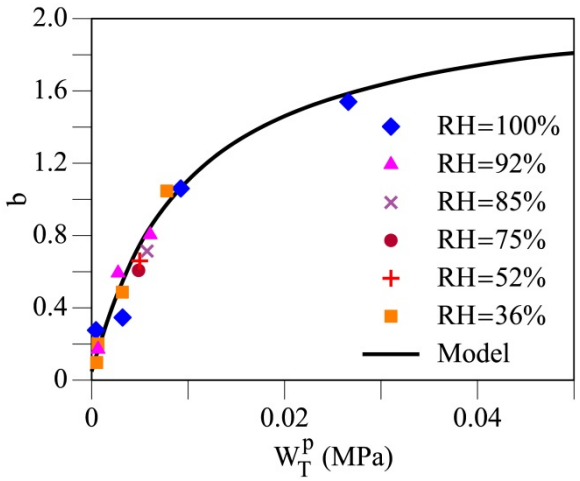

Figure 2-33 Evolution of *b* during the tests. Comparison between experimental data and model for unsaturated (RH=36%) and saturated conditions (RH=100%). (From Chávez (2003)).

Cap yield surface

The volumetric component of yield (cap) is based on the elastoplastic compressibility model for rockfill behaviour obtained by Oldecop and Alonso (2001) and described above. As we have seen, under isotropic compression, a threshold yield stress p_y marks the beginning of particle breakage. There is no suction effect for $p<p_y$.

The following expressions represent the cap yield surface:

For $p<p_y$:

$$f_p(p) = p(\psi) - p^* = 0 \quad (p<p_y) \tag{2:47}$$

For $p \geq p_y$:

$$f_p(p,\psi) = p\left[\lambda^i + \lambda^d(\psi) - \kappa\right] - p_y\lambda^d(\psi) - p^*\left[\lambda^i - \kappa\right] = 0 \tag{2:48}$$

where λ^i is the instantaneous compressibility index for a very dry state, κ is the elastic compressibility index, and $\lambda^d(\psi)$ is the compressibility index that depends on the applied total suction ψ, and can be calculated as follows:

$$\lambda^d(\psi) = \lambda_0^d + \alpha_s \ln\left(\frac{\psi + p_{atm}}{p_{atm}}\right) \tag{2:49}$$

where λ_0^d is the isotropic compressibility index for saturated conditions and α_s is a model parameter.

p^* is taken as the hardening parameter and is identified as the yield stress for very dry rockfill. The following strain hardening law controls p^*:

$$dp^* = \frac{d\varepsilon_q^p}{\lambda^i - \kappa} \tag{2:50}$$

Flow rules - Plastic Potential:

(a) *For the deviatoric part:* Non-associated flow rule is adopted.

$$Q_q = q - p\sin(\vartheta_m) \tag{2:51}$$

where ϑ_m is the dilatancy angle ($\vartheta_m = -\delta\varepsilon_p^p/\delta\varepsilon_q^p$), and it is calculated using the proposed expression by Wan and Guo (1998):

$$\sin(\vartheta_m) = \frac{\sin(\varphi_m) - \left(\frac{e}{e_{cr}}\right)^{\alpha}\sin(\varphi_{cr})}{1 - \left(\frac{e}{e_{cr}}\right)^{\alpha}\sin(\varphi_m)\sin(\varphi_{cr})} \tag{2:52}$$

where φ_m is the mobilized friction angle at a given yield state; φ_{cr} is the critical state value obtained from M_c; e_{cr} is the void ratio at critical state and is obtained from ν_{cr}; e is the current void ratio and α is a constant model parameter. φ_m is obtained as follows:

$$\sin(\varphi_m) = \frac{\eta_s}{\left(2 + \frac{1}{3}\eta_s\right)} \tag{2:53}$$

(b) *For the Isotropic part:* Associated flow rule is adopted.

$$Q_p = f_p(p) \tag{2:54}$$

In summary, the model uses 18 parameters that can be evaluated from isotropic and triaxial compression tests:

- **For deviatoric (shearing) behaviour:**

Yielding surface and hardening: k; y_0; α_y; m_{cr}; k_s; p_{atm}; M_{c0}; M_{cres}; a; B; c;

Deviatoric flow rule: α;

- **For isotropic compression (CAP):**

Yielding surface and hardening: p_y; λ^i; λ_0^d; α_s;

- **For elastic behaviour: κ; ν;**

Figure 2-34 shows the comparison between the experimental results of triaxial tests and the model predictions for samples S3 and D3, which are subjected to a confining stress σ_3=0.3MPa.

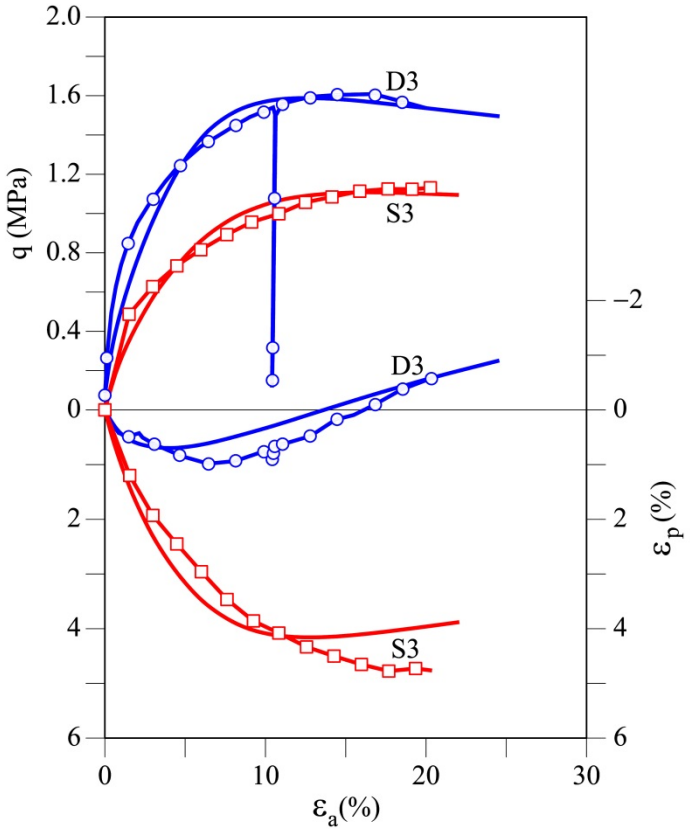

Figure 2-34 Triaxial behaviour: (a) stress-strain; (b) Volumetric change behaviour. Comparison between experimental triaxial tests on crushed slate gravels for unsaturated and saturated conditions ("dry" state: RH=36% - specimen D3; RH=100% - specimen S3) under σ_3=0.3MPa and model predictions. (From Chávez (2003)).

2.7.3 Compressibility of granular aggregates: Model of McDowell & Bolton (1998)

McDowell and Bolton (1998) explain, from a micromechanical perspective, the linear of the normal compression line (in a common space (void ratio *e*)–(logarithm of effective stress)) for a crushable aggregate which has been one-dimensionally compressed.

Figure 2-35 shows the compressibility curve of a one-dimensional compression test for dense silica sand obtained by Golightly (1990) (cited by McDowell and Bolton (1998)). Three regions are distinguished in the plot: (a) Small deformations in region 1, where the normalizing parameter should be the elastic modulus. However, small irrecoverable deformations may occur due to particle rearrangement; (b) Clastic yielding in region 2, where particle breakage is a prerequisite for further compaction: major irrecoverable deformations are permitted by the onset of particle fracture. Therefore, "*a clastic yield stress, $\bar{\sigma}_0$, is defined as the value of macroscopic stress which causes the maximum rate of grain fracture under increasing stress*" (McDowell and Bolton, 1998); (c) Plastic hardening in region 3 known as the 'normal compression'.

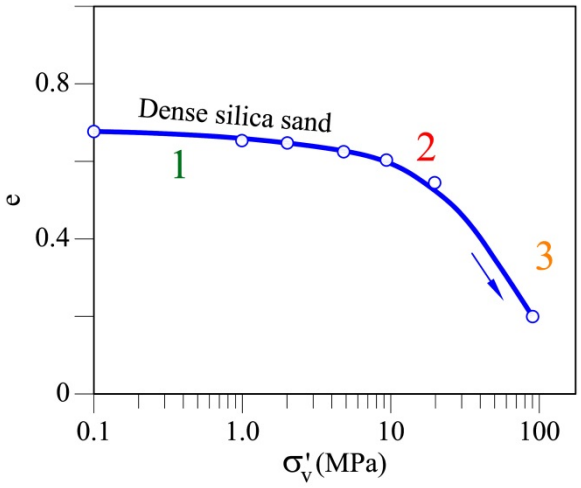

Figure 2-35 Compressibility curve: One-dimensional compression test on dense silica sand (Golightly (1990); cited by McDowell and Bolton (1998)).

The model takes into account a fractal behaviour for particle breakage and thus the grain size distribution evolves in a limited fractal geometry under increasing stress.

Based on the Weibull statistics of fracture of brittle ceramics, the tensile strength of a particle subjected to one-directional compression is defined. Furthermore, the model assumes that the clastic yield stress is proportional to the grain tensile strength.

Likewise, the model uses fracture mechanics laws to relate the particle strength and particle size.

In order to relate the evolution of a fractal geometry to the evolution of a normal compression line ((e – log $\bar{\sigma}$) space), McDowell and Bolton (1998) base their analysis on the original Cam Clay equation (Roscoe et al., 1963; Schofield and Wroth, 1968), taking into account the energy dissipated in the successive fracture of brittle particles (McDowell et al., 1996):

$$q\delta\varepsilon_q + p'\delta\varepsilon_v = Mp'\delta\varepsilon_q + \frac{\Gamma dS}{V_s(1+e)} \tag{2:55}$$

where dS is the increase in the surface area of a volume V_s of solids distributed in a total volume $V_s(1+e)$, and Γ is the surface energy related to the critical strain energy release rate G_c by $\Gamma = G_c/2$.

For one-dimensional normal compression with effective axial stress $\bar{\sigma}$ and axial strain $\bar{\varepsilon}$, the last equation is derived to:

$$\bar{\sigma}d\bar{\varepsilon} = \frac{2}{9}M\left(1+2K_0\right)\bar{\sigma}d\bar{\varepsilon} + \frac{\Gamma dS}{V_s(1+e)} \tag{2:56}$$

where K_0 is the lateral/axial effective stress ratio ($K_0 \approx 1-\sin\phi$).

Considering,

$$d\bar{\varepsilon} = -\frac{de}{(1+e)} \tag{2:57}$$

we obtain:

$$de = -\frac{\Gamma dS}{(1-\mu)\bar{\sigma}V_s} \tag{2:58}$$

where μ is a weak function solely of the angle of internal friction (McDowell, 1997).

Taking into account the aforementioned different aspect related to the fractal behaviour and fracture mechanics considerations, the model defined the following clastic hardening law:

$$de = -\left(\frac{1}{1-\mu}\frac{\beta_s}{\beta_v}\frac{\Gamma}{\bar{\sigma}_0 d_0}\right)\frac{d\bar{\sigma}}{\bar{\sigma}} = -\left(\frac{1}{1-\mu}\frac{\beta_s}{\beta_v}\frac{\Gamma/\sqrt{d_0}}{\bar{\sigma}_0\sqrt{d_0}}\right)\frac{d\bar{\sigma}}{\bar{\sigma}} = -\lambda\frac{d\bar{\sigma}}{\bar{\sigma}} \tag{2:59}$$

where λ is the compressibility index, the slope of a 'normal compression' line; β_s is the surface shape factor; β_v is the volume shape factor for the material; μ (function of the angle of internal friction) may vary from 0.4 for ϕ=20° to 0.6 for ϕ=40° (It is proposed to assume μ=0.5); Γ is the surface energy; $\bar{\sigma}_0$ is the clastic yield stress for the aggregate.

β_s can be calculated from this expression:

$$S(d) = \beta_s d^2 \tag{2:60}$$

where *S(d)* is the surface area of a particle of size *d*.

β_v can be derived from the calculation of the volume of a particle of size d, *M(d)*:

$$M(d) = \beta_v d^3 \tag{2:61}$$

Harr (1977) quotes values of β_s/β_v for crushed quartz in the range 14-18; Ashby and Jones (1986) give values of surface energy Γ for rocks of 25 J/m^2.

Finally, McDowell and Bolton (1998) suggest that λ may be seen as a material constant if the term [Γ / (d_0)$^{0.5}$] α 1, considering a value of the surface fractal dimension D_s=2.5, and [$\bar{\sigma}_0$ (d_0)$^{0.5}$] α K_{Ic}, the toughness value for mode I.

2.7.4 Elastoplastic constitutive model for coarse granular aggregates incorporating particle breakage (Based on triaxial tests: Deviatoric stress state): Model of Salim and Indraratna (2004)

2.7.4.1 Postulates

The model is based on two postulates:
(1) Coarse aggregates experience plastic strains when, and only when, there is a change in stress ratio, η=*q*/*p*. The model is based on the proposal of Pender (1978) for overconsolidated soils. This postulate is only valid for time-independent conditions (i.e. no creep effects).

Figure 2-36 shows this noncapped model, in which the yield loci are represented by constant stress ratio (η=constant). The yield locus moves kinematically along with its current stress ratio η_j as the stresses change. The yield function *f* is expressed as (Pender, 1978):

$$f = q - \eta_j p = 0 \tag{2:62}$$

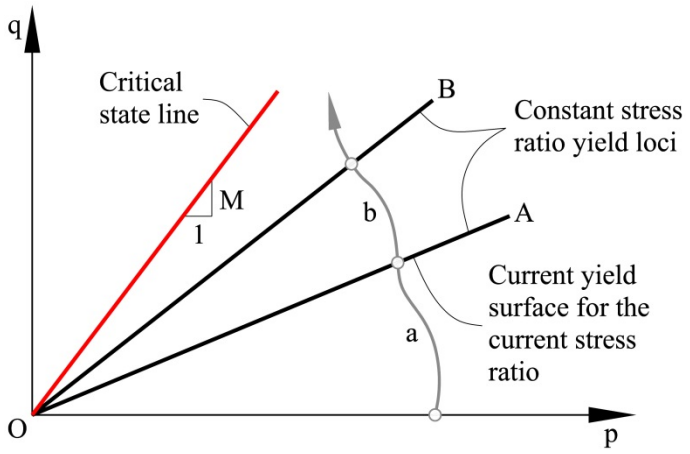

Figure 2-36 Model for yield loci represented by constant stress ratio lines in *p*-*q* plane (modified after Pender (1978); Cited by Salim and Indraratna (2004)).

(2) The undrained stress paths are parabolic in the *p*-*q* plane and are expressed by a relationship in Pender (1978), (**Figure 2-37**).

$$\left(\frac{\eta}{M}\right)^2 = \frac{p_{cs}}{p}\left[\frac{1-p_0/p}{1-p_0/p_{cs}}\right] \qquad (2:63)$$

Where p_{cs} is the value of p at the point on the critical state line corresponding to the current void ratio (value of p where the path comes to an end); p_0 is the intercept of the stress path on p axis (the starting point of the path).

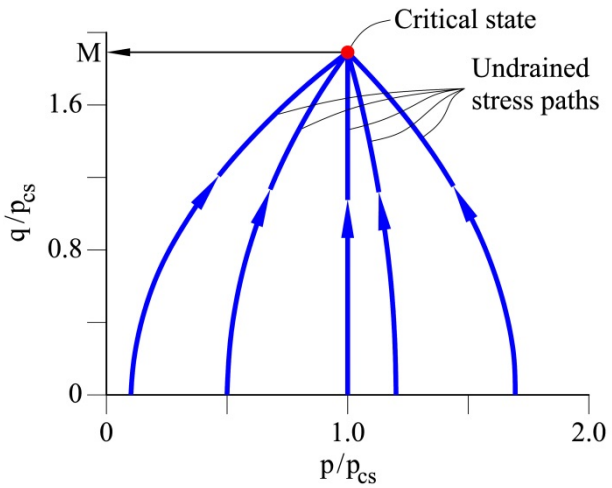

Figure 2-37 Parabolic undrained stress paths (modified after Pender (1978); Cited by Salim and Indraratna (2004)).

2.7.4.2 *Constitutive model*

The model derives from a simple expression of energy balance that takes into account the frictional resistance and the breakage of particles following the scheme presented in **Figure 2-38** which shows details of a triaxial specimen subjected to a compression load with a sawtooth deformation model (**Figure 2-38**a) and details of forces and deformation at the contact between two particles (**Figure 2-38**b). This is the energy balance equation:

$$F_{1i}dy_i - F_{3i}dx_i = N_i \tan\phi_f du_i + dE_{bi} \quad (2:64)$$

where F_{1i} and F_{3i} are the vertical and lateral forces at contact i; dE_{bi} is the amount of energy spent on particle breakage during the displacement du_i ; N_i is the normal force; ϕ_f is the basic angle of friction; dx_i and dy_i are the horizontal and vertical components of du_i, respectively.

The model relates this incremental energy spent on the particle breakage to the Marsal breaking index B_g (Marsal, 1967), which is calculated from the retained weight by sieves using the grain size distribution (gsd).

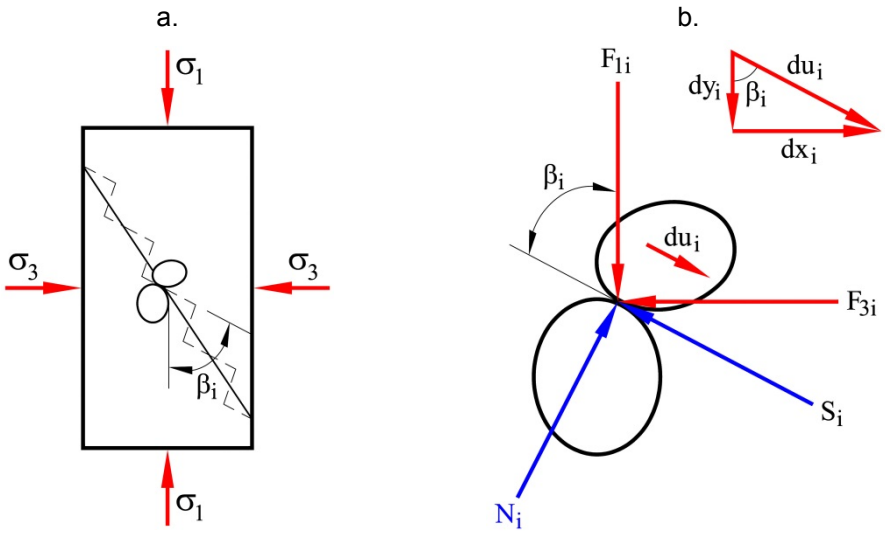

Figure 2-38 Coarse aggregate specimen subjected to triaxial compression: (a) axisymmetric specimen and sawtooth deformation model; (b) details of forces and deformation at the contact between two particles (after Indraratna and Salim (2002); Cited by Salim and Indraratna (2004)).

This model is also based on the critical state concept (**Figure 2-39** and **Figure 2-40**) and the theory of plasticity, taking into account a non-associated flow and a kinematic type yield locus (constant stress ratio). The plastic flow rule is formulated considering particle breakage. The following three equations represent the constitutive model:

(a) For stress ratio η:

$$d\eta = \frac{M^2\left(1+e_i\right)\left(2p_0/p-1\right)\left\{9\left(M-\eta^*\right)+B/p\left[\chi+\mu\left(M-\eta^*\right)\right]\right\}d\varepsilon_s^p}{2\alpha\kappa\left(p/p_{cs}\right)\left(1-p_{0(i)}/p_{cs(i)}\right)\left(9+3M-2\eta^*M\right)\eta} \quad (2:65)$$

(b) For plastic strain ratio:

$$\frac{d\varepsilon_v^p}{d\varepsilon_s^p} = \frac{9\left(M-\eta\right)}{9+3M-2\eta^*M} + \left(\frac{B}{p}\right)\left[\frac{\chi+\mu\left(M-\eta^*\right)}{9+3M-2\eta^*M}\right] \quad (2:66)$$

(c) For elastic volumetric strain increment:

$$d\varepsilon_v^e = \frac{\kappa}{1+e_i}\left(\frac{dp}{p}\right) \quad (2:67)$$

where:

η is the stress ratio: $\eta=q/p$;
q is the deviatoric stress: $q=\sigma_1-\sigma_3$;
p is the mean stress: $p=(\sigma_1+2\sigma_3)/3$;
ε_s^p is the plastic component of the distortional strain: $d\varepsilon_s^p = (d\varepsilon_s - d\varepsilon_s^e)$;
ε_s is the distortional strain: $\varepsilon_s = 2(\varepsilon_1 - \varepsilon_3)/3$;
ε_s^e is the elastic component of the distortional strain: $d\varepsilon_s^e = dq/(2G)$;
G is the elastic shear modulus;
ε_v^p is the plastic component of the volumetric strain: $d\varepsilon_v^p = (d\varepsilon_v - d\varepsilon_v^e)$;
ε_v^e is the elastic component of the volumetric strain;
ε_v is the volumetric strain: $\varepsilon_v = (\varepsilon_1+2\varepsilon_3)$;
M is the critical state friction ratio in compression: $M=(6\sin\phi_f)/(3-\sin\phi_f)$;
$\eta^* = \eta(p/p_{cs})$;
e_i is the initial void ratio at the start of shearing;
κ is the slope of the swelling-recompression line in the void ratio e – ln p plot;
p_{cs} is the value of p on the critical state line at the current void ratio, calculated in a plot [void ratio e] – [ln p]: $p_{cs} = \exp[(\Gamma - e)/\lambda_{cs}]$, (**Figure 2-40**);
λ_{cs}: slope of the critical state line in the space [void ratio e] – [ln p], (**Figure 2-40**);
Γ : void ratio (e) of the critical state line at p=1 in the space [void ratio e] – [ln p] , (**Figure 2-40**);
$p_{cs(i)}$ is the value of p_{cs} at the start of shearing;
$p_{(i)}$ is the value of p at the start of shearing;
p_0 is the value of p at the intersection of the initial stress ratio line with an imaginary undrained stress path passing through the current stress (p,q) point and the current (p_{cs}, Mp_{cs}) point corresponding to the current void ratio;
$p_{0(i)}$ is the initial value of p_0;

χ ; μ : material constants that define the rate of breakage. They are obtained from a plot [(dB_g / $d\varepsilon_s^p$) (ln ($p_{cs(i)}/p_{(i)}$))] vs. [M-η^*], whose relationship line may be described by this expression:

$$\left[\ln\left(p_{cs(i)} / p_{(i)}\right)\right]\left(\frac{dB_g}{d\varepsilon_s^p}\right) = \chi + \mu\left[M - \eta^*\right] \tag{2:68}$$

[(dB_g / $d\varepsilon_s^p$) (ln ($p_{cs(i)}/p_{(i)}$))], term from the left part of the last equation represents the rate of particle breakage and can be obtained from the adjusted curve in a plot [B_g (ln ($p_{cs(i)}/p_{(i)}$))] vs. ε_s^p]. θ and ν are material constants relating to the breakage of aggregates and are obtained from this curve:

$$B_g\left[\ln\left(p_{cs(i)} / p_{(i)}\right)\right] = \theta\left[1 - \exp\left(-\nu\varepsilon_s^p\right)\right] \tag{2:69}$$

α : constant relating to the initial stiffness of aggregates;
B : constant. It is calculated as follows:

$$B = \frac{\beta}{\ln\left(p_{cs(i)} / p_{(i)}\right)}\left[\frac{\left(9-3M\right)\left(6+4M\right)\right)}{6+M}\right] \tag{2:70}$$

β is the slope of a plot [$dE_B/d\varepsilon_1$] vs. [$dB_g/d\varepsilon_1$]: β = [$dE_B/d\varepsilon_1$] / [$dB_g/d\varepsilon_1$].

dE_B is the incremental energy spent on particle breakage per unit volume of aggregates during the incremental strain $d\varepsilon_1$. It is calculated from a back-analysis using this equation:

$$\frac{q}{p} = \frac{\left(1 - d\varepsilon_v / d\varepsilon_1\right)\tan^2\left(45 + \phi_f / 2\right) - 1}{\left[2/3 + 1/3\left(1 - d\varepsilon_v / d\varepsilon_1\right)\tan^2\left(45 + \phi_f / 2\right)\right]} + \frac{dE_B\left(1 + \sin\phi_f\right)}{pd\varepsilon_1\left[2/3 + 1/3\left(1 - d\varepsilon_v / d\varepsilon_1\right)\tan^2\left(45 + \phi_f / 2\right)\right]} \tag{2:71}$$

In summary, the model uses 11 parameters (M; λ_{cs}; Γ; κ; G; α; β; χ; μ; θ; ν) which can be evaluated using conventional drained triaxial tests with the measurement of particle breakage. **Figure 2-41** shows a comparison between the results of experimental data of drained triaxial shearing tests on crushed latite basalt performed by Indraratna and Salim (2001) and model predictions by Salim and Indraratna (2004).

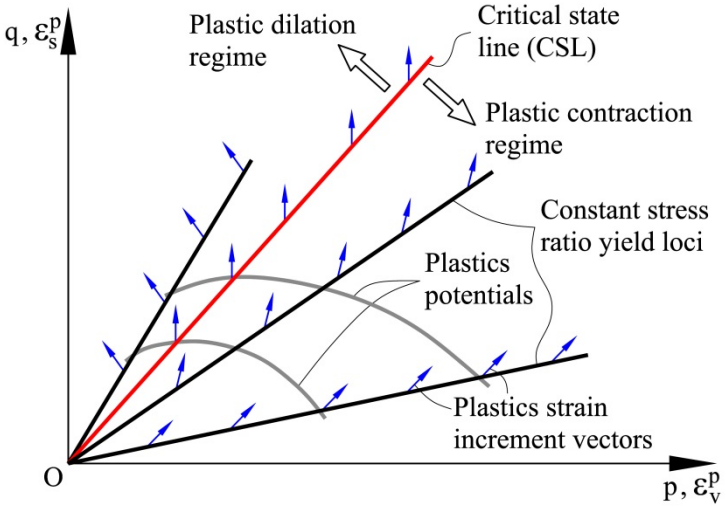

Figure 2-39 Critical state line in a space *p*-*q*, stress ratio yield loci, plastic potentials and plastic strain increment vectors (From Salim and Indraratna (2004)).

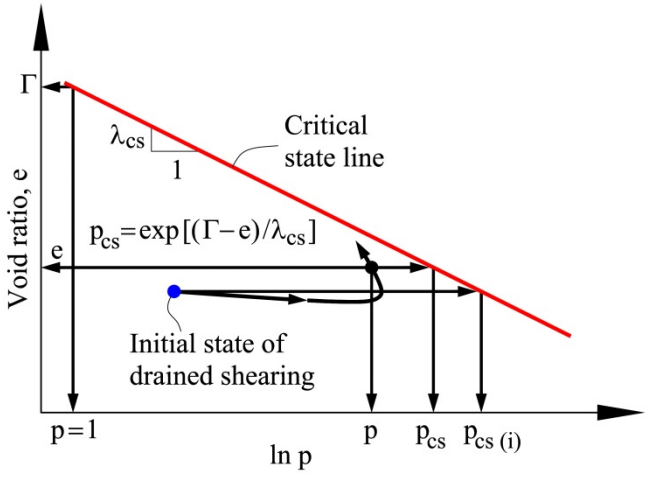

Figure 2-40 Critical state line in a space (void ratio (*e*) - ln *p*) and definition of p_{cs} in drained shearing (From Salim and Indraratna (2004)).

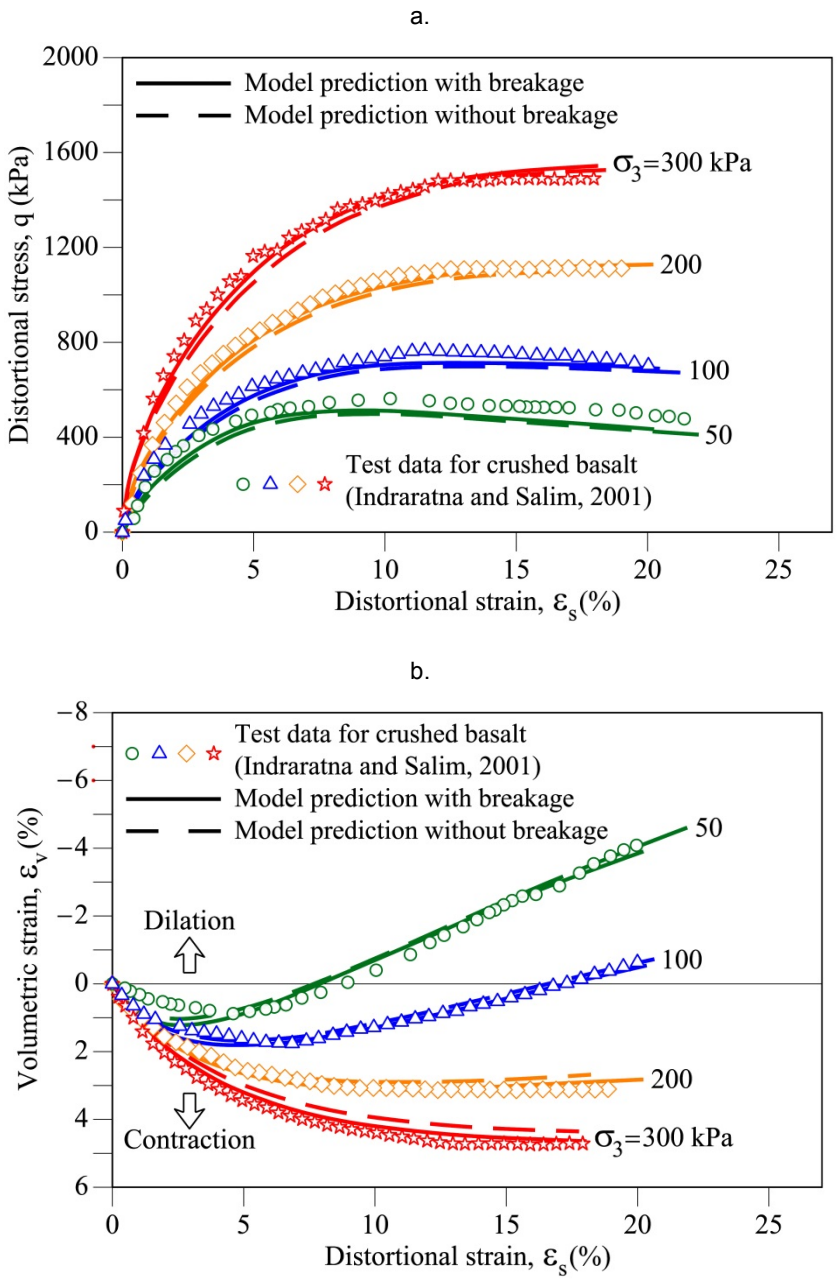

Figure 2-41 Triaxial shearing behaviour: (a) stress-strain; (b) Volume change behaviour. Comparison between experimental tests on crushed latite basalt (Indraratna and Salim, 2001) and model predictions (From Salim and Indraratna (2004)).

2.7.5 Hypoplastic modelling of moisture-sensitive weathered rockfill materials: Model of Bauer (2009)

This model is developed in a continuum approach and based on the hypoplasticity theory (Kolymbas, 1985), which was initially used in geotechnical engineering to describe the behaviour of sands (Bauer, 1996; Gudehus, 1996; Kolymbas, 1991; Niemunis and Herle, 1997; Wu et al., 1996) and continues to be generally used to model the behaviour of granular materials.

The model is applied to the rockfill material behaviour and takes into account the current void ratio, the effective stress, the strain rate and a moisture-dependent degradation of the solid hardness (h_{st}), which is a key parameter of the model.

This hypoplastic model is based on the following constitutive equations:

$$\overset{\circ}{\sigma}_{ij} = f_s\left[\hat{a}^2\dot{\varepsilon}_{ij} + \left(\hat{\sigma}_{kl}\dot{\varepsilon}_{kl}\right)\hat{\sigma}_{ij} + f_d\hat{a}\left(\hat{\sigma}_{ij} + \hat{\sigma}^*_{ij}\right)\sqrt{\dot{\varepsilon}_{kl}\dot{\varepsilon}_{kl}}\right] + \frac{\dot{h}_{st}}{h_{st}}\left(\frac{1}{3}\sigma_{kk}\delta_{ij} + \kappa\sigma^*_{ij}\right) \quad (2:72)$$

$$\dot{h}_{st} = h_{so}\dot{\psi}_t \quad (2:73)$$

$$\dot{\psi}_t = -\frac{1}{c}\left(\psi_t - \psi_w\right) \quad (2:74)$$

$$\dot{e} = \left(1+e\right)\dot{\varepsilon}_v \quad (2:75)$$

where:

$\overset{\circ}{\sigma}_{ij}$: effective stress rate;

σ_{ij} : effective Cauchy stress;

$\sigma^*_{ij} = \sigma_{ij} - \sigma_{kk}\,\delta_{ij}/3$: deviatoric part;

$\hat{\sigma}_{ij} = \sigma_{ij} / \sigma_{kk}$: normalized quantity;

$\hat{\sigma}^*_{ij} = \hat{\sigma}_{ij} - \delta_{ij}/3$: normalized quantity;

δ_{ij} : Kronecker delta ($\delta_{ij}=1$ if $i=j$; and $\delta_{ij}=0$ if $i \neq j$);

$\dot{\varepsilon}_{ij}$: strain rate;

$\dot{e}$: rate of void ratio;

$\dot{\varepsilon}_v = \dot{\varepsilon}_{kk}$: volumetric strain rate;

κ : parameter that controls the intensity of the creep velocity or the stress relaxation velocity. $\kappa = 0$ or 1;

$\dot{\psi}_t$: rate of the disintegration factor for a given time t. For the final state ($t \to \infty$): $\dot{\psi}_t = 0$;

ψ_t : disintegration factor for a given time t. ψ_t =1 for the initial state of the material, and ψ_t (t→∞) = ψ_w for the final state;

ψ_w : disintegration factor for the final state which depends on a given relative moisture content *w*; $\psi_w = h_{sw}/h_{so}$;

$\dot{h}_{st}$: rate of solid hardness;

h_{st} : Solid hardness (**Figure 2-42**) which decreases exponentially from the initial value h_{so} to the final value h_{sw} with an increase of the degradation parameter t/c:

$$h_{st} = h_{sw} + \left(h_{so} - h_{sw}\right)\exp\left[-t/c\right] \tag{2:76}$$

t : time;
c : constitutive constant of the model which has the dimension of time and scales the velocity of degradation;
h_{so} : Solid hardness (upper limit) at the initial dry state of the material (**Figure 2-42**);
h_{sw} : Final solid hardness after wetting, h_{st} (t→∞) (**Figure 2-42**);
$\hat{a}$: a function related to the critical stress state which can be reached asymptotically under large shearing. For this hypoplastic model, it can be calculated as follows:

$$\hat{a} = \frac{\sin\varphi_c}{3+\sin\varphi_c}\left[\sqrt{\frac{8/3 - 3\left(\hat{\sigma}^*_{kl}\hat{\sigma}^*_{kl}\right) + g\sqrt{3/2}\left(\hat{\sigma}^*_{kl}\hat{\sigma}^*_{kl}\right)^{3/2}}{1+g\sqrt{3/2}\left(\hat{\sigma}^*_{kl}\hat{\sigma}^*_{kl}\right)^{1/2}}} + \sqrt{\hat{\sigma}^*_{kl}\hat{\sigma}^*_{kl}}\right] \tag{2:77}$$

$$g = -\sqrt{6}\,\frac{\hat{\sigma}^*_{kl}\hat{\sigma}^*_{lm}\hat{\sigma}^*_{mk}}{\left(\hat{\sigma}^*_{pq}\hat{\sigma}^*_{pq}\right)^{3/2}} \tag{2:78}$$

φ_c : Intergranular friction angle for the critical state under triaxial compression;

For the critical state: $\overset{\circ}{\sigma}_{ij}$ =0 ; $\dot{\varepsilon}_v$ =0 ; $\dot{h}_{st}$ =0 ; $\hat{a} = \hat{a}_c$, and it is equal to Euclidian norm of the normalized stress deviator as shown in **Figure 2-43**.

f_d : density factor which relates the current void ratio *e*, the critical void ratio e_c, and the minimum void ratio e_d. It can be calculated as follows:

$$f_d = \left(\frac{e - e_d}{e_c - e_d}\right)^{\alpha} \tag{2:79}$$

α : constitutive constant; $\alpha < 0.5$;
f_s : stiffness factor which has the dimension of stress. f_s and f_d take into account the influence of the mean effective pressure and the current void ratio on the response of the constitutive equation. This stiffness factor can be calculated as follows:

$$f_s = \left(\frac{e_i}{e}\right)^{\beta} \frac{(1+e_i)}{n h_i e_i} \left(\frac{h_{st}}{3}\right)^{n} \frac{p^{(1-n)}}{\left(\hat{\sigma}^*_{kl}\hat{\sigma}^*_{kl}\right)} \qquad (2:80)$$

β ; n : constitutive constants;
e_i : maximum void ratio. **Figure 2-44** illustrates the compressibility curves for the maximum void ratio e_i, minimum void ratio e_d and critical void ratio e_c in relation to the mean stress p. The current void ratio e, and the other void ratios are related by the following equation:

$$\frac{e_i}{e_{i0}} = \frac{e_d}{e_{d0}} = \frac{e_c}{e_{c0}} = \exp\left[-\left(\frac{3p}{h_{st}}\right)^{n}\right] \qquad (2:81)$$

In summary, this hypoplastic model includes 11 constants (φ_c ; h_{so}; n; e_{i0}; e_{c0}; e_{d0}; α; β; h_{sw}; κ; c) which can evaluated from isotropic and triaxial compression tests. **Figure 2-45** compares some results obtained by Bauer (2009) from experimental triaxial tests and the model.

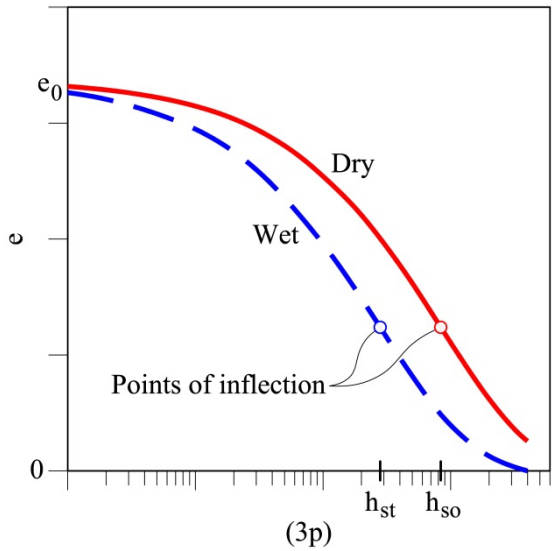

Figure 2-42 Compressibility curve in a space e-log (3p): Isotropic compression. Calculation of solid hardness h_s for dry and wet conditions. (From Bauer (2009)).

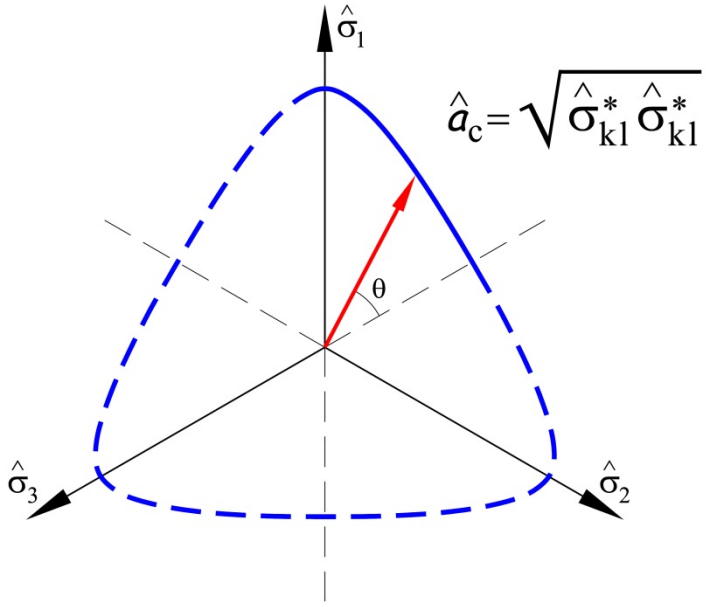

Figure 2-43 Critical stress state surface in the π-plane. (From Bauer (2009)).

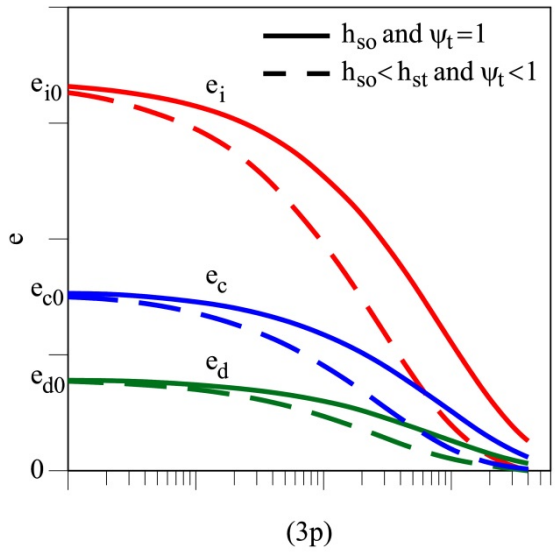

Figure 2-44 Compressibility curve in a space *e*-log (3*p*). Influence of the degradation of the solid hardness h_s on the limit void ratios. Solid curves are related to h_{so} and ψ_t =1; dashed curves are related to $h_{st} < h_{so}$ and $\psi_t < 1$. (From Bauer (2009)).

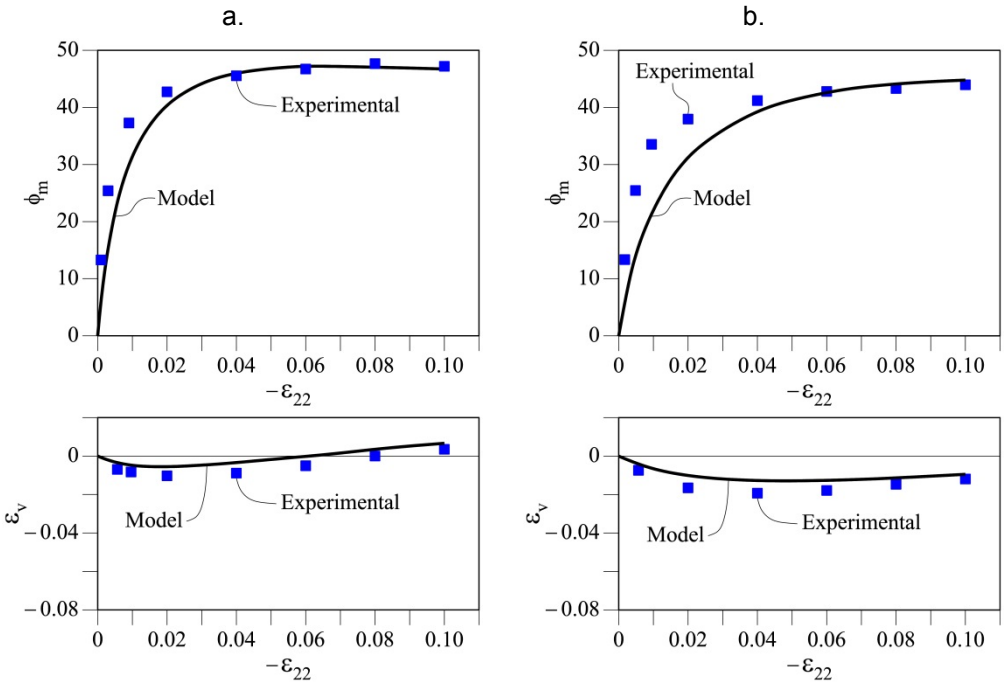

Figure 2-45 Triaxial compression behaviour under a constant mean pressure (p=0.8MPa) from an initial void ratio of: (a) e_o = 0.29 for dry state (ψ=1); (b) e_o = 0.285 for saturated state (ψ=0.34). Comparison between experimental results of weathered broken granite (dots) and model (solid curve). ϕ_m=mobilized friction angle; ε_v=volumetric strain; ε_{22}=vertical strain. (From Bauer (2009)).

2.7.6 Hyperbolic models applied to a rockfill dam: Models of LNEC of Lisbon and Swansea (Naylor et al., 1997, 1986)

These hypo-elastic models can be approximated as linear isotropic elastic over small increments of load. They were developed by the Laboratório Nacional de Engenharia Civil (LNEC) in Lisbon (Portugal) and the University College of Swansea (UK) and applied to simulate the behaviour of Beliche dam (Portugal). The models were based on the experimental research using large triaxial and oedometer equipment (**Table 2-1**) developed by the LNEC (Veiga Pinto, 1983) on scaled rockfill materials (hard greywacke and soft schist) of the dam, which is comprised of central clay and rockfill shells. The numerical simulations are based on finite element analyses. These models were compared and used to make predictions of the end of the construction performance (Naylor et al., 1986) and a back-analyses study (Naylor et al., 1997).

2.7.6.1 LNEC models: Hyperbolic model and EC-K_0 model

Hyperbolic model

In this model, the curve of deviator stress (σ_1-σ_3) – axial strain (ε_1) is approximated

by a hyperbola (Kondner, 1963). Likewise, the constitutive law is based on Duncan and Chang (1970) and can be expressed by the following equations:

$$E_t = Kp_a \left(\frac{\sigma_3}{p_{atm}} \right)^n X^2 \tag{2:82}$$

$$X = \left| 1 - \frac{R_f \left(\sigma_1 - \sigma_3 \right) \left(1 - \sin \phi \right)}{2\sigma_3 \sin \phi + 2 \cos \phi} \right| \tag{2:83}$$

$$\nu_t = \frac{G - F \log \left(\sigma_3 / p_{atm} \right)}{\left[1 - D \left(\sigma_1 - \sigma_3 \right) / Kp_a \left(\sigma_3 / p_{atm} \right)^n X \right]^2} \tag{2:84}$$

where:
E_t : tangential Young's modulus which is defined by the slope of the curve (σ_1-σ_3) vs. ε_1, for σ_3 constant, based on triaxial tests;
p_{atm} : atmospheric pressure,
c, ϕ : Mohr-Coulomb strength parameters
R_f : Reduction factor (model parameter)
K ; n : Constants to be determined experimentally
ν_t : Poisson ratio with is defined by the hyperbolic relationship between axial strain ε_1 and radial strain ε_3 for the shear stage of the triaxial test.
G ; F ; D : Parameters to be determined experimentally

For the failure envelope:

$$\phi = \phi_0 - \Delta\phi \log \left(\frac{\sigma_3}{p_{atm}} \right) \tag{2:85}$$

In summary, the model requires 8 parameters (without the unloading stage): K, c, ϕ, R_f, n, G, F and D. In addition, p_{atm} is a nominal atmospheric pressure.

EC-K_0 model

This model is proposed for materials subjected to similar conditions to one-dimensional tests. Parameters are calibrated from oedometer tests (lateral strain =0). The formulation was proposed by Veiga Pinto (1983). The model assumes the following relation between the vertical stress (σ_1) and strain (ε_1):

$$\sigma_1 = A_e p_{atm} \varepsilon_1^{B_e} \tag{2:86}$$

where p_{atm} is the atmospheric pressure; A_e and B_e are dimensionless constants to be found from the tests.

The following equations comprised the constitutive laws of the model:

$$E_c = \frac{d\sigma_1}{d\varepsilon_1} = A_e B_e p_{atm} \left(\frac{\sigma_1}{A_e p_{atm}} \right)^{(B_e - 1)/B_e} \quad (2:87)$$

$$K_0^t = \frac{d\sigma_3}{d\sigma_1} = A_0 + 2B_0 \frac{\sigma_1}{p_{atm}} \quad (2:88)$$

$$\nu_t = \frac{K_0^t}{1 + K_0^t} \quad (2:89)$$

$$E_t = \frac{(1+\nu_t)(1-2\nu_t)}{1-\nu_t} E_c \quad (2:90)$$

Where:
E_c : vertical constraint tangential modulus;
K_0^t : tangential K0 which is defined as $K_0 = \sigma_3 / \sigma_1$;
ν_t : tangential Poisson's ratio;
E_t : tangential Young modulus;
A_e ; B_e ; A_0 ; B_0 : Model parameters (dimensionless)

In summary, the model requires 4 parameters (without the unloading stage): A_e; B_e; A_0; B_0.

2.7.6.2 Swansea model: K-G model

Considering the plane strain analysis, the model assumes linear functions to relate the tangential bulk and shear moduli to the mean and deviatoric stress, respectively, as follows:

$$\bar{K} = \bar{K}_1 + \bar{\alpha}_K \sigma_s \quad (2:91)$$

$$G = G_1 + \alpha_G \sigma_s + \beta_G \sigma_d \quad (2:92)$$

where:
$\bar{K}$:plane strain bulk modulus which is also related to the conventional tangential bulk modulus K: $\bar{K} = K + G/3$;
G : tangential shear modulus;
σ_s : mean stress. $\sigma_s = (\sigma_1 + \sigma_3)/2$;
σ_d : deviatoric stress. $\sigma_d = (\sigma_1 - \sigma_3)/2$;
$\bar{K}_1$; G_1 ; $\bar{\alpha}_K$; α_G ; β_G : Material parameters of the model to be found experimentally.

The yield condition which is assumed when the stress state causes G to approach zero (G=0) and the Mohr Coulomb criterion are considered. Therefore, the

following equations are obtained:

$$\frac{\alpha_G}{-\beta_G} = 2\sin\phi \tag{2:93}$$

$$\frac{G_1}{-\beta_G} = 2c\cos\phi \tag{2:94}$$

where c and ϕ are the Mohr-Coulomb strength parameters.

In summary, the model requires 5 parameters (without the unloading stage): $\bar{K}_1$; G_1; $\bar{\alpha}_K$; α_G; β_G.

2.8 Conclusions

Particle breakage is a major cause of the deformation of the coarse aggregates (at common engineering stresses) because after the breakage a subsequent rearrangement of the granular mass occurs.

Rockfill/Gravel behaviour is dominated by particle breakage which is a consequence of the high concentrated loads acting at particle contacts. This phenomenon is significant at stresses prevailing in common engineering structures (embankments, dams).

The breakage is evidenced by the evolution of the grain size distribution (gsd) curve after both oedometer and triaxial tests. Isotropic and deviatoric stresses induce particle breakage. Volumetric and deviatoric hardening is expected.

Shear strength decreases with increasing particle breakage. Furthermore, the peak friction angle decreases as the breakage increases.

The particle breakage can be influenced by the humidity conditions and the particle size. Furthermore, it can be delayed in time.

The influence of the presence of water is evidenced both in field and in laboratory: In field, larger civil structures such as rockfill dams or embankments present considerable settlements due to collapse deformations during the reservoir impoundment and also after rainfall. In laboratory oedometer tests, coarse aggregates (i.e. gravels) present collapse in the volumetric strain when dry specimens are saturated, for example by flooding the samples or imposing 100% of Relative Humidity (RH): liquid water and water vapour have the same effect on the specimen.

In oedometer tests on coarse aggregates, higher compressibility is obtained for higher values of Relative Humidity or saturated specimens.

In triaxial tests (under controlled deformation), dry specimens experience collapse

in the deviatoric stress when they are saturated. If the test is resumed, the deviatoric stresses try to reach the strength of the tested specimens with saturated conditions from the beginning of the test.

In triaxial tests on coarse aggregates, higher strength is obtained for dry specimens than for saturated.

The strength enveloped is nonlinear for rockfill and gravels.

Critical states are difficult to find because dilatancy is significant at the maximum deviatoric strains of triaxial tests.

Time-dependent behaviour is also observed both in field and in laboratory: In field, settlements in larger civil structures such as rockfill dams or embankments have been recorded from the early stage of the construction until many years after the construction. In laboratory oedometer tests on coarse aggregates, delayed vertical strain also occurs when a specimen is subjected to a vertical load over time.

The breakage of particles can be explained by the crack propagation theory and the subcritical crack propagation theory. Subcritical crack propagation can be explained by the stress corrosion phenomenon which can occur at the crack tip. This phenomenon explains the effect of the liquid water or the water vapour (corrosive agent) and the hydrolysis process in the creation of weak links of hydroxyl groups that cause the decrease in the local toughness and lead to the crack propagation.

From one-directional compression tests on singular rock fragments, it has been evidenced that tensile strength in a particle decreases when the particle size increases. This size effect can be demonstrated by analytical solutions from fracture mechanics or the Weibull statistical approach.

Higher particles can have more inner flaws or defects and therefore they can have a higher probability of disintegrating and breaking than smaller particles.

The UPC has developed systematic research on unsaturated rockfill/gravel behaviour for the last fifteen years. Larger equipment for oedometer and triaxial tests with controlled suction have been built, and some constitutive models (compressibility and triaxial behaviour) for a continuum media based on experimental results have been proposed.

Plastic strains are very important in both oedometric and isotropic conditions. A cap yield was proposed in the UPC critical state model.

McDowell & Bolton model explains the linearity of the “normal compression line” from a micro-mechanical perspective.

Salim & Indraratna model takes into account particle breakage in a noncapped critical state model in a continuum media.

Bauer model based on the hypoplastic theory takes into account curves of void ratio evolution.

LNEC and Swansea models are based on hyperbolic models and explain the behaviour under one-dimensional compression and triaxial conditions. Mohr-Coulomb parameters are used in these models.

In summary, there are four key features in the rockfill and gravel behaviour based on both the behaviour of larger structures (dams and embankments) and laboratory experimental tests: Particle breakage during the process of deformation, scale or size effect, time-dependent effect and the influence of environmental conditions (water effect).

2.9 List of Notations

Notation		***Section***
A_e	Dimensionless constant; (LNEC EC-K_0 model, 1997; 1986); Eq. (2:86); (2:87)	2.7.6.1
A_0	Dimensionless constant; (LNEC EC-K_0 model, 1997; 1986); Eq. (2:88)	2.7.6.1
a	(1) Half-length of a crack inside a particle; Eq. (2:18) - (2:20)	(1) 2.5.4
	(2) Model parameter (triaxial tests): (model of Chávez and Alonso, 2003); Eq. (2:45)	(2) 2.7.2.2
$\hat{a}$	Function related to critical stress state; (model of Bauer, 2009); Eq. (2:72); (2:77)	2.7.5
$a(H_2O)$	Activity of the water; Eq. (2:6)	2.4.3
B	(1) Constant of the model (maximum value of parameter b); (triaxial tests): (model of Chávez and Alonso, 2003); Eq. (2:46)	(1) 2.7.2.2
	(2) Constant of the model; (model of Salim and Indraratna, 2004); Eq. (2:65); (2:66); (2:70)	(2) 2.7.4
B_e	Dimensionless constant; (LNEC EC-K_0 model, 1997; 1986); Eq. (2:86); (2:87)	2.7.6.1
B_g	Marsal breakage index	2.7.2.1 ; 2.7.4.2
B_r	Hardin breakage index	2.7.2.1
B_0	Dimensionless constant; (LNEC EC-K_0 model, 1997; 1986); Eq. (2:88)	2.7.6.1
b	(1) Material constant in some relationships	(1) 2.4.3

	that describe the subcritical crack propagation; Eq. (2:5) - (2:6)	
	(2) Constant in the relationship between tensile strength (σ_f) and the particle size (d); Eq. (2:10)	(2) 2.5.2
	(3) Parameter linked to the initial stiffness (triaxial tests): (model of Chávez and Alonso, 2003); Eq. (2:38); (2:46)	(3) 2.7.2.2
C	(1) Reference velocity – Charles's law; Eq. (2:2)	2.4.3;
	(2) Scaling parameter; Eq. (2:16) - (2:17)	2.5.3
C_{FM}	Scaling parameter; Eq. (2:21) - (2:22)	2.5.4
c	(1) Constant of the model (triaxial tests): (model of Chávez and Alonso, 2003); Eq. (2:46)	(1) 2.7.2.2
	(2) Constitutive constant; (model of Bauer, 2009); Eq. (2:76)	(2) 2.7.5
	(3) Mohr-Coulomb strength parameter; (LNEC Hyperbolic model, 1997; 1986)	(3) 2.7.6.1
	(4) Mohr-Coulomb strength parameter; Eq. (2:94)	(4) 2.7.6.2
D	Parameter of the model; (LNEC Hyperbolic model, 1997; 1986); Eq. (2:84)	2.7.6.1
D_s	Surface fractal dimension (model of McDowell and Bolton, 1998)	2.7.3
d	(1) Diameter of grain; Particle size ; Eq. (2:9) - (2:10); Eq. (2:14) - (2:16); Eq. (2:20) - (2:21)	(1) 2.5.2; 2.5.3; 2.5.4
	(2) Particle size (model of McDowell and Bolton, 1998); Eq. (2:60) - (2:61)	(2) 2.7.3
d_m	Average size of particle in the failure plane; Eq. (2:8)	2.5.2
dE_B	Incremental energy spent on particle breakage per unit volume of aggregates; (model of Salim and Indraratna, 2004); Eq. (2:71)	2.7.4
dE_{bi}	Amount of energy spent on particle breakage during the displacement du_i; (model of Salim	2.7.4

	and Indraratna, 2004); Eq. (2:64)	
dS	Increase in surface area of a volume V_s (model of McDowell and Bolton, 1998); Eq. (2:55) - (2:58)	2.7.3
du_i	Displacement; (model of Salim and Indraratna, 2004); Eq. (2:64)	2.7.4
dx_i	Horizontal component of du_i; (model of Salim and Indraratna, 2004); Eq. (2:64)	2.7.4
dy_i	Vertical component of du_i; (model of Salim and Indraratna, 2004); Eq. (2:64)	2.7.4
d_0	(1) Size of particle which is subjected to σ_0 mean tensile stress; Eq. (2:14) - (2:17)	(1) 2.5.3
	(2) Particle size (model of McDowell and Bolton, 1998); Eq. (2:59)	(2) 2.7.3
d_1	Size of particle which is subjected to σ_1 tensile stress; Eq. (2:14) - (2:17)	2.5.3
E	Activation Energy – modified Charles's law; Eq. (2:6)	2.4.3
E_c	Vertical constraint tangential modulus; (LNEC EC-K_0 model, 1997; 1986); Eq. (2:87); (2:90)	2.7.6.1
E_t	(1) Tangential Young's modulus; (LNEC Hyperbolic model, 1997; 1986); Eq. (2:82)	(1) 2.7.6.1
	(2) Tangential Young modulus; (LNEC EC-K_0 model, 1997; 1986); Eq. (2:90)	(2) 2.7.6.1
e	(1) Void ratio	(1) 2.7
	(2) Current void ratio (Triaxial tests) : (model of Chávez and Alonso, 2003); Eq. (2:52)	(2) 2.7.2.2
	(3) Current void ratio; (model of Bauer, 2009); Eq. (2:75); (2:79); (2:80)	(3) 2.7.5
$\dot{e}$	Rate of void ratio; (model of Bauer, 2009); Eq. (2:75)	2.7.5
e_c	Critical void ratio; (model of Bauer, 2009); Eq. (2:79); (2:81)	2.7.5
e_{cr}	Void ratio at critical state; obtained from ν_{cr} (Triaxial tests) : (model of Chávez and Alonso, 2003); Eq. (2:52)	2.7.2.2

e_d	Minimum void ratio; (model of Bauer, 2009); Eq. (2:79); (2:81)	2.7.5
e_i	(1) Initial void ratio at the start of shearing; (model of Salim and Indraratna, 2004); Eq. (2:65); (2:67)	(1) 2.7.4
	(2) Maximum void ratio; (model of Bauer, 2009); Eq. (2:80); (2:81)	(2) 2.7.5
e_0	Initial void ratio	2.7
F	Parameter of the model; (LNEC Hyperbolic model, 1997; 1986); Eq. (2:84)	2.7.6.1
F_f	Maximum load that causes the catastrophic failure; Eq. (2:9)	2.5.2
F_{1i}	Vertical force at contact *i*; (model of Salim and Indraratna, 2004); Eq. (2:64)	2.7.4
F_{3i}	Lateral force at contact *i*; (model of Salim and Indraratna, 2004); Eq. (2:64)	2.7.4
f_d	Density factor; (model of Bauer, 2009); Eq. (2:72); (2:79)	2.7.5
f_s	Stiffness factor; (model of Bauer, 2009); Eq. (2:72); (2:80)	2.7.5
G	(1) Parameter of the model; (LNEC Hyperbolic model, 1997; 1986); Eq. (2:84)	(1) 2.7.6.1
	(2) Tangential shear modulus; (Swansea K-G model, 1997; 1986); Eq. (2:91); (2:92)	(2) 2.7.6.2
G_c	Critical strain energy release rate (model of McDowell and Bolton, 1998)	2.7.3
G_1	Material parameter of the model; (Swansea K-G model, 1997; 1986); Eq. (2:92); (2:94)	2.7.6.2
g	Function of stresses; (model of Bauer, 2009); Eq. (2:77); (2:78)	2.7.5
gsd	Grain size distribution	2.2.1
H	Activation enthalpy – Charles's law; Eq. (2:2) - (2:5)	2.4.3
h_{so}	Solid hardness (upper limit) at the initial dry state; (model of Bauer, 2009); Eq. (2:73); (2:76)	2.7.5
h_{st}	Solid hardness; (model of Bauer, 2009); Eq. (2:76); (2:80); (2:81)	2.7.5

$\dot{h}_{st}$	Rate of solid hardness; (model of Bauer, 2009); Eq. (2:73)	2.7.5
h_{sw}	Final solid hardness after wetting; (model of Bauer, 2009); Eq. (2:76)	2.7.5
IDM	Instantaneous deformation mechanism	2.7.1.2
K	(1) Stress intensity factor; Eq. (2:6) - (2:7); Eq. (2:18)	(1) 2.4.3; 2.5.4
	(2) Constant of the model; (LNEC Hyperbolic model, 1997; 1986); Eq. (2:82); (2:84)	(2) 2.7.6.1
	(3) Tangential bulk modulus; (Swansea K-G model, 1997; 1986); Eq. (2:91)	(3) 2.7.6.2
$\overline{K}$	Plane strain bulk modulus; (Swansea K-G model, 1997; 1986); Eq. (2:91)	2.7.6.2
K_c	Toughness; Eq. (2:7); Eq. (2:19) - (2:22)	2.4.3; 2.5.4
K_I	Stress intensity factor (Mode I); Eq. (2:4) - (2:5)	2.4.3
K_{Ic}	Toughness value for mode I (model of McDowell and Bolton, 1998)	2.7.3
K_0	Lateral/axial effective stress ratio (model of McDowell and Bolton, 1998); Eq. (2:56)	2.7.3
K_0^t	Tangential K_0; (LNEC EC-K_0 model, 1997; 1986); Eq. (2:88); (2:89)	2.7.6.1
$\overline{K}_1$	Material parameter of the model; (Swansea K-G model, 1997; 1986); Eq. (2:91)	2.7.6.2
k	Constant of the model (triaxial tests): (model of Chávez and Alonso, 2003); Eq. (2:39)	2.7.2.2
k_s	Constant of the model (triaxial tests): (model of Chávez and Alonso, 2003); Eq. (2:44)	2.7.2.2
M	(1) Critical state stress ratio - Cam clay coefficient (model of McDowell and Bolton, 1998); Eq. (2:55); (2:56)	(1) 2.7.3
	(2) Critical stress friction ratio; (model of Salim and Indraratna, 2004); Eq. (2:63); (2:65); (2:66); (2:68)	(2) 2.7.4
$M_c(W_E^P, \psi)$	Critical state stress ratio (triaxial tests): (model of Chávez and Alonso, 2003); Eq. (2:38); (2:44)	2.7.2.2
$M_{cr}(W_E^P)$	Critical state stress ratio in relation to W_E^P	2.7.2.2

	(triaxial tests): (model of Chávez and Alonso, 2003); Eq. (2:44); (2:45)	
M_{cres}	Constant of the model (residual stress ratio for unsaturated conditions); (triaxial tests): (model of Chávez and Alonso, 2003); Eq. (2:45)	2.7.2.2
M_{c0}	Constant of the model (triaxial tests): (model of Chávez and Alonso, 2003); Eq. (2:45)	2.7.2.2
$M(d)$	Volume of a particle of size d (model of McDowell and Bolton, 1998); Eq. (2:61)	2.7.3
m	Weibull modulus; Eq. (2:11) - (2:17)	2.5.3
m_{cr}	Constant of the model (triaxial tests): (model of Chávez and Alonso, 2003); Eq. (2:40)	2.7.2.2
N_i	Normal force; (model of Salim and Indraratna, 2004); Eq. (2:64)	2.7.4
n	(1) Stress corrosion or subcritical crack growth index – Charles's law; Eq. (2:2) ; Eq (2:7)	(1) 2.4.3
	(2) Constitutive constants; (model of Bauer, 2009); Eq. (2:80)	(2) 2.7.5
	(3) Constant of the model; (LNEC Hyperbolic model, 1997; 1986); Eq. (2:82); (2:84)	(3) 2.7.6.1
n_d	Constant; Eq. (2:14) - (2:17)	2.5.3
P_a	Rupture load; Eq. (2:8)	2.5.2
$P_{survival}$	Survival probability; Eq. (2:11) - (2:12); Eq. (2:14)	2.5.3
p	Mean stress = $[(\sigma_1+2\ \sigma_3)/3]$; (Triaxial tests)	2.7
p^*	Hardening parameter; yield mean stress for a very dry rockfill (Triaxial tests) : (model of Chávez and Alonso, 2003); Eq. (2:47); (2:48); (2:50)	2.7.2.2
p_{atm}	Atmospheric pressure	2.7.1.2; 2.7.2.2; 2.7.6.1
p_{cs}	Value of p at the critical state line; (model of Salim and Indraratna, 2004); Eq. (2:63); (2:65)	2.7.4

$p_{cs(i)}$	Value of p_{cs} at the start of shearing; (model of Salim and Indraratna, 2004); Eq. (2:65); (2:68) - (2:70)	2.7.4
p_y	Threshold yield mean stress; (Triaxial tests) : (model of Chávez and Alonso, 2003); Eq. (2:47); (2:48)	2.7.2.2
p_0	Intercept of the stress path on p axis; (model of Salim and Indraratna, 2004); Eq. (2:63); (2:65)	2.7.4
$p_{0(i)}$	Initial value of p_0; (model of Salim and Indraratna, 2004); Eq. (2:65)	2.7.4
$p_{(i)}$	Value of p at the start of shearing; (model of Salim and Indraratna, 2004); Eq. (2:68) - (2:70)	2.7.4
Q_p	Plastic potential for isotropic stage (Triaxial tests) : (model of Chávez and Alonso, 2003); Eq. (2:54)	2.7.2.2
Q_q	Plastic potential for deviatoric stage (Triaxial tests) : (model of Chávez and Alonso, 2003); Eq. (2:51)	2.7.2.2
q	Deviatoric stress = $[\sigma_1-\sigma_3]$; (Triaxial tests)	2.7
R	Gas constant ; Eq. (2:2) - (2:6)	2.4.3
R_f	Reduction factor; (LNEC Hyperbolic model, 1997; 1986); Eq. (2:83)	2.7.6.1
RH	Relative Humidity	2.2; 2.4; 2.7.1; 2.7.2
r	Parameter that depends on the distance between ν_{cr} and ν (triaxial tests): (model of Chávez and Alonso, 2003) ; Eq. (2:38); (2:39)	2.7.2.2
r_c	Radius of curvature of the crack tip; Eq. (2:4)	2.4.3
$S(d)$	Surface area of a particle of size d (model of McDowell and Bolton, 1998); Eq. (2:60)	2.7.3
S_1	Proportion of d size; Eq. (2:20); (2:22)	2.5.4
T	Absolute temperature; Eq. (2:2) - (2:6)	2.4.3
TDM	Time-dependent deformation mechanism	2.7.1.2
t	(1) Time	(1) 2.7

	(2) Time; (model of Bauer, 2009); Eq. (2:76)	(2) 2.7.5
V	Volume; Eq. (2:11)	2.5.3
V_s	Volume of solids (model of McDowell and Bolton, 1998); Eq. (2:55) - (2:58)	2.7.3
V_0	Reference volume; Eq. (2:11) - (2:13)	2.5.3
V_1	Volume under tensile stress σ_1; Eq. (2:13)	2.5.3
V^*	Activation volume; Eq. (2:4)	2.4.3
v	Velocity of crack propagation – modified Charles's law; Eq. (2:4) - (2:7)	2.4.3
v_x	Velocity of crack propagation or penetration velocity of crack tip in the x direction	2.4.3
v_0	Reference velocity – modified Charles's law; Eq. (2:4) - (2:7)	2.4.3
W^P	Plastic work (triaxial tests): (model of Chávez and Alonso, 2003)	2.7.2.2
W_E^P	"Effective" plastic work (triaxial tests): (model of Chávez and Alonso, 2003) ; Eq. (2:38); Eq. (2:42); Eq. (2:45)	2.7.2.2
W_R^P	Plastic work associated with particle rearrangement (triaxial tests): (model of Chávez and Alonso, 2003) ; Eq. (2:42)	2.7.2.2
W_T^P	Total plastic work (triaxial tests): (model of Chávez and Alonso, 2003) ; Eq. (2:38); Eq. (2:43); Eq. (2:46)	2.7.2.2
w	Gravimetric humidity	2.7.1; 2.7.2
X	Function of strength; (LNEC Hyperbolic model, 1997; 1986); Eq. (2:82); (2:83)	2.7.6.1
x	Crack depth – Charles's law; Eq. (2:2)	2.4.3
x_{cr}	Crack depth for spontaneous rupture – Charles's law; Eq. (2:2)	2.4.3
y_0	Constant of the model (triaxial tests); (model of Chávez and Alonso, 2003); Eq. (2:41)	2.7.2.2
$y(\psi)$	Specific volume in relation to the suction (triaxial tests); (model of Chávez and Alonso, 2003); Eq. (2:40); (2:41)	2.7.2.2

α	(1) Constant model parameter (Triaxial tests): (model of Chávez and Alonso, 2003); Eq. (2:52)	(1) 2.7.2.2
	(2) Model constant relating to the initial stiffness of aggregates; (model of Salim and Indraratna, 2004); Eq. (2:65)	(2) 2.7.4
	(3) Constitutive constant; (model of Bauer, 2009); Eq. (2:79)	(3) 2.7.5
α_G	Material parameter of the model; (Swansea K-G model, 1997; 1986); Eq. (2:92); (2:93)	2.7.6.2
$\bar{\alpha}_K$	Material parameter of the model; (Swansea K-G model, 1997; 1986); Eq. (2:91)	2.7.6.2
α_s	Model parameter (Triaxial tests) : (model of Chávez and Alonso, 2003); Eq. (2:49)	2.7.2.2
α_y	Constant of the model (triaxial tests): (model of Chávez and Alonso, 2003); Eq. (2:41)	2.7.2.2
α_ψ	Model parameter (model of Oldecop and Alonso, 2001); Eq (2:25); (2:27)	2.7.1.2
β	(1) Dimensionless coefficient used in the calculation of the stress intensity factor; Eq. (2:18) - (2:22)	(1) 2.5.4
	(2) Model parameter; (model of Salim and Indraratna, 2004); Eq. (2:70)	(2) 2.7.4
	(3) Constitutive constants; (model of Bauer, 2009); Eq. (2:80)	(3) 2.7.5
β_G	Material parameter of the model; (Swansea K-G model, 1997; 1986); Eq. (2:92); (2:93); (2:94)	2.7.6.2
β_s	Surface shape factor (model of McDowell and Bolton, 1998); Eq. (2:59) - (2:60)	2.7.3
β_v	Volume shape factor for the material (model of McDowell and Bolton, 1998); Eq. (2:59); (2:61)	2.7.3
Γ	(1) Surface energy related to G_c (model of McDowell and Bolton, 1998); Eq. (2:55) - (2:59)	(1) 2.7.3
	(2) Void ratio (e) of the critical state line at p=1; (model of Salim and Indraratna, 2004);	(2) 2.7.4

	Figure 2-40	
δ_{ij}	Kronecker delta; (model of Bauer, 2009); Eq. (2:72)	2.7.5
ε	Strain	2.7
$\overline{\varepsilon}$	Axial strain (model of McDowell and Bolton, 1998); Eq. (2:56)	2.7.3
$\dot{\varepsilon}_{ij}$	Strain rate; (model of Bauer, 2009); Eq. (2:72)	2.7.5
$\dot{\varepsilon}_v$; $\dot{\varepsilon}_{kk}$	Volumetric strain rate; (model of Bauer, 2009); Eq. (2:75)	2.7.5
ε_a ; ε_1	Axial strain (Triaxial tests)	2.7
ε_3	Lateral strain (Triaxial tests)	2.7
ε_p ; ε_v	Volumetric strain = [$\varepsilon_1+2\varepsilon_3$]; (Triaxial tests)	2.7
ε_q ; ε_s	Deviatoric strain (Distorsional strain) = [$(2/3)*(\varepsilon_1-\varepsilon_3)$]; (Triaxial tests)	2.7
ε_q^e ; ε_s^e	Deviatoric elastic strain (Distorsional elastic strain); [$d\varepsilon_s^e = dq / (2G)$]; (Triaxial tests)	2.7
ε_q^p ; ε_s^p	Deviatoric plastic strain (Distorsional plastic strain); [$d\varepsilon_s^p = (d\varepsilon_s - d\varepsilon_s^e)$]; (Triaxial tests)	2.7
ε_p^e ; ε_v^e	Volumetric elastic strain; (Triaxial tests)	2.7
ε_p^p ; ε_v^p	Volumetric plastic strain; [$d\varepsilon_v^p = (d\varepsilon_v - d\varepsilon_v^e)$]; (Triaxial tests)	2.7
ε^e	(1) Elastic strain	(1) 2.7
	(2) Elastic strain due to stress increment (Oedometer tests): (model of Oldecop and Alonso, 2001); Eq. (2:28)	(2) 2.7.1.2
ε^p	(1) Plastic strain	(1) 2.7
	(2) Plastic strain (Oedometer tests): (model of Oldecop and Alonso, 2001); Eq. (2:34) - (2:36)	(2) 2.7.1.2
ε^{ψ}	Elastic strain due to suction changes (Oedometer tests): (model of Oldecop and Alonso, 2001); Eq. (2:29)	2.7.1.2
η	(1) Constant; Eq. (2:8)	(1) 2.5.2
	(2) Stress ratio, [$\eta=q/p$]; (model of Salim and Indraratna, 2004); Eq. (2:62) - (2:68)	(2) 2.7.4

η^*	Function of stress ratio, $[\eta(p/p_{cs})]$; (model of Salim and Indraratna, 2004); Eq. (2:65); (2:66); (2:68)	2.7.4
η_s	Stress ratio (triaxial tests): (model of Chávez and Alonso, 2003); Eq. (2:38); (2:53)	2.7.2.2
θ	Material constants of the model; (model of Salim and Indraratna, 2004); Eq. (2:69)	2.7.4
ϑ_m	Dilatancy angle (Triaxial tests) : (model of Chávez and Alonso, 2003); Eq. (2:51)(2:52)	2.7.2.2
κ	(1) Elastic compressibility index (Triaxial tests) : (model of Chávez and Alonso, 2003); Eq. (2:48)	(1) 2.7.2.2
	(2) Slope of the swelling-recompression line in the void ratio e – ln p plot; (model of Salim and Indraratna, 2004); Eq. (2:65); (2:67)	(2) 2.7.4
	(3) Model parameter to control the stress relaxation velocity; (model of Bauer, 2009); Eq. (2:72)	(3) 2.7.5
$\underline{\kappa}$	Elastic stress-related compressibility index (Oedometer tests): (model of Oldecop and Alonso, 2001); Eq. (2:28)	2.7.1.2
κ_ψ	Relationship between suction and elastic strain (Oedometer tests): (model of Oldecop and Alonso, 2001); Eq. (2:27); (2:29)	2.7.1.2
λ	(1) Constant; Eq. (2:8)	(1) 2.5.2
	(2) Compressibility index (slope of a 'normal compression' line) (model of McDowell and Bolton, 1998); Eq. (2:59)	(2) 2.7.3
$\lambda^d(\psi)$	Isotropic compressibility index that depends on the applied total suction ψ (Triaxial tests) : (model of Chávez and Alonso, 2003); Eq. (2:48) ; Eq. (2:49)	2.7.2.2
λ_0^d	Isotropic compressibility index for saturated conditions (Triaxial tests) : (model of Chávez and Alonso, 2003); Eq. (2:49)	2.7.2.2
λ^i	Isotropic instantaneous compressibility index for a very dry state (Triaxial tests) : (model of Chávez and Alonso, 2003); Eq. (2:48); (2:50)	2.7.2.2

λ_t	Long term compressibility index	2.7.1.1
$\underline{\lambda}$	Compressibility index: slope of the curve ε – ln σ (Oedometer tests): (model of Oldecop and Alonso, 2001)	2.7.1.2
$\underline{\lambda}^i$	Minimum compressibility index which corresponds for a very dry state: slope of the curve ε – ln σ (Oedometer tests): (model of Oldecop and Alonso, 2001)	2.7.1.2
$\underline{\lambda}^r$	Compressibility index for $\sigma_0 < \sigma_y$ (particle rearrangement stage): slope of the curve ε – ln σ (Oedometer tests): (model of Oldecop and Alonso, 2001)	2.7.1.2
$\underline{\lambda}_0$	Maximum compressibility index corresponding to the saturated material (ψ=0): slope of the curve ε – ln σ (Oedometer tests): (model of Oldecop and Alonso, 2001)	2.7.1.2
μ	(1) Friction coefficient (function of the angle of internal friction) (model of McDowell and Bolton, 1998); Eq. (2:58); (2:59)	(1) 2.7.3
	(2) Material constants of the model; (model of Salim and Indraratna, 2004); Eq. (2:65); (2:66); (2:68)	(2) 2.7.4
ν	(1) Current value of specific volume (triaxial tests): (model of Chávez and Alonso, 2003) Eq. (2:39)	(1) 2.7.2.2
	(2) Material constants of the model; (model of Salim and Indraratna, 2004); Eq. (2:69)	(2) 2.7.4
ν_{cr}	Critical state specific volume (triaxial tests): (model of Chávez and Alonso, 2003) Eq. (2:39); (2:40)	2.7.2.2
ν_t	(1) Poisson ratio; (LNEC Hyperbolic model, 1997; 1986); Eq. (2:84)	(1) 2.7.6.1
	(2) Tangential Poisson's ratio; (LNEC EC-K_0 model, 1997; 1986); Eq. (2:89); (2:90)	(2) 2.7.6.1
σ	(1) Applied tensile stress; Eq. (2:11) - (2:14); Eq. (2:18)	(1) 2.5.3; 2.5.4

	(2) Normal vertical stress (Oedometer tests): (+) Compression	(2) 2.7.1
$\bar{\sigma}$	Effective axial stress (model of McDowell and Bolton, 1998); Eq. (2:56)	2.7.3
σ_{ij}	Effective Cauchy stress; (model of Bauer, 2009); Eq. (2:72)	2.7.5
$\overset{\circ}{\sigma}_{ij}$	Effective stress rate; (model of Bauer, 2009); Eq. (2:72)	2.7.5
$\hat{\sigma}_{ij}$	Normalized stress quantity; (model of Bauer, 2009); Eq. (2:72)	2.7.5
σ^*_{ij}	Deviatoric part; (model of Bauer, 2009); Eq. (2:72)	2.7.5
$\hat{\sigma}^*_{ij}$	Normalized stress quantity – deviatoric part; (model of Bauer, 2009); Eq. (2:72)	2.7.5
σ_a	Applied stress ; Figure 2-10	2.4.3
σ_{cr}	Rupture strength – Charles's law; Eq. (2:3)	2.4.3
σ_d	Deviatoric stress; [$\sigma_d = (\sigma_1 - \sigma_3)/2$]; (Swansea K-G model, 1997; 1986); Eq. (2:92)	2.7.6.2
σ_f	Tensile strength of grains; Eq. (2:9) - (2:10); Mean tensile strength Eq. ((2:16); Eq. (2:19)	2.5.2; 2.5.3; 2.5.4
σ_m	Tip stress – Charles's law; Eq. (2:3)	2.4.3
σ_s	Mean stress; [$\sigma_s = (\sigma_1 + \sigma_3)/2$]; (Swansea K-G model, 1997; 1986); Eq. (2:91); (2:92)	2.7.6.2
σ_v	Normal vertical stress (Oedometer tests): (+) Compression	2.7.1
σ_y	Clastic yield stress	2.7.1
σ_0	(1) Tensile stress σ such that 36.7879% of the total number of blocks survive ; Eq. (2:11) - (2:17)	(1) 2.5.3
	(2) Current applied normal vertical stress (Oedometer tests): (model of Oldecop and Alonso, 2001)	(2) 2.7.1.2
σ_0^*	Yield stress of the dry state rockfill (Oedometer tests): (model of Oldecop and Alonso, 2001)	2.7.1.2

σ_0^{ch}	Threshold stress where starts the clastic hardening stage (Oedometer tests): (model of Oldecop and Alonso, 2001)	2.7.1.2
$\bar{\sigma}_0$	Clastic yield stress for the aggregate (model of McDowell and Bolton, 1998); Eq. (2:59)(2:41)	2.7.3
σ_1	(1) Tensile stress which acts in a block material of V_1 volume; Eq. (2:13); (2:15)	(1) 2.5.3
	(2) Axial (normal) stress; (Triaxial tests)	(2) 2.7
σ_3	Lateral (normal) stress or confining stress; (Triaxial tests)	2.7
φ_c	Intergranular friction angle for the critical state under triaxial compression; (model of Bauer, 2009); Eq. (2:77)	2.7.5
φ_{cr}	critical state friction angle obtained from Mc (Triaxial tests) : (model of Chávez and Alonso, 2003); Eq. (2:52)	2.7.2.2
φ_m	Mobilized friction angle at a given yield state (Triaxial tests) : (model of Chávez and Alonso, 2003); Eq. (2:52); (2:53)	2.7.2.2
ϕ	(1) Angle of internal friction (model of McDowell and Bolton, 1998); ; Eq. (2:56)	(1) 2.7.3
	(2) Mohr-Coulomb strength parameter; (LNEC Hyperbolic model, 1997; 1986); Eq. (2:83); (2:85)	(2) 2.7.6.1
	(3) Mohr-Coulomb strength parameter; Eq. (2:93); (2:94)	(3) 2.7.6.2
ϕ_f	Basic angle of friction; (model of Salim and Indraratna, 2004); Eq. (2:64); (2:71)	2.7.4
χ	(1) activated complex;	(1) 2.4.3
	(2) Material constants of the model; (model of Salim and Indraratna, 2004); Eq. (2:65); (2:66); (2:68)	(2) 2.7.4
χ_ψ	Relationship between suction and collapse strain (Oedometer tests): (model of Oldecop and Alonso, 2001); Eq. (2:27)	2.7.1.2
ψ	Total suction	2.7.1 - 2.7.2

ψ_t	Disintegration factor for a given time t; (model of Bauer, 2009); Eq. (2:74)	2.7.5
$\dot{\psi}_t$	Rate of the disintegration factor for a given time t; (model of Bauer, 2009); Eq. (2:73); (2:74)	2.7.5
ψ_w	Disintegration factor for the final state which depend on a given relative moisture content *w*; (model of Bauer, 2009); Eq. (2:74)	2.7.5

2.10 References

Alonso, E.E., Olivella, S., Pinyol, N.M., 2005. A review of Beliche Dam. Géotechnique 55, 267–285.

Ashby, M.F., Jones, D.R.H., 1986. Engineering materials 2. Pergamon Press, Oxford.

Atkinson, B.K., 1984. Subcritical crack growth in geological materials. J. Geophys. Res. 89, 4077–4114.

Atkinson, B.K., 1979. A fracture mechanics study of subcritical tensile cracking of quartz in wet environments. Pure Appl. Geophys. PAGEOPH 117, 1011–1024. doi:10.1007/BF00876082

Atkinson, B.K., Meredith, P.G., 1987. The theory of subcritical crack growth with applications to minerals and rocks, in: Atkinson, B.K. (Ed.), Fracture Mechanics of Rock. Academic Press, London (U.K), pp. 111–166.

Bauer, E., 2009. Hypoplastic modelling of moisture-sensitive weathered rockfill materials. Acta Geotech. 4, 261–272. doi:10.1007/s11440-009-0099-y

Bauer, E., 1996. Calibration of a comprehensive hypoplastic model for granular materials. Soils Found. 36, 13–26.

Bazant, Z.P., 1999. Size effect on structural strength: A review. Arch. Appl. Mech. 69, 703–725. doi:10.1007/s004190050252

Bazant, Z.P., 1984. Size effect in Blunt Fracture: Concrete, Rock, Metal. J. Eng. Mech. 110, 518–535. doi:10.1061/(ASCE)0733-9399(1984)110:4(518)

Been, K., Jefferies, M.G., 1985. A state parameter for sands. Géotechnique 35, 99–112. doi:10.1680/geot.1985.35.2.99

Caproni, N., Armelin, J.L., 1998. Deformabilidade de um enrocamento obtida em ensaios de compressão unidimensional, in: Proceedings of XI Congreso Brasileiro de Mecânica Dos Solos E Engenharia Geotécnica, Brasilia, Brasil, 2. pp. 705–712.

Charles, J.A., Watts, K.S., 1980. The influence of confining pressure on the shear strength of compacted rockfill. Géotechnique 30, 353–367.

Charles, R.J., 1958a. Static fatigue of glass. I. J. Appl. Phys. 29, 1549–1553. doi:10.1063/1.1722991

Charles, R.J., 1958b. Static fatigue of glass. II. J. Appl. Phys. 29, 1554–1560. doi:10.1063/1.1722992

Charles, R.J., Hilling, W.S., 1962. Kinetics of glass failure of stress corrosion, in: Symposium Sur La Resistance Du Verre et Les Moyens de l'Ameliorer. Union Scientifique Continentale du Verre, Charleroi (Belgium), pp. 511–527.

Chávez, C., 2003. Estudio del comportamiento triaxial de materiales granulares de tamaño medio con énfasis en la influencia de la succión. PhD. Thesis. Technical University of Catalonia. UPC, Barcelona, Spain (in Spanish).

Chávez, C., Alonso, E.E., 2003. A constitutive model for crushed granular aggregates which includes suction effects. Soils Found. 43, 215–227.

Chrismer, S.M., 1985. Considerations of factors affecting ballast performance. Rep. No. WP-110, Administration of American Railroads, Research and Test Department, Bulletin 704, American Railway Engineering Association. pp 118-150.

Clements, R.P., 1981. The deformation of rockfill: inter-particle behaviour, bulk properties and behaviour in dams. PhD thesis. London University, London, UK.

Craig, R.F., 2004. Soil mechanics, Seventh ed. ed. Spon Press, Taylor & Francis Group, London, UK.

Duncan, J.M., Chang, C.V., 1970. Nonlinear analysis of stress and strain in soils. J. Soil Mech. Found. Div. ASCE 96, 1629–1654.

Evans, A.G., 1972. A method for evaluating the time-dependent failure characteristics of brittle materials - and its application to polycrystalline alumina. Mater. Sci. 7, 1137–1146.

Freiman, S.W., 1984. Effects of Chemical Environments on Slow Crack Growth in Glasses and Ceramics. Geophys. Res. 89, 4072–4076.

Frossard, E., Hu, W., Dano, C., Hicher, P.-Y., 2012. Rockfill shear strength evaluation : a rational method based on size effects. Géotechnique 62, 415–427.

Fumagalli, E., 1969. Tests on cohensionless materials for rockfill dams. J. Soil Mech. Found. Div. ASCE 95, 313–330.

Golightly, C.R., 1990. Engineering properties of carbonate sands. PhD. thesis. Bradford University.

Gudehus, G., 1996. A comprehensive constitutive equation for granular materials. Soils Found. 36, 1–12.

Hardin, B.O., 1985. Crushing of soil particles. J. Geotech. Eng. ASCE 111, 1177–1192.

Harr, M.E., 1977. Mechanics of particulate media. McGraw-Hill, New York, NY, USA.

Holtz, R.D., Kovacs, W.D., 1981. An introduction to geotechnical engineering. Prentice Hall, Inc, Englewood Cliffs, NJ, USA.

Holtz, W.G., Gibbs, H.J., 1956. Triaxial shear tests on pervious gravelly soils. J. Soil Mech. Found. Div. ASCE 82, 1–22.

Indraratna, B., Ionescu, D., Christie, H.D., 1998. Shear behaviour of railway ballast based on large-scale triaxial tests. J. Geotech. Geoenvironmental Eng. ASCE 439–449.

Indraratna, B., Salim, W., 2002. Modelling of particle breakage of coarse aggregates incorporating strength and dilatancy. Proc. Inst. Civ. Eng. London 155, 243–252.

Indraratna, B., Salim, W., 2001. Shear strength and degradation characteristics of railway ballast, in: Ho, K.K.S., Lo, K.S. (Eds.), Proceedings of the 14th Southeast Asian Geotechnical Conference, Hong Kong. A.A. Balkema, Rotterdam, The Netherlands, p. Vol. 1, 521-526.

Indraratna, B., Salim, W., Rujikiatkamjorn, C., 2011. Advanced rail geotechnology – ballasted track. Balkema, CRC Press, Taylor & Francis Group, London, UK.

Indraratna, B., Wijewardena, L.S.S., Balasubramaniam, A.S., 1993. Large-scale triaxial testing of greywacke rockfill. Géotechnique 43, 37–51. doi:10.1680/geot.1994.44.3.539

Islam, M.N., Siddika, A., Hossain, M.B., Rahman, A., Asad, M.A., 2011. Effect of particle size on the shear strength behaviour of sands. Aust. Geomech. 46, 75–86.

Jaeger, J.C., 1967. Failure of rocks under tensile conditions. Int. J. Rock Mech. Min. Sci. 4, 219–227.

Kjaernsli, B., Sande, A., 1963. Compressibility of some coarse-grained materials, in: Proceedings of the 1st European Conference on Soil Mechanics and Foundation Engineering, Weisbaden, Germany, Vol. 1. pp. 245–251.

Kolbuszewski, J., Frederick, M.R., 1963. The significance of particle shape and size on the mechanical behaviour of granular materials, in: European Conference on Soil Mechanics and Foundation Engineering. Sec. 4, Paper 9. Wiesbaden, Germany, pp. 253–263.

Kolymbas, D., 1991. An outline of hypoplasticity. Arch. Appl. Mech. 61, 143–151. doi:10.1007/BF00788048

Kolymbas, D., 1985. A generalized hypoplastic constitutive law, in: Proceedings of the Eleventh International Conference on Soil Mechanics and Foundation Engineering, San Francisco, 12-16 August , 1985. Vol. 5. Balkema, 1988, San Francisco, p. 2626.

Kondner, R.L., 1963. Hyperbolic stress-strain response: cohesive soils. J. Soil Mech. Found. Div. ASCE 89, 115–143.

Lade, P., Yamamuro, J., Bopp, P., 1996. Significance of particle crushing in granular materials. J. Geotech. Eng. ASCE 122, 309–316. doi:10.1061/(ASCE)0733-9410(1996)122:4(309)

Lee, D.M., 1992. The angles of friction of granular. PhD. dissertation. University of Cambridge, Cambridge, UK.

Lee, K., Farhoomand, I., 1967. Compressibility and crushing of granular soil in anisotropic tiraxial compression. Can. Geotech. J. 4, 68–86. doi:10.1139/t67-012

Marachi, N.D., Chan, C.K., Seed, H.B., 1972. Evaluation of properties of rockfill materials. J. Soil Mech. Found. Div. ASCE 98, 95–114.

Marachi, N.D., Chan, C.K., Seed, H.B., Duncan, J.M., 1969. Strength and deformation characteristics of rockfill materials. Berkeley, CA, USA.

Marsal, R.J., 1973. Mechanical properties of rockfill, in: Hirschfeld, R.C., Poulos, S.J. (Eds.), Embankment Dam Engineering. Casagrande Volume I. John Wiley & Sons, New York, NY, USA, pp. 110–200.

Marsal, R.J., 1967. Large-scale testing of rockfills materials. J. Soil Mech. Found. Div. ASCE 93, 27–44.

Marsal, R.J., Resendiz, D., 1975. Presas de tierra y enrocamiento, Editorial. ed. Mexico City, Mexico.

McDowell, G.R., 1997. Clastic soil mechanics. PhD. dissertation. University of Cambridge.

McDowell, G.R., Bolton, M.D., 1998. On the micromechanics of crushable aggregates. Géotechnique 48, 667–679.

McDowell, G.R., Bolton, M.D., Robertson, D., 1996. The fractal crushing of granular materials. J. Mech. Phys. Solids 44, 2079–2102.

Michalske, T., Freiman, S.W., 1982. A molecular interpretation of stress corrosion in silica. Nature 295, 511–512.

Muir Wood, D., Belkheir, K., Liu, D.F., 1994. Strain softening and state parameter for sand modelling. Géotechnique 44, 335–339. doi:10.1680/geot.1994.44.2.335

Nakata, Y., Hyodo, M., Hyde, A.F.L., Kato, Y., Murata, H., 2001. Microscopic particle crushing of sand subjected to high pressure one-dimensional compression. Soils Found. 41, 69–82.

Naylor, D.J., Maranha, J.R., Maranha das Neves, E., Veiga Pinto, A.A., 1997. A back-analysis of Beliche Dam. Géotechnique 47, 221–233.

Naylor, D.J., Maranha Das Neves, E., Mattar, D., Veiga Pinto, A.A., 1986. Prediction of construction performance of Beliche Dam. Géotechnique 36, 359–376.

Niemunis, A., Herle, I., 1997. Hypoplastic model for cohesionless soils with elastic strain range. Mech. Cohesive-frictional Mater. 2, 279–299.

Nobari, Duncan, 1972. Effect of reservoir filling on stresses and movements in earth and rockfill dams.

Oldecop, L.A., 2000. Compresibilidad de escolleras. Influencia de la humedad. PhD. Thesis. Technical University of Catalonia. UPC, Barcelona, Spain (in Spanish).

Oldecop, L.A., Alonso, E.E., 2013. Rockfill mechanics, in: (eds), C. et al. (Ed.), Advances in Unsaturated Soils - Proceedings of the 1st Pan-American Conference on Unsaturated Soils. Cartagena de Indias (Colombia), February 20th–22nd, 2013. Taylor & Francis Group, Cartagena de Indias (Colombia), pp. 61–86.

Oldecop, L.A., Alonso, E.E., 2007. Theoretical investigation of the time-dependent behaviour of rockfill. Géotechnique 57, 289–301.

Oldecop, L.A., Alonso, E.E., 2004. Testing rockfill under relative humidity control. Geotech. Test. J. 27, 269–278.

Oldecop, L.A., Alonso, E.E., 2003. Suction effects on rockfill compressibility. Géotechnique 53, 289–292.

Oldecop, L.A., Alonso, E.E., 2001. A model for rockfill compressibility. Géotechnique 51, 127–139.

Ortega, E., 2008. Comportamiento de materiales granulares gruesos - Efecto de la succión. PhD. Thesis. Technical University of Catalonia. UPC, Barcelona, Spain (in Spanish).

Parish, O.O., Putnam, T.W., 1977. Equations for the determination of humidity from dewpoint and psychrometric data. Edwards, California (USA).

Parkin, A.K., Adikari, G.S.N., 1981. Rockfill deformation from large-scale tests, in: Proceedings of 10th Int. Conf. Soil Mech. And Found. Engg. (ICSMFE), Stockholm, 4. pp. 727–731.

Pender, M.J., 1978. A model for the behaviour of overconsolidated soil. Géotechnique 28, 1–25. doi:10.1680/geot.1978.28.1.1

Penman, A., Charles, J., 1976. The quality and suitability of rockfill used in dam construction, in: Penman, A.D.M., Charles, J.A., Moore, J.F.A. (Eds.), Dams and Embankments, A.D.M. Penman, J.A. Charles, J.F.A. Moore (Eds.). Edited By: The Building Research Establishment, The Construction Press, Garston, Watford, UK, pp. 72–85.

Roscoe, K.H., Schofield, A.N., Thurairajah, A., 1963. Yielding of clays in states wetter than critical. Géotechnique 13, 211–240. doi:10.1680/geot.1963.13.3.211

Russell, A.R., Muir Wood, D., 2009. Point load tests and strength measurements for brittle spheres. Int. J. Rock Mech. Min. Sci. 46, 272–280. doi:10.1016/j.ijrmms.2008.04.004

Salim, W., Indraratna, B., 2004. A new elastoplastic constitutive model for coarse granular aggregates incorporating particle breakage. Can. Geotech. J. 41, 657–671. doi:10.1139/t04-025

Saouma, V.E., 2007. Lecture notes in fracture mechanics. Barcelona (Spain).

Schofield, A.N., Wroth, C.P., 1968. Critical state soil mechanics. McGraw-Hill, London, UK.

Shipway, P.H., Hutchings, I.M., 1993. Fracture of brittle spheres under compression and impact loading. I. Elastic stress distributions. Philos. Mag. A 67, 1389–1404.

Soriano, A., Sánchez, F.J., 1999. Settlements of railroad high embankments, in: Proceedings of XII European Conference on Soil Mechanics and Geotechnical Engineering. Netherlands.

Sowers, G.F., Williams, R.C., Wallace, T.S., 1965. Compressibility of broken rock and settlement of rockfills, in: Proceedings of the 6th ICSMFE, Montreal, Canada, Vol. 2. pp. 561–565.

Takei, M., Kusakabe, O., Hayashi, T., 2001. Time-dependent behavior of crushable materials in one-dimensional compression tests. Soils Found. 41, 97–121.

Thom, N.H., Brown, S.F., 1989. The mechanical properties of unbounded aggregates from various sources, in: Jones, R.H., Dawson, A.R. (Eds.),

Unbound Aggregates in Roads. pp. 130–142.

Thom, N.H., Brown, S.F., 1988. The effect of grading and density on the mechanical properties of a crushed dolomitic limestone, in: Proceedings of 14th ARRB Conf., Vol. 14, Part 7. pp. 94–100.

Tsoungui, O., Vallet, D., Charmet, J.C., 1999. Numerical model of crushing of grains inside two-dimensional granular materials. Powder Technol. 105, 190–198. doi:10.1016/S0032-5910(99)00137-0

Vallerga, B.A., Seed, H.B., Monismith, C.L., Cooper, R.S., 1957. Effect of shape, size and surface roughness of aggregate particles on the strength of granular materials, in: Road and Paving Materials. pp. 63–74.

Veiga Pinto, A.A., 1983. Previsao do comportamento estrutural de barragens de enrocamento. PhD. Thesis. Laboratorio Nacional de Engenharia Civil, Lisbon, Portugal (in Portuguese).

Vesic, A.S., Clough, G.W., 1968. Behaviour of granular materials under high stresses. J. Soil Mech. Found. Div. ASCE 94, 661–668.

Wan, R.G., Guo, P.J., 1998. A simple constitutive model for granular soils: Modified stress-dilatancy approach. Comput. Geotech. 22, 109–133.

Weibull, W., 1951. A statistical distribution function of wide applicability. J. Appl. Mech. 18, 293–297.

Weibull, W., 1939. A statistical theory of the strength of materials, in: Proceedings of the Royal Swedish Institute of Engineering Research, 151.

Wiederhorn, S.M., 1978. Mechanisms of subcritical crack growth in glass, in: Bradt, R.C., Hasselman, D.P.H., Lange, F.F. (Eds.), Fracture Mechanics of Ceramics, Vol. 4. Plenum Press, pp. 549–580.

Wiederhorn, S.M., 1974. Subcritical crack growth in ceramics, in: Bradt, R.C., Hasselman, D.P.H., Lange, F.F. (Eds.), Fracture Mechanics of Ceramics, Vol. 2. Plenum Press, New York, pp. 613–646.

Wiederhorn, S.M., Boltz, L.H., 1970. Stress corrosion and static fatigue of glass. J. Am. Ceram. Soc. 53, 543–548.

Wiederhorn, S.M., Freiman, S.W., Fuller, E.R., Simmons, C.J., 1982. Effects of water and other dielectrics on crack growth. Mater. Sci. 17, 3460–3478.

Wu, W., Bauer, E., Kolymbas, D., 1996. Hypoplastic constitutive model with critical state for granular materials. Mech. Mater. 23, 45–69. doi:10.1016/0167-6636(96)00006-3

Yamamuro, J., Lade, P., 1996. Drained sand behaviour in axisymmetric tests at high pressures. J. Geotech. Eng. ASCE 122, 109–119.

Yasuda, N., Matsumoto, N., 1994. Comparison of deformation characteristics of rockfill materials using monotonic and cycling loading laboratory tests and in situ tests. Can. Geotech. J. 31, 162–174.

Yasuda, N., Matsumoto, N., Yoshioka, R., Takahashi, M., 1997. Undrained monotonic and cyclic strength of compacted rockfill material from triaxial and torsional simple shear tests. Can. Geotech. J. 34, 357–367. doi:10.1139/cgj-34-3-357

Chapter 3

Basic features of DEM

The discrete (or distinct) element method (DEM) has been developed in order to investigate and model the micro- and macro-mechanical behaviour of granular media. DEM is based on the modelling of the movement of each distinct element and its interactions with others.

This chapter presents the fundamentals of the discrete (distinct) element methods (DEM). The main basic features of DEM such as contact models, force-displacement laws at the inter-particle contacts and the analysis of the particle motion will be described here. Some other aspects such as damping and critical timestep are also presented.

With respect to the DEM model used in this research, presented in chapter 5, clump structures are also defined in order to model rigid macroparticles. Special emphasis is placed on the presentation of different DEM models that are found in the literature and simulate breakage in crushable soils.

Finally, the main characteristics of the software adopted in this research, the PFC3D code, are presented.

3.1 Introduction

The "Distinct Element Method", DEM, was introduced by Peter Cundall (Cundall and Strack, 1979a; Cundall, 1971). Subsequently, the acronym DEM has evolved to include the Discrete Element Methods.

In DEM, each grain is treated independently; this is the reason for "distinct" (distinct element), (**Figure 3-1**). The DEM grains interact at contacts through some law of contacts.

DEM particles are generally considered circular (2D) or spherical (3D). Other shapes could also be taken into account but the contact detection processes between particles require more sophisticated methods and most likely an increase in the computational costs. The following other shapes can be found in the literature:

- **Polyhedral shapes:** (Chang and Chen, 2008; Cundall, 1988a; Dubois and Jean, 2003; Dubois, 2011; Nezami et al., 2004; Perales, 2007; Saussine, 2004; Saussine et al., 2004).
- **Rounded shapes:** Super-ellipsoids (Hogue, 1998); spheroids (Lee et al., 2003); spherocylinders (Pournin et al., 2005); spheropolyhedra (Galindo-Torres and Pedroso, 2010).
- **Assembly of disk/spheres:** Using clumps (Itasca, 2008) or clusters (Cheng et al., 2003).

This work uses clumps, which are explained below (3.5), in order to take into account the irregular shapes of the gravels and rockfill.

DEM techniques could also be divided into two categories according to the type of contacts (From Duran (2000), cited by O'Sullivan (2011); and Jean (2011)): Smooth methods (soft sphere models) and Non-Smooth methods (hard sphere models).

The first, Smooth methods, use a frictional contact law taking into account fine physical effects (realistic or not, e.g. springs) and computed using fine-time-step explicit schemes. The Distinct Element Method of Cundall (Cundall and Strack, 1979a) and Molecular Dynamics method, MD (McNamara, 2011a), are in this group.

The Non-Smooth methods, such as the Non-Smooth Contact Dynamics, NSCD (Jean, 2011), and Event-Driven methods, ED, (McNamara, 2011b), use rough laws and do not allow the inter-penetration of the particles during an impact ("Hard" particle approach). These methods require implicit iterative numerical algorithms and accept large timesteps (Jean, 2011).

In the literature there is a wide range of models that can be considered particulate models (or based on particle models), such as the "Discrete Element Methods". However, there are some particulate models that are not considered DEM models, for example the SPH (Smoothed-Particle Hydrodynamics), which is a meshless method, and the MPM (Material Point Method), which is a "Finite Element Method" FEM based on a particle model. These models are not explained here. O'Sullivan (2011) shows an excellent summary of some particulate models. Radjai and Dubois (2011) also describe some of them in detail. At present, there are some techniques to combine DEM models with FEM models but they are not considered here. Likewise, DEM developments (Butlanska, 2014) advance the improvement of the contact detection algorithms, the increase in the number of particles, the considerations of actual shapes, the interactions between solid particles and fluids, and the formulation or validation of constitutive models that explain the behaviour of materials more realistically.

3.1.1 DEM fundamentals

This work uses Cundall's DEM, and therefore a smooth method: Particles are infinitely stiff, i.e. they always conserve their shape and can overlap with other neighboring particles. DEM allows finite displacements and rotations of the

particles, and recognizes new contacts around the particles during the process (Figure 3-1b).

A discrete media is composed of particles and boundaries. Generally, to begin to use a DEM it is necessary to input the position of the particles and boundaries and their properties which are related to the constitutive model at contacts (for instance stiffnesses, friction coefficients, densities).

Particle interactions result from a dynamic process of particle motion. DEM monitors these movements for every singular particle: particle position, contacts and contact forces around the particle are checked during the process. Force balance (dynamic equilibrium) in every timestep is performed for each particle (Figure 3-1b).

Particle motion is caused by an unbalance of forces. For an equilibrium system, this motion could be introduced by the application of external forces or the motion of a boundary system, e.g.

a. b.

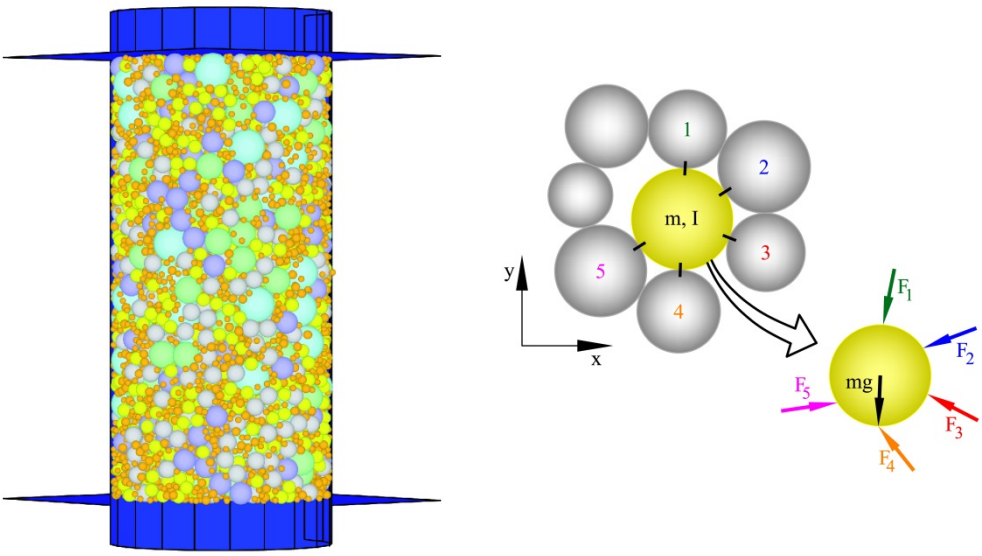

Figure 3-1 DEM model for particles: (a) Particle aggregate specimen; (b) Interaction between particles – Contact forces and gravity force acting on a particle.

The DEM procedure is summarized in the following steps:

I. At the beginning (initial time $t=t_0=0$):
   1. Definition and location of particles and boundaries (system geometry).
   2. Definition of contact model.
   3. Input of properties of particles and boundaries.

II. Small increment of time, Δt ($t=t_1=t_0+\Delta t$). For each particle:
   4. Identification of particle and boundary positions, and contacts around the particles.
   5. Application of Contact Law at each contact: Calculation of contact forces.
   6. Application of dynamic equilibrium (balance of forces): Calculation of resultant force and moment; body forces and external forces could be taken into account.
   7. Application of Law of Motion: Calculation of accelerations, velocities, displacements and rotations of particles.
   8. Updating particle and boundary positions.

III. Small increment of time, Δt ($t=t_1+\Delta t$): See step II.

DEM applies Newton's second law of motion to the particles and a law of force-displacement to the contacts. Translational and rotational movements for each particle are obtained using the motion law after the analysis of the forces acting on each particle. The force-displacement law (Figure 3-2) applied to each contact around a particle is used to update the contact forces which have been generated by particle motion.

The explicit finite difference method is used to calculate the motion of the particles.

After the balance of forces, the acting force and moment are found in each particle. Subsequently, acceleration (linear and angular) is calculated applying the law of motion. The increment in displacement is obtained by integrating the acceleration equations twice under a very small timestep, so acceleration can be considered constant in this interval.

Extending this procedure to all the particles or grains, a new “geometry” is obtained which makes it possible to return to the first step, i.e. the calculation of the new contact forces in each particle.

Fundamentals of DEM and modelling using DEM are discussed in detail in O’Sullivan (2011), Radjai and Dubois (2011), Itasca (2008) and more recently in Thornton (2015).

3.2 Inter-Particle contacts – Force-Displacement Laws

Some features of the contact models and law of motion that are used by the PFC3D code (Itasca, 2008) and relate to the proposed model are presented below.

3.2.1 Simple linear contact model

This model considers normal and tangential springs in the contact between two particles (or particle-wall interaction) and a “slider mechanism” which controls shear strength (see Figure 3-2).

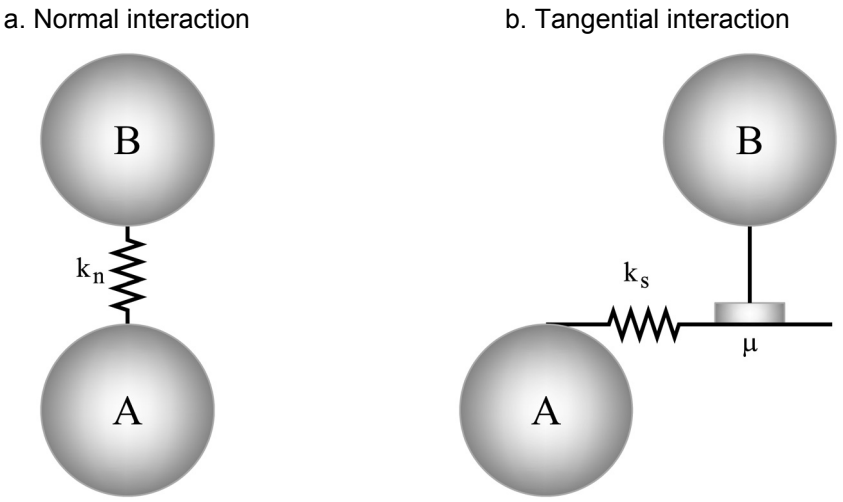

Figure 3-2 Law of force-displacement in the simple contact model between particles A and B.

Six parameters are considered in the contacts, three parameters per particle. The following parameters are considered for each particle:

• Normal and shear stiffness, k_n and k_s
• Coefficient of friction μ

This contact model is considered in the DEM model proposed in this research and presented in chapter 5.

3.2.1.1 Stiffnesses and Contact Forces

The contact force vector, F_i, which represents the action of the particle A on the particle B (Figure 3-3), is calculated as follows:

$$F_i = F^n n_i + F^s t_i \tag{3:1}$$

where:
F^n: Normal force component (related to the contact plane);
F^s: Shear (or tangential) force (related to the contact plane);
n_i, t_i: Unit vectors which define the contact plane.

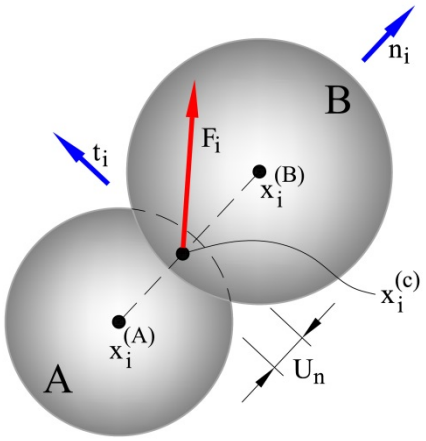

Figure 3-3 Contact Force F_i in the simple contact model between particles A and B: *n* is the normal direction to contact plane; *t* is tangential direction to contact plane.

The contact normal force is calculated as follows:

$$F^n = K^n U^n \tag{3:2}$$

where:
U^n: Overlap;
K^n: Normal contact stiffness (secant stiffness modulus which relates the total displacement and force). This is calculated by:

$$K^n = \frac{k_n^{(A)} k_n^{(B)}}{k_n^{(A)} + k_n^{(B)}} \tag{3:3}$$

where $k_n^{(A)}$ and $k_n^{(B)}$ are the normal stiffnesses of the particles A and B respectively;

The contact shear force is calculated incrementally: It is zero when the contact is formed, and a subsequent relative shear-displacement increment (ΔU^s) results in an increment of elastic shear force (ΔF^s) which is added to the current value. Thus, this increment of elastic shear force can be obtained as follows:

$$\Delta F^s = -k^s \Delta U^s \tag{3:4}$$

where k^s is the shear contact stiffness (tangential stiffness modulus which relates the displacement and force increments) and can calculated by:

$$k^s = \frac{k_s^{(A)} k_s^{(B)}}{k_s^{(A)} + k_s^{(B)}} \tag{3:5}$$

where $k_s^{(A)}$ and $k_s^{(B)}$ are the shear stiffnesses of the particles A and B respectively.

The contact stiffnesses for the linear contact model are calculated assuming that the stiffnesses of the two contact particles act in series (Eq. (3:3) and (3:5)).

3.2.1.2 Sliding behaviour

A slider mechanism is also considered in this model (**Figure 3-2**b), such that the two particles may slip relative to one another. The contact shear force F^s can only reach a maximum value related to the contact normal force F^n and the friction coefficient at the contact between particles μ (dimensionless):

$$F^s = \mu F^n \quad if \quad F^s > \mu F^n \tag{3:6}$$

$$\mu = \min(\mu^{(A)}, \mu^{(B)}) \tag{3:7}$$

where $\mu^{(A)}$ and $\mu^{(B)}$ are the Friction coefficients of the particles A and B respectively. μ is taken to be the minimum friction coefficient of the two particles.

The contact is checked for slip conditions in each timestep by calculating the maximum allowed shear contact force, $F^s_{\max}$:

$$F^s_{\max} = \mu \left| F^n \right| \tag{3:8}$$

If $\left|F^s\right| > F^s_{\max}$, then the slip is allowed to occur (for the next timestep) by setting the magnitude of F^s equal to $F^s_{\max}$.

3.2.2 Simple contact Bond

The contact bond (or simple contact bond) can be seamed as a point of glue at a contact or as a pair of elastic springs with normal and shear stiffnesses and with shear and tensile normal strengths. This model does not permit the action of the slider mechanism which was considered in the previous section. Bonds can support loads and break.

The bond breaks if one of the two following possibilities occurs:

(1) When the tensile normal contact force equals or exceeds the normal contact bond strength, and then both the normal and shear contact forces are set to zero.
(2) When the shear contact force equals or exceeds the shear contact bond strength, and then the contact force is not altered.

Therefore, a contact bond is defined by two parameters: normal contact bond strength F_c^n (force) and shear contact bond strength F_c^s (force).

3.2.3 Parallel Bond - Bonded Particle Method, BPM

The Bonded Particle Method, BPM, was proposed by Potyondy and Cundall (2004). This model simulates the rock as a very dense aggregate of circular or spherical particles which stay together using bonds at their contacts. This model is available in PFC3D under the name of Parallel Bond.

BPM has the assumptions of DEM:

• The particles are rigid disks or spheres with a finite mass;
• The particles move independently and can rotate;
• The particles interact only at the contacts. A contact is composed of two particles;
• There may be overlaps between particles (small overlaps compared to the particle size);
• Bonds can exist at a contact. They can support loads and break;
• The law of force-displacement relates the particle motion and the forces and moments at the contacts;
• The contacts can have rotational stiffness.

3.2.3.1 Mechanical behavior of particle-bond (Grain-cement) system

The following loads act in a bonded contact as illustrated in Figure 3-4:

• Particle-particle contact – Overlap between particles (grain behavior):

F_i load

• Bond (cement behaviour):

$\bar{F}_i$ load;

$\bar{M}_i$ Moment

These loads and moment contribute to the resultant force and moment that act on the contact between two particles.

If there is no bond at a contact, then only the force-displacement behavior between particles is considered.

3.2.3.2 Particle-Particle contact behaviour

The particle-particle contact behaves like the simple contact (Figure 3-4b) and therefore it considers the following parameters for each particle:

• Normal and shear stiffness, k_n and k_s
• Coefficient of friction μ

The contact laws and the behaviour of the springs and slider are the same as with

the simple contact.

3.2.3.3 *Parallel bond behaviour*

A bond simulates the mechanical behavior of brittle cement between two elastic particles. This bond acts in parallel in relation to the behavior of the particle-particle contact, so it is also called "*parallel bond*". Sliding could also occur.

This parallel bond is simulated as a set of elastic springs distributed over a rectangular (2D case) or circular section (3D case) resting on the contact plane and centered on the point of contact. This parallel bond is represented as a cylinder of $\overline{L}$ length and $2\,\overline{R}$ diameter, as illustrated in Figure 3-4a and Figure 3-4c.

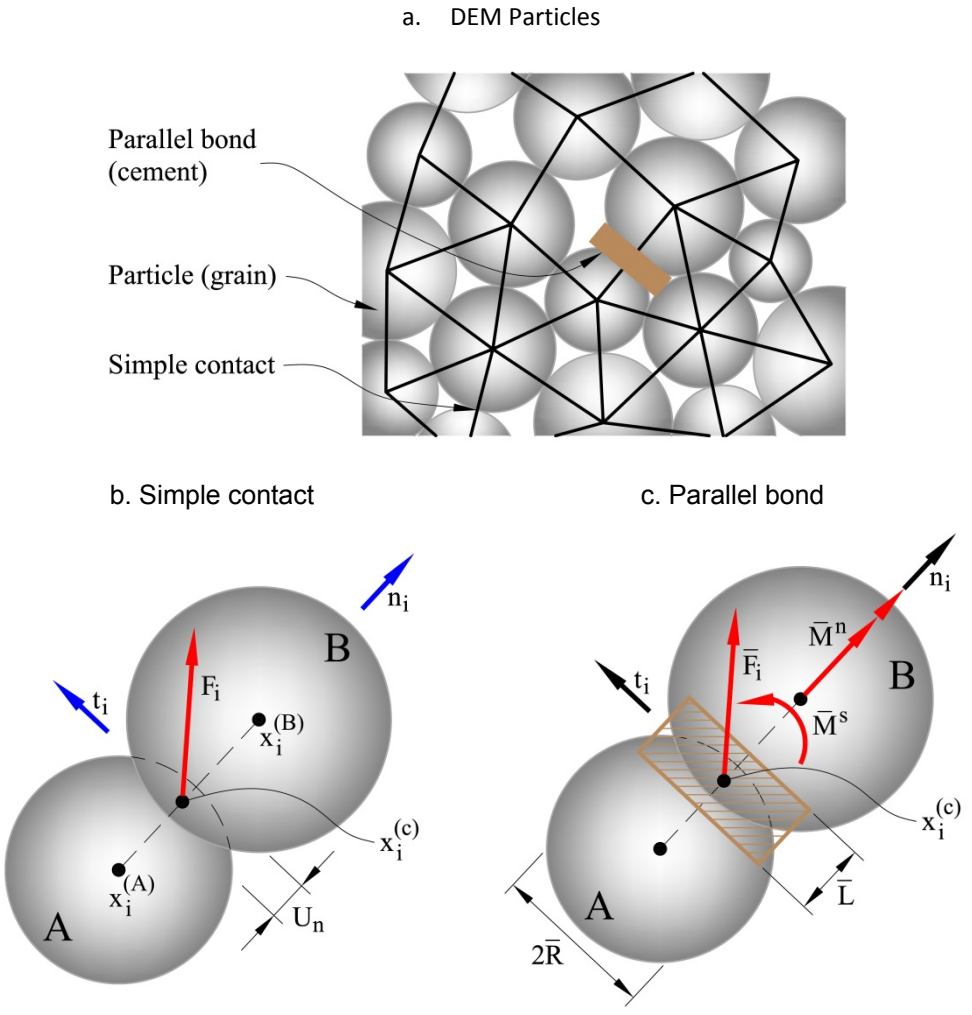

Figure 3-4 Force-displacement behavior of the Model BPM or Parallel Bond between particles A and B (Modified from Potyondy and Cundall (2004)).

Five parameters are considered in this parallel contact bond (**Figure 3-4**c):

• Normal and shear stiffness per unit area, $\overline{k}^n$ and $\overline{k}^s$;
• Tensile and shear strength, $\overline{\sigma}_c$ and $\overline{\tau}_c$;
• Bonded multiplier factor, $\overline{\lambda}$, so that the radius of the bond is:

$$\overline{R} = \overline{\lambda} \min(R^{(A)}, R^{(B)}) \tag{3:9}$$

where $R^{(A)}$ and $R^{(B)}$ are the radii of the particles A and B, respectively.

The total force $\overline{F}_i$ and moment $\overline{M}_i$, which represent the action of the bond on the particle B, are calculated as follows:

$$\overline{F}_i = \overline{F}^n n_i + \overline{F}^s t_i \tag{3:10}$$

$$\overline{M}_i = \overline{M}^n n_i + \overline{M}^s t_i \tag{3:11}$$

where:
$\overline{F}^n$: Axial force;
$\overline{F}^s$: Shear force;
$\overline{M}^n$: Axial moment (for the 2D case: it is equal to 0);
$\overline{M}^s$: Shear moment (Bending moment). For the 2D case, it acts in the out-of-the-plane direction;
n_i, t_i: Unit vectors which define the contact plane;

The following expressions are used in the model in order to calculate the forces and moments due to the parallel bond:

$$\Delta\overline{F}^n = \overline{k}^n A \Delta U^n \tag{3:12}$$

$$\Delta\overline{F}^s = -\overline{k}^s A \Delta U^s \tag{3:13}$$

$$\Delta\overline{M}^n = -\overline{k}^s J \Delta\theta^n \tag{3:14}$$

$$\Delta\overline{M}^s = -\overline{k}^n I \Delta\theta^s \tag{3:15}$$

where A is the area of the bond disk; I is the moment of Inertia of the disk cross-section; and J is the polar moment of inertia of the disk cross-section. They are calculated by:

$$A = \pi \bar{R}^2 \tag{3:16}$$

$$I = \frac{1}{4}\pi \bar{R}^4 \tag{3:17}$$

$$J = \frac{1}{2}\pi \bar{R}^4 \tag{3:18}$$

Strengths of the parallel bond ($\bar{\sigma}_c$ and $\bar{\tau}_c$) are compared with the maximum tensile $\bar{\sigma}^{\max}$ and shear $\bar{\tau}^{\max}$ stresses acting on the bond which are calculated as follows:

$$\bar{\sigma}^{\max} = \frac{-\bar{F}^n}{A} + \frac{\left|\bar{M}^s\right|\bar{R}}{I} < \bar{\sigma}_c \tag{3:19}$$

$$\bar{\tau}^{\max} = \frac{\left|\bar{F}^s\right|}{A} + \frac{\left|\bar{M}^n\right|\bar{R}}{J} < \bar{\tau}_c \tag{3:20}$$

If $\bar{\sigma}^{\max} \geq \bar{\sigma}_c$, or $\bar{\tau}^{\max} \geq \bar{\tau}_c$, then the parallel bond breaks.

3.3 Particle motion

Following the procedure of DEM in section 3.1.1, it can be seen that after the calculation of the contact forces, and taking into account the body forces and external forces that can act on each particle, a dynamic equilibrium is carried out at each particle in order to obtain the resultant force and momentum. DEM applies Newton's second law of motion to calculate the acceleration of the particles due to resultant forces. A time integration approach using the explicit centered finite difference method is then used to obtain the velocities and displacements. A very small time increment Δt is used. Consequently, the following procedure is employed to find the displacements:

Forces and moments acting on a particle:

For a resultant force vector (F_i) at a particle *i*, (sum of all externally applied forces acting on the particle):

$$F_i = m(\ddot{x}_i - g_i) \tag{3:21}$$

where *m* is the mass of the particle; $\ddot{x}_i$ is the acceleration vector of the particle *i*; and g_i is the body force acceleration vector (gravity).

For rotational motion, the resultant moment vector (M_i) acting on a spherical particle is given by:

$$M_i = I\dot{\omega}_i = \left(\frac{2}{5}mR^2\right)\dot{\omega}_i \tag{3:22}$$

where *I* is the moment of Inertia, *R* is the radius of the particle, $\dot{\omega}_i$ is the angular acceleration vector.

Accelerations of a particle:

The translational acceleration vector $\ddot{x}_i(t)$ of a particle in a current time *t* is given by:

$$\ddot{x}_i(t) = \frac{1}{\Delta t}\left[\dot{x}_i\left(t+\frac{\Delta t}{2}\right) - \dot{x}_i\left(t-\frac{\Delta t}{2}\right)\right] \tag{3:23}$$

The rotational (angular) acceleration vector $\dot{\omega}_i(t)$ of a particle in a current time *t* is given by:

$$\dot{\omega}_i(t) = \frac{1}{\Delta t}\left[\omega_i\left(t+\frac{\Delta t}{2}\right) - \omega_i\left(t-\frac{\Delta t}{2}\right)\right] \tag{3:24}$$

where $\dot{x}_i\left(t+\frac{\Delta t}{2}\right)$ and $\omega_i\left(t+\frac{\Delta t}{2}\right)$ are the velocity and angular velocity vectors respectively of a particle in a time $\left(t+\frac{\Delta t}{2}\right)$; $\dot{x}_i\left(t-\frac{\Delta t}{2}\right)$ and $\omega_i\left(t-\frac{\Delta t}{2}\right)$ are the velocity and angular velocity vectors respectively of a particle in a time $\left(t-\frac{\Delta t}{2}\right)$; *t* is the current time, and Δt is an increment time.

Velocities of a particle:

The velocity vector $\dot{x}_i\left(t+\frac{\Delta t}{2}\right)$ of a particle in a time $\left(t+\frac{\Delta t}{2}\right)$ is given by:

$$\dot{x}_i\left(t+\frac{\Delta t}{2}\right)=\dot{x}_i\left(t-\frac{\Delta t}{2}\right)+\left[\left(\frac{F_i(t)}{m}\right)+g_i\right]\Delta t \tag{3:25}$$

where $F_i(t)$ is the resultant force vector of a particle for a current time *t*.

Similarly, the angular velocity vector $\omega_i\left(t+\frac{\Delta t}{2}\right)$ of a particle in a time $\left(t+\frac{\Delta t}{2}\right)$ is given by:

$$\omega_i\left(t+\frac{\Delta t}{2}\right)=\omega_i\left(t-\frac{\Delta t}{2}\right)+\left[\frac{M_i(t)}{m}\right]\Delta t \tag{3:26}$$

where $M_i(t)$ is the resultant moment vector of a particle for a current time *t*.

Displacements of a particle:

The velocities are used to update the position of the particle center vector $x_i(t+\Delta t)$ in a time $(t+\Delta t)$ as follows:

$$x_i(t+\Delta t)=x_i(t)+\dot{x}_i\left(t+\frac{\Delta t}{2}\right)\Delta t \tag{3:27}$$

where $x_i(t)$ is the position vector of a particle for a current time *t*.

The values of $F_i(t+\Delta t)$ and $M_i(t+\Delta t)$, which are used in the next timestep, are obtained by the application of the force-displacement law as illustrated in Figure 3-5 following the PFC3D procedure (Itasca, 2008).

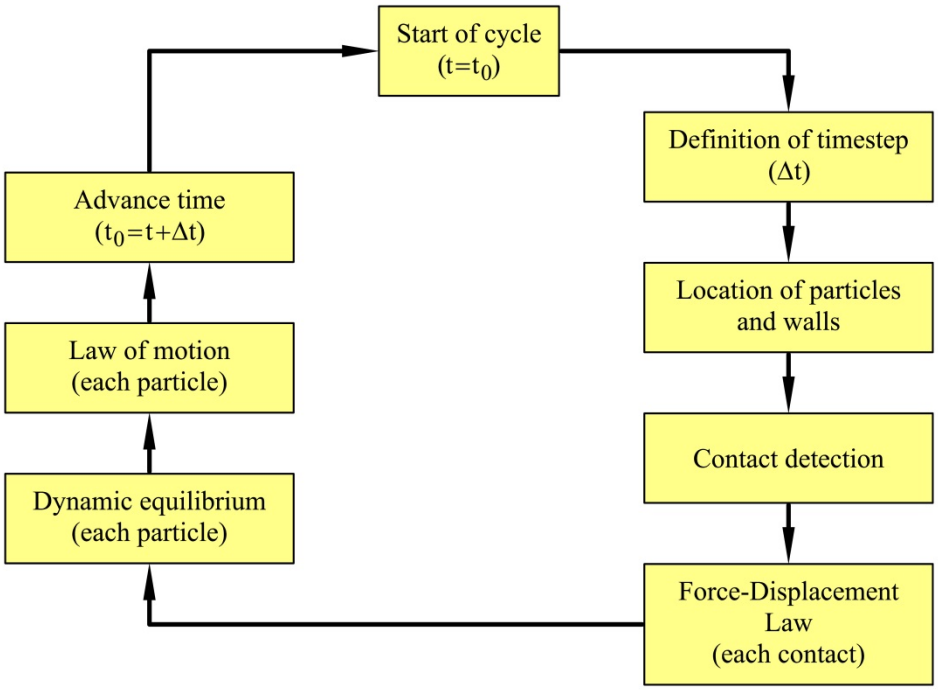

Figure 3-5 Particle motion in a calculation cycle in PFC3D.

3.3.1 Critical timestep

The solutions of the previous motion equations, which were obtained by explicit centered finite difference procedure, are stable only if the timestep does not exceed a critical timestep.

For a simple one-dimensional mass-spring system comprised of a mass *m* and a spring with a stiffness *k*, the critical time step t_{crit} that corresponds to a second-order finite difference scheme can be calculated as (Bathe and Wilson, 1976):

$$t_{crit} = \frac{T}{\pi} \tag{3:28}$$

where *T* is the period of the system and is given by:

$$T = 2\pi\sqrt{\frac{m}{k}} \tag{3:29}$$

For a generalized multiple mass-spring system (considering that springs are in series) the critical timestep for a translational motion can be calculated as:

$$t_{crit} = \sqrt{\frac{m}{k}} \tag{3:30}$$

The critical timestep is calculated for each particle (assuming an uncoupled system of degrees of freedom). The minimum of all the calculated critical timesteps is taken as the timestep (procedure followed by the PFC3D code (Itasca, 2008)).

3.4 Damping of particle motion

It is necessary to introduce a damping in the particulate system in order to dissipate kinetic energy and avoid instability of the system. The damping can be applied to each ball (local damping) or each contact (viscous damping). Itasca (2008) recommends using the local damping for compacted assemblies and conducting quasi-static deformation simulations, and using the viscous damping for problems involving free flight of particles and/or impacts between particles.

3.4.1 Local damping

Local damping applies a damping force to each ball. This damping force (F^d) is added to the equations of motion. This force is given by:

$$F^d = -\alpha \left|F\right| sign\left(V\right) \tag{3:31}$$

where:

α	=	Damping coefficient.
$\|F\|$	=	Magnitude of the force that acts on the particle
sign(V)	=	Sign (positive or negative) of the particle velocity

Typical value of the damping coefficient is α = 0.7.

3.4.2 Viscous damping

Viscous damping adds normal and shear dashpots at each contact. They act in parallel with the current contact model, and provide forces that are proportional to the relative velocity difference between the particles.

A damping force (D_i) which acts to oppose motion is added to the contact force and is calculated as follows:

$$D_i = c_i \left|V_i\right| \tag{3:32}$$

Where subscript i refers to the component of the contact force ($i=n$ for normal; $i=s$ for shear); V_i is the relative velocity at the contact; and c_i is the damping constant which is calculated by:

$$c_i = \beta_i c_i^{crit} \tag{3:33}$$

Where β_i is the critical damping ratio (parameters of the model: β_n ; β_s) and c_i^{crit} is

the critical damping constant which is obtained as follows:

$$c_i^{crit} = 2\sqrt{mk_i} \tag{3:34}$$

Where k_i is the contact tangent stiffness; m is the effective system mass which is equal to the particle (ball) mass in a particle (ball)-wall contact, or depends on the mass of the particles in contact ($m^{(A)}$ and $m^{(B)}$) for a particle-particle contact and is given by:

$$m = \frac{m^{(A)}m^{(B)}}{m^{(A)} + m^{(B)}} \tag{3:35}$$

3.5 Macroparticles using Clumps

Special comments about this kind of grouping of particles follow here because it is used in the proposed model of this research (see chapter 5).

A clump is an assembly of particles (spheres in this work) that behaves as a rigid body which cannot break, i.e. the particles remain at a fixed distance from each other. This particle grouping tool is available in PFC3D (Itasca, 2008) and the equations here follow its considerations.

In this research, a macroparticle, which simulates an actual singular grain or rock fragment, is composed of a clump, and the particles (spheres) that comprise it are named microparticles, i.e. a macroparticle is an assembly of some microparticles which are rigid and have a finite mass.

The internal contact forces that exist between the microparticles inside the clump are not considered. In PFC3D, the contacts internal to the clump are skipped during the calculation cycle in order to save computing time. However, in the proposed DEM model (chapter 5), internal stresses are calculated and the macroparticles can break.

3.5.1 Inter-Macroparticle contacts - Force-displacement law

Macroparticles interact at the contacts (each contact comprises two macroparticles), i.e. a macroparticle (clump) has a "*deformable*" boundary. There may be overlaps between the macroparticles; there are normal and shear stiffnesses at contacts, as well as friction between the macroparticles.

The law of force-displacement at contacts is applied to the contact between singular particles in the same way as discussed previously because the contacts between macroparticles are contacts between microparticles located in the boundaries.

3.5.2 Basic mass properties of a macroparticle (clump)

The total mass *m* of a clump, which is composed of N_p microparticles, is obtained as follows:

$$m = \sum_{p=1}^{N_p} m^{[p]} \tag{3:36}$$

where $m^{[p]}$ is the mass of the microparticle *p*.

The location of the center of mass of a clump $x_i^{[G]}$ is given by:

$$x_i^{[G]} = \frac{1}{m} \sum_{p=1}^{N_p} m^{[p]} x_i^{[p]} \tag{3:37}$$

where $x_i^{[p]}$ is the centroid location of the microparticle *p*; $m^{[p]}$ is the mass of the microparticle *p*; and *m* is the total mass of the clump.

The moment and product of inertia of the clump, I_{ii} and I_{ij}, are given by:

$$I_{ii} = \sum_{p=1}^{N_p} \left\{ m^{[p]} \left(x_j^{[p]} - x_j^{[G]} \right) \left(x_j^{[p]} - x_j^{[G]} \right) + \frac{2}{5} m^{[p]} R^{[p]} R^{[p]} \right\} \tag{3:38}$$

$$I_{ij} = \sum_{p=1}^{N_p} \left\{ m^{[p]} \left(x_i^{[p]} - x_i^{[G]} \right) \left(x_j^{[p]} - x_j^{[G]} \right) \right\}; \quad (j \neq i) \tag{3:39}$$

where $R^{[p]}$ is the radius of a microparticle *p*.

3.5.3 Macroparticle (Clump) motion

The translational motion of the center of mass of the macroparticle is described in terms of its position x_i, velocity $\dot{x}_i$, and acceleration $\ddot{x}_i$. The rotational motion of the macroparticle is described in terms of its angular velocity ω_i, and angular acceleration $\dot{\omega}_i$.

The equations of motion (3:21) and (3:22) are given now as follows:

For the resultant force F_i (translational motion):

$$F_i = m(\ddot{x}_i - g_i) \tag{3:40}$$

where *m* is now the total mass of the clump; g_i is the body force acceleration vector; and F_i is the resultant force which is now calculated as:

$$F_i = \tilde{F}_i + \sum_{p=1}^{N_p} \left(\tilde{F}_i^{[p]} + \sum_{c=1}^{N_c} F_i^{[p,c]} \right) \tag{3:41}$$

where $\tilde{F}_i$ is the externally applied force acting on the clump; $\tilde{F}_i^{[p]}$ is the externally applied force acting on microparticle *p*; $F_i^{[p,c]}$ is the force acting on microparticle *p* at contact *c*; N_p is the total number of microparticles that comprise the macroparticle; N_c is the total number of contacts around the microparticle *p*.

For the resultant moment M_i (rotational motion):

$$M_i = \dot{H}_i \tag{3:42}$$

where the resultant moment M_i and the angular momentum $\dot{H}_i$ can now be calculated by:

$$M_i = \tilde{M}_i + \sum_{p=1}^{N_p} \left(\tilde{M}_i^{[p]} + \varepsilon_{ijk} \left(x_j^{[p]} - x_j^{[G]} \right) F_k^{[p]} + \sum_{c=1}^{N_c} \varepsilon_{ijk} \left(x_j^{[c]} - x_j^{[p]} \right) F_k^{[p,c]} \right) \tag{3:43}$$

$$\dot{H}_i = \dot{\omega}_i I_{ii} - \dot{\omega}_j I_{ij} + \varepsilon_{ijk} \omega_j \left(\omega_k I_{kk} - \omega_l I_{kl} \right); \quad \left(j \neq i; l \neq k \right) \tag{3:44}$$

where $\tilde{M}_i$ is the externally applied moment acting on the clump; $\tilde{M}_i^{[p]}$ is the externally applied momentum acting on microparticle *p*; $F_k^{[p]}$ is the resultant force acting on microparticle *p* at its centroid; $F_k^{[p,c]}$ is the force acting on microparticle *p* at contact *c*; N_p is the total number of microparticles that comprise the macroparticle; N_c is the total number of contacts around the microparticle *p*; $x_j^{[p]}$ is the position vector of microparticle *p*; $x_j^{[c]}$ is the position vector of contact *c*; $x_j^{[G]}$, I_{ii} and I_{ij} are basic mass properties (see previous section).

Following section 3.3 for particle motion, equations (3:40) and (3:42) are also integrated using an explicit centered finite difference procedure in order to obtain (translational and angular) velocities and displacements of the macroparticles.

3.6 Particle breakage DEM models

The literature presents some techniques to model the breakage of the particles. Some of them are described here.

3.6.1 Cluster of particles using contact bonds: simple and parallel contact bonds

This technique consists of the simulation of the grains as a cluster of particles (disks or spheres) which are put together usually by simply touching or with a small overlap between them and using breakage bonds at their contacts which support tensile and shear strength and follow previous considerations of section 3.2.2 and 3.2.3 for simple contact bond or parallel contact bond models, respectively. For a considerable number of broken bonds, the cluster is divided into two or more smaller clusters. There is a breakage limit that takes into account the smallest particle size of the cluster. A 2D-scheme from an intact and a broken cluster of bonded particles can be appreciated in Figure 3-6 (O'Sullivan, 2011).

The system of equations for a cluster considers the individual particles. For each particle, all contact forces around the particle are considered: the contact forces at the bond contacts (between the particles of the same cluster) and at other contacts (i.e. between particles belonging to a different cluster).

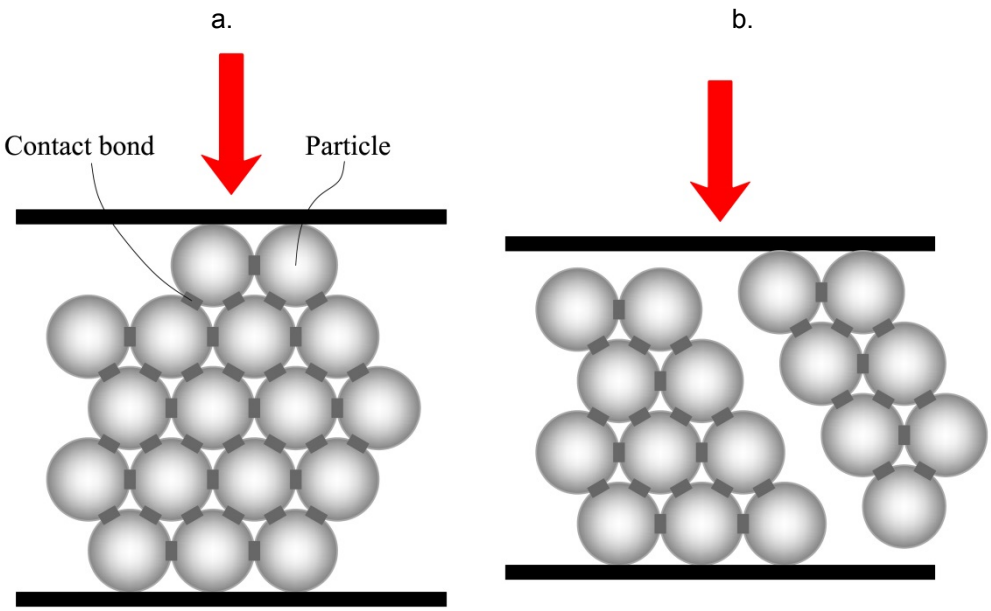

Figure 3-6 Scheme of a cluster of breakage bonded particles: (a) Intact cluster; (b) Broken cluster (From O'Sullivan (2011)).

Some of the examples from literature that have used these kinds of crushable clusters are commented below.

Kafui and Thornton (2000) used agglomerates of equal-sized bonded spheres in face-centred cubic arrangement to simulate a sub-millimetre sized crystalline agglomerate, using the granular dynamics code GRANULE (Aston University version), an improved version of the TRUBAL code (Cundall and Strack, 1979b; Cundall, 1988b). They studied the micro-mechanical behaviour caused by impacts on the agglomerate and reported numerical simulations of orthogonal impacts with a target wall at different impact velocities and for different inter-particle bond strengths. They concluded that for any given bond strength there was an impact velocity which produced a complete set of fracture planes. Subsets of this fracture pattern were produced at lower impact velocities. The fracture was shear-induced. Figure 3-7a shows a face-centred cubic arrangement used by them. Similarly, Thornton and Liu (2004) used the same technique as Kafui and Thornton (2000) to explain the breakage of an agglomerate of powders (polydisperse cuboidal agglomerate using particles of 16-24μm in size) that collides with a target wall (Figure 3-7b and Figure 3-7c).

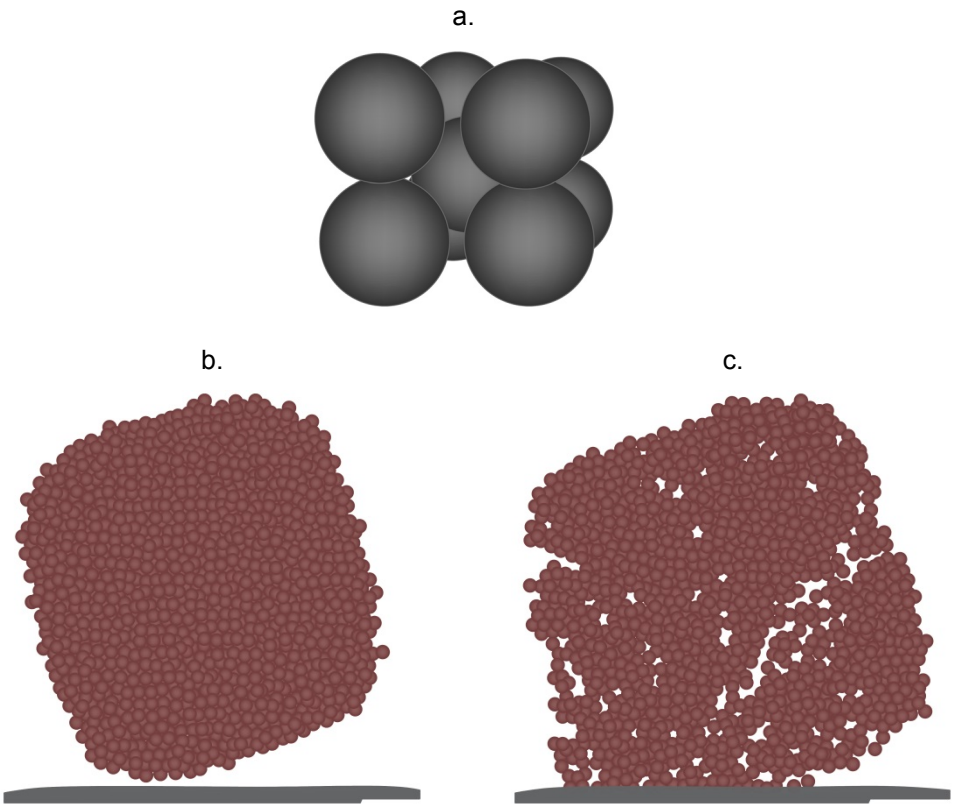

Figure 3-7 Agglomerates of rigid particles with bond contacts using GRANULE code: (a) Agglomerate microstructure: nine equal-sized bonded spheres in face-centred cubic arrangement (From Kafui and Thornton (2000)); (b) Polydisperse cuboidal agglomerate before impact; (c) Cuboidal agglomerate after impact-t=11μs (From Thornton and Liu (2004)).

Robertson (2000) and Robertson and Bolton (2001) applied this technique to a geotechnical field. They used regular “crystalline” (spherical shape) assemblies of balls using simple contact bonds in order to simulate crushable soils (Figure 3-8). The Weibull statistical analysis was taken into account by introducing randomly flawed bonds with 5% of the strength value of unflawed bonds. The PFC3D code was used in the numerical modelling. One-dimensional tests and triaxial tests were analyzed. Figure 3-8a and Figure 3-8b show an intact and broken cluster or assembly of bonded particles, respectively; Figure 3-8c shows an assembly of clusters in a numerical uniaxial compression test.

Cheng et al. (2003) also used clusters (or agglomerates) of bonded spheres but in a hexagonal close packing in order to reduce voids between clusters (Figure 3-9a). The spheres were put together without any initial overlap. The bonds were simple contact bonds. In order to take into account the Weibull statistical variability of the strength and shape of the agglomerates, similar to real sand grains, each sphere had an 80% probability of survival, i.e. 20% of the spheres were eliminated from an original agglomerate composed of 57 spheres. Figure 3-9 shows some of the different clusters used at the beginning of the simulations. The particle contact parameters were calibrated comparing experimental and numerical results from crushing tests for a single particle. The PFC3D code was also used and triaxial tests simulated to study the behaviour of sands.

McDowell and Harireche (2002) have also used aggregates with simple contact bonds between particles to simulate the silica sand behaviour in one-dimensional compression tests (PFC3D). Similarly, Lim and McDowell (2005) simulated single particle crushing tests and oedometer tests (PFC3D) on railway ballast using regular (spherical shape) aggregates of spheres with simple contact bonds. The size of a singular aggregate was 48mm. Compared with the experimental data, the DEM model produced an acceptable normal compression line; however, the DEM yield stress was less than for the real ballast. The authors concluded that further compression could arise in the unloading stage from a rolling effect caused by the use of contact bonds which allow the rolling of one ball relative to another without breakage. They do not show the evolution of grain size distributions.

In order to consider the abrasion of ballast, Lu and McDowell (2006) mixed two techniques to model aggregates: a simple two-ball rigid clump with two small bonded balls (asperities). The balls were joined to the clump using parallel contact bonds which could break (Figure 3-10a). They also used PFC3D and simulated a box test on railway ballast (Figure 3-10b).

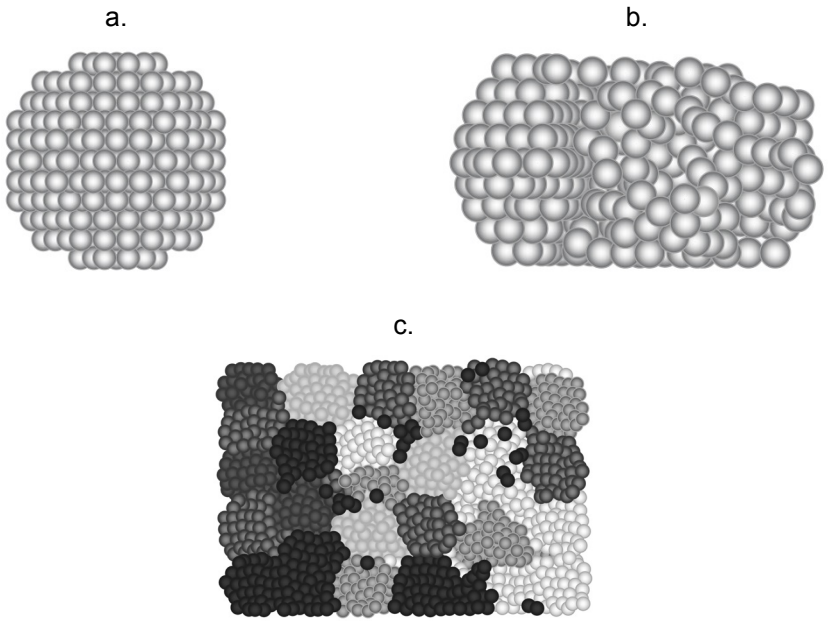

Figure 3-8 Crushable cluster using simple contact bonds: (a) Regular "crystalline" (spherical shape) assembly of balls; (b) Broken cluster; (c) Assembly of cluster in a numerical uniaxial compression test (From Robertson and Bolton (2001)).

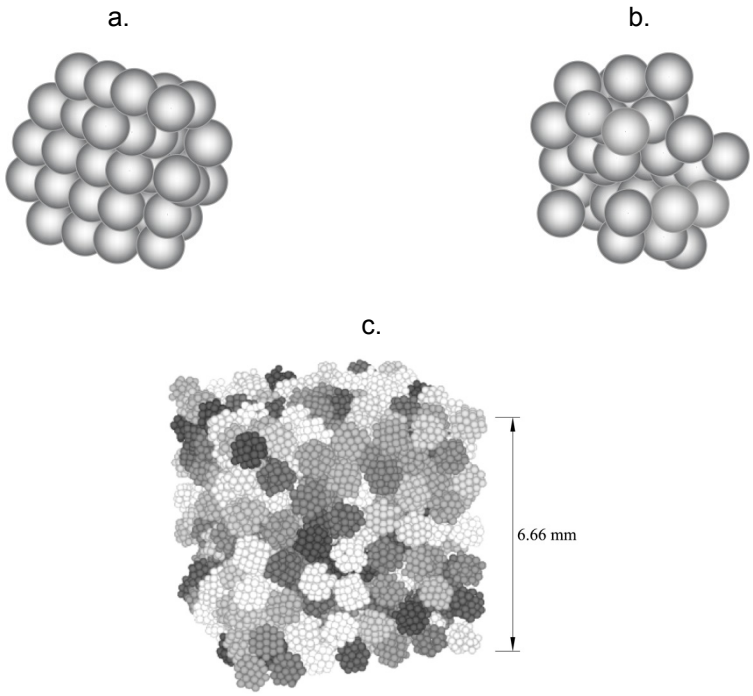

Figure 3-9 Aggregates of simple bonded particles in hexagonal packing: (a) cluster of 50 spheres and 177 bonds; (b) cluster of 36 spheres and 88 bonds; (c) Cubical assembly of clusters (From Cheng et al. (2003)).

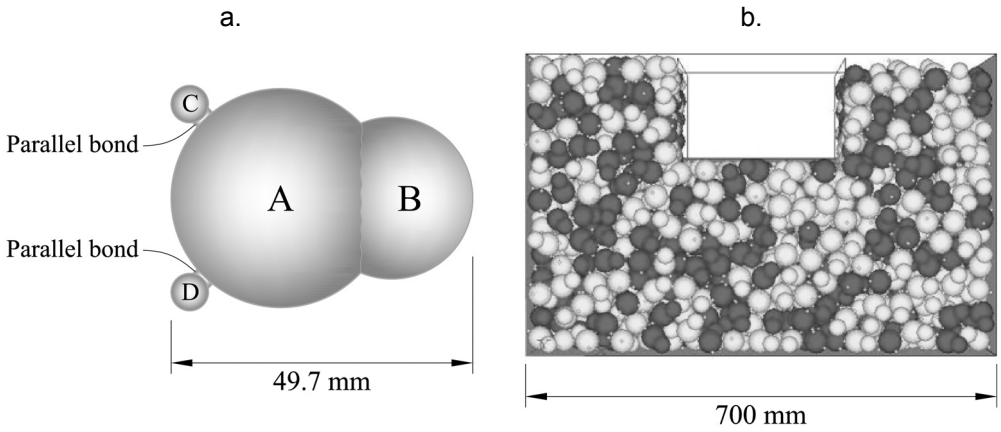

Figure 3-10 Mix of clump with small particles using parallel contact bonds: (a) Two-Ball Clump with two-parallel bonded balls; (b) DEM aggregates in a box test (From Lu and McDowell (2006)).

Deluzarche and Cambou (2006) used a similar technique in order to model breakable rockfill material and reproduce different block shapes using fewer balls: clumps (rigid blocks or sub-clumps) with simple contact bonds between them (**Figure 3-11**). Their model is 2D and uses the PFC2D code. Each sub-clump has at least two bond contacts with the others in order to avoid the rolling between sub-clumps. The clump strength was adapted to the experimental results of crushing tests. The relationships between 2D and 3D parameters were also taken into account. The authors simulated oedometer and biaxial compression tests and compared them with experimental results from the literature.

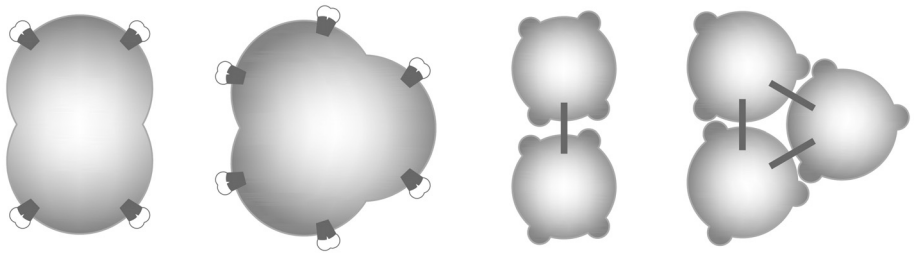

Figure 3-11 Types of breakable cluster of clumps with simple contact bonds in order to model rockfill material (From Deluzarche and Cambou (2006)).

3.6.2 Replacement of broken particles by smaller fragment-particles

This technique consists of replacing a particle which has reached a predefined failure criterion with an equivalent assembly of smaller particles in a multigenerational approach. The following applications can be found in the literature for 2D:(Astrom and Herrmann, 1998; Ben-Nun and Einav, 2010, 2008; Lobo-Guerrero and Vallejo, 2005; Tsoungui et al., 1999); and for 3D consideration: (Bruchmüller et al., 2011; Ciantia et al., 2015; Marketos and Bolton, 2009; Marketos, 2007; McDowell and De Bono, 2013). Some of these models are detailed below.

Tsoungui et al. (1999) considered the breakage of particles using a 2D code based on the Molecular Dynamic method – MD, which is also a smooth DEM method (see 3.1). Their breakage technique has been used in works that apply Cundall's DEM. They replaced the particle by 12-disk particles of four different sizes when it reached the failure criterion (Figure 3-12). The failure criteria is based on the grain fracture under diametric compression. They imposed a certain lower limit on the grain size to consider the breakage. The MD simulations were compared with experimental oedometric compression tests on moulding plaster disks of uniform thickness.

Following the work of Tsoungui et al. (1999), Lobo-Guerrero and Vallejo (2005) replaced the particle (a disk) with eight disks as shown in Figure 3-13. The PFC2D code was used for DEM simulations. The particle "breaks" when an induced tensile stress (which is calculated as in the Brazilian test considering the particle under diametrical compression, taking the highest value of the contact forces acting on the disk particle) reaches the tensile strength of the particle. Only particles with a coordination number equal to or smaller than 3 can break. There is no mass conservation in this method. This model was used in the simulation of direct shear tests. Pöschel and Schwager (2005) follow a similar methodology but take into account the conservation of mass when new particles are created. Overlaps between particles are generated and "nonphysical" energy is introduced to the system (O'Sullivan, 2011).

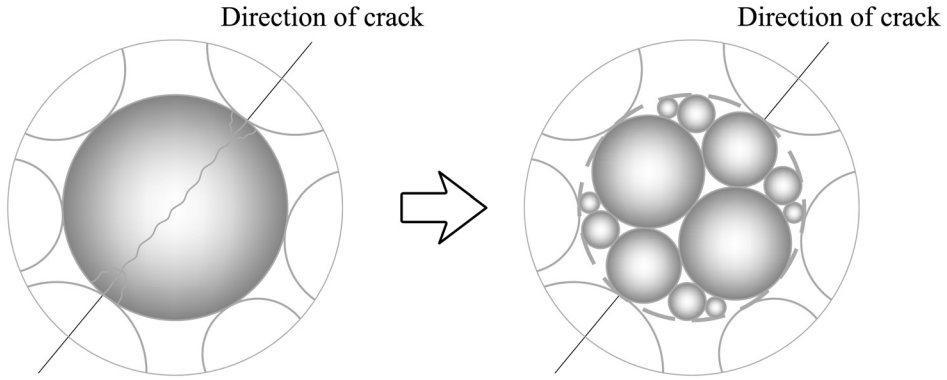

Figure 3-12 Breakage technique by replacement of a "broken" disk particle by smaller disk particles-using a 2D code based on MD method (From Tsoungui et al. (1999)).

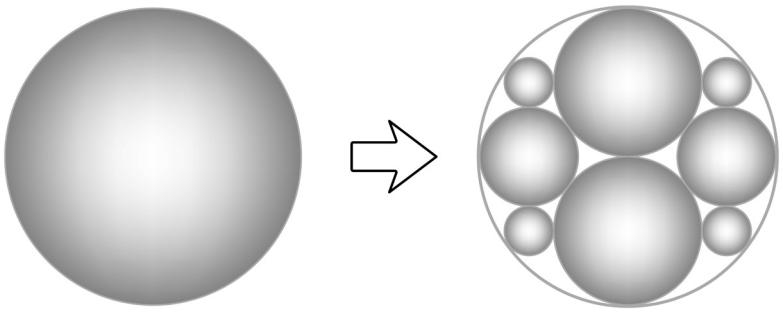

Figure 3-13 Replacement of a "broken" disk particle by smaller disk particles- 2D analysis (From Lobo-Guerrero and Vallejo (2005)).

Marketos and Bolton (2009) compared different techniques to model the fragmentation of particles while using the same failure criterion: A particle breaks if a characteristic stress inside it (defined as the ratio of the maximum normal contact force on the particle and the square of its diameter) exceeds its crushing strength. They used the PFC3D code (3D case) and simulated one-dimensional (uniaxial) compression tests in order to reproduce breakage localization and compaction bands on high-porosity sandstone. They utilized spheres (balls) of 1-2mm which were cemented together by parallel bonds. In addition, they considered three different methods to model the fragmentation of the particles:

(1) Fragmentation of the broken particles.
(2) Removal of broken particles.
(3) Reducing the contact stiffness.

The last two methods are explained later in sections 3.6.4 and 3.6.5, respectively. The first method follows the idea that has been treated in this section. Small fragments were introduced into the granular sample that replaced the broken particle: an eight-ball assembly with half the mass of the original replaced ball (Figure 3-14). Different values of parallel bond strength were used (400, 200 and 80 MPa): for lower values of bond strength the sample was more stable, the ductility was increased, the sample strength decreased and localization was less marked. For a high bond strength, a large brittle peak was observed in the curve axial stress-axial strain, associated with a sudden stress-drop. This behaviour is explained by the number of bonds that break: as the bond strength decreased, the number of bonds broken before significant particle crushing increased, progressively turning the sandstone to sand.

(Ben-Nun and Einav, 2010) also used this replacement method (in 2D analysis) considering three different disk-particle assembly configurations (Figure 3-15) to replace the original disk when it reaches a failure criterion. Two interesting failure criteria were considered: The first is an improved version of the criterion used by (Tsoungui et al., 1999) based on the "Brazilian test" criterion (Mode I-Tensile criterion) – the equations are formulated in terms of nominal and critical forces; the second criterion is based on the mode II of fracture and considers isotropic condition – and it compares the average of the normal component of the contact forces against a critical force which depends on the critical force of the first criterion, the coordination number and the curvature of the loading particles.

Regarding the fragmentation process, to conserve the mass, the replacement was done in two phases as shown in Figure 3-15: Firstly, in phase 1 the replacement is done taking into account the diameter of the original particle in order to avoid overlaps and the particle assembly is randomly rotated, and then, in phase 2, an expansion of the particle is applied to gain back the overall solid mass. After simulations of confined uniaxial compression tests were performed, it was concluded that the gsd curve tended asymptotically towards an ultimate fractal distribution, according to its outstanding particle breakage mechanics (Einav, 2007a, 2007b, 2007c).

Ciantia et al. (2015) worked in a 3D space and used the PFC3D code to simulate silica sand behaviour. They analyzed some sphere configurations in order to perform the replacements and chose a 14-ball packing (Figure 3-17). During the breakage process, there is a lower ball diameter limit to apply breakage, the number of particles is limited, finer particles are excluded and upscaling technique is applied in order to reduce computational costs. There are mass losses of about 47%, which are distributed in finer fractions in order to obtain the porosity and the grain size distribution curves.

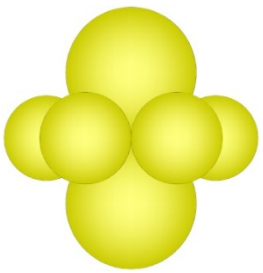

Figure 3-14 Fragmentation of a broken particle: replacement by an 8-ball assembly (From Marketos and Bolton (2009)).

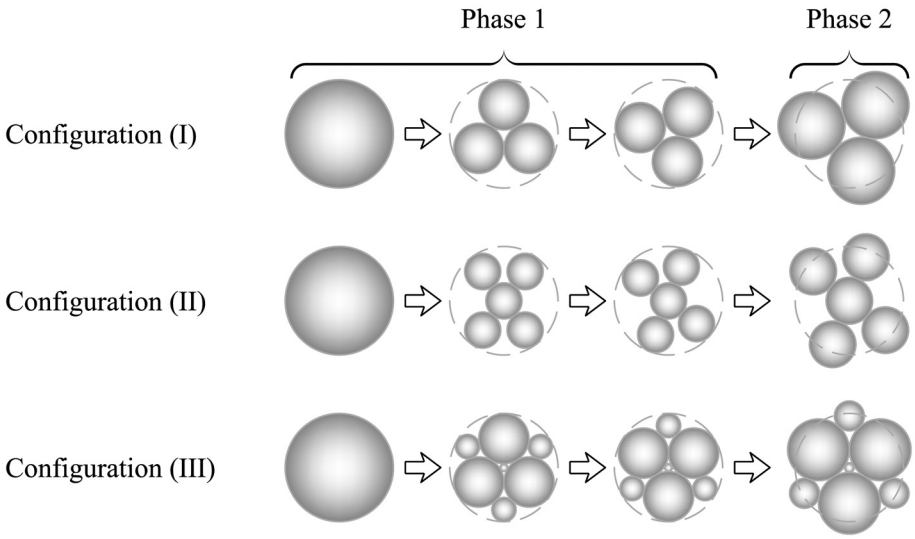

Figure 3-15 Post-crushing fragmentation process of disk-particles (2D analysis): replacements using three different disk-assembly configurations (From Ben-Nun and Einav (2010)).

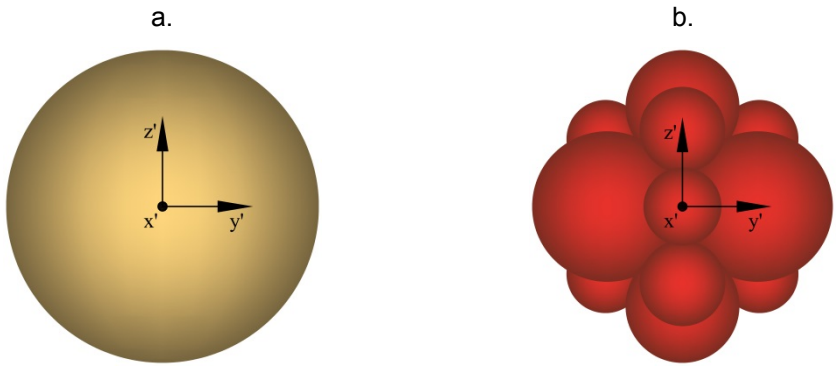

Figure 3-16 Multigenerational replacement approach in a 3D space: (a) intact sphere; (b) 14-sphere configuration after breakage (From Ciantia et al. (2015)).

3.6.3 Releasing Clumps

This methodology consists of using clumps (rigid particles which do not break, see 3.5) and releasing their particles when certain failure criterion is reached. This technique was used in a 2D analysis by Alaei and Mahboubi (2012) in the simulation of rockfill material (5.7 - 7.6cm size) using the PFC2D code. They used three different clump shapes. Figure 3-17 shows one of them: an intact clump at the beginning (intact clump) and after crushing during an indirect tensile test. The clump is composed of three main sub-clumps. Each sub-clump is made of one bigger disk with three small disks around it. When the clump reaches a failure criterion, the sub-clumps are released. The authors based this breakage criterion on Lobo-Guerrero and Vallejo (2005), but considered a contact force orientation anisotropy concept instead of the coordination number concept in order to take into account the confinement effect in the clumps. These sub-clumps cannot break. Single crushing tests and biaxial compression tests were simulated.

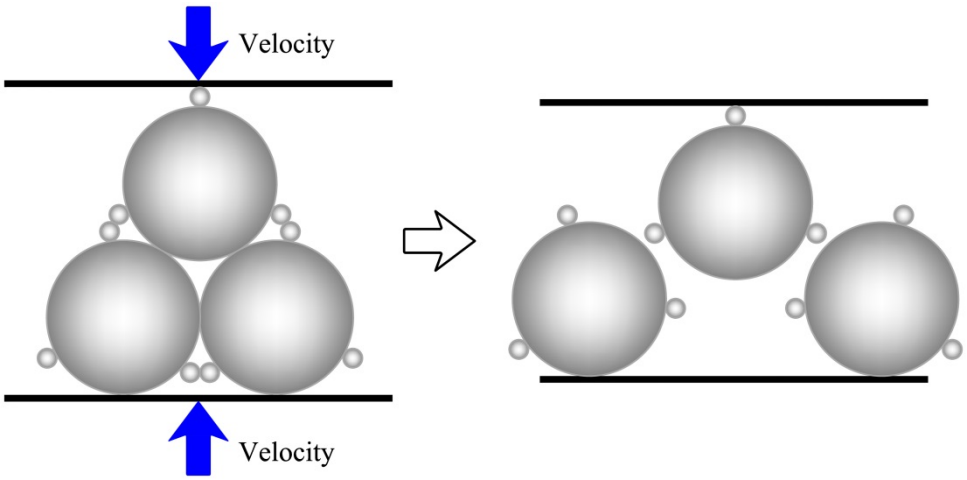

Figure 3-17 Releasing clumps technique: A clump before (right) and after crushing during an indirect tensile test- 2D analysis (From Alaei and Mahboubi (2012)).

3.6.4 Removing particles from clusters

Couroyer et al. (2000) used an improved version of the TRUBAL code (Cundall and Strack, 1979b) and simulated the behaviour of spherical porous alumina beads in the size range of 1.70–2.00mm. Bulk crushing strength (BCS) tests were simulated as compression tests on a particle assembly (3D). During the tests, when the maximum normal contact force of a particle reaches its crushing strength value, the particle is removed from the assembly. The authors justified their methodology arguing that the removal of broken particles does not affect the stress-strain relationship.

As stated in section 3.6.2, Marketos and Bolton (2009) also used this method of removing the broken particles in a 3D analysis using the PFC3D code. They explained that this case is thought to represent cases where the parent grain is crushed to dust that falls into the large inter-particle void space. They concluded that this method does not reproduce the stiffening of the sample at large strains but it is useful for their proposal, the study of compaction band formation at a relatively small strain interval. They found little difference in the sample behaviour between simulations where grain crushing was modelled by particle removal and simulations where the broken particle was replaced by 8 fragments. This was concluded to result from the grain fragments falling into the inter-grain space and being unable to carry forces.

3.6.5 Reducing stiffnesses in contacts

Marketos and Bolton (2009) used this technique to model the crushing of particles and compared it with two other methods, as was explained in sections 3.6.2 and 3.6.4, using the PFC3D code in order to simulate breakage localization and compaction bands on high-porosity sandstone.

As explained in section 3.6.2, when a particle reaches the failure criteria, a reduction of the contact stiffness of the particle by some factor (it was arbitrarily set to 2) is applied. Particles were only allowed to break once. This method simulates cases where the fragments could still carry some force immediately after breakage, with the deformation of inter-fragment voids making the local response less stiff. Additionally, all parallel bonds at the contacts of the broken particle are deleted, causing a further, small reduction in contact stiffness. This method has the advantage of reducing the local implosive behaviour observed in the previous particle breakage methods when a broken particle is removed or replaced by smaller particles. In fact, with this method it was observed that the sample behaviour is less unstable.

However, this method does not consider the evolution of the grain size distribution.

3.7 Software adopted

For the three-dimensional DEM simulations, this research uses the commercial code PFC^{3D} (PFC3D- Particle Flow Code in 3 Dimensions), version 4.0, developed

by Itasca Consulting Group, Inc.

PFC3D models the movement and interaction of stressed assemblies of distinct particles, bodies that occupy a finite amount of space, using Cundall's DEM (Cundall and Strack, 1979a): a soft contact approach method, where distinct particles (spheres) are rigid, move independently of one another, and interact only at contacts or interfaces between particles; they may overlap at the contacts, as described in sections 3.1 - 3.5. PFC3D is a simplified implementation of DEM because of the restriction to rigid spherical particles; although it also provides the clump tool which allows the modelling of macroparticles of arbitrary shape (see section 3.5). The theory, specifications and features of the code can be found in the PFC3D manual (Itasca, 2008).

In addition to spheres (balls), PFC3D provides boundary elements: "walls", which make it possible to confine the assemblies of balls. The walls can be moved applying certain velocity. The balls and walls can interact via the forces at contacts. The motion of the walls should be specified by the user and remains constant regardless of the contact forces acting on it. There can only be ball-ball contact or ball-wall contact.

PFC3D allows users to introduce their modelling using a programming language called FISH. Also, new contact models can be written in C++ language and compiled as a DLL (dynamic link library). In this research, the DEM model and the numerical simulations of the tests have been introduced via FISH programming.

FISH allows the defining of new variables and functions which may be used to extend PFC3D's usefulness or add user-defined features. These FISH programs are embedded in a data file and executed by PFC3D. The new FISH Functions may invoke other Functions, which may invoke others. The characteristics of FISH programming are detailed in the PFC3D manual (Itasca, 2008).

Some features to take into account for DEM simulations using PFC3D are described below. The details of commands that are used in this procedure can be found in the PFC3D manual (Itasca, 2008). However, some of these features that are used in the programming of the DEM model, described in chapter 5, and numerical test simulations of this research are detailed in chapters 5-7.

3.7.1 Generation of the assembly of particles

3.7.1.1 Definition of entities

Characteristics such as size and shape should be defined for the following entities:

- Balls: Spheres, Clusters of spheres.
- Walls: The walls can be of different types: Flat, cylinder, disk, spiral, sphere, ring and line3D.
- Clumps.

GENERATE, BALL, WALL and CLUMP commands are used.

3.7.1.2 Definition of the contact model and assignation of properties of entities

The following properties should be specified depending on the contact model:

- Friction coefficient.
- Normal and shear stiffnesses.
- Bond properties.
- Damping coefficient.
- Timestep.
- Other properties that depend on the contact model used in the simulations.

PROPERTY, WALL, CLUMP, and DAMP commands are used. Unusual distributions of properties and non-standard properties require the introduction of new FISH functions.

3.7.1.3 Allocation of walls

Walls act as boundaries for the system of particles. WALL command is used.

3.7.1.4 Creation of an assembly of particles

Particles (Balls, clusters, clumps) are allocated in a “physical” space. GENERATE, BALL, WALL and CLUMP commands are used. Special particle generations and distributions require new FISH functions.

3.7.1.5 Generation of the assembly of particles with a required porosity

This procedure requires a new FISH function.

3.7.2 Definition of a breakage model (optional)

The introduction of functions to consider particle breakage is required in this research.

3.7.3 Numerical simulation

The numerical simulation of a test or a certain motion condition for the system of particles requires the introduction of new functions that are generally related to the following aspects:

- Motion of the walls.
- Motion of the particles.
- Application of forces on the particles.
- Servo-control system in numerical tests.

- Calculation of stresses, strains and other variables.

3.7.4 Monitoring of variables

Standard PFC3D variables (contact forces; particle and wall positions) and new variables can be monitored during the DEM simulation via the following:

- Using HISTORY command: Variables can be stored during a model run.
- Output data file.
- Visualization on the screen of the evolution of variables of the particle system using the PLOT command: For example, particle positions, contact forces, velocity and displacement vectors for particles, and others variables which have been stored using the HISTORY command.

New FISH functions are required to plot or print new variables.

3.8 Conclusions

DEM (Discrete Element Method) is a numerical model capable of describing the mechanical behaviour of assemblies of particles which tend to be disks (2D analysis) and spheres (3D analysis). It was introduced by Peter Cundall (Cundall and Strack, 1979a; Cundall, 1971) and originally named Distinct Element Method ("original DEM"). Over the years, other techniques based on the original DEM of Cundall have been developed. Many of these models can be grouped as Discrete Element Methods (DEM), where a particle occupies a finite amount of space (not a single point). Particulate methods or modelling (or particle-based methods) include DEM and other methods which are based on particle behaviour.

This research uses the DEM of Cundall, i.e. a smooth method or soft contact approach method, where distinct particles (spheres) are infinitely stiff (i.e. they always conserve their shape) but may overlap at the contacts, move independently of one another, and interact only at contacts or interfaces between them. DEM allows finite displacements and rotations of the particles.

In DEM, the interaction of the particles is monitored contact by contact and the motion of the particles is modelled particle by particle. DEM applies a law of force-displacement in the contacts and Newton's second law of motion in the particles. DEM (of Cundall) uses the explicit finite difference method to calculate the displacements of the particles. This explicit scheme uses a fine-time-step (timestep) which should not exceed a critical value in order to obtain a stable solution.

DEM uses a frictional contact law that considers fine-physical effects at the contacts (e.g. springs). For example, the simple linear contact considers a friction coefficient between particles and normal and shear contact stiffnesses. DEM can also consider a bond at the contact (simple or parallel contact bond) in order to model a "glue or cement" behaviour at the contact between two particles. A simple contact bond can only resist tensile normal and shear forces, and it is defined by

normal tensile contact bond strength and shear contact bond strength. The parallel contact bond resists tensile normal and shear forces and moments. It is defined by the normal and shear stiffness per unit area, and the tensile and shear strength.

DEM also uses dashpot elements to consider a damping effect in order to dissipate kinetic energy and avoid instability of the system. Damping can be applied to each ball (local damping) or to each contact (viscous damping).

The use of DEM provides information concerning the micro-mechanical behaviour of a granular mass (assembly of particles) and it may provide an important and useful tool to understand the macro-mechanical behaviour.

This research uses the commercial code PFC^{3D} (PFC3D- Particle Flow Code for 3 Dimensions), version 4.0, developed by Itasca Consulting Group, Inc. This code allows the introduction of new functions through subroutines in FISH programming language in order to include new variables, failure criteria, servo-control systems, specific motion of particles and boundaries, numerical modelling of tests, etc.

PFC3D is a discrete element code and adopts the DEM of Cundall.

PFC3D can employ three entities that comprise the DEM system: balls (spheres), walls (boundaries), and clumps. The balls can be grouped and form clusters using contact bonds. Different types of walls could be used: flat, cylinder, ring, etc. The clumps are assemblies of balls that behave as rigid bodies and cannot break.

Some techniques to model particle breakage that can be found in the literature have been described in this chapter. Many of them have used the PFC code (PFC2D or PFC3D). These techniques can be summarized in five types: (1) Breakage of a cluster of particles (disks or spheres) which use simple or parallel contact bonds; (2) Replacement of broken particles (disks or spheres) by smaller fragment-particles (disks or spheres); (3) Releasing Clumps; (4) Removing particles from clusters; and (5) Reducing stiffness at contacts. The first two techniques are the most widely used.

Although previous techniques to model the breakage have reproduced the macro-mechanical behavior of particle aggregates subjected to some numerical tests, they should pay special attention to solving certain problems. Information about two- or three-dimensional analysis is indicated in parentheses:

- For the first technique: ensuring the rigidity of the whole cluster that should behave as a rigid macroparticle; avoiding a rolling effect caused by the use of contact bonds which allow the rolling of one ball relative to another without breakage. (2D and 3D analysis).
- For the second: ensuring the mass conservation. (2D and 3D analysis).
- For the third: computational cost. (2D analysis).
- For the fourth: mass loss. (2D and 3D analysis).
- The fifth technique does not consider the evolution of the grain size distribution. (3D analysis).

3.9 List of Notations

Notation		*Section*
A	Area of the parallel bond disk; Eq. (3:12); (3:13); (3:16)	3.2.3.3
BPM	Bonded Particle Method	3.2.3
C++	Programming language	3.7
c_i	Damping constant that acts on the contact for the *i* component of the contact force (*i*=*n* for normal; *i*=*s* for shear); (viscous damping); Eq. (3:32); (3:33)	3.4.2
c_i^{crit}	Critical damping constant that acts on the contact for the *i* component of the contact force (*i*=*n* for normal; *i*=*s* for shear); (viscous damping); Eq. (3:33); (3:34)	3.4.2
D_i	Damping force at the contact for the *i* component of the contact force (*i*=*n* for normal; *i*=*s* for shear); (viscous damping); Eq. (3:32)	3.4.2
DLL	Dynamic link library	3.7
DEM	(1) Discrete Element Method (2) Distinct Element Method	(1) 3 (2) 3 ; 3.1 ; 3.1.1
ED	Event-Driven method	3.1
F	Force	3.1.1
$\|F\|$	Magnitude of the force that acts on the particle (local damping); Eq. (3:31)	3.4.1
F_i	(1) Contact force vector; Eq. (3:1) (2) Force at particle-particle contact (at parallel contact bond) (3) Resultant force vector at a particle *i*; Eq. (3:21) (4) Resultant force vector of the macroparticle or clump; Eq. (3:40); (3:41)	(1) 3.2.1.1 (2) 3.2.3 (3) 3.3 (4) 3.5.3
$\bar{F}_i$	Force at bond (at parallel contact bond) - action of the bond on the particle; Eq. (3:10)	3.2.3

$\tilde{F}_i$	Externally applied force vector acting on the clump; Eq. (3:41)	3.5.3
$F_i(t)$	Resultant force vector of a particle *i* for a current time *t*; Eq. (3:25)	3.3
$F_i(t+\Delta t)$	Resultant force vector of a particle *i* for a time ($t+\Delta t$)	3.3
F^d	Damping force that acts on the particle (local damping); Eq. (3:31)	3.4.1
F^n	Contact normal force component; Eq. (3:1); (3:2)	3.2.1.1
$\overline{F}^n$	Axial force at bond (at parallel contact bond) - action of the bond on the particle; Eq. (3:10); (3:12); (3:19)	3.2.3.3
F^s	Contact shear (or tangential) force; Eq. (3:1); (3:4); (3:6)	3.2.1.1 ; 3.2.1.2
$\overline{F}^s$	Shear force at bond (at parallel contact bond) - action of the bond on the particle; Eq. (3:10); (3:13); (3:20)	3.2.3.3
F_c^n	Normal contact bond strength (force)	3.2.2
F_c^s	Shear contact bond strength (force)	3.2.2
$\tilde{F}_i^{[p]}$	Externally applied force vector acting on microparticle *p*; Eq. (3:41)	3.5.3
$F_i^{[p,c]}$	Force vector acting on microparticle *p* at contact *c*; Eq. (3:41)	3.5.3
$F_k^{[p]}$	Resultant force vector acting on microparticle *p* at its centroid; Eq. (3:43)	3.5.3
$F_k^{[p,c]}$	Force vector acting on microparticle *p* at contact *c*; Eq. (3:43)	3.5.3
$F_{\max}^s$	Maximum allowed shear contact force; Eq. (3:8)	3.2.1.2
FEM	Finite Element Method	3.1
FISH	Programming language embedded in the PFC3D code	3.7
g_i	(1) Body force acceleration vector (gravity); Eq. (3:21)	(1) 3.3
	(2) Body force acceleration vector of the macroparticle or clump; Eq. (3:40)	(2) 3.5.3

gsd	Grain size distribution	3.6
$\dot{H}_i$	Angular momentum vector of the macroparticle or clump; Eq. (3:42); (3:44)	3.5.3
I	(1) Moment of Inertia of the disk cross-section; Eq. (3:15); (3:17); (3:19)	(1) 3.2.3.3
	(2) Moment of Inertia; Eq. (3:22)	(2) 3.3
I_{ii}	Moment of inertia of the clump; Eq. (3:38); (3:44)	3.5.2
I_{ij}	Product of inertia of the clump; Eq. (3:39); (3:44)	3.5.2
J	Polar moment of inertia of the disk cross-section; Eq. (3:14); (3:18); (3:20)	3.2.3.3
K^n	Normal contact stiffness (secant stiffness modulus) – Contact between two particles; Eq. (3:2); (3:3)	3.2.1.1
k	Stiffness (one-dimensional mass-spring system); Eq. (3:29); (3:30)	3.3.1
k_i	Contact tangent stiffness that acts on the contact for the *i* component of the contact force (*i*=*n* for normal; *i*=*s* for shear); (viscous damping); Eq. (3:34)	3.4.2
k_n	(Contact) Normal stiffness of a particle	3.2
$k_n^{(A)}$	Normal stiffnesses of the particle A; Eq. (3:3)	3.2.1.1
$k_n^{(B)}$	Normal stiffnesses of the particle B; Eq. (3:3)	3.2.1.1
k^s	Shear contact stiffness (tangential stiffness modulus) – Contact between two particles; Eq. (3:4); (3:5)	3.2.1.1
k_s	(Contact) Shear stiffness of a particle	3.2
$k_s^{(A)}$	Shear stiffness of the particle A; Eq. (3:5)	3.2.1.1
$k_s^{(B)}$	Shear stiffness of the particle B; Eq. (3:5)	3.2.1.1
$\overline{k}^n$	Normal stiffness per unit area at parallel contact bond; Eq. (3:12); (3:15)	3.2.3.3
$\overline{k}^s$	Shear stiffness per unit area at parallel contact bond; Eq. (3:13); (3:14)	3.2.3.3
$\overline{L}$	Length of (cylinder) parallel bond	3.2.3.3
M_i	(1) Resultant moment vector acting on a spherical particle *i*; Eq. (3:22)	(1) 3.3

	(2) Resultant moment vector of the macroparticle or clump; Eq. (3:42); (3:43)	(2) 3.5.3
$\bar{M}_i$	Moment at bond (at parallel contact bond) - action of the bond on the particle; Eq. (3:11)	3.2.3
$\tilde{M}_i$	Externally applied moment vector acting on the clump; Eq. (3:43)	3.5.3
$M_i(t)$	Resultant moment vector of a particle *i* for a current time *t*; Eq. (3:26)	3.3
$M_i(t+\Delta t)$	Resultant moment vector of a particle *i* for a time ($t+\Delta t$)	3.3
$\bar{M}^n$	Axial moment at bond (at parallel contact bond) - action of the bond on the particle; Eq. (3:11); (3:14); (3:20)	3.2.3.3
$\bar{M}^s$	Shear moment (Bending moment) at bond (at parallel contact bond) - action of the bond on the particle; Eq. (3:11); (3:15); (3:19)	3.2.3.3
$\tilde{M}_i^{[p]}$	Externally applied momentum vector acting on microparticle *p*; Eq. (3:43)	3.5.3
MD	Molecular Dynamics method	3.1
MPM	Material Point Method	3.1
m	(1) Mass of the particle; Eq. (3:21)	(1) 3.3
	(2) Mass (one-dimensional mass-spring system); Eq. (3:29); (3:30)	(2) 3.3.1
	(3) Effective system mass; (viscous damping); Eq. (3:34); (3:35)	(3) 3.4.2
	(4) Total mass of a clump; Eq. (3:36); (3:40)	(4) 3.5.2; 3.5.3
$m^{(A)}$	Mass of the particle A; (viscous damping); Eq. (3:35)	3.4.2
$m^{(B)}$	Mass of the particle B; (viscous damping); Eq. (3:35)	3.4.2
$m^{[p]}$	Mass of the microparticle *p*; Eq. (3:36) - (3:39)	3.5.2
N_c	Total number of contacts around the microparticle *p*; Eq. (3:41); (3:43)	3.5.3
N_p	Number of microparticles; Eq. (3:36) - (3:39); (3:41); (3:43)	3.5.2; 3.5.3

NSCD	Non Smooth Contact Dynamics method	3.1
n_i	Component of unit vector which define the contact plane: normal direction to contact plane; Eq. (3:1); (3:10); (3:11)	3.2.1.1; 3.2.3.3
PFC	Particle Flow Code	3.2 ; 3.6 ; 3.7
PFC2D ; PFC^{2D}	Particle Flow Code in 2 Dimensions	3.6
PFC3D ; PFC^{3D}	Particle Flow Code in 3 Dimensions	3.2 ; 3.6 ; 3.7
R	Radius of the particle; Eq. (3:22)	3.3
$\overline{R}$	Radius of (cylinder) parallel bond; Eq. (3:9); (3:16) - (3:20)	3.2.3.3
$R^{(A)}$	Radius of the particle A; Eq. (3:9)	3.2.3.3
$R^{(B)}$	Radius of the particle B; Eq. (3:9)	3.2.3.3
$R^{[p]}$	Radius of a microparticle *p*; Eq. (3:38)	3.5.2
SPH	Smoothed-Particle Hydrodynamics method	3.1
sign(V)	Sign (positive or negative) of the particle velocity (local damping); Eq. (3:31)	3.4.1
T	Period of the one-dimensional mass-spring system; Eq. (3:28); (3:29)	3.3.1
t	(1) Time (2) Time; Eq. (3:23) - (3:27)	(1) 3.1.1 (2) 3.3
t_{crit}	Critical time step; Eq. (3:28); (3:30)	3.3.1
t_i	Component of unit vector which define the contact plane: tangential direction to contact plane; Eq. (3:1) ; (3:10); (3:11)	3.2.1.1; 3.2.3.3
t_0	Initial time	3.1.1
U^n	Overlap; Eq. (3:2)	3.2.1.1
V_i	Relative velocity at the contact for the *i* component of the contact force (*i*=*n* for normal; *i*=*s* for shear); (viscous damping); Eq. (3:32)	3.4.2
x_i	(1) Position vector of the center of particle *i* (2) Position of the (centroid) macroparticle or clump	(1) 3.3 (2) 3.5.3

$\dot{x}_i$	(1) Velocity vector of a particle *i* (2) Velocity of the macroparticle or clump	(1) 3.3 (2) 3.5.3
$\ddot{x}_i$	(1) Acceleration vector of the particle *i*; Eq. (3:21) (2) Acceleration of the macroparticle or clump; Eq. (3:40)	(1) 3.3 (2) 3.5.3
$x_i^{[G]}$	Location of the center of mass of a clump *i*; Eq. (3:37) - (3:39); (3:43)	3.5.2
$x_i^{[p]}$	Centroid location of the microparticle *p* that belongs to the clump *i*; Eq. (3:37) - (3:39)	3.5.2
$x_i(t)$	Position vector of the center of particle *i* for a current time *t*; Eq. (3:27)	3.3
$x_i(t+\Delta t)$	Position vector of the center of particle center *i* for a current time (t+Δt); Eq. (3:27)	3.3
$\dot{x}_i\left(t+\frac{\Delta t}{2}\right)$	Velocity vector of a particle *i* in a time (t+Δt/2); Eq. (3:23); (3:25)	3.3
$\dot{x}_i\left(t-\frac{\Delta t}{2}\right)$	Velocity vector of a particle *i* in a time(t-Δt/2); Eq. (3:23)	3.3
$\ddot{x}_i(t)$	Translational acceleration vector of a particle *i* in a current time *t*; Eq. (3:23)	3.3
$x_j^{[p]}$	Position vector of the microparticle *p*; Eq. (3:43)	3.5.3
$x_j^{[c]}$	Position vector of the contact *c*; Eq. (3:43)	3.5.3

2D	Two Dimensional	3
3D	Three Dimensional	3

α	Damping coefficient that acts on the particle (local damping); Eq. (3:31)	3.4.1
β_i	Critical damping ratio for the *i* component of the contact force (*i*=*n* for normal, β_n ; *i*=*s* for shear, β_s); (viscous damping); Eq. (3:33)	3.4.2
ΔF^s	Increment of elastic shear force; Eq. (3:4)	3.2.1.1

Δt	(1) Increment of time; timestep	(1) 3.1.1
	(2) Time increment; Eq. (3:23) - (3:27)	(2) 3.3
ΔU^s	Relative shear-displacement increment; Eq. (3:4)	3.2.1.1
$\bar{\lambda}$	Bonded multiplier factor for parallel contact bond; Eq. (3:9)	3.2.3.3
μ	(1) Coefficient of friction of a particle	(1) 3.2
	(2) Coefficient of friction at the contact between two particles; Eq. (3:6); (3:7); (3:8)	(2) 3.2.1.2
$\mu^{(A)}$	Friction coefficient of the particle A; Eq. (3:7)	3.2.1.2
$\mu^{(B)}$	Friction coefficient of the particle B; Eq. (3:7)	3.2.1.2
$\bar{\sigma}_c$	Tensile parallel contact bond strength; Eq. (3:19)	3.2.3.3
$\bar{\sigma}^{\max}$	Maximum tensile stress acting on the parallel bond; Eq. (3:19)	3.2.3.3
$\bar{\tau}_c$	Shear parallel contact bond strength; Eq. (3:20)	3.2.3.3
$\bar{\tau}^{\max}$	Maximum shear stress acting on the parallel bond; Eq. (3:20)	3.2.3.3
ω_i	(1) Angular velocity of the particle	(1) 3.3
	(2) Angular velocity of the macroparticle or clump; Eq. (3:44)	(2) 3.5.3
$\dot{\omega}_i$	(1) Angular acceleration vector of the particle; Eq. (3:22)	(1) 3.3
	(2) Angular acceleration of the macroparticle or clump; Eq. (3:44)	(2) 3.5.3
$\dot{\omega}_i(t)$	Rotational (angular) acceleration vector of a particle *i* in a current time *t*; Eq. (3:24)	3.3
$\omega_i\left(t+\frac{\Delta t}{2}\right)$	Angular velocity vector of a particle *i* in a time (t+Δt/2); Eq. (3:24); (3:26)	3.3
$\omega_i\left(t-\frac{\Delta t}{2}\right)$	Angular velocity vector of a particle *i* in a time (t-Δt/2); Eq. (3:24)	3.3

3.10 References

Alaei, E., Mahboubi, A., 2012. A discrete model for simulating shear strength and deformation behaviour of rockfill material, considering the particle breakage phenomenon. Granul. Matter 14, 707–717.

Astrom, J.A., Herrmann, H.J., 1998. Fragmentation of grains in a two-dimensional packing. Eur. Phys. J. B 5, 551–554.

Bathe, K.J., Wilson, E.L., 1976. Numerical Methods in Finite Element Analysis. Prentice-Hall, Englewood Cliffs.

Ben-Nun, O., Einav, I., 2008. A refined DEM study of grain size reduction in uniaxial compression, in: Proocedings of the 12th International Conference of the International Association for Computer Methods and Advances in Geomechanics (IACMAG). Goa, India, pp. 702–708.

Ben-Nun, O., Einav, I., 2010. The role of self-organization during confined comminution of granular materials. Philos. Trans. R. Soc. London A 231–247.

Bruchmüller, J., Van Wachem, B.G.M., Gu, S., Luo, K.H., 2011. Modelling discrete fragmentation of brittle particles. Powder Technol. 208, 731–739. doi:10.1016/j.powtec.2011.01.017

Butlanska, J., 2014. Cone penetration tests in a virtual calibration chamber. PhD. Thesis. Universitat Politècnica de Catalunya, Barcelona, Spain.

Chang, S.W., Chen, C.S., 2008. A non-iterative derivation of the common plane for contact detection of polyhedral blocks. Int. J. Numer. Methods Eng. 74, 734–753.

Cheng, Y.., Nakata, Y., Bolton, M.D., 2003. Discrete element simulation of crushable soil. Géotechnique 53, 633–641. doi:10.1680/geot.2003.53.7.633

Ciantia, M.O., Arroyo, M., Calvetti, F., Gens, A., 2015. An approach to enhance efficiency of DEM modelling of soils with crushable grains. Géotechnique 65, 91–110.

Couroyer, C., Ning, Z., Ghadiri, M., 2000. Distinct element analysis of bulk crushing: effect of particle propertiesand loading rate. Powder Technol. 109, 241–254. doi:10.1016/S0032-5910(99)00240-5

Cundall, P.A., 1971. A computer model for simulating progressive large-scale movements in blocky rock systems, in: Proocedings of the Symposio of the International Society of Rock Mechanics, Nancy 2. p. No. 8.

Cundall, P.A., 1988a. Formulation of a three-dimensional Distinct Element Model—Part I. A scheme to detect and represent contacts in a system composed of many polyhedral blocks. Int. J. Rock Mech. Min. Sci. 25, 107–116. doi:10.1016/0148-9062(88)92293-0

Cundall, P.A., 1988b. Micromechanics of Granular Materials, in: Satake, M., Jenkins, J.T. (Eds.), . Elsevier, pp. 113–123.

Cundall, P.A., Strack, O.D.L., 1979a. A discrete numerical model for granular assemblies. Géotechnique 29, 47–65.

Cundall, P.A., Strack, O.D.L., 1979b. The distinct element method as a tool for research in granular media, Part I.

Deluzarche, R., Cambou, B., 2006. Discrete numerical modelling of rockfill dams. Int. J. Numer. Anal. Methods Geomech. 30, 1075–1096. doi:10.1002/nag

Dubois, F., 2011. Numerical modeling of granular media composed of polyhedral particles, in: Radjai, F., Dubois, F. (Eds.), Discrete-Element Modeling of Granular Materials. ISTE Ltd; John Wiley & Sons, Inc., London, UK, pp. 233–261.

Dubois, F., Jean, M., 2003. LMGC90 une plateforme de développement dédiée à la modélisation des problèmes d'interaction, in: Sixième Coloque National En Calcul Des Structures, Vol. 1. pp. 111–118.

Duran, J., 2000. Sands, Powders, and Grains. An introduction to the Physics of Granular Materials. Springer, New York.

Einav, I., 2007a. Breakage mechanics - Part I: Theory. J. Mech. Phys. Solids 55, 1274–1297. doi:10.1016/j.jmps.2006.11.003

Einav, I., 2007b. Breakage mechanics - Part II: Modelling granular materials. J. Mech. Phys. Solids 55, 1298–1320. doi:10.1016/j.jmps.2006.11.004

Einav, I., 2007c. Fracture propagation in brittle granular matter. Proc. R. Soc. A Math. Phys. Eng. Sci. 463, 3021–3035. doi:10.1098/rspa.2007.1898

Galindo-Torres, S., Pedroso, D., 2010. Molecular dynamics simulations of complex-shaped particles using Voronoi-based spheropolyhedra. Phys. Rev. E 81, 1–9.

Hogue, C., 1998. Shape representation and contact detection for discrete element simulations of arbitrary geometries. Eng. Comput. 15, 374–390.

Itasca, 2008. Manuals of PFC3D v.4.0, 4th ed. USA.

Jean, M., 2011. Contact Dynamic Method, in: Radjai, F., Dubois, F. (Eds.), Discrete-Element Modeling of Granular Materials. ISTE Ltd; John Wiley & Sons, Inc., London, UK, pp. 27–66.

Kafui, K., Thornton, C., 2000. Numerical simulations of impact breakage of a spherical crystalline agglomerate. Powder Technol. 109, 113–132.

Lee, Y., Yang, C.T., Chien, C.S., 2003. A 3D ellipsoid-based model for packing of granular particles. Int. J. Comput. Appl. Technol. 17, 148–155.

Lim, W.L., McDowell, G.R., 2005. Discrete element modelling of railway ballast. Granul. Matter 7, 19–29. doi:10.1007/s10035-004-0189-3

Lobo-Guerrero, S., Vallejo, L.E., 2005. Discrete Element Method Evaluation of Granular Crushing Under Direct Shear Test Conditions. J. Geotech. Geoenvironmental Eng. ASCE 131, 1295–1300.

Lu, M., McDowell, G.R., 2006. Discrete element modelling of ballast abrasion. Géotechnique 56, 651–655.

Marketos, G., 2007. An investigation of crushing and compaction bands in granular material. PhD. Thesis. Cambridge University, U.K.

Marketos, G., Bolton, M.D., 2009. Compaction bands simulated in discrete element methods. J. Struct. Geol. 31, 479–490.

McDowell, G.R., De Bono, J.P., 2013. On the micro mechanics of one-dimensional normal compression. Géotechnique.

McDowell, G.R., Harireche, O., 2002. Discrete element modelling of soil particle fracture. Géotechnique 52, 131–135.

McNamara, S., 2011a. Molecular Dynamics Method, in: Radjai, F., Dubois, F. (Eds.), Discrete-Element Modeling of Granular Materials. ISTE Ltd; John Wiley & Sons, Inc., London, UK, pp. 1–25.

McNamara, S., 2011b. Event-driven Method, in: Radjai, F., Dubois, F. (Eds.), Discrete-Element Modeling of Granular Materials. ISTE Ltd; John Wiley & Sons, Inc., London, UK, pp. 103–121.

Nezami, E.G., Hashash, Y.M.A., Zhao, D., Ghaboussi, J., 2004. A fast contact detection algorithm for 3-D discrete element method. Comput. Geotech. 31, 575–597.

O'Sullivan, C., 2011. Particulate Discrete Element Modelling. A Geomechanics perspective. Spon Press, Taylor & Francis Group, Abingdon, Oxon, Uk.

Perales, R., 2007. Modélisation du comportement mécanique par éléments discrets des ouvrages maçonnés tridimensionnels. Contribution à la définition d'éléments de contacts surfaciques. PhD. Thesis. University of Montpellier 2.

Pöschel, T., Schwager, T., 2005. Computational Granular Dynamics. Models and Algorithms. Springer-Verlag, Berlin, Germany.

Potyondy, D.O., Cundall, P.A., 2004. A bonded-particle model for rock. Int. J. Rock Mech. Min. Sci. 41, 1329–1364. doi:10.1016/j.ijrmms.2004.09.011

Pournin, L., Weber, M., Tsukahara, M., Ferrez, J.A., Ramaioli, M., Liebling, T.M., 2005. Three-dimensional distinct element simulation of spherocylinder crystallization. Granul. Matter 7, 119–126.

Radjai, F., Dubois, F. (Eds.), 2011. Discrete-element Modelling of Granular Materials. ISTE Ltd; John Wiley & Sons, Inc., London, UK.

Robertson, D., 2000. Computer simulations of crushable aggregates. PhD. Thesis. Cambridge University.

Robertson, D., Bolton, M.D., 2001. DEM simulations of crushable grains and soils, in: Proceedings of the 4th International Conference on Micromechanics of Powders and Grains. Sendai, Japan, pp. 623–626.

Saussine, G., 2004. Contribution à la modélisation de granulats tridimensionnels: application au ballast. PhD. Thesis. University of Montpellier 2.

Saussine, G., Cholet, C., Dubois, F., Bohatier, C., Gauthier, P., 2004. Modélisation du comportment du ballast par une méthode d'éléments discrets. Reveu Eur. des Eléments Finis 13, 725–736.

Thornton, C., 2015. Granular Dynamics, Contact Mechanics and Particle System Simulations. A DEM study, Particle Technology Series. Springer International Publishing. doi:10.1007/978-3-319-18711-2

Thornton, C., Liu, L., 2004. How do agglomerates break? Powder Technol. 143-144, 110–116.

Tsoungui, O., Vallet, D., Charmet, J.C., 1999. Numerical model of crushing of grains inside two-dimensional granular materials. Powder Technol. 105, 190–198. doi:10.1016/S0032-5910(99)00137-0

Chapter 4

Compressibility, grain breakage and time-dependent behaviour of a gap-graded crushable material

Breakage of particles is one of the main mechanisms which contribute to the deformation in coarse aggregates because it introduces instability in the granular mass structure as it can be described in chapter 2. Therefore, the comprehension of the mechanisms of particle breakage is essential to study the mechanical behavior of the coarse aggregates.

This chapter presents results of an alternative, simple but powerful procedure to experimentally investigate the behaviour of a crushable, brittle granular material: sugar cubes (27.4x17.6x12.2mm) placed in two different initial arrangements, a low porosity and ordered cubes piling (e = 0.2) and a high porosity (e = 0.8) disordered mass. Cubes are made by compacting slightly moistened saccharose crystals (size close to 0.45mm). Sugar cube arrangements are a case of a gap graded granular material. Results of a set of one dimensional compression tests are presented. Grain size distributions (gsd) were determined for increasing vertical stress (max. 640kPa). Against an intuitive initial guess, the gsd at the end of the loading process for both porosity types exhibited an almost identical shape made of two S-shaped curves. Comminution and split particle mechanisms have been identified and related with the compressibility and the evolution of grain sizes during loading.

Finally, breakage particle analysis on time is also presented.

4.1 Introduction

In coarse crushable soils and rockfill, the breakage of particles during loading constitutes a key feature that controls their mechanical behaviour. Testing granular soils at stresses capable of grain breakage require either very high stresses in the case of sands (Coop and Lee, 1993; Nakata et al., 2001) or large and costly equipment for gravel and rockfill (Caproni and Armelin, 1998; Clements, 1981; Marachi et al., 1969; Marsal, 1967; Naylor et al., 1986; Oldecop and Alonso, 2004; Parkin and Adikari, 1981; Penman and Charles, 1976).

On the other hand, it is not easy manipulate the samples in order to obtain certain initial arrangements, especially for small initial void ratio. In the laboratory, it may

also be limitations on the magnitude of the applying loads.

Therefore, it would be desirable to test a crushable granular material that would work with different initial porosities and break with a relatively small stresses: sugar cubes.

Particle breakage depends on some material properties and features which were identified in the chapter 2: particle toughness, shape and size of particles, defects inside particles, type and magnitude of the applied load, and environmental conditions that could induce stress corrosion processes inside the material. Mineralogy by itself is not significant “per se” but through its relationship with controlling variables.

Mineralogy and bonding among crystals are “represented”, when explaining breakage by fracture mechanics concepts, by “toughness”. For a given geometry and loading scheme, once toughness is found, the underlying mineralogy, bonding and microstructure, in a general sense, are no longer invoked to explain fracture. Of course, this is part of a modelling concept but it seems to capture well the deformation of brittle rock aggregates. From this perspective, the sugar grains have a given toughness and this is the mechanical information required. No conceptually different, if one accepts fracture mechanics, from other brittle materials (rocks, which may also be extremely different in mineralogy and internal structure). Therefore, the relevant crushing mechanisms of rock particles could be present in a crushable and brittle particle (the sugar cube) which experiences splitting and comminution damage, just as rock particles do, when they are under stress concentrations. The purpose of this chapter is to identify the deformation mechanisms and not to establish a direct relationship with geologic materials in quantitative terms.

An objective of this part of the research is to get relevant results by means of a simple and cheap procedure which, because of the regular geometry of the cubes, could allow the testing of widely different initial porosities and geometric arrangements, a possibility which escapes from typical gravel shapes. In fact, the initial sample void ratio which could be achieved when using parallelepipedic shapes could be as different as e_o=0.2 and e_o=0.8, as shown below.

Sugar cubes are aggregates of saccharose crystals. They are manufactured by compacting slightly moistened saccharose crystals (size close to 0.45 mm and density of 1.588 g/cm3). The mean size of a sugar cube (large “macro” grain) is 27.4x17.6x12.2mm. A collection of sugar cubes is a good example of a gap graded granular material having two characteristic sizes: the cube itself and the basic saccharose crystal. Both “units” are brittle bodies.

Sugar cubes are placed in two widely different initial arrangements: a low porosity and ordered face-to-face piling of the cubes (e_o=0.2) and a high porosity (e_o=0.8) disordered mass.

Additionally, results about the time dependence behavior are presented motived by the found evidence in the literature (Takei et al. 2001; Oldecop & Alonso 2007). The regular initial geometry of cubes is an advantage when trying to identify the breakage mechanisms during loading or in the course of time. One of the

objectives of the experiments was to investigate yielding conditions in a macroscopic sense and their relationship with breakage mechanisms. In addition, special attention was given to check the existence of a limiting attractor for the grain size distribution when the initial particle arrangement is widely different. Major changes in the initial granular soil fabric are difficult to achieve with subrounded, angular or "natural" granular geometries but are easily achieved with a regular cubic geometry of particles, as shown below.

4.2 Some properties of the sugar cube

Sugar cubes (**Figure 4-1**) are commercialized in rectangular prisms of compacted and dried saccharose crystals or sugar grains (**Figure 4-2**) extracted from beet or sugarcane. Sugar cubes are obtained from a mix of sugar and water in a very small amount (1%), subjected to drying and aeration processes. After stabilization, the final humidity should be less than 0.06%. **Table 4-1** and **Table 4-2** list some properties of the sugar crystals and the sugar cubes.

Figure 4-1 Sugar cube (27.4x17.6x12.2 mm).

Figure 4-2 Sugar crystals (0.45mm).

Several simple compression tests were made (**Figure 4-3**) using cubes sugar samples. **Table 4-3** shows some features and results (also see Appendix 4). Unconfined compression strength (**Figure 4-4**) indicated a mean strength of 2325 kPa and a standard deviation of 305 kPa. A brittle failure was measured at axial strains in the range 0.7% - 1.3%. Accordingly, sugar cubes are stiff material, with Young Modulus around to 230 MPa, fragile material, and relatively strong material.

Table 4-1 Properties of sugar crystals.

Mean grain size*:	0.45 ± 0.15 mm
Density*:	1.588 g/cm^3
Saccharose*:	≥ 99.9%
Humidity*:	≤ 0.04%

* Data from "La Azucarera" Company (Spain).

Table 4-2 Properties of sugar cubes.

Dimensions:	27.4 x 17.6 x 12.2 mm
Mean density:	1.027 ± 0.016 g/cm^3
Water content:	0.33 ± 0.13 %

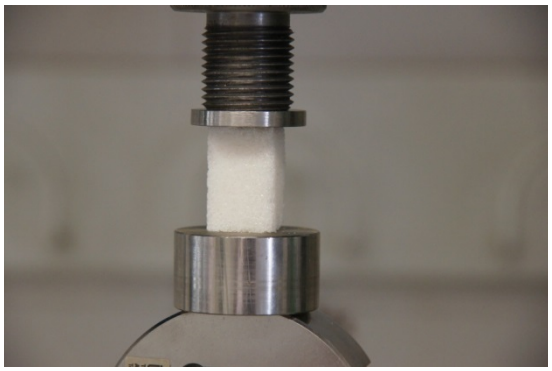

Figure 4-3 Simple compression tests on sugar cube samples.

Table 4-3 Features and results of Simple Compression tests on sugar cube samples.

Sample	Water content	Density	Simple compression strength
	(%)	g/cm^3	kPa
CS1	0.38	1.011	1998.9
CS2	0.17	1.011	2216.5
CS3	0.35	1.011	2625.8
CS4	0.35	1.020	2600.6
CS5	0.17	1.019	1868.4
CS6	0.17	1.060	2686.6
CS7	0.34	1.043	2585.0
CS8	0.34	1.041	1952.3
CS9	0.51	1.020	2400.4
CS10	0.51	1.030	2312.2
Mean	0.33	1.027	2324.7
Standard Deviation	0.13	0.017	304.8

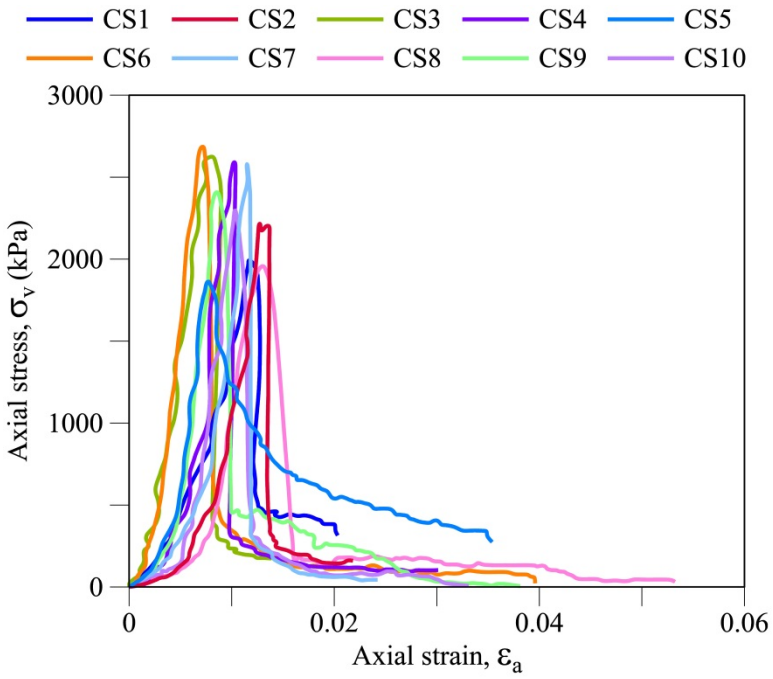

Figure 4-4 Results of unconfined compression strength tests on sugar cube samples.

Friction angle between sugar cubes was measured on regular cube arrangements by means of a tilting table following test details described in Bruce et al. 1989. In these tests, two regular blocks are in contact through a flat surface. The lower block (or plate block) is fixed, and the upper block (or slider block) can move or slide over the lower block. The inclination at which the slider first moves on the plate is known as the friction angle. The inclination of the tilting table was done by hand with a velocity about 8º/min.

Plates were comprised of regular cube arrangements. Two types of arrangements were tested for the sliders: regular cube arrangements of sugar cubes as the plates blocks (M1A arrangements, **Figure 4-5**) and samples of individual sugar cubes (M2A arrangements, **Figure 4-6**).

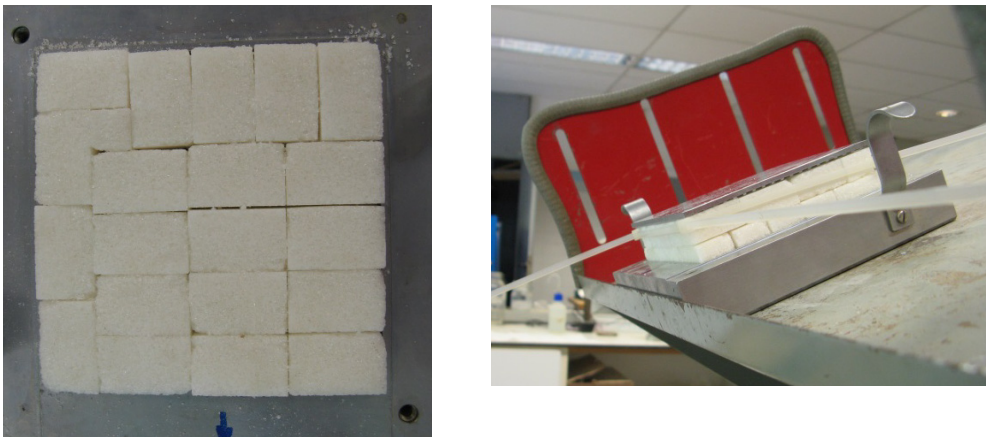

a. b.

Figure 4-5 M1A slider arrangements (10x10cm): (a) Plate block; (b) Tilting table test: Slider and plate blocks.

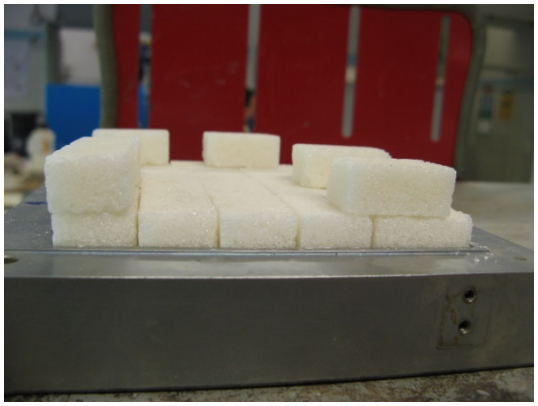

Figure 4-6 M2A slider arrangements (individual sugar cubes). Tilting table test: sliders over a plate block.

A small vertical stress which not exceeds 20 kPa could be applied in some tests. **Table 4-4** and **Table 4-5** show some features and results of the tests.

Table 4-4 Features and results of Friction angles tests using tilt table.

Type of Slider Arrangement	Contact Area (cm2)	Description	Mean Friction Angle (°)	
M1A	100.0	Cube arrangements of sugar cubes assembly	31.8±3.5	31.7±3.5
M2A	4.9	Individual sugar cubes	31.3±3.4	

Table 4-5 Details and results of Friction angles tests using tilt table.

Type of Slider Arrangement	Normal stress (kPa)	Friction angle (°)						Mean Velocity (°/min)
		Test 1	Test 2	Test 3	Test 4	Test 5	Average	
M1A	0.3	28	28	30	-	-	28.7	8.0
	0.5	34	35	-	-	-	34.5	7.9
	0.9	32.5	32.5	-	-	-	32.5	8.0
	1.6	33	35	-	-	-	34.0	8.0
	2.1	36	36.5	-	-	-	36.3	8.0
	3.9	34.5	35	-	-	-	34.8	8.1
	9.4	28	25	-	-	-	26.5	8.0
	18.2	25.5	29	-	-	-	27.3	8.2
M2A	0.1	40	29	36	36	37	35.6	8.2
	0.1	31	31	31	31	31	31.0	8.1
	0.1	26	26	30	-	-	27.3	8.4

The derived mean friction angle and standard deviation (31.8º±3.5º) decreased slightly with confining stress (**Figure 4-7**).

The following expression can be used to calculate the fiction angle, *FA*:

$$FA = 31.429 * \left(\frac{\sigma_N}{\sigma_0}\right)^{-0.012} \quad (4:1)$$

where *FA* = Friction angle in decimal grades (°); σ_N = normal stress in kPa, and σ_0=reference stress equal to 1kPa.

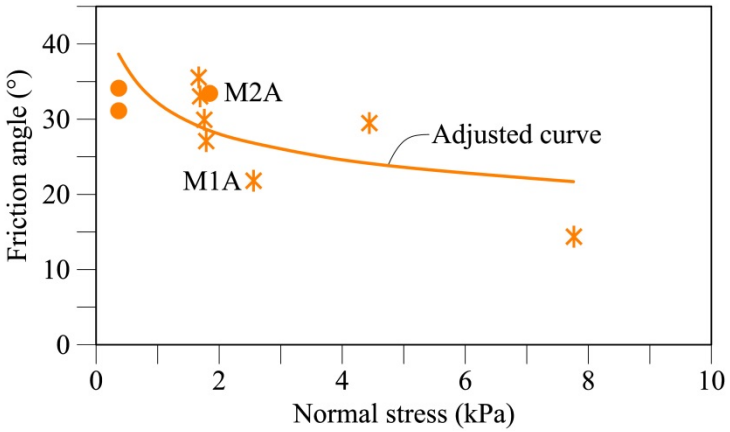

Figure 4-7 Results of friction angle tests using tilting table.

4.3 Particle breakage and compressibility

Two different arrangements have been tested:

a. An ordered pile of sugar cubes in a face-to -face structure, resulting in a low void ratio, approximately e_o= 0.18 (**Figure 4-8**).
b. A disordered aggregate of cubes in a random arrangement, having a high void ratio in the vicinity of e_o= 0.78 (**Figure 4-9**).

Tests were performed in a 152 mm inner diameter Rowe oedometer cell (**Figure 4-10**). The height of samples was 95 mm for the disordered arrangement and 75 mm for the ordered arrangement. Grease was applied to the internal surface of the oedometer cell to minimize friction effects.

In the ordered arrangements, sugar cubes were placed by layers following a certain orientation of the larger side of the cubes. This orientation was changed in each layer by rotating 90° the orientation of major cube axis. There were spaces between the cell and the cubes due to the shape of the sugar cubes compared with the circular geometry of the oedometer ring. The rotation of cube layers during the preparation of the samples tended to homogenize the geometry of voids. All aggregate samples were built in the same manner for all tests. A maximum number of cubes (intact or original cubes) were used per layer in order to obtain a lowest value of void ratio. The contact loads around the cubes at the outside border in

each layer are not uniform in comparison with the cubes in the inner part. However, this effect was common for all the tests performed. It is believed that the overall sample density dominates the sample behaviour.

The relationship between oedometer cell dimensions and sugar cubes follow criteria used for oedometer tests on rockfill and coarse aggregates as it can be appreciated in **Table 4-6**. Published relationships between sample diameter and maximum grain size of particles are in a range from 5.0 to 8.0 for oedometer tests on gravels and rock fragments, and about 7.8 and 6.9 for ordered and disordered arrangement of sugar cubes tests respectively. Likewise, reported relationships between sample height and maximum grain size of particles are in a range from 2.6 to 7.7 for oedometer tests on gravels and rock fragments, and about 4.4 and 4.3 for ordered and disordered arrangement of sugar cubes tests reported here.

The set of tests performed are defined in **Table 4-7**, and their laboratory data are shown in Appendix 4. They were designed to investigate the evolution of the grain size distribution with applied stress. Therefore, five reference (maximum) stresses in increasing order were applied to the ordered samples and four maximum stresses to the disordered arrangements. Some variability in the initial void ratio was unavoidable. For each one of the tests performed stresses were applied in steps, shown in the compressibility curves given in **Figure 4-11** (ordered arrangements) and **Figure 4-12** (disordered arrangements).

At the end of each test a grain size distribution was carried out by means of a sieving technique. This sieving process was performed very carefully minimizing the energy used and performing the gsd test in steps: one for each sieve. Bigger broken particles were separated by hand in each sieve. In this process, separation of some sugar crystal grains from the sugar aggregates due to some weak bonds can occur and therefore increase the “finer” particle size.

Figure 4-8 Ordered arrangement sample (e_o=0.18) inside the oedometer cell (diameter 152mm).

Figure 4-9 Disordered arrangement sample (e_o =0.78) inside the oedometer cell (diameter 152mm).

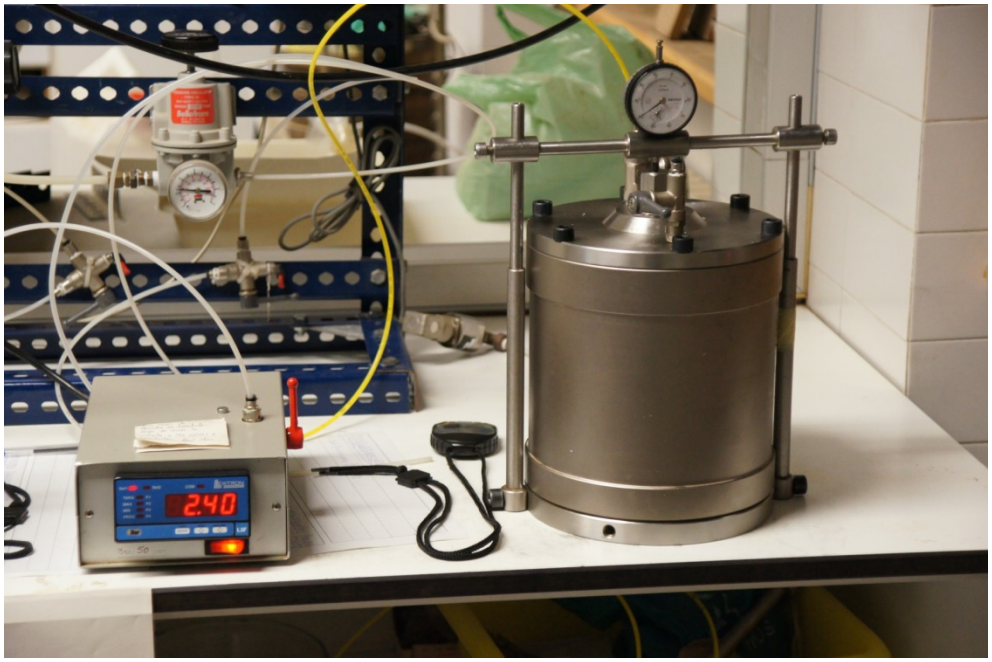

Figure 4-10 Oedometer equipment - Rowe cells (Inner diameter 152mm).

Table 4-6 Features of oedometer tests on gravels and rock fragments (Modified from Table 2-1).

Reference	Sample Dimension		Maximum grain size (m)	Relationship [Sample diameter /Grain size]	Relationship [Sample height /Grain size]
	Diameter (m)	Height (m)			
Norwegian Geotechnical Institute (Norway): Kjaernsli and Sande (1963)	0.50	0.25	0.064	7.8	3.9
Georgia Inst. of Technoloy (USA): Sowers et al. (1965)	0.19	0.10	0.038	5.0	2.6
UNAM – CFE (Mexico): Marsal (1973, 1967)	1.13	1.13	0.20	5.7	5.7
ISMES (Italy): Fumagalli (1969)	0.10; 0.50; 1.30	0.20; 1.00; 2.00	0.26	5.0	7.7
Build. Research Establishment (UK): Penman and Charles (1976)	0.60; 1.00	0.50	0.125	8.0	4.0
Build. Research Establishment (UK): Clements (1981)	0.45	0.225	0.076	5.9	3.0
Monash U. (Australia): Parkin and Adikari (1981)	0.635	0.61	0.09	7.1	6.8
LNEC (Portugal): Naylor et al. (1986); Veiga Pinto (1983)	0.50	0.50	0.10	5.0	5.0
Brasil: Caproni and Armelin (1998)	1.00	1.00	0.20	5.0	5.0
UPC (Spain): Oldecop and Alonso (2001)	0.30	0.20	0.04	7.5	5.0
UPC (Spain): Ortega (2008)	0.30	0.20	0.04	7.5	5.0
Ordered sugar cubes (This research)	0.152	0.075	[0.027;0.012];0.017	7.8	4.4
Disordered sugar cubes (This research)	0.152	0.095	0.022	6.9	4.3

Table 4-7 Oedometer tests performed.

Sample		σ_{vmax} kPa	$e_{o(Initial)}$	$e_{(Final\ \sigma vmax)}$	$e_{(Final\ Unloading)}$
Ordered:	M1	120	0.20	0.20	0.20
	M2	240	0.18	0.17	0.17
	M3	240	0.17	0.16	0.16
	M5	440	0.18	0.16	0.17
	M9	640	0.17	0.16	0.16
Disordered:	M7	30	0.80	0.79	0.79
	M6	60	0.74	0.73	0.73
	M4	120	0.87	0.82	0.82
	M8	440	0.72	0.66	0.66

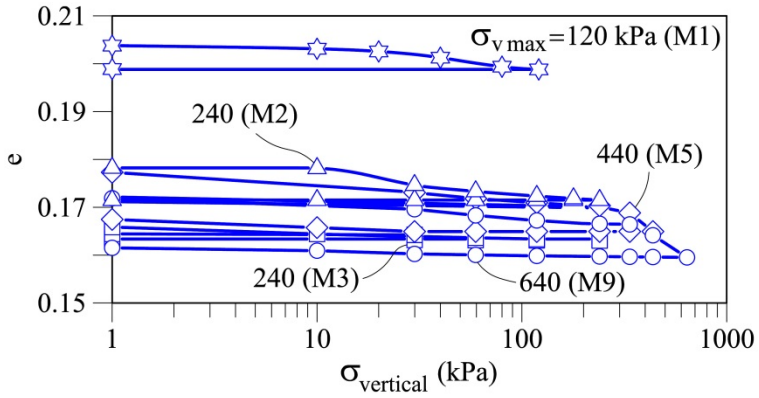

Figure 4-11 Compressibility curves for ordered arrangements.

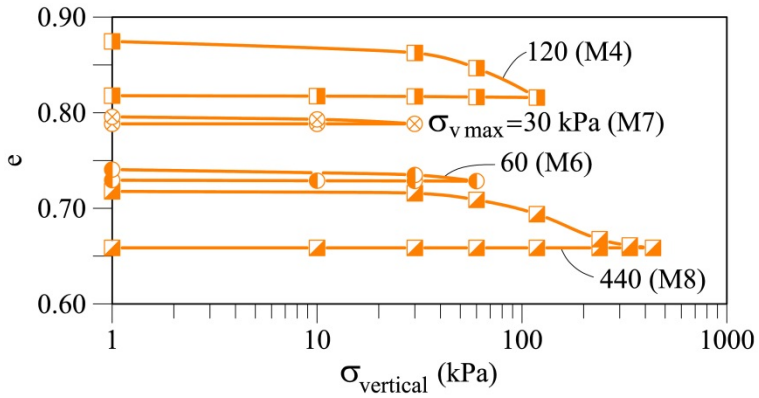

Figure 4-12 Compressibility curves for disordered arrangements.

A yield stress at about 250 kPa for the ordered arrangement and 60 kPa for the disordered sample may be approximated. These are rough estimates but more precise values can be derived if the change in void ratio is represented in terms of applied stress (**Figure 4-13**). The acceleration of change of void ratio with stress (in log scale) is also found at 250 kPa and 60 kPa, approximately, for the ordered and disordered samples.

The evolution of grain size curves with applied maximum stress is given in **Figure 4-14** and **Figure 4-15**. A remarkable result is that the gsd for the maximum applied stress of the two extremely "distant" initial (and final) arrangements is essentially the same. This is shown in **Figure 4-16**, which compares the two grain size distributions at the maximum applied stress for both arrangements (640 and 440 kPa). They are almost identical.

One may wonder if the gsd of the tested cube arrangements have reached an ultimate state at the maximum applied stress of the experiments. This issue was further examined by calculating the number of particles during the process of loading. This is done by assuming an equivalent spherical diameter for particles retained between two successive sieves. The resulting cumulative distribution of number of particles, *N(d)*, for the ordered arrangement is shown in **Figure 4-17**. The curves for 440 kPa and 640 kPa are very close. This result indicates that further crushing under increasing stress is unlikely.

Note also that the sugar cubes behaviour is similar to the gap-graded materials (Zhang and Baudet, 2013) in the sense that the gsd curves are evolving into two regular "S" shaped partial distributions with a "knee pivot" (see below).

Further support for the closeness to a unique attractor gsd is given by the evolution of Breakage indices calculated later (**Figure 4-26** and **Figure 4-27**). They tend towards an asymptotic state, a result consistent with an ultimate state in terms of gsd.

A second remarkable result of the set of gsd curves in **Figure 4-14**, **Figure 4-15** and **Figure 4-16** is the "composite" shape of the curves which describe the mixture of two regular "S" shaped partial distributions. Each one of these S shape curves shows the evolution of the two original grain sizes: the big identical sugar cubes and the small identical crystals. The two families evolve in an independent manner during the breakage process. This is better appreciated if the proportions of each particular grain size are plotted for increasing stress in a common diagram (**Figure 4-18**). The plot shows two distinct grain sizes for the resulting gsd: 11 mm for the coarse part and 0.4 mm for the small (crystal) size. These two values correspond approximately to half the reference (average) size of the sugar cubes (**Figure 4-19**c and **Figure 4-22**c) and the initial crystal size (**Figure 4-19**h and **Figure 4-22**h). This result has also been found by Zhang & Baudet 2013, when testing gap graded granular mixtures.

Note also the significant grain breakage for stresses above the yield values when examining the evolution of grain size distributions in **Figure 4-14**, **Figure 4-15** and **Figure 4-18**. This is in agreement with results obtained when testing geo-materials: McDowell and Bolton (1998), who discussed the results of Golightly (1990) on carbonate and silica sands and Nakata et al. (2001) on sands.

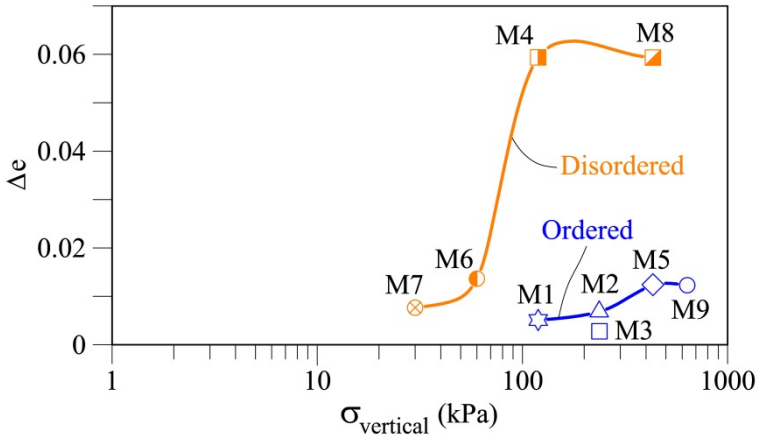

Figure 4-13 Variation of void ratio with applied vertical stress for ordered (e_o =0.18) and disordered (e_o =0.78) arrangements.

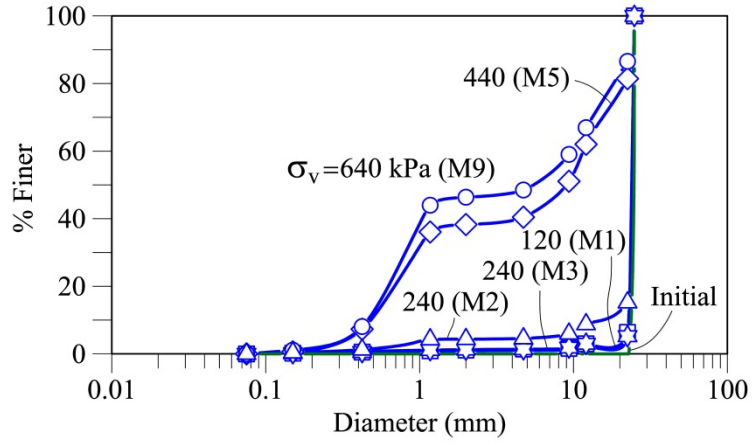

Figure 4-14 Evolution of grain size distributions with maximum applied stress for ordered arrangement.

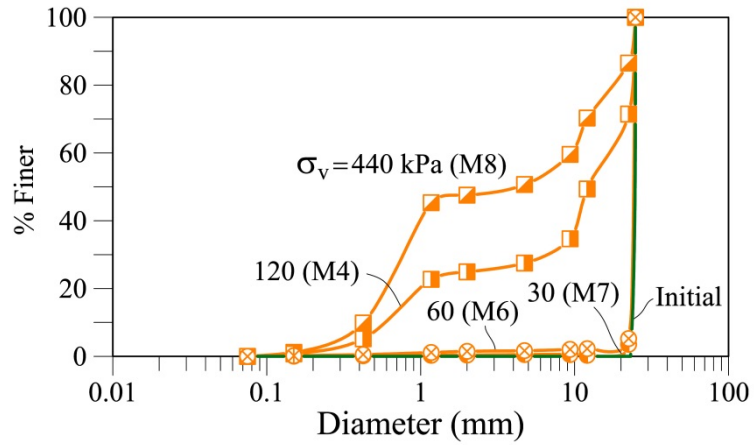

Figure 4-15 Evolution of grain size distributions with applied stress for disordered arrangement.

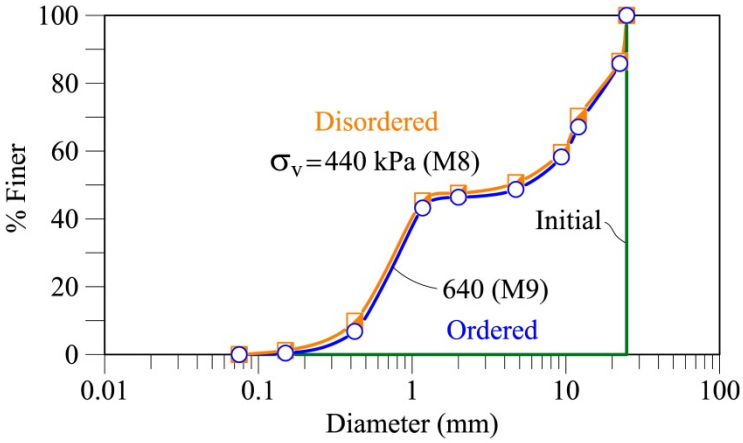

Figure 4-16 Comparison of grain size distribution for both ordered (M9, e_o =0.18) and disordered (M8, e_o =0.78) arrangements, at the maximum vertical stress.

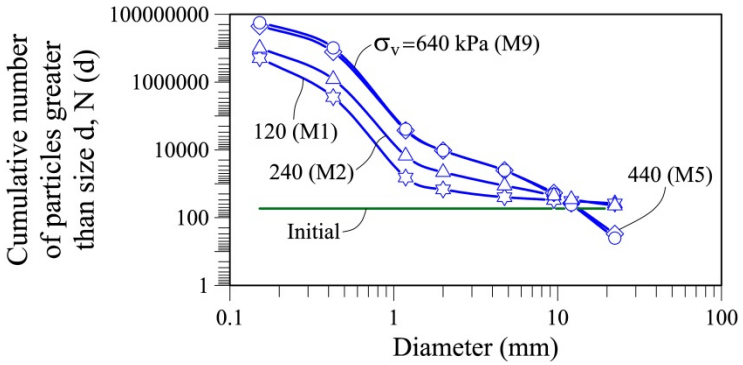

Figure 4-17 Evolution of cumulative number of particles with maximum applied stress for ordered arrangements (e_o=0.18).

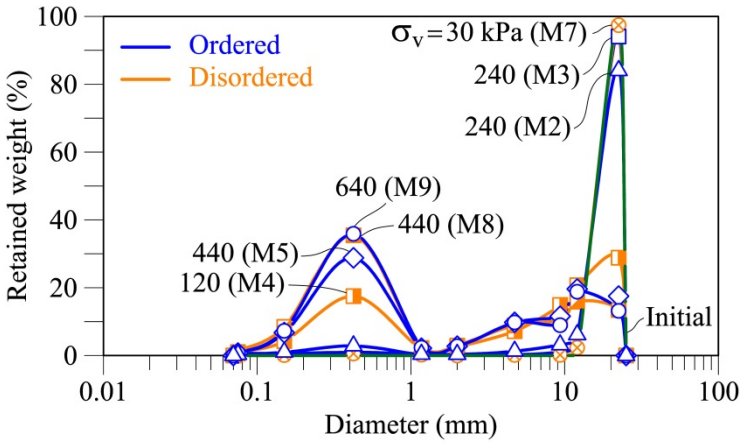

Figure 4-18 Evolution of the distribution of retained weight by sieve at the end of incremental vertical loading for both ordered (e_o =0.18) and disordered (e_o =0.78) arrangements.

4.3.1 Further insight into the crushing mechanisms

4.3.1.1 Crushing mechanisms

The breakage process was analyzed in more detail by examining the shape of particles in a breakage process (see **Figure 4-19**). In general terms two types of breakage could be observed, either a local crushing in the vicinity of highly stressed contacts (**Figure 4-20**) or a splitting failure, which typically results in two half-size particles (**Figure 4-21**). The local crushing will also be termed a "comminution" mechanism. It produces particles significantly smaller than the original particle (s).

4.3.1.2 Analysis of crushing mechanisms based on a sieving process

Consider now the sieving process and let us start by the size and shape of particles retained in sieve #0.5" (12.7 mm). The particles retained by this sieve size will belong only to the three first categories (a, b, c) shown in **Figure 4-19** and **Figure 4-22**a,b,c (intact, a small defect or a first-split-particle). The total weight of split particles retained in the #0.5" sieve, $W_{RT0.5"}$, is a measure of the splitting mechanism associated with the largest particle size. The number of split particles ($NP_{0.5"}$) retained by this sieve can be approximated by dividing $W_{RT0.5"}$ by the weight of an equivalent sphere defining the sieve size. Note also that the number of divisions (splitting events) experienced by the original cubes originating the previous number of split particles will be $NP_{0.5"}/2$.

The next sieve (3/8" = 9 mm) will retain only those particles which derive from a first division of the original cubes and a second split. Therefore the number of splitting events associated with the retained particles will be given by half the calculated values of retained particles.

It will be assumed that the splitting mechanism produces particles which are retained by the sieves 0.5" (**Figure 4-22**c), 3/8" (**Figure 4-22**d), #4 (4.75 mm) (**Figure 4-22**e) and #10 (2mm) (**Figure 4-22**f). For sizes smaller than this sieve the hypothesis is that particles originate from local crushing events. This hypothesis may look somewhat arbitrary but the results presented below show a consistent picture of the observed results. It should be added that the analysis refer to the breakage mechanisms of the large cubes.

Summarizing and generalizing the preceding discussion, the number of equivalent particles retained at a given sieve size i (i goes from 12.7 to 2 mm), NP_i are approximated by Eq. (4:2):

$$NP_i = \frac{6 * W_{RTi}}{\gamma * \pi * d_i^3} \tag{4:2}$$

where W_{RTi} = weight retained in the sieve i; γ = total unit weight for sugar cubes; d_i= equivalent diameter for particles retained in sieve i.

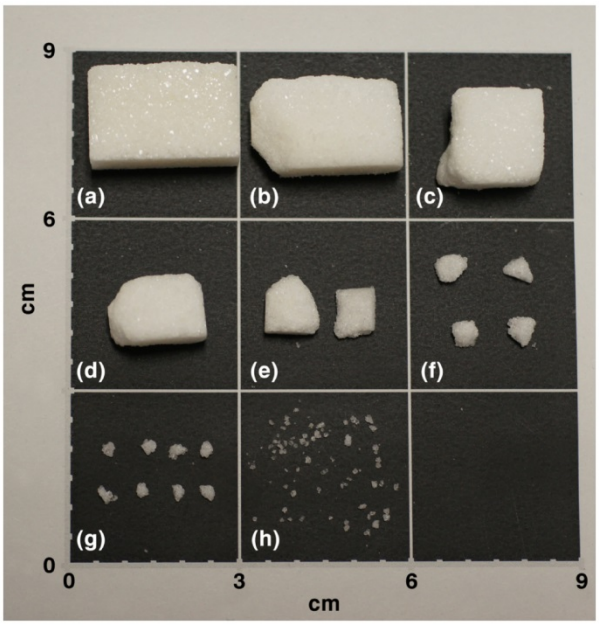

Figure 4-19 Relevant shapes of particles: a) original cube; b) original cube damaged locally; c) cube after a first splitting of the original cube (particles retained in sieve 1/2"- 12.7 mm); d) particles after splitting (retained in sieve 3/8" - 9.5 mm); e) particles after splitting (retained in sieve #4 – 4.75 mm); f) particles after splitting (retained in sieve #10 - 2 mm) ; g) particles after comminution (retained in sieve #16 – 1.2 mm) ; h) sugar crystals (retained in sieve #40 – 0.4 mm).

Figure 4-20 Local or Comminution crushing.

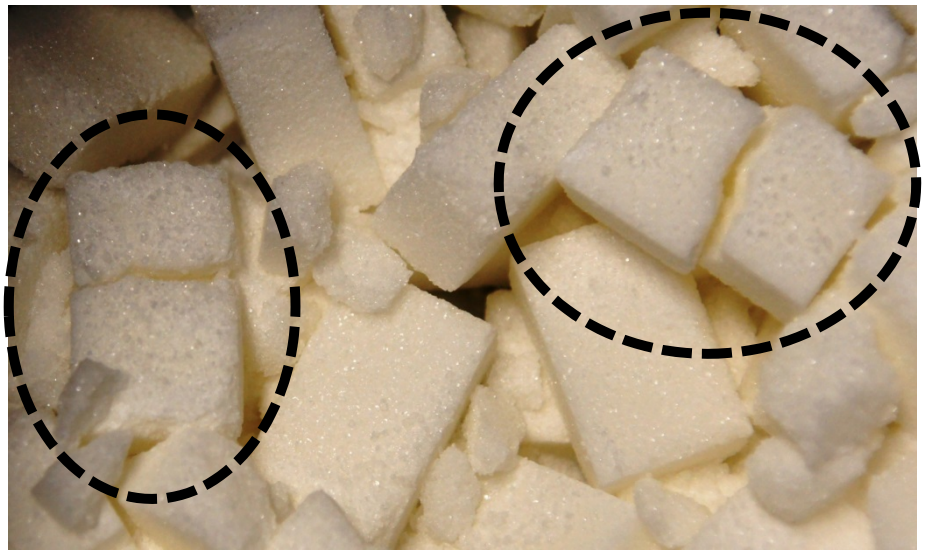

Figure 4-21 Splitting crushing.

The number of division events by splitting (equal volume breakage) for the sieve size *i*, ND_i is given by Eq. (4:3):

$$ND_i = NP_i * \chi \tag{4:3}$$

where χ is a fraction which is equal to ½ for sieves 0.5" and 3/8" and becomes 3/4 and 7/8 for sieves #4 and #10 respectively. **Table 4-8** and **Figure 4-23** show squemes of the division process by splitting or equal volume mechanism from an original particle ($P_{original}$) associated to the original sugar cube until retained particles by sieve ($P_{sieve\ i}$). **Figure 4-23** also illustrates the calculation of χ. The total amount of splitting breakage events is obtained by adding the set of ND_i values defined previously.

It was further accepted that all particles retained in #16 sieve (1.18 mm) are mainly a result of local crushing effects associated with the initial cubes (**Figure 4-22**g). Particles with smaller sizes (**Figure 4-22**h) are not included in this group because they are the result of the combination of different mechanisms including splitting, comminution, and/or decay processes of the sugar cubes.

Therefore, the following expression is used to calculate the amount of divisions due to comminution crushing, ND_{com}:

$$ND_{com} = NP_{\#16} \tag{4:4}$$

where $NP_{\#16}$ is the amount of particle retained in sieve #16.

The preceding calculations were performed at the end of each one of the tests performed and therefore the statistics on particle breakage can be related to the stress applied.

a. Intact Particles: Retained in Sieve 1/2"- 12.1mm

b. Local or Comminution Crushing: Retained in Sieve 1/2"- 12.1mm

c. Splitting Crushing: Retained in Sieve 1/2"- 12.1mm

d. Splitting Crushing: Retained in Sieve 3/8"- 9.5mm

e. Splitting Crushing: Retained in Sieve # 4 - 4.75mm

f. Splitting Crushing: Retained in Sieve # 10 - 2.0mm

g. Local or Comminution Crushing: Retained in Sieve # 16 - 1.18mm

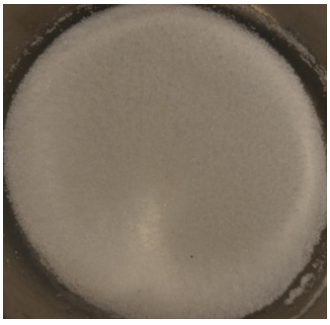

h. Sugar Crystals: Retained in Sieve # 40 - 0.425mm

Figure 4-22 Breakage mechanisms associated to sieving process after oedometer test: retained particles by sieve, $\sigma_{v\,max}$=240 kPa.

Table 4-8 Division process by splitting or equal volume mechanism.

Sequence of Division by Splitting or Equal Volume Crushing (EQC)	Number of accumulated divisions EQC occurred from original particle until retained particle by sieve	Maximum amount of new particles created by EQC division from 1 original particle
1 $P_{original}$ → 1 $P_{s½"\ or\ s3/8"}$ + 1 $P_{s½"\ or\ s3/8"}$	1	2
1 $P_{s½"or\ s3/8"}$ → 1 $P_{s\#4}$ + 1 $P_{s\#4}$	3	4
1 $P_{s\#4}$ → 1 $P_{s\#10}$ + 1 $P_{s\#10}$	7	8

$P_{original}$: original particle (original sugar cube); P_{si}: retained particle by sieve i.

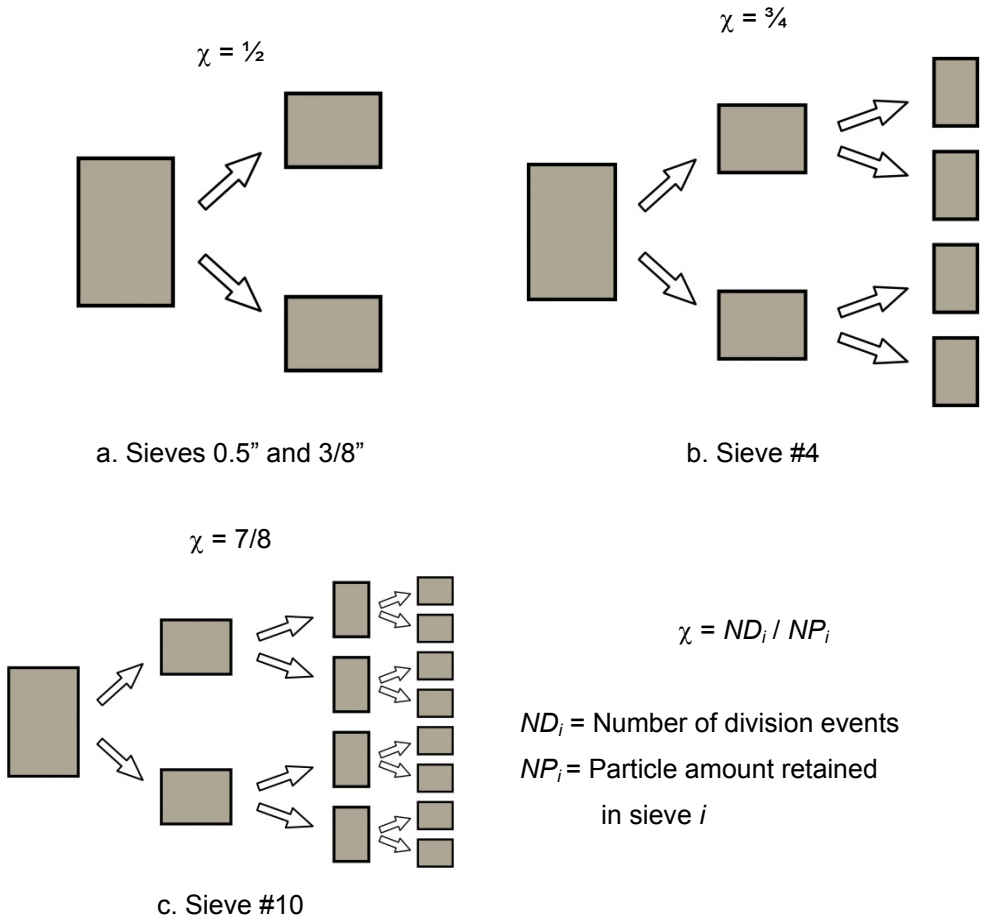

Figure 4-23 Squeme of division events for splitting mechanisms from an original particle until retained particle by sieve and calculation of χ.

The relevance of each one of the defined mechanisms is better appreciated if the number of particle divisions is normalized with respect to the total number of divisions. These normalized values, PND_{ij} are represented in **Figure 4-24** in terms of the applied stress for the two sample arrangements (low and high void ratio).

Eq. ((4:5) is used to calculate PND_{ij} in order to know the distribution of rupture mechanisms in percentage that acts in the breakage processes due to an apply load.

$$PND_{ij} = \left(\frac{ND_{ij}}{ND_{Tj}}\right) * 100\% \quad (4:5)$$

where:

PND_{ij} = Percentage of particle divisions for the *i* breakage mechanism (splitting or comminution), with respect to the total number of divisions, for a vertical stress *j*;
ND_{ij} = Amount of divisions for the *i* breakage mechanism (splitting or comminution), for a vertical stress *j*;
ND_{Tj} = Total number of divisions for a vertical stress *j* (=$ND_{(splitting)\ j}$ + $ND_{(comminution)\ j}$).

From **Figure 4-24**, consider the disordered samples (e_0 = 0.78). For applied stresses below the yield stress (around 60 kPa) 90% of the breakage events are comminution events. The remaining 10% corresponds to splitting mechanisms. However, when the stress increases beyond the yield stress the splitting mechanism increases substantially to reach 25 – 30% of the total number of breakage events. Interestingly, the distribution of the two mechanisms becomes very similar for the two sample arrangements for stresses beyond 120 kPa, again a remarkable result if one considers the widely different initial void ratios. The increasing importance of the splitting breakage mechanism above the yield stress was also reported by Nakata et al. (2001), testing silica sands. They performed high pressure one-dimensional compression tests (oedometer tests with maximum vertical stress of 92 MPa), on uniform silica sands (1.4 mm - 1.7 mm diameter) and found that for vertical stresses less than a yield stress all the damage was concentrated at the particle contacts while for higher values than the yield stress the splitting failure corresponded to 50% of the total damage. The results of this research are in the same way to their results.

If the “steady state” gsd for high stresses (**Figure 4-16**) is adopted as a suitable reference to normalize results, the number of particle breakage events should be compared with the calculated values for the maximum applied stress. Then comminution and splitting events are normalized by their counterparts for the maximum stress. Therefore these ratios, $PND_{ij(\sigma vmax)}$, vary between 0 (for a small applied stress) to 1 (for the maximum stress), and can be calculated by the Eq. (4:6):

$$PND_{ij(\sigma vmax)} = \left[\frac{ND_{ij}}{ND_{i(\sigma vmax)} * \left(\frac{NP_{0j}}{NP_{0(\sigma vmax)}}\right)}\right] * 100\% \quad (4:6)$$

where:

$PND_{ij(\sigma vmax)}$ = Percentage of particle divisions for the *i* breakage mechanism (splitting or comminution), for a vertical stress *j* normalized by their counterparts for the maximum vertical stress σ_{vmax};
ND_{ij} = Number of divisions for the *i* breakage mechanism (splitting or comminution), for a vertical stress *j*;
$ND_{i(\sigma vmax)}$ = Number of divisions for the *i* breakage mechanism (splitting or comminution), for a maximum applied vertical stress σ_{vmax};
NP_{0j} = Total number of initial particles in the test under an applied vertical stress *j*;
$NP_{0(\sigma vmax)}$ = Total number of initial particles in the test under a maximum applied vertical stress σ_{vmax}.

The calculations of $PND_{ij(\sigma vmax)}$ are plotted in **Figure 4-25** in terms of the applied stress. The plot shows two distinct trends for the high porosity, disordered samples and for the low porosity ordered samples. In both cases the amount of breakage events increases fast for stresses in excess of the yield stress. The increase is not so rapid for the dense sample.

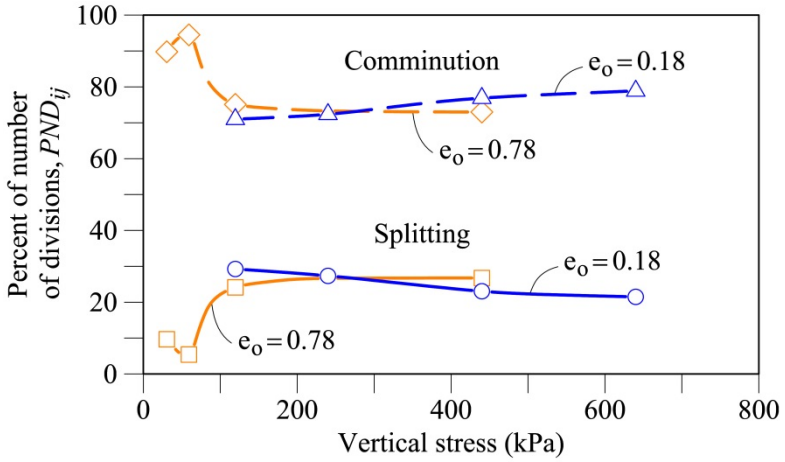

Figure 4-24 Comparison of the evolution of the percentage of amount of divisions according to breakage mechanisms, PND_{ij}, in relation to applied vertical load for both ordered (e_o =0.18) and disordered (e_o =0.78) arrangements.

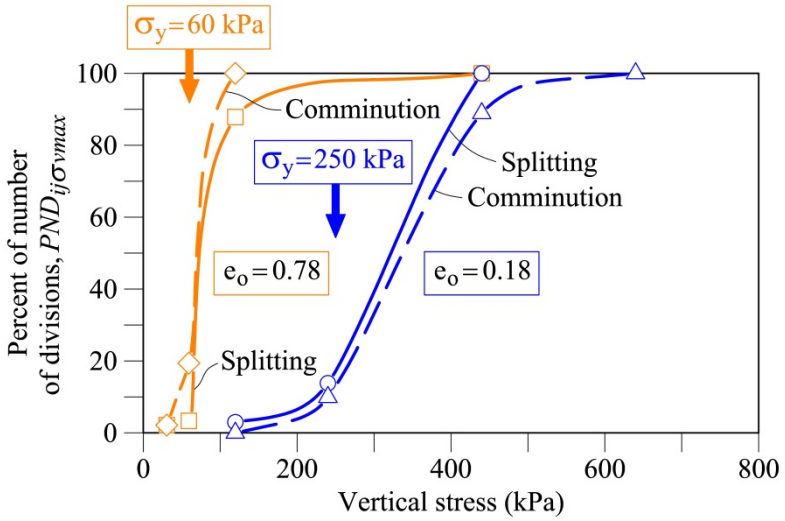

Figure 4-25 Comparison of the evolution of the percentage of amount of particle divisions according to breakage mechanism (splitting or comminution), for a certain vertical stress related to those divisions for a maximum applied vertical stress σ_{vmax}, $PND_{ij\sigma vmax}$, for both ordered (e_o =0.18) and disordered (e_o =0.78) arrangements.

Even if the hypothesis made to distinguish the breakage mechanism may look somewhat crude, what is important is to investigate their relative change with the initial sample structure and with the applied stress. The parameters derived proved to be very indicative of the evolution of breakage mechanisms with stress and in particular the role of the yield stress as the initial point to trigger a rapid development of splitting mechanisms. Interestingly, the differences in this regard between the two widely different particle arrangements are minor.

4.3.1.3 Analysis of particle breakage using Breaking Indices

A further indication of the nature of the breakage mechanisms is given by the evolution of Breaking Indices with the imposed stress. This information is given in **Figure 4-26** and **Figure 4-27** for the Hardin (Hardin, 1985) and Marsal (Marsal, 1967) indices. These indices were obtained from the grain size curves at the end of the oedemeter tests.

Both provide the same result: breaking indices remain small for stresses below the yield stress and increase fast in the vicinity of the yield stress. Note also that the two indices tend towards an asymptotic value for the highest applied stresses, which is consistent with the previously reported steady state common grain size distribution for the two particle arrangements.

One might think that the size of the sugar crystals (retained in sieve #40 - 0.4mm) would be a limit to calculate the relative breakage indices, but actually there were also particles retained in sieves #100-0.15mm (about 8%) and #200-0.075mm (about 1%), i.e. there was also breakage in the crystal grain. For the maximum stresses in both ordered and disordered arrangements, there no were particles

less than 0.074mm. Therefore, the limit of 0.074mm is suitable to calculate the (relative) Hardin breakage index, Br.

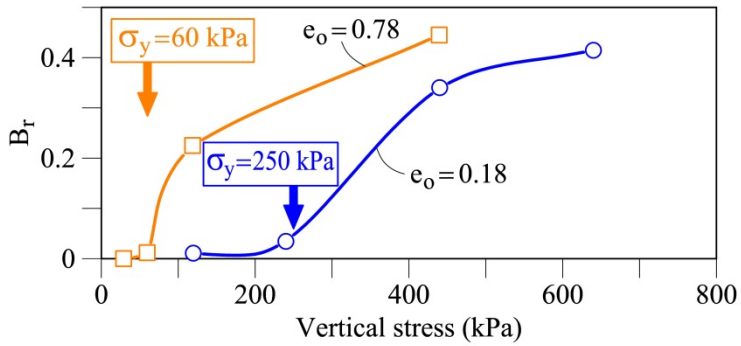

Figure 4-26 Evolution of Hardin Breakage Index, *Br*, after applied vertical load for both ordered (e_o =0.18) and disordered (e_o =0.78) arrangements.

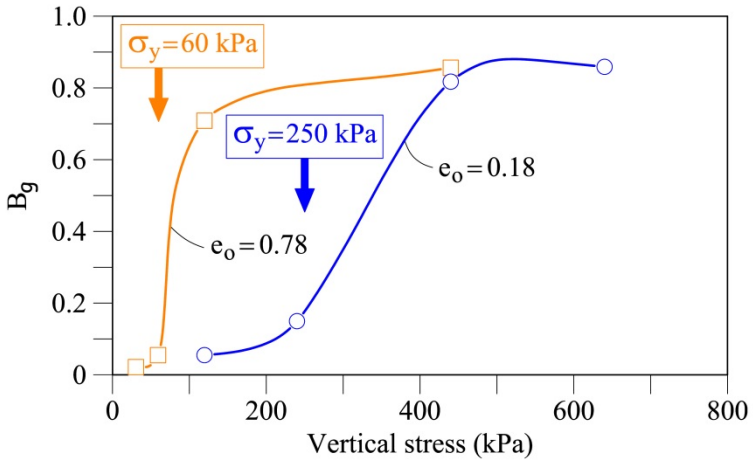

Figure 4-27 Evolution of Marsal Breakage Index, *Bg*, after applied vertical load for both ordered (e_o =0.18) and disordered (e_o =0.78) arrangements.

4.4 Time dependent behaviour

Time effects were investigated in oedometer tests in which the applied stress (240 kPa) was maintained during a certain period of time (10, 107, 1000, 9874, 69952, and 226815 minutes -157.5 days-). Grain size distributions were obtained at the end of the loading period. In all cases the samples were loaded in short time steps (30, 60, 120, 240 kPa) before reaching the target vertical confining stress.

The time-dependent response was only measured for the disordered arrangements. Disordered samples, having an average void ratio e_o= 0.81 were

selected for these tests. The final vertical confining stress is well above the yielding stress (60 kPa) reported previously for these samples. **Table 4-9** defines the set of tests performed, and their laboratory data are shown in Appendix 4. The compressibility curves are shown in **Figure 4-28**.

Since the evolution of particle size distributions for both ordered and disordered arrangements followed a similar trend above the yield stress (previous section) it is believed that the time dependent behaviour discussed below applies also to the ordered arrangements.

The decrease in void ratio with time, in natural and logarithmic scales, is represented in **Figure 4-29**. It can be appreciated that the sample continues to deform on time. However the velocity of deformation decreases after 9874 min have elapsed (**Figure 4-29**a). The sample densification increases linearly with the logarithm of time for the time intervals selected (**Figure 4-29**b). The following expression has been found:

$$\Delta e = \left[0.004 * ln\left(\frac{t}{t_0}\right)\right] + 0.0038 \quad (4:7)$$

where t is the time (in min) and t_o is a reference time = 1 min.

Table 4-9 Oedometer tests performed for time dependent analysis.

Sample (Disordered Arrangements)	σ_{vmax} (1)	Elapsed time for imposed stress [Creeping time]	$e_{o(Initial)}$	$e_{(Final\ \sigma vmax)}$	$e_{(Final\ Unloading)}$
	(kPa)	(min)			
T8E	240	10	0.809245705	0.790909666	0.791532895
T2E	240	107	0.759049899	0.739213254	0.739833719
T3E	240	1000	0.807452312	0.779265908	0.779849742
T4E	240	9874	0.844370781	0.80574562	0.80649063
T9E	240	69952	0.831542131	0.788748828	0.789498366
T6E	240	226815	0.798627015	0.736368893	0.736643796

(1) : Imposed load by steps.

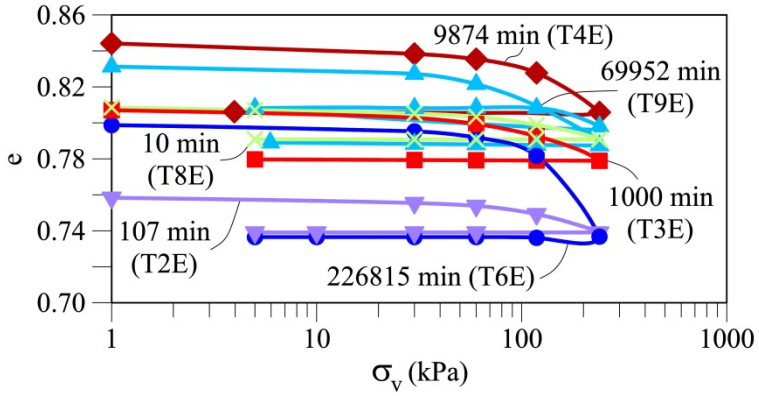

Figure 4-28 Compressibility curves for disordered arrangements (e_o=0.81) under a vertical stress of 240 kPa at different creeping times.

a. Horizontal axis in arithmetic scale

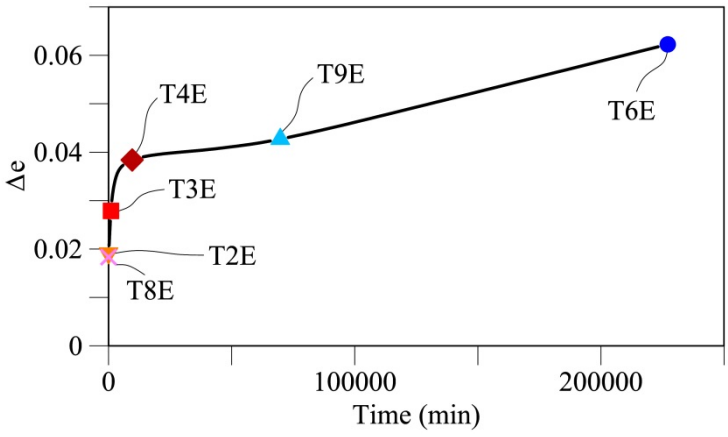

b. Horizontal axis in logarithmic scale

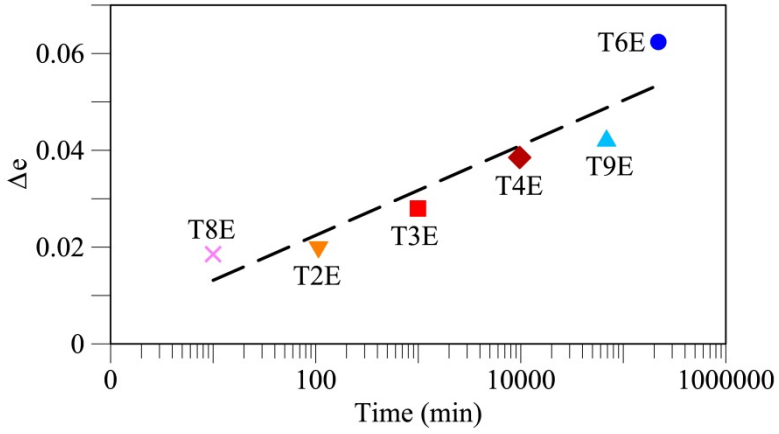

Figure 4-29 Increase in void ratio with creeping time under a vertical stress of 240 kPa for disordered (e_o = 0.81) samples: a) natural time scale; b) logarithmic time scale.

Grain size distributions could be determined at the end of each one of the testing periods. The evolution of grain size distributions at the end of the tests (**Figure 4-30**) progressively adopts two dominant sizes as determined previously in tests performed at increasing confining stress (**Figure 4-15**). The "creeping" mechanism is therefore not substantially different from a pure "loading" effect. This is shown in **Figure 4-31**, which compares the gsd of a previous test under a vertical stress of 440 kPa and the gsd under 240 kPa and a creeping time of 157.5 days. Obviously, the breakage of particles depends on time. Note that the shape of the evolving creeping grain sizes is remarkable similar to the previously determined shapes for increasing confining stress. In view of the results given in **Figure 4-15**, it is clear that the final grain size distribution for t = 157.5 days has not yet achieved the degree of breakage expected in a "final attractor". However, this concept is perhaps not so clearly defined in view of the continuous increase in breakage with time resulting from **Figure 4-29** and **Figure 4-30**. In other words, the attractor gsd, depends on time, even if its variation is slow (logarithmic) beyond a certain time.

During the breaking process on time, the two dominant grain size families (11 mm for the coarse part and 0.4 mm for the small –crystal- size) also evolve in an independent manner as in the case of increasing confining stresses previously described. The two dominant sizes correspond approximately to half the reference (average) size of the sugar cubes and the initial crystal size. If the proportions of each particular grain size are plotted for increasing elapsed time in a common diagram (**Figure 4-32**) the grain size evolution in time is essentially the same of the grain size evolution with applied stress (**Figure 4-18**).

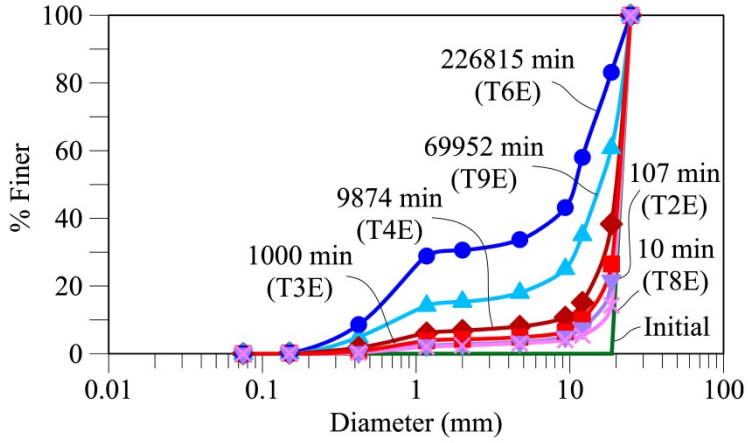

Figure 4-30 Evolution of grain size distributions for disordered arrangements (e_o = 0.81) under an applied vertical stress of 240 kPa at different creeping times.

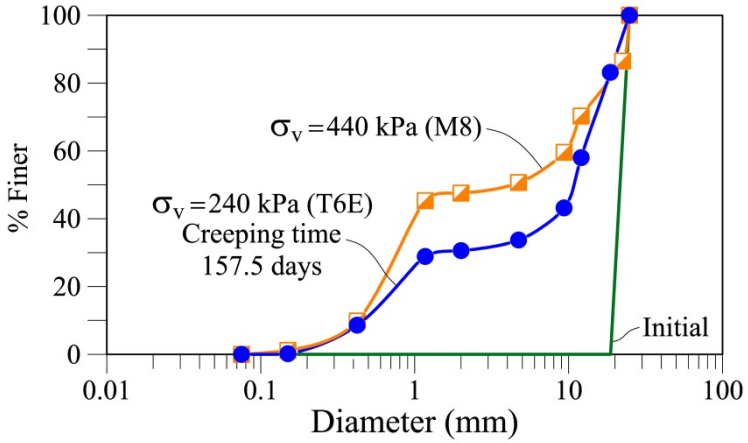

Figure 4-31 Comparison between grain size distributions for σ_v = 440 kPa (loading time: 70.9 days) and σ_v = 240 kPa (loading time =157.5 days). Disordered arrangements (e_o=0.81).

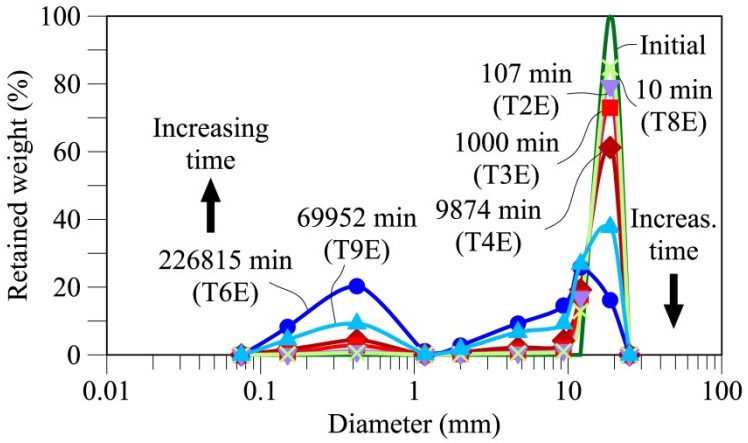

Figure 4-32 Evolution in time of the distribution of retained weight at a given sieve size for disordered arrangements (e_o=0.81) and applied vertical stress of 240 kPa.

4.4.1 Analysis of crushing mechanisms in time

Consider again the retained particles by sieve ½", shown in **Figure 4-22** (a, b, and c) and **Figure 4-19** (a, b and c). The time evolution of the three identified types of particles is shown in **Figure 4-33**. Particles type 1 correspond to intact original particles, type 2 describes to original cubes damaged locally (local crushing), and type 3 describes to cubes after a first splitting of the original sugar cubes (their size is half the original size, approximately). **Figure 4-33** shows that increasing the elapsed time results in a decrease of the percentage of original particles (type 1): 54% of retained particles for a creeping time of 10 min, 14% for 69952 min and 2% for 226815 min. Likewise, the amount of type 3 particles increases with time: 9%, 27% and 25% for the same increments of creeping time respectively.

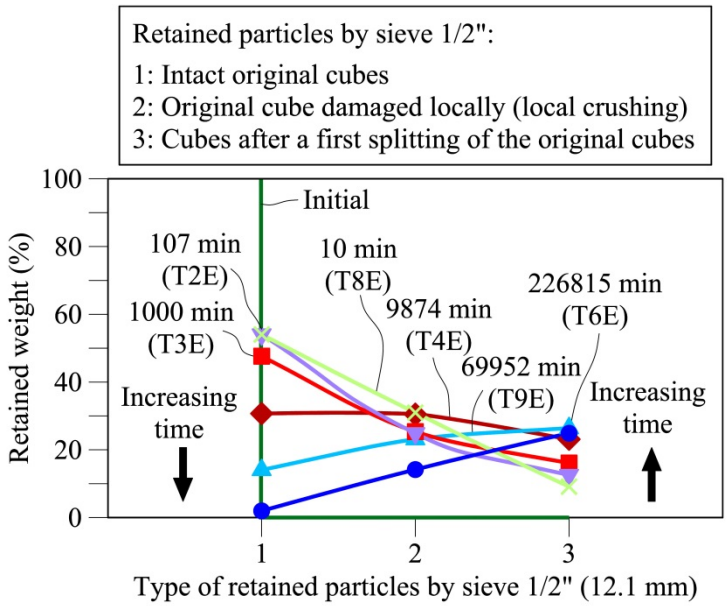

Figure 4-33 Evolution of the largest particle sizes (retained particles by sieve ½"), for disordered arrangements (e_o=0.81) and applied vertical stress of 240 kPa at different elapsed times.

Equations (4:3) and (4:4) describe the number of division events by splitting and comminution crushing mechanisms respectively. They referred to the previous analysis for particle breakage and compressibility (section 4.3.1.2.). Similar expressions may be proposed to analyze particle divisions taking place in time, at a constant applied stress:

$$PND_{ijt} = \left(\frac{ND_{ijt}}{ND_{Tjt}}\right) * 100\% \quad (4:8)$$

where:
PND_{ijt} = Percentage of particle divisions for the *i* breakage mechanism (splitting or comminution), with respect to the total number of divisions, for a vertical stress *j* at an elapsed time *t*;
ND_{ijt} = Amount of divisions for the *i* breakage mechanism (splitting or comminution), for a vertical stress *j* at an elapsed time *t*;
ND_{Tjt} = Total number of divisions for a vertical stress *j* at an elapsed time *t* (= $ND_{(splitting)\,jt}$ + $ND_{(comminution)\,jt}$).

Normalized values, PND_{ijt} are represented in **Figure 4-34** in terms of the creeping time under an imposed stress of 240 kPa for a disordered arrangement. The figure shows that the distribution of the crushing mechanisms remains approximately constant at all times: 30 to 40% of rupture processes for splitting breakage and 60-70% of rupture processes by comminution crushing.

In a similar manner, the number of divisions may be normalized with respect to the situation at the maximum creeping time (157.5 days; **Figure 4-31**). Then, the normalized evolution of breakage, either splitting, comminution or total breakage could be calculated as a function of time.

The calculated ratios, $PND_{ijt(tmax)}$, vary between 0 (for a short elapsed time) to 1 (for the maximum elapsed time). They were calculated with the help of the following equation:

$$PND_{ijt(tmax)} = \left[\frac{ND_{ijt}}{ND_{ij(tmax)} * \left(\frac{NP_{0jt}}{NP_{0j(tmax)}}\right)}\right] * 100\% \quad (4:9)$$

where:

$PND_{ijt(tmax)}$ = Percentage of particle divisions for the *i* breakage mechanism (splitting or comminution) or total crushing events (sum of comminution and splitting), for a vertical stress *j* at an elapsed time *t* normalized by their counterparts for the maximum elapsed time, *tmax*;
ND_{ijt} = Number of divisions for the *i* breakage mechanism (splitting or comminution) or total crushing events, for a vertical stress *j* at an elapsed time *t*;
$ND_{ij(tmax)}$ = Number of divisions for the *i* breakage mechanism (splitting or comminution) or total crushing events, for a vertical stress *j* at a maximum elapsed time *tmax*;
NP_{0jt} = Total number of initial particles in the test at creeping time *t* under the applied stress *j*;
$NP_{0j(tmax)}$ = Total number of initial particles in the test at maximum creeping time *tmax* (157.5 days) under the applied stress *j*.

Values of $PND_{it(tmax)}$ are plotted in Figure 4-35 in terms of the creeping time (disordered arrangement; constant applied stress of 240 kPa). The plot shows a rapid increase in crushing events at early times (shorter than 1000 min). The crushing events represent only 20% of the crushing events for a long time. The rate of breakage (splitting, comminution or total) decreases continuously with time.

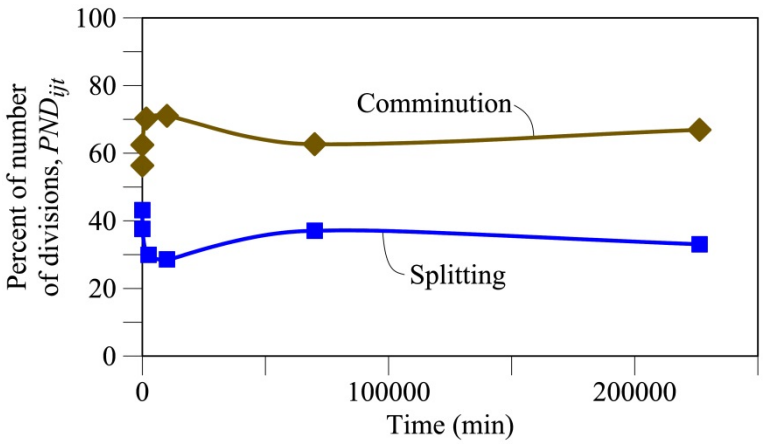

Figure 4-34 Evolution in time of the percentage of divisions for two breakage mechanisms, PND_{ijt}. Disordered arrangements (e_o=0.81) and applied vertical stress of 240 kPa.

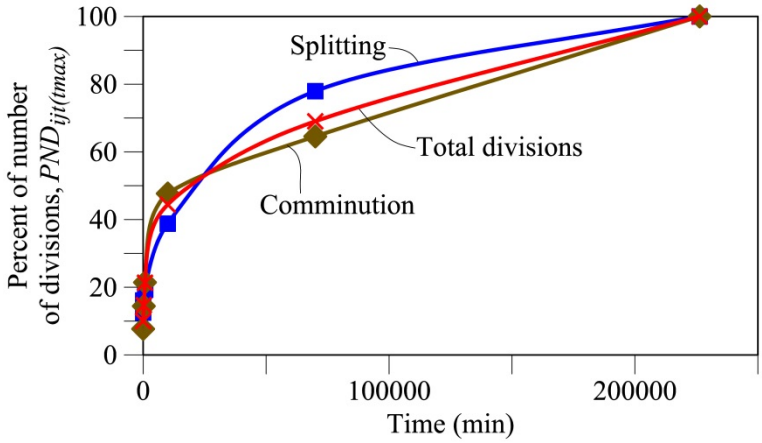

Figure 4-35 Evolution in time of the percentage of particle divisions for the different breakage mechanism (splitting, comminution and total), $PND_{ijt(tmax)}$. Disordered arrangements (e_o=0.81) and applied vertical stress of 240 kPa

4.4.2 Evolution of Breaking Indices

Hardin, B_r (Hardin, 1985), and Marsal, B_g (Marsal, 1967) Breakage Indices, were obtained from the grain size curves at the end of each of the creep tests performed. They are plotted against time in **Figure 4-36** and **Figure 4-37**. The plots may be described by power functions of time:

$$B = A * \left(\frac{t}{t_0}\right)^{\beta} \tag{4:10}$$

where B is the breakage index (B_r ; B_g); t_0 is a reference time (1 minute in the plots); the β exponent is around 0.15 (Marsal) - 0.20 (Hardin); A coefficient is around 0.036 (Hardin) - 0.094 (Marsal).

Thus, the following expressions are obtained to calculate the B_r and B_g, respectively:

$$B_r = 0.0357 * \left(\frac{t}{t_0}\right)^{0.20} \tag{4:11}$$

$$B_g = 0.0939 * \left(\frac{t}{t_0}\right)^{0.15} \tag{4:12}$$

The coefficients of determination, R^2, were equals to 0.9404 and 0.9752 for B_r and B_g respectively.

Breakage indices B_r and B_g evolve in time in a manner similar to the evolution of the normalized number of divisions (**Figure 4-35**): a fast initial increase and a sustained increase in breakage, at reduced rates, as time increases. No indications of an asymptotic stabilization were found, despite the relatively high maximum

creeping time.

At beginning, B_r and B_g increase rapidly until to reach an elapsed time of 10000min, after this time the rate of increasing decreases. However, the values of these indices for time shorter than 10000min are small compared with those obtained for a long elapsed time: Respectively, B_r and B_g are less than 0.17 and 0.38 for a shorter time than 10000min, and then they are increased until to reach values of 0.52 and 0.83 for a time equal to 226815min.

Obviously, this is once again evidence that the rupture processes are dependence on time.

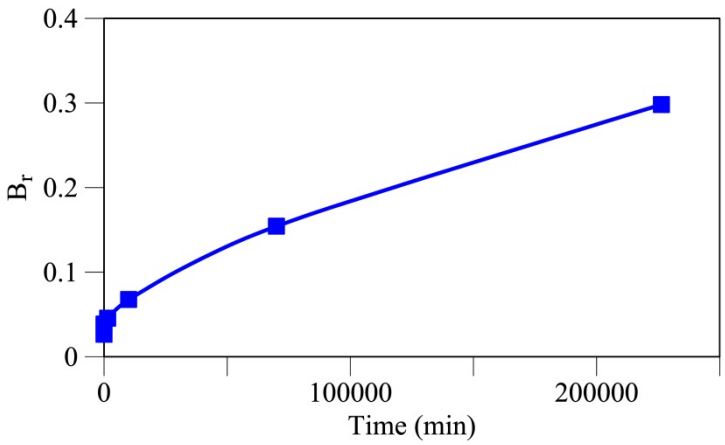

Figure 4-36 Evolution in time of Hardin Breakage Index, B_r, for disordered arrangements (e_o=0.81) and applied vertical stress of 240 kPa.

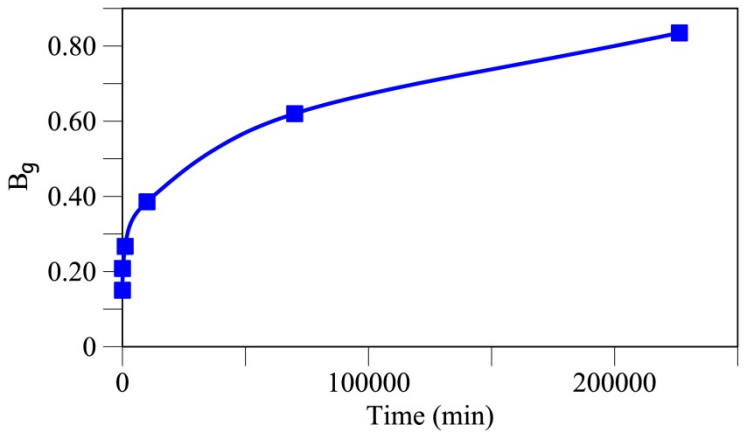

Figure 4-37 Evolution in time of Marsal Breakage Index, B_g, for disordered arrangements (e_o=0.81) and applied vertical stress of 240 kPa.

4.5 Conclusions

Particle breakage mechanisms in loaded coarse aggregates could be analysed from testing of regular blocks of a brittle material of relatively low strength (sugar cubes) in a simple but very informative procedure. Two very different initial porosities (very low and high) of specimens could be obtained by two different piling methods (ordered and disordered arrangement) of the regular parallelepiped cubes. After loading process at a relatively high confining stress, in a remarkable result far from intuitive, the gsd curves of these two widely different arrangements converged into a unique grain distribution. Therefore it confirms that the grain size distribution, irrespective of the initial fabric, evolves into an "attractor" curve during loading.

The gsd curves evolve around two families of grain sizes which are related to the initially two sizes, in an apparently independent manner. The final gsd could be defined as a superposition of two limiting "attractors". However, it remains to be shown that the same conclusion holds if the initial sizes of the gap graded granular mixture are close enough.

In loading processes, the evolution of the grain sizes is explained by the action of the following breakage mechanisms which were identified: local crushing (comminution) which generates particles significantly smaller than the original particle, and particle splitting which divides in roughly two halves the broken particle. The development of breakage was investigated in more detail using a procedure, based on interpreting the mass fractions retained at each particular sieve. It was found that:

- Particle breakage is very limited for stresses below the yield stress.
- The intensity of the two breakage mechanisms increase fast in the vicinity of the yielding stress.

Conventional breakage indices also increase rapidly at stresses close to the yield stress. In fact, the yield stress is better identified in the tests performed by gsd-related criteria than on the basis of the classical interpretation of compression behaviour in e vs. $\log(\sigma)$ plots.

Long term tests at constant confining stress supported a creep law relating deformations with the logarithm of time. The evolution of breakage was analyzed by examining samples at different creeping times. It was found that the evolution of grain size distributions followed a pattern entirely similar to the pattern observed during a (fast) increase in stress. In particular, creeping was also explained by the emergence of a dominant grain size associated with the crystal size and the reduction of sizes associated with the initial size of cubical particles. No evidence of an asymptotic exhaustion of long term deformations was found despite the maximum duration of tests (157.5 days). It appears that the gsd attractor is, in fact, a function of time. Breakage rates evolved from maximum values at early times towards a progressive reduction of breakage rates as time increases.

The fact that increasing stress and increasing time at constant stress result in common patterns of gsd suggests that a unified phenomenon explains both phenomena. The subcritical crack propagation within particles was proposed by

Oldecop and Alonso (2007, 2001) as a suitable mechanism to explain the response of gravels to confined loading. The present results support also this mechanism.

The results of this experimental research are useful for a better understanding of the breakage mechanisms taking place in coarse crushable aggregates (gravels and rockfill) subjected to one dimensional compression conditions. It is believed that some of the findings presented could be of application to generalized stress-strain paths.

The two crushing mechanisms described are associated with the distribution of stresses in particles due to the action of concentrated loads which act around the particle. Splitting failure could be associated with tensile stresses and comminution crushing to shear stresses. The magnitude and distribution of the stresses inside particles depend on the mechanical properties of the particle (e.g. elastic/elasto-plastic parameters), shape of the particle, magnitude and contact area of the applied load, roughness surface, etc. In this regard, a random package of sugar cubes is probably not much different from gravel made of particles having three similar dimensions and sharp edges and vertices. An ordered set of cubes is close to a regular stone fabric in a wall or in a variety of masonry structures. The interest of the tests on sugar cubes is the possibility of examining the two extremes of rockfill fabric in an easy manner.

4.6 List of Notations

Notation		***Section***
A	Coefficient which is used to calculated breakage indices; Eq. (4:10)	4.4.2
B	Breakage index; Eq. (4:10)	4.4.2
B_r	Hardin breakage index; Eq. (4:11)	4.3.1.3; 4.4.2
B_g	Marsal breakage index; Eq. (4:12)	4.3.1.3; 4.4.2
d_i	Equivalent diameter for particles retained in sieve i; Eq. (4:2)	4.3.1.2
EQC	Equal Volume Crushing; Table 4-8	4.3.1.2
e	Void ratio	4; 4.3
e_o	Initial void ratio	4.3
FA	Friction angle; Eq. (4:1)	4.2
gsd	Grain size distribution	4
ND_{com}	Amount of divisions due to comminution crushing; Eq. (4:4)	4.3.1.2
ND_i	Number of division events by splitting (equal volume breakage) for the sieve size i; Eq.	4.3.1.2

	(4:3)	
ND_{ij}	Amount of divisions for the *i* breakage mechanism (splitting or comminution), for a vertical stress *j* ; Eq. (4:5) ; (4:6)	4.3.1.2
ND_{ijt}	Number of divisions for the *i* breakage mechanism (splitting or comminution) or total crushing events, for a vertical stress *j* at an elapsed time *t*; Eq. (4:8); (4:9)	4.4.1
$ND_{ij(tmax)}$	Number of divisions for the *i* breakage mechanism (splitting or comminution) or total crushing events, for a vertical stress *j* at a maximum elapsed time *tmax* ; Eq. (4:9)	4.4.1
$ND_{i(\sigma vmax)}$	Number of divisions for the *i* breakage mechanism (splitting or comminution), for a maximum applied vertical stress σ_{vmax} ; Eq. (4:6)	4.3.1.2
ND_{Tj}	Total number of divisions for a vertical stress *j*; Eq. (4:5)	4.3.1.2
ND_{Tjt}	Total number of divisions for a vertical stress *j* at an elapsed time *t*; Eq. (4:8)	4.4.1
NP_i	Number of equivalent particles retained at a given sieve size *i*; Eq. (4:2); (4:3); (4:4)	4.3.1.2
NP_{0j}	Total number of initial particles in the test under an applied vertical stress *j* ; Eq. (4:6)	4.3.1.2
NP_{0jt}	Total number of initial particles in the test at creeping time *t* under the applied stress *j*; Eq. (4:9)	4.4.1
$NP_{0j(tmax)}$	Total number of initial particles in the test at maximum creeping time *tmax* (157.5 days) under the applied stress *j*; Eq. (4:9)	4.4.1
$NP_{0(\sigma vmax)}$	Total number of initial particles in the test under a maximum applied vertical stress σ_{vmax} ; Eq. (4:6)	4.3.1.2
PND_{ij}	Percentage of particle divisions for the *i* breakage mechanism (splitting or comminution), with respect to the total number of divisions, for a vertical stress *j*;	4.3.1.2

	Eq. (4:5)	
PND_{ijt}	Percentage of particle divisions for the *i* breakage mechanism (splitting or comminution), with respect to the total number of divisions, for a vertical stress *j* at an elapsed time *t*; Eq. (4:8)	4.4.1
$PND_{ijt(tmax)}$	Percentage of particle divisions for the *i* breakage mechanism (splitting or comminution) or total crushing events (sum of comminution and splitting), for a vertical stress *j* at an elapsed time *t* normalized by their counterparts for the maximum elapsed time, *tmax* ; Eq. (4:9)	4.4.1
$PND_{ij(\sigma vmax)}$	Percentage of particle divisions for the *i* breakage mechanism (splitting or comminution), for a vertical stress *j* normalized by their counterparts for the maximum vertical stress σ_{vmax} ; Eq. (4:6)	4.3.1.2
t	Elapsed time	4.4
t_0	Reference time which is used to calculated breakage indices; Eq. (4:10); (4:11); (4:12)	4.4.2
W_{RTi}	Weight of particles retained in the sieve *i*; Eq. (4:2)	4.3.1.2
β	Exponent which is used to calculated breakage indices; Eq. (4:10)	4.4.2
γ	Total unit weight for sugar cubes; Eq. (4:2)	4.3.1.2
Δe	Variation of void ratio; Figure 4-13; Figure 4-29; Eq. (4:7)	4.3; 4.4
σ	Normal stress	4
σ_N	Normal stress; Eq. (4:1)	4.2
σ_v	Vertical normal stress	4.3
σ_{vmax}	Maximum vertical normal stress applied	4.3
σ_y	Yield stress	4.3

σ_0	Reference stress; Eq. (4:1)	4.2
χ	Dimensionless coefficient used in the calculation of the number of division events by splitting for the sieve size *i*, ND_i. It is a fraction of NP_i ; Eq. (4:3)	4.3.1.2

4.7 References

Bruce, I.. G., Cruden, D.M., Eaton, T.M., 1989. Use of a tilting table to determine the basic friction angle of hard rock samples. Can. Geotech. J. 26, 474–479.

Caproni, N., Armelin, J.L., 1998. Deformabilidade de um enrocamento obtida em ensaios de compressão unidimensional, in: Proceedings of XI Congreso Brasileiro de Mecânica Dos Solos E Engenharia Geotécnica, Brasilia, Brasil, 2. pp. 705–712.

Clements, R.P., 1981. The deformation of rockfill: inter-particle behaviour, bulk properties and behaviour in dams. PhD thesis. London University, London, UK.

Coop, M.R., Lee, I.K., 1993. The behaviour of granular soils at elevated stresses, in: Telford, T. (Ed.), Predictive Soil Mechanics. London, pp. 186–198.

Fumagalli, E., 1969. Tests on cohensionless materials for rockfill dams. J. Soil Mech. Found. Div. ASCE 95, 313–330.

Golightly, C.R., 1990. Engineering properties of carbonate sands. PhD. thesis. Bradford University.

Hardin, B.O., 1985. Crushing of soil particles. J. Geotech. Eng. ASCE 111, 1177–1192.

Kjaernsli, B., Sande, A., 1963. Compressibility of some coarse-grained materials, in: Proceedings of the 1st European Conference on Soil Mechanics and Foundation Engineering, Weisbaden, Germany, Vol. 1. pp. 245–251.

Marachi, N.D., Chan, C.K., Seed, H.B., Duncan, J.M., 1969. Strength and deformation characteristics of rockfill materials. Berkeley, CA, USA.

Marsal, R.J., 1973. Mechanical properties of rockfill, in: Hirschfeld, R.C., Poulos, S.J. (Eds.), Embankment Dam Engineering. Casagrande Volume I. John Wiley & Sons, New York, NY, USA, pp. 110–200.

Marsal, R.J., 1967. Large-scale testing of rockfills materials. J. Soil Mech. Found. Div. ASCE 93, 27–44.

McDowell, G.R., Bolton, M.D., 1998. On the micromechanics of crushable aggregates. Géotechnique 48, 667–679.

Nakata, Y., Hyodo, M., Hyde, A.F.L., Kato, Y., Murata, H., 2001. Microscopic particle crushing of sand subjected to high pressure one-dimensional compression. Soils Found. 41, 69–82.

Naylor, D.J., Maranha Das Neves, E., Mattar, D., Veiga Pinto, A.A., 1986.

Prediction of construction performance of Beliche Dam. Géotechnique 36, 359–376.

Oldecop, L.A., Alonso, E.E., 2007. Theoretical investigation of the time-dependent behaviour of rockfill. Géotechnique 57, 289–301.

Oldecop, L.A., Alonso, E.E., 2004. Testing rockfill under relative humidity control. Geotech. Test. J. 27, 269–278.

Oldecop, L.A., Alonso, E.E., 2001. A model for rockfill compressibility. Géotechnique 51, 127–139.

Ortega, E., 2008. Comportamiento de materiales granulares gruesos - Efecto de la succión. PhD. Thesis. Technical University of Catalonia. UPC, Barcelona, Spain (in Spanish).

Parkin, A.K., Adikari, G.S.N., 1981. Rockfill deformation from large-scale tests, in: Proceedings of 10th Int. Conf. Soil Mech. And Found. Engg. (ICSMFE), Stockholm, 4. pp. 727–731.

Penman, A., Charles, J., 1976. The quality and suitability of rockfill used in dam construction, in: Penman, A.D.M., Charles, J.A., Moore, J.F.A. (Eds.), Dams and Embankments, A.D.M. Penman, J.A. Charles, J.F.A. Moore (Eds.). Edited By: The Building Research Establishment, The Construction Press, Garston, Watford, UK, pp. 72–85.

Sowers, G.F., Williams, R.C., Wallace, T.S., 1965. Compressibility of broken rock and settlement of rockfills, in: Proceedings of the 6th ICSMFE, Montreal, Canada, Vol. 2. pp. 561–565.

Takei, M., Kusakabe, O., Hayashi, T., 2001. Time-dependent behavior of crushable materials in one-dimensional compression tests. Soils Found. 41, 97–121.

Veiga Pinto, A.A., 1983. Previsao do comportamento estrutural de barragens de enrocamento. PhD. Thesis. Laboratorio Nacional de Engenharia Civil, Lisbon, Portugal (in Portuguese).

Zhang, X., Baudet, B., 2013. Particle breakage in gap-graded soil. Géotechnique Lett. 3, 72–77.

Chapter 5

Particle model for rockfill and crushable coarse aggregate behaviour

In this chapter, particle crushing is introduced into a discrete model for rockfill and crushable coarse aggregates by a novel approach which combines a closed form solution for stress distribution inside particles and a crack propagation criterion derived from fracture mechanics concepts.

Two breakage modes are simulated: a local contact crushing and an equal volume splitting. The occurrence of both modes derives from experimental observations.

Three main parameters control the model performance: contact stiffness, basic friction angle of the particle material and the particle toughness.

Contact stiffness and friction were determined by experiments. A large diameter oedometer test on hard limestone gravel was successfully simulated. The simulation includes the prediction of the compression response and the evolution of grain size distribution. Rock toughness and basic friction angle were determined independently from the oedometer results.

Subsequently, large scale triaxial tests on the same material were simulated. Model parameters fitting the oedometer test were maintained unchanged. The predicted triaxial response (deviatoric stress-strain response, volumetric behaviour and final grain size distribution) was close to actual measurements.

5.1 Introduction

As it was shown in chapter 2, rockfill and coarse granular aggregates are commonly found in civil engineering structures (earth and rockfill dams, embankments, protection dykes, railway ballast) and mining installations (spoil heaps). Their deformability, strength, long-term behaviour and effect of water have been investigated by testing programs that involve heavy equipment, because of the specimen size adopted. Table 2-1 collects sample dimensions and maximum grain sizes in oedometer and triaxial tests performed over the last five decades. Laboratory testing requires, in most cases, a reduction of grain size if compared with prototype dimensions. In fact, testing real rockfill dimensions is an unrealistic

proposition. This difficulty opens the question of the representativity of scaled samples.

The set of references listed in Table 2-1 revealed key aspects of rockfill deformation:

(a) Deformation involves and is, to a large extent, a consequence of particle breakage. This is the case for stresses in the range of engineering applications. Particle breakage explains most of the features of rockfill behaviour.
(b) Shear strength is a nonlinear function of confining stress.
(c) Increasing confining stress eliminates peak strength behaviour and increases sample ductility. It also increases compressive behaviour under shear straining. Critical states are difficult to find because dilatancy is significant at the maximum deviatoric strains of triaxial tests.
(d) Yielding under isotropic compression is very significant. Yield loci include a "cap" and their geometry is qualitatively similar the yield shapes found in fine grained materials.
(e) Sample wetting results in collapse volumetric strains.
(f) Rockfill exhibits a marked time dependent behaviour that is controlled by stress and the ambient Relative Humidity.
(g) Grain size effects affect the entire stress-strain-time behaviour.

Tests results referenced in Table 2-1 were in most cases described in phenomenological terms. However, as it can be seen in chapter 2, elastoplastic models have also been developed (Alonso et al., 2005; Bauer, 2009; Chávez and Alonso, 2003; Indraratna et al., 2011; Naylor et al., 1997, 1986; Oldecop and Alonso, 2001; Salim and Indraratna, 2004). Einav (2007a, 2007b) developed an elegant elastoplastic model based on the evolution of the grain size distribution during material stressing.

These models reproduce some of the aspects listed above, but a comprehensive "continuum" model has not yet been proposed.

Scale effects on strength have been approached by incorporating breakage size effects of individual particles into a nonlinear strength criterion for the entire aggregate (Frossard et al., 2012; Ovalle et al., 2014). Ramon et al. (2008) examined size effects by interpreting tests for different grain size distributions by means of an elastoplastic compressibility model. Scale effects have not yet received a comprehensive modelling approach.

The modelling alternative explored in this research is to perform a direct simulation of the grain structure by means of a Distinct Element Method (DEM). This is an attractive scenario because the number of particles of the large scale tests listed in Table 2-1 may be reproduced without major difficulties. Probably larger structures, such as rockfill embankments, could be represented in the near future by a particle arrangement close to real conditions, at least under some regularity or symmetry conditions (plane strain, for instance). Of course, particle methods offer the

possibility of simulating properly the actual behaviour. A necessary feature of a particle model is the simulation of particle breakage. As it can be seen in chapter 3, previous attempts reported (Cheng et al., 2004, 2003; Lim and McDowell, 2005; Lu and McDowell, 2006; McDowell and Harireche, 2002; Robertson and Bolton, 2001; Robertson, 2000) simulate particle breakage through the rupture of a "bond" among particles previously introduced in the model formulation. Another approach is to substitute a given particle by smaller ones when certain particle strength is reached (Ben-Nun and Einav, 2010; Ciantia et al., 2015; Lobo-Guerrero and Vallejo, 2005; Marketos and Bolton, 2009; Pöschel and Schwager, 2005; Tsoungui et al., 1999). Also, there are other techniques for considering the breakage as the removing particles from clusters (Couroyer et al., 2000; Marketos and Bolton, 2009), and the reducing stiffnesses in contacts (Marketos and Bolton, 2009).

The breakage criteria introduced in this work is substantially different from previous proposals. A particle breaks when it meets certain conditions associated with the propagation of cracks inside particles. This concept, which was analysed in some detail in Oldecop and Alonso (2007, 2001) may account for the main aspects of rockfill deformation mentioned above. Creep behaviour, suction and scale effects may be approached by the same basic idea but they are outside the scope of this chapter and they will be analyzed in chapters 6 and 7.

The present chapter describes the model adopted and the procedure to identify model parameters from laboratory tests. Oedometer and triaxial tests reported by Ortega (2008) (see Table 2-1) for very dry conditions (Relative Humidity of 10%) will be reproduced. It is argued that all the complexity of the deformation and particle breakage, even if it associated with oedometric conditions, may be captured by the model. If this is the case, the model parameters identified should ideally be capable of predicting the response of a similar sample under triaxial conditions. This proposition is discussed in the final part of the chapter.

5.2 Stress state and breakage of a loaded particle

Early experimental work on the distribution of forces at contacts, in loaded granular media (Dantu, 1968, 1967; De Josselin de Jong and Verruijt, 1969) as well as in numerical analysis based on DEM (Cundall and Strack, 1979), show the development of "chains" of highly loaded particles, which isolate areas or volumes slightly loaded. These chains suggest that a loading condition leading to a particle breakage may be approximated by two opposite concentrated forces acting on the particle. Consider this condition in Figure 5-1. An elastoplastic circular disk, 3 cm in diameter, is loaded against a very rigid base ($E = 2 \times 10^6$ MPa; $\nu = 0.3$) by a concentrated loading P acting at the top. The curved contact at the base facilitates the numerical analysis. The effect of the concentrated load is observed in the upper half of the disk. The rock disk is characterised by elastic parameters E = 400 MPa, $\nu = 0.25$; a shear strength of 54 MPa, zero friction and a tension cut-off of 10 MPa. A Plaxis program was used in calculations. The load P was taken to its maximum value, P_{max} = 49.5 kN/m, under plane strain conditions. Tensile horizontal stresses (positive σ_{xx}) are calculated in most of the cylinder. However, strong and rapidly varying horizontal compression stresses are calculated in the vicinity of the application of the load. Very large shear stresses develop in this localised area.

Additional contact points, even if their concentrated loads are a fraction of the dominant *P* load, are also expected. This situation is approximated in Figure 5-2 by introducing two concentrated loads ($P = P_{max}/4$) in the position shown. Nothing changes essentially in terms of the distribution of stresses if compared with the previous case.

Consider now a polygonal shape in Figure 5-3. The vertical loads act on the upper vertex. Shearing in the vicinity of the vertex increases but tensile horizontal stresses dominate most of the particle volume as in previous cases. The failure load P_{max} now increases to P_{max} = 56.2 kN/m. Plastic points are represented in Figure 5-4. Close to the concentrated force, shear loading ("Mohr Coulomb points") develops. Inside the particle the tensile strength is the limiting condition.

However, a rock particle behaves as a brittle material and the simple analysis performed will be inaccurate but it suggests that two breakage mechanisms will coexist: a local "abrasion", "trituration" or "comminution" and a global splitting failure that divides the particle by means of a tensile rupture plane into two pieces of approximately equal volume. This is indicated in Figure 5-5. The photographs in Figure 5-5 were taking after dismantling an oedometer test on hard sandstone gravels. The maximum vertical stress applied was 0.4 MPa for Figure 5-5b and 2.8 MPa for Figure 5-5d.

In a loading process of increasing intensity the nature of the breaking process changes. For the lower range of contact forces, small particles detach from the contact area. We will refer to a comminution process in this research. Nakata et al. (2001) performed oedometer tests on uniform silica sand (diameters of particles varying between 1.4 mm and 1.7 mm) and found evidence of a yield stress, σ_y. They report that for vertical stresses $\sigma < \sigma_y$ all the damage was concentrated at the particle contacts. In this research, testing arrangements of parallelepipedic sugar cubes (chapter 4), it was found that below a yielding stress, 90% of the damage could be associated with contact crushing, while the remaining 10% was identified as tensile stress-driven splitting in approximately equal volumes.

Beyond σ_y, Nakata et al. (2001) found that damage was evenly distributed between comminution (50%) and splitting (50%). In this research, in chapter 4, it was found somewhat different proportions (70% and 30% respectively). In fact, even if a yield stress σ_y could be approximately found by examining the oedometric stress-strain compression curve, the best identification of the yielding point was the sudden surge of splitting divisions.

In the model developed these finding were taken into account as follows: for stresses below σ_y comminution and splitting breakages amount to 90% and 10% respectively. Above σ_y these proportions become 60% and 40%. This "yield stress" was estimated at 0.6MPa from the experimental oedometer tests reported by Ortega (2008).

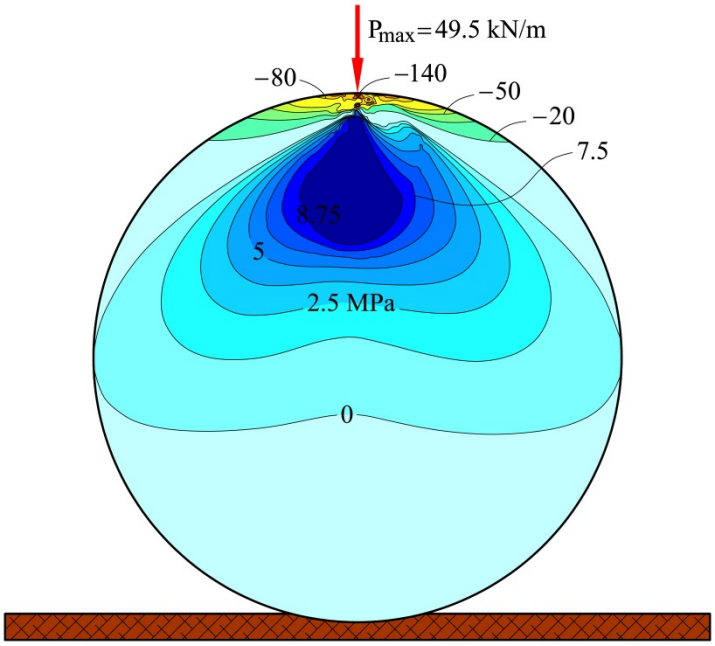

Figure 5-1 Calculated σ_{xx} stresses in horizontal direction inside an elasto-plastic circular disk over a rigid surface, subjected to a vertical concentrated compression load *P* at the top. *E*=400MPa, ν=0.25, c_u=54MPa, ϕ=0, σ_t=10MPa. Disk radius=1.5cm.

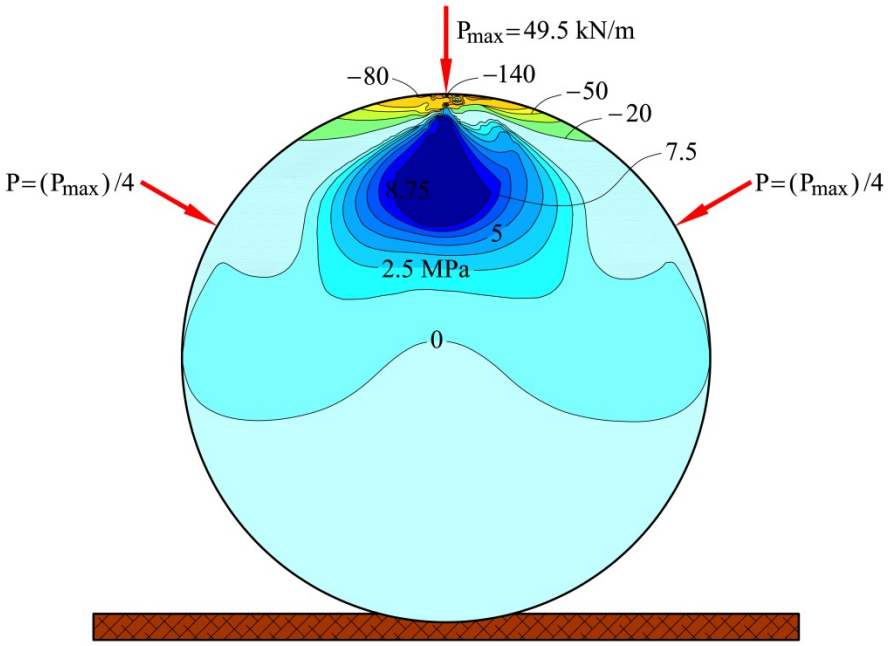

Figure 5-2 Calculated σ_{xx} stresses in horizontal direction inside an elasto-plastic circular disk over a rigid surface, subjected to a vertical concentrated compression load *P* at the top and two additional concentrated loads in the positions shown. *E*=400MPa, ν=0.25, c_u=54MPa, ϕ=0, σ_t=10MPa. Disk radius=1.5cm.

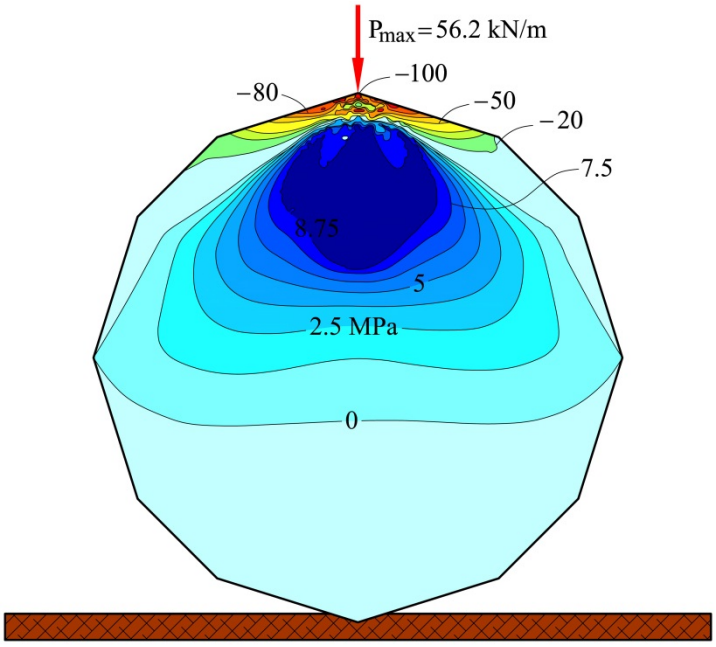

Figure 5-3 Calculated σ_{xx} stresses in horizontal direction inside an elasto-plastic polygon over a rigid surface, subjected to a vertical concentrated compression load *P* at the top. *E*=400MPa, ν=0.25, c_u=54MPa, ϕ=0, σ_t=10MPa. External disk radius=1.5cm.

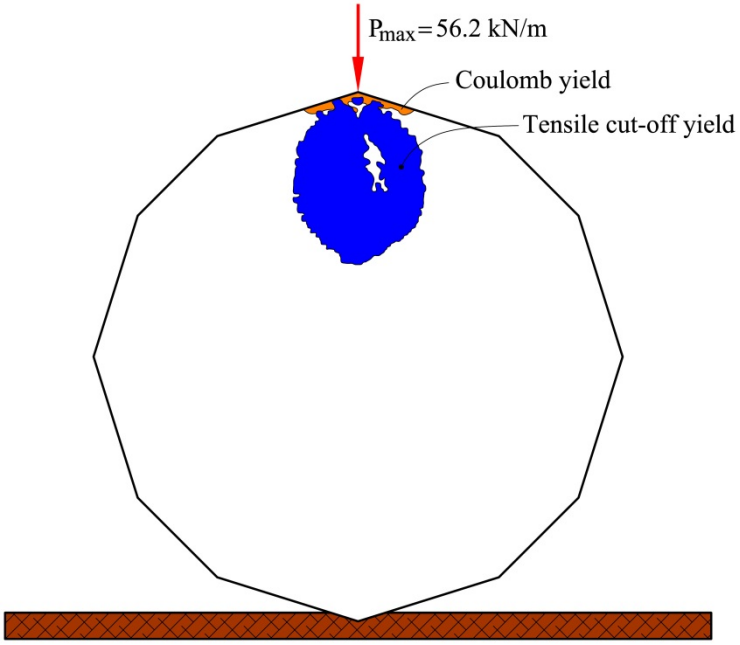

Figure 5-4 Distribution of Coulomb shear and tensile yielding zones in the case represented in **Figure 5-3**.

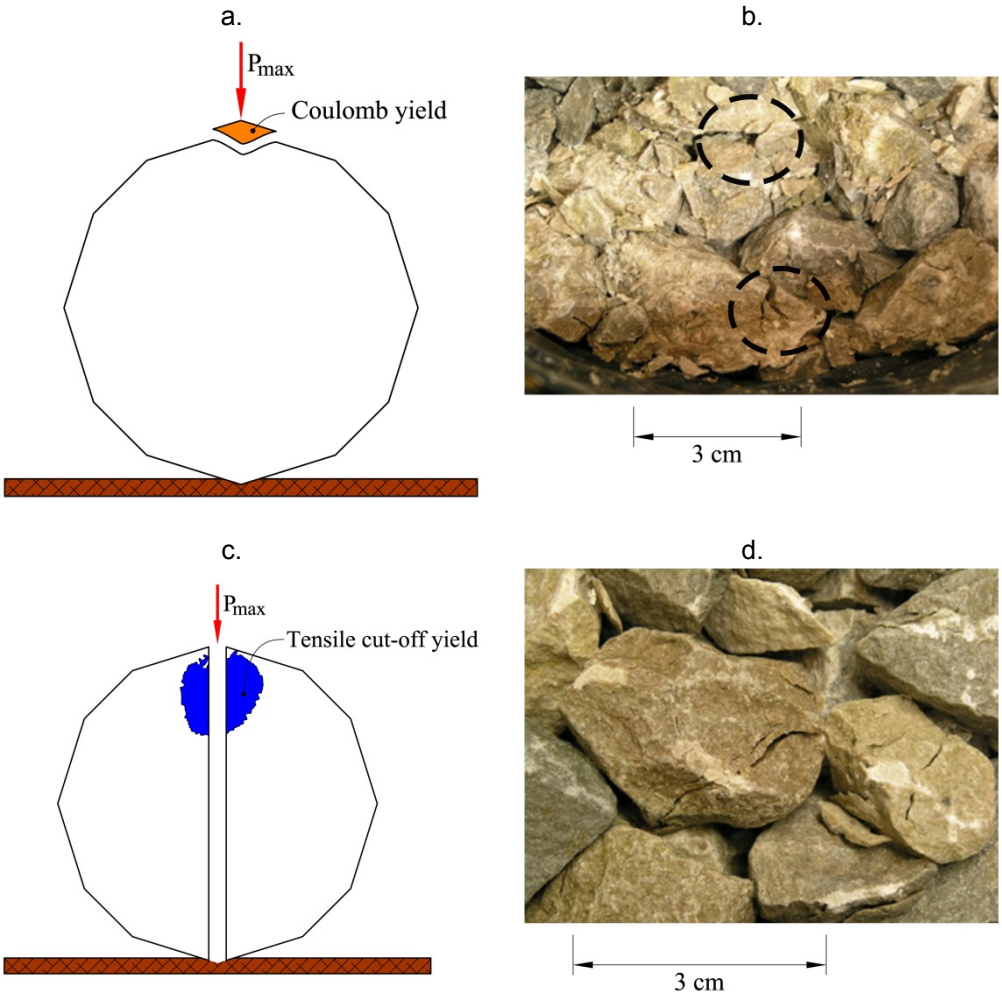

Figure 5-5 Breakage mechanisms: (a) Comminution crushing: Scheme of rupture process mainly attributed to shear stresses; (b) Observed contact crushing in sandstone gravels subjected to a vertical stress of 0.4 MPa under oedometric conditions; (c) Splitting breakage: Scheme of rupture process associated with tensile stresses; (d) Observed particle splitting in sandstone gravels subjected to a vertical stress of 2.8 MPa under oedometric conditions. (Photos (b) and (d) are courtesy of the Professor L.A. Oldecop).

Hiramatsu and Oka (1966) performed loading tests, by two diametrically opposed forces, on rock particles of irregular shape, and compared the results with the behaviour of spherical particles. Their conclusions support the previous discussion summarized in Figure 5-1 to Figure 5-5. This is convenient in order to develop a computational model for rockfill because stresses inside the irregular particles may be approximated by stresses calculated in spheres.

Russell and Muir Wood (2009) have provided analytical results for point loading on brittle spheres. A point load is an idealization of a more complex contact shape. Micro-asperities at the contact area between two particles would crush or plastify, and the point load is better conceived as a distributed stress on a finite surface.

This loading condition was introduced by Russell and Muir Wood (2009) in the manner indicated in Figure 5-6. The stress p is assumed to act on a circular "cap" area defined by the solid angle $2\theta_0$. The concentrated force F is given by $F = p\pi R^2 \sin 2\theta_0$, R being the sphere radius.

With reference to Figure 5-6, tensile stress acting on vertical diameter is given by:

$$\sigma_\theta = \left[\frac{1}{2} + \nu - \frac{(1+\nu)}{\left(1+\left(\frac{w}{z}\right)^2\right)^{0.5}} + \frac{1}{2*\left(1+\left(\frac{w}{z}\right)^2\right)^{1.5}} \right] * p \qquad (5:1)$$

where ν is Poisson ratio, z is the vertical coordinate shown in the figure and w is the radius of the loaded area.

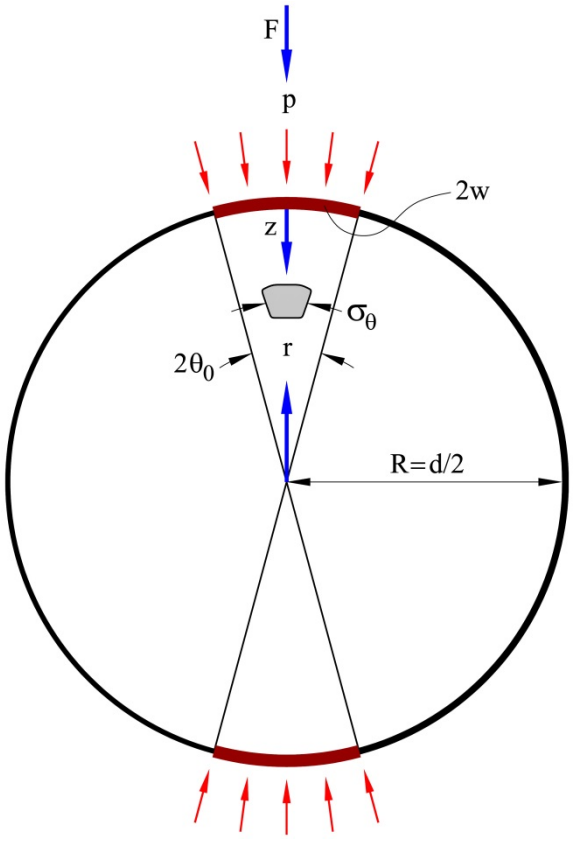

Figure 5-6 Modelling roughness effect: Contact load applied to a small circular area. After Russell and Muir Wood (2009).

Equation (5:1) is represented in Figure 5-7a for different Poisson ratios and a solid angle $\theta_0 = \pi/36 = 5^o$. The solution is highly dependent on ν. Compression σ_θ loads are calculated in the vicinity of the applied load. For a value $\nu = 0.25$, the maximum tensile stress is at a distance $z = 0.1925R$ of the centre of the applied stress. Tensile stresses extend towards the centre of the sphere. The effect of the loaded area (θ_0) is very significant in the proximity of the loaded area. This is shown in Figure 5-7b. A concentrated load ($\theta_0 = \pi/200 = 0.9^o$) induces a tensile stress ($\sigma_\theta = 44F/\pi R^2$) fifteen times higher than the stress calculated for $\theta_0 = \pi/50 = 3.6^o$.

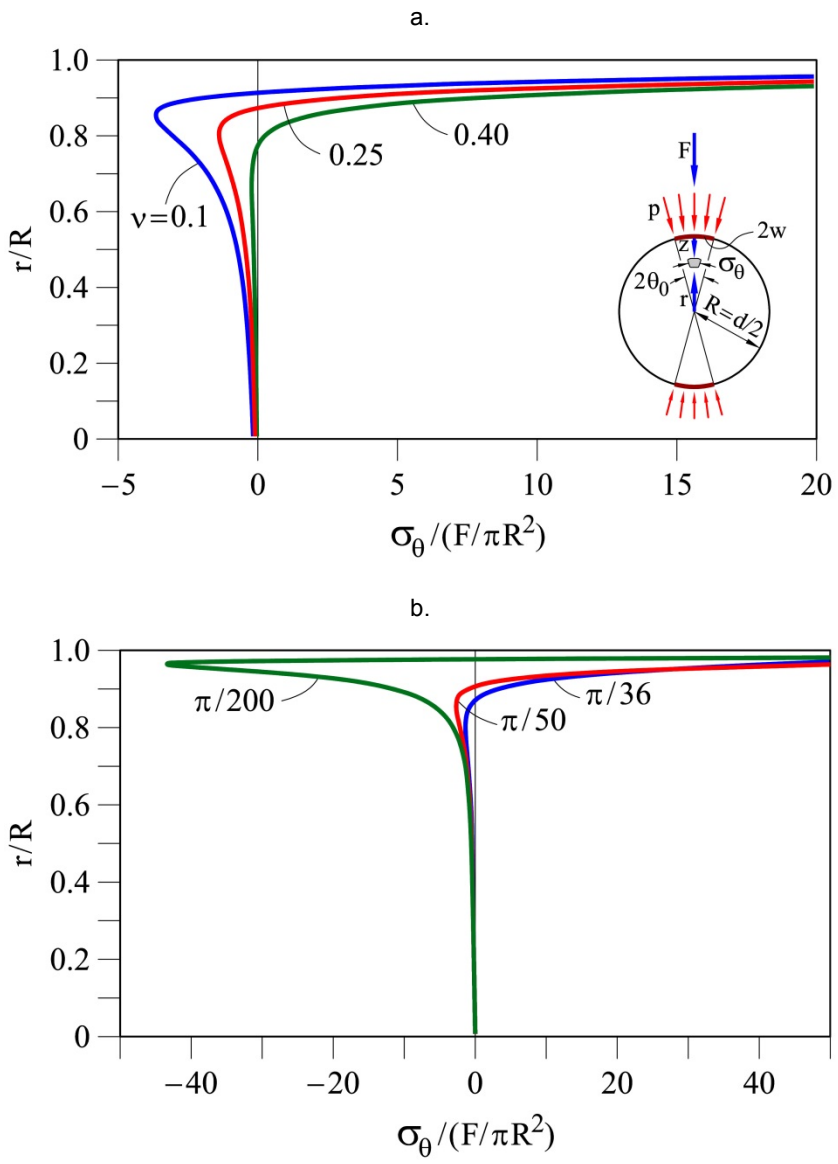

Figure 5-7 Dimensionless horizontal stress ($\sigma_\theta/(F/\pi R^2)$) in particle axis, for different: (a) Poisson ratios and $\theta_0=(\pi/36)$; (b) θ_0 values and ν=0.25.

In the model developed θ_0 was approximated by three alternative methods which take into account the contact stiffness and the contact roughness (rock macroparticles, described later, were considered as equivalent spheres):

(a) Calculation of θ_0 by Hertz's theory:

The effect of contact stiffness on θ_0 was first obtained by Hertz's theory (Santamarina et al., 2001), by calculating the contact interface radius (r_c) between two elastic spheres (radius R) subjected a normal load (F). Properties of limestone fragments used in the model were: Young's modulus, E = 6800 MPa; Poisson's ratio, ν = 0.25 and particle diameter of 2.8cm. The following expressions were used to calculate θ_0:

$$\frac{r_c}{R} = \left[\frac{3\left(1-\nu^2\right)F}{4ER^2} \right]^{1/3} \tag{5:2}$$

$$\sin\theta_o = \frac{r_c}{R} \tag{5:3}$$

$$\theta_o = \sin^{-1}\left(\left[\frac{3\left(1-\nu^2\right)F}{4ER^2} \right]^{1/3} \right) \tag{5:4}$$

(b) Calculation of θ_0 based on contact stiffness tests:

Values of θ_0 were also obtained from the results of contact stiffness tests which are described below when discussing parameter identification of DEM modelling (see section 5.6.2). The measured mean value of elastic contact stiffness (k_n) of 5.8 MN/m allowed the calculation of θ_0: The normal force, F, between two spheres, which induce a δ overlap is

$$F = k_n\delta \tag{5:5}$$

and

$$\theta_o = \cos^{-1}\left(1 - \frac{F}{2Rk_n}\right) \tag{5:6}$$

(c) Calculation of contact angle θ_0 based on surface roughness:

A third method for calculating θ_0 relies on the roughness of the particle surfaces. The procedure follows Russell and Muir Wood (2009), which uses expressions from Bahrami et al. (2005) and Hertz's theory. Summarizing, two spheres in contact (one rough and the other smooth)

having the same modulus *E* and radius *R* are considered equivalent to a smooth rigid sphere indenting a rough elastic half space. The radius of equivalent smooth sphere *r'* and the modulus *E'* of the elastic half space can be estimated as follows:

$$r' = \frac{R}{2} \tag{5:7}$$

$$\frac{1}{E'} = \frac{2(1-\nu^2)}{E} \tag{5:8}$$

The contact radius r_L of the loaded rough surface is calculated as:

$$r_L = r_L' r_c \tag{5:9}$$

where:
r_c is the contact radius for smooth spheres, calculated as in Equation (5:2) and r_L' is a dimensionless parameter given by

$$r_L' = \begin{cases} 1.605 / \sqrt{P_o'} & for \quad 0.01 \le P_o' \le 0.47 \\ 3.51 - 2.51 P_o' & for \quad 0.47 \le P_o' \le 1 \end{cases} \tag{5:10}$$

where

$$\alpha' = \frac{s\, r'}{r_c^2} \tag{5:11}$$

$$\beta' = \frac{E'}{H_{mic}} \sqrt{\frac{r'}{s}} \tag{5:12}$$

$$P_o' = \frac{1}{1 + 1.22\alpha' (\beta')^{-0.16}} \tag{5:13}$$

In these expressions,

- *s* is the root mean square of the asperity heights of the rough surface. It was taken as the R_a roughness experimentally determined for the #80 polished limestone surfaces. (R_a = 3.7mm, see section 5.6.1)
- H_{mic} is the effective microhardness of the asperities. It has and has units of stress and it was assumed equal to *E'*.
- P_o' is the maximum dimensionless contact pressure and it is related to a pressure distribution across the contact area. This pressure was considered uniform. For smooth spheres the value of P_o' is 1. It decreases for rough surfaces.

Finally, θ_0 is calculated as:

$$\tan\theta_o = \frac{r_L}{R} \tag{5:14}$$

Figure 5-8 illustrates the calculated θ_0 values, by the three methods as a function of applied load *F*. Interestingly, the three methods predict similar values. The value of θ_0 increases moderately with the contact force for values in excess of 500 N. The constant value $\theta_0 = \pi/36$, adopted in all calculations, looks like a reasonable compromise.

Russell and Muir Wood (2009) analytical solution was adopted to estimate maximum tensile stresses inside the irregular particles, which will be defined below in the computational model. For the purposes of this calculation an equivalent spherical radius was calculated for the irregular particles.

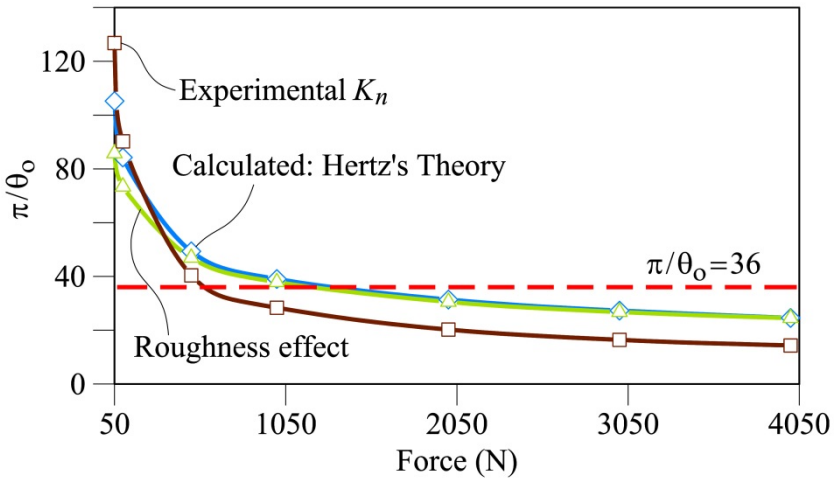

Figure 5-8 Calculated values of θ_0 when the load between two spheres in contact increases from 50 to 4050 N. Three calculation methods are indicated: Hertz's theory for smooth spheres, a method based on experimental stiffness and a roughness-based method. (E=6800 MPa; ν=0.25; Particle diameter=0.028m).

5.3 The model

Particles in DEM interact at their contacts by means of a simple frictional model (linear contact model). Particles will break in a granular assembly being loaded in time when a pre-existing crack or defect propagates and reaches the particle boundary.

Crack propagation is instantaneous when a stress intensity factor, which is calculated for every single particle, reaches the toughness, K_c, of the particle. A stress intensity factor for a Mode I of crack propagation (propagation in a uniform tensile field) is defined as:

$$K = \beta\sigma\sqrt{(\pi a)} \tag{5:15}$$

where a is the half-length of the defect, β is a dimensionless coefficient that depends on the particle geometry, the position of the defect, the intensity and direction of loading and the ratio of defect and particle size. For a disk of brittle material having a central defect of length $2a$ in the direction of two opposite point loads (Oldecop and Alonso, 2007):

$$\beta = \left(\frac{1}{1-\alpha}\right) * \begin{bmatrix} 1 - 0.4964*\alpha + 1.5582*\alpha^2 - 3.1818*\alpha^3 + 10.0962*\alpha^4 \\ -20.7782*\alpha^5 + 20.1342*\alpha^6 - 7.5067*\alpha^7 \end{bmatrix} \quad (5:16)$$

where $\alpha = 2a/D$; D is the diameter of the disk.

In the model developed σ is taken as the maximum tensile stress given by Equation (5:1).

However, even if $K < K_c$, defects propagate at a certain speed. This is known as subcritical crack propagation (Atkinson, 1984), such as it has been presented in chapter 2. The velocity of crack propagation may be written:

$$v = v_0 * \left(\frac{K}{K_c}\right)^n \quad (5:17)$$

which is a normalized version of the original Charles's law (Charles 1958a, 1958b). v_0 is a reference velocity and n is a parameter which depends on the ambient Relative Humidity. For dry conditions, n adopts high values (60 to 200). Data on crack propagation on a number of rock types (and glass) collected by Oldecop and Alonso (2007) suggest that $v_0 \approx 0.1$ m/s, a value adopted in the simulations reported below.

The form of Equation (5:17), when n is a large number, implies that the cracks remain essentially dormant until the stress intensity factor becomes close to the rock toughness. This result implies (Oldecop and Alonso, 2007) that the time to break, for a given stress state, essentially depends on the initial crack length, $2a$.

5.3.1 Particle shape

The model will be applied to reproduce the test reported by Ortega (2008) (Table 2-1) on hard crushed limestone used in railway ballast. Figure 5-9 shows a photograph of the material tested under oedometer and triaxial conditions. Minimum and maximum sieve sizes in Figure 5-9 are 25 and 30 mm.

Gravel geometry is characterized by sharp edges and relatively flat faces. After several trials, exploring the shapes of arrangements of spherical microparticles, a pyramidal shape defined by 14 equal micro spheres was adopted as a representative initial shape. The 14 micro-particle "clump" was selected because the evolution of particle size distribution induced by the breakage process was

reasonably well reproduced, at an affordable computational cost. In the Appendix 2, it is presented a sensitive analysis using different number of microparticles in order to also see the effect of the shape of the particles.

Micro spheres are rigidly attached, following the logic of “clumps” or macroparticles included in the DEM computer program PFC3D (Itasca, 2008). This program plays the role of a basic computational kernel for the extensive re-programming performed as it was seen in chapter 3.

In a uniform granular sample, all macroparticles have the same shape and dimensions but their orientation follows a random pattern. Figure 5-10 shows the shape of the 14-sphere macroparticle and the side view of two testing arrangements: an oedometer specimen 25 cm in diameter and 25 cm in height and a triaxial specimen (25 cm in diameter and 50 mm in height). The oedometer specimen requires 471 macroparticles against 971 for the triaxial specimen in order to obtain the initial porosity of the simulated laboratory samples.

Any contact between particles is characterized by two linear stiffness parameters (k_n, k_s) and a friction coefficient μ. In this work $k_n = k_s$. A third material coefficient is the rock toughness, K_c. The process of calibrating the three material parameters will be detailed below.

Figure 5-9 Hard limestone gravels from a quarry in Vallirana (Barcelona, Spain). Material tested by Ortega (2008).

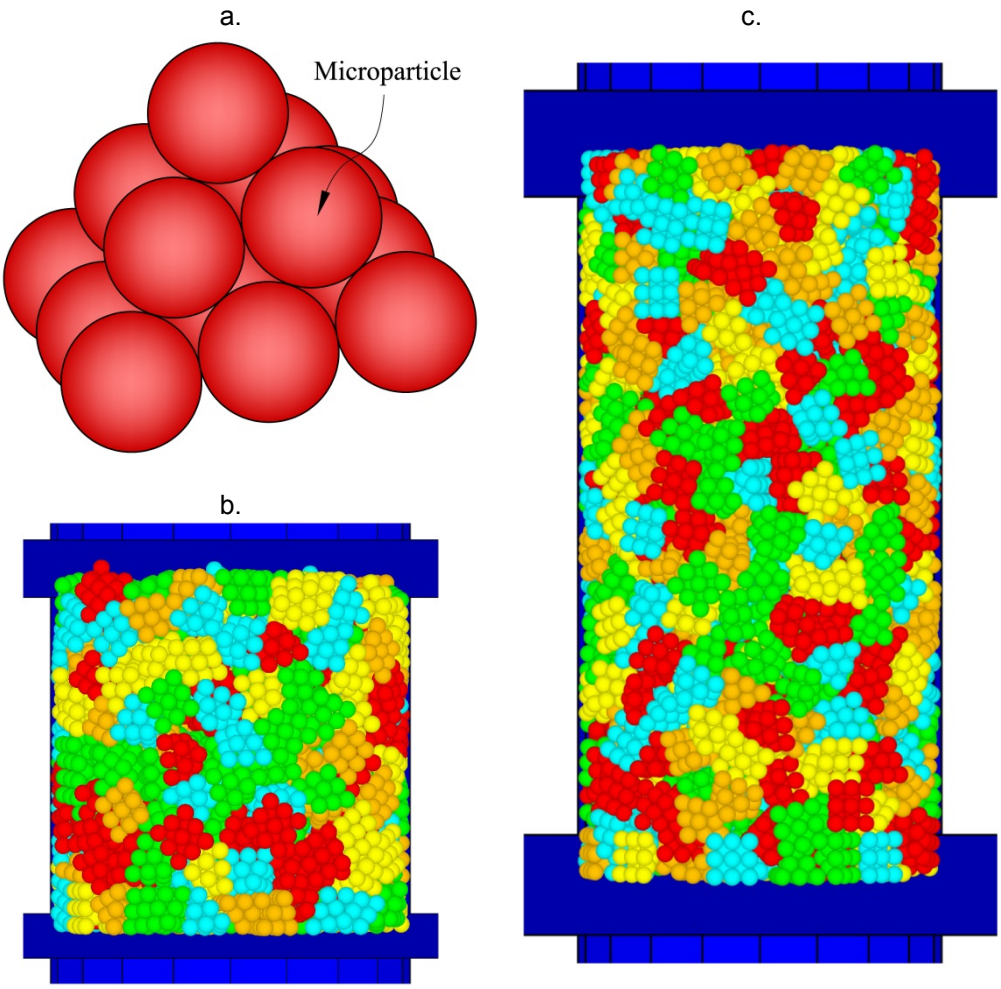

Figure 5-10 (a) Macroparticle DEM model: Clump of 14 microparticles; (b) model representation of oedometer test: Cylindrical sample (0.25x0.25m) made of 471 macroparticles; (c) model representation of triaxial test: Cylindrical sample (0.25x0.50m) made of 971 macroparticles.

5.4 Sample generation and division criteria

With the purpose of modelling, samples of uniform grain size distribution were generated. The attained porosity, very close to 0.53, reproduces the actual value tested by Ortega (2008). An initial geometrical layout of pyramidal particles, randomly generated, may result in concentrations of internal forces due to particles overlap. These stresses should be relaxed before the application of testing loads. The technique adopted to get a stress-free aggregation of particles, after checking other alternatives, was as follows: The number of particles leading to a target porosity in a given volume is first estimated. Spheres having the volume of the uniform gravel particles are randomly distributed in the sample volume. Their diameter is reduced to avoid force interactions and they are substituted by the

equivalent (equal volume) pyramidal macroparticles. The size of the macroparticles is then increased in steps, in a slow process in which internal interaction forces are systematically reduced to zero at the end of each step. A small contact friction coefficient (μ< 0.1) is applied to facilitate the elimination of internal forces.

Once the particle arrangement is defined a “defect” is assigned to each of the macroparticles. In practice, this defect may be any fissure, open or closed crack, crystal to crystal interface, etc. The defect is introduced as a “virtual crack length” in each macroparticle. Defect lengths follow a random uniform distribution between two limits directly related to the macroparticle diameter: 0.001D to 0.5D. Macroparticle shape is not taken into account in the propagation of the crack (Figure 5-11). A sensitivity analysis using different probabilistic distributions of the crack length is presented in Appendix 1.

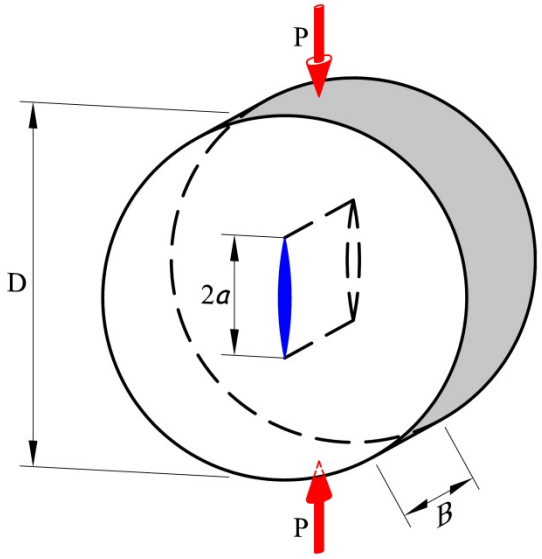

Figure 5-11 Macroparticle model to calculate crack propagation due to tensile stress (mode I). (Oldecop and Alonso, 2007).

The particle division procedure starts by examining the largest force applied to every particle. This force is then assumed to act as a double concentrated force at the ends of a particle diameter. The velocity of crack propagation is calculated by Equations (5:15), (5:16) and (5:17). The calculation proceeds in time and the crack length is updated at each time instant:

$$a = a_0 + \mathrm{v}^*\Delta t \tag{5:18}$$

where a_0 and a are the crack half lengths before and after a time increment Δt.

A particle division is achieved whenever $K \geq K_c$ or $2a \geq D$. Two possibilities are considered: comminution or splitting breakage. Once a fracture propagates in a given macro-particle the type of breakage follows previous discussion: for sample

stresses $\sigma < \sigma_y$ the probability of a comminution or splitting breakage to occur are 0.9 or 0.1 respectively. For $\sigma > \sigma_y$ these probabilities change to 0.6 and 0.4. This is performed as follows:

(a) In a comminution type of breakage the microparticle which receives the maximum contact force is removed in the manner indicated in Figure 5-12a. A new macroparticle made of 13 spheres and a new particle made of one sphere is generated. The 13-sphere macroparticle may be subjected to further comminution or may decide to split into roughly equal volume macroparticles. Under a continuous comminution process the initial macroparticle may eventually end into one simple sphere: 14 → 13 + 1; 13 → 12 + 1; 12 → 11 + 1; 11 → 10 + 1; 10 → 9 + 1; 9 → 8 + 1; 8 → 7 + 1; 7 → 6 + 1; 6 → 5 + 1; 5 → 4 + 1; 4 → 3 + 1; 3 → 2 + 1; 2 → 1 + 1.

The resulting individual spheres may still break into smaller particles. This is achieved by building an additional subparticle structure in them. This is shown in Figure 5-12c. The original spherical particle becomes in fact a "macroparticle" able to break following a comminution or a splitting type of division. Figure 5-12c shows the subdivision of an original spherical particle into an approximately spherical arrangement of 13 subparticles whose joint diameter is very similar to the original sphere, which may undergo further comminution or splitting breakage. For the comminution type of division, the rule already described applies to the spherical subparticles.

In the simulations reported here the largest initial macroparticles had a mean diameter of 2.8 cm. The spherical particles integrating the initial macroparticles had a diameter of 1.185 cm and the finest spherical subparticle becomes 0.395 cm.

For every particle resulting from a division, except for the finest subparticles, a defect of random size is introduced again. The final subdivision of a spherical particle into 13 subparticles does not preserve mass, and whenever this subdivision is performed a few microspheres are added in the vicinity of the original spherical macroparticle to enforce mass conservation.

(b) In a "splitting" type of breakage, a macroparticle is divided in two parts trying to follow a "equal volume" criteria. The initial big macroparticle and its subdivisions are split according to the scheme (Figure 5-12b): 14 → 8 + 6; 8 → 4 + 4; 6 → 3 + 3; 4 → 2 + 2; 3 → 2 + 1; 2 → 1 + 1. The position of the new macroparticles remains in the original locations and a set of new contacts are activated.

In a similar way to comminution division, the resulting individual and original spheres are replaced by 13 subparticles (Figure 5-12c) that may still break in a splitting or a comminution type.

For the 13 subparticle spheres and the resulting macroparticles from a comminution process, a similar equal volume criterion is adopted. For

instance, a particle made of 11 subparticles evolves as follows in a splitting process: 11 → 6 + 5; 6 → 3 + 3; 5 → 3 + 2; 3 → 2 + 1; 2 → 1 + 1.

Under a splitting mode of breakage and in the case of arriving to one spherical particle in the division process, the additional replacement by an assemblage of 13 subparticles requires the addition of small subparticles to ensure mass conservation.

5.5 Sensitivity analysis

The response of the model described is controlled by three main parameters: the contact stiffness, k_n, the toughness of particles, K_c, and the friction contact, μ. The model includes also "hidden" parameters, which have been listed in Table 5-1. Some of them have a numerical character (the contact damping) and others are not supposed to change in a significant way when modelling different rock materials under dry conditions (v_0, n: Eq. (5:17)). σ_y is an input parameter and depends on the material. As mentioned above it can be derived from the compressibility curves of oedometer test. For the analyzed case (limestone fragments with sizes between 2.5 and 3.0cm) this value was equal to 0.6MPa.

Table 5-1 Parameter of DEM model.

Parameter	Notation	Units	Observations
MAIN:			
Contact stiffness	k_n	MN/m	$k_n = k_s$
Contact friction coefficient	μ	-	
Toughness	K_c	MPa*m$^{0.5}$	
OTHER:			
Damping	η	-	Selected value (η = 0.7) to reduce uncontrolled particle motion
Reference velocity for crack propagation in Charles model	v_0	m/s	v_0 = 0.1 m/s for different rock types
Yield stress	σ_y	MPa	σ_y = 0.6 MPa for limestone fragments
Solid angle describing contact stresses	θ_0	Radians	$\theta_0 = \pi/36$. This value takes into account the roughness and stiffness of contacts for the calculation of the contact radius of applied load

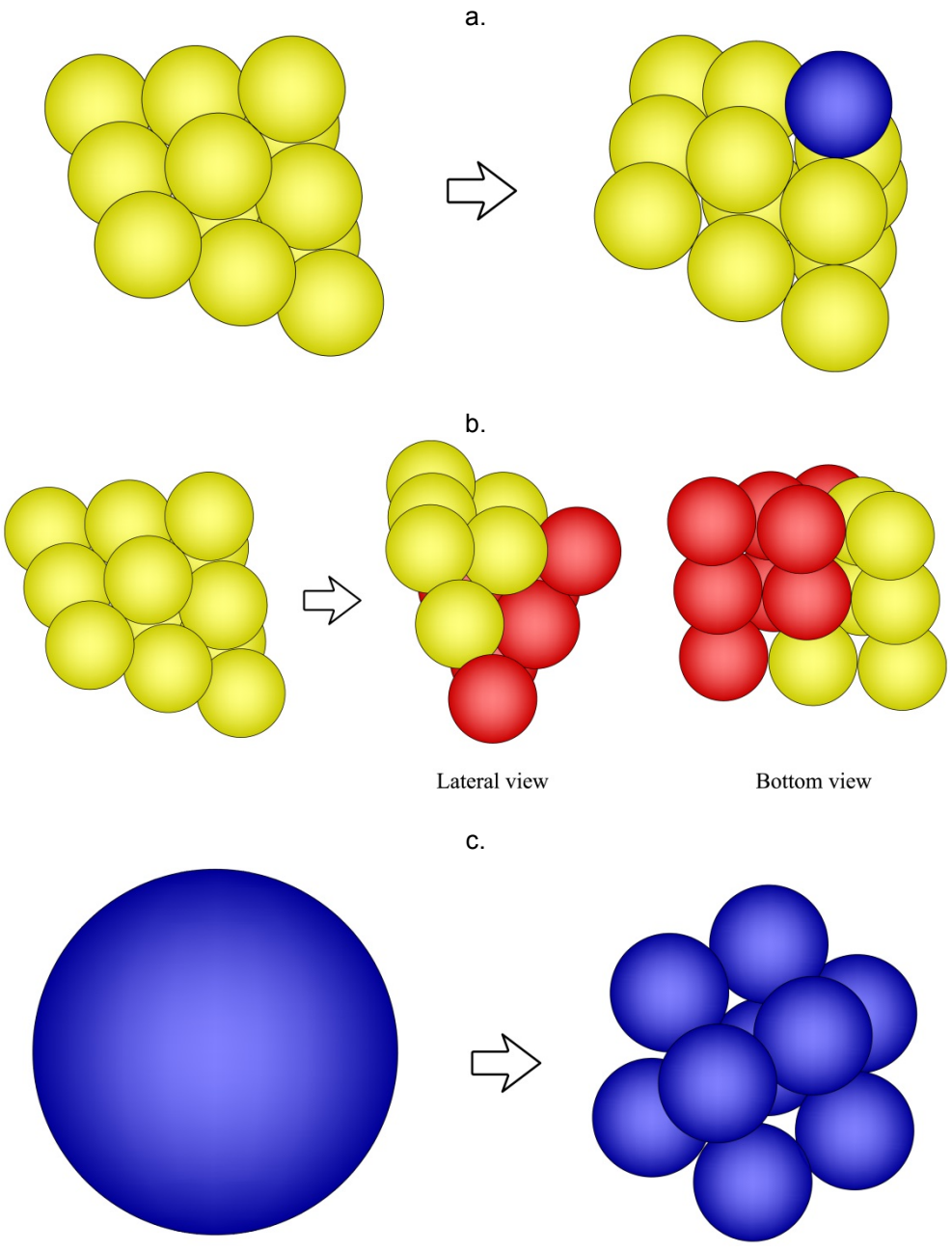

Figure 5-12 (a) Crushing by comminution: first division of the macroparticle: 14→ 13+1; (b) crushing by splitting: first division of the macroparticle: 14→ 8+6; (c) substitution of the original microsphere, once it is isolated, by a new macroparticle (clump) of 13 spherical elementary particles (13 subparticles).

Parameters k_n, K_c and μ will be calibrated by means of an oedometer test (Figure 5-10b). Before this is done, it was found useful to perform a sensitivity analysis aimed at knowing the effect of the three parameters on the sample response.

An oedometer test provides a compressibility curve and a grain size distribution at the end of the test, which may be quantified by a breakage index (for instance, the Hardin (1985), B_r index). B_r index provides a continuous measurement of the breakage at the current load applied.

Intuitively K_c should explain better the intensity of breakage than other parameters. Figure 5-13a shows the effect of K_c on the calculated B_r for different contact friction angles and a common k_n value. The numerical tests were performed by loading a 25 cm × 25 cm cylindrical oedometer sample initially made of 471 macroparticles (n_0 = 0.53). The loading increases in steps to a maximum of 2.8 MPa. Each one of the points represented in Figure 5-13a corresponds to a numerical test. Increasing toughness reduces particle breakage. Toughness controls the "resistance" to crack propagation: particle breaks catastrophically when stress intensity factor K exceeds K_c, and K_c also controls the crack propagation velocity (Equation (5:17)).

As a reference to interpret the scale of the horizontal axis, toughness values for mode I (tensile) fracture varies between 0.4 MPa $m^{0.5}$ and 4 MPa $m^{0.5}$ when comparing different types of rock and rock quality (Alehossein and Boland, 2004; Ayatollahi and Aliha, 2008; Backers, 2004; Chang et al., 2002; Saouma, 2007; Zhixi et al., 1997). The lowest range (0.4-1 MPa $m^{0.5}$) is found in sedimentary rocks (shale, sandstone, limestone) and the higher range (1.5-4 MPa $m^{0.5}$) is measured in intrusive rocks (granite, diorite).

The contact friction coefficient and stiffness (Figure 5-13 and Figure 5-14) have also some effect on breakage. Coefficient μ has no appreciable effects either for very low values of K_c (K_c = 0.5 MPa $m^{0.5}$) where breakage is very high, or for very high values (K_c = 10 MPa $m^{0.5}$) where almost no breakages occur (Figure 5-13a). However, it is observed that for values of μ > 0.3 increasing μ increases particle breakage. The interpretation is that low friction favours displacement of particles and results in higher sample density. Then, more contact points around particles are generated and less breakage is expected. The plot in Figure 5-14a (B_r against μ) also indicates in a more clear way the limited effect of internal friction on breakage. Contact stiffness has some effect on breakage as shown in Figure 5-13b. However, its effect is very limited. This is better shown if breakage index is plotted in terms of k_n (Figure 5-14b). B_r remains almost constant for changes in k_n. The reason for this result is not obvious. With the purpose of investigating this effect in more detail, force chains in the oedometer sample, subjected to a vertical stress of 2.8MPa, were calculated for different values of k_n (Figure 5-15). Increasing k_n results in a reduced number of force chains and an increase in the forces carried by them. These are counterposed effects which explain the limited effect of contact stiffness on breakage.

It is concluded that the calibration of K_c should preferentially be based on the evolving grain size distributions during loading.

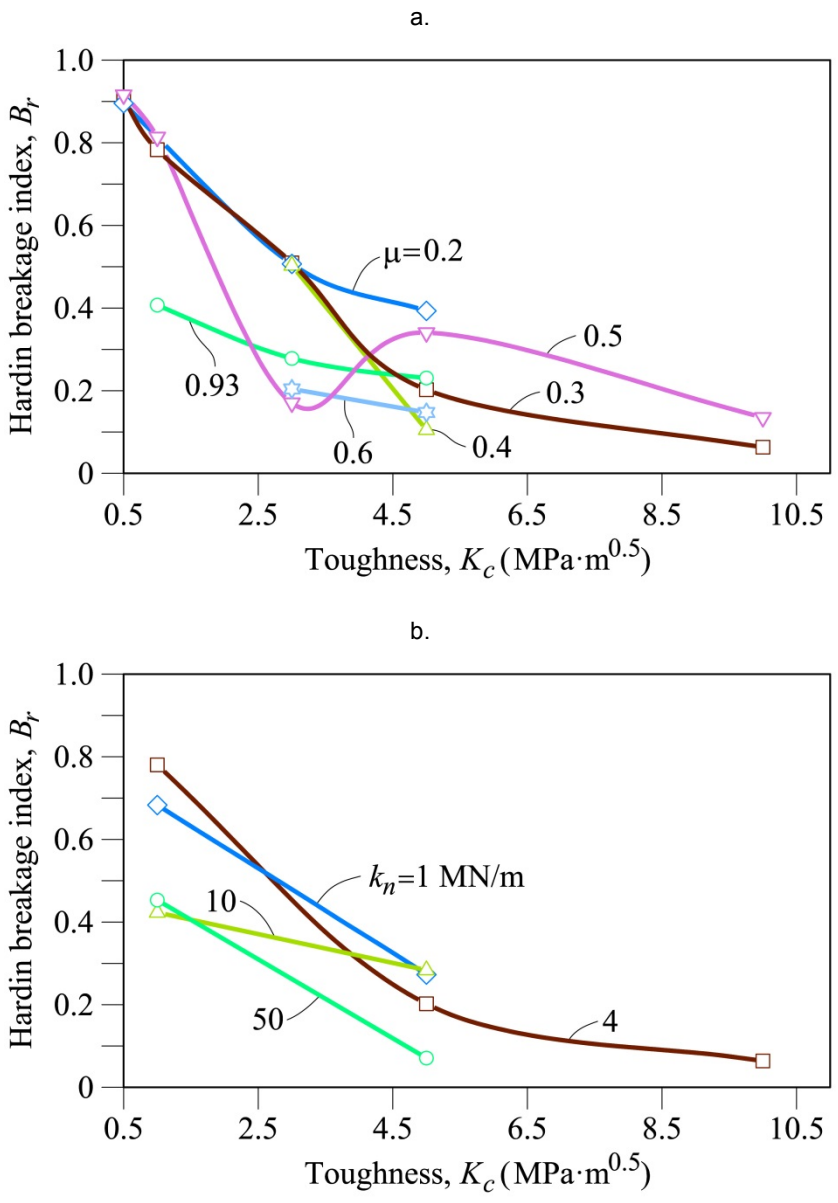

Figure 5-13 Variation of Hardin Breakage Index B_r with rock toughness K_c for: a) different friction coefficients μ, and k_n=4MN/m; b) different contact stiffness k_n and μ = 0.3. DEM simulations of oedometer test at σ_{max} =2.8 MPa.

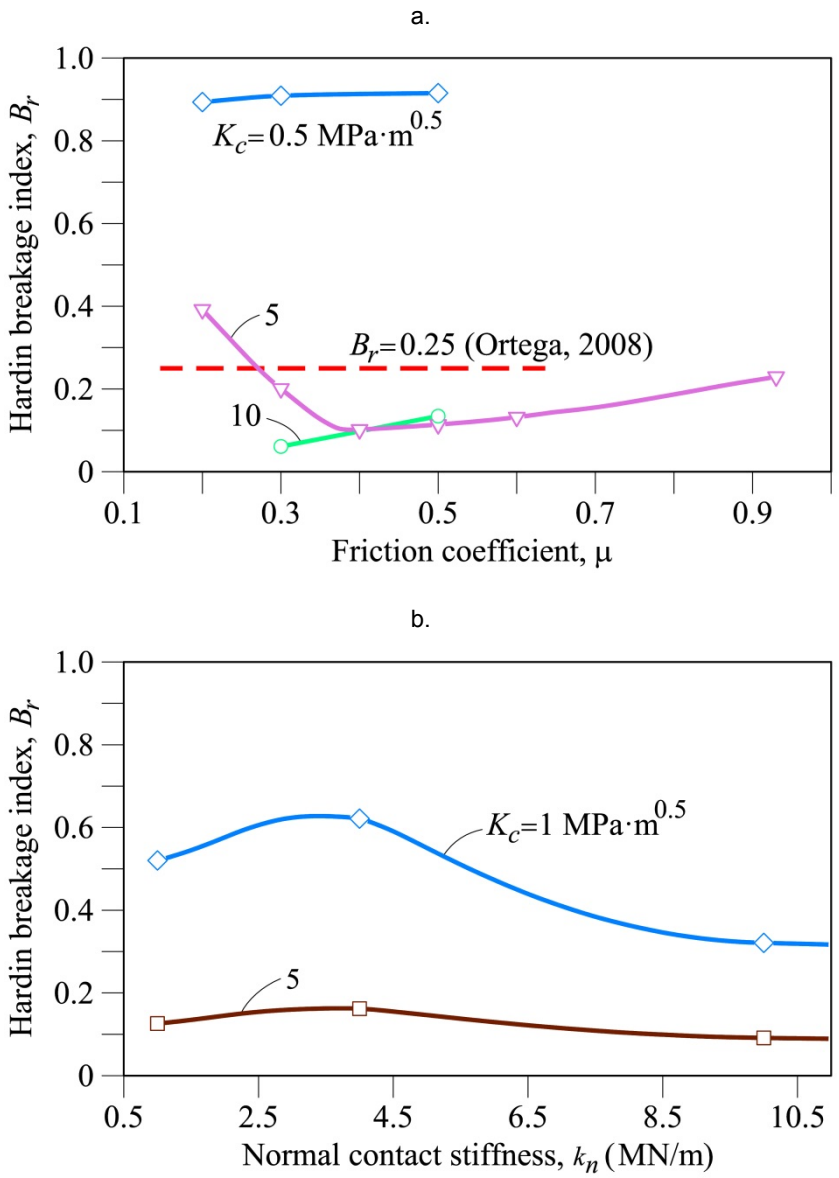

Figure 5-14 Variation of Hardin Breakage Index B_r with: (a) friction coefficient for three values of rock toughness K_c and k_n =4MN/m; (b) normal contact stiffness k_n for two values of rock toughness K_c and μ =0.3. DEM simulations of oedometer test at σ_{max} =2.8 MPa.

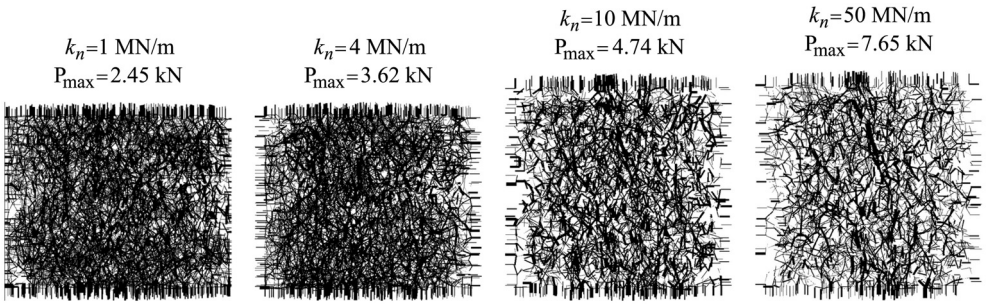

Figure 5-15 Comparison of force chains at σ_v =2.8 MPa varying k_n values. DEM simulation of oedometer tests. DEM parameters: μ =0.3; K_c=1 MPa*m$^{0.5}$. Value of maximum contact force P_{max} is indicated.

Consider now the compressibility of the oedometric sample. It will be characterized by the slope λ of the semi-logarithmic *e* vs. lnσ plot at high stress (say $\sigma \geq$ 0.5 MPa). Values of λ are represented in Figure 5-16 in terms of k_n for two values of K_c (1 MPa m$^{0.5}$; 5 MPa m$^{0.5}$; the first value is more likely to characterize the toughness of a hard limestone). A constant friction μ = 0.3 was selected in this case. k_n has a significant effect on λ. Sample compressibility is a result of deformation at contacts but also a consequence of particle breakage and subsequent re-arrangement of particles. Therefore, the three main parameters defining the model (k_n, K_c, μ) are expected to contribute in a significant manner. In a DEM model the overlap between particles, determined through k_n contributes to the overall deformation. Therefore compressibility will decrease when k_n increases. This is shown in Figure 5-16. The relationship between λ and k_n is shown to be nonlinear probably as a result of the effect of k_n on the evolution of geometry and contact points during the loading process.

Contact friction effect on λ, for different values of K_c, is given in Figure 5-17. Low friction values effectively control λ because they facilitate the structure re-arrangement. As friction increases the mobility of grains is restricted and compressibility decreases markedly. This effect is also shown in Figure 5-18, where λ is plotted in terms of toughness for different friction values. Friction coefficients in excess of 0.4 do not lead to any further increase in compressibility. The effect of material toughness is also shown in Figure 5-19 which shows the joint effect of k_n and K_c on λ. As expected, increasing toughness reduces compressibility because particle breakage is progressively reduced. High friction values are however capable of reducing significantly the effect of toughness (Figure 5-18).

Also represented in previous Figure 5-14 to Figure 5-19 are the B_r and λ values derived from Ortega (2008) test. They help to perform the back analysis because they show in a rapid way the range model parameters leading to a good representation of the test.

Summarizing the previous discussion, it can be concluded that K_c has a significant effect on the evolution of the grain size distribution, unlike the friction coefficient. Compressibility, on the other hand is significantly controlled by k_n as well as by the

friction coefficient. The backanalysis of a “complex” oedometer test which integrates the joint behaviour of a large assembly of breakable particles and provides also information of the evolution of the grain size distribution is a powerful procedure to determine model constants. But they may also be determined experimentally. This double approach, which helps to provide consistency to the entire modelling approach, is addressed in the next section.

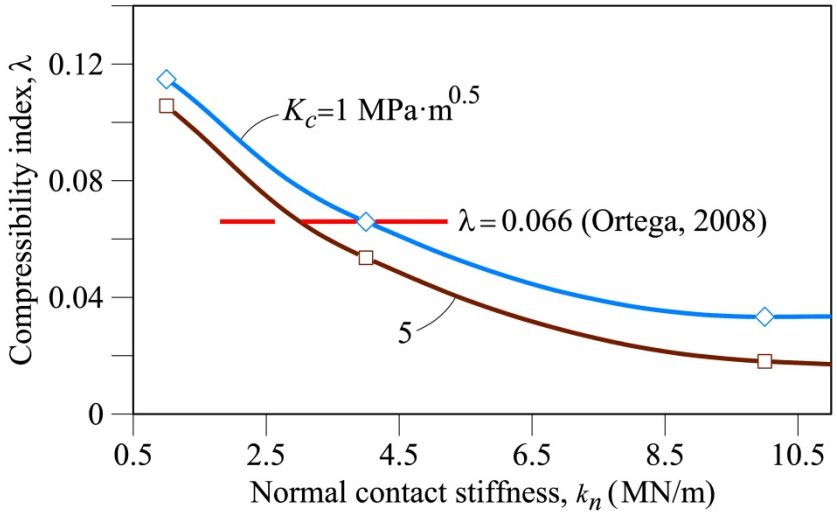

Figure 5-16 Influence of k_n on compressibility index λ for two K_c values, and μ=0.3. DEM simulations of oedometer test at σ_{max} =2.8 MPa.

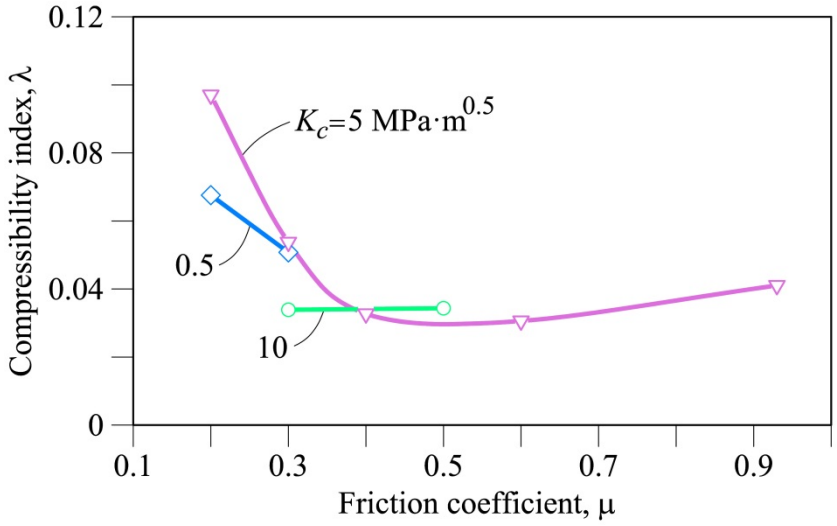

Figure 5-17 Influence of μ on compressibility index λ for three K_c values, and k_n =4MN/m. DEM simulations of oedometer test at σ_{max} =2.8 MPa.

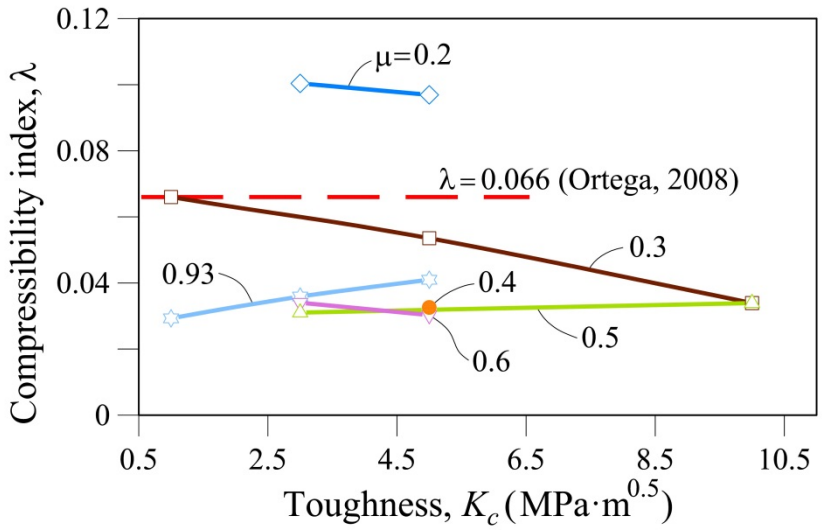

Figure 5-18 Influence of K_c on compressibility index λ for different μ values and k_n =4 MN/m. DEM simulation of oedometer test, σ_{max} =2.8 MPa.

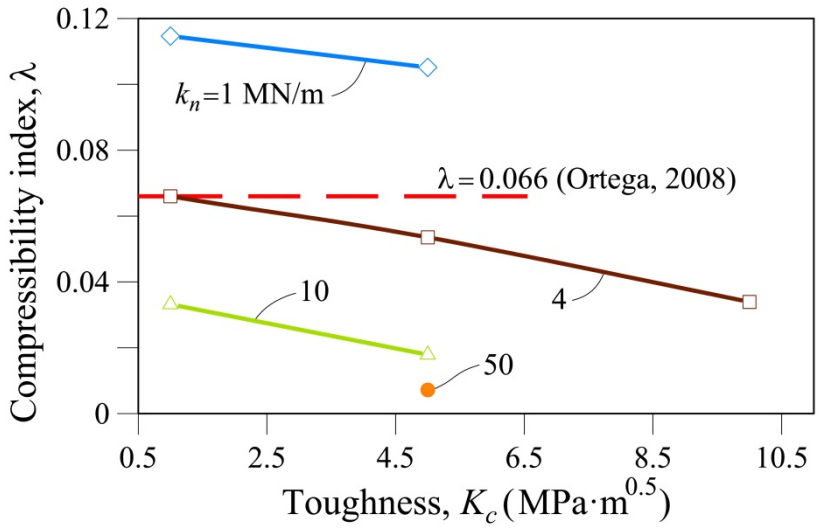

Figure 5-19 Influence of K_c on compressibility index λ for different k_n values and μ =0.3. DEM simulation of oedometer test, σ_{max} =2.8 MPa.

5.6 Oedometer test on crushed limestone, parameter identification and modelling

Ortega (2008) performed suction-controlled oedometer and triaxial tests on crushed gravel of a hard microcrystalline limestone used as railway ballast. Basic

properties of the limestone are given in Table 5-2.

Table 5-2 Properties of crushed limestone tested by Ortega (2008).

Unconfined compression strength	67–146 MPa
Tensile strength (Brazilian test)	2.2–11 MPa
Solids density	2.76 Mg/m^3
Young's modulus, E	6800 MPa
Absorption	0.38%
Porosity (estimated from absorption value)	1%
Los Angeles abrasion coefficient	17.8

Porosity of rock fragments was estimated from the water absorption value. Pores are probably not connected. The grain size distribution of the tested sample in the 25 cm by 25 cm oedometer cell is shown in Figure 5-20. Gravel passing the 30 mm sieve and retained by the 25 mm sieve was selected for the test. The gravel was maintained in a very dry state (Relative Humidity = 10%) during the test by means of a vapour circulation system. The gravel was poured into the oedometer cell and slightly compacted (statically) in four layers. The achieved void ratio was close to 1 (n_0 = 0.5). The vertical stress was applied in steps: 0.1; 0.2; 0.4; 0.6; 0.8; 1.2; 1.6; 2.0; 2.4 and 2.8 MPa. After stabilization under this stress the sample was flooded and finally unloaded. The grain size distribution after dismantling the test is shown in Figure 5-20. A breaking index B_r = 0.25 is determined for the grain size distribution after testing.

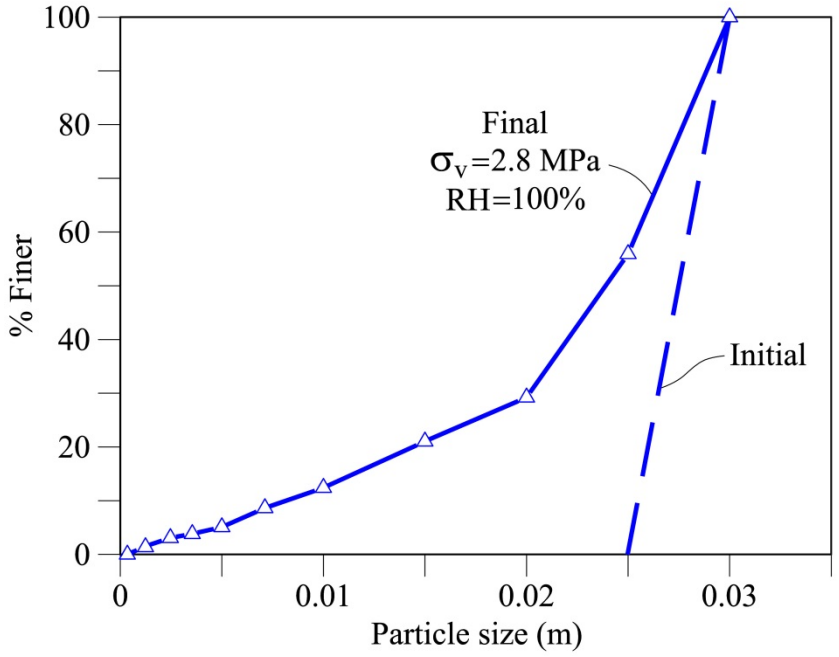

Figure 5-20 Initial and final grain size distribution for limestone gravel sample tested in an oedometer by Ortega (2008).

The simulated granular arrangement is shown in Figure 5-10b. The sample was initially represented by 471 macroparticles, each one of them integrating 14 spherical microparticles in a pyramidal configuration. The porosity of this arrangement was n_0 = 0.53, slightly higher than the porosity of the real sample. The lateral steel cylindrical surface was simulated by a stiff outer boundary having a normal stiffness k_n = 3.2x10^9 N/m.

5.6.1 Contact friction between particles and surface roughness

Particle methods become more effective and useful if their basic parameters have a physical interpretation and their values can be determined through specific tests, not directly based on testing the granular aggregate. Concerning the contact friction, it was decided to perform an experimental investigation on the limestone gravel tested by Ortega (2008). The conditions of a limestone-limestone contact could be categorized in three classes regarding the roughness of the contact:

(a) A rough surface. This may be the case of the cutting surface left by a rock saw.
(b) A “basic” roughness, leading to a basic friction between rock surfaces polished to certain fineness.
(c) Highly polished rock surfaces leading to mineral friction.

Bruce et al. (1989) provided guidelines for the preparation of rock surfaces for the determination of basic and mineral friction coefficients. For the basic friction, they suggested polishing with sand paper #80 of the two surfaces in contact. For the mineral friction, they suggested to test a #80 polished surface against a surface first polished to the #1000 paper followed by an additional polishing with tin oxide.
Shear tests were performed in two devices: a tilting table and a direct shear box. The procedure suggested by Bruce et al. (1989) was followed for the tilt tests applying an average inclination speed of 8º/min (by hand). Sets of two blocks were tested under several normal loads. The bottom block was fixed to the table whereas the upper block was able to slide. When determining mineral friction, the fixed block had a #1000 polished surface, and the sliding block a #80 polished surface.

Direct shear tests on conventional equipment were also performed at a shearing rate of 0.005 mm/min. The moving block (#80 polishing) slid on a polished (#1000) fixed block.

The available samples belonged to two groups: “small” samples (approximately 5 × 5 cm in size) and “large” samples (approximately 12 × 15 cm). Table 5-3 summarises the limestone samples prepared for the tilt and direct shear tests and the roughness of the sheared surface. The results of the tilt table and shear box tests are collected in Figure 5-21. Note the large difference in normal stress. However, the two experiments provide a consistent result: a basic friction angle of 17º-18º and a mineral friction angle of 12º were determined for the tested limestone.

A basic friction angle (ϕ_b = 18º; μ = 0.3) was selected for DEM simulations. It was judged that the point contacts had a relatively low roughness but not as low as to justify a mineral friction angle.

Table 5-3 Limestone samples for tilt table and direct shear tests.

Sample	Area (cm2)	Description	Roughness
M1R	164	Large. Irregular section	Rough
M2R	42.8	Small. Rectangular section	Rough
M1P	27.8	Small. Rectangular section	Basic
M4G	159.9	Large. Rectangular section	Basic
M5G	163.2	Large. Irregular section	Basic
M2P	24.5	Small. Rectangular section	Mineral
M3P	28.8	Small. Rectangular section	Mineral
M6G	207.2	Large. Rectangular section	Mineral

A compendium of results of performed tilt table and direct shear tests on limestone fragments is in the Appendix 5.

The roughness of the surfaces tested for basic and mineral frictions were also measured. This determination was used for the estimation of the contact angle discussed in a previous section. Thin sections were cut from limestone blocks polished to #80 and #1000 grades. Ten micro photographed profiles were analyzed per section. Figure 5-22 shows two of the analyzed profiles for #80 and #1000 polished surfaces.

R_a roughness (Thomas, 1999) was determined. This roughness corresponds to the arithmetic average of the deviations of the curved profile with respect to the midline of the profile. Five representative points per each profile were selected for measuring deviations.

For the #80 polished surface, the roughness R_a ranged between 2.2 µm and 6.0 µm, with a mean value of 3.7 µm. This surface roughness can be observed by naked eye. Roughness R_a of the #1000 polished surface, ranged between 0,5 µm y 3,7 µm, with a mean value of 1.7 µm . This roughness cannot be appreciated by the naked eye.

Details of the roughness tests on limestone fragments are found in Appendix 5.

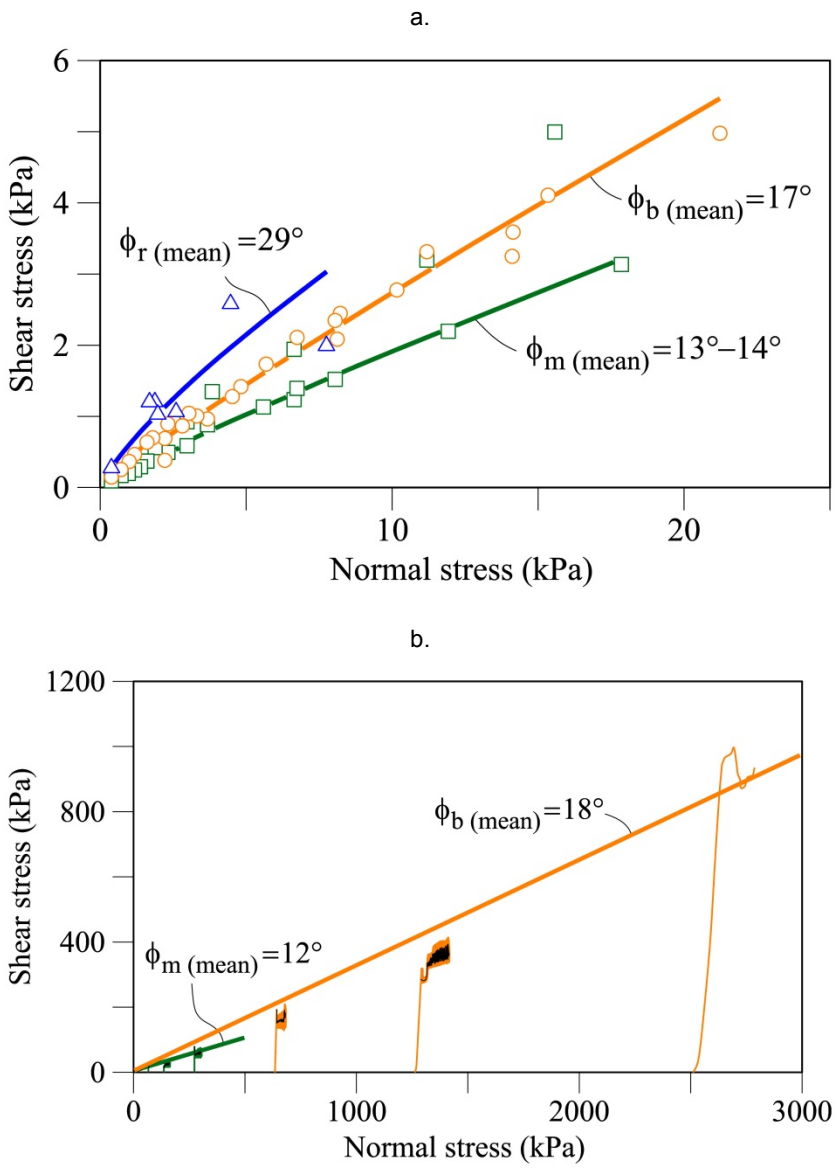

Figure 5-21 Limestone friction angle determined in shear tests on polished planar joints (rough surfaces (ϕ_r); basic friction angle (ϕ_b); mineral friction angle (ϕ_m)): (a) Tilt table results; (b) Direct shear test results.

a.

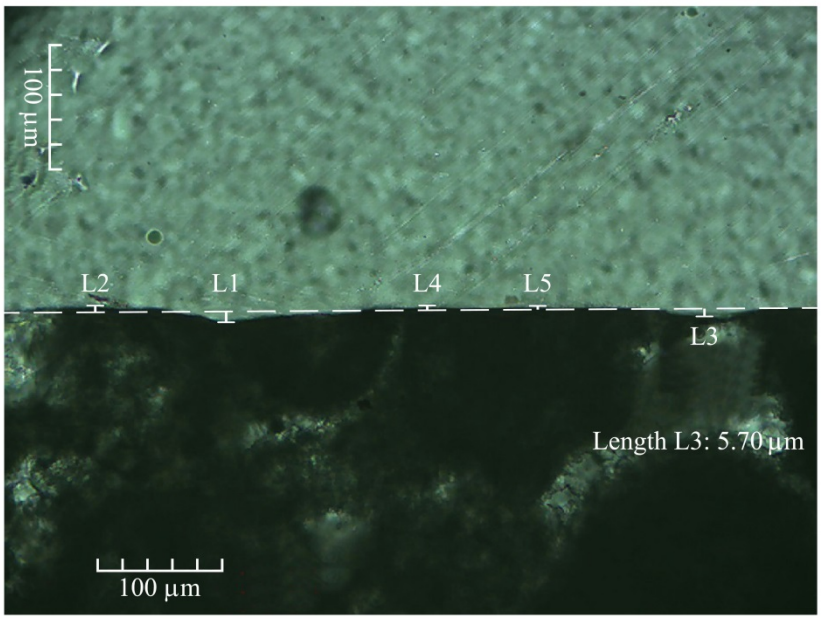

b.

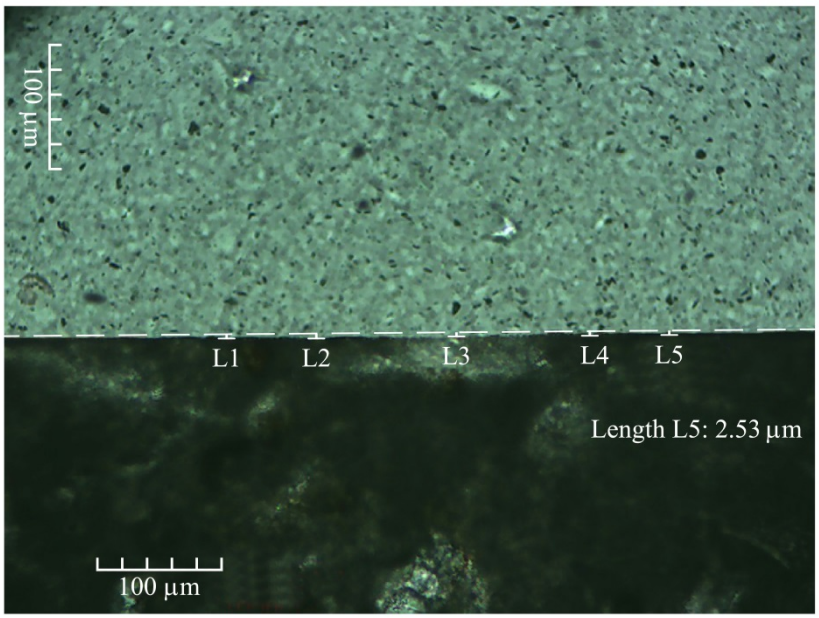

Figure 5-22 Roughness measurement: Profiles of thin sections of limestone by microscope examination. (a) #80 polished surface; (b) #1000 polished surface. (Limestone in dark color in the lower part. Epoxy resin –upper part- covers the rock).

5.6.2 Contact stiffness between particles

Laboratory tests were performed to measure the contact stiffness k_n. Prisms of limestone (square section 2.5 x 2.5 cm and 6 cm height) were prepared. One edge of the prisms was subsequently carved into a pyramidal shape having apex angles varying between 70^o and 90^o. Samples were subjected to compressive loads against a limestone flat surface (Figure 5-23).

Test results are shown in Figure 5-24. 90º apex angle prism samples exhibit a stiffer reaction than 70º samples. There is some scatter in results, which manifests also when stiffness coefficient k_n is calculated. Stiffness values varying between 1 and 7 MN/m were measured for the range of loads applied (0 to 800 N). Unloading-reloading lead to an increase in stiffness: the calculated mean k_n was 5.8 MN/m. Also shown in the figure are the results predicted by Hertz's theory for the contact between elastic spheres (E = 6800 MPa, ν = 0.25; sphere diameter: 2.8 cm). The load–displacement relationship is nonlinear and shows a stiffer reaction than the measurements when the concentrated load exceeds 150-200 N. This is explained by the different geometrical definition of the contact between two spheres and the point-flat surface indentation experiments performed. Note also that the tested rock samples include some degree of local roughness, unlike the Hertz model. Two representative values for k_n, derived from the Hertzian curve, are 2.1 MN/m (applied load: 1.5-100 N) and 6.2 MN/m (100-1000N). Despite the scatter of experiments the measured response of the loading rock contacts are in reasonable agreement with Hertz's model.

Experimental data of these contact stiffness tests on limestone fragments are found in Appendix 5.

5.6.3 Simulation of oedometer test on limestone gravel

No specific tests were performed to determine the K_c value. However, the review of K_c values published (for mode I fracture), summarised before, suggests that a hard, dense and sound limestone may have a K_c value on the vicinity of 1 MPa $m^{0.5}$.

The experimental oedometer compression curve reported by Ortega (2008) was well reproduced (Figure 5-25) by the following parameters defining the DEM model: μ = 0.3, K_c = 1 MPa $m^{0.5}$ and k_n = 4 MN/m. μ and K_c are amenable to independent direct determination. k_n is more linked to the nature of DEM modelling and seems to be better determined by a backanalysis of test results on particle aggregates. Nevertheless, the "ad hoc" experiments performed on manufactured contacts indicate that the back analyzed k_n value is not far from expected (real) local stiffness at particle to particle contacts.

a.

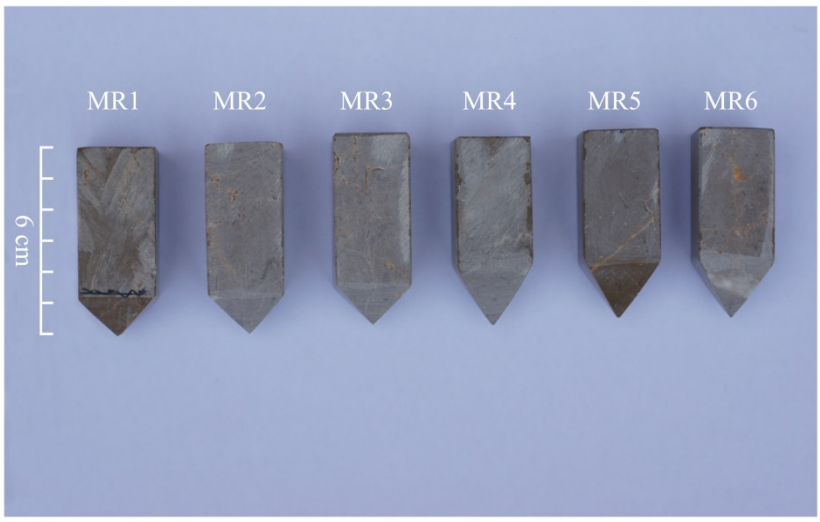

b.

Figure 5-23 a) Limestone samples for contact stiffness tests: MR1, MR2, and MR3 (90º apex angle); MR4, MR5 and MR6 (70º apex angle). Height of samples: 6 cm; Cross section: 2.5 cm x 2.5 cm; b) detail of testing arrangement.

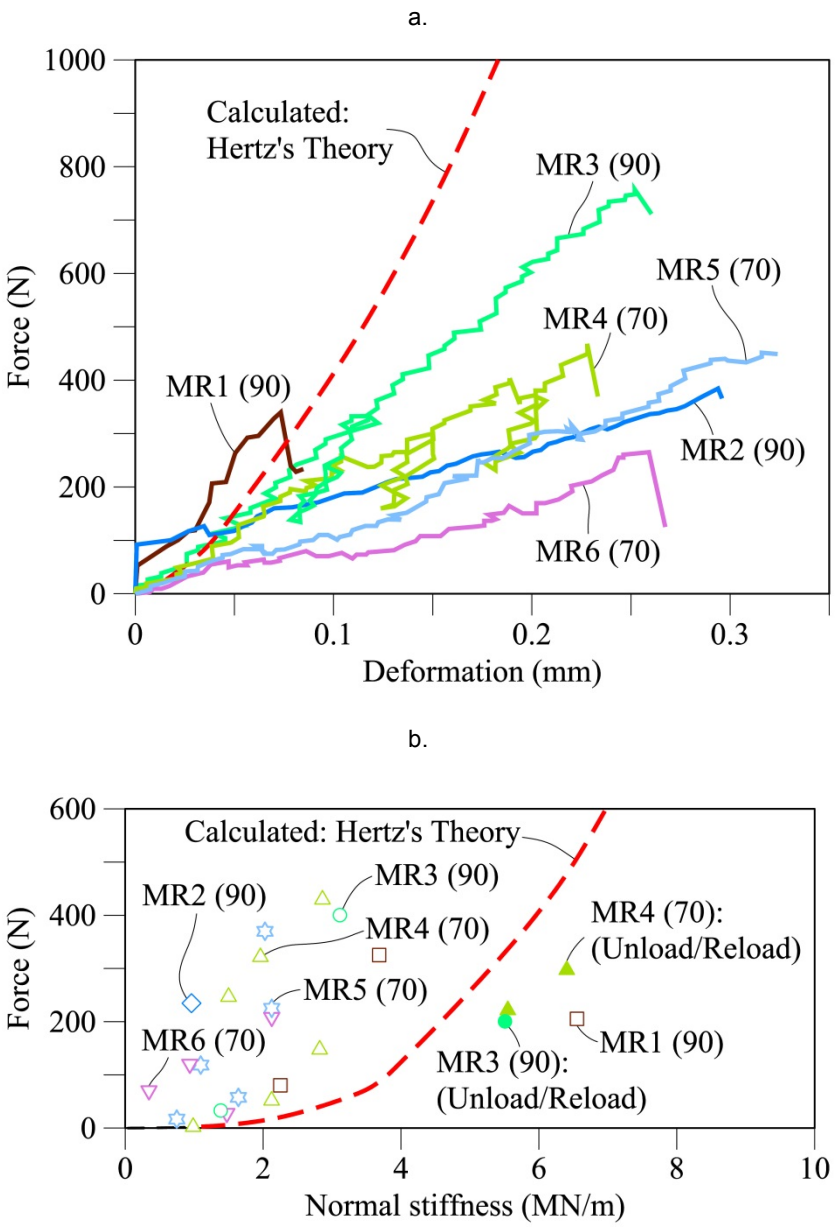

Figure 5-24 a) Force-deformation response of limestone pyramidal samples. Tests (MR1-MR6); b) Normal stiffness plotted against applied load (wedge angle indicated in parenthesis). Also shown are results of Hertz's theory (E=6800 MPa; ν=0.25; particle diameter=0.028m).

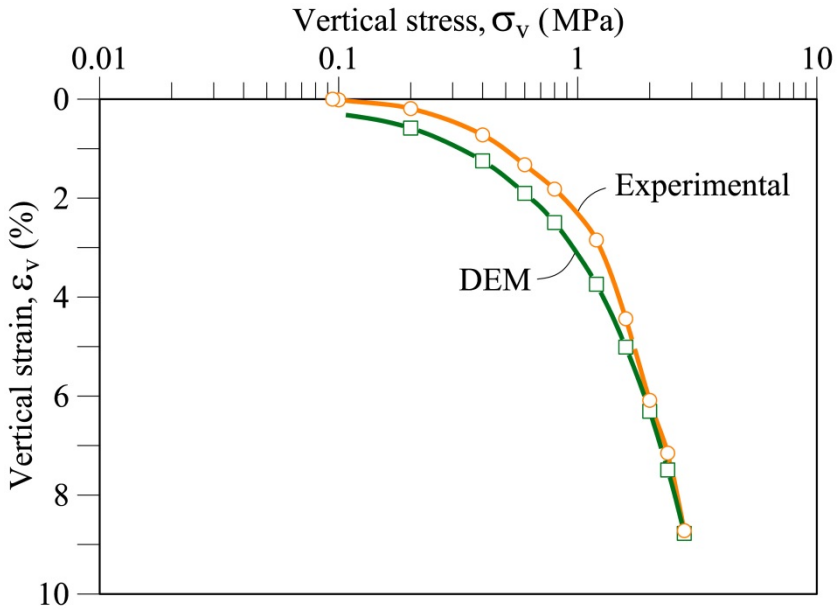

Figure 5-25 Measured and calculated oedometer compressibility of the limestone gravel sample. DEM parameters: μ=0.3; K_c=1 MPa*m$^{0.5}$; k_n=4 MN/m.

5.6.4 Grain size evolution

An additional check of the capability of the model is possible because the grain size distribution at the end of the test is also available. There is a difficulty, however, because Ortega (2008) did not report the grain size distribution at the end of the loading (at σ_v = 2.8 MPa) but after collapsing the sample by full wetting under the maximum stress.

The methodology described in this chapter was extended to deal with suction effects and long-term deformations of rockfill (see chapter 7). In fact, the velocity of crack propagation (Eq. (5:17)) is also a function of Relative Humidity. These developments are outside the scope of this chapter, but the collapse imposed by Ortega (2008) was also simulated in the model described and the grain size distribution could be calculated. Figure 5-26 shows the calculated grain size distributions at the end of loading, after wetting. The latter compares well with the actual measurements. The figure indicates also the initial, essentially uniform, grain size distribution and the truly uniform distribution adopted in the model. The coefficient of uniformity evolves from unity to a value of 3 for the loaded and collapsed sample. The breaking index B_r increases from zero to B_r = 0.23.

The evolution of the number of particles broken during the reported test is given in Figure 5-27a. The initial small number of large uniform particles (471) results in 12146 particles at the end of the test. The number of non-broken initial macroparticles becomes 183, somewhat above one third of the initial arrangement (Figure 5-27b).

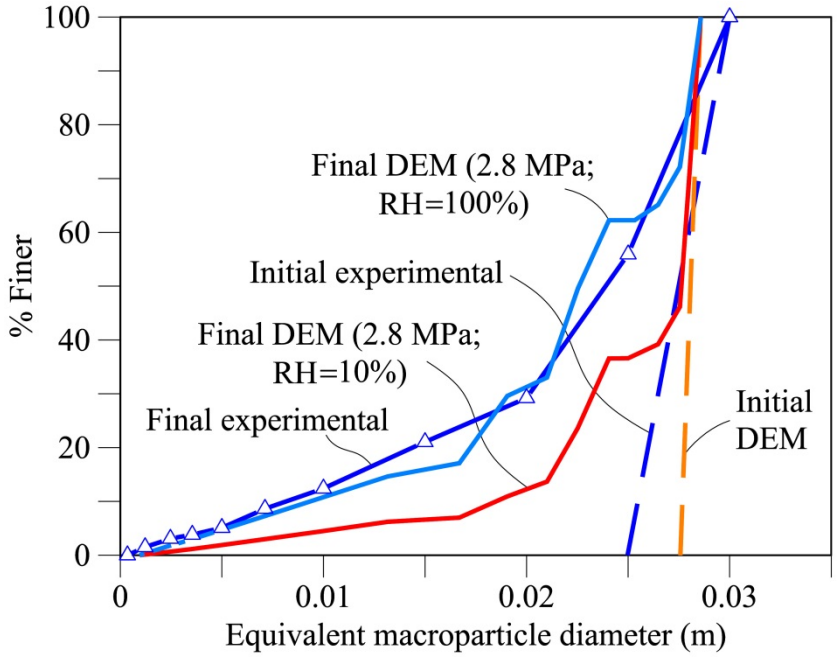

Figure 5-26 Evolution of particle size distribution in oedometer test. Actual results reported by Ortega (2008) are compared with DEM simulations.

The calculated evolution of grain size distribution as well as the Hardin breakage index B_r is given in Figure 5-28 and Figure 5-29. Particle breakage develops immediately after the beginning of loading. Its intensity (measured in terms of the breaking index) increases fast when the splitting mechanism becomes more widespread ($\sigma_v > \sigma_y$). For high stresses (in our case, when $\sigma_v > 2$ MPa) breakage decreases rapidly and it approaches a limiting situation (an “attractor”) for the maximum applied stress. This behaviour is consistent with experimental observations by Nakata et al. (2001) and the previous results of the chapter 4.

The evolution of grain size distribution (gsd) curves toward an "ultimate" distribution in compacted crushable aggregates under high confined pressure has been described in the literature: Turcotte (1986) examined fragments of several crushable materials and concluded that any distribution of particles tends to a fractal distribution; McDowell and Bolton (1998) argued that the evolution of gsd tends to be fractal; they also presented results of (Bard, 1993) about gsd evolution curves for one-dimensionally compressed petroleum coke at high confined stresses (5 - 100 MPa). Einav (2007a) developed a continuum theory for granular crushable materials which uses the “distance” between initial and ultimate gsd distributions. The evolution of gsd curves is supported by experimental results of Coop et al. (2004). They found the Hardin breakage index, B_r, increases with increasing shear strain, and tends to an asymptotic value for high values of deformation.

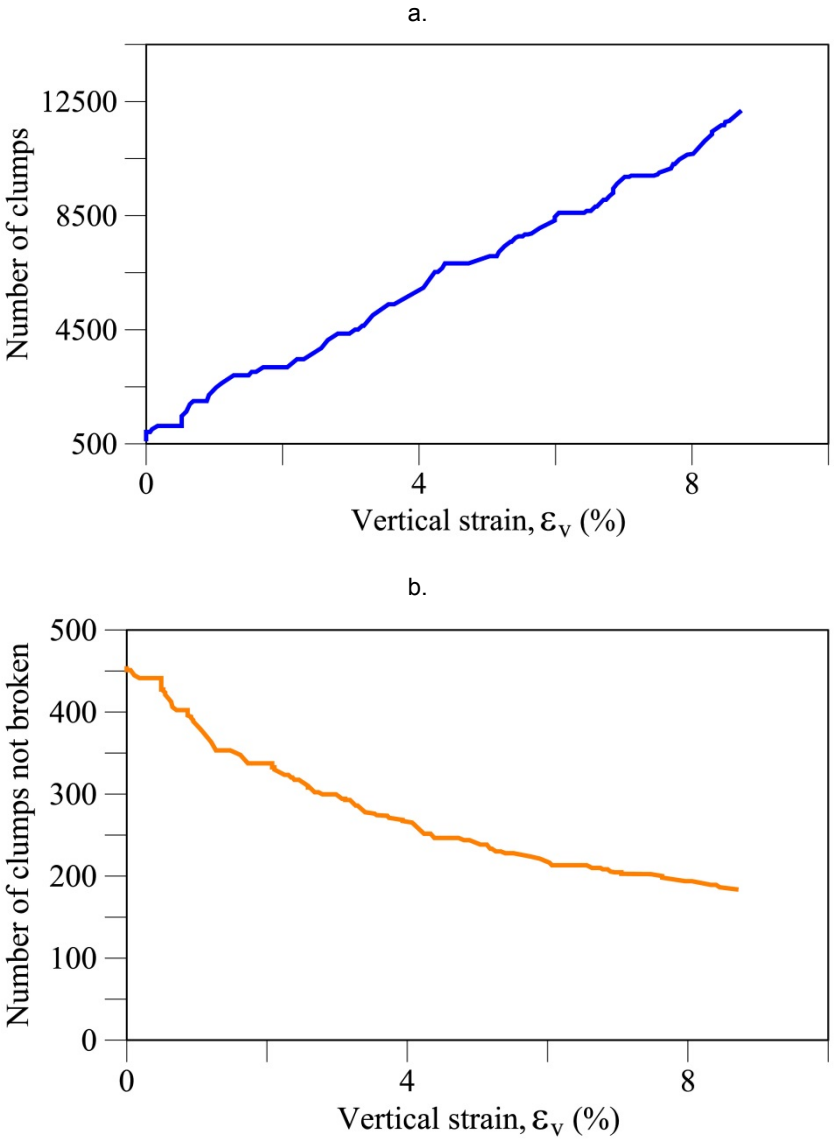

Figure 5-27 Evolution of (a) broken and (b) non-broken macroparticles during the numerical oedometer test.

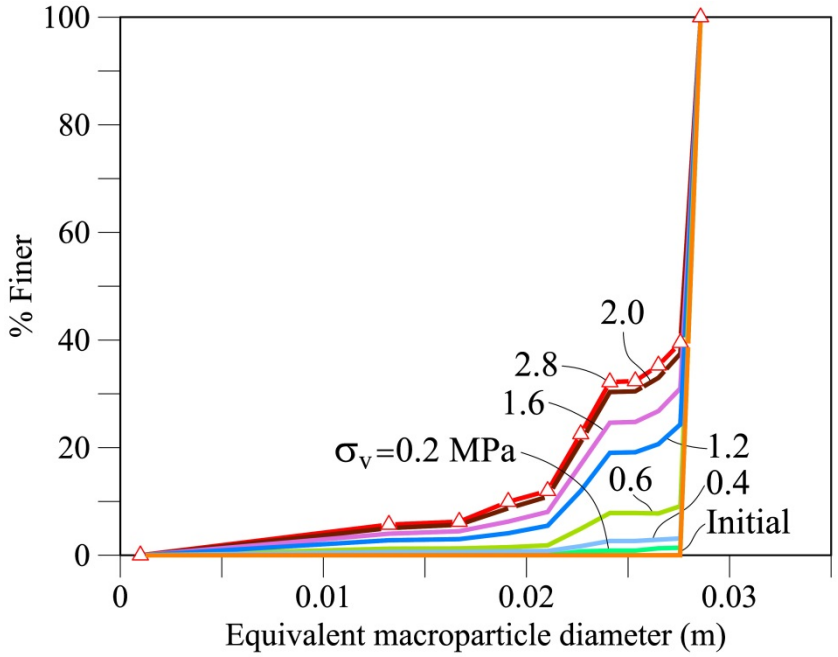

Figure 5-28 Evolution of grain size distribution: DEM simulation of oedometer test. DEM properties: μ=0.3; k_n=4 MN/m; K_c=1MPa•m$^{0.5}$. σ_y = 0.6 MPa.

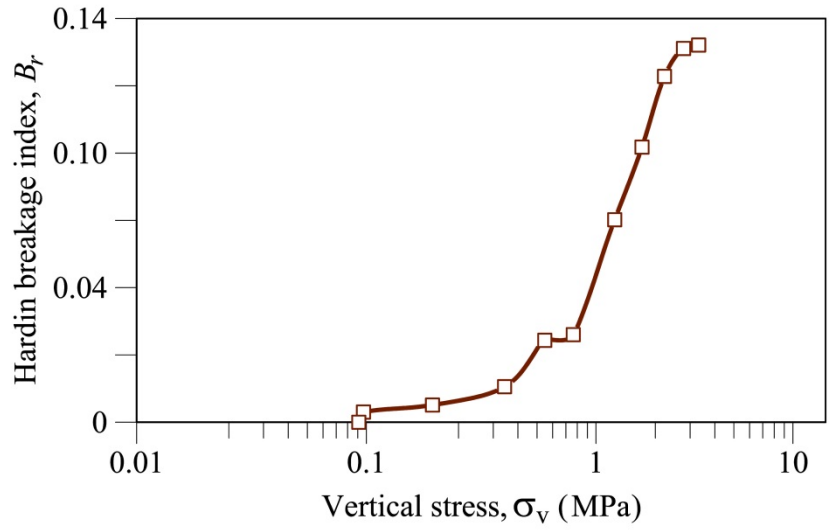

Figure 5-29 Evolution of Hardin breakage index: DEM simulation of oedometer test. DEM properties: μ =0.3; k_n =4 MN/m; k_n =1MPa•m$^{0.5}$. σ_y = 0.6 MPa.

The evolution of particle breakage during loading may also be followed by examining the evolution and arrangements of particles in the model. Figure 5-30 shows two views of the initial oedometer sample and three reference planes of observation: two vertical ones (I-I'; II-II'), and one horizontal through the centre of the sample (III-III'). The effect of loading the sample is detailed in Figure 5-31 and Figure 5-32. Breakage of particles may be followed by examining the colour (shading) of particles represented in the two figures. Table 5-4 indicates the colour (shade) associated with the number of microparticles in a given macroparticle.

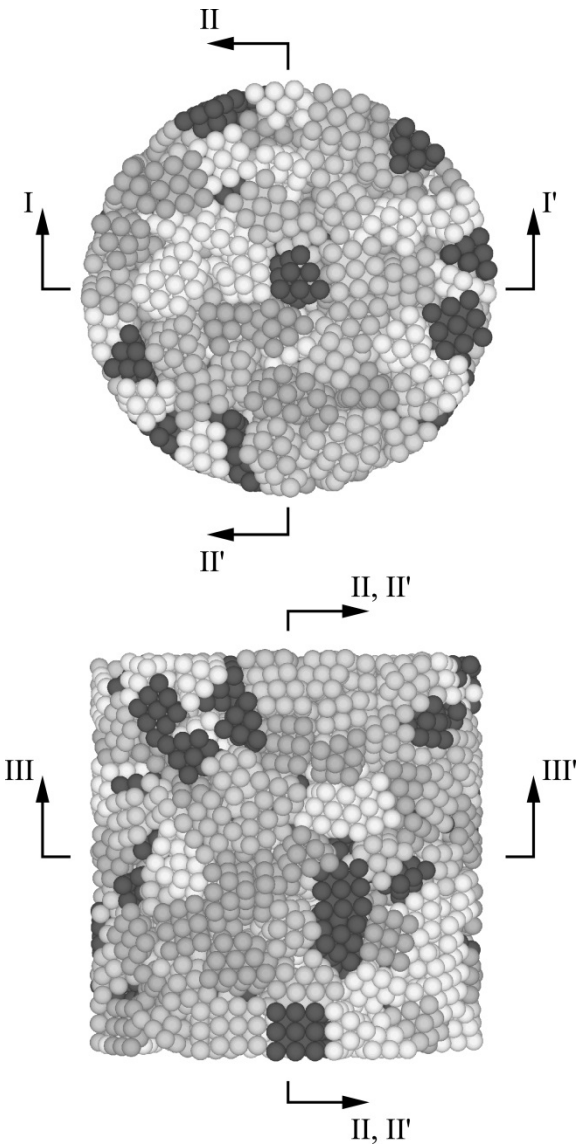

Figure 5-30 Particulate model of oedometer test. Position of cross sections I-I', II-II' and III-III'. A grey scale is introduced to identify initial macroparticles.

Table 5-4 Shading code of broken macroparticles (Figure 5-31 and Figure 5-32).

Shade	Colour of Macroparticles	Number of microparticles
	Orange (initial)	14
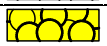	Yellow	13
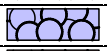	Light blue	12
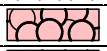	Light red	11
	Gray	10
	White	9
	Blue	8
	Light green	7
	Red	6
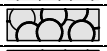	Light gray	5
	Cyan	4
	Green	3
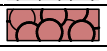	Brown	2

Single microparticles are replaced by a new “clump” of 13 additional subparticles, which may be seen in Figure 5-31.

Figure 5-31 shows a cross section of the sample when looking at planes I-I’ and II-II’ at four applied stresses: A: Initial; B: 0.2 MPa; C: 1.2 MPa and D: 2.8 MPa. The plot shows the voids and the solid particles. The evolution of some resisting chains of load has been marked in Figure 5-31a. Some macroparticles in the chain begin to break at vertical stress as low as 0.2 MPa. At σ_v = 1.2 MPa, a significant proportion of particles in the chain have experienced breakages of varying intensity. At σ_v = 2.8 MPa, the entire chain has suffered breakages.

The figures also show that several macroparticles have survived at their original shape. They appear surrounded by broken particles. They can be identified in Figure 5-31 by their shade (see Table 5-4). Figure 5-32 shows a horizontal section III-III’ of the sample. One set of figures shows voids and solids. The second set is an “optical” planar view: voids are not visible. It would be the result of a photograph of the sample taken from above the sample. The damaged particles show the position of subvertical chains developing inside the sample. Undamaged macroparticles at the maximum load applied are also shown to be protected by broken grains. This protection explains their survival, which is confirmed by the grain size distributions. This explanation has also been given in McDowell and Bolton (1998); Nakata et al. (2001); Tsoungui et al. (1999).

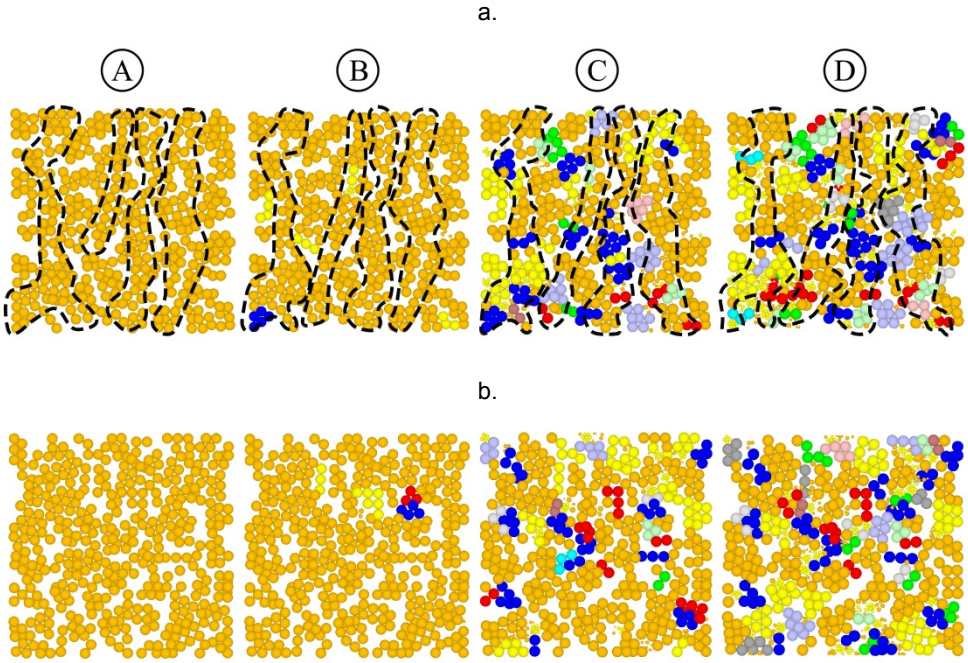

Figure 5-31 Vertical sections of oedometer test for increasing vertical stress: A: Initial; B: 0.2MPa; C: 1.2MPa; D: 2.8MPa: (a) Section I-I'; (b) Section II-II'.

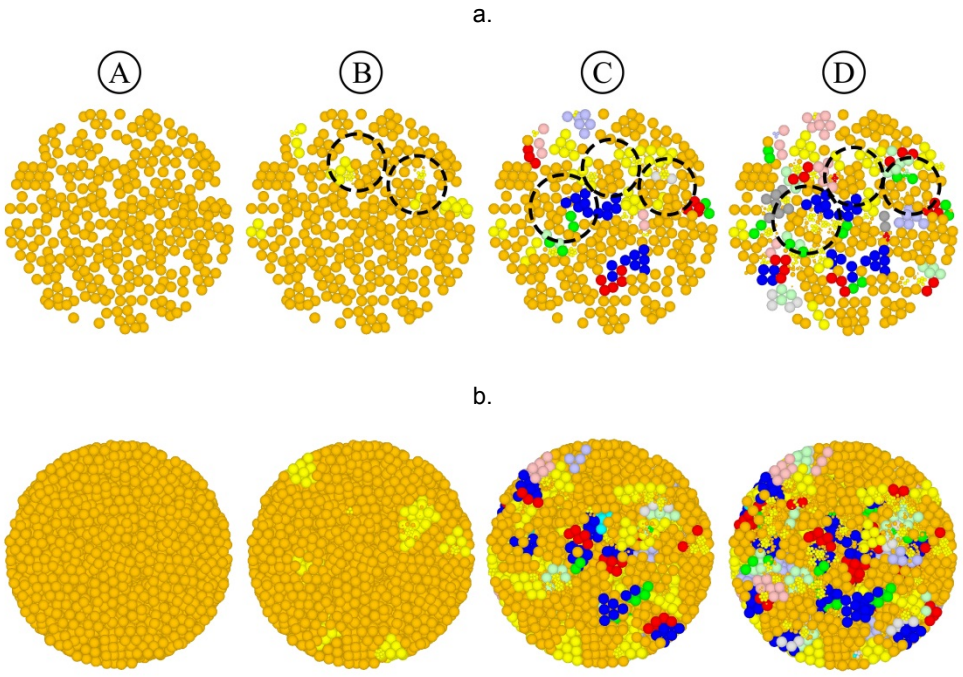

Figure 5-32 Horizontal sections (Plane III-III') of oedometer test for increasing vertical stress: A: Initial; B: 0.2MPa; C: 1.2MPa; D: 2.8MPa: (a) Planar cross section; (b) "Optical" planar view (voids are not visible).

5.7 Predicting triaxial tests

The oedometer path, despite not approaching shear failure conditions of a sample, subjects the granular aggregates to different modes of fracture and certainly it induces shear failures at the contacts and an intense particle breakage. It may be accepted that an oedometer mobilises all the deformation mechanisms associated with particle breakage, which is a fundamental phenomenon to explain the overall macroscopic behaviour. Then, the idea was to check if the particle model developed, calibrated against an oedometer test, could reproduce triaxial tests.

Ortega (2008) performed a triaxial test on a uniform sample of the same limestone gravel under dry conditions (RH = 10%), compacted at a similar porosity (n_0 = 0.50). The sample (25 cm in diameter, 50 cm in height; see Figure 5-10c) was first subjected to a confining stress of 1 MPa and then the vertical stress was increased at a constant horizontal stress. The sample was taken to failure conditions and it was fully wetted at a large vertical strain (10%) when the sample was close to limiting conditions. Unfortunately Ortega (2008) did not report the deformation of the sample during the initial confining period. However, the simulation followed the entire stress path. Figure 5-33 shows a comparison of model and experimental results. The volumetric behaviour is well captured. The calculated deviatoric response remains below the experimental values and the (dry) strength is underestimated by approximately 30%. The grain size distribution after wetting and dismantling the sample was also available. It is compared with model predictions in Figure 5-34. The agreement is very good (suction effects and their modelling are not discussed in this chapter but they are found in chapter 7).The Hardin breakage index B_r for the experimental triaxial test and the DEM simulation are 0.29 and 0.26 respectively.

If measured grain size distributions for triaxial and oedometer tests are compared, both curves are very similar (Figure 5-35). The maximum deviatoric stress of the experimental triaxial test was 2.5 MPa (for fully wetted sample at 10% vertical strain), which can be compared with the maximum deviatoric stress of the oedometer (1.9 MPa for RH=10% and wetted afterwards). The maximum mean stresses for the experimental triaxial and oedometer tests were 1.8 and 1.6 MPa respectively (horizontal stresses were measured in the oedometer test). The corresponding DEM calculated mean stresses were 1.7 and 1.8 MPa respectively. It is concluded that the intensity of mean stress was rather similar in both tests. Deviatoric stresses were higher for the triaxial test.

Measured B_r indices after testing was similar in both cases: 0.29 (triaxial) and 0.25 (oedometer). These values can be compared with DEM simulation of both tests: 0.26 and 0.20 respectively. The model performed reasonably well in both cases.

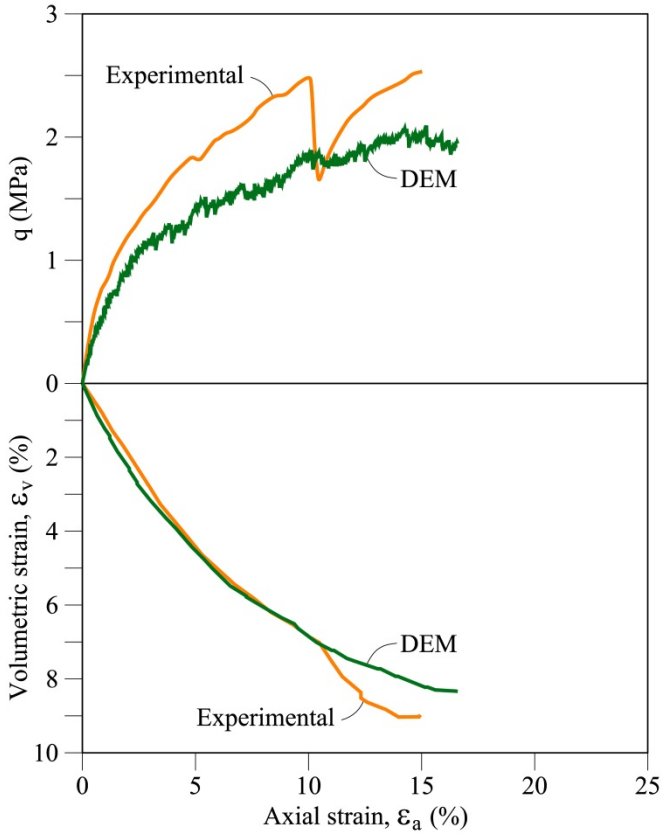

Figure 5-33 Comparison of triaxial test results reported by Ortega (2008) and model predictions. DEM parameters: μ=0.3; K_c=1 MPa*m$^{0.5}$; k_n=4 MN/m.

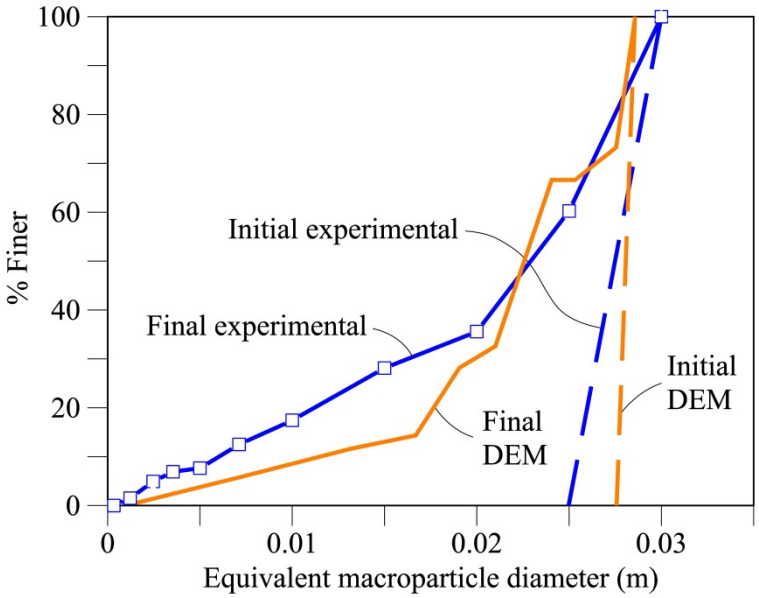

Figure 5-34 Measured and calculated grain size distributions of triaxial tests.

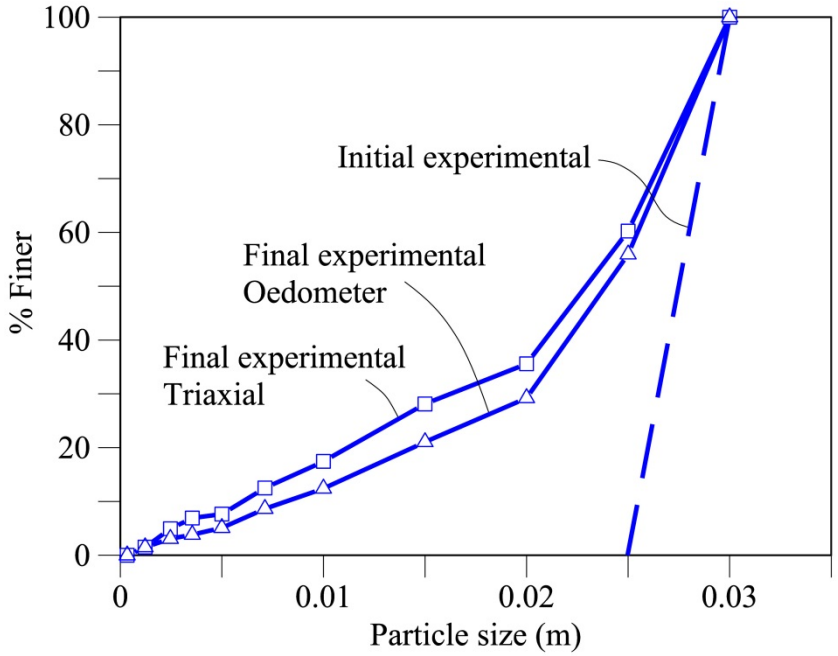

Figure 5-35 Measured grain size distributions of experimental triaxial and oedometer tests (Modified from Ortega, 2008).

Additional large scale triaxial tests on the same material and different grain size distributions were simulated in order to study size effects. They are presented in chapter 6.

The results are very encouraging. However, one may wonder why the fit was not better. The model, in terms of key parameters (k_n, K_c, μ) is remarkably simple and all of them are rock material properties. Contact stiffness, k_n, is probably the most uncertain one, a conclusion that has also been supported by the specific tests reported in this chapter. If the other two are assumed to be reliable, the reason for the mismatch may be attributed to k_n. But this is somewhat inconsistent: the oedometer test, which was well captured by the model, would not be well reproduced if k_n changes.

A possible explanation lies in a "hidden" part of the model: the geometrical representation of particles and their evolution during breakage. Grain size distributions are well reproduced in general, but the triaxial deviatoric response is controlled to a large extent by the degree of interlocking between particles, probably more than the interlocking operating in an oedometer test. The actual particles had sharp edges (Figure 5-9) and their breakage will lead also to sharp edges of the split particles. These geometries facilitate interlocking. These shapes are not well reproduced by the particle geometry and its evolution adopted in this research. Despite this limitation, the results are very promising.

5.8 Conclusions

Rockfill and gravel aggregates experience significant particle breakage when loaded at stresses commonly found in engineering applications. This phenomenon explains, to a large extent, their stress-strain behaviour. Rock particles are brittle solids and their breakage has been represented by fracture mechanics concepts. This approach is believed to provide a more accurate description of real phenomena than other techniques, computationally oriented, which rely in concepts such as particle bonding.

The model requires the estimation of stresses inside particles and the propagation of existing cracks or defects. They have been described by analytical solutions under a certain set of assumptions. In this way, the calculations associated with the breakage or survival of a given particle may be performed in a fast manner within the overall numerical approach.

The shape of particles and its evolution during loading is also a key aspect. It controls the degree of interlocking and the modification of grain size distribution. The protocol developed is based on initial pyramidal shapes, which upon breakage, transform into smaller pyramidal and irregular parallelepipedic geometries. These bodies are represented by sets of spheres, an assumption that may be relaxed in subsequent work. An interesting feature was the automatic subdivision of smaller particles into a set of elementary particles of yet smaller size, during the calculation process. This technique proved to be useful to reproduce observed grain size distributions after oedometric and triaxial testing of gravel aggregates.

Special attention was given to the nature of breakage and its evolution under increasing loading. Experiments indicate that contact-related comminution breakage predominates at small contact forces, whereas “equal volume” splitting becomes dominant beyond a given “yielding” stress. The model reproduces these observations.

In terms of material parameters, the model is remarkably simple: it requires the contact stiffness (k_n), the rock toughness (K_c) and the friction coefficients (μ) at particle contacts. K_c and μ may be determined by rock characterization tests. In this work K_c was calibrated by the after-test grain size distribution. Contact friction was experimentally determined for hard limestone. Special tests were also performed to estimate the contact stiffness between particles. “Blind” simulation of real triaxial tests, accepting the model parameters, the geometrical characterization of particles and the entire calculation protocol, used previously to interpret an oedometer test, led to a fairly successful prediction which refers to the deviatoric stress-strain behaviour, the volumetric sample response, the grain size distribution and the correct identification of size effects.

5.9 List of Notations

Notation		*Section*
a	Half-length of the defect; Eq. (5:15) ; (5:18)	5.3; 5.4
a_0	Half-length of the defect before a time increment; Eq. (5:18)	5.4
B_r	Hardin breakage index	5.5; 5.6.4; 5.7
c_u	Undrained shear strength	5.2
D	Particle Diameter; Eq. (5:16)	5.3; 5.4
DEM	Discrete/Distinct Element Method	5
E	Young's modulus; Eq. (5:2); (5:4); (5:8)	5.2; 5.6; 5.6.2
E'	Equivalent modulus of an elastic half space; Eq. (5:8); (5:12)	5.2
F	(1) Normal concentrated force (Figure 5-6) (2) Normal load; Eq. (5:2) - (5:6)	(1) 5.2; (2) 5.2;
gsd	Grain size distribution	5.6.4; 5.7
H_{mic}	Effective microhardness of the asperities; Eq. (5:12)	5.2
K	Stress intensity factor; Eq. (5:15); (5:17)	5.3; 5.4
K_c	Toughness; Eq. (5:17)	5.3; 5.3.1; 5.4; 5.5; 5.6.3; 5.6.4; 5.7
k_n	Contact (normal) stiffness; Eq. (5:5); (5:6)	5.2; 5.3.1; 5.5; 5.6.2; 5.6.3; 5.6.4; 5.7
k_s	Contact shear stiffness	5.3.1; 5.5
n	Parameter for crack propagation in Charles model; Eq. (5:17)	5.3
n_0	Porosity	5.4; 5.5; 5.6; 5.7
P	Concentrated load	5.2
PFC3D	Particle Flow Code in 3 Dimensions	5.3.1
P_{max}	Maximum concentrated load or maximum contact force	5.2; 5.5

P_o'	Maximum dimensionless contact pressure; Eq. (5:10); (5:13)	5.2
p	(1) Contact stress due roughness effect (Figure 5-6); Eq. (5:1)	(1) 5.2;
	(2) Mean stresses	(2) 5.7
q	Deviatoric stress	5.7
R	Particle Radius; Eq. (5:2) - (5:7); (5:14)	5.2
RH	Relative Humidity	5.1; 5.3; 5.6; 5.7
R_a	Arithmetic average roughness; Eq. (5:11); (5:12)	5.2; 5.6.1
r	Radial coordinate inside particle (Figure 5-6)	5.2
r_c	Contact interface radius (Hertz theory); Eq. (5:2); (5:3); (5:9); (5:11)	5.2
r'	Radius of equivalent smooth sphere; Eq. (5:7); (5:11); (5:12)	5.2
r_L	Contact radius of loaded rough surface; Eq. (5:9); (5:14)	5.2
r_L'	Dimensionless parameter used by calculation of r_L; Eq. (5:9); (5:10)	5.2
s	Root mean square of the asperity heights of the rough surface; Eq. (5:11); (5:12)	5.2
v	Crack propagation velocity; Eq. (5:17); (5:18)	5.3; 5.4
v_0	Reference velocity for crack propagation in Charles model; Eq. (5:17)	5.3; 5.5
w	Radius of the loaded area or contact stress (Figure 5-6); Eq. (5:1)	5.2
z	Vertical coordinate inside particle under *F* applying (Figure 5-6); Eq. (5:1)	5.2
α	Dimensionless coefficient used in calculation of stress intensity factor; Eq. (5:16)	5.3
α' ; β'	Dimensionless parameters used in calculation of θ_0 by surface roughness method; Eq. (5:11); (5:12); (5:13)	5.2
β	Dimensionless coefficient used in calculation	5.3

	of stress intensity factor; Eq. (5:15); (5:16)	
Δt	Time increment; Eq. (5:18)	5.4
δ	Overlap between two spheres; Eq. (5:5)	5.2
ε_a	Axial or vertical strain	5.6.3; 5.6.4; 5.7
ε_v	Volumetric strain	5.7
η	Damping	5.5
θ_0	Solid angle describing contact stresses (Figure 5-6); Eq. (5:3); (5:4); (5:6); (5:14)	5.2; 5.5; 5.6.1
λ	Compressibility index	5.5
μ	Contact friction coefficient	5.3.1; 5.4; 5.5; 5.6.1; 5.6.3; 5.6.4; 5.7
ν	Poisson ratio; Eq. (5:1);(5:2); (5:4); (5:8)	5.2; 5.6.2
σ	(1) Maximum tensile stress inside particle; Eq. (5:15); (5:1)	(1) 5.3;
	(2) Vertical stress	(2) 5.2
σ_{max}	Maximum vertical stress	5.5
σ_t	Tensile strength	5.2
σ_v	Vertical stress	5.6.4
σ_{xx}	Stress in horizontal direction	5.2
σ_y	Yield stress	5.2; 5.4; 5.5; 5.6.4
σ_θ	Tensile stress acting on vertical diameter inside macroparticle (Figure 5-6); Eq. (5:1)	5.2
ϕ	Friction angle	5.2; 5.6.1
ϕ_b	Basic friction angle	5.6.1
ϕ_m	Mineral friction angle	5.6.1
ϕ_r	Friction angle on a rough surface	5.6.1

5.10 References

Alehossein, H., Boland, J.N., 2004. Strength, toughness, damage and fatigue of rock, in: Proc. Structural Integrity and Fracture International Conference (SIF'04). 26-29/09/2004. Brisbane (Australia).

Alonso, E.E., Olivella, S., Pinyol, N.M., 2005. A review of Beliche Dam. Géotechnique 55, 267–285.

Atkinson, B.K., 1984. Subcritical crack growth in geological materials. J. Geophys. Res. 89, 4077–4114.

Ayatollahi, M.R., Aliha, M.R.M., 2008. Mixed mode fracture analysis of polycrystalline graphite-a hite-a modified MTS criterion. Carbon N. Y. 46, 1302–1308.

Backers, T., 2004. Fracture toughness determination and micromechanics of rock under mode I and mode II loading. PhD. Thesis. University of Postdam. Postdam, Germany.

Bahrami, M., Yovanovich, M., Culham, J., 2005. A compact model for spherical rough contacts. ASME, J. Tribol. 127, 884–889.

Bard, E., 1993. Comportement des materiaux granulaires secs et a liant hydrocarbone. PhD. Thesis. Ecole Centrale de Paris. Châtenay-Malabry, France (in French).

Bauer, E., 2009. Hypoplastic modelling of moisture-sensitive weathered rockfill materials. Acta Geotech. 4, 261–272. doi:10.1007/s11440-009-0099-y

Ben-Nun, O., Einav, I., 2010. The role of self-organization during confined comminution of granular materials. Philos. Trans. R. Soc. London A 231–247.

Bruce, I.. G., Cruden, D.M., Eaton, T.M., 1989. Use of a tilting table to determine the basic friction angle of hard rock samples. Can. Geotech. J. 26, 474–479.

Chang, S.H., Lee, C.I., Jeon, S., 2002. Measurement of rock fracture toughness under modes I and II and mixed-mode conditions by using disc-type specimens. Eng. Geol. 66, 79–97. doi:10.1016/S0013-7952(02)00033-9

Charles, R.J., 1958a. Static fatigue of glass. I. J. Appl. Phys. 29, 1549–1553. doi:10.1063/1.1722991

Charles, R.J., 1958b. Static fatigue of glass. II. J. Appl. Phys. 29, 1554–1560. doi:10.1063/1.1722992

Chávez, C., Alonso, E.E., 2003. A constitutive model for crushed granular aggregates which includes suction effects. Soils Found. 43, 215–227.

Cheng, Y.., Bolton, M.D., Nakata, Y., 2004. Crushing and plastic deformation of soils simulated using DEM. Géotechnique 54, 131–141. doi:10.1680/geot.2004.54.2.131

Cheng, Y.., Nakata, Y., Bolton, M.D., 2003. Discrete element simulation of crushable soil. Géotechnique 53, 633–641. doi:10.1680/geot.2003.53.7.633

Ciantia, M.O., Arroyo, M., Calvetti, F., Gens, A., 2015. An approach to enhance efficiency of DEM modelling of soils with crushable grains. Géotechnique 65, 91–110.

Coop, M.R., Sorensen, K.K., Bodas Freitas, T., Georgoutsos, G., 2004. Particle breakage during shearing of a carbonate sand. Géotechnique 54, 157–163.

Couroyer, C., Ning, Z., Ghadiri, M., 2000. Distinct element analysis of bulk crushing: effect of particle propertiesand loading rate. Powder Technol. 109, 241–254. doi:10.1016/S0032-5910(99)00240-5

Cundall, P.A., Strack, O.D.L., 1979. The distinct element method as a tool for research in granular media, Part I.

Dantu, P., 1967. Etude expérimentale d'un milieu pulvérulent compris entre deux plans verticaux et parallèle. Ann. des Ponts Chaussées 4, 193–202.

Dantu, P., 1968. Etude statistique des forces intergranulaires dans un milieu pulverulen. Géotechnique 18, 50–55.

De Josselin de Jong, G., Verruijt, A., 1969. Étude photo-élastique d'un empilement de disques. Cah. du Groupe Français Rhéologie 2, 73–86.

Einav, I., 2007a. Breakage mechanics - Part I: Theory. J. Mech. Phys. Solids 55, 1274–1297. doi:10.1016/j.jmps.2006.11.003

Einav, I., 2007b. Breakage mechanics - Part II: Modelling granular materials. J. Mech. Phys. Solids 55, 1298–1320. doi:10.1016/j.jmps.2006.11.004

Frossard, E., Hu, W., Dano, C., Hicher, P.-Y., 2012. Rockfill shear strength evaluation : a rational method based on size effects. Géotechnique 62, 415–427.

Hardin, B.O., 1985. Crushing of soil particles. J. Geotech. Eng. ASCE 111, 1177–1192.

Hiramatsu, Y., Oka, Y., 1966. Determination of the tensile strength of rock by a compression test of an irregular test piece. Int. J. Rock Mech. Min. Sci. 3, 89–99.

Indraratna, B., Salim, W., Rujikiatkamjorn, C., 2011. Advanced rail geotechnology – ballasted track. Balkema, CRC Press, Taylor & Francis Group, London, UK.

Itasca, 2008. Manuals of PFC3D v.4.0, 4th ed. USA.

Lim, W.L., McDowell, G.R., 2005. Discrete element modelling of railway ballast. Granul. Matter 7, 19–29. doi:10.1007/s10035-004-0189-3

Lobo-Guerrero, S., Vallejo, L.E., 2005. Discrete Element Method Evaluation of Granular Crushing Under Direct Shear Test Conditions. J. Geotech. Geoenvironmental Eng. ASCE 131, 1295–1300.

Lu, M., McDowell, G.R., 2006. Discrete element modelling of ballast abrasion. Géotechnique 56, 651–655.

Marketos, G., Bolton, M.D., 2009. Compaction bands simulated in discrete element methods. J. Struct. Geol. 31, 479–490.

McDowell, G.R., Bolton, M.D., 1998. On the micromechanics of crushable aggregates. Géotechnique 48, 667–679.

McDowell, G.R., Harireche, O., 2002. Discrete element modelling of soil particle fracture. Géotechnique 52, 131–135.

Nakata, Y., Hyodo, M., Hyde, A.F.L., Kato, Y., Murata, H., 2001. Microscopic particle crushing of sand subjected to high pressure one-dimensional compression. Soils Found. 41, 69–82.

Naylor, D.J., Maranha Das Neves, E., Mattar, D., Veiga Pinto, A.A., 1986. Prediction of construction performance of Beliche Dam. Géotechnique 36, 359–376.

Naylor, D.J., Maranha, J.R., Maranha das Neves, E., Veiga Pinto, A.A., 1997. A back-analysis of Beliche Dam. Géotechnique 47, 221–233.

Oldecop, L.A., Alonso, E.E., 2001. A model for rockfill compressibility. Géotechnique 51, 127–139.

Oldecop, L.A., Alonso, E.E., 2007. Theoretical investigation of the time-dependent behaviour of rockfill. Géotechnique 57, 289–301.

Ortega, E., 2008. Comportamiento de materiales granulares gruesos - Efecto de la succión. PhD. Thesis. Technical University of Catalonia. UPC, Barcelona, Spain (in Spanish).

Ovalle, C., Frossard, E., Dano, C., Hu, W., Maiolino, S., Hicher, P.-Y., 2014. The effect of size on the strength of coarse rock aggregates and large rockfill samples through experimental data. Acta Mech. 225, 2199–2216. doi:10.1007/s00707-014-1127-z

Pöschel, T., Schwager, T., 2005. Computational Granular Dynamics. Models and Algorithms. Springer-Verlag, Berlin, Germany.

Ramon, A., Alonso, E.E., Romero, E.E., 2008. Grain size effects on rockfill constitutive behavior, in: Toll, Augarde, Gallipolli, Wheeler (Eds.), In: Unsaturated Soils. Advances in Geo-Engineering: Proceedings of the 1st European Conference on Unsaturated Soils, Durham (U.K.). Taylor and Francis Group, London (U.K), pp. 341–347.

Robertson, D., 2000. Computer simulations of crushable aggregates. PhD. Thesis. Cambridge University.

Robertson, D., Bolton, M.D., 2001. DEM simulations of crushable grains and soils, in: Proceedings of the 4th International Conference on Micromechanics of Powders and Grains. Sendai, Japan, pp. 623–626.

Russell, A.R., Muir Wood, D., 2009. Point load tests and strength measurements for brittle spheres. Int. J. Rock Mech. Min. Sci. 46, 272–280. doi:10.1016/j.ijrmms.2008.04.004

Salim, W., Indraratna, B., 2004. A new elastoplastic constitutive model for coarse granular aggregates incorporating particle breakage. Can. Geotech. J. 41, 657–671. doi:10.1139/t04-025

Santamarina, J.C., Klein, K., Fam, M., 2001. Load deformation behaviour, in: Soils and Waves: Particulate Materials Behaviour, Characterization and Process Monitoring. John Wiley & Sons, Ltd., Chichester (UK), pp. 104–106.

Saouma, V.E., 2007. Lecture notes in fracture mechanics. Barcelona (Spain).

Thomas, T.R., 1999. Amplitude Parameters, in: Rough Surfaces. Imperial College Press, London (UK), pp. 133–150.

Tsoungui, O., Vallet, D., Charmet, J.C., 1999. Numerical model of crushing of grains inside two-dimensional granular materials. Powder Technol. 105, 190–198. doi:10.1016/S0032-5910(99)00137-0

Turcotte, D.L., 1986. Fractals and fragmentation. Journal of Geophysical Research- Solid Earth. J. Geophys. Res. Solid Earth 91, 1921–1926.

Zhixi, C., Mian, C., Yan, J., Rongzun, H., 1997. Determination of rock fracture toughness and its relationship with acoustic velocity. Int. J. Rock Mech. Min. Sci. 34, 49.e1–49.e11.

Chapter 6

Scale effect in rockfill behaviour

Particle sizes in large rockfill structures such as dams prevent laboratory testing. Prediction of field behaviour requires the development of models that integrate size effects. This chapter focuses the discussion on the influence of the particle size on rockfill and coarse aggregates behaviour. The distinct element method (DEM) model proposed in the previous chapter is applied to study the behaviour of the loaded aggregates under one-directional conditions: oedometer tests have been simulated.

The DEM model includes the following features: a) Grains are characterized by aggregations of a maximum of 14 elementary spherical particles. The resulting particle shape approaches real geometries and allows a reasonable breakage evolution; b) Particle breakage criterion involves the subcritical propagation of fissures in the grain. Time effects are included through the velocity of crack propagation, a function of stress state and defect size, which is introduced as a random set of varying lengths. However, time effects are studied in the next chapter.

The DEM model was used to simulate the stress-strain response, the evolution of grain size distribution and creep behaviour under oedometric conditions. The model has been used to simulate size effects in the range 2.8-560 mm of initial particle size (uniform distributions were tested). Compressibility and creep were partially validated by comparing calculations with test results covering a reduced range of particles. This chapter also presents the evolution of short-term compressibility and creep indices in terms of particle size.

Finally, the DEM model is also applied in the simulation of large scale triaxial tests on the same material simulated in chapter 5, but varying the initial particle sizes: 18.5mm and 38.5mm. Model parameters fitting the oedometer test in chapter 5 were maintained unchanged. Results are compared with experimental data obtained by Ortega (2008).

The model is a useful and novel tool to extrapolate laboratory results from scaled grain size distributions to prototype dimensions.

6.1 Introduction

Rockfill is often used in large civil engineering structures such as embankments and dams. Particle sizes range from a few millimetres to more than one meter. Common D_{50} sizes in rockfill dams are in the range 10–40 cm. Testing such a granular aggregate under oedometric, direct shear or triaxial conditions is unreasonable. After a literature review, Table 2.1 (chapter 2) shows a compendium of large diameter testing cells, their overall dimensions and the largest acceptable particle size for triaxial and oedometer tests on gravels and rock fragments. Even the largest testing cells described (Marachi et al., 1972, 1969; Marsal, 1973, 1967; Nobari and Duncan, 1972) are capable of testing rockfill aggregates having maximum particle sizes not exceeding 15-20cm. The largest particle sizes (0.15-0.18m) could be tested in huge triaxial cells developed in the 60's in connection with rockfill dams being built in the U.S. and Mexico. In recently built equipment the largest particle seldom exceeds 10 cm.

Summary, the experimental results of rockfill reported by the literature have been performed on smaller sized of rock fragments due to the limitation of the size of the equipment.

As in contrast, the range of particle sizes in rockfill embankments and dams is much bigger, a procedure to overcome the change in scale, often reported when justifying testing of gravel size in an attempt to determine parameters for larger particle sizes is to test a 'scaled' grain size distribution (**Figure 6-1**). Accordingly, published experimental information on the mechanical behaviour of rockfill is based on tests on scaled grain size distributions.

However, the intrinsic scale effects associated with particle breakage make this hypothesis wrong. Rockfill behaviour is grain size scale dependent in a significant way as demonstrated by test performed on "similar" grain size distributions but having a varying mean grain size (Alonso et al., 2005; Marachi et al., 1969; Marsal, 1973, 1967).

Scale effects affect particle breakage, a key phenomenon controlling all aspects of the stress-strain-time behaviour of rockfill and gravels. It is therefore expected that scale effects are present in the constitutive behaviour of rockfill. Since testing real size is impossible in practice, alternative procedures should be derived to extrapolate the known behaviour at a reduced scale to 'in situ' conditions.

In some applications specific aspects of behaviour are required: strength, compressibility and collapse upon wetting, and long term creep behaviour. Examples related to dam engineering are given by Alonso et al. (2005) and Frossard et al. (2012). Rules have been proposed to scale some rockfill properties such as strength (Frossard et al., 2012). This is a useful contribution but difficulties arise when considering other aspects of constitutive behaviour. The distinct element method (DEM) (Cundall and Strack, 1979) offers an interesting alternative to simulate size effects provided it is capable of integrating properly grain failure mechanisms. This is the purpose of this chapter.

The model developed will be applied to the simulation of oedometer and triaxial tests.

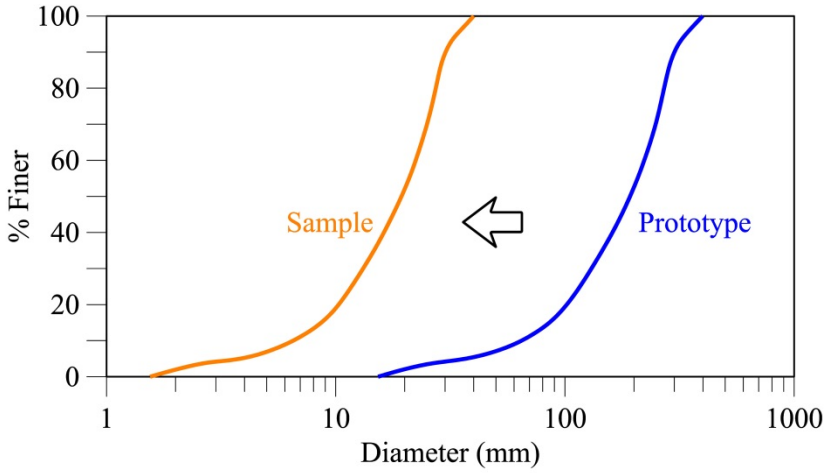

Figure 6-1 Grain size distributions of prototype and scaled sample.

6.2 The nature of scale effects

In section 2.5 (chapter 2), it was discussed the influence of the grain size in coarse aggregates behaviour. Now, the nature of this scale effect is resumed.

Laboratory experiments show that increasing grain size leads to an increase in compressibility and a reduction in strength (although there may be controversy, i.e. Kolbuszewski and Frederick (1963), see section 2.5.1). These are important considerations when translating laboratory-determined parameters to field scale.

Scale effects on grain breakage may be approached from the Weibull (1951, 1939) theory of strength of materials. It is also known as a weak-link approach. Weibull proposed the following equation (see also Eq. 2:14) for the probability of survival of a sample of size D subjected to a tensile stress σ:

$$P_{survival}(D,\sigma) = \exp\left[-\left(\frac{D}{D_0}\right)^{n_d}\left(\frac{\sigma}{\sigma_0}\right)^{m}\right] \tag{6:1}$$

where D_0, σ_0 are reference states and n_d, m are experimental parameters.

For a given probability of survival (see also Eq. 2:16),

$$\sigma_f = C\, D^{-n_d/m} \tag{6:2}$$

which explains that the stress inducing failure depends on sample size.

Fracture mechanics (Bazant, 1984) (see Fig. 2-15, chapter 2) explains also this dependency in brittle materials (see section 2.5.4). The figure shows the relationship between the stress at failure and size of a given sample. When sample size increases, linear elastic and nonlinear fracture mechanics predict that sample strength is proportional to the inverse of the square root of sample size.

In fracture mechanics, failure is understood as a consequence of a full propagation of an existing defect or crack. In fact, linear elastic fracture mechanics for a mode I type of failure (failure in extension) predicts failure when the stress intensity factor K_i of a given sample (say particle *i* of a loaded granular aggregate),

$$K_i = \beta_i \sigma_i \sqrt{\pi a_i} \tag{6:3}$$

becomes equal to a material property (toughness K_c). Failure is understood as a rapid propagation of a critical fracture leading to a particle breakage. In Equation (6:3) σ_i is the tensile stress, β_i depends on particle geometry, position and size of a potentially active microcrack, and a_i is the half length of the crack.

Therefore, at failure (see Eq. 2:19 - 2:22, in chapter 2)

$$\sigma_i = \sigma_f = \frac{K_c}{\beta_i \sqrt{(\pi a_i)}} \propto a_i^{-1/2} \approx D_i^{-1/2} = \frac{1}{\sqrt{D_i}} \tag{6:4}$$

(Note that in statistical terms particle size (D_i) and the length of a critical crack are directly correlated).

Point load tests on rock specimens reported by many authors (see Fig. 2-12, chapter 2) support Eq. (6:4) and (6:2).

If a given rock mass is assumed to host a distribution of cracks of different lengths, the larger the particle under consideration the higher the probability of having large-size cracks within the particle. In other words, the size of the particle and the size of maximum crack are equivalent. The particle fracture, in view of Equation (6:3), will be dependent on particle size.

The next step would be to relate the macroscopic behaviour to the scale dependent particle breakage. This is an 'automatic' outcome of a DEM simulation. Therefore, size effects will be obtained if scale dependent laws are used to simulate particle breakage.

Scale effects in granular assemblies, not undergoing particle breakage, were investigated by Kuhn and Bagi (2009) through DEM simulations of biaxial tests. They found a slight size effect which was attributed to two sources: the development of localization bands and "boundary layers" effects. The first source is attributed to the observation that, as the assembly size increases, deformation is localized within a smaller volume of material. This phenomenon was found analogous to the fracture mechanics size effect. The second source was associated with the restriction imposed by the test boundary conditions (caps, lateral restraints) to shear band development. The key point, however, is that calculated size effects were minor. Particle breakage modifies substantially this conclusion.

6.3 A distinct element model for crushable particle aggregates

The numerical model presented in chapter 5 follows previous experimental and theoretical research on the behaviour of rockfill (Oldecop and Alonso, 2007, 2001).

The possibilities offered by the Distinct Element Method (Cundall and Strack, 1979; Itasca, 2008; Potyondy and Cundall, 2004) to investigate scale effects are explored here.

As it was presented in chapter 5, model particles approximate the real shape by aggregating several spheres as a rigid body. Initial macroparticles (or "clumps") integrate 14 spheres in the work described here. **Figure 6-2** shows the picture of a limestone gravel taken from an experimental program referred to later, the pyramidal shape of the selected macroparticles and the initial arrangement of 471 macroparticles which define the oedometer sample analyzed. The selection of the number of spheres simulating a particle was a trade-off between the capability of the assemblage to reproduce a realistic initial shape of particles and the computational cost of the model. A clump of 14 spheres allows a basic three dimensional pyramidal shape which was judged adequate.

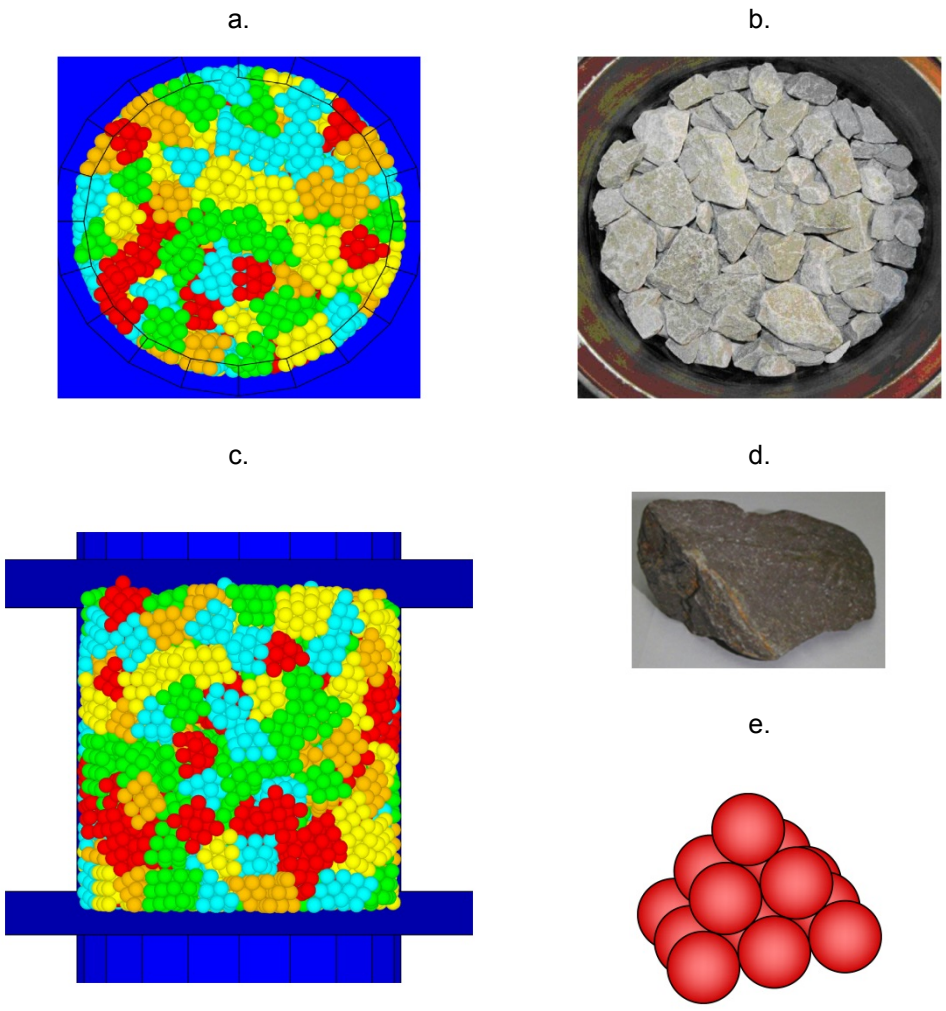

Figure 6-2 a,c) DEM model of Oedometer test: sample of 471 macroparticles; b) Crushed gravel in oedometer cell (Alonso et al., 2009); d) Limestone gravel (approximate size: 2.5cm) tested by Ortega (2008); e) 14-spheres macroparticle (DEM model).

Macroparticles interact through contact friction and normal and shear stiffness coefficients (**Table 6-1**). Defects are attributed randomly to all particles, keeping their maximum length limited by the initial size of particles. Maximum defect length was limited to half the size of the particle. A uniform probability density function was simply selected for the distribution of crack sizes among particles.

Table 6-1 Properties of the discrete particles in DEM model.

Normal contact stiffness, k_n: N/m	4 x 10^6
Shear contact stiffness, k_s: N/m	4 x 10^6
Friction Coefficient, μ	0.3
Toughness, K_c: MPa.$m^{1/2}$	5.0

As it was discussed in the previous chapter, particles will fail if, at some instant during sample loading, $K = K_c$. However, particles may also fail even if $K < K_c$. This is known as a "subcritical" failure condition, analyzed in (Atkinson, 1984; Oldecop and Alonso, 2007, 2001; Wiederhorn et al., 1980) in the context of rockfill behaviour. Fractures propagate in time at a velocity controlled by K and the prevailing relative humidity (RH). The second dependence, which explains collapse deformation upon wetting, is not analyzed here (see chapter 7). A dry rockfill is assumed in the simulations performed.

The determination of the tensile stress σ necessary to calculate K, follows the analysis given by Russell and Muir Wood (2009) as it was indicated in the previous chapter. In the vicinity of a spherical particle subjected to a loading stress ρ (force per unit area of application), the tensile stress is given by:

$$\sigma = \left[\frac{1}{2} + \nu - \frac{(1+\nu)}{\left(1+(\frac{w}{z})^2\right)^{0.5}} + \frac{1}{2*\left(1+(\frac{w}{z})^2\right)^{1.5}} \right] * \rho \qquad (6:5)$$

where ν is Poisson`s ratio, z the distance below the centre of the loaded area and w the radius of a loaded circular area. Macroparticles are, for the purposes of calculating σ, assimilated to spheres of equivalent radius r. Maximum tensile stress is calculated at a distance z = 0.1925r under the center of the loaded area on the boundary of the sphere, for ν = 0.25 and a solid angle "seen" from the center of the particle, $2\theta_0 = \pi/18$, which defines the small area of stress application.

Crack propagation velocity, V, is described by a modified Charles law (Charles, 1958a, 1958b; Oldecop and Alonso, 2007):

$$V = da/dt = V_0 \left(K / K_C \right)^n \qquad (6:6)$$

where V_0 is a reference velocity taken as V_0 = 0.1m/s in view of the data given in

Charles (1958a, 1958b) and exponent n was taken in this scale effect study equal to 181.5 for a dry condition (RH = 10%). For a given time increment dt, the crack length increment da is calculated following equations (6:6) and (6:3). In this chapter, the time increment has a value of 1000 s and this is related to real time. Crack lengths are updated at each step in calculations, $a = a_0 + da$, where a_0 is the previous crack length. The particle is assumed to be broken when the updated crack length reaches the mean dimension of the particle.

The macroparticle divides following the splitting mechanism described in chapter 5 which takes into account the number of particles integrated in a "clump" and its pyramidal shape. Comminution mechanism was not considered in the scale effect study for the numerical simulation of oedometer tests. The following division rule is applied:

$$14 \rightarrow 8+6;\ 8 \rightarrow 4+4;\ 6 \rightarrow 3+3;\ 4 \rightarrow 2+2;\ 2 \rightarrow 1+1.$$

It tends to divide particles into two new particles of approximately equal shape and size.

Calculation of stresses, the determination of failure criteria for particles as well as the conditions and performance protocol of oedometer tests were introduced in a program developed in FISH language, which is included in the program PFC3D v4 (Itasca, 2008). Any clump which reaches the established failure criterion (length of crack reaching the clump size) divides in the manner described above. The two new particles (clumps) are integrated into the model. Therefore, the number of clumps increases continuously during the "test" and the grain size distribution is modified accordingly.

6.4 Model response

Once validated the DEM model, see the previous work in chapter 5, it offers the possibility of investigating scale effects at a limited cost. If the objective is the variation of compressibility with grain size, one possibility is to run a series of numerical oedometric tests changing only the particle size.

The performed exercise is defined in **Table 6-2**. Four 'samples' of increasing size were tested. Sample dimensions, initial porosity and initial equivalent diameter of particles are given in **Table 6-2**. The soil had initially a uniform particle size ranging from 2.8mm to 560mm (there was a scaling factor of 20 when comparing maximum and minimum sizes). This wide range helps to identify scale effects. It is also a range of particles that may be easily found in practice. Also indicated in the **Table 6-2** is the necessary size of a testing cell to accommodate the four materials. They are, except for the smaller particles outside a reasonable cell size. All tests had the same relationship between the diameter of the odemeter cell and the diameter of the initial equivalent macroparticle diameter equal to 8.93. Initial porosity is essentially the same in all cases (0.53) to avoid density effects.

Table 6-2 Dimensions of sample and macroparticles in the numerical simulation of oedometer tests.

Sample	Scale	Sample size		Equivalent macroparticle diameter (mm)	Initial porosity
		Height (mm)	Diameter (mm)		
S25	0.1	25	25	2.8	0.5314
S250	1.0	250	250	28	0.5314
S1250	5.0	1250	1250	140	0.5337
S5000	20.0	5000	5000	560	0.5314

6.4.1 Short-term compressibility

Model parameters (**Table 6-1**) were adjusted to simulate results of real oedometer tests performed on uniform limestone gravel (Ortega, 2008)**.** Ortega tested 40-30 mm, 30-25 mm, 25-20 mm and 20-25 mm gravels having an initial porosity of 0.49 in a 300 mm diameter by 200 mm height cell.

Model calculations for a particle size of 28 mm are compared in **Figure 6-3**, with experimental results for the 30-25 mm range of limestone particles. This figure provides plots of deformations measured along time for a series of increasing stress increments. In all cases the RH was maintained constant and equal to RH = 10%.

The agreement of the (DEM) calculated and (experimental) measured deformation-time records demonstrate the capability of the model to reproduce rockfill deformation phenomena. All time records follow a similar pattern: An immediate deformation is followed by a delayed accumulation of strains. Calculated deformations are very similar to experimental results. The slope of the delayed response is small and it cannot be distinguished in **Figure 6-3**. It is a consequence of the rupture of clumps and the subsequent re-arrangement of particles. The calculated slopes given later (see **Figure 6-9**) show the long term compressibility values. Note that the transition time from short term compressibility to long term behaviour is somewhat different when comparing model and experiments.

If deformations for a particular instant (5 x 10^8 s was selected) are plotted in terms of vertical stress, conventional deformation-stress plots are calculated (**Figure 6-4**). These calculated compression curves were taken to a maximum vertical stress of 2.8 MPa.

They show the type of compression behaviour reported by Oldecop and Alonso (2003) for samples of uniform compacted gravel of slate. Scale effects are clearly shown. Larger size particles result in an increase in compressibility index, λ, defined as:

$$\lambda = \frac{d\,\varepsilon_v}{d(\ln \sigma_v)} \tag{6:7}$$

where ε_v is the vertical deformation and σ_v is the vertical stress.

a.

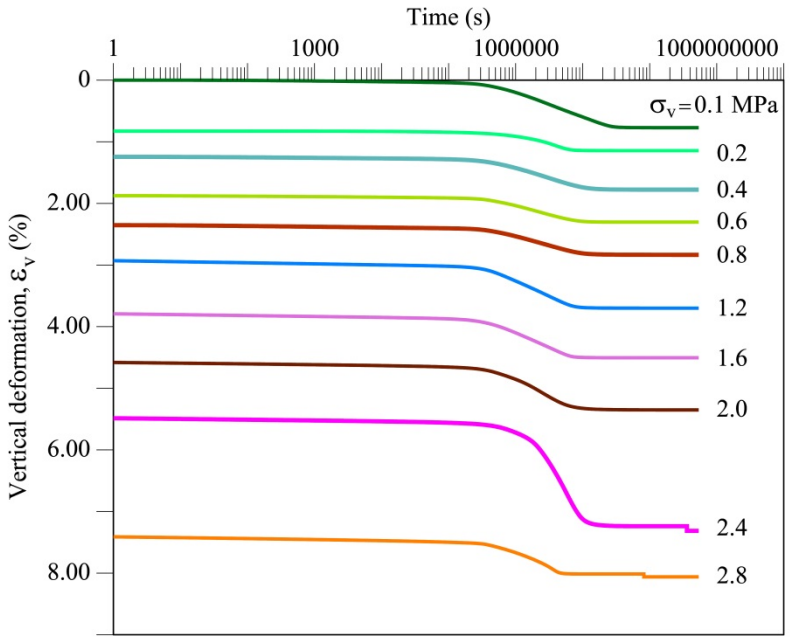

b.

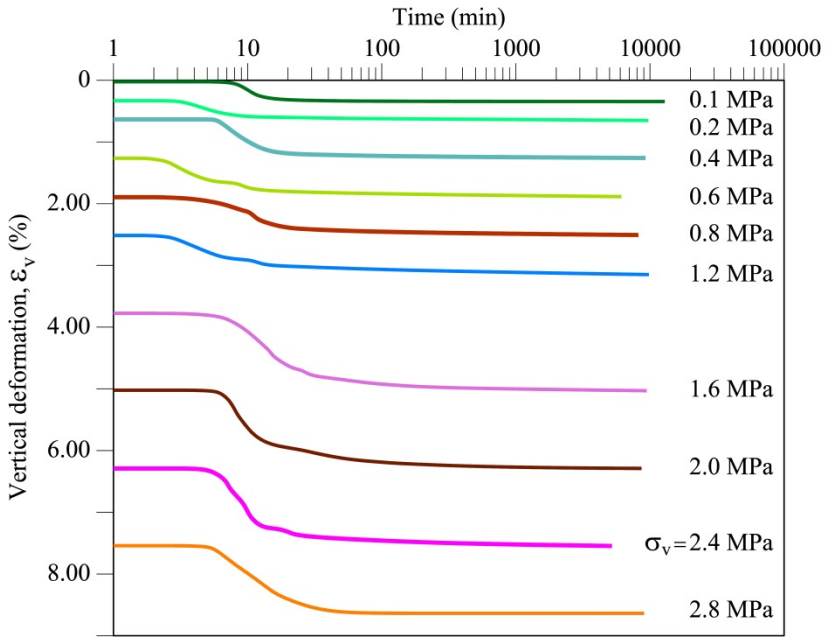

Figure 6-3 a) DEM simulations: Calculated deformation – time records, under the vertical stresses indicated; equivalent particle size 28mm; RH=10%. b) Experimental results: Measured deformation – time records in an oedometer test on compacted limestone gravel having equivalent diameter sizes in the range 25-30mm; RH=10% (Ortega, 2008).

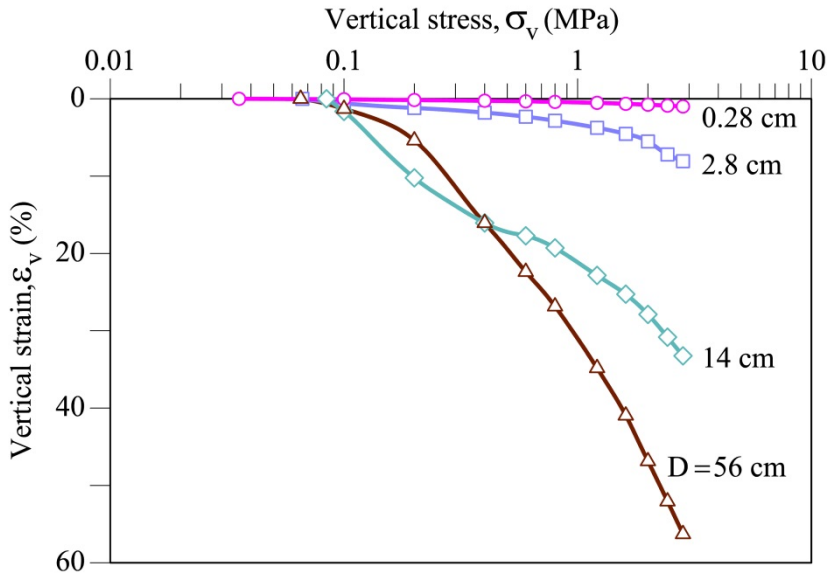

Figure 6-4 Calculated compressibility of samples of increasing initial equivalent particle size *D*. *RH=10%*.

Calculated λ values are represented in **Figure 6-5**. For σ_v = 2 MPa, the compression coefficient ranges from 0.005 to 0.27, when the grain size changes from 0.28 cm to 56 cm (200 times). The calculated average compressibility indices for vertical stresses in excess of 1.2 MPa are given in **Figure 6-6**. Size effects can be appreciated in this figure. Also plotted are λ values reported by Ortega (2008) for three specimen sizes (1.5-2cm; 2.5-3cm; 3-4cm). They show the expected scale effect but points are concentrated in a narrow range of sizes. The experimental data is concentrated around a particle size D = 3cm and no test data on significantly lower or higher sizes is available. Nevertheless, the numerical value for D = 2.8cm is reasonably close to measurements. The plot shows also the significant increase in compressibility with particle size. The plotted regression curve is given by:

$$\lambda = 0.02*(D)^{0.7} \tag{6:8}$$

where D is the particle size and it is given in cm.

Equation (6:8) could be normalized respect to certain reference compressibility index (λ_{ref}), which corresponds to the value of the compressibility index for an aggregate with an initial diameter of D_{ref}, and therefore, the following expression is obtained:

$$\frac{\lambda}{\lambda_{ref}} = \mathrm{A}*\left(\frac{D}{D_{ref}}\right)^{b} \tag{6:9}$$

where *A* and *b* are the coefficient and exponent of the model respectively.

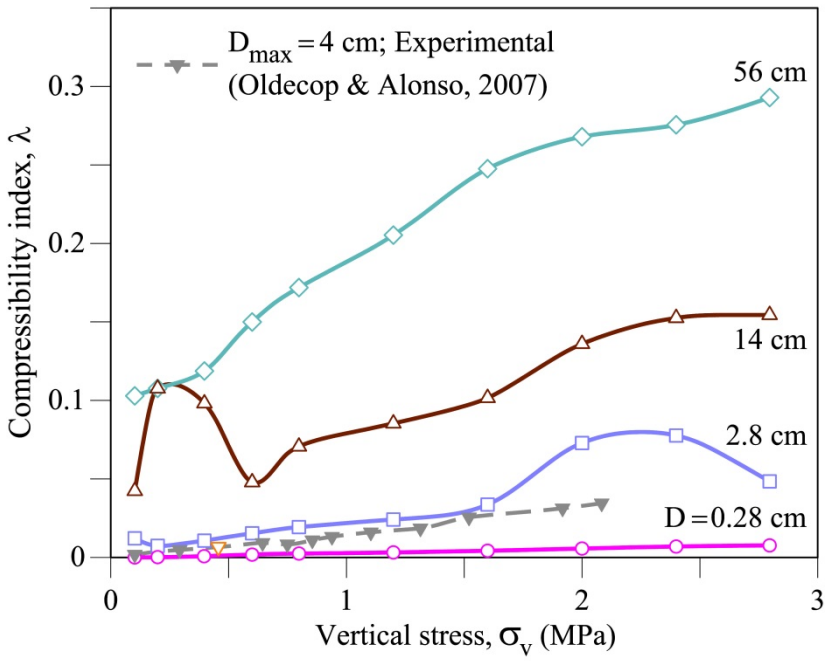

Figure 6-5 Calculated compressibility index λ. Also indicated are λ values for an oedometer test on compacted dry quartzitic slate (Oldecop and Alonso, 2007).

Figure 6-7 shows the relationship between (λ/λ_{ref}) and (D/D_{ref}) for a D_{ref}=2.8cm (λ_{ref}=0.05976). For this case, A = 0.7 and b = 0.7. However, if this exercise is also made for the other reference diameters (D_{ref}=0.28cm; 14cm; 56cm), it could be found a general expression with A=1.0 and b=0.7. **Figure 6-8** shows the relationship between (λ/λ_{ref}) and (D/D_{ref}) for all referenced sizes (D_{ref}=0.28cm; 2.8cm; 14cm; 56cm). The new plotted regression curve is given by:

$$\frac{\lambda}{\lambda_{ref}} = \left(\frac{D}{D_{ref}}\right)^{0.7} \qquad (6:10)$$

Figure 6-8a shows the relationship in a logarithmic scale for (D/D_{ref}) and **Figure 6-8**b in a natural scale.

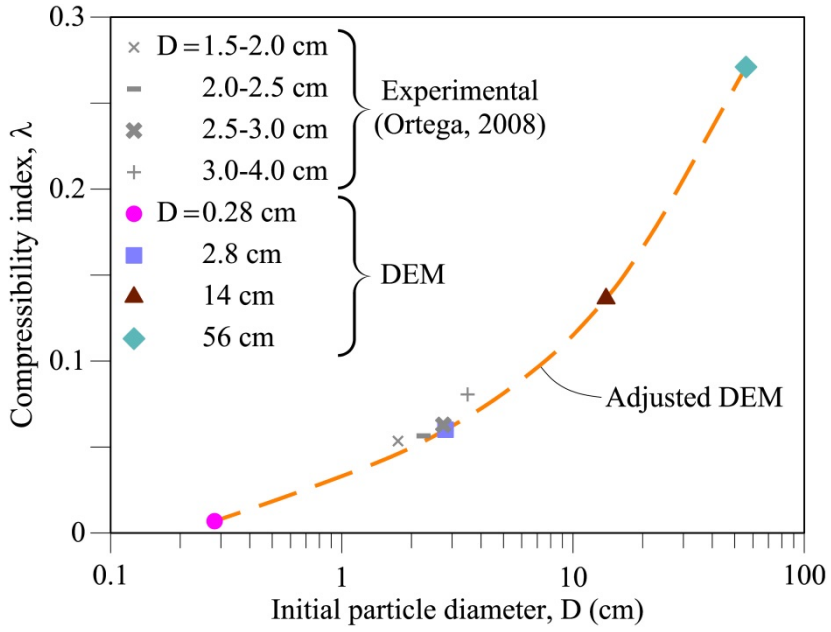

Figure 6-6 Calculated average compressibility indices for vertical stresses in excess of 1.2 MPa for different initial particle diameter. RH=10%. Comparison with results of laboratory tests of Ortega (2008).

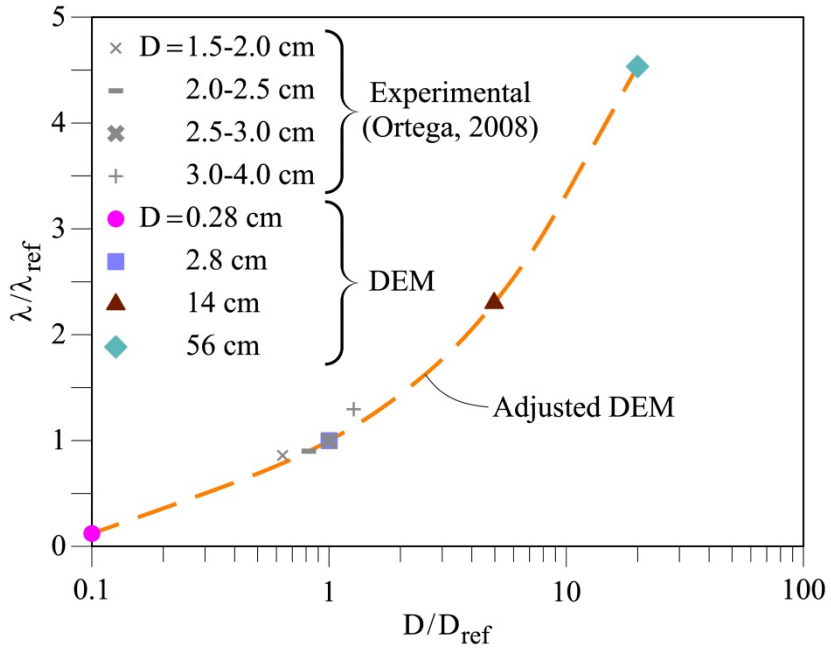

Figure 6-7 Size effect on normalized calculated average compressibility indices (for vertical stresses in excess of 1.2 MPa) for D_{ref} =2.8cm (λ_{ref} =0.0598): λ/λ_{ref} vs. D/D_{ref}. RH=10%. Comparison with results of laboratory tests of Ortega (2008).

a.

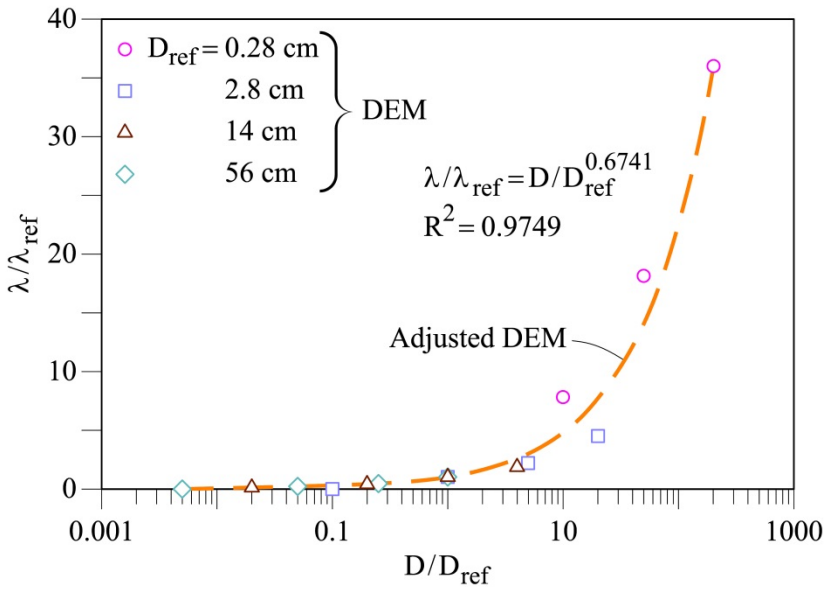

b.

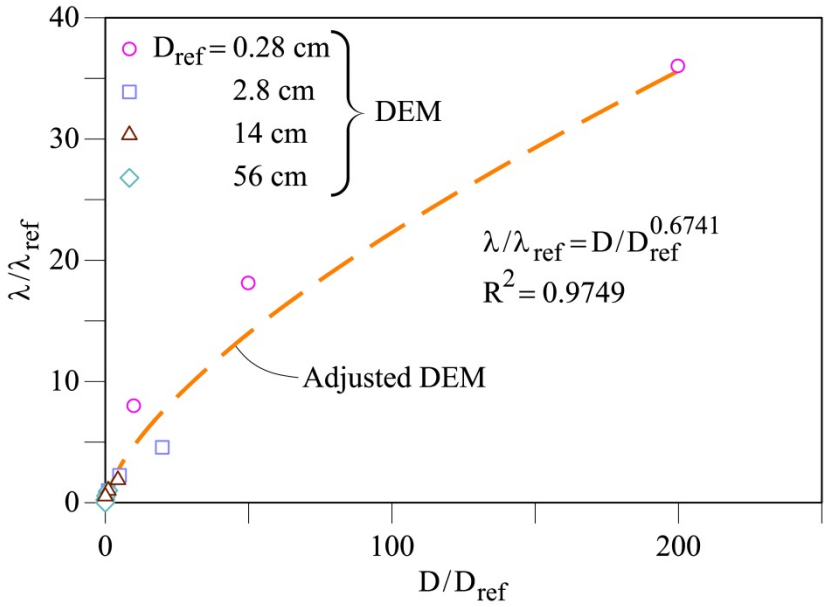

Figure 6-8 Size effect on normalized calculated average compressibility indices (for vertical stresses in excess of 1.2 MPa) for different values of D_{ref}: λ/λ_{ref} vs. D/D_{ref}. RH=10%. (a) Logarithmic scale for D/D_{ref}; (b) natural scale for D/D_{ref}.

6.4.2 Long-term (creep) compressibility

Long-term deformations are found in the numerical calculations performed (**Figure 6-3**) to be linearly related to log(time). This is also the case of the real experiments reported in the same figure. The long-term compressibility index, defined as:

$$\lambda_t = \frac{d\varepsilon_v}{d(\ln t)} \tag{6:11}$$

increases with the applied stress. Equation (6:11) was applied in discrete form ($\lambda_t = \Delta\varepsilon_v / \ln(t_2/t_1)$) for two times of the strain record: the time corresponding to the total simulation period ($t_2 \approx 5\text{x}10^8$ s) and a previous time ($t_1 \approx 5\text{x}10^7$ s) located also within the delayed "flat" response. **Figure 6-9** shows the calculated values in terms of the confining vertical stress for D_{max} = 2.8 cm. Calculations compare well with experimental results for uniform aggregates of similar size and porosity.

A definite scale effect was also found. This is to be expected because λ and λ_t are known to be closely related parameters. Oldecop and Alonso (2007) provided a theoretical explanation for the constant ratio λ_t/λ observed in creep tests on rockfill.

Computed λ and λ_t values exhibit an approximately constant ratio (**Figure 6-10**). **Figure 6-10** also includes experimental data: the range of λ_t/λ values reported by Oldecop and Alonso (2007) for oedometer tests on compacted slate (as well as other data) and the λ_t/λ values reported by Ortega (2008) on limestone gravels is given. The calculated (λ_t,vs. λ) values are close to a unique relationship,

$$\lambda_t = 0.004 * \lambda \tag{6:12}$$

which is close to the lower ratio reported by Oldecop & Alonso (2007). This lower ratio corresponds, consistently, to oedometer tests on very dry samples. The values reported by Ortega (2008) span the limits of the λ_t/λ relationship found in other experiments as well as in the present set of calculations.

Model results indicate that aggregates with very large particles follow the λ_t/λ relationship reported for tests on dry specimens of compacted gravels reasonably well.

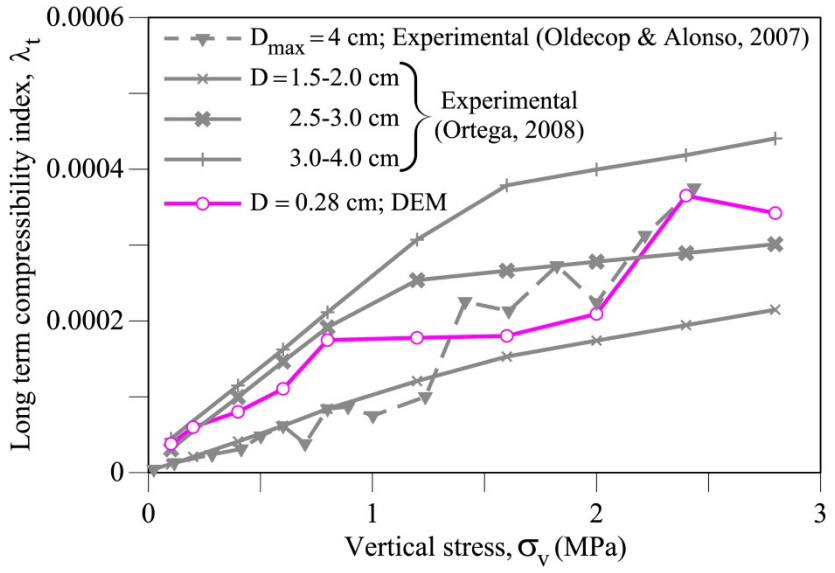

Figure 6-9 Calculated long-term compressibility index λ_t (for *D*=2.8cm) and experimental results based on Ortega (2008) and Oldecop & Alonso (2007).

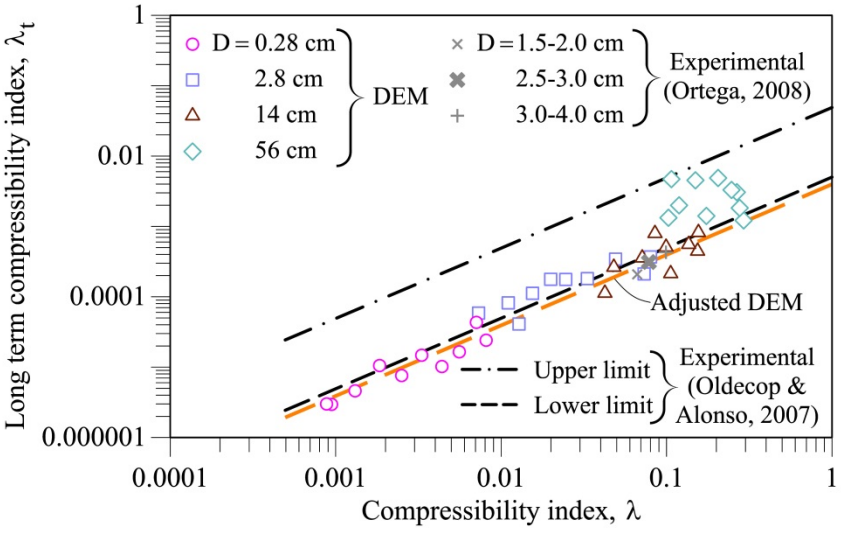

Figure 6-10 Correlation between calculated long-term compressibility index λ_t and compressibility index λ and experimental results based on Ortega (2008) and Oldecop & Alonso (2007).

6.4.3 Particle breakage

Figure 6-11 shows an example of the evolution of the grain size distribution of the 2.8 cm particle size sample when the vertical stress reached 2.8 MPa. The final grain size distribution is not a continuous function which is probably a result of the limited number of particles defining a macroparticle but, also, the relatively low number of "clumps" used in the simulation. Nevertheless the attained distributions allow calculating breakage indices (Hardin, 1985; Marsal, 1973). The calculated Hardin index (B_r) is shown in **Figure 6-12** in terms of grain size; three values reported by Ortega (2008) are also shown in the figure. Apparently, the calculated breakage indices stabilise beyond a certain grain size (2.8 cm) and even decrease slowly. However, **Figure 6-12** should be considered a preliminary result subjected to further analysis with increasing number of particles.

Comparing size effect in the evolution of gsd curves for specimens subjected at the same stress (σ_v=2.8MPa), **Figure 6-13** shows the calculated gsd for the samples S25 (D=0.28cm) and S250 (D=2.8cm) at the initial and final tests: the sample with greater particle size presented higher breakage for this size range. These results are agree with experimental tests performed by Ortega (2008) (see **Figure 6-12**).

Therefore, as it was argued in comments at the end of section 6.1, the hypothesis about the assignation of the same mechanical behaviour for larger particle sizes than for a scaled grain size (**Figure 6-1**) is wrong because the intrinsic scale effects are associated with particle breakage.

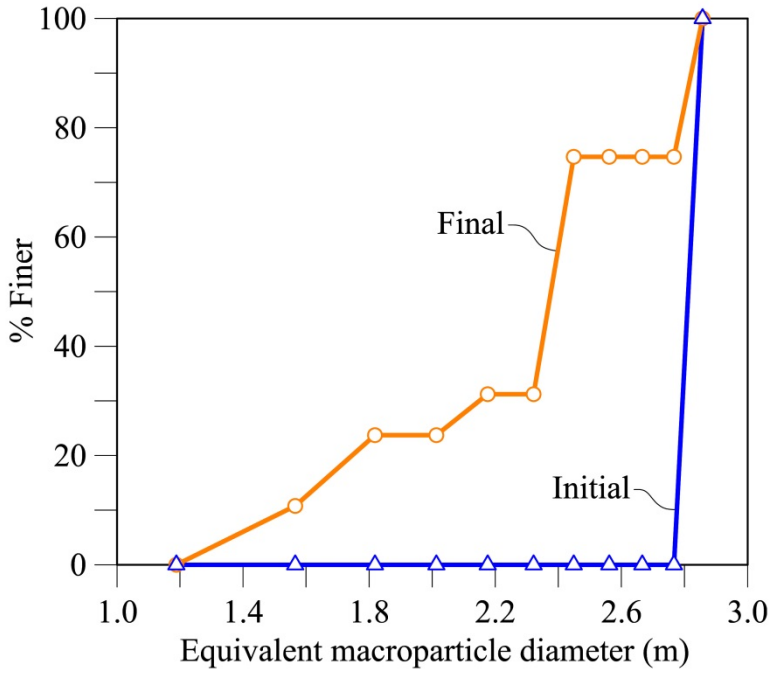

Figure 6-11 Calculated grain size distribution of test *D*=2.8cm at the end of the test (σ_v=2.8MPa; RH=10%).

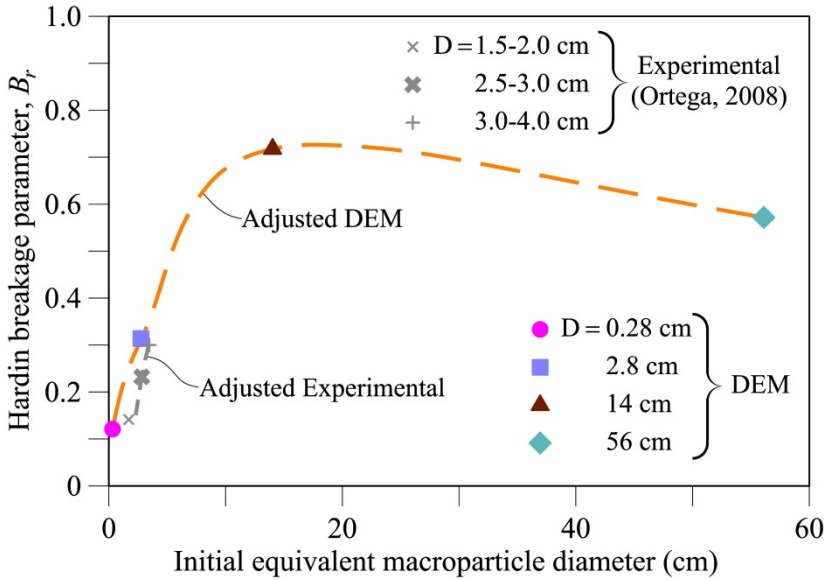

Figure 6-12 Hardin breakage parameter (B_r) derived from DEM calculations and B_r values derived from test results (Ortega, 2008).

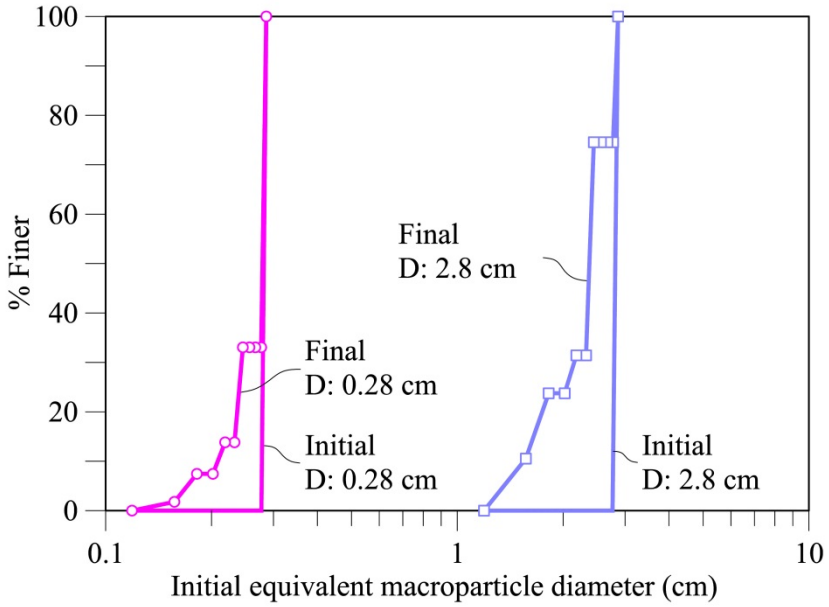

Figure 6-13 Calculated grain size distribution of the tests *D*=0.28cm and D=2.8cm at the initial and end of the tests (σ_v=2.8MPa; RH=10%).

6.5 Predicting triaxial tests

Once validated in the manner discussed in chapter 5 the model offers the opportunity to investigate size effects, a subject of practical interest.

The capability of the model to simulate scale effects was further checked by performing numerical triaxial tests on samples of uniform particle sizes (18.5mm and 38.5 mm) which could be compared with actual laboratory tests performed by Ortega (2008). The gravel in this case was Garraf limestone and the model parameters μ = 0.3; K_c = 1 MPa.m$^{0.5}$; k_n = k_s = 4 MN/m were already discussed in the chapter 5. For this exercise, the entire calculation protocol used in chapter 5 was followed: comminution and splitting mechanisms were taken into account.

The limestone gravels of Ortega (15-20 mm and 30-40 mm) were compacted to an initial porosity n_0 = 0.49. The DEM samples had an initial porosity of 0.53. The confining radial stress in the triaxial tests was 1 MPa. Tests were under dry conditions (RH = 10%). Actual samples were flooded when the axial deformation reached 13% and the shear strength was already very close. This final part of tests was not simulated here but is presented in chapter 7.

Figure 6-14 compares experimental results and model calculations. DEM predicts shear strengths (for an axial deformation of 12%) which are 90% (finer aggregate) and 80% (coarser aggregate) of test results. DEM-calculated volumetric compression (**Figure 6-14**) is smaller than testing results but overall the agreement is reasonably good. Size effects are well captured by the model: finer aggregates exhibit a stiffer response, an increased strength (measured before “residual” conditions) and a reduced volumetric compression during shear than coarser samples.

Figure 6-15 and **Figure 6-16** show the evolution of grading curves (end of tests compared with initial grading) and the breaking index B_r respectively. Measured and calculated values are compared in these figures. The agreement is quite good for the smallest gravel size. Measured breakage for the largest size is more pronounced than model predictions. In fact, B_r for DEM simulations varies from 0.21 to 0.22, for 18.5mm and 38.5mm initial sizes whereas measured B_r varies between 0.24 to 0.29, for the 15-20mm and 30-40mm initial sizes.

Overall, the blind simulation of the triaxial tests described is very good: the volumetric behaviour and the grain size evolution were reasonably well predicted and the mobilized deviatoric stress reached 70%-90% of measured values. Size effects were well captured, a very significant aspect of coarse granular aggregates. This capability is directly associated with the fracture mechanics-based model for grain breakage.

Frossard et al. (2012) describe an analytical procedure to estimate size effects for uniform granular materials of different sizes. Their approach is limited to strength envelopes or linear compressibility parameters. The advantage of the DEM approach is that it may refer to any aspect of behaviour and it may handle arbitrary grain size distributions.

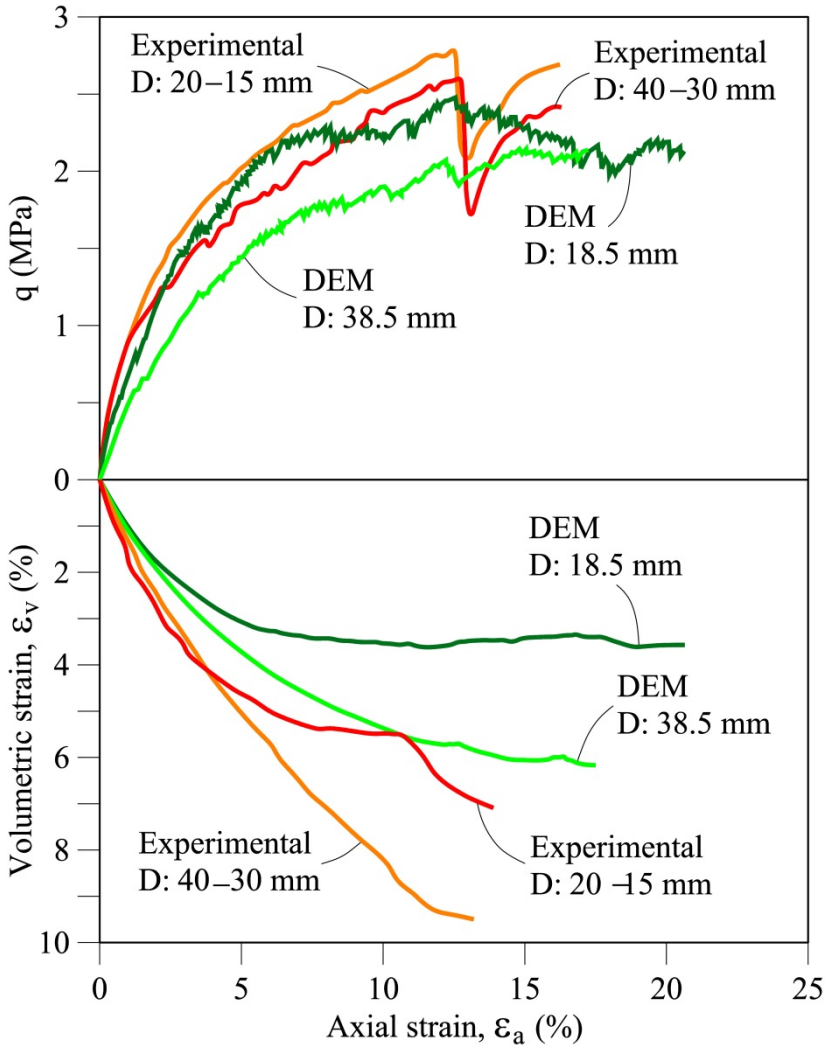

Figure 6-14 Experimental and simulated triaxial tests on uniform limestone gravels of different initial grain size. Experimental data reported by Ortega (2008). DEM parameters: μ=0.3; K_c=1 MPa*m$^{0.5}$; k_n=4 MN/m.

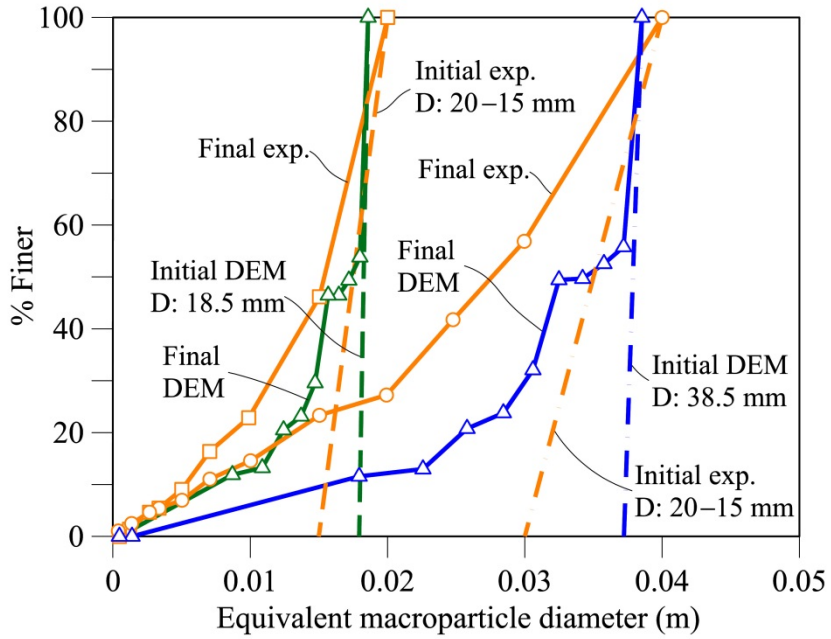

Figure 6-15 Triaxial tests on two coarse aggregates. Comparison of measured and calculated grain size distribution at the end of tests. Experimental data reported by Ortega (2008). DEM parameters: μ=0.3; K_c=1 MPa*m$^{0.5}$; k_n=4 MN/m.

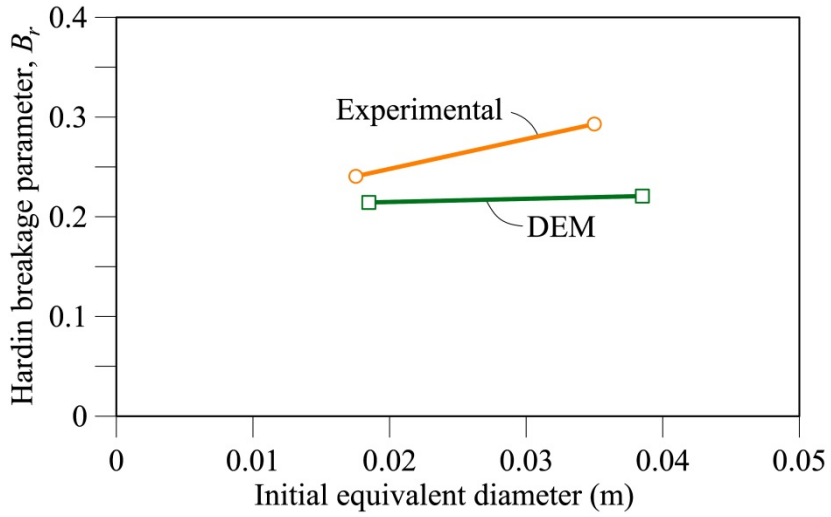

Figure 6-16 Triaxial tests on two coarse aggregates. Comparison of measured and calculated breaking Index parameter B_r. Experimental data reported by Ortega (2008). DEM parameters: μ=0.3; K_c=1 MPa*m$^{0.5}$; k_n=4 MN/m.

6.6 Conclusions

Scale effects on rockfill behaviour can be successfully approached through a DEM modelling provided a particle breakage criterion incorporating the mechanics of crack propagation in brittle materials is included in the model. This opens the possibility of quantifying scale effects in rockfill, a subject of practical interest.

The model developed simulates particle shapes of a roughly pyramidal shape and proposes a particular subdivision law. The subdivision is achieved when a critical defect or crack propagates through the particle. The time to the final stage of crack propagation is derived from an analysis of the subcritical crack growth under a mode I type of loading, which is accepted as a reasonable mode in granular assemblages in which diametral loading of particles is the dominant mechanism.

The model parameters have been calibrated through the results of real oedometer tests performed on samples having an average particle diameter of 2.8 cm, such as in previous chapter. Once this is achieved, the model is used as a virtual laboratory to explore size effects.

Numerical simulations were then carried out, testing particle sizes in the range 0.28-56 cm (initial particle average size) in order to evaluate the compressibility of the rockfill at different scales. The results were compared with real oedometer tests.

The model is capable of a precise reproduction of long-term (oedometer) tests. Short-term compressibility (λ) increases with particle size, as well as the creep or secondary coefficient. The ratio λ_t/λ was found in reasonable agreement with experimental results derived for different granular materials. The model provides also information of the evolution of grain size distribution during loading of specimens for a wide range of particle sizes.

Similarly to the previous work in chapter 5, “blind” simulations of real triaxial tests on different size particle for the same material, using the model parameters and the entire calculation protocol used to interpret the oedometer test of the chapter 5, also led to a quite successful prediction of the deviatoric stress-strain behaviour, the volumetric sample response, and the grain size distribution.

6.7 List of Notations

Notation		***Section***
A	Coefficient of the model; Eq. (6:9)	6.4.1
a	Half-length of the defect/crack	6.3
a_i	Half-length of the defect/crack for a particle i; Eq. (6:3); (6:4)	6.2

a_0	Previous or initial half-length of the defect/crack	6.3
B_r	Hardin breakage index	6.4.3; 6.5
b	Exponent of the model; Eq. (6:9)	6.4.1
C	Scaling parameter; Eq. (6:2)	6.2
D	Diameter of grain; Particle size; Sample size; Eq.(6:1); (6:8) - (6:10)	6.2; 6.4; 6.5
D_i	Diameter of grain i; Size of particle i; Eq. (6:4)	6.2
D_{max}	Maximum diameter of grain; Maximum particle size; Initial grain/particle size	6.4.2
D_{ref}	Reference initial diameter; Eq. (6:9); (6:10)	6.4.1
D_0	Reference diameter; Eq.(6:1)	6.2
D_{50}	Diameter through which 50% of the total soil mass is passing	6.1
DEM	Discrete/Distinct Element Method	6
da	Crack length increment; Eq. (6:6)	6.3
dt	Time increment; Eq. (6:6)	6.3
FISH	Programming language embedded in the PFC3D code	6.3
gsd	Grain size distribution	6.4.3; 6.5
K	Stress intensity factor; Eq. (6:6)	6.3
K_c	Toughness; Eq. (6:4); (6:6)	6.2; 6.3; 6.5
K_i	Stress intensity factor of a given particle i; Eq. (6:3)	6.2
k_n	Normal contact stiffness	6.3; 6.5
k_s	Shear contact stiffness	6.3; 6.5
m	Experimental parameter; Weibull modulus; Eq. (6:1); (6:2);	6.2
n	Exponent of Charles law; Eq. (6:6)	6.3
n_d	Constant; Eq. (6:1); (6:2);	6.2
n_0	Initial porosity	6.5
$P_{survival}(D,\sigma)$	Probability of survival of a sample of size D subjected to a tensile stress σ; Eq.(6:1)	6.2
PFC3D	Particle Flow Code in 3 Dimensions	6.3

RH	Relative Humidity	6.4; 6.5
r	Equivalent radius	6.3
t	Time; Eq. (6:11)	6.4.2
V	Crack propagation velocity; Eq. (6:6)	6.3
V_0	Reference velocity; Eq. (6:6)	6.3
w	Radius of a loaded circular area; Eq. (6:5)	6.3
z	Distance below the centre of the loaded area; Eq. (6:5)	6.3
β_i	Dimensionless coefficient for a particle i used in the calculation of the stress intensity factor; Eq. (6:3); (6:4)	6.2
ε_v	Vertical deformation; Eq. (6:7); (6:11)	6.4.1; 6.4.2
θ_0	Solid angle which defines the small area of stress application	6.3
λ	Compressibility index; Eq. (6:7) - (6:10); (6:12)	6.4.1
λ_{ref}	Reference compressibility index; Eq. (6:9); (6:10)	6.4.1
λ_t	Long-term compressibility index; Eq. (6:11); (6:12)	6.4.2
μ	Friction coefficient	6.3; 6.5
ν	Poisson`s ratio; Eq. (6:5)	6.3
ρ	Loading stress; Eq. (6:5)	6.3
σ	Tensile stress; Eq.(6:1) ; (6:5)	6.2; 6.3
σ_f	Mean tensile strength; Eq. (6:2); (6:4)	6.2
σ_i	Tensile stress for a particle i; Eq. (6:3); (6:4)	6.2
σ_v	Vertical stress; Eq. (6:7)	6.4.1
σ_0	Reference tensile stress (value of tensile stress σ such that 36.7879% of the total number of tested blocks survive); Eq.(6:1)	6.2

6.8 References

Alonso, E.E., Oldecop, L., Pinyol, N., 2009. Long term behavior and size effects of coarse granular iedia, in: Kolymbas, D., Viggiani, G. (Eds.), Mechanics of Natural Solids. Springer-Verlag, Berlin, Germany, pp. 255–281.

Alonso, E.E., Olivella, S., Pinyol, N.M., 2005. A review of Beliche Dam. Géotechnique 55, 267–285.

Atkinson, B.K., 1984. Subcritical crack growth in geological materials. J. Geophys. Res. 89, 4077–4114.

Bazant, Z.P., 1984. Size effect in Blunt Fracture: Concrete, Rock, Metal. J. Eng. Mech. 110, 518–535. doi:10.1061/(ASCE)0733-9399(1984)110:4(518)

Charles, R.J., 1958a. Static fatigue of glass. I. J. Appl. Phys. 29, 1549–1553. doi:10.1063/1.1722991

Charles, R.J., 1958b. Static fatigue of glass. II. J. Appl. Phys. 29, 1554–1560. doi:10.1063/1.1722992

Cundall, P.A., Strack, O.D.L., 1979. A discrete numerical model for granular assemblies. Géotechnique 29, 47–65.

Frossard, E., Hu, W., Dano, C., Hicher, P.-Y., 2012. Rockfill shear strength evaluation : a rational method based on size effects. Géotechnique 62, 415–427.

Hardin, B.O., 1985. Crushing of soil particles. J. Geotech. Eng. ASCE 111, 1177–1192.

Itasca, 2008. Manuals of PFC3D v.4.0: Theory and Background, 4th ed. Minneapolis, Minnesota, USA.

Kolbuszewski, J., Frederick, M.R., 1963. The significance of particle shape and size on the mechanical behaviour of granular materials, in: European Conference on Soil Mechanics and Foundation Engineering. Sec. 4, Paper 9. Wiesbaden, Germany, pp. 253–263.

Kuhn, M.R., Bagi, K., 2009. Specimen Size Effect in Discrete Element Simulations of Granular Assemblies. J. Eng. Mech. ASCE 135, 485–492.

Marachi, N.D., Chan, C.K., Seed, H.B., 1972. Evaluation of properties of rockfill materials. J. Soil Mech. Found. Div. ASCE 98, 95–114.

Marachi, N.D., Chan, C.K., Seed, H.B., Duncan, J.M., 1969. Strength and deformation characteristics of rockfill materials. Berkeley, CA, USA.

Marsal, R.J., 1973. Mechanical properties of rockfill, in: Hirschfeld, R.C., Poulos, S.J. (Eds.), Embankment Dam Engineering. Casagrande Volume I. John Wiley & Sons, New York, NY, USA, pp. 110–200.

Marsal, R.J., 1967. Large-scale testing of rockfills materials. J. Soil Mech. Found. Div. ASCE 93, 27–44.

Nobari, Duncan, 1972. Effect of reservoir filling on stresses and movements in earth and rockfill dams.

Oldecop, L.A., Alonso, E.E., 2007. Theoretical investigation of the time-dependent behaviour of rockfill. Géotechnique 57, 289–301.

Oldecop, L.A., Alonso, E.E., 2003. Suction effects on rockfill compressibility. Géotechnique 53, 289–292.

Oldecop, L.A., Alonso, E.E., 2001. A model for rockfill compressibility. Géotechnique 51, 127–139.

Ortega, E., 2008. Comportamiento de materiales granulares gruesos - Efecto de la succión. PhD. Thesis. Technical University of Catalonia. UPC, Barcelona, Spain (in Spanish).

Potyondy, D.O., Cundall, P.A., 2004. A bonded-particle model for rock. Int. J. Rock Mech. Min. Sci. 41, 1329–1364. doi:10.1016/j.ijrmms.2004.09.011

Russell, A.R., Muir Wood, D., 2009. Point load tests and strength measurements for brittle spheres. Int. J. Rock Mech. Min. Sci. 46, 272–280. doi:10.1016/j.ijrmms.2008.04.004

Weibull, W., 1951. A statistical distribution function of wide applicability. J. Appl. Mech. 18, 293–297.

Weibull, W., 1939. A statistical theory of the strength of materials, in: Proceedings of the Royal Swedish Institute of Engineering Research, 151.

Wiederhorn, S.M., Fuller, E.R., Thomson, R., 1980. Micromechanisms of crack growth in ceramics and glasses in corrosive environments. Met. Sci. 14, 450–458. doi:http://dx.doi.org/10.1179/msc.1980.14.8-9.450

Chapter 7

Influence of relative humidity and time effect on coarse granular aggregates

This chapter presents the considerations and implementation of the relative humidity and time-dependent behaviour in the proposed DEM model.

The theory of subcritical crack propagation due to stress corrosion is considered in order to take into account the relative humidity in the breakage of particles. Three models of subcritical crack propagation are proposed.

The influence of the relative humidity is also studied through the performance of numerical oedometer and triaxial tests using the DEM model. These numerical tests simulate experimental tests from Ortega (2008). Furthermore, size effects are analyzed in some numerical (DEM) triaxial tests taking into account the relative humidity.

Finally, time-dependent behaviour is analyzed by conducting a numerical oedometer test and also comparing it with an experimental test from Ortega (2008).

7.1 Introduction

The effect of the relative humidity (or suction) on the mechanical behaviour and the time-dependent behaviour of rockfill and gravels have been evidenced in both laboratory tests on scaled material and field research on bigger engineering structures such as dams and embankments, as we can see below. The breakage of particles and the subsequent rearrangement of the particles are key aspects of this mechanical behaviour.

7.1.1 Relative Humidity effect

7.1.1.1 Laboratory tests

Results of one-directional compression tests in a Relative Humidity (RH)-controlled

oedometer cell on coarse aggregates (slate and limestone gravels between 0.4 and 40 mm in size, see chapter 2, section 2.7.1) show that the higher the humidity, the greater the compressibility of the aggregates and, furthermore, collapse of volumetric deformation occurs when dry aggregates are subjected to wetting and reach a saturated condition (Oldecop, 2000; Oldecop and Alonso, 2003, 2001; Ortega, 2008). In addition, the gravels exhibit a time-dependent behaviour controlled by stresses and the surrounding relative humidity (Oldecop and Alonso, 2007).

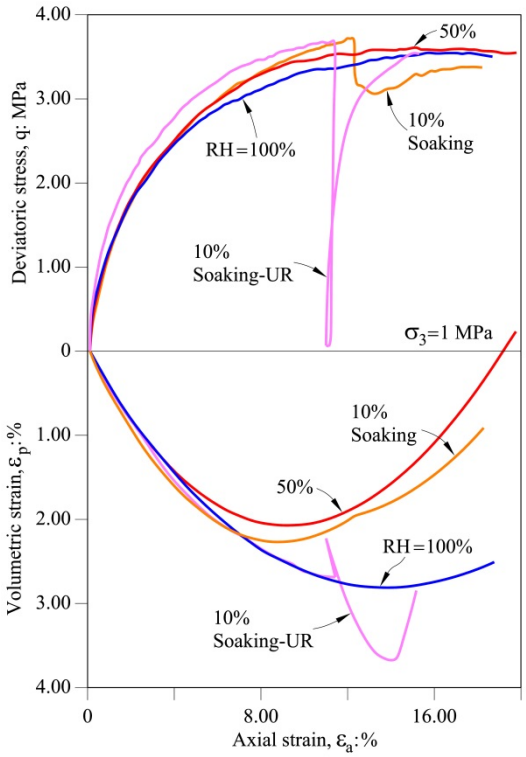

Figure 7-1 Deviatoric behaviour of well-graded aggregates of Garraf limestone gravels (Diameter size: 1.4-40mm). Results of suction-controlled triaxial tests for σ_3=1MPa and different Relative Humidity conditions: 10%, 50% and 100%. One of the samples at RH=10% was flooded at $\varepsilon_a \approx$12% (10%-Soaking curve) and the other one was unloaded at $\varepsilon_a \approx$ 11% and then flooded, before resuming the test (10%-Soaking-UR curve). (From Alonso et al. (2016)).

On the other hand, results of RH-controlled triaxial tests on the same material tested in oedometers (slate and limestone gravels, see chapter 2, section 2.7.2) show that the lower the humidity, the greater the resistance of the gravel samples (Alonso et al., 2016; Chávez, 2003; Chávez and Alonso, 2003; Ortega, 2008). Likewise, collapse in the deviatoric stress is observed when dry samples are flooded. For limestone gravels, Alonso et al. (2016) found that relative humidity affects the evolution of grain size distribution, the deviatoric stress–strain response and the dilatancy rules. For a certain confining stress, dry samples present more dilatancy than saturated samples. They found that for different confining stresses (0.3; 0.5 and 1.0 MPa), in a deviatoric stress - axial strain space, the deviatoric stress is smaller for the saturated samples (RH=100%) (see **Figure 2-28** in chapter 2 and **Figure 7-1** for limestone gravels with confining stresses σ_3 of 0.3 MPa and 1

MPa respectively). The behaviour of the samples with RH=10% and 50% was very similar and fell within the range of experimental variability. The positive dilatancy or contractancy behaviour is present at the beginning of the applications of deviatoric stresses as a consequence of particle breakage. Dilatancy rates decrease until they reach a value of zero when the shearing conditions are also reached. After this stage, negative dilatancy or expansion is present at constant shearing strength. Dry samples present more dilatancy rate (in the negative range or expansion) than saturated samples. At the end of the tests (axial strain ε_a=16-18%), a decrease in the dilatancy rate could not be evidenced. This behaviour was also found by Chávez (2003) for slate gravels (see **Figure 2-34** in chapter 2).

The grain size distribution (gsd) curves at the end of these experimental triaxial tests evidence the effect of the relative humidity on the breakage of particles. For instance, **Figure 2-27**, in chapter 2, shows the evolution of gsd curves for the Pancrudo slate gravels tested by Chávez and Alonso (2003). **Figure 7-2** shows the evolution of gsd curves for these slate gravels at the end of the triaxial tests with RH=36% and 100% with a confining stress σ_3 of 0.3 MPa (**Figure 7-2a**) and 0.8 MPa (**Figure 7-2b**). They show a reduction of a greater size and an emergence of a fine grain size. The effect of the Relative Humidity on the evolution of breakage can also be followed by the calculation of the Hardin (B_r) and Marsal (B_g) breaking indexes: these values can be appreciated in **Figure 7-2**c.

Therefore, deformation involves and is in fact a consequence of the breakage of particles. Particle breakage explains most of the mechanical behaviour of rockfill. This breakage is enhanced by the presence of water (Clements, 1981; Nobari and Duncan, 1972; Ortega, 2008). Breakage can occur both when stress and/or humidity increases.

Some constitutive models for rockfill compressibility behaviour (Oldecop and Alonso, 2001) and triaxial behaviour (Chávez and Alonso, 2003), presented in chapter 2, sections 2.7.1.2 and 2.7.2.2, have been proposed based on the continuum media and include the suction or Relative Humidity effect.

7.1.1.2 Field observations

Alonso et al. (2005) also present evidence of the effect of water on the rockfill. They analyze previous work on the mechanical behaviour of the Beliche dam (Naylor et al., 1997, 1986). Beliche is an earth and rockfill dam, 54 meters high, located in Algarve, Portugal (core of low plasticity clay of rockfill shoulders - Central core of low-plasticity clay with 2 rockfill shells). They correlated rainfall records for a period of 10 years (1995-1994) and the vertical settlements for a point (J40) located on the downstream rockfill shoulder (see **Figure 2-7**, in chapter 2).

In similar fashion, **Figure 2-8** (in chapter 2) shows the influence of humidity (associated with rainfall records) on the vertical settlement of the crest of a rockfill embankment standing 40m high (composed of schist and shales fragments) in the railway of High Velocity Trains (AVE) Madrid-Seville (Soriano and Sánchez, 1999).

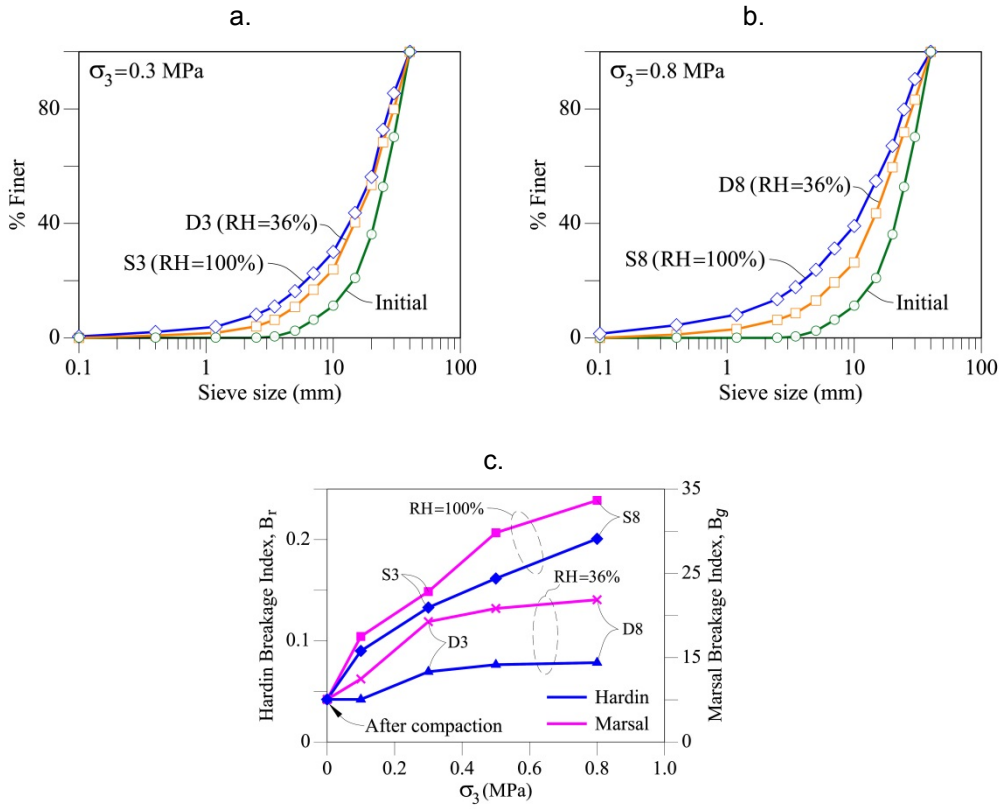

Figure 7-2 Evolution of grain size curve during triaxial tests on coarse aggregates of slate gravels from Pancrudo River, Spain (Modified from (Alonso et al., 2016; Chávez, 2003; Chávez and Alonso, 2003)): (a) Samples with RH=36% (sample D3) and RH=100% (sample S3) with confining stress σ_3=0.3MPa ; (b) Samples with RH=36% (sample D8) and RH=100% (sample S8) with confining stress σ_3=0.8MPa; (c) Evolution of breaking index.

7.1.2 Time-dependent behaviour

7.1.2.1 Laboratory tests

Regarding time effects in the rockfill and the behaviour of coarse aggregates, there are some studies which relate the time-dependent behaviour with particle crushing:

In order to design gravel drains and soil filters in dams, Lee and Farhoomand (1967) performed isotropic and anisotropic triaxial compression tests on a granular soil and studied the compressibility at high pressures. They suggested that crushing and compressibility are time-dependent phenomena. They reported cracking sounds during the loading stage in triaxial tests.

Vesic and Clough (1968) demonstrated the time-dependent behaviour based on experimental isotropic compression tests on granular materials at high pressures (e.g. 62MPa). They also related the compressibility with the breakdown of particles and argued that a similarity with the behaviour of secondary consolidation should

be expected.

Leung et al. (1996) studied the settlement of piles in sand using centrifuge modelling and observed that settlements incremented almost linearly with the logarithm of time and were also dependent upon the load magnitude and relative density of sands. Furthermore, they performed one-dimensional compression tests on the same sands and associated the pile creep to the progressive breakage of sand grains.

In the isotropic compression stage, results of triaxial tests on decomposed granites performed by Galer (1999) also showed time-dependent behaviour: after applying an isotropic stress increment and the stabilization of pore water pressure, a progressive increase in volume was produced and it was attributed to the particle breakage (Takei et al., 2001).

Takei et al. (2001) reported experimental evidence of time behaviour for some crushable materials (chalk and talc cylindrical bars, spherical Glass beads, and quartz particle specimens) subjected to one-directional compression tests: the strain continued to increase smoothly with time after the stress was imposed and remained constant during the tests; this continued increment of strain was due to particle crushing and subsequent rearrangement of particles. They also observed and studied some crushing mechanisms from single particle crushing tests (Brazilian tests) and the above-mentioned one-dimensional compression tests: local crushing at contact areas, continuous cracks in vertical splitting mode or sideways splitting mode - (for chalk and talc bars); collapse of angular edges of particles, local crushing at contact areas, splitting mode - (for quartz particles); and instant crushing (burst) into a number of fragments - (for glass beads). They argued that the time-dependent behaviour due to particle crushing under one-dimensional compression conditions may be considered to progress with the occurrence of particle crushing, subsequent rearrangement of fragments and stress redistribution.

The works of Oldecop and Alonso (2007) and Ortega (2008) also show time behaviour based on experimental data in large-diameter oedometer tests on compacted slates and limestone fragments respectively: long-term strain records demonstrated that strains could be linearly related with the logarithm of time.

Chapter 4 presented the time-dependent behaviour of sugar cubes subjected to long term oedometric tests at constant confining stress: particle breakage occurred over time and gsd curves evolved following a pattern similar to the pattern observed during a (fast) increase in stress; likewise, the samples supported a creep law relating deformations with the time.

7.1.2.2 Field observations

Barksdale and Blight (1997) show examples of field observation of creep settlement of structures founded on residual soils: After the end of construction, settlements occurred during several years.

Based on experimental data from both geotechnical structures and coarse

aggregate samples tested in the laboratory, Oldecop and Alonso (2007) studied the time dependence of the mechanical behaviour of rockfill and also the effect of suction. **Figure 2-5** (in chapter 2) shows a data compilation of crest settlements in several dams: the largest settlements occur in rockfill dams over some time – deformation begins in the early stages of construction and continues for many years.

7.1.3 DEM modelling

With regard to the action of water in saturated conditions, there are DEM models which consider the interaction of the fluid phase and solid particles, calculating forces caused by the fluid and applying them to the solids at contacts, but which do not take into account the particle breakage (e.g. in order to study the consolidation process of saturated samples (Catalano et al., 2011)).

Regarding the study of the effect of suction using DEM models, Gili and Alonso (2002) presented a 2D model for unsaturated granular media considering capillary forces due to the suction acting on the contacts. This model takes into account the interaction of particles, pores and water menisci. Chareyre and Scholtès (2011) and Chareyre et al. (2009) also consider capillary forces in the contacts in unsaturated conditions. However, the effect of capillary forces between contacts is not relevant in the rockfill behaviour. It is necessary to study the suction effect through a model that involves the relative humidity (RH) around the particles.

DEM models presented in chapter 3 take into account the breakage of particles but address neither the suction effect nor the time-dependent behaviour.

This chapter presents the results of the 3D DEM model which was presented in chapter 5, taking into account the time-dependent behaviour and the influence of the relative humidity.

7.2 DEM Model

The DEM model which is based on the distinct (discrete) element method DEM (Cundall and Strack, 1979) was already presented in chapter 5. The computer program PFC3D (Itasca, 2008) was used for the numerical simulations. Simulations of the breakage of rock fragments and the mechanical behaviour of rockfill and coarse aggregates were presented for dry conditions. Now, the effects of the Relative Humidity (RH) are introduced. They will be explained below and detailed in section 7.3. On the other hand, time effects are included by using the fracture mechanics and crack propagation concepts.

As explained in chapter 5, each rock fragment in this model is represented by a macroparticle composed of an assembly of strongly bonded and very stiff microspheres (microparticles) which form a clump of particles (**Figure 7-3**).

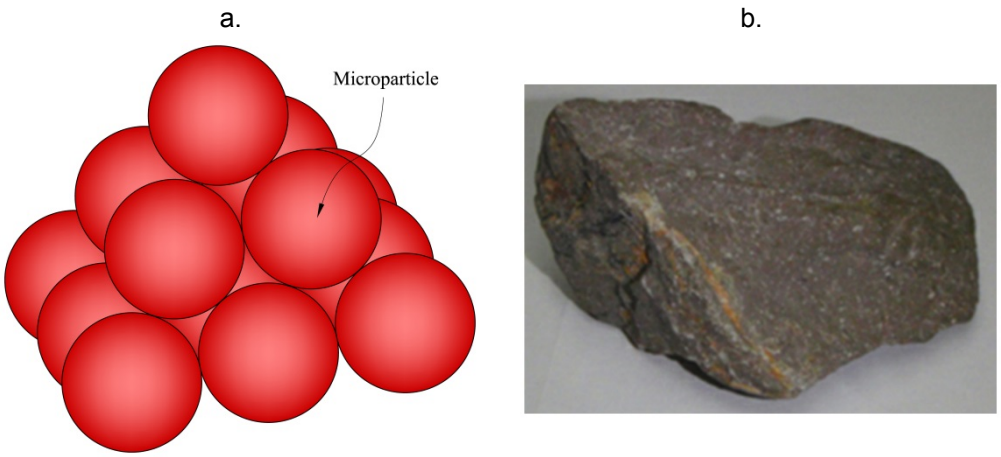

Figure 7-3 Macroparticle model: (a) Clump of 14 microparticles; (b) Limestone fragment about 3 cm in size.

A summary of the model is presented below. The following procedure is performed for the simulation of particle breakage:

(a) Calculation of stresses inside the macroparticles
(b) Application of the failure criteria
(c) Division of the macroparticles that reach the criterion of failure.

7.2.1 Calculation of stresses inside the macroparticles

In rockfill and coarse aggregates subjected to confining compressive stress, the loads are transmitted through the contact between aggregates. Chains of forces are generated inside the sample. For example, **Figure 7-4** shows these chains in an aggregate of spherical particles under a numerical simulation of triaxial test using DEM for a confining pressure σ_3 = 0.5 MPa. **Figure 7-4a** corresponds to the loaded sample (deviatoric stress condition) at an instance shown in **Figure 7-4b** when axial strain is close to 28%.

These chains of forces generally follow certain preferential directions according to applied external loads and the arrangement of the particles. Some contacts carry more load than others.

Chapter 5 showed the stress distribution inside an elasto-plastic disc resting on a rigid surface subjected to a vertical load. The effect of having another load close to a higher one as well as the effect of the disc shape were also analyzed. Stress distribution along the axis under maximum load is very similar in all those cases.

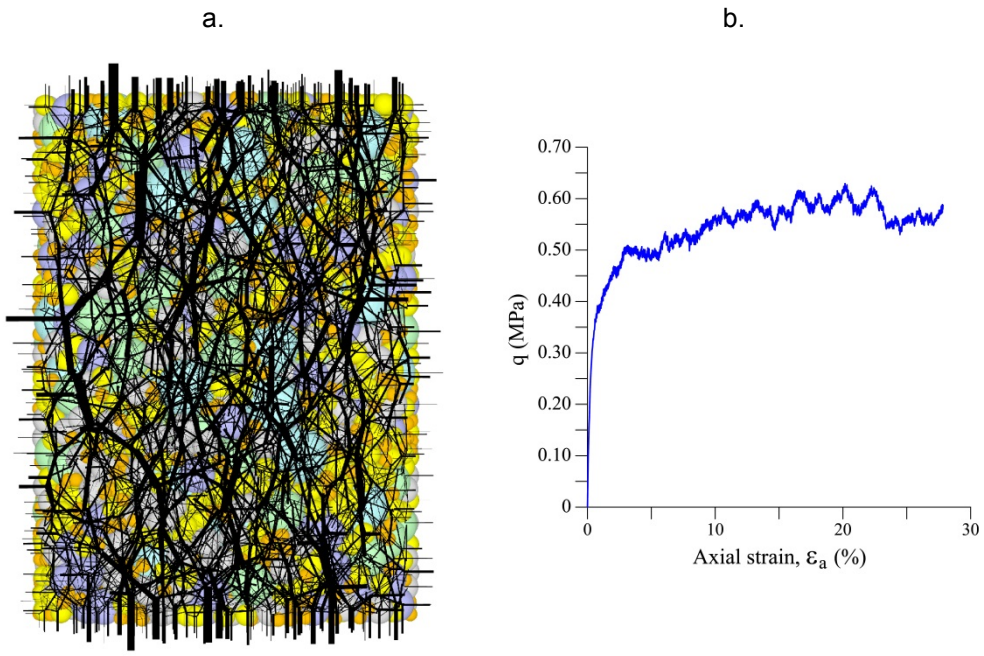

Figure 7-4 Chain forces inside coarse aggregates subjected to confining and deviatoric compressive stress. DEM triaxial simulation: (a) Chain of forces; (b) q-ε_a curve. DEM properties: μ=0.5; k_n=k_s=2x10^{7}N/m; σ_3=0.5MPa.

These results agree with those obtained by Hiramatsu and Oka (1966), who performed load tests under two diametrically opposed forces on rock samples with different shapes (spherical and irregular particles).

Therefore, the model assumes that the maximum load around the particle causes more damage, and that the particle may be compared to a sphere under diametrically opposite loads in order to calculate the stresses inside.

Furthermore, when a particle is subjected to these compressive loads, high concentrations of compressive and shear stresses occur inside it very close to the load application, and tensile stresses occur between the center of the particle and a point located at a certain distance under the load application. If the load is increased until it reaches the failure and a Mohr-Coulomb with Tensile cut-off failure criteria is applied, yielding areas are generated by shear stresses near the application load zones and tensile yielding zones around the maximum tensile stress (see **Figure 5-4** in chapter 5).

Consequently, the model considers that a macroparticle can be affected by either of the two following types of failure mechanisms: (a) Local crushing or Comminution crushing due to shear stress that causes the separation of small pieces of rock fragment; (b) Splitting failure due to tensile stress which consists of separating two blocks with similar volumes. These failure mechanisms were shown in coarse aggregates after one-dimensional compression tests on silica sands (Nakata et al., 2001) and oedometer tests on sugar cubes (see chapter 4).

These experimental results have shown that the intensity of breaking mechanisms acting on the particles is related to the "yield stress, σ_y" obtained from the compressibility curve. According to the experimental results presented in chapter 4 and by Nakata et al. (2001), the model assumes that for $\sigma < \sigma_y$, 90% of the particle breakage is due to "Comminution" mechanism and the remaining 10% to "Splitting failure". Once the "yield stress" is reached, 60% of the breakage is “Comminution” and 40% "Splitting Failure".

With regard to the calculation of stresses, **Figure 7-5** shows the generated stresses inside a sphere subjected to a diametrically opposite load *F* (the maximum compression contact load around the macroparticle). Tensile stresses σ_θ are calculated according to Russell and Muir Wood (2009). The roughness of the contacts is taken into account when the contact load *F* is applied in a small circular area, as shown in **Figure 5-6** (chapter 5).

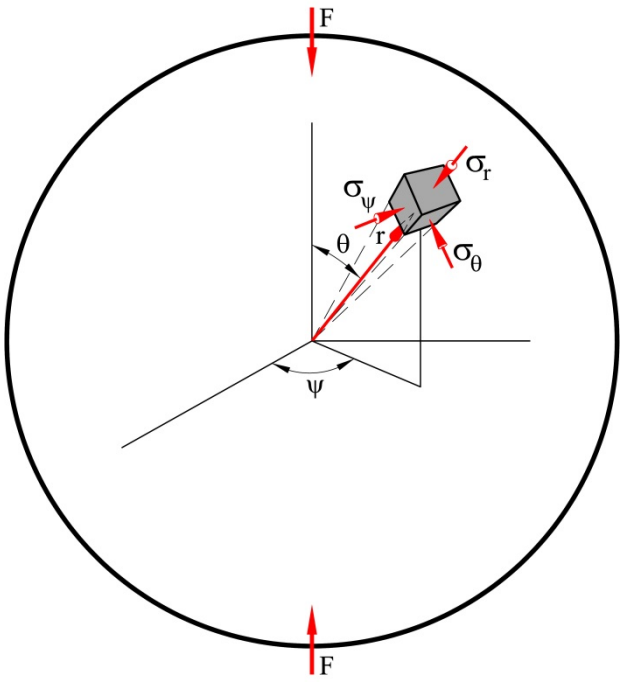

Figure 7-5 Stress calculations inside macroparticles.

Thus, the maximum tensile stress occurs under the axis of load application (θ=0°) and is calculated as follows, considering that it is produced at *z*=0.17*R*, distance of load application (see **Figure 5-6** in chapter 5), where *R* is the radius of the sphere:

$$\sigma = \left[\frac{1}{2} + \nu - \frac{(1+\nu)}{\left(1+(\frac{w}{z})^2\right)^{0.5}} + \frac{1}{2*\left(1+(\frac{w}{z})^2\right)^{1.5}} \right] * p \qquad (7:1)$$

where:

$$p = \left[\frac{F}{\pi R^2 \sin^2 \theta_0} \right] \quad (7:2)$$

R = Radius of the sphere
$2\theta_0$ = Solid Angle (see **Figure 5-6**)
ν = Poisson ratio
z = Vertical coordinate
w = Radius of loaded area

7.2.2 Failure criteria

For coarse aggregates, it is assumed that particles break when a pre-existing inner crack or defect is propagated and reaches the surface (see **Figure 5-11** in chapter 5).

Crack propagation is instantaneous when stress intensity factor K reaches the value of the particle toughness K_c. K is calculated for a Mode I (tensile) as follows:

$$K = \beta\sigma\sqrt{(\pi a)} \quad (7:3)$$

where:
a = crack half-length
β = Dimensionless coefficient dependent on the geometry of the particle, location of the crack, load intensity and direction, and the ratio between the defect and particle size. It is calculated as follows for a brittle disc with an inner defect in the center of $2a$ length, subject to two opposite contact loads (Oldecop and Alonso, 2001):

$$\beta = \left(\frac{1}{1-\alpha} \right) * \begin{bmatrix} 1 - 0.4964*\alpha + 1.5582*\alpha^2 - 3.1818*\alpha^3 + 10.0962*\alpha^4 \\ -20.7782*\alpha^5 + 20.1342*\alpha^6 - 7.5067*\alpha^7 \end{bmatrix} \quad (7:4)$$

where: $\alpha = 2a / D$; D = Diameter of disc.

σ is taken as the maximum tensile stress given by equation (7:1).

When the value of K is less than the toughness, the inner crack or defect is propagated with a certain velocity v, a phenomenon known as subcritical crack propagation (Atkinson, 1984). The velocity v is calculated by the following expression, a normalized version of the Charles's law (Charles, 1958):

$$\mathrm{v} = \mathrm{v}_0 * \left(\frac{K}{K_c} \right)^n \quad (7:5)$$

where v_0 is a reference velocity; n is a variable that depends on the Relative Humidity RH and will be detailed below when the influence of RH is treated (section 7.3).

For a small time increment Δt, the crack half-length is increased Δa:

$$\Delta a = v^* \Delta t \tag{7:6}$$

The crack half-length is calculated as follows:

$$a = a_0 + v^* \Delta t \tag{7:7}$$

where a_0 is the crack half-length before propagation.

7.2.3 Division of macroparticles

The highest contact force around the macroparticle is used to calculate the maximum tensile stress (Eq. (7:1)). If the failure is reached, i.e., whether $K \geq K_c$, or when $2a = D$ (equivalent macroparticle diameter), the division of the macroparticle into two parts occurs. **Figure 7-6** shows the algorithm used for the implementation of the division.

As explained in section 7.2.1, this division is performed by applying one of the two breakage mechanisms shown above: Comminution (local crushing), or Splitting failure.

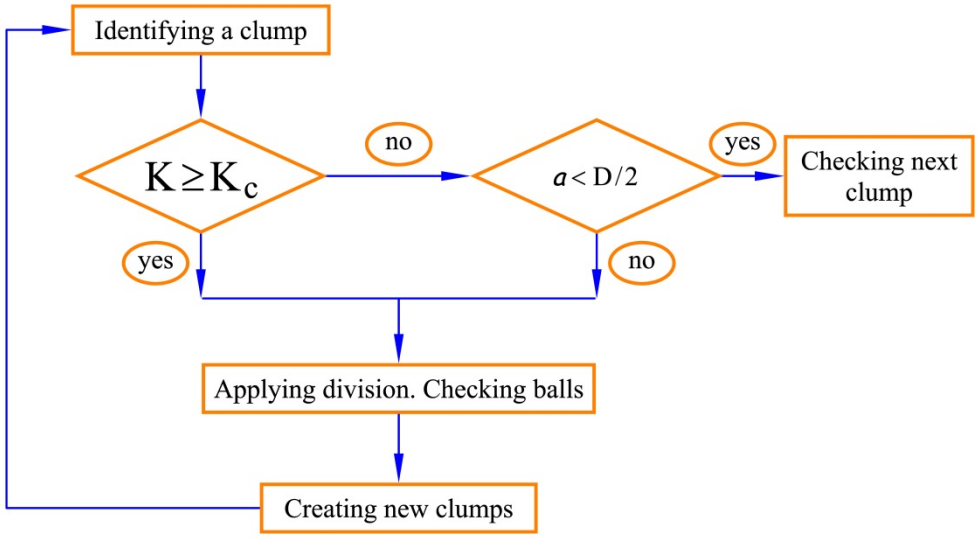

Figure 7-6 Algorithm to apply the Failure Criteria to each macroparticle (clump) in the DEM model.

The selection of the breakage mechanisms follows a probabilistic method using a uniform probabilistic distribution based on the experimental evidence as discussed above. This selection takes into account the external load applied σ (vertical stress σ_v for oedometer test and confinement stress σ_c for triaxial test) and the "yield stress σ_y" calculated from the experimental data of oedometer tests: when $\sigma < \sigma_y$, 90% of the particle breakage is due to "Comminution" mechanism and the remaining 10% to the "Splitting failure"; when $\sigma \geq \sigma_y$, 60% of the breakage is "Comminution" and 40% "Splitting Failure".

7.2.3.1 Comminution crushing mechanism

This breakage simulates a local failure, thus the microparticle that supports the highest contact force is separated from the clump (see **Figure 5-12a** in chapter 5).

This microsphere is then replaced by a new macroparticle of 13 subparticles (see **Figure 5-12c** in chapter 5) with the same diameter. This new macroparticle can also break until it reaches a subparticle level, considering both crushing mechanisms.

The rest of the old macroparticle can also be broken by either of the two crushing mechanisms.

The "Comminution" breakage process that a macroparticle of 14 microparticles can suffer is the following (see **Figure 5-12a** in chapter 5): 14→13+1; 13→12+1; 12→11+1; 11→10+1; 10→9+1; 9→8+1; 8→7+1; 7→6+1; 6→5+1; 5→4+1; 4→3+1; 3→2+1; 2→1+1.

The "Comminution" breakage process for a new macroparticle of 13 subparticles (including the initial replacement of a microparticle for the new subparticles) is the following: 1→13; 13→12+1; 12→11+1; 11→10+1; 10→9+1; 9→8+1; 8→7+1; 7→6+1; 6→5+1; 5→4+1; 4→3+1; 3→2+1; 2→1+1.

7.2.3.2 Splitting failure mechanism

In this type of breakage, the particle is divided into approximately two halves (see **Figure 5-12b** in chapter 5).

This is the "Splitting failure" process followed by a macroparticle of 14 microparticles: 14→8+6; 8→4+4; 6→3+3; 4→2+2; 3→2+1; 2→1+1.

As in the previous criterion, when there is only one separated microparticle, it is replaced by a new macroparticle of 13 subparticles. This new macroparticle can also keep breaking until it reaches a subparticle level (subparticles cannot be broken), considering both crushing mechanisms.

The rest of the old macroparticle can also be broken by either of the two crushing mechanisms.

For instance, for a macroparticle of 13 microparticles or a new macroparticle of 13 subparticles, this is the “Splitting failure” process: 13→7+6; 7→4+3; 6→3+3; 4→2+2; 3→2+1; 2→1+1.

7.2.4 DEM simulations for oedometer and triaxial tests

This chapter presents an analysis of the effects of suction (in terms of the Relative Humidity RH) and time dependence on the mechanical behaviour of rockfill and coarse aggregates. This study is done based on the results of the numerical simulations of oedometric and triaxial tests. These DEM tests simulate actual experimental results (Ortega, 2008) of limestone fragments, the same material used for dry conditions in chapter 5 (see **Figure 5-9**) with uniform size around 3 cm (**Figure 7-7**). **Table 7-1** shows some properties of limestone.

Table 7-1 Properties of crushed limestone.

Unconfined compression strength [1]	67–146 MPa
Tensile strength (Brazilian test) [1]	2.2–11 MPa
Solids density [1]	2.76 Mg/m^3
Young’s modulus, E [1]	6800 MPa
Basic friction angle, ϕ_b [2]	17^o – 18^o
Mineral friction angle, ϕ_m [2]	12^o – 14^o

[1] Tested by Ortega (2008)
[2] Tested in this research

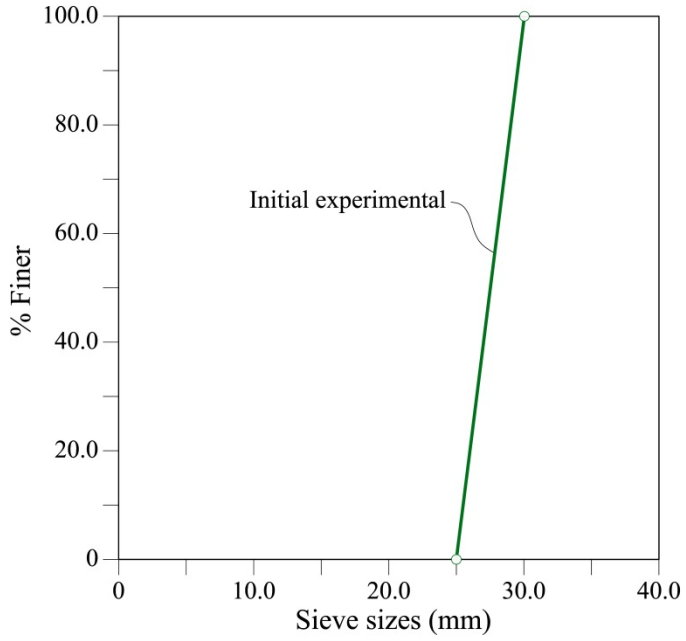

Figure 7-7 Initial grain size distribution of hard limestone gravels tested by (Ortega, 2008).

Cylindrical specimens of macroparticles have a diameter of 25cm and a height of 25cm for oedometer tests and they are 25cm x 50cm for triaxial tests. Pyramidal macroparticles are put inside the cylinder randomly following the procedure described in chapter 5.

For both DEM oedometer and triaxial tests, the initial porosity of the samples is around 53%, avoiding overlap between macroparticles (null contact forces). The initial porosity of the experimental samples of limestone fragments was around 49%.

Figure 7-8 shows macroparticle specimens before the oedometric and triaxial tests. 471 macroparticles of an initial equivalent diameter of 28mm were used in the oedometer, while 942 were used in the triaxial.

In this DEM model, macroparticles interact through their contact points by friction and stiffness. The model considers the following properties: friction coefficient μ, normal and shear contact stiffness (k_n=k_s), and particle toughness K_c. Chapter 5 described the method for obtaining these properties by conducting oedometer tests and the subsequent application in the simulation of triaxial tests. The properties found there are used in this chapter: μ = 0.3; k_n = 4 MN/m; K_c = 1 MPa.m$^{0.5}$.

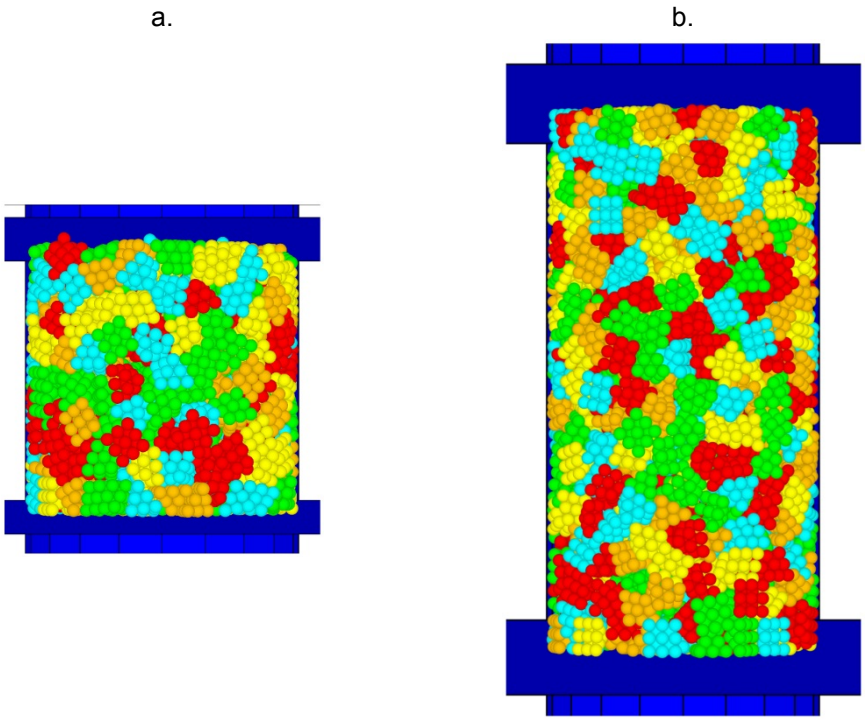

Figure 7-8 (a) Model representation of oedometer test: Cylindrical sample (0.25x0.25m) made of 471 macroparticles; (b) Model representation of triaxial test: Cylindrical sample (0.25x0.50m) made of 971 macroparticles.

7.3 Influence of Relative Humidity

7.3.1 General features of subcritical crack propagation due to stress corrosion

As previously explained, the particle breakage model is based on fracture mechanics and considers that a particle breaks when an inner crack or defect propagates until it reaches the surface: This can occur instantaneously when the value K reaches the toughness value K_c, or be deferred for $K \leq K_c$ (this phenomenon is known as subcritical crack propagation, see Wachtman et al. (2009)), where crack will propagate with a velocity according to Eq. (7:5).

Some authors have argued that there is a lower limit of the stress intensity factor or threshold stress intensity factor, K_0, below which no crack propagation occurs (Atkinson, 1984; Meredith and Atkinson, 1983; Oldecop and Alonso, 2007). K_0 is also known as the subcritical crack growth limit.

K_0 was proposed based on the work on glass and ceramics by Wiederhorn (Wiederhorn, 1978, 1974), who found values around 0.1-0.25 K_c. However, there is no experimental verification of this K_0 limit for rocks (Atkinson, 1984; Wilkins, 1980). This could be due to the difficulty of obtaining very low velocities with the performed tests. Wilkins' (1980) experimental research and studies of crack propagation velocities on granite did not find any limit for the slowest velocities from 10^{-11} to 10^{-12} m/s. Experimental results from recent tests have not been found in the literature.

7.3.1.1 Mechanisms

Aspects related to the phenomenological explanation of the subcritical crack propagation under certain environmental, chemical conditions which were discussed in section 2.4.3 (chapter 2) are now considered again in order to incorporate these aspects into the DEM model.

As previously seen, the subcritical crack propagation has been studied by several researchers: Atkinson and Meredith, 1987; Atkinson, 1984, 1982, 1979a, 1979b; Charles and Hilling, 1962; Charles, 1958a, 1958b; Evans, 1972; Freiman, 1984; Meredith and Atkinson, 1983; Oldecop, 2000; Wiederhorn, 1978, 1974; Wiederhorn et al., 1982.

Some mechanisms that cause crack propagation were presented in chapter 2 (section 2.4.3): stress corrosion, dissolution, diffusion, ion exchange, and microplasticity (Atkinson, 1984; Wiederhorn et al., 1982). These mechanisms are influenced by the chemical effects of pore water.

I will focus on one of them, the stress corrosion. This is a key mechanism because strong molecular bonds resulting from the presence of water and the action of hydrolysis processes can lead to weak bonds in hydroxyl groups (Atkinson, 1984). For instance, **Figure 2-9** (in chapter 2) shows the chemical reactions which occur mainly at the tip of the crack by strained Si-O bonds in vitreous silica and the

reaction with H_2O molecule of gas or liquid: two new bonds are formed that replace the previous Si-O bond (Si-O_{water} and H-O_{silica}) and the weak bond between the O_{water} and H is broken by the mechanical action of the stress state (Freiman, 1984; Michalske and Freiman, 1982).

Therefore, the velocity of crack propagation is controlled by the corrosion reaction under a given stress. This corrosion reaction is caused by a corrosive agent which may be related to the action of water vapour (Wiederhorn et al., 1982) or the relative humidity RH in the environment.

For this reason, the influence of the RH may be considered for calculating the velocity of crack propagation: see previous Equations 2:6 – 2:7 (Freiman, 1984; Oldecop and Alonso, 2007); based on the approaches of (Charles, 1958a; Charles and Hilling, 1962; Wiederhorn and Boltz, 1970).

7.3.1.2 Crack growth models in the literature

Chapter 2 (section 2.4.3) presented several equations for describing the subcritical crack propagation: Equations (2:2) to (2:7). Generally, these equations relate the crack growth velocity with the stress at the crack tip and the rupture strength and they are based on the Charles's law (Charles, 1958a, 1958b), see Eq. (2:3). Equations (2:4) to (2:7) were formulated in terms of fracture mechanics, thus the crack propagation velocity, v, was related to the stress intensity factor (Mode I), K.

Subcritical crack propagation tests in Mode I-Tensile could be performed to find the fracture toughness K_c of a material and to relate the stress intensity factor (K) with the velocity of crack propagation (v) under a given environmental condition.

Based on experimental results and the formulations of the subcritical crack propagations, **Figure 7-9**a shows a common schematic K-v diagram which describes the subcritical tensile crack propagation behaviour for a certain environmental condition due to stress corrosion mechanism (Atkinson, 1984, 1979a; Freiman, 1984; Meredith and Atkinson, 1983). This behaviour is explained by three regions: Most K-v data results reported in the literature fall into Region 1. For $K>K_0$, the velocity of crack propagation v is controlled by stress corrosion reactions at the tip of the crack. In Region 2, at higher values of K, v is almost constant and controlled by the rate of transport of the corrosive agent (water vapour) to the crack tip through diffusion mechanisms. In Region 3, when the stress intensity factor (K) approaches the K_c value, the crack growth occurs too rapidly and is mainly controlled by mechanical rupture. The K-v curve in Region 3 does not depend on the chemical environment.

Atkinson (1984) suggested the schematic K-v diagram shown in **Figure 7-9**b, which takes into account the variation in the pressure of the fluid in the crack (in this case, H_2O).

Finally, Oldecop and Alonso (2007) explained their conceptual model for crack propagation through the diagram shown in **Figure 7-9**c, based on the aforementioned works. For them, the increment in the relative humidity (RH) increases the velocity of the crack propagation. Equation (2:7) is valid for Region 1.

The authors suggested that stress corrosion curves under different RH values were nearly parallel except for dry conditions.

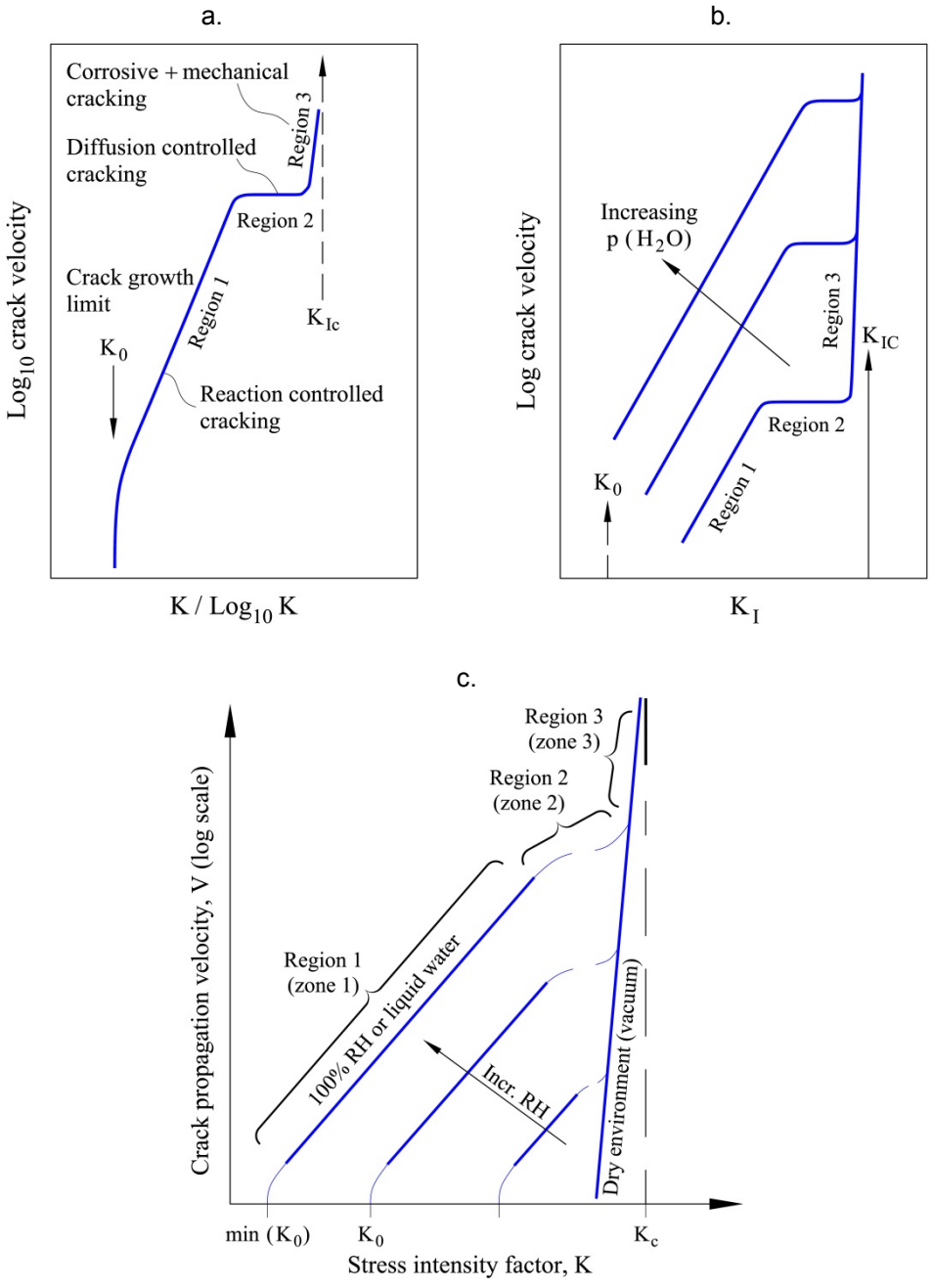

Figure 7-9 Schematic diagrams for subcritical crack propagation due to stress corrosion by Atkinson, 1984, 1979a; Freiman, 1984; Meredith and Atkinson, 1983; Oldecop and Alonso, 2007: (a) Mechanisms in a K-v curve (From Meredith and Atkinson, 1983); (b) Including water effect (From Atkinson, 1984) ; (c) Including Relative Humidity effect – (From Oldecop and Alonso, 2007).

7.3.2 Subcritical Crack Propagation Model with RH influence

Some experimental data results from literature will be shown before presenting the model of the Subcritical Crack Propagation, which takes into account the relative humidity under stress corrosion mechanism.

As presented previously, subcritical propagation tests for Mode I (tensile) are performed in order to describe the behaviour of *K*-*v* curves and find the fracture toughness value K_c. The most common test is the Double Torsion testing method (Atkinson, 1984; Meredith and Atkinson, 1983; Outwater et al., 1974; Swanson, 1984; Williams and Evans, 1973). For instance, **Figure 7-10**a shows curves *K*-*v* (stress intensity factor for Mode I "tensile", *K,* vs. crack propagation velocity, *v*) for different specimens of quartz (natural and synthetic) at room temperature and for different RH conditions (Atkinson, 1984): the samples with higher humidity had higher velocities of propagation. **Figure 7-10**b shows the same data results but in a log-log scale. The slopes of the curves log (*K*) – log (*v*) are the values of the *n* index of Eq. (7:5) for every environmental condition. The *n* calculated values for the synthetic quartz were 14 at RH=100% and 21 at RH=68%; for the natural quartz they were, respectively, 47 and 46 for the two specimens at RH=62.5%.

Regarding the experimental results on rock specimens, for instance **Figure 7-11** shows the *K*-v relations under different relative humidities which were obtained from the subcritical tensile crack growth data for some specimens of Kumamoto andesite (**Figure 7-11**a) and Oshima granite (**Figure 7-11**b). The tests were perfomed by Nara et al., (2010). The temperature is indicated in the figures: they were between 16.9°C and 21.9°C (290-295K). The results also indicated that the specimens with higher humidity had higher velocities of propagation. The *n* calculated values are indicated in the curves:

- For Kumamoto andesite: *n* is between 37 and 48 for RH=90% (mean *n*= 41), between 57 and 59 for RH=55% (mean *n*= 58), and between 57 and 63 for RH=25% (mean *n*= 60).
- For Oshima granite: *n* is between 39 and 54 for RH=90% (mean *n*= 54), and between 74 and 105 for RH=24% (mean *n*= 91).

Similarly, **Figure 7-12** shows a compendium made by Oldecop and Alonso (2007) of stress corrosion experimental data for different rocks, quartz and glass. Curves (K / K_c)-v are presented for different environmental conditions of humidity. Furthermore, estimated *n* values (slope of the curve log (K / K_c) vs. log (*v*)) are also plotted. These curves evidence again that *n* may be associated with the humidity: lowest *n* values for samples immersed in liquid water (and highest propagation velocity), and highest *n* values for dry samples.

Returning to the data results for the quartz specimens which were shown in **Figure 7-10b**, **Figure 7-13** illustrates the same *K*-*v* curves (in log-log scale) but distinguishing each kind of quartz (**Figure 7-13a** for natural quartz and **Figure 7-13b** for synthetic quartz) in order to highlight some features. **Figure 7-13a** shows the previously described three regions of *K*-*v* behaviour for one specimen of the natural quartz (solid red circles). Although it is not entirely clear, the curves for the synthetic quartz (**Figure 7-13b**) seem to suggest that Region 2 is reached for the specimen with RH=68% at a lower crack velocity than for the specimen with

RH=100%. Unfortunately, Region 2 for the specimen at RH=100% was not obtained.

On the other hand, if the straight lines of Region 1 are prolonged (extrapolating data) for all the cases (see **Figure 7-13a and b**), then we can observe that:

- For the natural quartz (**Figure 7-13*a*)**, the lines tend to intersect when K≈1.1 MPa•m$^{0.5}$ and v=1 m/s. This value of K corresponds to the fracture toughness of the solid red curve.
- For the synthetic quartz (**Figure 7-13**b**)**, the lines of Region 1 for the cases RH=100% and RH=68% tend to intersect when K≈1 MPa•m$^{0.5}$ and v=0.0032 m/s. This value of K is close to the fracture toughness for synthetic quartz, K_c=0.8 – 1 MPa•m$^{0.5}$ (see **Table 7-2**).

Similarly, for the K-v curves of the rock specimens of the **Figure 7-11**, if the straight lines of Region 1 are prolonged (extrapolating data) for the both cases of Kumamoto andesite and Oshima granite (see **Figure 7-14**a and b), then we can observe that:

- For Kumamoto andesite (**Figure 7-16**a), the lines tend to intersect when K≈2.1 MPa•m$^{0.5}$ and v=10 m/s. This value of K corresponds to the fracture toughness (see **Table 7-2**).
- For Oshima granite (**Figure 7-14**b**)**, the lines tend to intersect when K≈2 MPa•m$^{0.5}$ and v=1 m/s. This value of K is similar to the fracture toughness (K_c =2.15 MPa•m$^{0.5}$, see **Table 7-2**).

Taking into account these observations and considering the action of the stress corrosion mechanism, three models for the Subcritical Crack Propagation behaviour (in a space K-v) are proposed below. All three models are based on Eq. (7:5) - the Charles's law (Charles, 1958a, 1958b; Oldecop and Alonso, 2007) and the models therefore consider that the following factors influence the subcritical crack propagation: inner crack length, crack propagation due to tensile stresses (Mode I), stress intensity factor K, rock toughness K_c, and the action of the water (vapour or liquid) acting as a corrosive agent. Furthermore, in all three models the reference velocity v_0 is considered a constant that depends on the material, and n index depends on the environmental condition which is evaluated by the Relative Humidity RH, as will be explained in section 7.3.2.4.

There is experimental evidence that temperature and the "activity" of the fluid at the crack are important for the K-v behaviour: If the temperature rises, then the velocity of crack propagation also increases and it seems that toughness K_c decreases (if deformation is brittle); on the other hand, the higher the activity of the agent, the greater the velocity of crack propagation due to stress corrosion at constant stress intensity factor and temperature (Atkinson, 1984). However, these aspects (influence of temperature and activity of the corrosive agent) will not be considered in this research.

These models were implemented in the DEM code proposed in this research.

a.

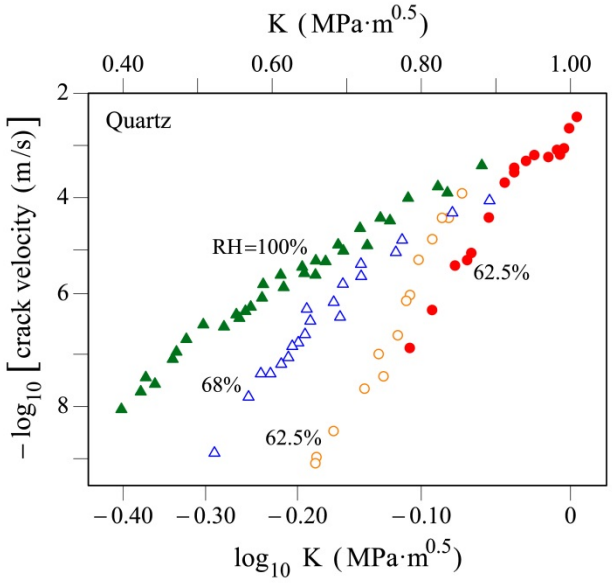

b.

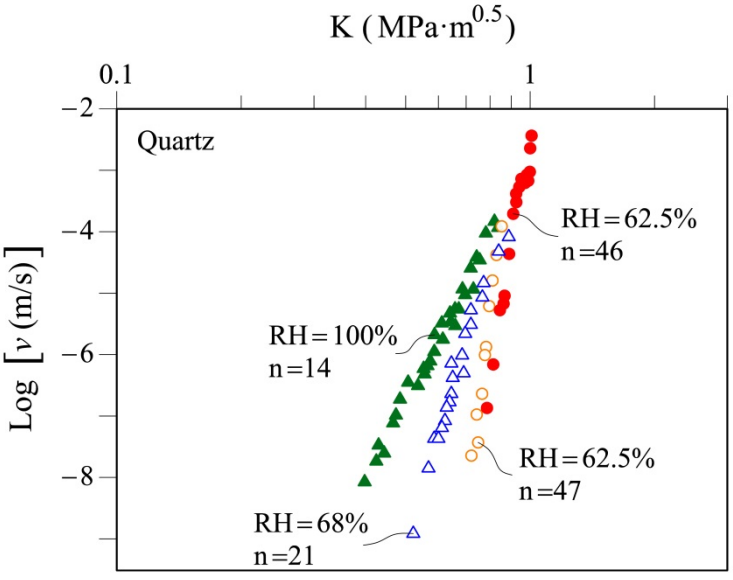

Figure 7-10 Subcritical tensile crack growth data for quartz at room temperature (stress intensity factor K_I – crack velocity data): Solid and open circles are for two specimens of natural quartz at 62.5% relative humidity (Bruner, 1980); Solid triangles are for synthetic quartz in liquid water (Atkinson, 1979a); Open triangles are for synthetic quartz at 68% relative humidity (Atkinson, 1979a). (a) *K* - Log (*v*) (Taken from (Atkinson, 1984)); (b) Log (*K*) – Log (*v*) curve.

a.

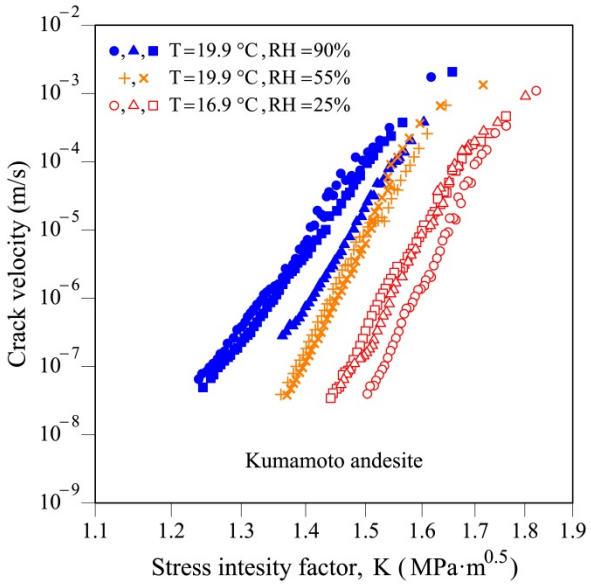

b.

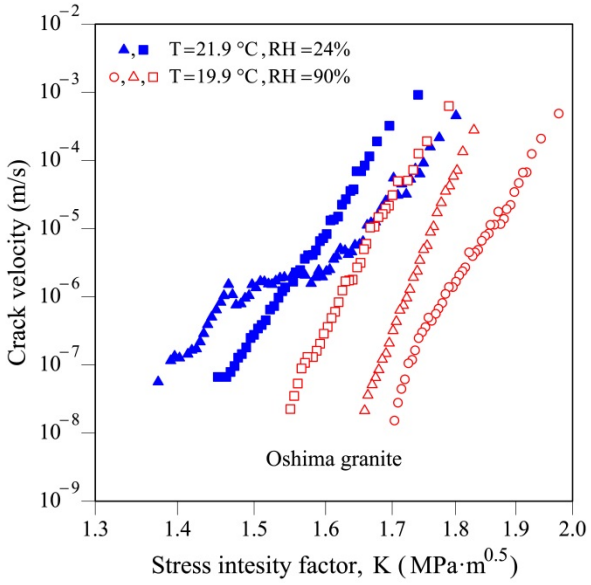

Figure 7-11 Subcritical tensile crack growth data for some rocks under diferent relative humidities (RH) at the same temperature (Curves of stress intensity factor *K*– crack velocity). (a) Kumamoto andesite; (b) Oshima granite.(From Nara et al., (2010)).

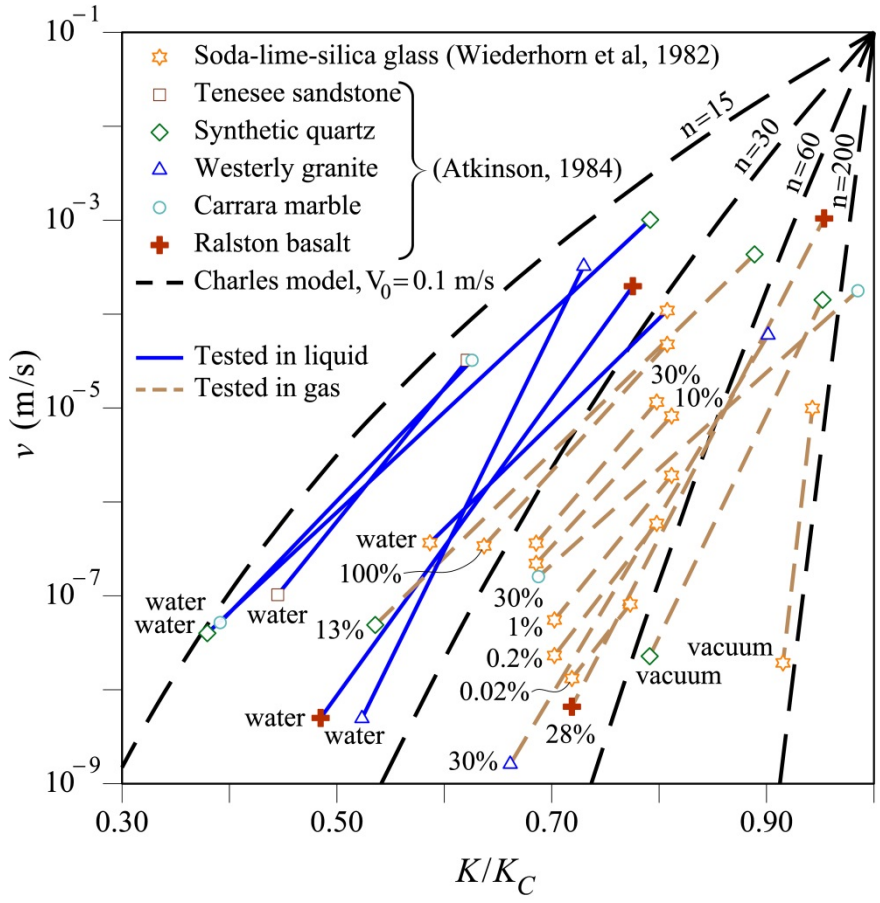

Figure 7-12 Charles Model and stress corrosion experimental data for different materials: rocks, quartz and glass, in different environmental conditions (immersed in liquid water, relative humidity conditions (%), and vacuum). (Oldecop and Alonso, 2007).

a.

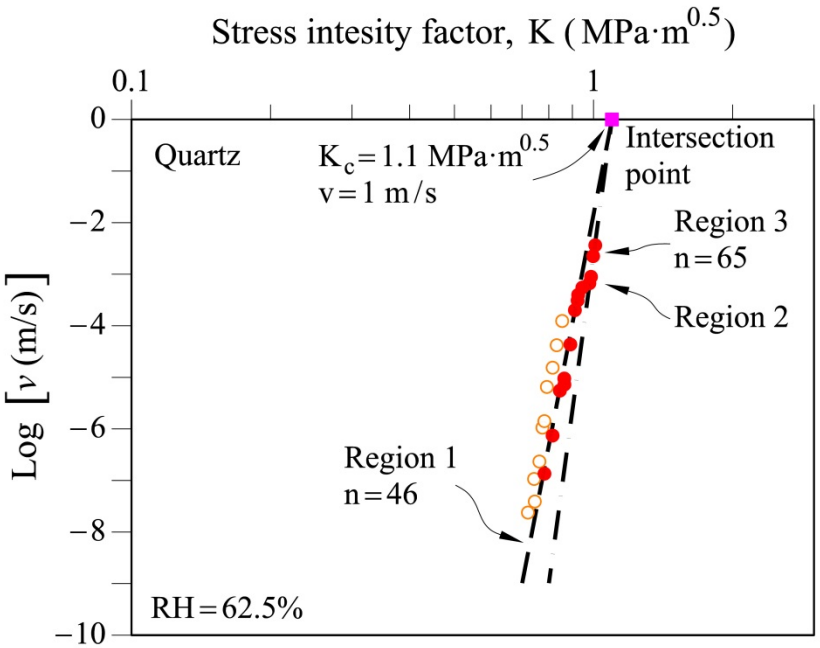

b.

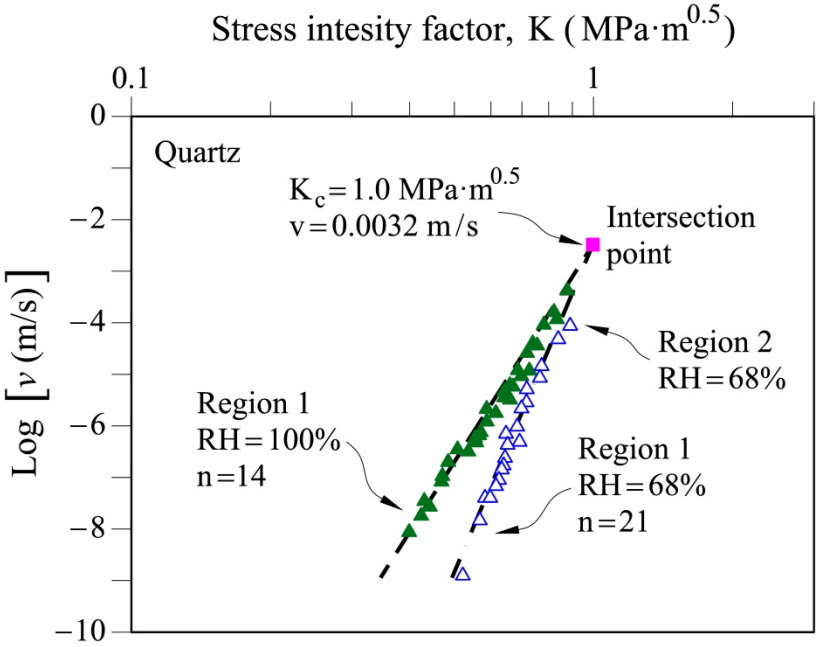

Figure 7-13 Analysis of Region of *K-v* behaviour in log-log scale for data results of **Figure 7-10**: (a) Synthetic quartz at RH=100% and 68%; (b) Two specimens of natural quartz at RH=62.5%.

a.

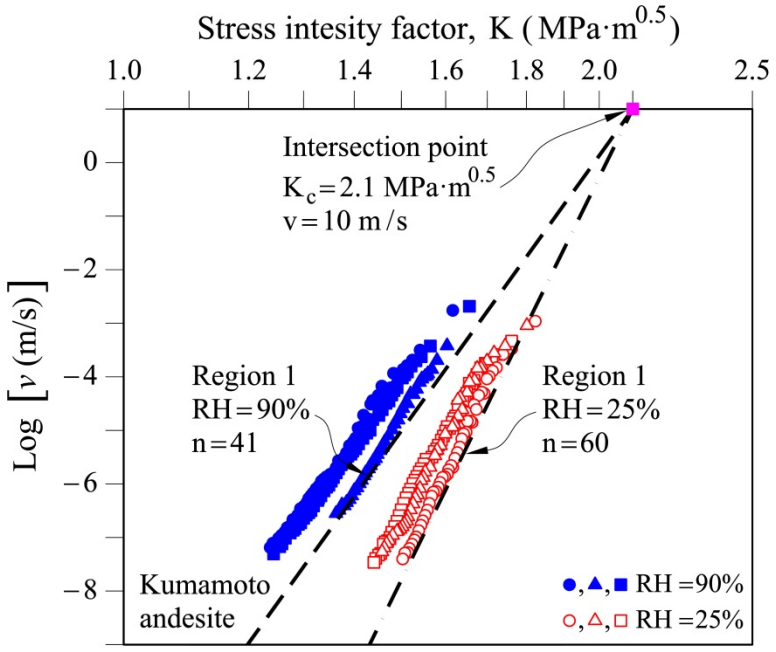

b.

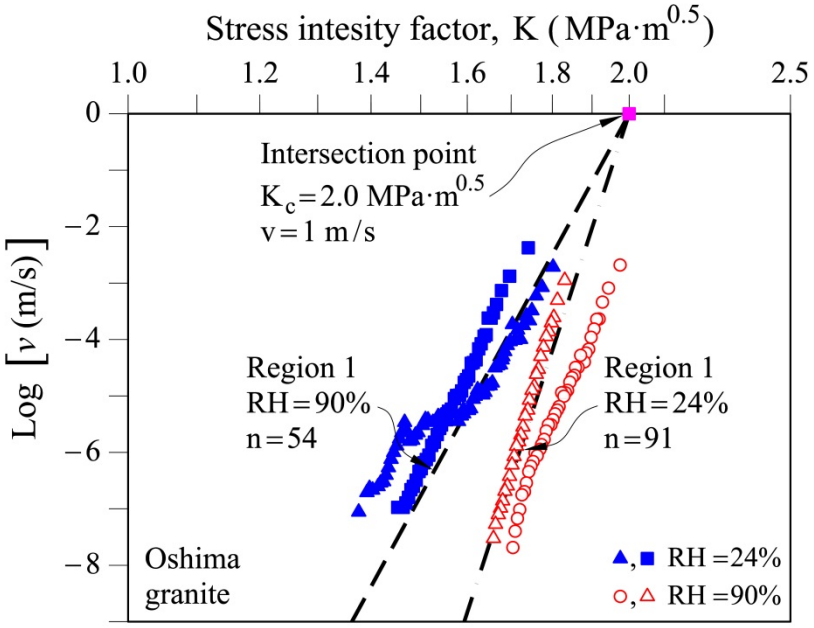

Figure 7-14 Analysis of Region of *K-v* behaviour in log-log scale for data results of **Figure 7-11**: (a) Kumamoto andesite; (b) Oshima granite.

7.3.2.1 *Model 1 of Subcritical Crack Propagation behaviour (Generalized model)*

Figure 7-15 shows the proposed model which is described for the three *K*-*v* regions. The formulations for each region are presented below. In the figure, RH_i and RH_j are the Relative Humidity for the given RH conditions when RH=i and j respectively.

The model considers three regions, which are conceptually explained as in previous work (Atkinson, 1984; Freiman, 1984; Meredith and Atkinson, 1983; Oldecop and Alonso, 2007): the subcritical crack propagation occurs under stress corrosion mechanisms. In Region 1, the velocity of crack propagation (*v*) is controlled by stress corrosion reactions at the tip of the crack; in Region 2, at higher values of *K*, *v* is constant and controlled by diffusion mechanisms; and in Region 3, the crack propagation velocity does not depend on the environmental condition because the stress intensity factor (*K*) is close to the K_c value and the crack growth is controlled by mechanical rupture and occurs too rapidly, as previously explained.

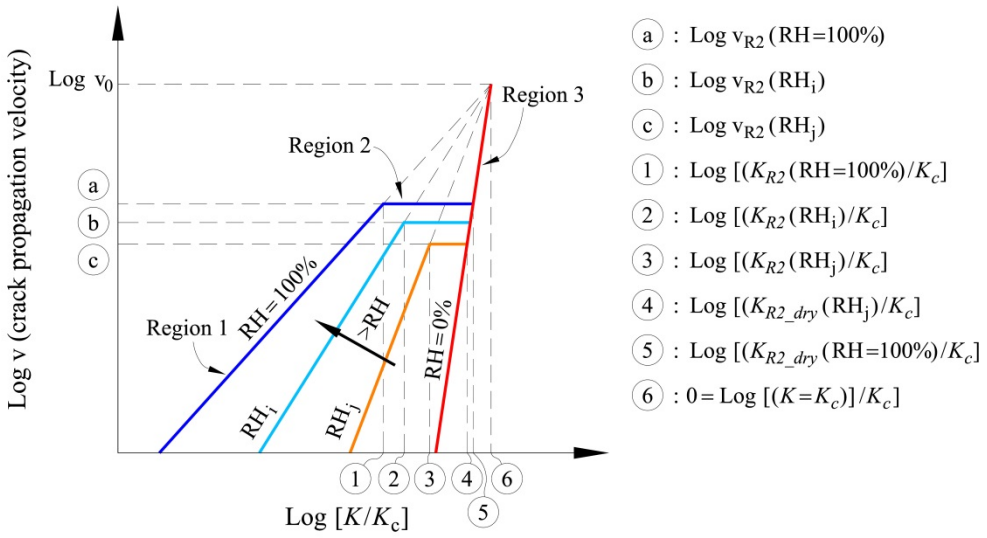

Figure 7-15 Generalized Subcritical Crack Propagation Model (Model 1).

a) For Region 1: $0 \le RH \le 100\%$ and $K \le K_{R2}(RH)$:

$$v = v_0 * \left(\frac{K}{K_c} \right)^{n(RH)} \tag{7:8}$$

where:
v is the velocity of the crack propagation for a given RH condition;
K is the stress intensity factor (Mode I);

v_0 is a reference velocity for the material. This is a parameter of the model;
K_c is the toughness of the material. This is a parameter of the model;
n(RH) is the subcritical crack propagation index or stress corrosion index that depends on the relative humidity. It corresponds to the slope of the straight line of the relation Log (K/K_c) – Log (v) and is calculated as indicated in section 7.3.2.4;
$K_{R2}(RH)$ is the value of the stress intensity factor for a given RH condition when v= $v_{R2}(RH)$ and is calculated as follows:

$$K_{R2}(RH) = K_c * \left(\frac{v_{R2}(RH)}{v_0} \right)^{\frac{1}{n(RH)}} \quad (7:9)$$

$v_{R2}(RH)$ is a reference velocity that limits Region 1 and Region 2 for a given RH condition. This is a parameter of the model;

b) For Region 2: 0 ≤ RH ≤ 100% and $K_{R2}(RH) \leq K \leq K_{R2\_dry}(RH)$:

$$v = v_{R2}(RH) \quad (7:10)$$

where:
$K_{R2\_dry}(RH)$ is the value of the stress intensity factor for RH=0% condition when v= $v_{R2}(RH)$ and is calculated as follows:

$$K_{R2\_dry}(RH) = K_c * \left(\frac{v_{R2}(RH)}{v_0} \right)^{\frac{1}{n(RH=0\%)}} \quad (7:11)$$

$v_{R2}(RH)$ is a reference velocity that limits Region 1 and Region 2 for a given RH condition. This is a parameter of the model;
n(RH=0%) is the subcritical crack propagation index or stress corrosion index when RH=0% and is calculated as indicated in section 7.3.2.4;

c) For Region 3: 0 ≤ RH ≤ 100% and $K_{R2\_dry}(RH) \leq K \leq K_c$:

$$v = v_0 * \left(\frac{K}{K_c} \right)^{n(RH=0\%)} \quad (7:12)$$

where:
n(RH=0%) is the subcritical crack propagation index or stress corrosion index when RH=0% and is calculated as indicated in section 7.3.2.4;

In this model, K_c and v_0 are constants and parameters of the model. $v_{R2}(RH)$ depends on the RH but it is also a parameter of the model. All these parameters can be found in the subcritical crack propagation tests (for instance, with the Double Torsion testing method). K_0 has not been considered here but if it was found in the tests, then the velocity of crack propagation in Region 1 would be calculated for the range $K_0 \leq K \leq K_{R2}(RH)$. For $K < K_0$ no crack propagation occurs.

7.3.2.2 *Model 2 for Subcritical Crack Propagation behaviour with common Region 2*

This proposed model also considers three regions and differs from the previous because it considers a unique Region 2 which does not depend on the Relative Humidity. **Figure 7-16** shows this model. In the figure, RH_i is the Relative Humidity for a given RH=i. The conceptual explanation of the three Regions is the same as in the previous model.

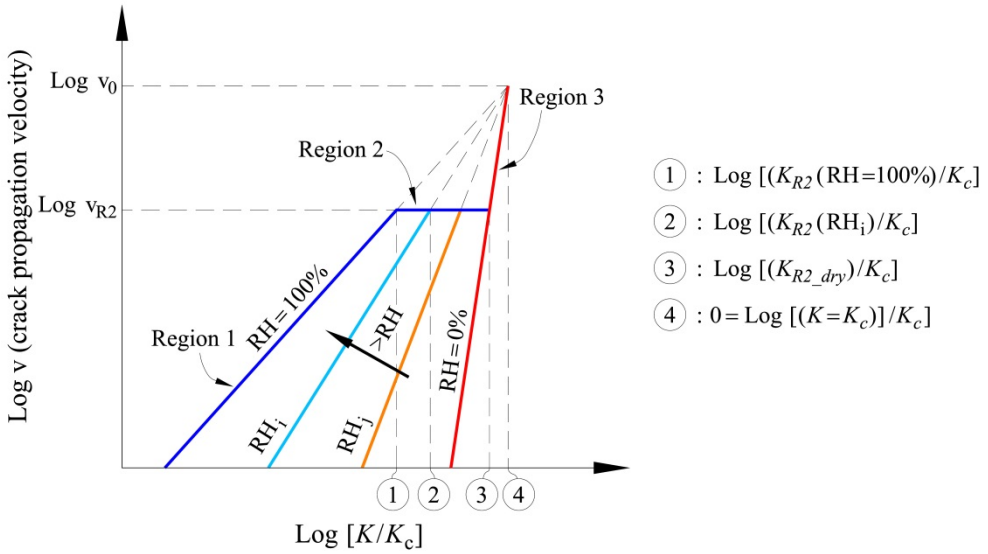

Figure 7-16 Subcritical Crack Propagation Model with common Region 2 (Model 2).

a) For Region 1: 0 ≤ RH ≤ 100% and $K \le K_{R2}(RH)$:

$$v = v_0 * \left(\frac{K}{K_c} \right)^{n(RH)} \tag{7:13}$$

where:
v is the velocity of the crack propagation for a given RH condition;
K is the stress intensity factor (Mode I);
v_0 is a reference velocity for the material. This is a parameter of the model;
K_c is the toughness of the material. This is a parameter of the model;
n(RH) is the subcritical crack propagation index or stress corrosion index that depends on the relative humidity and is calculated as indicated in section 7.3.2.4. It corresponds to the slope of the straight line of the relation Log (K/K_c) – Log (*v*);
$K_{R2}(RH)$ is the value of the stress intensity factor for a given RH condition when v= v_{R2} and is calculated as follows:

$$K_{R2}(RH) = K_c * \left(\frac{v_{R2}}{v_0} \right)^{\frac{1}{n(RH)}} \tag{7:14}$$

v_{R2} is a reference velocity for the material that limits Region 1 and Region 2. For this model, the value does not depend on the RH. This is a parameter of the model;

b) For Region 2: 0 ≤ RH ≤ 100% and $K_{R2(RH)} \leq K \leq K_{R2\_dry}$:

$$v = v_{R2} \tag{7:15}$$

where:
K_{R2_dry} is the value of the stress intensity factor for RH=0% condition when v= v_{R2}. For this model, this value does not depend on the RH. It is calculated as follows:

$$K_{R2\_dry} = K_c * \left(\frac{v_{R2}}{v_0} \right)^{\frac{1}{n(RH=0\%)}} \tag{7:16}$$

v_{R2} is a reference velocity for the material that limits Region 1 and Region 2. For this model, this value does not depend on the RH. This is a parameter of the model;
n(RH=0%) is the subcritical crack propagation index or stress corrosion index when RH=0% and is calculated as indicated in section 7.3.2.4;

c) For Region 3: 0 ≤ RH ≤ 100% and $K_{R2\_dry} \leq K \leq K_c$:

$$v = v_0 * \left(\frac{K}{K_c} \right)^{n(RH=0\%)} \tag{7:17}$$

where:
n(RH=0%) is the subcritical crack propagation index or stress corrosion index when RH=0% and is calculated as indicated in section 7.3.2.4;

In this model, K_c, v_0 and v_{R2} are constants and parameters of the model.

As in the previous model, all the parameters can be found in the subcritical crack propagation tests. K_0 has not been considered here but if it was found in the tests, then the velocity of crack propagation in Region 1 would be calculated for the range $K_0 \leq K \leq K_{R2(RH)}$. For $K < K_0$ no crack propagation occurs.

7.3.2.3 Model 3: Simplified model for Subcritical Crack Propagation behaviour (used in the DEM tests)

This model is a simplification of models 1 and 2. It has been proposed because in the review of experimental tests of subcritical crack propagation on rocks, most of the results (almost all) of the *K-v* behaviour fall in Region 1 or in Region 3; points in Region 2 were apparently sometimes found in a high crack velocity for tests in environmental conditions involving water vapour, for instance in tests on quartz specimens, and some granite and dolerite specimens (Atkinson, 1984). Region 2

seems to be difficult to capture.

For this reason, this model proposes a unique region (Region 1) for describing the *K*-*v* behaviour for the subcritical crack propagation under stress corrosion (see **Figure 7-17**).

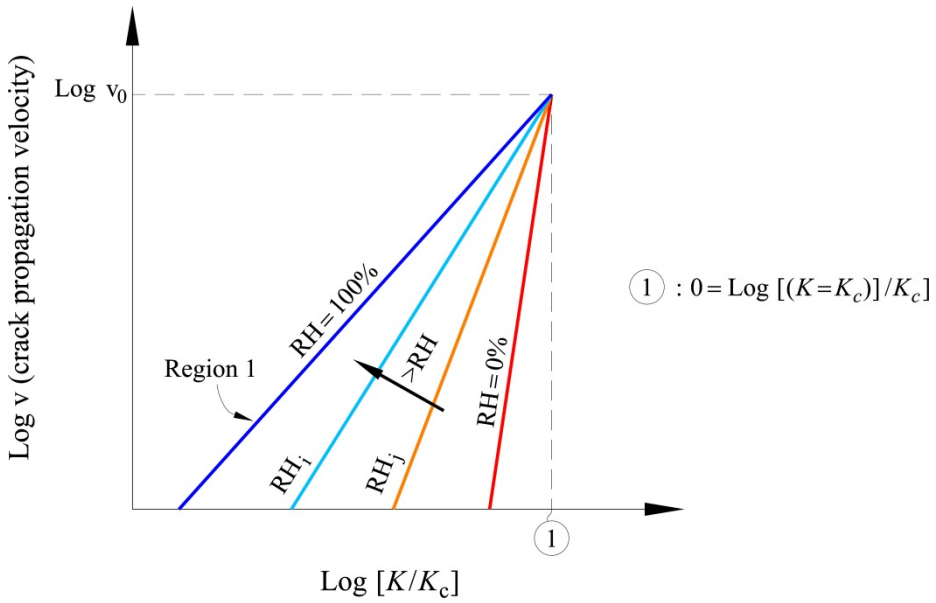

Figure 7-17 Simplified Subcritical Crack Propagation Model (Model 3). Model used in the DEM tests.

Unique Region 1: 0 ≤ RH ≤ 100% and $K \leq K_c$:

$$v = v_0 * \left(\frac{K}{K_c} \right)^{n(RH)} \tag{7:18}$$

where:
v is the velocity of the crack propagation for a given RH condition;
K is the stress intensity factor (Mode I);
v_0 is a reference velocity for the material. This is a parameter of the model;
K_c is the toughness of the material. This is a parameter of the model;
n(RH) is the subcritical crack propagation index or stress corrosion index that depends on the relative humidity and is calculated as indicated in section 7.3.2.4. It corresponds to the slope of the straight line of the relation Log (K/K_c) – Log (*v*).

In this model, K_c and v_0 are constants and parameters of the model. These parameters can be found from the subcritical crack propagation tests (for instance, the Double Torsion testing method). K_0 has not been considered here but if it was found in the tests, then the velocity of crack propagation in Region 1 would be calculated for the range $K_0 \leq K \leq K_{R2}(RH)$. For $K < K_0$ no crack propagation occurs.

7.3.2.4 Calculation of n index

Atkinson (1984) created a compendium of test results of subcritical crack propagation (in Mode I-Tensile) for different geological materials, comparing properties such as toughness $K_{c,}$ and calculated values of subcritical crack growth index *n* of the Charles's law (Charles, 1958a, 1958b) for different rocks in different environmental conditions of humidity and temperature.

Table 7-2 shows data results of this compilation and complemented data results from others authors (Atkinson, 1984, 1979a; Meredith and Atkinson, 1983; Nara et al., 2013, 2011, 2010, 2009; Swanson, 1984; Wiederhorn et al., 1982). When *K*-*v* curves were available in the references, the *n* values were calculated again based on these *K*-*v* curves (*n* is the slope of the "log *K*- log *v*" straight line in Region 1): the original value of *n,* which was presented in the reference, was written between parentheses in these cases. Furthermore, it took into account the environmental conditions in terms of relative humidity (RH) around the crack for all the tests: For cases where the RH was not specified, RH=100% was assigned for samples immersed in liquid water and RH=30% for dry conditions. Additionally, when only the pressure of water vapour and temperature had been reported, the RH was calculated as follows:

$$RH = \left(\frac{p_v}{p_{vs}} \right) * 100\% \tag{7:19}$$

$$Log_{10}\left[p_{vs} \right] = \left(7.5 * \frac{T(^oK) - 273.15}{T(^oK) - 35.85} + 2.7858 \right) \tag{7:20}$$

where:

p_v is the partial pressure of water vapour or actual vapour pressure at the temperature *T*;
p_{vs} is the equilibrium vapour pressure of water at the same temperature T or the saturation vapour pressure; p_{vs} is given in (Pa) for equation (7:20);
T is the temperature in Kelvin degrees.

Most of the subcritical crack propagation tests (Mode I), whose data results are shown in **Table 7-2**, were performed at room temperature between 20ºC and 25 ºC using the Double Torsion (DT) testing method (Atkinson, 1984; Meredith and Atkinson, 1983; Outwater et al., 1974; Swanson, 1984; Williams and Evans, 1973).

Similarly, **Table 7-3** shows the calculated *n* values for the data results for the materials presented in **Figure 7-12**, compilation data presented by Oldecop and Alonso (2007). The values of *n* were calculated based on the *n*-curves proposed by the authors.

Table 7-2 Compilation of subcritical crack growth parameters for geological materials in mode I (Adapted/Modified from Atkinson (1984) and others: complemented data from (Atkinson, 1984, 1979a; Meredith and Atkinson, 1983; Nara et al., 2013, 2011, 2010, 2009; Swanson, 1984; Wiederhorn et al., 1982)). Calculated n values from *K*- v curves; original value of *n* -presented in the reference- is written between parentheses. Subcritical crack propagation tests: DT is Double Torsion; 3PB is Three Point Bend.

MATERIAL		Environment Conditions and reference	T (^{o} C)	n	RH (%)	K_c (MPa.m$^{0.5}$)	Test
Quartz Rock	Tennessee Sandstone (Q1)	Air, 30% RH (Atkinson, 1984)	20	17.2	30	0.45	DT
		Water (Atkinson, 1984)	20	13.7	100		DT
	Arkansas Novaculite (Q2)	Water (Atkinson, 1980)	20	25	100	1.34	DT
	Mojave Quartzite (Q3)	Water (Atkinson, 1984)	20	34	100	2.1	DT
			40	39.1	100		DT
Calcite Rock	Falerans Micrite (C1)	Air (Henry and Paquet, 1976)	20	130	30	1.01	3PB
		Water + $CaCO_3$ (Henry and Paquet, 1976)	20	23 (26)	100		
	Solnhofen Limestone (C2)	Carbonated water (Atkinson, 1984)	20	25 (26)	100	1.01 (Perpen-dicular); 0.87 (parallel)	DT
	Carrara Marble (C3)	Air, 30% RH (Atkinson, 1984)	20	20 (18.8)	30	0.64	DT
		Water (Atkinson, 1984)	20	15 (15.3)	100		DT
	St. Pons Marble (C4)	Water , Direction #1 (Henry and Paquet, 1976). #1 and #3 are perpendicular	20	24 (26-29)	100	0.70 (parallel to foliation) 1.39; 1.07 (perpen-dicular)	3PB
		Water , Direction #3 (Henry and Paquet, 1976). #1 and #3 are perpendicular	20	23 (26-29)	100		
Basic Rock	Black Gabbro (B1)	Air, 30% RH (Atkinson and Rawlings, 1981)	20	32.1	30	2.88	DT
		Water (Atkinson and Rawlings, 1981)	20	28.6	100		
	Ralston Basalt (B2)	Air, 28-45% RH (Meredith and Atkinson, 1983; Swanson, 1984)	20	70.7 (44.4-97)	36,5	2.58	DT
		Water (Meredith and Atkinson, 1983)	20	23.5	100		DT

(continuation 1/4 of **Table 7-2**)

MATERIAL		Environment Conditions and reference	T (° C)	n	RH (%)	K_c (MPa.m$^{0.5}$)	Test
Basic Rock	Ralston Basalt (B2)	Air, 40-50% RH (Swanson, 1984)	20	97	45	-	DT
	Kinosaki Basalt (B3)	Air (Waza et al., 1980)	30	34	30	-	-
		Water (Waza et al., 1980)	25	33	100		
	Whin Sill Dolerite (B4)	Air, 30% RH (Meredith and Atkinson, 1983)	20	31.2	30	3.28	DT
		Water (Meredith and Atkinson, 1983)	20	29	100		DT
	Murata Basalt (B5)	Air (Sano and Ogino, 1980)	20	22	30	-	-
Interme-diate Rock	Kumamoto Andesite (A1A)	In air, RH=44%, water vapour pressure: 570 Pa (Nara et al., 2009)	10.9	39.7	44	2.1	DT
		In distilled water, pH=6 (Nara et al., 2009)	11.9	34.8	100		DT
	Kumamoto Andesite (A1B)	Air, RH=25%, water vapour (Nara et al., 2010)	16.9	60.3 (58)	25		DT
		Air, RH=55%, water vapour (Nara et al., 2010)	19.9	58.2 (61)	55		DT
		Air, RH=90%, water vapour (Nara et al., 2010)	19.9	41.4 (45)	90		DT
	Kumamoto Andesite (A1C)	In air, RH=49-52% (Nara et al., 2013)	54.9	47 (47)	50.5		DT
		In distilled water, pH=5 (Nara et al., 2013)	54.9	28 (28)	100		DT
	Kumamoto Andesite (A1D)	In air, RH=50% (Nara et al., 2013)	72.9	40 (40)	50		DT
		In distilled water, pH=5 (Nara et al., 2013)	72.9	22 (22)	100		DT

(continuation 2/4 of**Table 7-2**)

MATERIAL		Environment Conditions and reference	T (^{o} C)	n	RH (%)	K_c (MPa.m$^{0.5}$)	Test
Granitic Rock	Westerly Granite (G1)	Toluene, 11.3% RH (Swanson, 1980)	20	51	11.3	-	DT
		Air, 30% RH (Atkinson and Rawlings, 1981)	20	39.1	30	1.74	DT
		Water (Atkinson and Rawlings, 1981)	20	34.8	100		DT
		Air, 40-50% RH (Swanson, 1984)	20	69	45	-	DT
		Water (Swanson, 1980)	20	53	100	-	DT
	Yugawara Andesite (G2)	Air (Waza et al., 1980)	25	31	30	-	-
		Water (Waza et al., 1980)	25	26	100	-	-
	Oshima Granite (G3)	Air (Sano and Ogino, 1980)	20	30	30	-	-
	Oshima Granite (G3A)	In air, RH=44%, water vapour pressure: 570 Pa; Orientation 3-2 (Nara et al., 2009)	10.9	70.2	44	2.15	DT
		In distilled water (Nara et al., 2009)	10.9	49.4	100		DT
	Oshima Granite (G3B)	In air, RH=22-26%, water vapour; Cracks always propagated in a direction normal to the grain plane and parallel to the rift plane (Nara et al., 2010)	21.9	91.2 (75)	24		DT
		In air, RH=88-91%, water vapour; Cracks always propagated in a direction normal to the grain plane and parallel to the rift plane (Nara et al., 2010)	19.9	53.9 (65)	89.5		DT
	Oshima Granite (G3C)	In air, RH=2%; Orientation 2-3 (Nara et al., 2013)	55.4	69 (69)	2		DT
		In air, RH=71%; Orientation 2-3 (Nara et al., 2013)	55.4	49 (49)	71		DT

(continuation 3/4 of **Table 7-2**)

MATERIAL		Environment Conditions and reference	T (° C)	n	RH (%)	K_c (MPa.m$^{0.5}$)	Test
Granitic Rock	Oshima Granite (G3C)	In air, RH=86%; Orientation 2-3 (Nara et al., 2013)	55.4	41 (41)	86	2.15	DT
		In distilled water, pH=5-7; Orientation 2-3 (Nara et al., 2013)	55.4	36 (36)	100		DT
	Oshima Granite (G3D)	In air, RH=2%; Orientation 2-1 (Nara et al., 2013)	56.9	80 (80)	2		DT
		In air, RH=71%; Orientation 2-1 (Nara et al., 2013)	56.9	61 (61)	71		DT
	Lac du Bonnet Granite (G4)	Air (Wilkins, 1980)	20	58.5	30	-	-
		Air (Wilkins, 1980)	20	55.9	30	-	-
	Inada Granite (G5)	In air, RH=53%; Orientation 2-1 (Nara et al., 2013)	19.9	59 (59)	53	1.89	DT
		In distilled water, pH=7-8; Orientation 2-1 (Nara et al., 2013)	19.9	43 (43)	100		DT
Sedi-mentary Rock	Devonian Shale (S1)	Air, 40-50% RH (Swanson, 1984)	20	82.6 (80)	45	-	DT
	Kushiro Sandstone (S2)	In air, RH=21-25%; Cracks propagated parallel to the bedding plane (Nara et al., 2011)	17.9	44 (44)	23	0.89	DT
		In air, RH=54-55%; Cracks propagated parallel to the bedding plane (Nara et al., 2011)	19.9	35 (35)	54.5		DT
		In air, RH=85-88%; Cracks propagated parallel to the bedding plane (Nara et al., 2011)	19.9	26 (26)	86.5		DT
	Shirahama Sandstone (S3)	In air, RH=53-56%; Cracks propagated parallel to the bedding plane (Nara et al., 2011)	19.9	37 (37)	54.5	0.73	DT
		In air, RH=90-92%; Cracks propagated parallel to the bedding plane (Nara et al., 2011)	19.9	30 (30)	91		DT

(continuation 4/4 of **Table 7-2**)

MATERIAL		Environment Conditions and reference	T (^{o} C)	n	RH (%)	K_c (MPa.m$^{0.5}$)	Test
Quartz (Mineral)	Natural Quartz (QM1)	RH=62.5% A plane, normal to r (Bruner, 1980). See **Figure 7-10**	20	47 (-)	62.5	-	-
		RH=62.5% A plane, normal to r (Bruner, 1980). See **Figure 7-10**	20	46 (-)	62.5		-
	Synthetic Quartz (QM2)	vacuum (0.1-0.5Pa) A plane, normal to z (Atkinson, 1984; Meredith and Atkinson, 1982)	20	40 (41)	0	1.0 (perpen-dicular to z) 0.85 (perpen-dicular to r)	DT
		Water vapour (300Pa) A plane, normal to z (Atkinson, 1984; Meredith and Atkinson, 1982)	20	18 (18)	12.83		DT
		Water vapour (2000 Pa) A plane, normal to z (Meredith and Atkinson, 1982)	20	13.3	85.56		DT
		Liquid Water; RH=100% A plane, normal to z (Atkinson, 1979a). See **Figure 7-10**	20	13 (-)	100		DT
		2N HCl A plane, normal to z (Meredith and Atkinson, 1982)	20	19.3	100	-	DT
Other	Soda-lime-silica Glass (OG)	RH: 0% (Wiederhorn et al., 1982)	20	41 (-)	0	-	-
		RH: 0.2% - 1% (Wiederhorn et al., 1982)	20	32 (-)	1	-	-
		Water, RH=100% (Wiederhorn et al., 1982)	20	17 (-)	100	-	-

Table 7-3 Calculated values of n for different geological materials based on the compilation of experimental results by Oldecop and Alonso (2007) and presented in **Figure 7-12**.

MATERIAL		Environment Conditions	n	RH (%)
Quartz Rock	Tennessee Sandstone (Q1)	Water	18	100
Calcite Rock	Carrara Marble (C3)	Air, 30% RH(Atkinson, 1984)	55	30
		Water	17	100
Basic Rock	Ralston Basalt (B2)	Air, 28% RH	60	28
		Water	27	100
Granitic Rock	Westerly Granite (G1)	Air, 30% RH	54	30
		Water	26	100
Quartz (Mineral)	Synthetic Quartz (QM2)	Vacuum	108	0
		13% RH	30	13
		Water	20	100
Other	Soda-lime-silica Glass (OG)	Vacuum	188	0
		1% RH	50	1
		10% RH	43	10
		30% RH	40	30
		Water	28	100

These experimental results suggest that *n* index is related to the environmental conditions in the crack propagation. For this reason, in this research the influence of the relative humidity on *n* values uses the compilation of stress corrosion experimental data, which is shown in **Table 7-2** and **Table 7-3** and carried out by Atkinson (1984), Oldecop and Alonso (2007) and others (Atkinson, 1984, 1979a; Meredith and Atkinson, 1983; Nara et al., 2013, 2011, 2010, 2009; Swanson, 1984; Wiederhorn et al., 1982).

It is important to highlight the fact that there could be dispersion of n values when they are obtained using different experimental techniques for the propagation of cracks in Mode I-Tensile: Double Torsion (for most of the tests), Three Point Bend; Double Cantilever Beam, etc. As previously mentioned, most of the results considered here are from Double Torsion tests.

Figure 7-18 shows *n*- RH correlations for different geological materials based on data results from literature, which are shown in **Table 7-2** and **Table 7-3**. **Figure 7-18a** illustrates all the results without any distinction between materials. We can see much dispersion in the results. For this reason, it is better to distinguish the

results for different types of material (see **Figure 7-18b)**. In **Figure 7-18b**, the *n*-RH results from **Table 7-3** have also been drawn using curves according to the type of material. We can observe that quartz and glass are in the lower part of the graph for wetted environment but the values of n increase significantly in the dry part (vacuum). **Figure 7-18c** shows the *n*-RH curves taking into account each type of geological material.

In order to analyze only the *n*-RH relation in rocks, the results of quartz and glass were removed from previous figures (see **Figure 7-19a**). **Figure 7-19b** shows only the *n*-RH curves calculated from the *n*-values found in **Figure 7-12** by Oldecop and Alonso (2007).

There is in fact a relationship between *n* index and the Relative Humidity RH. However, this relation also depends on the type of material. For rocks, especially limestone, whose behaviour is studied and modeled in this research, the following relationship *n*-RH may be obtained from **Figure 7-19a** and **Figure 7-19b**:

$$\mathrm{n} = 100 * e^{(-0.015*RH)} \tag{7:21}$$

This n-RH curve has been drawn in **Figure 7-18** and **Figure 7-19** in order to compare it with experimental results.

Thus, a higher relative humidity causes lower *n* values and a higher velocity of crack propagation. This *n* index is the exponent used in the previous models of subcritical crack propagation -Equations (7:8) to (7:18)- as has been explained above.

As already discussed, the relative humidity controls the rate of particle breakage in granular coarse aggregates.

Since the relative humidity around the fragments is associated with the total suction s_ψ, it can be argued that the total suction controls the particle breakage in coarse aggregates. Total suction s_ψ and relative humidity RH are related by the psychrometric law, as follows:

$$s_\Psi = -\frac{RT}{M_w}\rho_l \ln(RH) \tag{7:22}$$

where R=Gas constant=8.134 J/(mol ^oK) ; T = Temperature in ^oK; M_w= Molecular weight of water =0.018kg/mol; ρ_l = Density of liquid (water); RH= Relative Humidity.

The effects of changes in relative humidity in the oedometer and triaxial tests are discussed below.

(Fig. 7.18a.)

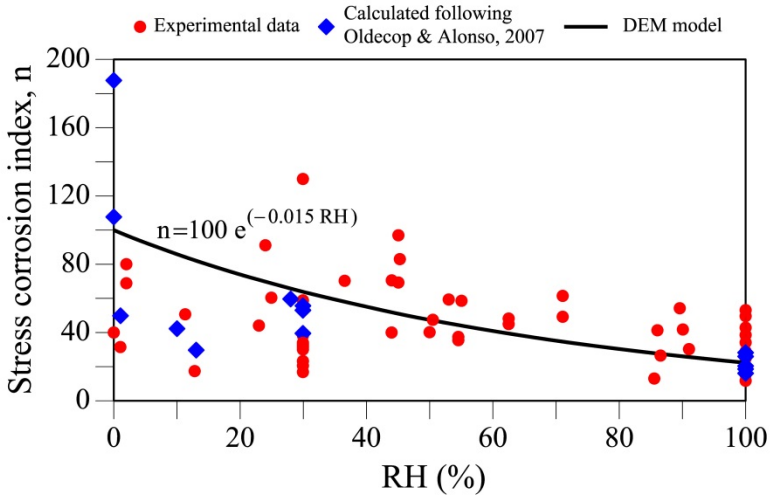

(Fig. 7.18b.)

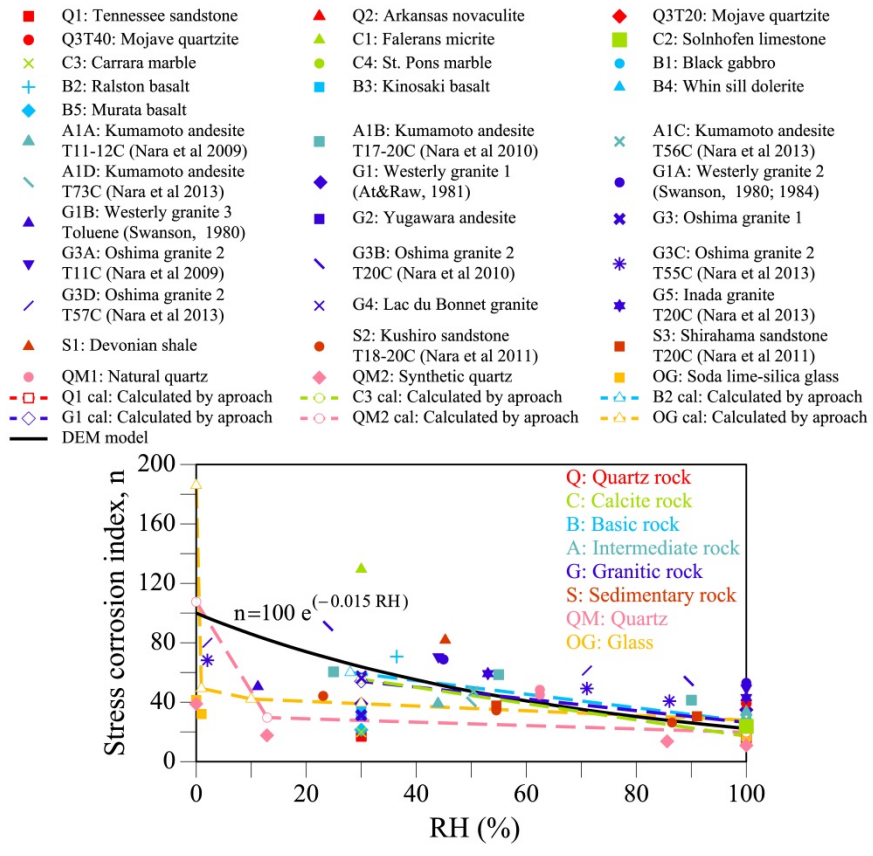

(Fig. 7.18c.)

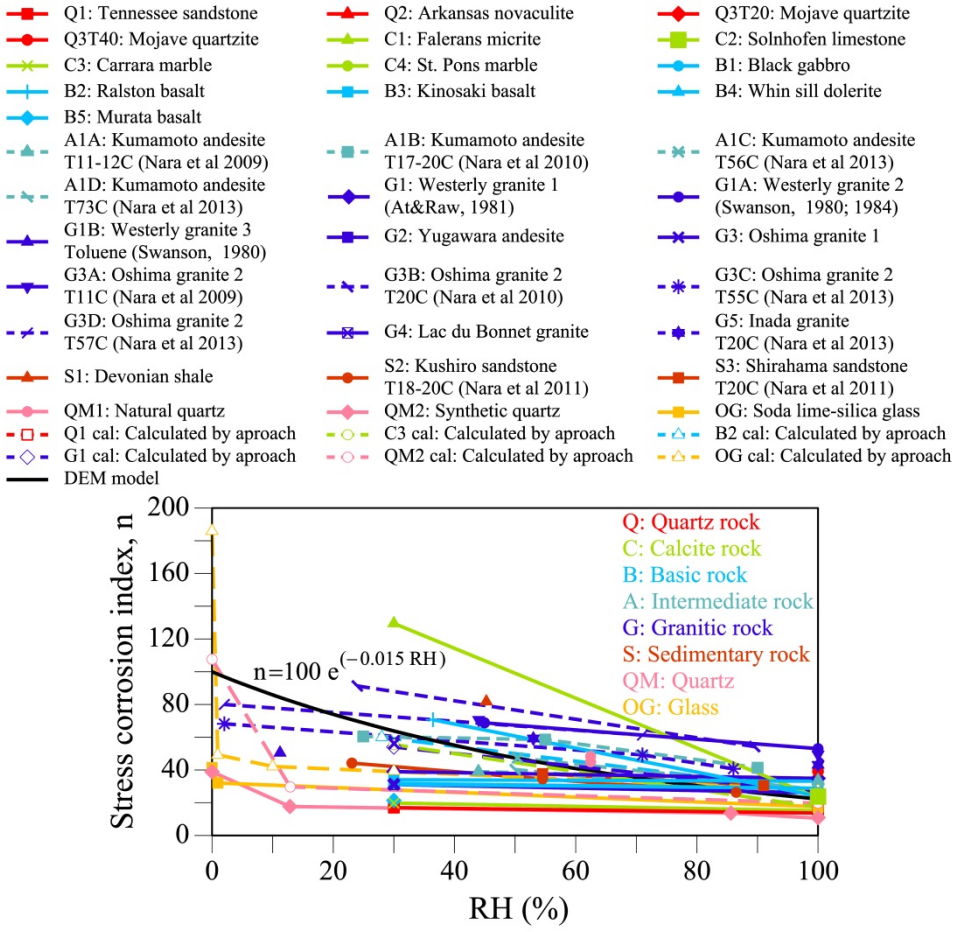

Figure 7-18 Correlation between stress corrosion index *n* and relative humidity RH for DEM model based on stress corrosion tests for different geological materials. Compiled experimental data from Atkinson, 1984, 1979a; Meredith and Atkinson, 1983; Nara et al., 2013, 2011, 2010, 2009; Oldecop and Alonso, 2007; Swanson, 1984; Wiederhorn et al., 1982. Comparison between *n*-RH model, experimental data and calculated *n* values from Oldecop and Alonso (2007). (a) *n*-RH experimental point data; (b) *n*-RH experimental point data taking into account the kind of geological material; (c) *n*-RH experimental curves taking into account each type of geological material.

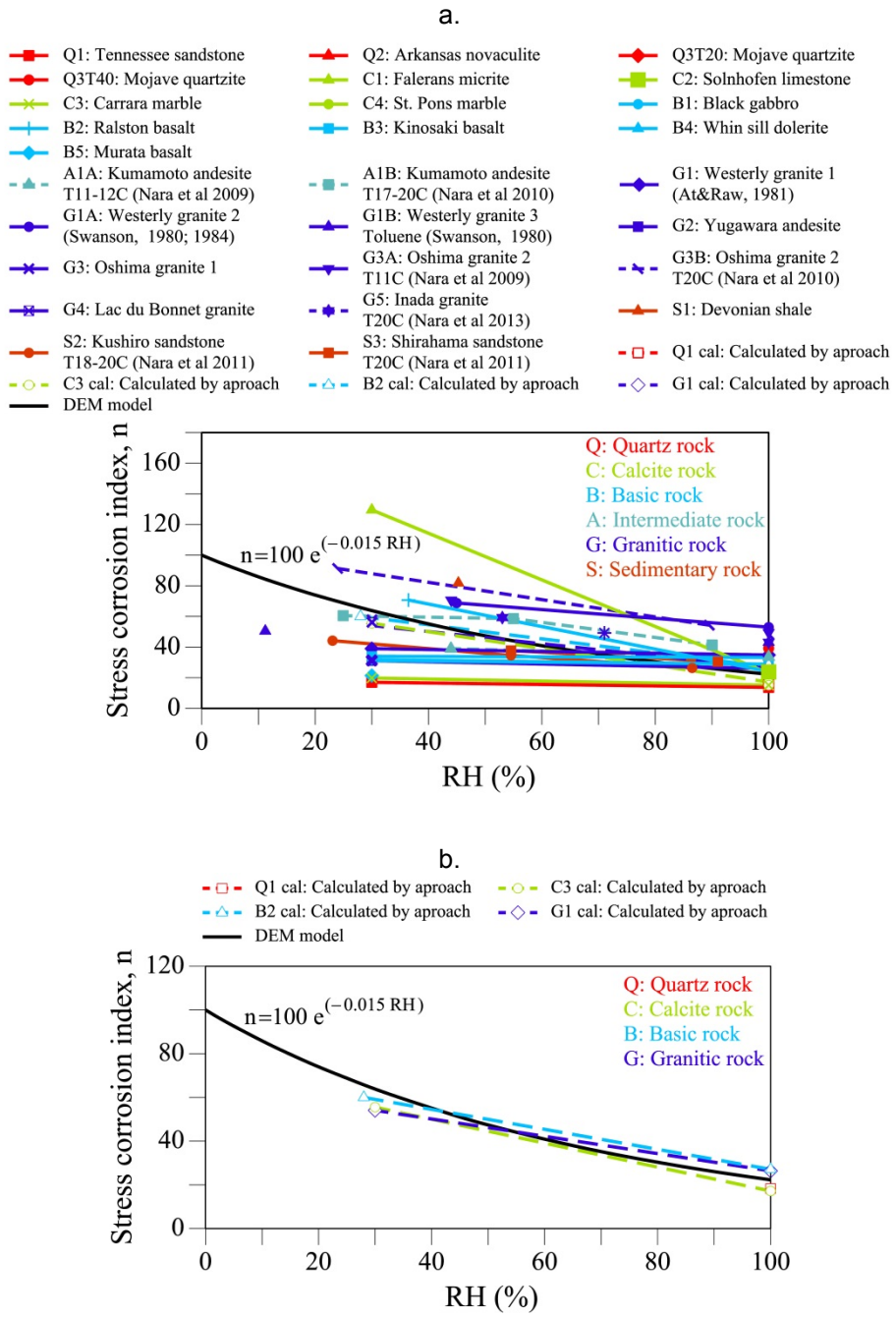

Figure 7-19 Correlation for rocks between stress corrosion index *n* and relative humidity RH for DEM model based on stress corrosion tests. Compiled experimental data from Atkinson, 1984, 1979a; Meredith and Atkinson, 1983; Nara et al., 2013, 2011, 2010, 2009; Oldecop and Alonso, 2007; Swanson, 1984; Wiederhorn et al., 1982. Comparison between *n*-RH model, experimental data and calculated n values from Oldecop and Alonso (2007). (a) *n*-RH experimental curves taking into account experimental data of rocks; (b) Taking into account the *n*-curves used by Oldecop and Alonso (2007).

7.3.3 Oedometer tests

Numerical oedometer tests (**Figure 7-8a**) were performed simulating the experimental tests from Ortega (2008) on limestone fragments (**Figure 7-3b**). A same vertical stress path was applied: 0.1; 0.2; 0.4; 0.6; 0.8; 1.2; 1.6; 2.0; 2.4; 2.8 MPa. A relative humidity of 10% was maintained during the loading path.

In order to keep any sudden increment load from leading to excessive overlap between macroparticles, the load was applied by small increments, allowing the sample some time to relax after these increments until the axial deformation was stabilized. Time effect will be discussed below.

After reaching the maximum vertical load of 2.8 MPa at RH=10% and getting a stabilized sample deformation, the relative humidity was increased up to 100%. RH=100% has the same effect as flooding the sample with liquid water until total saturation.

Two unloading paths were also performed: The first path was applied after the maximum vertical stress of 2.8 MPa at RH=10%. Unloading was applied by steps and it followed the same experimental vertical stress path: 2.4; 2.0; 1.6; 1.2; 0.8; 0.6; 0.4; 0.2 MPa. The second unload path was applied after imposing 100% RH at 2.8 MPa. The previous unloading path was also applied.

7.3.3.1 Compressibility behaviour

The compressibility curve is shown in **Figure 7-20** for the DEM simulation in the loading path in a log-"natural" graph: log-horizontal axis for vertical stress (σ_v); and "natural" axis for axial (vertical) strain (ε_a=ε_v). This curve illustrates a collapse due to the flooding of the sample (application of RH = 100%). The experimental compressibility curve can be appreciated in **Figure 7-21**: It is compared with the calculated DEM simulation. A very good approximation is discernible. At the end of the loading of 2.8 MPa for RH = 10%, the axial (vertical) strain (ε_a=ε_v) was 0.085 (8.5%) for the DEM simulation while it was 0.088 (8.8%) for the experimental test. At the end of the collapse, the axial strain was 0.130 (13.0%) for the DEM model and 0.133 (13.3%) for the experimental data.

Figure 7-22 illustrates the compressibility curves –for the DEM and experimental results- in a "natural" scale for both axes: vertical stress (σ_v) and axial (vertical) strain (ε_a=ε_v). In this figure, the curves seem more like straight lines. The unloading paths are also shown in **Figure 7-22**. At the end of the unloading path for σ_v =0.4 MPa, the experimental data did not show practically any recovery of axial strain for any unload path: ε_a =8.6% for RH=10%; and ε_a = 13.1% for RH=100%; i.e. recovered strain (elastic strain) = 0.2% for both cases. However, DEM simulations showed a certain recovery of axial strain: ε_a =5.5% for RH=10%, i.e. recovered strain (elastic strain) = 3.0%; and ε_a = 9.9% for RH=100%, i.e. recovered strain (elastic strain) = 3.1%; main recovered strain (elastic strain) = 3.0% for both cases. This elastic behaviour in DEM simulations could be caused by the elastic overlapping between macroparticles, and the plastic behaviour (not recovering

strain) follows from the breakage and rearrangement of particles. The actual results show that breakage and rearrangement control the compressibility behaviour in this assembly of hard limestone fragments.

The compressibility of the sample can be characterized by the compressibility index λ (slope of the curve ε_a – ln σ, and it is calculated by the following expression:

$$\lambda = \frac{d(\varepsilon_a)}{d(\ln \sigma)} \tag{7:23}$$

Figure 7-23 compares the compressibility index λ depending on the vertical stress applied σ_v to the DEM and experimental results. A good correlation for loads less than 2.4 MPa is observed. The DEM curve shows decreasing compressibility for σ_v ≥2.0 MPa. The average value of λ for loads between 1.2 and 2.0 MPa is 0.06 for the DEM case, while it is 0.05 for the experimental data. The maximum value of λ is 0.068 for DEM (it occurs for 1.6 MPa) while it is 0.078 for the experimental data (it occurs for 2.8 MPa).

On the other hand, regarding the deformability of the sample, the findings for the DEM results were as follows: the void ratio was 1.13 at the beginning of the test and 0.92 at the end of 2.8 MPa for RH=10% (see **Figure 7-24**). **Figure 7-24**a and **Figure 7-24**b illustrate respectively the curves *e*-*p* (void ratio – mean stress) and *e*-σ_v (void ratio – vertical stress): these curves show the collapse caused by the wetting of the sample while the vertical stress approximately 2.8 MPa is maintained (this load corresponds to a mean stress *p* between 1.7 for a final dry stage and 1.8 MPa for a final wetting stage); *e* decreases from 0.92 to 0.84 (RH=100%). The mean stress *p* was calculated as (σ_v +2 σ_h)/3 where σ_v is the vertical stress imposed to the sample and σ_h is the horizontal stress measured in the wall of the cylinder.

As the σ_h was measured in both the experimental and DEM tests, the lateral coefficients of earth pressure K_o was calculated for each load applied during the tests (see **Figure 7-25**). For the DEM test, K_o remained almost constant around 0.4, while for the experimental data K_o increased from close to 0 at the beginning up to a value of 0.32 at σ_v =2.8MPa for RH=10%. For σ_v >1MPa, the K_o behaviour was similar in both tests. For instance, at the end of the dry tests (RH=10%) at σ_v =2.8MPa, K_o was 0.43 for the DEM and 0.32 for the experimental data; after the wetting (RH=100%), K_o increased up to 0.48 for the DEM and 0.36 for the experimental data.

On the other hand, **Figure 7-26** shows the evolution of the porosity (n_o) in relation to the axial strain (ε_a) of the sample: For the dry part (RH = 10%), n_o varies from 0.53 at the beginning of the test to 0.48 in the final test of 2.8 MPa when axial strain becomes 0.085 (8.5%). After the wetting, the porosity decreases until it reaches a value of 0.45 when axial strain is around 0.13 (13%).

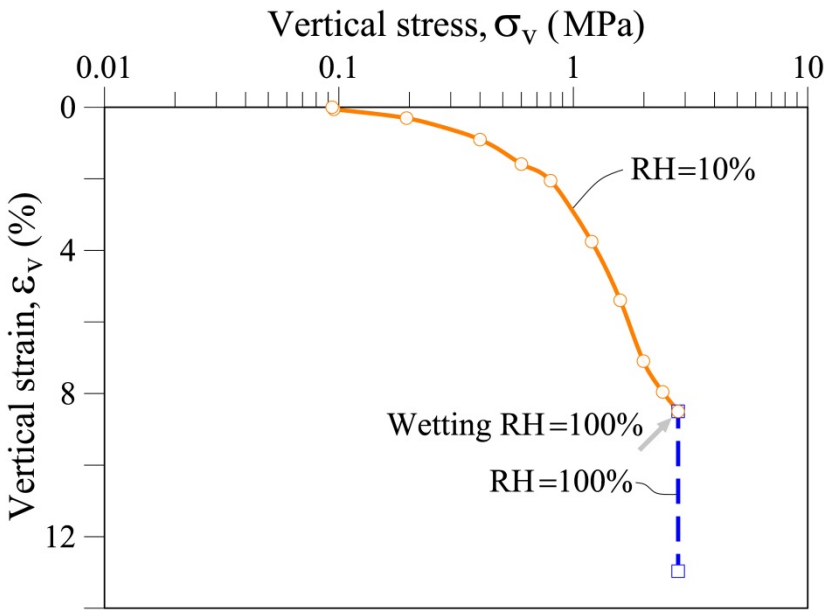

Figure 7-20 DEM simulation of oedometer test: Compressibility curve. DEM properties: μ=0.3; k_n=4 MN/m; K_c=1MPa•m$^{0.5}$.

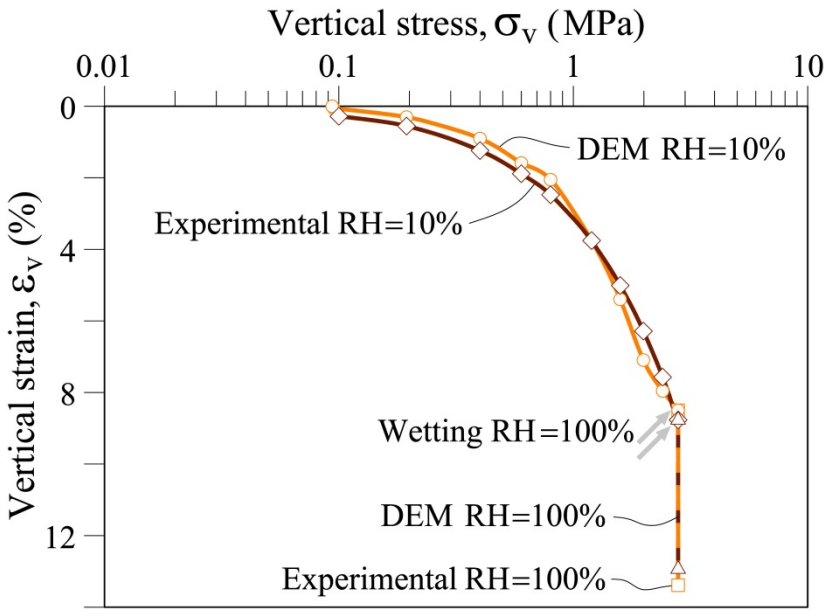

Figure 7-21 Compressibility curves: Comparison between DEM simulation and experimental oedometer test on limestone gravels. DEM properties: μ=0.3; k_n=4 MN/m; K_c=1MPa•m$^{0.5}$. Horizontal axis which corresponds to vertical stress is in a log scale.

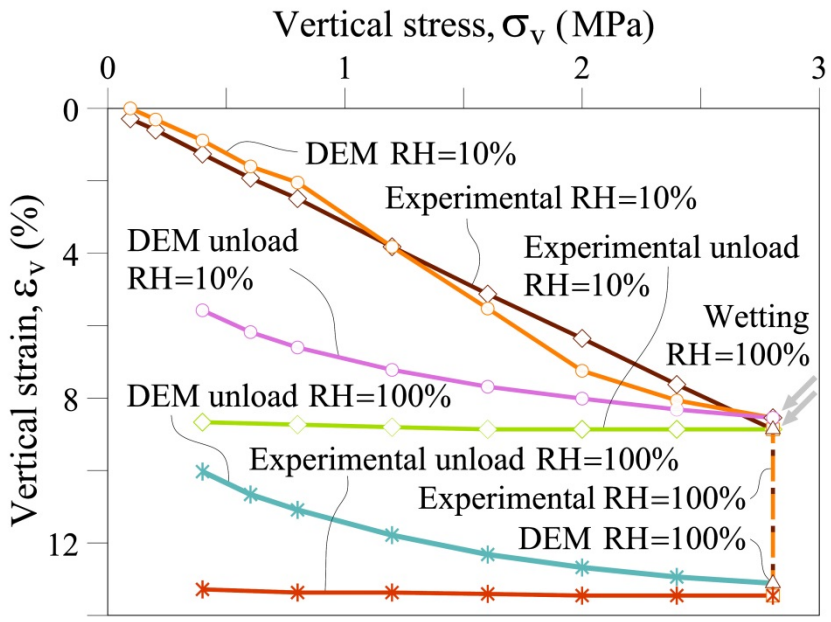

Figure 7-22 Compressibility curves – Loading and unloading paths: Comparison between DEM simulation and experimental oedometer test. DEM properties: μ=0.3; k_n=4 MN/m; K_c=1MPa•m$^{0.5}$. Horizontal and vertical axes which correspond to vertical stress and vertical strain are in a "natural" scale.

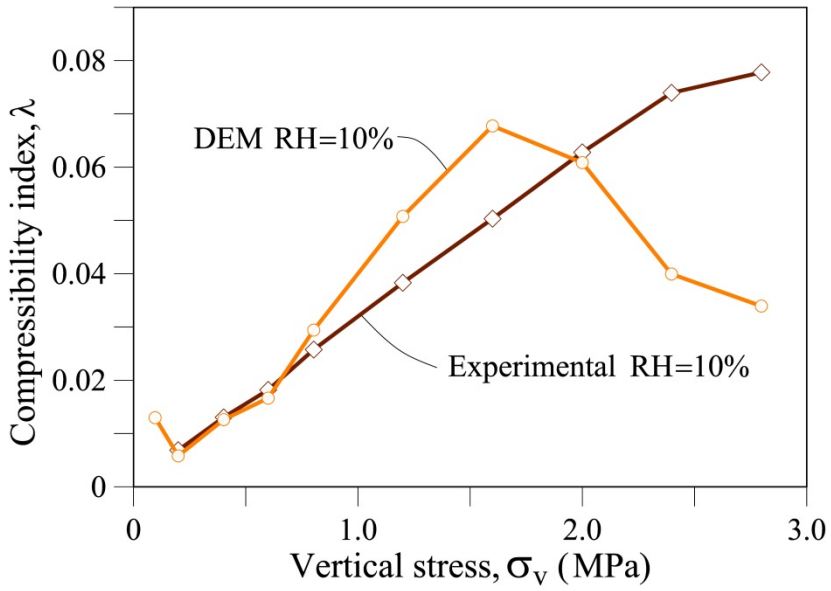

Figure 7-23 Evolution of compressibility index, λ: Comparison between DEM simulation and experimental oedometer test. DEM properties: μ=0.3; k_n=4 MN/m; K_c=1MPa•m$^{0.5}$. (RH=10%).

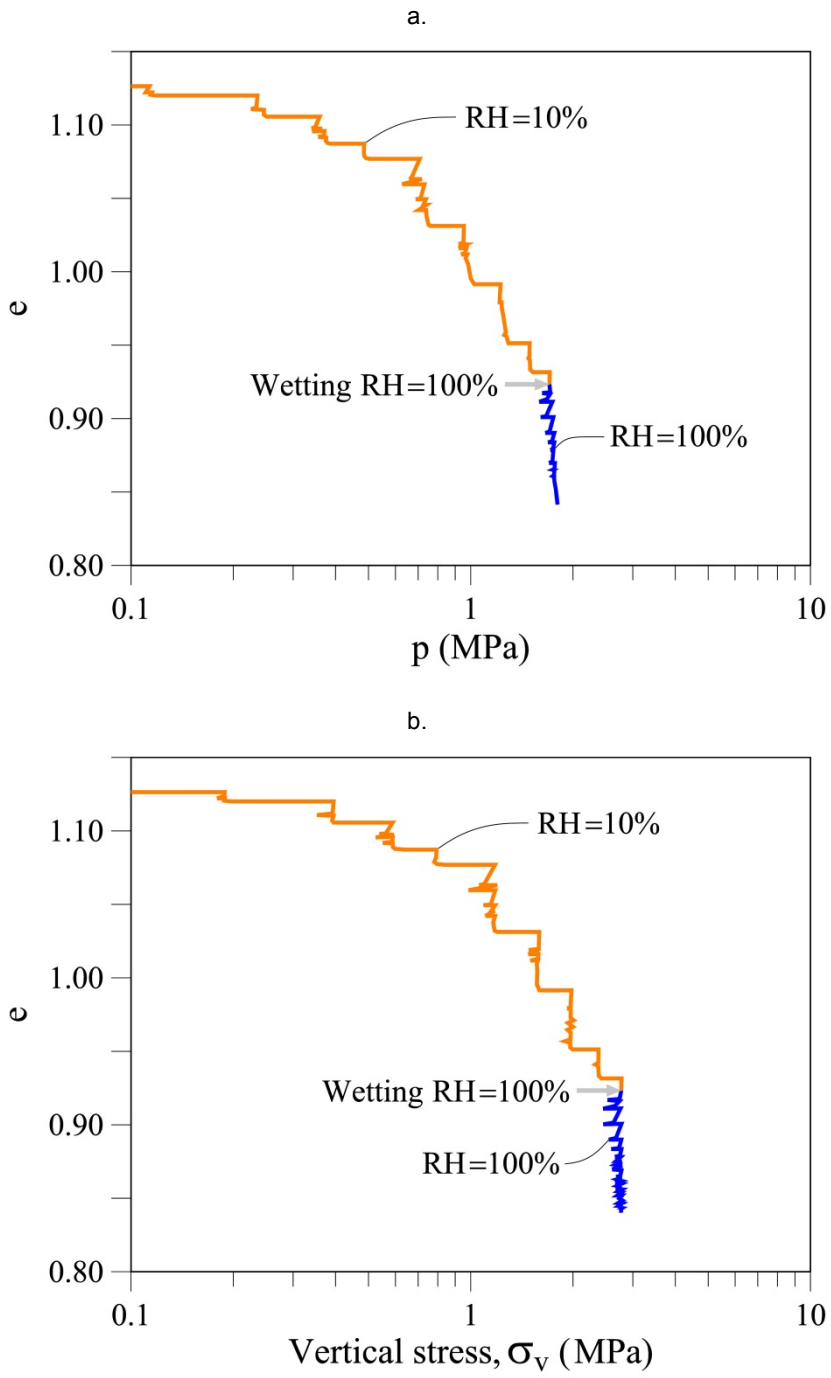

Figure 7-24 Compressibility curves: (a) *e*-*p*; (b) *e*-σ_v: DEM simulation of oedometer test. DEM properties: μ=0.3; k_n=4 MN/m; K_c=1MPa•m$^{0.5}$.

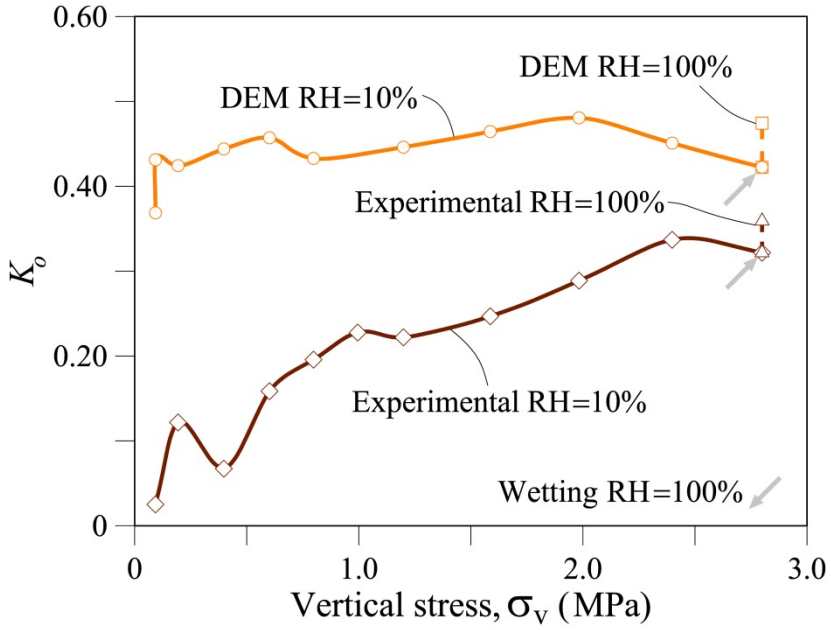

Figure 7-25 Evolution of K_o with applied vertical stresses – Relative Humidity Effect: DEM simulation of oedometer test. DEM properties: μ=0.3; k_n=4 MN/m; K_c=1MPa•m$^{0.5}$.

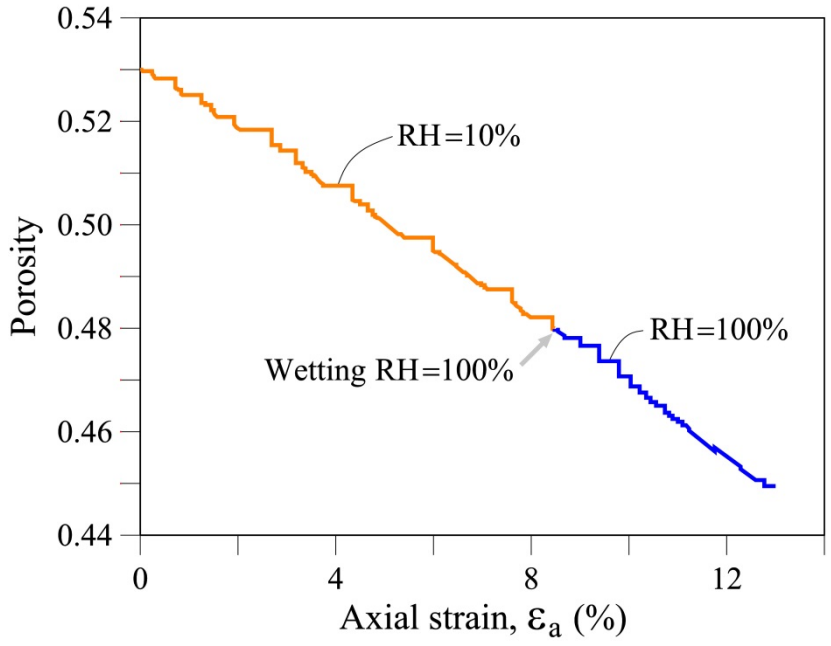

Figure 7-26 Evolution of porosity: DEM simulation of oedometer test. DEM properties: μ=0.3; k_n=4 MN/m; K_c=1MPa•m$^{0.5}$.

7.3.3.2 Particle breakage

Figure 7-27 illustrates a comparison of the following gsd curves: at the beginning of the DEM and experimental tests; at the end of applied load of 2.8 MPa with RH=10% for the DEM simulation; at the end of the flooding (RH=100%) with the imposed load of 2.8 MPa for the DEM simulation; and at the end of the experimental test (Ortega, 2008) after a 2.8MPa load applied for the fully saturated material. The DEM and experimental gsd are similar at the end of the tests and show the accuracy of the model.

Figure 7-28 shows the evolution of the DEM grading curves throughout the test after applying several vertical stresses for a constant value of the relative humidity, RH=10%. The evolution of these curves during the test shows the evolution of particle breakage depending on the applied load. Similarly, the evolution of breakage indexes of Hardin (B_r) and Marsal (B_g) in relation to applied load are observed in **Figure 7-29** and **Figure 7-30**. Calculated (DEM) values of 0.13 and 0.40 for B_r and B_g, respectively, were reached at the end of the vertical stress of 2.8 MPa for RH=10%. The wetting effect can also be seen: B_r and B_g increase up to values of 0.23 and 0.57 respectively when RH=100% is applied. Values of 0.25 for B_r and 0.56 for B_g were found for the experimental data at the end of the test, i.e. after RH=100% was imposed at a maximum vertical stress of σ_v=2.8MPa. The DEM results were very close to the experimental data.

Likewise, the evolution of the particle breakage can also be observed if we plot the retained weight by each equivalent sieve size after every load increment (see **Figure 7-31**). This figure shows that the number of original macroparticles (0.028m for the initial equivalent diameter) decreases during the test: They account for about 60% of the total weight at the end of the test for the dry stage RH=10% at σ_v=2.8MPa. Moreover, there are three macroparticle sizes that appear and stand out during the breaking process: 0.0235m, 0.019m and <0.014m (see **Figure 7-31**). This figure also illustrates the particle breakage caused by the wetting effect: when the sample is subjected to RH=100% while maintaining a load of 2.8 MPa, the evolution of the particle breakage which is reflected in the evolution of certain particle sizes continues with the same previous tendency. The number of original macroparticles (0.028m for the initial equivalent diameter) decreases until it reaches a value of 43% of the total weight at the end of the test (after the saturation of the sample RH=100% at σ_v=2.8MPa).

Another way to analyze the particle breaking process is to follow the evolution of the number of macroparticles inside the sample during the test (**Figure 7-32**): At the beginning of the test there were 471 particles, while at the end of the loading process (2.8 MPa) for RH = 10% there were 11307 particles when ε_a = 8.5%. The number of macroparticles increases to 21383 particles at the end of wetting process.

The number of initial macroparticles (clumps comprised of 14 microparticles 2.8cm in size) that are not broken during the test decreases from 471 at the beginning to 202 at the end with an applied load of 2.8 MPa for RH=10%. This number of unbroken macroparticles decreases until it reaches a value of 117 particles when the wetting is imposed (**Figure 7-33**).

Figure 7-34 and **Figure 7-35** also show the evolution of the total number of macroparticles and unbroken macroparticles respectively but depending on the applied load. These curves show more clearly the effect of wetting on the particle breakage.

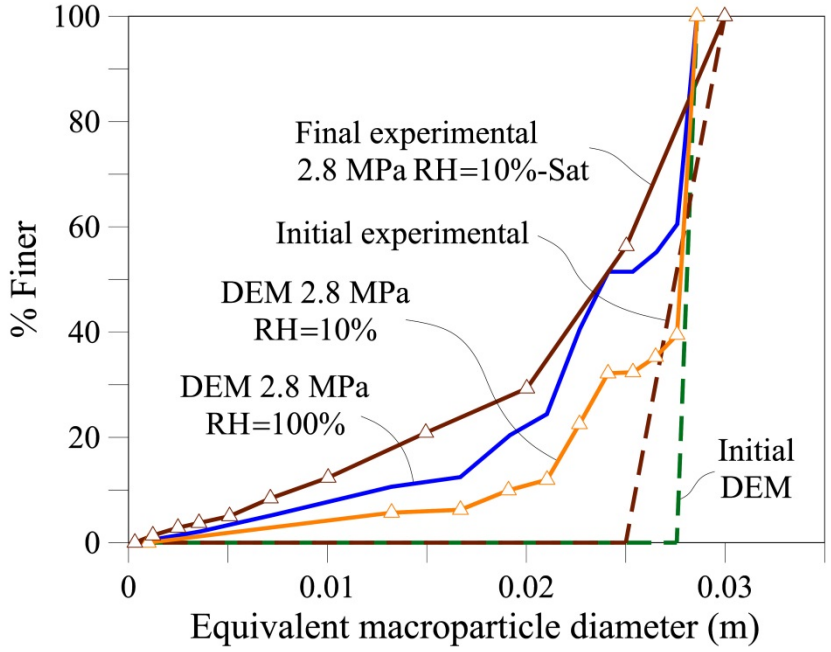

Figure 7-27 Evolution of grain (particle) size distribution: Comparison between DEM simulation and experimental oedometer test. DEM properties: μ=0.3; k_n=4 MN/m; K_c=1MPa•m$^{0.5}$.

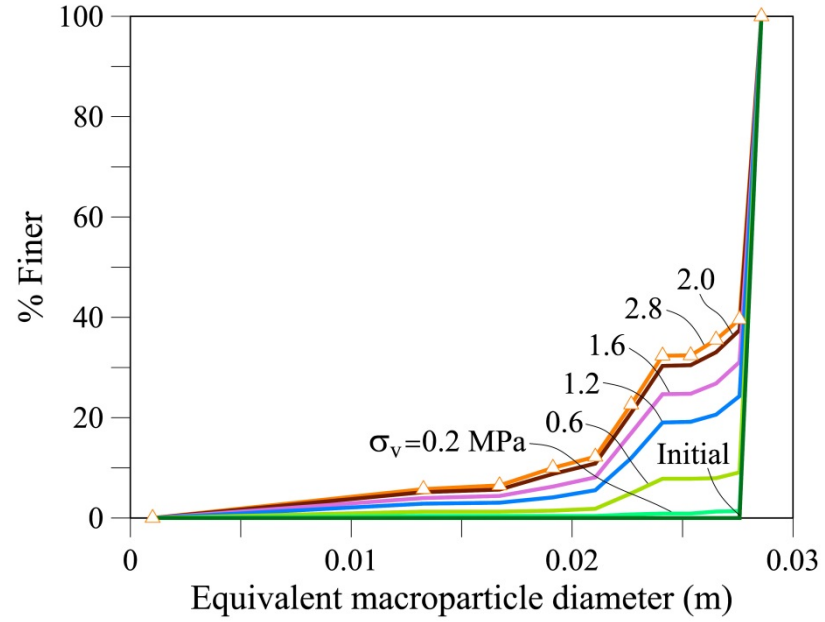

Figure 7-28 Evolution of grain (particle) size distribution for several applied loads (RH=10%): DEM simulation of oedometer test. DEM properties: μ=0.3; k_n=4 MN/m; K_c=1MPa•m$^{0.5}$.

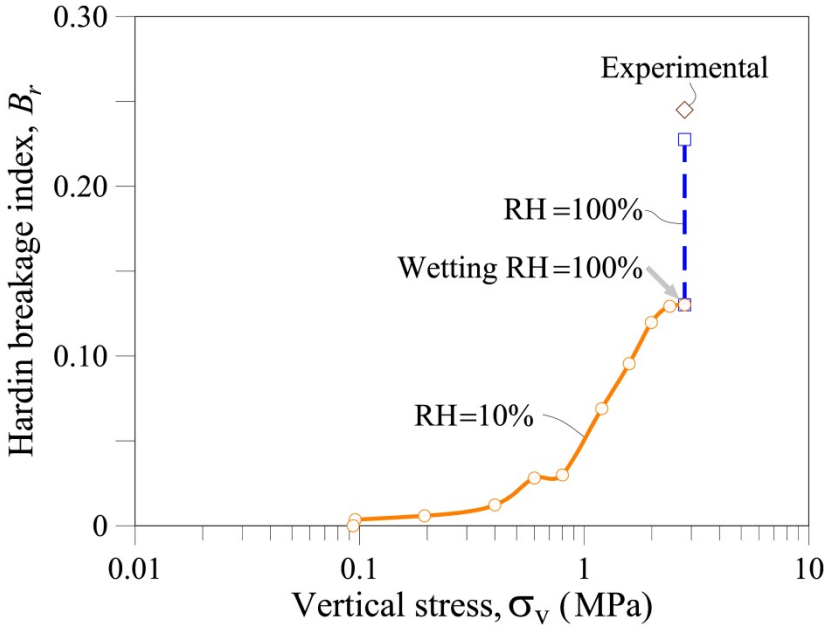

Figure 7-29 Evolution of Hardin breakage index – Relative Humidity Effect: DEM simulation of oedometer test. DEM properties: μ=0.3; k_n=4 MN/m; K_c=1MPa•m$^{0.5}$.

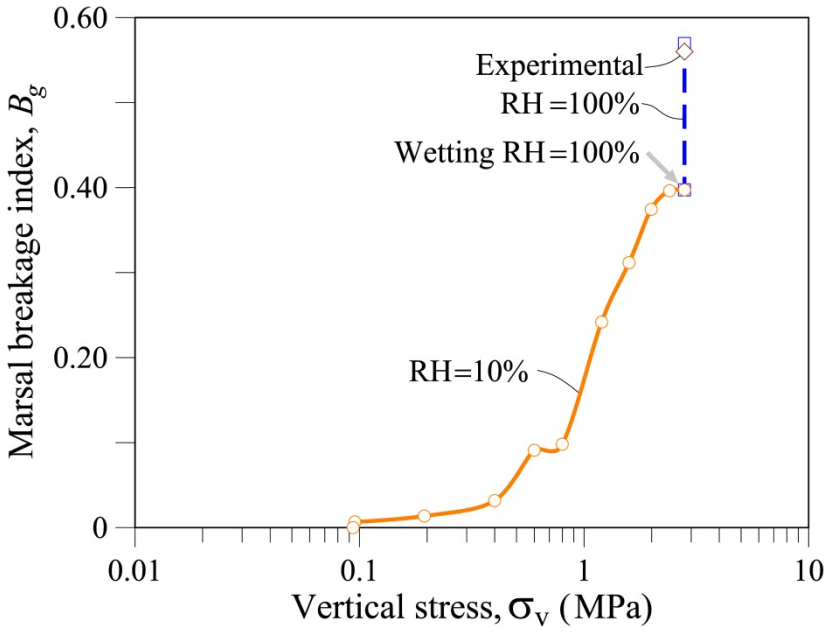

Figure 7-30 Evolution of Marsal breakage index – Relative Humidity Effect: DEM simulation of oedometer test. DEM properties: μ=0.3; k_n=4 MN/m; K_c=1MPa•m$^{0.5}$.

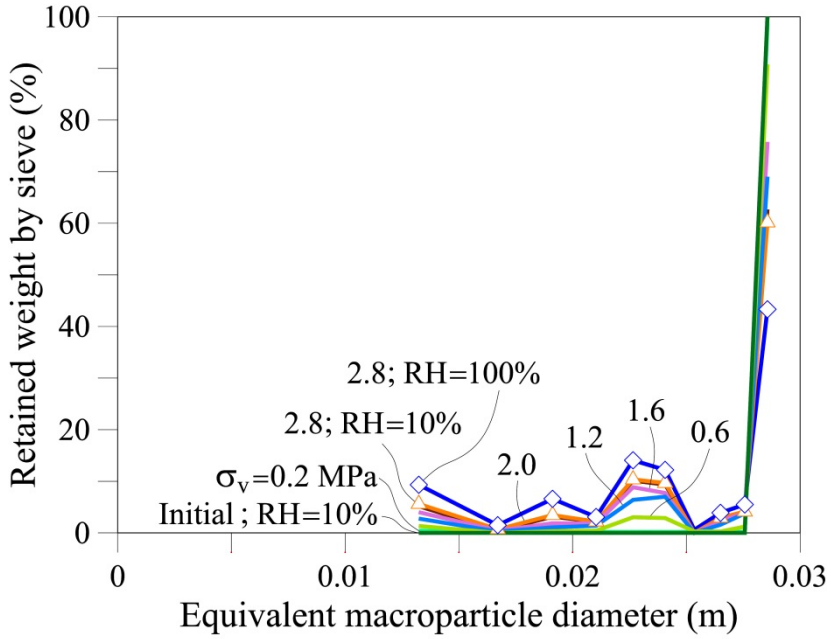

Figure 7-31 Evolution of macroparticle size: DEM simulation of oedometer test. DEM properties: μ=0.3; k_n=4 MN/m; K_c=1MPa•m$^{0.5}$.

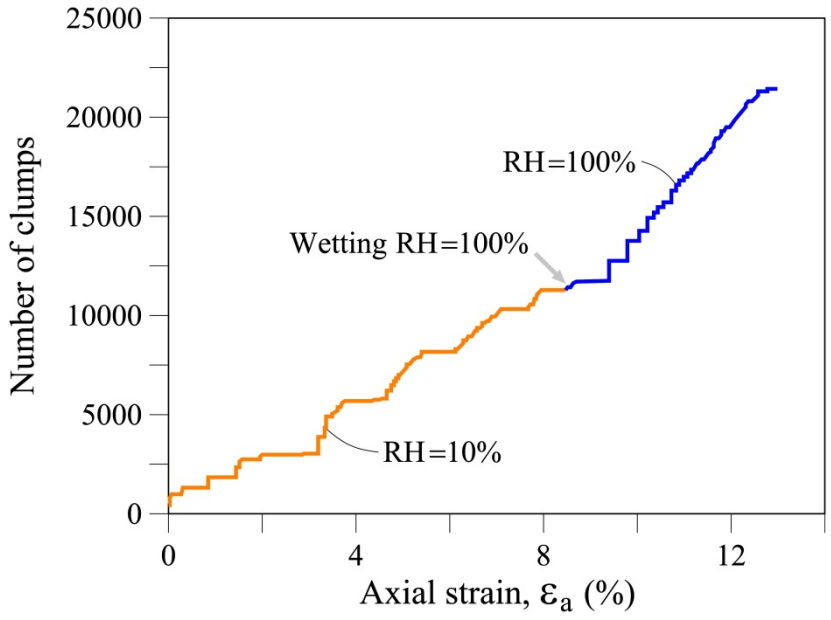

Figure 7-32 Evolution of number of macroparticles (clumps): DEM simulation of oedometer test. DEM properties: μ=0.3; k_n=4 MN/m; K_c=1MPa•m$^{0.5}$.

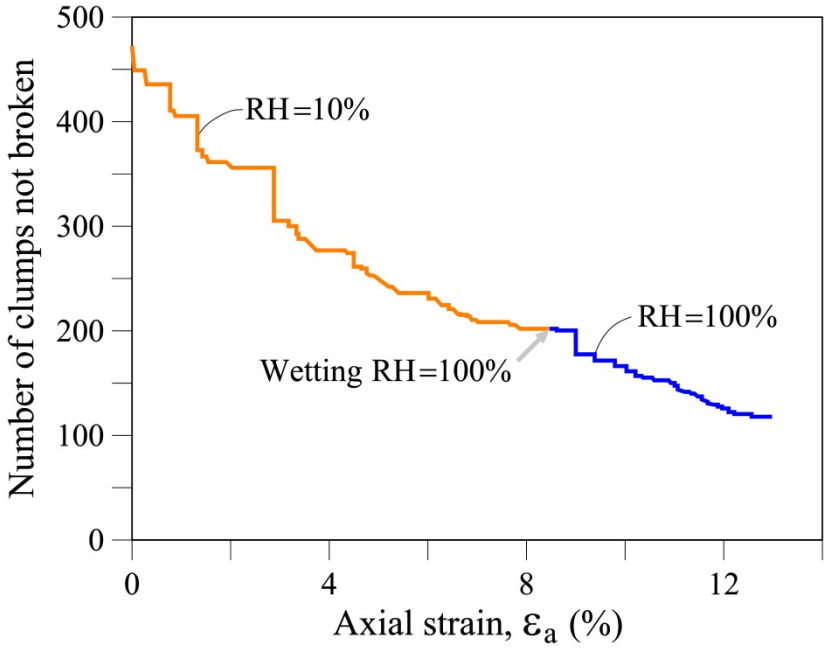

Figure 7-33 Evolution of number of macroparticles (clumps) not broken: DEM simulation of oedometer test. DEM properties: μ=0.3; k_n=4 MN/m; K_c=1MPa•m$^{0.5}$.

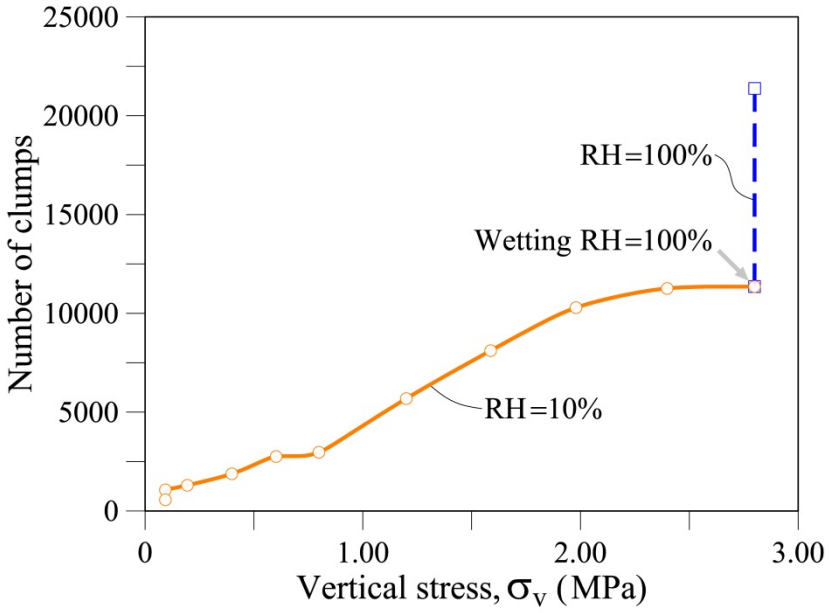

Figure 7-34 Evolution of Number of Macroparticles (Clumps) with applied vertical stresses – Relative Humidity Effect: DEM simulation of oedometer test. DEM properties: μ=0.3; k_n=4 MN/m; K_c=1MPa•m$^{0.5}$.

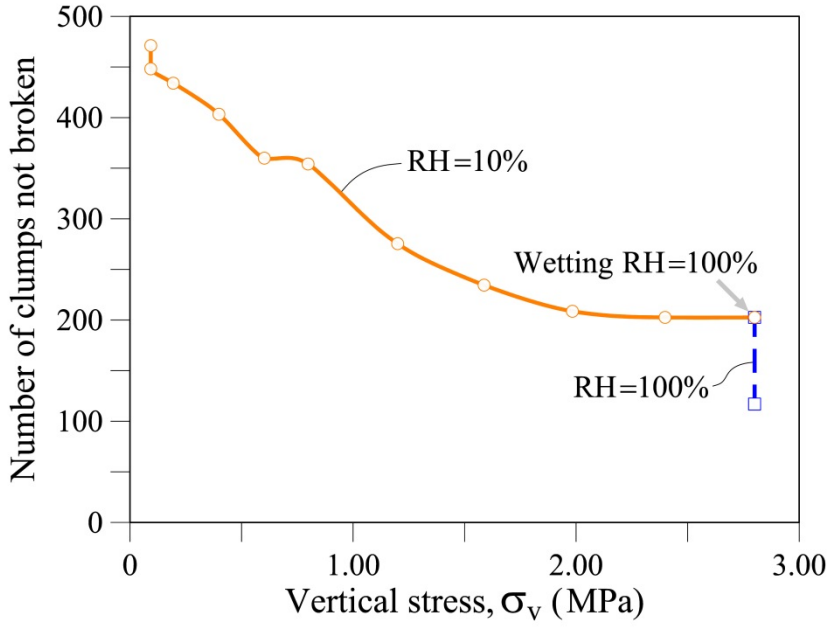

Figure 7-35 Evolution of Number of Macroparticles (Clumps) not broken with applied vertical stresses – Relative Humidity Effect: DEM simulation of oedometer test. DEM properties: μ=0.3; k_n=4 MN/m; K_c=1MPa•m$^{0.5}$.

7.3.3.3 Energy

An energy balance check for discrete element simulations is useful in order to investigate the evolution of energy input and dissipation behaviour and to check numerical instabilities, e.g. in a loading/deformation process.

Belytschko et al. (2000) argued that instabilities could lead to a “false” generation of energy and therefore also lead to a violation of the conservation of energy. O’Sullivan and Bray (2004) and O’Sullivan (2011) use the approach of Belytschko et al. (2000) for the energy balance check.

At each stage in a loading/deformation process, the law of energy conservation is given by (O’Sullivan and Bray, 2004; Wang and Yan, 2012):

$$E_{ext} = E_k + E_{\text{int}} \tag{7:24}$$

where:
E_{ext} = External energy of the system;
E_k = Kinetic energy of the system;
E_{int} = Internal energy of the system.

The energy terms can be calculated using an incremental approach (Itasca, 2008; O’Sullivan, 2011).

a. External energy, E_{ext}

$$E_{ext}^{t+\Delta t} = E_{bodyforce}^{t+\Delta t} + E_{externalappliedforces}^{t+\Delta t} + E_{w}^{t+\Delta t} \quad (7:25)$$

where:

$$E_{bodyforce}^{t+\Delta t} = E_{bodyforce}^{t} + \sum_{i=1}^{N_p} m_i g_i \Delta_i \quad (7:26)$$

$$E_{externalappliedforces}^{t+\Delta t} = E_{externalappliedforces}^{t} + \sum_{i=1}^{N_p} F_i^{applied} \Delta_i \quad (7:27)$$

$$E_{w}^{t+\Delta t} = E_{w}^{t} + \sum_{i=1}^{N_w} F_i \Delta u_i \quad (7:28)$$

$E_{ext}^{t+\Delta t}$: External energy of the system at time (t+Δt);

$E_{bodyforce}^{t+\Delta t}$; $E_{bodyforce}^{t}$: Energy associated with body forces, such as gravity, acting on the particles, at time (t+Δt) and (t) respectively. In our case, $E_{bodyforce}$=0;
N_p = Number of particles;
m_i = Mass of the particle i;
g_i = Vector of gravitational acceleration acting on i;
Δ_i = Incremental displacement of particle i;
$E_{externalappliedforces}^{t+\Delta t}$; $E_{externalappliedforces}^{t}$: Energy associated with any externally applied loads acting on the particles, at time (t+Δt) and (t) respectively. In our case, $E_{externalappliedforces}$=0;
$F_i^{applied}$ = Applied external force acting on i;

$E_{w}^{t+\Delta t}$; E_{w}^{t}: Work done on the system by the rigid boundaries, at time (t+Δt) and (t) respectively. In our case, E_w is the work done by all the walls on the sample (surfaces that confine the sample: cylinder and upper and lower plates). It takes into account the resulting forces (F_i) acting on these surfaces (at the beginning of the current timestep) and displacements (Δu_i) that occur during the current time increment or timestep ($t \rightarrow (t+\Delta t)$). E_w is named here as boundary energy;
N_w = Number of walls.

Therefore, in our case:

$$E_{ext}^{t+\Delta t} = E_{w}^{t+\Delta t} \quad (7:29)$$

Figure 7-36 shows the evolution of E_w (axial strain-E_w curve) during the numerical oedometric test. This figure illustrates the behaviour during the loading test which includes the saturation stage maintaining the vertical stress of 2.8 MPa, (ε_a>0.085). At the end of the loading process (σ_v=2.8MPa) for RH = 10%, when ε_a=0.085, E_w reaches a value of 1382.8 J, and increases after saturation up to a value of 2723.7 J at ε_a=0.130.

Figure 7-36 also shows the behaviour during loading and unloading processes. For unloading in dry conditions (RH=10%), i.e. unloading from 2.8 MPa to 0.2 MPa, which corresponds to axial strain ε_a from 0.085 to 0.047, E_w decreases to a value of 932.3 J. Similarly, for saturated conditions (RH=100%), i.e. unloading from 2.8 MPa to 0.2 MPa, which corresponds to axial strain ε_a from 0.130 to 0.079, E_w also decreases from 2723.7 J to 2300.1 J. In short, in the unloading process, there was a recovery of energy (liberation of stored energy in the loading process) about 32.6% in dry conditions and 15.6% for RH=100%.

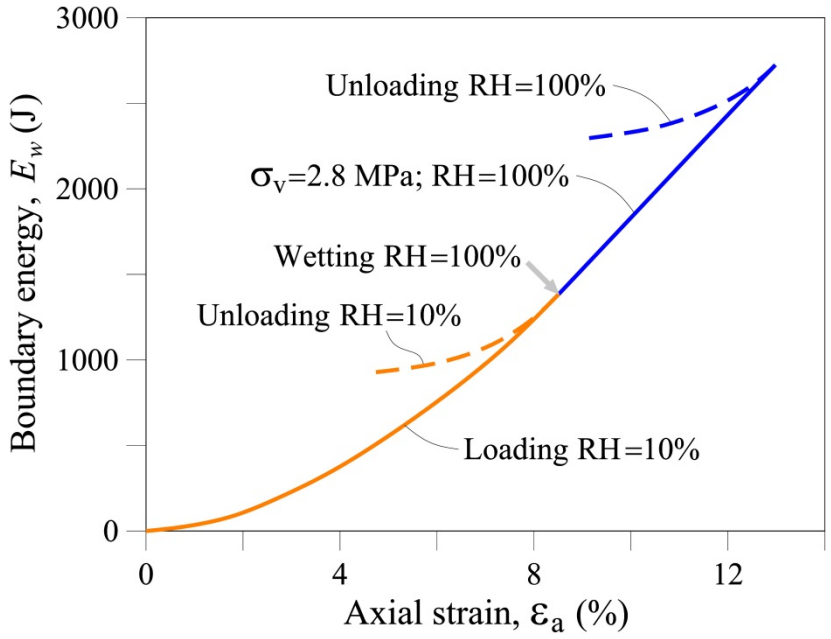

Figure 7-36 Evolution of total boundary energy, E_w: DEM simulation of oedometer test. DEM properties: μ=0.3; k_n=4 MN/m; K_c=1MPa•m$^{0.5}$. Loading [0-2.8MPa] and Unloading [2.8 – 0.2MPa] processes in different relative humidity conditions –RH=10% and RH=100%–. Continuous line after wetting corresponds to the behaviour under σ_v=2.8MPa.

b. Kinetic energy, E_k

$$E_k = \frac{1}{2}\sum_{i=1}^{N_p}\left(m_i V_i^2 + I_i w_i \cdot w_i\right) \qquad (7:30)$$

where:
N_p = Number of macroparticles
m_i = Inertial mass
I_i = Inertia tensor
V_i = Translational velocity for macroparticle *i*
w_i= Rotational velocity for macroparticle *i*

As might be expected, the total kinetic energy of all the particles, E_k, takes into account the movement of all of them. It is generally zero during the test, with peak values (sudden increments which return to zero again) when load increments are applied and the suction is changed, or when particles break and rearrangement occurs (see **Figure 7-37**).The maximum peak value of E_k was about 4 J, which represents a very low value in comparison with E_w (approximately, E_k ≈0.0% of E_w). In the unloading process for dry and wet conditions, there were not any significant peak values (E_k ≈0J).

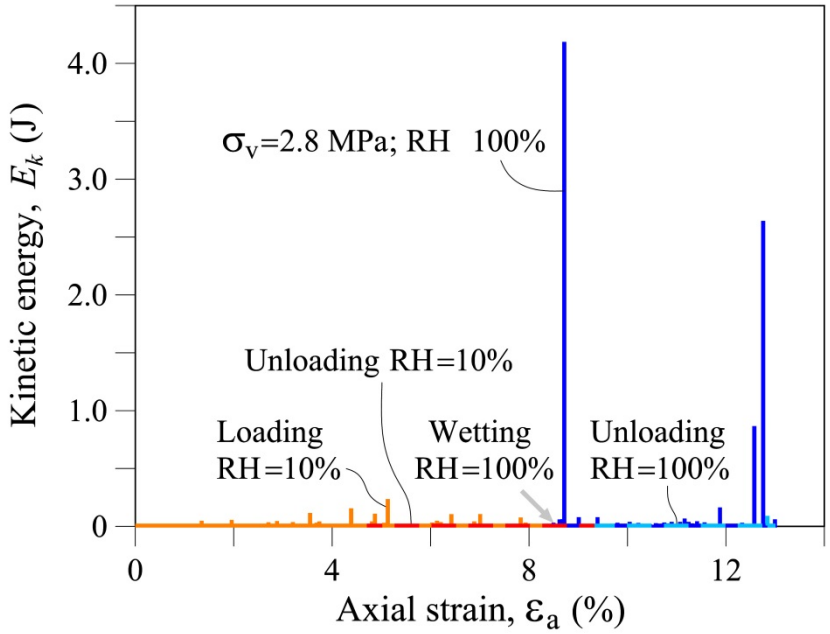

Figure 7-37 Evolution of total kinetic energy, E_k: DEM simulation of oedometer test. DEM properties: μ=0.3; k_n=4 MN/m; K_c=1MPa•m$^{0.5}$. Loading [0-2.8MPa] and Unloading [2.8 – 0.2MPa] processes in different relative humidity conditions –RH=10% and RH=100%–. Continuous line after wetting corresponds to the behaviour under σ_v=2.8MPa.

c. Internal energy, E_{int}

$$E_{\text{int}}^{t+\Delta t} = E_s^{t+\Delta t} + E_b^{t+\Delta t} + E_f^{t+\Delta t} + E_d^{t+\Delta t} \tag{7:31}$$

where:

$E_{\text{int}}^{t+\Delta t}$ = Internal energy of the system at time (t+Δt);

$E_s^{t+\Delta t}$ = (Elastic) Strain energy at time (t+Δt);

$E_b^{t+\Delta t}$ = Bond energy at time (t+Δt); corresponds to the elastic strain energy stored in a parallel bond. It is lost when the bond is broken. In our DEM model, there are no parallel bonds so its value is equal to 0.

$E_f^{t+\Delta t}$ = Frictional energy at time (t+Δt); this is the energy dissipated by frictional sliding.

$E_d^{t+\Delta t}$ = Damping dissipation energy at time (t+Δt);

c1. Strain energy, E_s

Figure 7-38 shows the evolution of the total strain energy, E_s, of the entire sample stored at all contacts assuming a contact-stiffness linear model. E_s is calculated as follows for the current time increment ($t \rightarrow (t+\Delta t)$):

$$E_s^{t+\Delta t} = \frac{1}{2}\sum_{i=1}^{N_c}\left(\frac{\left|F_i^n\right|^2}{k^n} + \frac{\left|F_i^s\right|^2}{k^s}\right) \qquad (7:32)$$

where: N_c = Number of contacts; $|F_i^n|$ and $|F_i^s|$ are the magnitudes of the normal and shear components of the contact force at contact i; k^n and k^s are the normal and shear contact stiffnesses.

Figure 7-38 shows the behaviour during the loading test which includes the saturation stage maintaining the vertical stress of 2.8 MPa, (ε_a>0.085), and also illustrates the behaviour during unloading processes for dry and wet conditions.

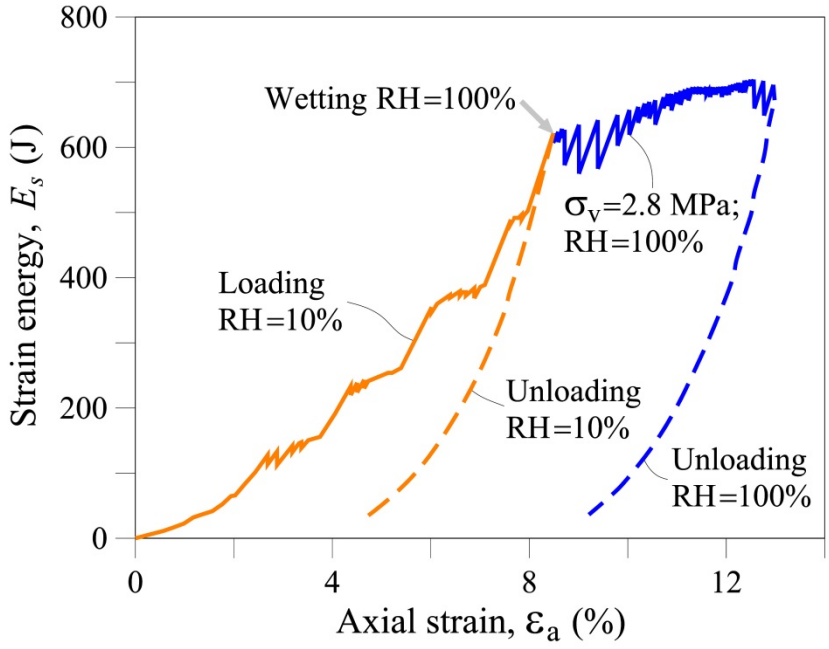

Figure 7-38 Evolution of total strain energy, E_s: DEM simulation of oedometer test. DEM properties: μ=0.3; k_n=4 MN/m; K_c=1MPa•m$^{0.5}$. Loading [0-2.8MPa] and Unloading [2.8 – 0.2MPa] processes at different relative humidity conditions –RH=10% and RH=100%–. Continues line after wetting corresponds to the behaviour under σ_v=2.8MPa.

At the end of the loading process for RH = 10% (σ_v=2.8MPa; ε_a=0.085), E_s reaches a value of 621.0 J, and increases to 694.8 J at the end of the wetting (σ_v=2.8MPa; ε_a=0.130). The rate of the energy increase is lower for the wetting stage than for the dry part.

For the unloading process in dry conditions (unloading from 2.8 MPa to 0.2 MPa which corresponds to axial strain ε_a from 0.085 to 0.047), E_s decreases to a value of 37.2 J. Similarly, for the unloading process in saturated conditions (unloading from 2.8 MPa to 0.2 MPa which corresponds to ε_a from 0.130 to 0.079), E_s also decreases from 694.8 J to 31.9 J, almost the same value as for unloading in dry conditions. In short, for the unloading process, there was practically a total recovery of strain energy (liberation of stored energy in the loading process): 94.0% in dry conditions and 95.4% for RH=100%.

c2. Frictional energy, E_f

Figure 7-39 shows the evolution of total frictional work, E_f, the total energy that has been dissipated by frictional sliding at all contacts. E_f is calculated by the following expression for the current time increment ($t \rightarrow (t+\Delta t)$):

$$E_f^{t+\Delta t} = E_f^t + \sum_{i=1}^{N_c} \left(\left\langle F_i^s \right\rangle \left(\Delta u_i^s \right)^{slip} \right) \tag{7:33}$$

where: N_c = Number of contacts.

E_f takes into account the shear forces (F_i^s) at contact i and the increment of slip displacement ($(\Delta u_i^s)^{slip}$) that occurs when the contact shear force exceeds the shear strength force due to friction, at the current timestep. The increment of slip displacement is calculated as follows:

$$\begin{aligned} \left(\Delta u_i^s \right)^{slip} &= \Delta u_i^s - \left(\Delta u_i^s \right)^{elast} \\ &= \Delta u_i^s + \frac{\left(\Delta F_i^s \right)^{elast}}{k^s} = \Delta u_i^s + \frac{\left(F_i^s \right)^{(t+\Delta t)} - \left(F_i^s \right)^t}{k^s} \end{aligned} \tag{7:34}$$

where k^s is the contact shear stiffness.

Figure 7-39 illustrates the frictional energy behaviour during loading test which includes the saturation stage maintaining the vertical stress of 2.8 MPa, (ε_a>0.085), and also shows the behaviour during unloading processes for dry and wet conditions.

E_f has a value of 541.9 J at the end of the loading process (σ_v=2.8MPa; ε_a=0.085) for RH = 10%, and increases to 1379.9 J at the end of the wetting (σ_v=2.8MPa; ε_a=0.130).

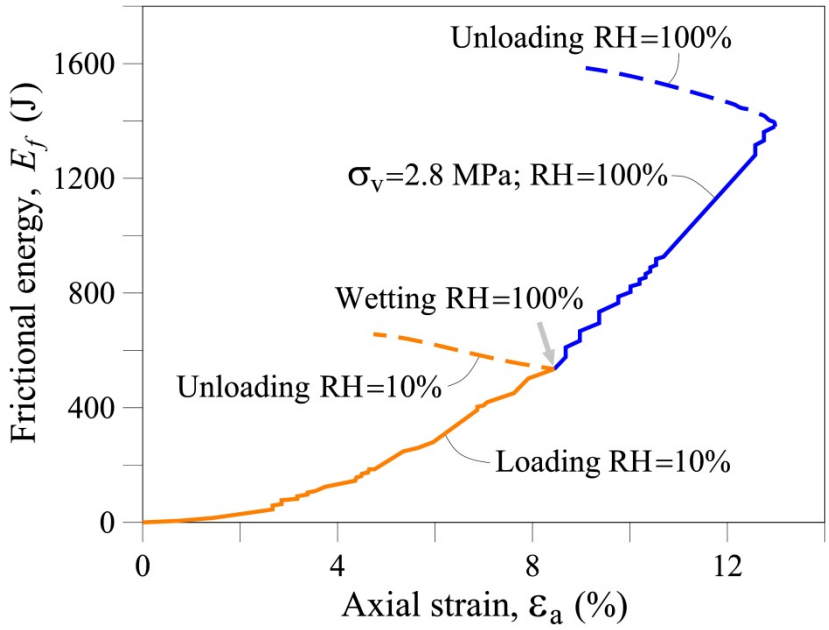

Figure 7-39 Evolution of total frictional energy, E_f: DEM simulation of oedometer test. DEM properties: μ=0.3; k_n=4 MN/m; K_c=1MPa•m$^{0.5}$. Loading [0-2.8MPa] and Unloading [2.8 – 0.2MPa] processes in different relative humidity conditions –RH=10% and RH=100%–. Continuous line after wetting corresponds to the behaviour under σ_v=2.8MPa.

In contrast to the E_s behaviour for the unloading process in dry conditions (unloading from 2.8 MPa to 0.2 MPa; ε_a from 0.085 to 0.047), E_f increases until it reaches a value of 658.5 J. Also for the unloading process in saturated conditions (unloading from 2.8 MPa to 0.2 MPa; ε_a from 0.130 to 0.079), E_f increases from 1379.9 J to 1585.4 J. In short, for the unloading process, there was a small generation of frictional energy about 21.5% in dry conditions and 14.9% for RH=100%.

c3. Damping dissipation energy, E_d

Figure 7-40 compares the behaviour of the evolution of the external energy E_w (black curve) and the sum of the kinetic energy E_k and the internal energies E_s and E_f (brown and blue curve). Loading and unloading paths for the different environmental (saturation) conditions are shown.

The sum of the values of the energies (E_k+E_s+E_f) is about 1162.9 J at the end of the loading process for RH = 10% (σ_v=2.8MPa; ε_a=0.085), which corresponds to 0.84*E_w, and increases to 2074.7 J at the end of the wetting (σ_v=2.8MPa; ε_a=0.130), which corresponds to 0.76*E_w.

For the unloading process in dry conditions (unloading from 2.8 MPa to 0.2 MPa; ε_a from 0.085 to 0.047), the sum (E_k+E_s+E_f) decreases until a value of 695.7 J in reached, which corresponds to 0.75*E_w. For the unloading process in saturated

conditions (unloading from 2.8 MPa to 0.2 MPa; ε_a from 0.130 to 0.079), the sum (E_k+E_s+E_f) also decreases from 2074.7 J to 1617.2 J, which corresponds to 0.70*E_w.

The difference between curves could be explained by the damping used in the DEM model.

Figure 7-41 shows the behaviour of the damping dissipation energy E_d during loading test which includes the saturation stage maintaining the vertical stress of 2.8 MPa, (ε_a>0.085). Likewise, **Figure 7-41** also shows the behaviour during loading and unloading process for dry and wet conditions.

E_d has a value of 219.9 J at the end of the loading process (σ_v=2.8MPa; ε_a=0.085) for RH = 10%, and increases to 649.0 J at the end of wetting (σ_v=2.8MPa; ε_a=0.130).

For the unloading process in dry conditions (unloading from 2.8 MPa to 0.2 MPa; ε_a from 0.085 to 0.047), E_d increases in a small proportion (7.6%) up to a value of 236.6 J. Similarly, for the unloading process in saturated conditions (unloading from 2.8 MPa to 0.2 MPa; ; ε_a from 0.130 to 0.079), E_d also increases in a small proportion (5.2%) from 649.0 J to 683.0 J. In short, for the unloading process, there was a very small generation of damping energy about 6% in dry and wet conditions; this kind of energy remained practically constant.

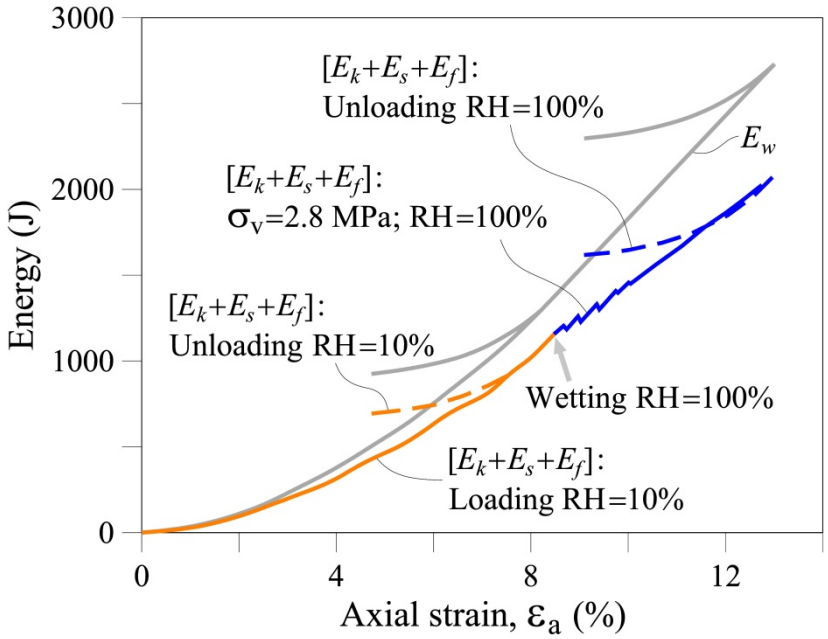

Figure 7-40 Comparison of the evolution of total boundary energy (E_w) and the sum of the strain, frictional and kinetic energies, [E_s + E_f + E_k]: DEM simulation of oedometer test. DEM properties: μ=0.3; k_n=4 MN/m; K_c=1MPa•m$^{0.5}$. Loading [0-2.8MPa] and Unloading [2.8 – 0.2MPa] processes in different relative humidity conditions –RH=10% and RH=100%–. Continuous line after wetting corresponds to the behaviour under σ_v=2.8MPa.

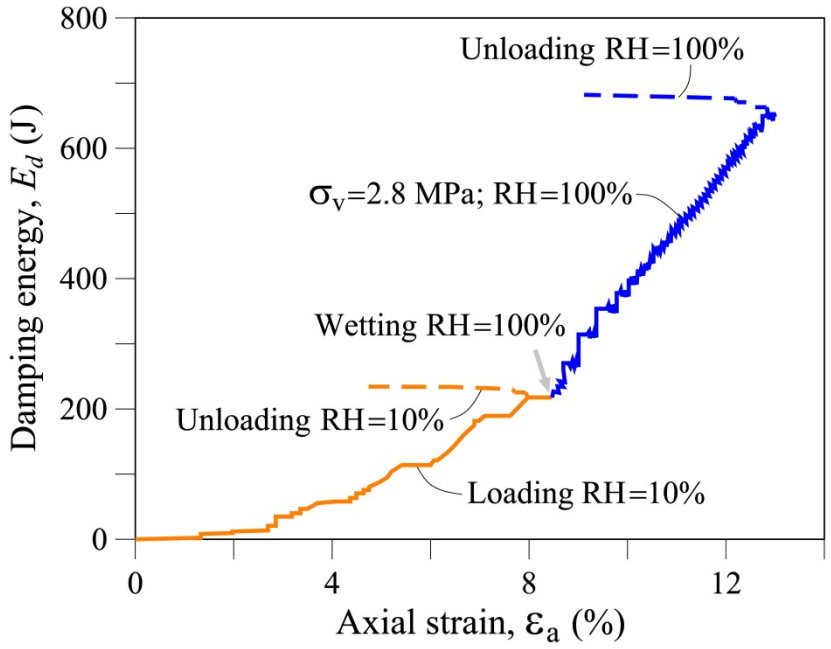

Figure 7-41 Evolution of total damping dissipation energy, E_d: DEM simulation of oedometer test. DEM properties: μ=0.3; k_n=4 MN/m; K_c=1MPa•m$^{0.5}$. Loading [0-2.8MPa] and Unloading [2.8 – 0.2MPa] processes at different relative humidity conditions –RH=10% and RH=100%–. Continues line after wetting corresponds to the behaviour under σ_V=2.8MPa.

d. Analysis of the evolution of the energy

A comparison of the evolution of all the energies during the test is shown in **Figure 7-42**a: External energy (Boundary energy E_w), Kinetic energy E_k, and Internal energies −Strain (E_s), Frictional (E_f) and Damping (E_d)−. **Figure 7-42**b also shows a comparison between the behaviour of these energies but in terms of the ratio E/E_w, i.e. all the values of each type of energy are related to the external (boundary) energy. The ratio E_s/E_w always decreases during the entire test and is greater than E_f/E_w for ε_a<0.054 (σ_V<1.6 MPa). For 1.6≤σ_V≤2.8 MPa at RH=10%, E_s/E_w and E_f/E_w are close to 0.4: for instance, at σ_V=2.8MPa (ε_a=0.085): E_s/E_w =45% and E_f/E_w = 39%. In contrast to E_s/E_w, E_f/E_w increases during the entire test and this evidences that the displacements due to sliding and particle rearrangement (and also due to particle breakage and rearrangement of particles) are increasingly relevant especially in the wetting stage maintaining the load σ_V=2.8 MPa (0.085≤ε_a≤0.130).

At the end of the wetting at ε_a=0.130; E_s/E_w =26% and E_f/E_w = 51%.

At the end of the unloading process, for both dry and wetting conditions, the relationship E_f/E_w tends to a value of 0.7 (E_f/E_w=71% for RH=10%; E_f/E_w=69% for RH=100%) and E_s/E_w tends to zero (E_s/E_w=4% for RH=10%; E_s/E_w=1% for RH=100%).

Regarding the damping energy, just like E_f/E_w, E_d/E_w increases during the entire test but in a lower proportion: at σ_v=2.8MPa for dry conditions (ε_a=0.085), E_d/E_w =16%; at the end of the wetting at ε_a=0.130 (σ_v=2.8MPa), E_d/E_w =24%; at the end of the unloading process, for both dry and wetting conditions E_d/E_w tends to 0.3 (E_d/E_w=25% for RH=10%; E_d/E_w=30% for RH=100%).
.
As previously commented, the values of kinetic energy are negligible compared to the other types of energy.

On the other hand, based on the behaviour of the energies (see **Figure 7-42**a) and following the approach by Wang and Yan (2012), these energies can be grouped into two types: elastic strain and plastic dissipation energy. Thereby Equations (7:24) and (7:31) can be rewritten as:

$$E_{ext} = E_e + E_p \tag{7:35}$$

where:
E_{ext} = External energy of the system. In our case: E_{ext} =E_w.
E_e = Elastic strain energy of the system. In our case: E_e = E_s.
E_p = Plastic dissipation energy of the system. In our case: E_p = E_f + E_d.

Figure 7-43 shows a comparison of the behaviour of E_w, E_e and E_p during the test. **Figure 7-43**a illustrates the evolution of the values of the energies. In **Figure 7-43**b, the comparison of the energy behaviour is given in terms of the relationship between the value of the energy and E_w, i.e. E_e/E_w. and E_p/E_w ;

Just like E_s behaviour, at the end of the loading process for RH = 10% (σ_v=2.8MPa; ε_a=0.085), E_e has a value of 621.0 J, which corresponds to 0.449*E_w, and increases to 694.8 J, which corresponds to 0.255*E_w at the end of the wetting (σ_v=2.8MPa; ε_a=0.130). For the unloading process in dry conditions (unloading from 2.8 MPa to 0.2 MPa; ε_a from 0.085 to 0.047), E_e decreases to a value of 37.2 J, which corresponds to 0.040*E_w. For the unloading process in saturated conditions (unloading from 2.8 MPa to 0.2 MPa; ε_a from 0.130 to 0.079), E_e also decreases from 694.8 J to 31.9 J, which corresponds to 0.014*E_w.

Regarding the plastic dissipation energy, E_p has a value of 761.8 J at the end of the loading process for RH = 10% (σ_v=2.8MPa; ε_a=0.085) which corresponds to 0.551*E_w, and increases to 2028.9 J at the end of the wetting (σ_v=2.8MPa; ε_a=0.130), which corresponds to 0.745*E_w. For the unloading process in dry conditions (unloading from 2.8 MPa to 0.2 MPa; ε_a from 0.085 to 0.047), E_p increases from 761.8 J to 895.07 J, which corresponds to 0.960*E_w. For the unloading process in saturated conditions (unloading from 2.8 MPa to 0.2 MPa; ε_a from 0.130 to 0.079), E_p also increases from 2028.9 J to 2268.3 J, which corresponds to 0.986*E_w.

Obviously, at the end of the unloading process E_e tends to zero and E_p tends to E_w.

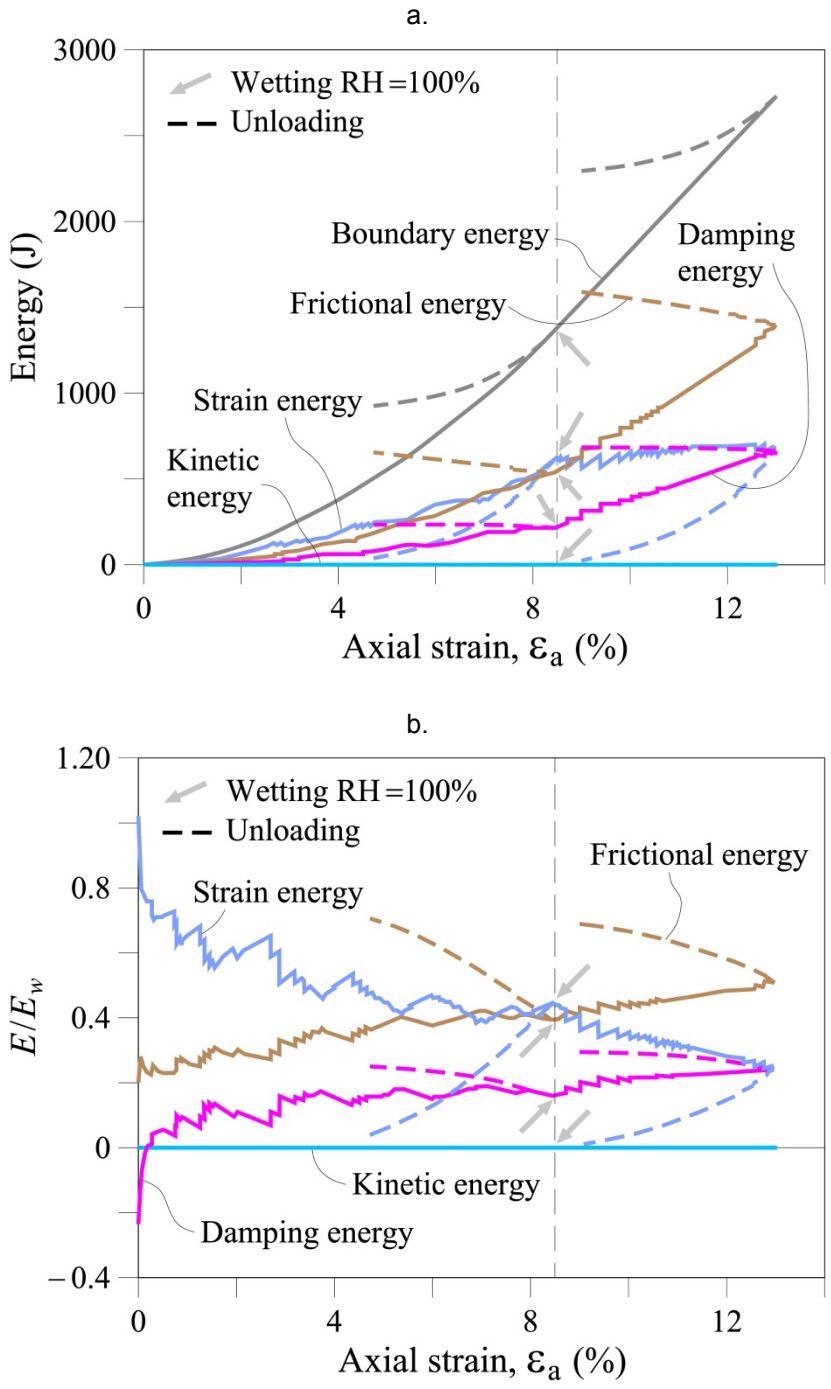

Figure 7-42 Comparison of the evolution of total energies: boundary (E_w), strain (E_s), frictional (E_f), kinetic (E_k) and damping (E_d) energies. DEM simulation of oedometer test. DEM properties: μ=0.3; k_n=4 MN/m; K_c=1MPa•m$^{0.5}$. (a) Total energies; (b) Relationship of the energy in relation to the total boundary energy (E/E_w).

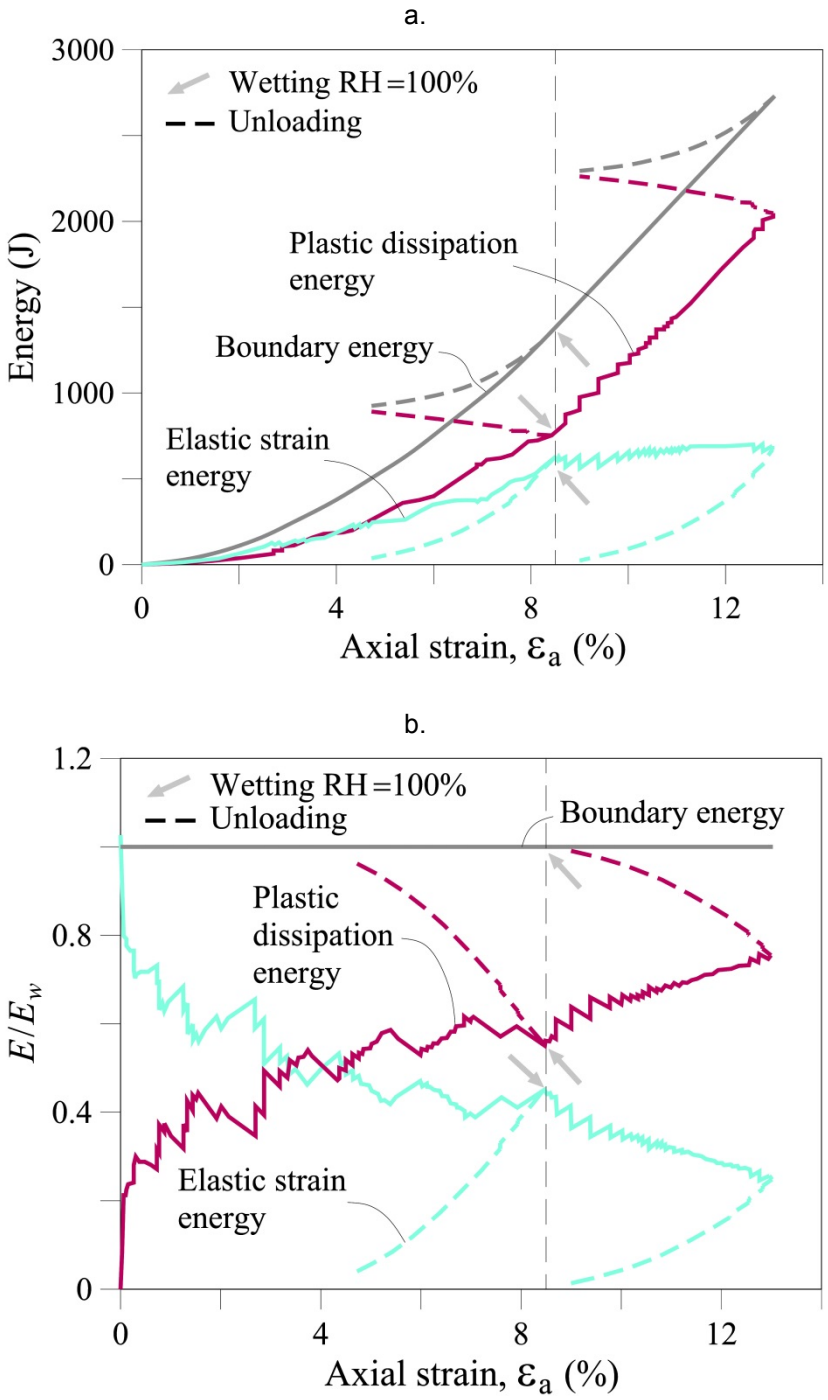

Figure 7-43 Comparison of the evolution of total boundary energy (E_w) , Elastic strain energy (E_e) and Plastic dissipation energy (E_p): DEM simulation of oedometer test. DEM properties: μ=0.3; k_n=4 MN/m; K_c=1MPa•m$^{0.5}$. (a) Total energies; (b) Relationship of the energy in relation to the total boundary energy (E/E_w).

7.3.4 Predicting triaxial tests

In this section, the results of the DEM simulations of triaxial tests are presented. The DEM parameters used in the tests are the same as those found for the previous oedometer tests: μ = 0.3; k_n = 4 MN/m; K_c = 1 MPa.m$^{0.5}$. These DEM numerical tests simulate the experimental test performed by Ortega (2008) on the same limestone fragments tested in the oedometer tests. In the first instance, a confining pressure of 1.0 MPa is applied and maintained during the entire test. Thereafter, deviatoric stresses are applied.

The following two DEM simulations of triaxial tests are presented:

- Test I: RH=10% is maintained from the beginning until an axial strain of about 10% is reached. Then the RH is changed to 100% in order to simulate the flooding or total saturation of the sample, case provided for the experimental test.
- Test II: RH=10% is maintained during the entire test.

The numerical and experimental results are shown in **Figure 7-44**: curves ε_a - q (axial strain- deviatoric stress) and ε_a - ε_v (axial strain – volumetric strain).

The collapse in the deviatoric stress caused by wetting can be appreciated in the Test I (**Figure 7-44**). After this collapse, the test is resumed and the ε_a - q curve tries to reach the RH=10% curve although a smaller strength value is obtained.

Despite the differences between the strength achieved in the DEM and experimental tests (maximum deviatoric stress, q_{max}: 2.5 MPa (for Experimental); 2.0 MPa (for DEM)), the behaviour of the curves is similar.

Figure 7-44 also shows the collapse of the volumetric strain caused by the wetting for both the experimental and the DEM tests. Comparing tests I and II, it is noteworthy that at the end of numerical tests (ε_a =18%), ε_v =8.4% for RH=10% test and ε_v =12% for the wet sample (RH = 100%). For the experimental data, the volumetric strain reached 8.0%, but the test was performed only up to an axial strain of about ε_a =14%.

Comparing the stress path and failure envelope for the two DEM samples (RH = 10% and RH = 10-100%) in a p-q space (mean stress – deviatoric stress), calculated M values (M=q/p at maximum deviatoric stress q) are very similar in both cases: M = 1.28 (ϕ = 32°) (**Figure 7-45**).

The following results were obtained in the experimental test: ϕ =34.6º for RH=10% and ϕ =34.1º for RH=100%.

For numerical and experimental tests, compressibility behaviour in a p-e space (mean stress - void ratio) can be appreciated in **Figure 7-46**. Although the experimental test began the deviatoric stage (p=1MPa) with a lower void ratio

(*e*=0.87 for experimental; *e*=1.04 for DEM), similar behaviours are obtained. This difference between the initial void ratio conditions could explain the difference between strength values for the DEM and experimental tests.

Figure 7-47 and **Figure 7-48** show the evolution of void ratio and porosity respectively for DEM tests. "Initial compaction" of the sample due to the application of confining pressure of 1 MPa can be observed in **Figure 7-48**: initial porosity changes from 0.53 to 0.51; axial strain behaviour is not shown in this stage. Both figures show the deformation collapse caused by wetting. At the end of testing for an axial strain of 18%, void ratios are 0.94 and 0.88 for RH = 10% test and RH=10-100% test respectively, and porosities are 0.49 and 0.47 for RH = 10% test and RH=10-100% test respectively.

On the other hand, gsd curves are very similar at the end of the experimental and DEM tests after applying the wetting; the agreement is very good (**Figure 7-49**). This figure shows the particle size distribution at the beginning and end of the tests: the particle breakage during loading process is evident.

Figure 7-50 presents a comparison of DEM gsd curves for these cases: Before wetting the sample (RH = 10% and ε_a = 10%) and after wetting and resuming the test (RH = 100%; ε_a = 15%). The “jump” in the evolution of the gsd curve evidences the breakage of particles caused by the wetting.

Similarly, in order to appreciate the wetting effect, **Figure 7-51** shows the grading curves at the end of the following stages for the DEM tests: RH=10% -100% test (Test I) for ε_a = 0.20 (initially dry and then saturated at ε_a = 10%); RH=10% test (Test II) for ε_a = 0.19 (dry condition during the entire test); and RH=10% test for ε_a = 0.10 (dry condition during the entire test). Experimental curve is also presented. By comparing the curves of RH = 10% test (ε_a = 0.19) and RH = 10-100% test (ε_a = 0.20), it can be concluded that if wetting had not been imposed, the breakage would be less.

Figure 7-52 shows the evolution of the particle size distribution for RH=10-100% DEM numerical test (dry at the beginning, wetting at ε_a = 10%, and resuming the test). The gsd curves for different load stages are presented. These curves show the evolution of particle breakage during the entire test. The values of the deviatoric stress (q) and the axial strain (ε_a) are indicated in each gsd curve.

For the same loading stages indicated in the previous figure, **Figure 7-53** shows the evolution of retained weight percentage by size ranges: decrease in the original size (0.028cm) and a significant increase of 0.0235m, 0.019m and <0.014m in size are observed.

The evolution of breakage can also be appreciated by monitoring the breaking indexes of Hardin (B_r) and Marsal (B_g) (see **Figure 7-54** and **Figure 7-55**). These figures illustrate the breakage behaviour for the dry test (RH=10%) and dry-wet test (RH=10-100%). An instant after the sample is flooded and the collapse occurs, B_r and B_g increase rapidly: B_r changes from 0.17 to 0.20 (**Figure 7-54**) and B_g changes from 0.52 to 0.6 (**Figure 7-55**). At the end of the tests, for ε_a =20%, B_r are 0.20 and 0.27 for the dry and flooded samples respectively, and B_g are 0.60 and

0.72 for also dry and flooded samples respectively, indicating that the breakage particle is greater in the wet sample. Experimental data are also indicated in the figures: B_r =0.29 and B_g =0.6 at the end of the test. As already seen, these results also indicate a good fit of the model.

The particle breakage caused by the applied load and wetting can also be seen in the increase in macroparticles during the tests (**Figure 7-56**). The number of macroparticles is 941 at the beginning of the triaxial tests, 3800 at the end of the dry test and 4500 for the flooded sample. In this last test (flooded sample), when the wetting is imposed (ε_a =0.10), the number of macroparticles increases from 3200 to 3700.

Figure 7-57 shows the evolution of the number of macroparticles that did not break during the tests for dry and flooded samples: the original macroparticles (clumps of 14 microparticles) decrease during the entire test. At ε_a =18%, there are 260 and 180 unbroken macroparticles for the dry and wet sample, respectively. For the flooded test, when the wetting is imposed (ε_a =0.10) the number of unbroken macroparticles decreases from 320 to 230 approximately.

Concerning the evolution of total energy, it can be appreciated in **Figure 7-58** that the total boundary energy E_w always increases during the test. E_w reaches a value of 7000J for the dry test. However, it can be seen that this increase is smaller for the wetted test: the explanation is that after the collapse in the deviatoric stress due to wetting the strength is not completely recovered when the test is resumed.

This collapse of the load can be also appreciated in the evolution curve of total elastic strain energy, E_s, due to wetting (**Figure 7-59**): E_s decreases approximately from 1100J to 740J at the flooding instant. At the end of the testing E_s is 1350J for the dry test and 930J for the wetted test.

Moreover, the total friction energy E_f (**Figure 7-60**) increases from 2500J to 3000J when the sample is wetted (ε_a =0.10). However, at the end of the tests E_f tends to be the same for both tests: E_f reaches a value of 4300 J for an axial strain of 15%.

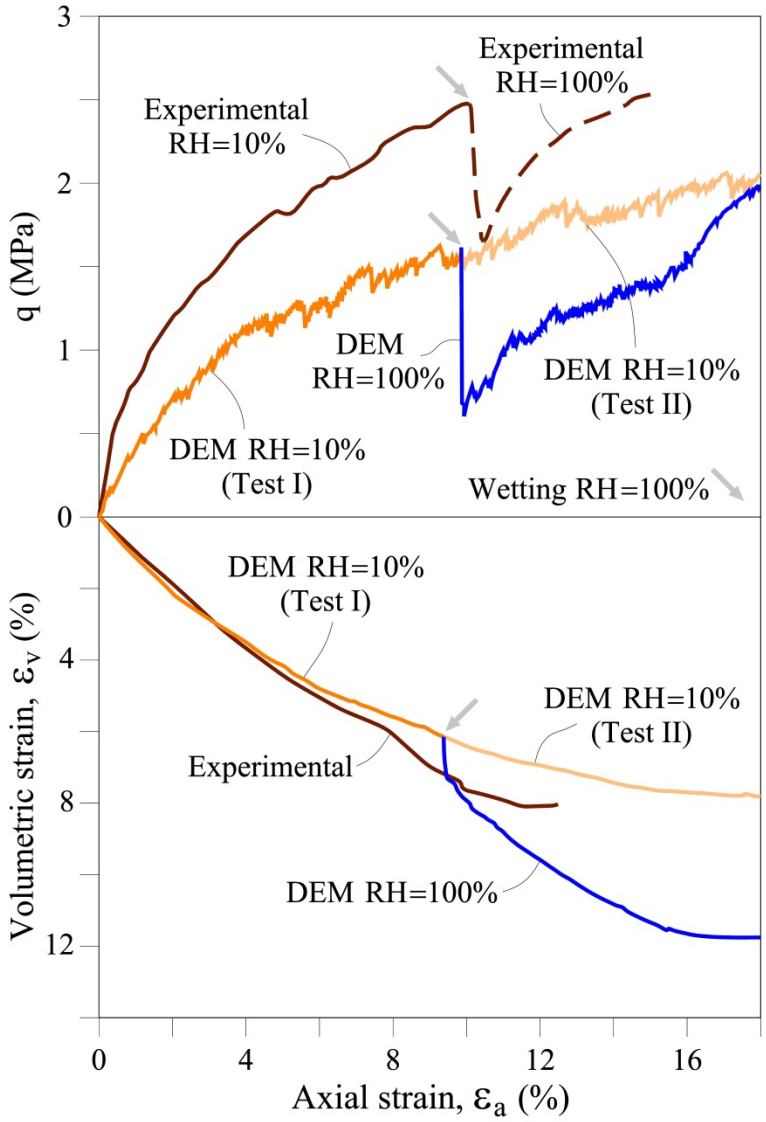

Figure 7-44 Deviatoric stress and volumetric strain behaviour: DEM simulation of triaxial test. Comparison between DEM and experimental results. DEM properties: μ=0.3; k_n=4 MN/m; K_c=1MPa•m$^{0.5}$. Test I: Dry conditions (RH=10%) at the beginning and then wetting (RH=100%) at ε_a≈10 %; Test II: Dry conditions (RH=10%) during the entire test.

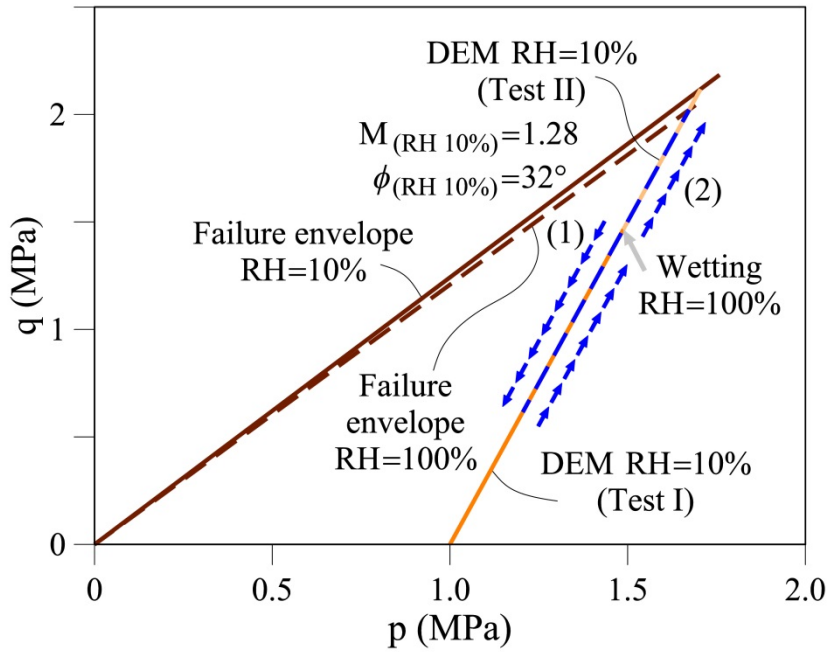

Figure 7-45 Stress path in *p*:*q* stress plane: DEM simulation of triaxial test. DEM properties: μ=0.3; k_n=4 MN/m; K_c=1MPa•m$^{0.5}$. Test I: Dry conditions (RH=10%) at the beginning and then wetting (RH=100%) at ε_a≈10 %: (1) corresponds to the collapse on *q* due to wetting, and (2) Resuming of test I after wetting; Test II: Dry conditions (RH=10%) during the entire test.

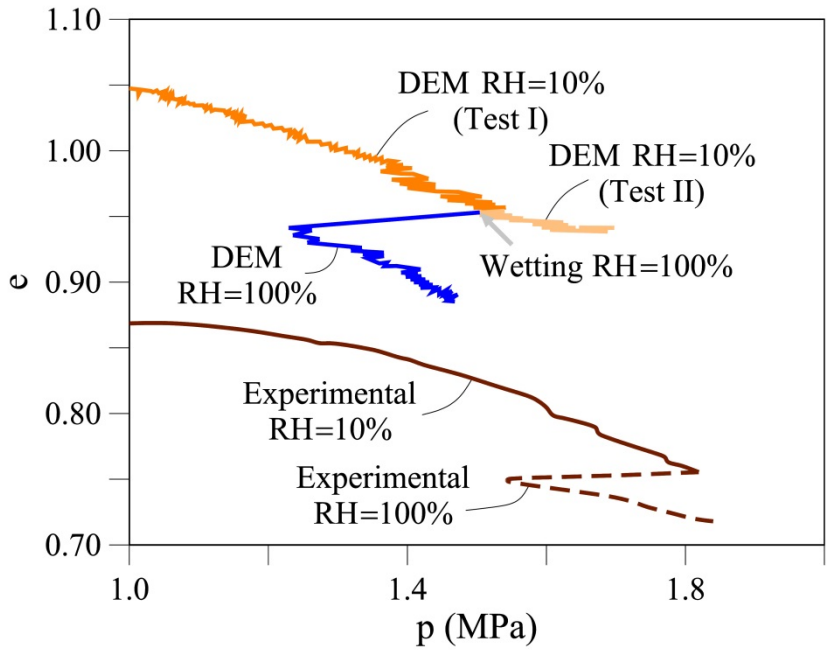

Figure 7-46 *e*:*p* compression plane: DEM simulation of triaxial test. Comparison between DEM and experimental results. DEM properties: μ=0.3; k_n=4 MN/m; K_c=1MPa•m$^{0.5}$. Test I: Dry conditions (RH=10%) at the beginning and then wetting (RH=100%) at ε_a≈10 %; Test II: Dry conditions (RH=10%) during the entire test.

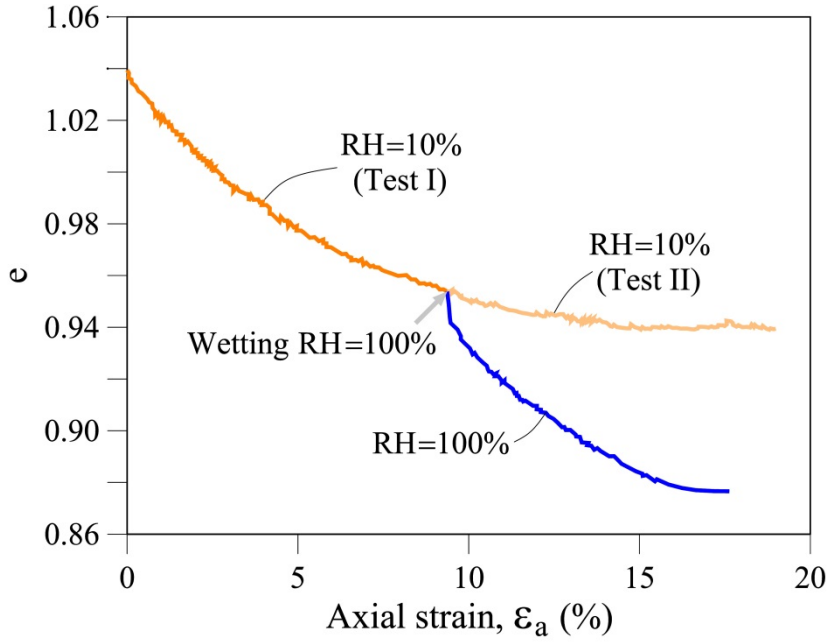

Figure 7-47 Evolution of void ratio: DEM simulation of triaxial test. DEM properties: μ=0.3; k_n=4 MN/m; K_c=1MPa•m$^{0.5}$. Test I: Dry conditions (RH=10%) at the beginning and then wetting (RH=100%) at ε_a≈10 %; Test II: Dry conditions (RH=10%) during the entire test.

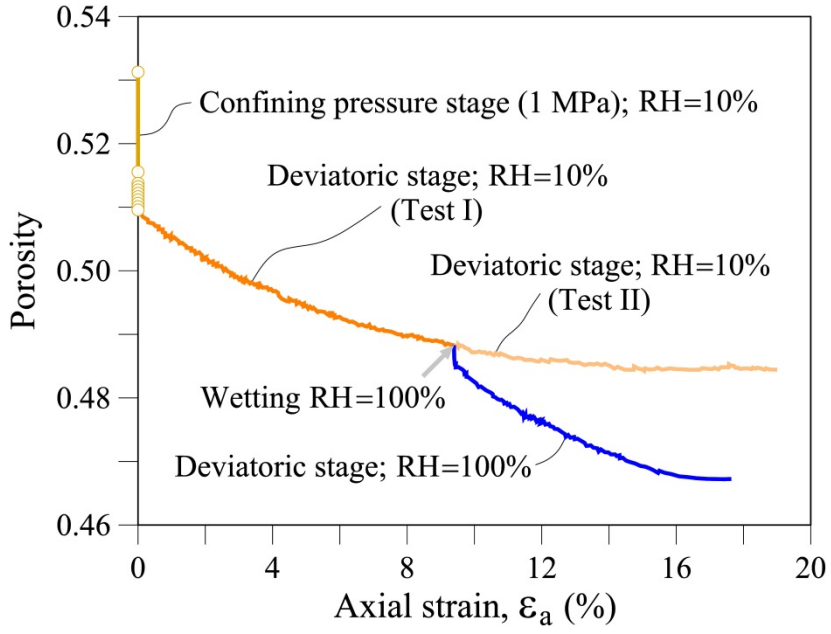

Figure 7-48 Evolution of porosity: DEM simulation of triaxial test. DEM properties: μ=0.3; k_n=4 MN/m; K_c=1MPa•m$^{0.5}$. Test I: Dry conditions (RH=10%) at the beginning and then wetting (RH=100%) at ε_a≈10 %; Test II: Dry conditions (RH=10%) during the entire test. Axial strain behaviour is not shown during the stage of initial confining pressure application.

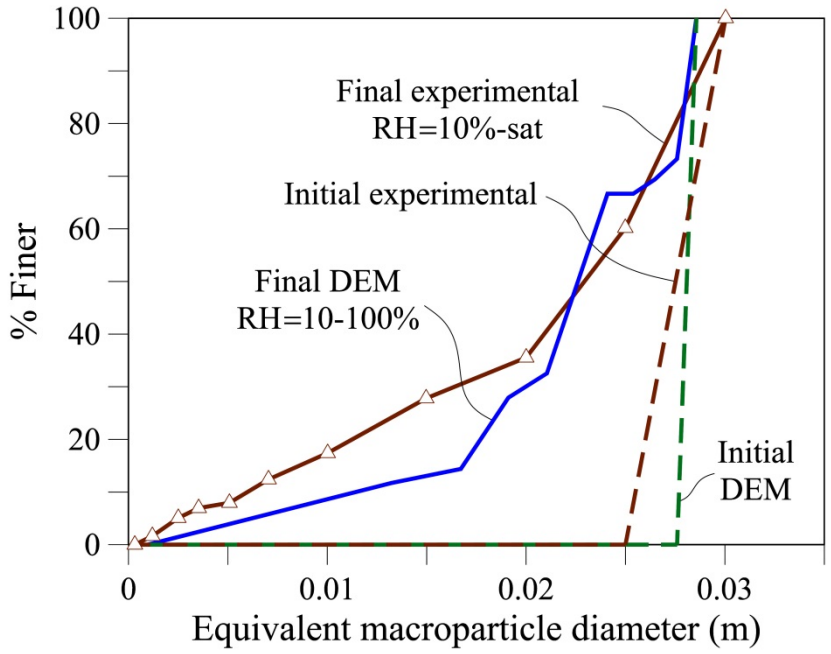

Figure 7-49 Evolution of grain (particle) size distribution: Comparison between DEM simulation and experimental triaxial test. DEM properties: μ=0.3; k_n=4 MN/m; K_c=1MPa•m$^{0.5}$.

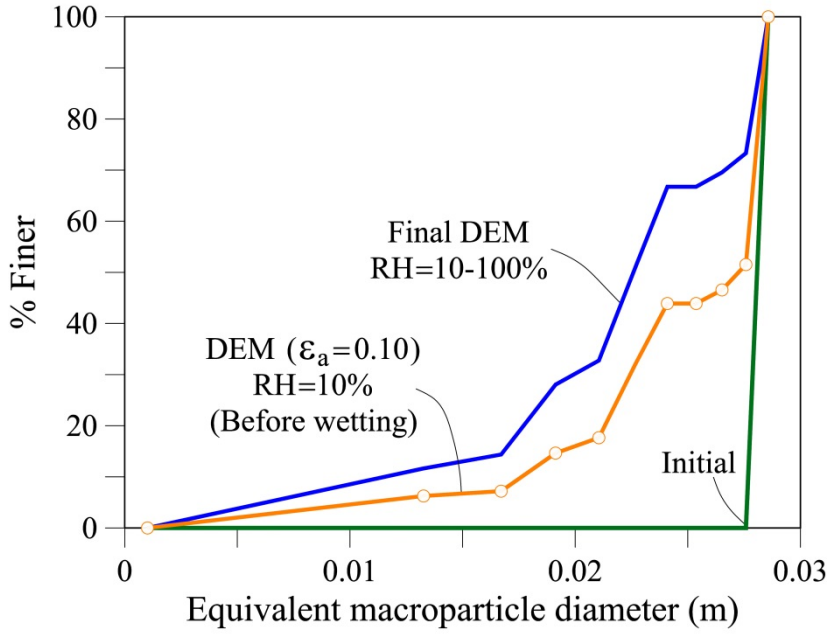

Figure 7-50 Evolution of grain (particle) size distribution in Test I – Relative Humidity effect: DEM simulation of triaxial test. DEM properties: μ=0.3; k_n=4 MN/m; K_c=1MPa•m$^{0.5}$.

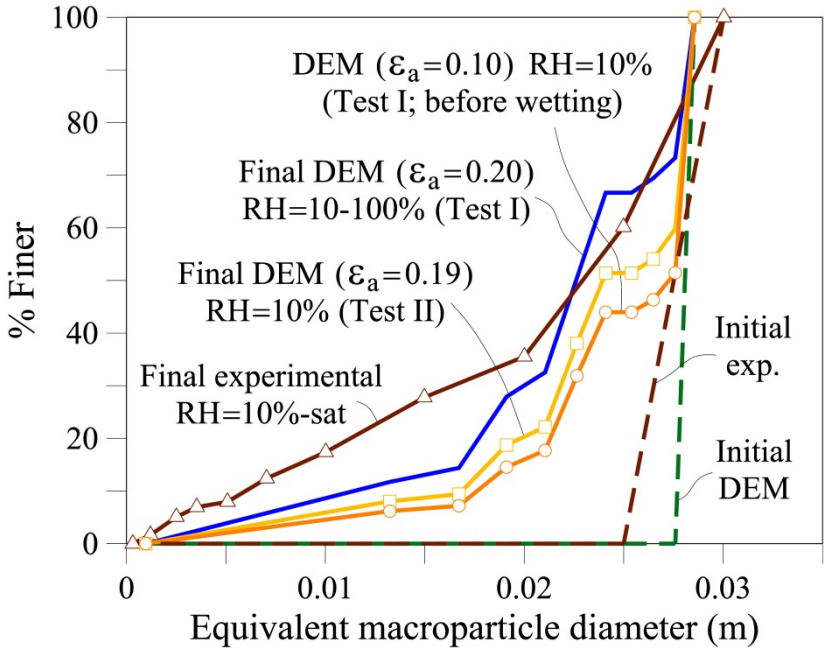

Figure 7-51 Evolution of grain (particle) size distribution in Tests I and II – Relative Humidity Effect: Comparison between DEM simulation and experimental triaxial test. DEM properties: μ=0.3; k_n=4 MN/m; K_c=1MPa•m$^{0.5}$. Test I: Dry conditions (RH=10%) at the beginning and then wetting (RH=100%) at ε_a≈10 %; Test II: Dry conditions (RH=10%) during the entire test.

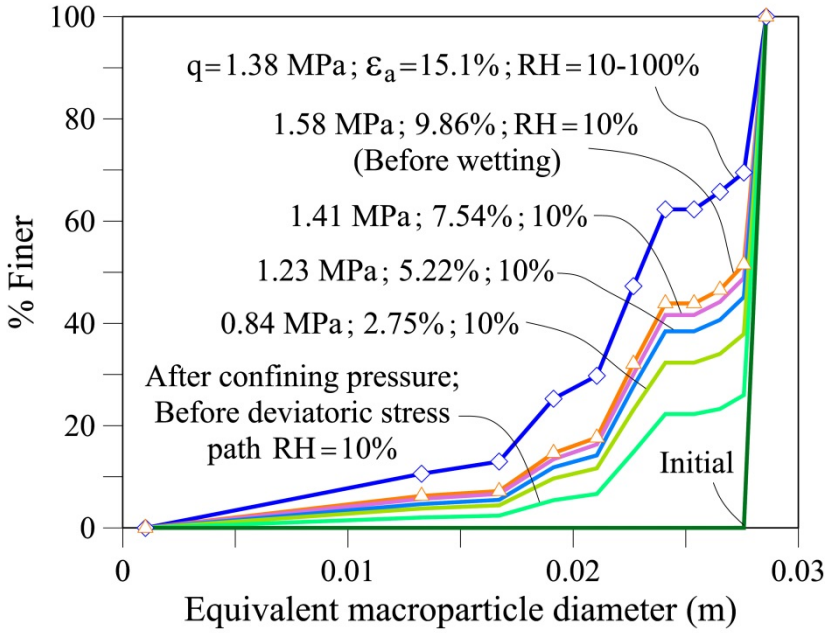

Figure 7-52 Evolution of grain (particle) size distribution in Test I – Relative Humidity Effect: DEM simulation of triaxial test. DEM properties: μ=0.3; k_n=4 MN/m; K_c=1MPa•m$^{0.5}$. Values of q and ε_a are indicated.

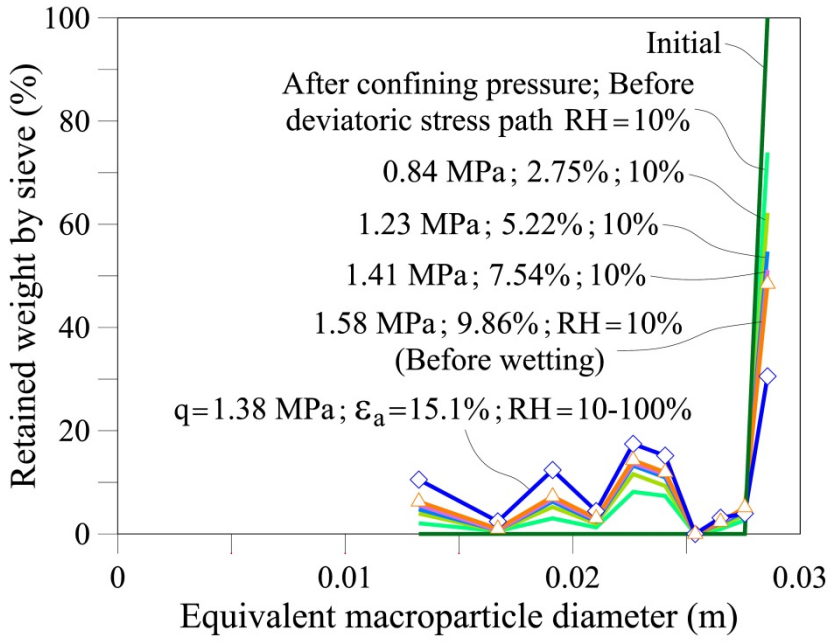

Figure 7-53 Evolution of macroparticle size – Relative Humidity Effect: DEM simulation of triaxial test. DEM properties: μ=0.3; k_n=4 MN/m; K_c=1MPa•m$^{0.5}$. Values of q and ε_a are indicated.

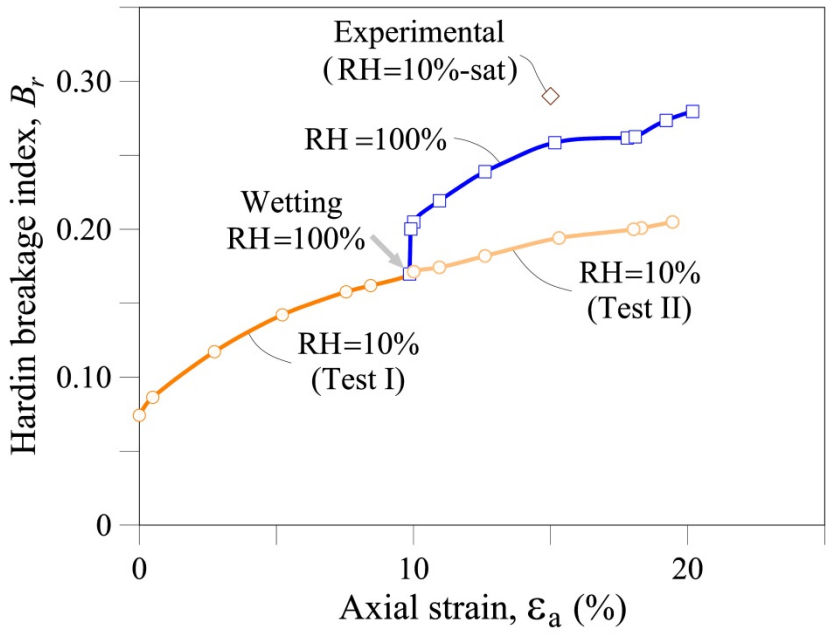

Figure 7-54 Evolution of Hardin breakage index – Relative Humidity Effect: DEM simulation of triaxial test. DEM properties: μ=0.3; k_n=4 MN/m; K_c=1MPa•m$^{0.5}$. Test I: Dry conditions (RH=10%) at the beginning and then wetting (RH=100%) at ε_a≈10 %; Test II: Dry conditions (RH=10%) during the entire test.

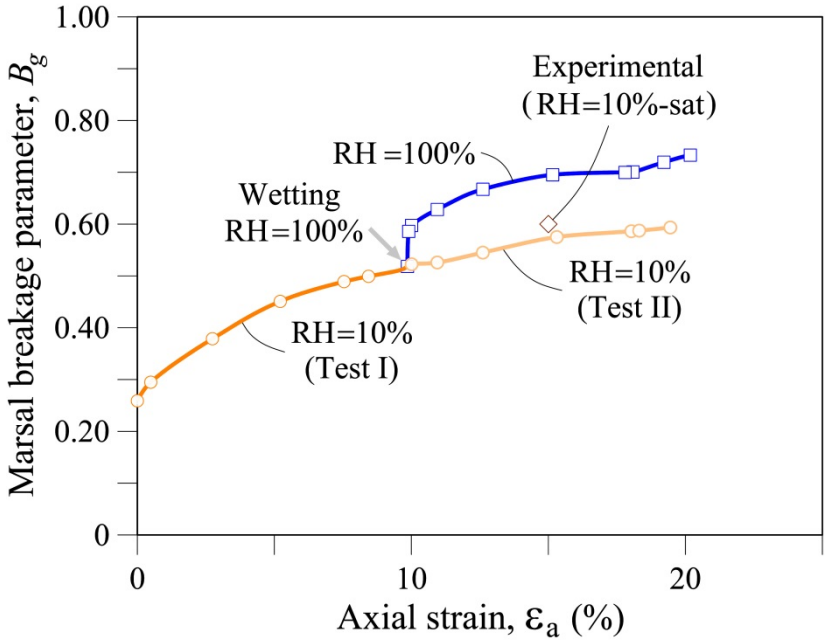

Figure 7-55 Evolution of Marsal breakage index – Relative Humidity Effect: DEM simulation of triaxial test. DEM properties: μ=0.3; k_n=4 MN/m; K_c=1MPa•m$^{0.5}$. Test I: Dry conditions (RH=10%) at the beginning and then wetting (RH=100%) at ε_a≈10 %; Test II: Dry conditions (RH=10%) during the entire test.

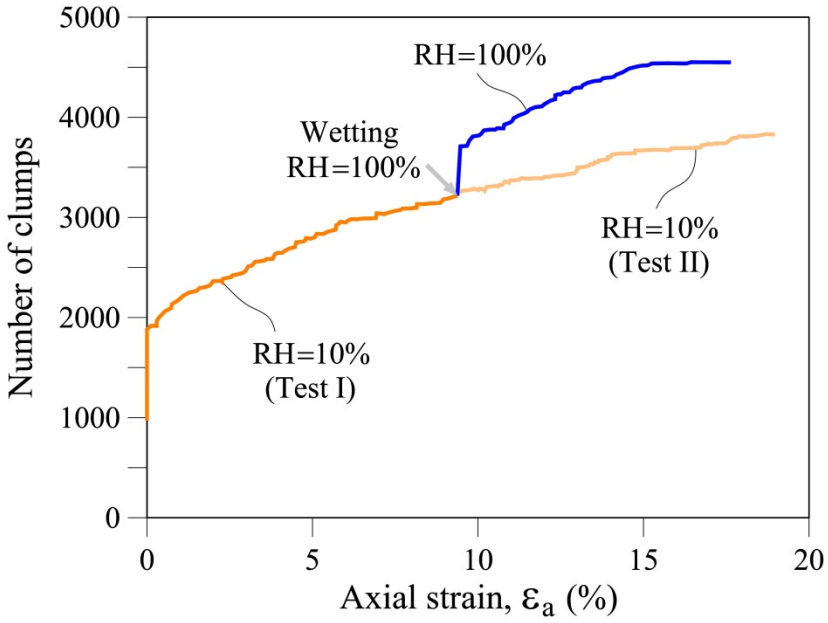

Figure 7-56 Evolution of number of macroparticles (clumps) – Relative Humidity Effect: DEM simulation of triaxial test. DEM properties: μ=0.3; k_n=4 MN/m; K_c=1MPa•m$^{0.5}$. Test I: Dry conditions (RH=10%) at the beginning and then wetting (RH=100%) at ε_a≈10 %; Test II: Dry conditions (RH=10%) during the entire test.

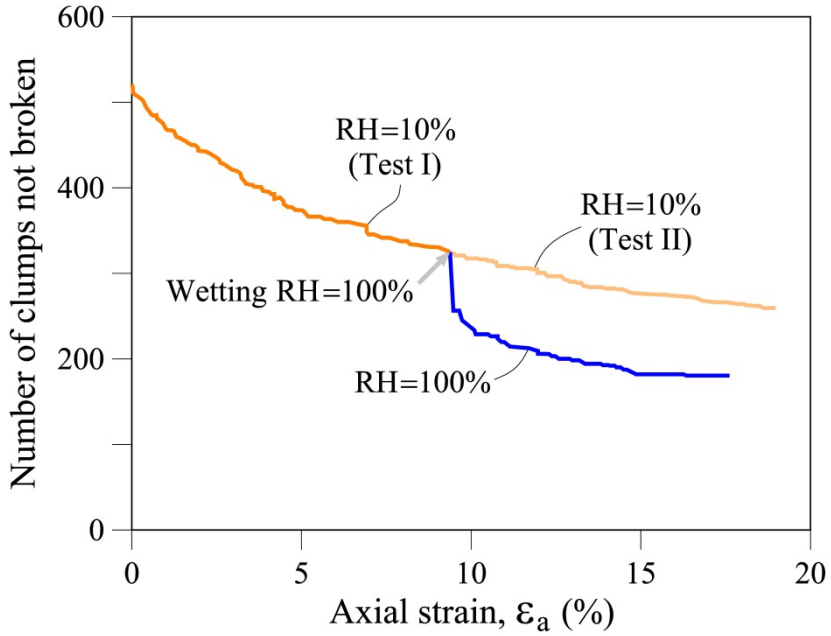

Figure 7-57 Evolution of number of macroparticles (clumps) not broken – Relative Humidity Effect: DEM simulation of triaxial test. DEM properties: μ=0.3; k_n=4 MN/m; K_c=1MPa•m$^{0.5}$. Test I: Dry conditions (RH=10%) at the beginning and then wetting (RH=100%) at ε_a≈10 %; Test II: Dry conditions (RH=10%) during the entire test.

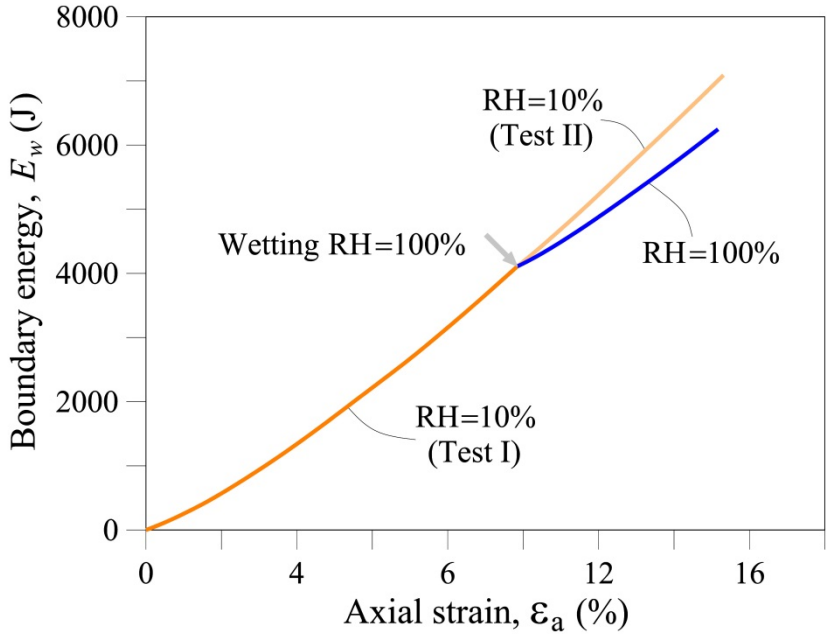

Figure 7-58 Evolution of total boundary energy, E_w – Relative Humidity Effect: DEM simulation of triaxial test. DEM properties: μ=0.3; k_n=4 MN/m; K_c=1MPa•m$^{0.5}$. Test I: Dry conditions (RH=10%) at the beginning and then wetting (RH=100%) at ε_a≈10 %; Test II: Dry conditions (RH=10%) during the entire test.

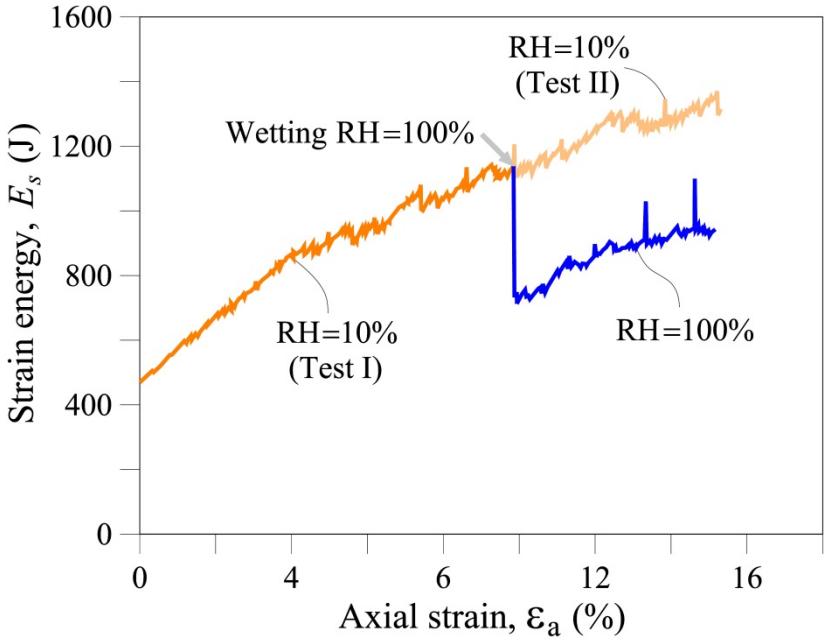

Figure 7-59 Evolution of total strain energy, E_s – Relative Humidity Effect: DEM simulation of triaxial test. DEM properties: μ=0.3; k_n=4 MN/m; K_c=1MPa•m$^{0.5}$. Test I: Dry conditions (RH=10%) at the beginning and then wetting (RH=100%) at ε_a≈10 %; Test II: Dry conditions (RH=10%) during the entire test.

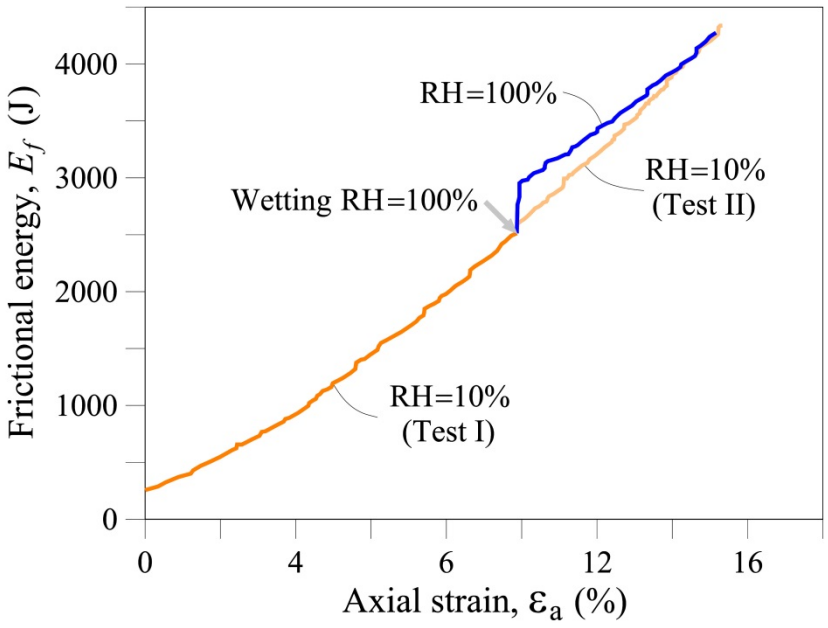

Figure 7-60 Evolution of total frictional energy, E_f – Relative Humidity Effect: DEM simulation of triaxial test. DEM properties: μ=0.3; k_n=4 MN/m; K_c=1MPa•m$^{0.5}$. Test I: Dry conditions (RH=10%) at the beginning and then wetting (RH=100%) at ε_a≈10 %; Test II: Dry conditions (RH=10%) during the entire test.

7.3.4.1 Scale effects

In order to study the scale effects and the RH influence in triaxial tests, additional DEM triaxial tests were performed varying the initial size of the macroparticles.

Two additional sizes were used in an initial uniform gsd: equivalent diameters of 18.5mm and 38.5mm.

The sizes of the specimens were also changed: 0.325m x 0.1625m for the 18.5mm macroparticles and 0.675m x 0.3375m for the 38.5mm macroparticles. The initial porosity of the specimens was the same in both cases: n_o=0.53; and also the initial number of macroparticles: 942. The DEM parameters were also the same as previously: μ = 0.3; k_n = 4 MN/m; K_c = 1 MPa.m$^{0.5}$.

In the first instance, a confining pressure of 1.0MPa was also applied and then deviatoric stresses were applied.

For each size, two DEM tests were performed following different RH conditions in a similar way to the previous tests on 28.5mm size:

- Test I: RH=10% is maintained from the beginning until an axial strain of about 13%. Then the RH is changed to 100% in order to simulate the flooding or total saturation of the sample, as was done in the experimental tests which are presented below.
- Test II: RH=10% is maintained during the entire test.

Figure 7-61 shows the results of the deviatoric stress and volumetric strain behaviour:

For dry conditions (RH=10%):

a) A specimen with a smaller size is stiffer and has a higher peak strength (maximum deviatoric stress): q_{max}= 2.48MPa at ε_a = 12.6% for 18.5mm; and q_{max}= 2.14MPa at ε_a = 17.4% for 38.5mm.
b) For large axial strain, “residual” strength tends to the same: q_{max}= 2.10MPa at ε_a = 18% for both sizes.
c) Larger specimens are more deformable (compressive): ε_v = 6.2% at ε_a = 17.5% for 38.5mm; and ε_v = 3.6% at ε_a = 20.6% for 18.5mm.

For wetting conditions (RH=10-100%):

a) The collapse in deviatoric stress and volumetric strain are presented in both tests when RH=100% is imposed (wetting of the specimens – saturated conditions):

For 18.5mm, *q* falls from 2.40MPa to 1.28MPa at about ε_a = 13%;
For 38.5mm, *q* falls from 1.96MPa to 1.29MPa at about ε_a = 13%;
At the end of the tests: for 18.5mm, ε_v = 3.6% at RH=10%; and ε_v = 7.0% at RH=100%; and for 38.5mm, ε_v = 6.2% and 8.7% at RH=10% and 100% RH conditions, respectively.

b) For both sizes, strength tends to be recovered when tests are resumed after wetting.

These DEM tests (dry conditions at the beginning and then wetting – RH=10-100%) were performed in order to simulate experimental tests carried out by Ortega (2008) on the same previous limestone fragments for initial uniform gsd: 20-15mm and 40-30mm in size, respectively. The initial porosity of the actual specimens was similar to the DEM samples: n_o=0.49. **Figure 7-62** shows a comparison of the results of the numerical and experimental tests. A good agreement was obtained for all the tests:

A. For 18.5mm size:

a) Before wetting (RH=10%) at ε_a = 13% approximately:
q= 2.40MPa for DEM and *q*= 2.78MPa for experimental;
ε_v = 3.6% for DEM and ε_v = 5.5% for experimental.

b) After wetting (RH=100%) at the end of the tests:
q= 1.96MPa for DEM and *q*= 2.69MPa for experimental;
ε_v = 7.0% for DEM and ε_v = 7.1% for experimental.

B. For 38.5mm size:

c) Before wetting (RH=10%) at ε_a = 10% approximately:
q= 1.96MPa for DEM and *q*= 2.59MPa for experimental;
ε_v = 5.8% for DEM and ε_v = 8.4% for experimental.

d) After wetting (RH=100%) at the end of the tests:
q= 1.77MPa for DEM and *q*= 2.41MPa for experimental;
ε_v = 8.7% for DEM and ε_v = 9.5% for experimental.

Figure 7-63 illustrates a comparison of the gsd curves at the end of the DEM and experimental tests. There is a very good agreement between them. These gsd evolutions also show a scale or size effect, a typical feature of rockfill and gravels as presented previously (chapters 2 and 6). Gsd curves do not evolve in the same way.

Figure 7-64 and **Figure 7-65** show the evolution of the Hardin and Marsal breakage indices. Breakage of particles increases with the initial size. This effect was more marked in the experimental tests than in the DEM tests: For the DEM, B_r values were 0.29 and 0.31 for 18.5mm and 38.5mm, respectively; B_g values were 0.69 and 0.73 for 18.5mm and 38.5mm, respectively. For the experimental tests: B_r was 0.24 and 0.29 for D20-15mm and D30-40mm, respectively; B_g was 0.46 and 0.57 for D20-15mm and D30-40mm, respectively.

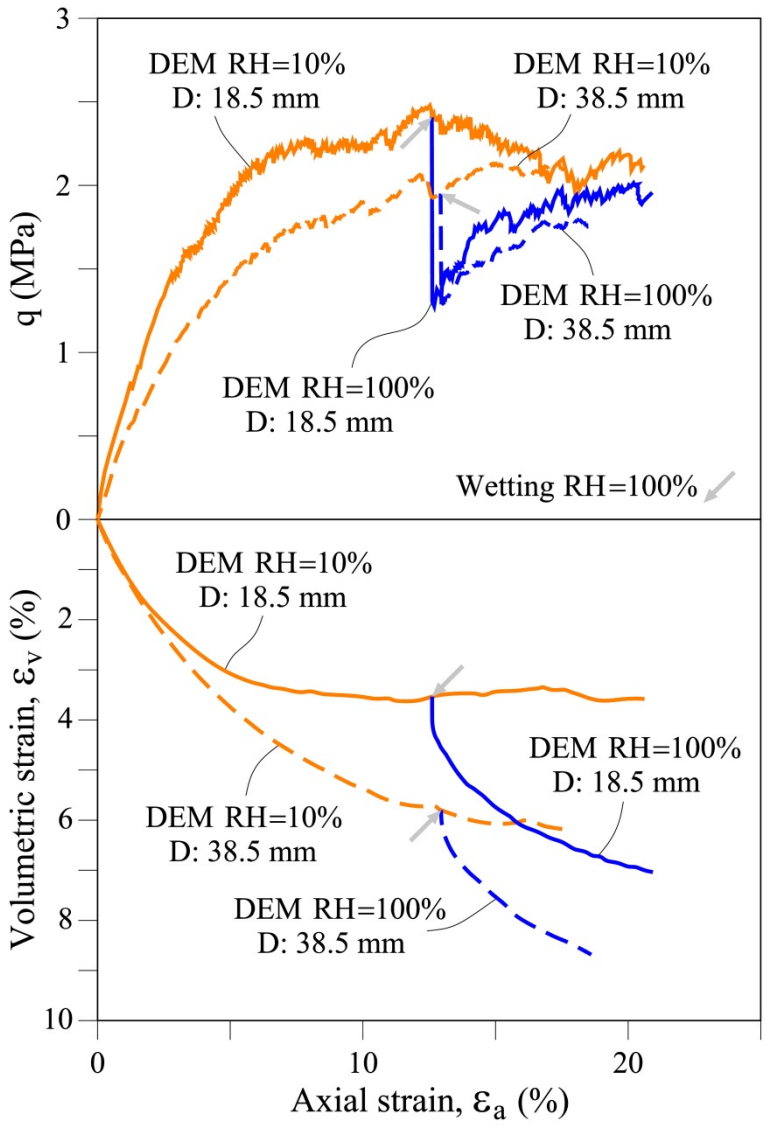

Figure 7-61 Scale effect and influence of Relative Humidity in DEM triaxial tests: Deviatoric stress and volumetric strain behaviour. DEM properties: μ=0.3; k_n=4 MN/m; K_c=1MPa•m$^{0.5}$. Comparison between two initial macroparticle sizes: 18.5mm and 38.5mm; for two types of tests: dry conditions (RH=10%) at the beginning and then wetting (RH=100%) at $\varepsilon_d \approx$ 13%; and dry conditions (RH=10%) during the entire test.

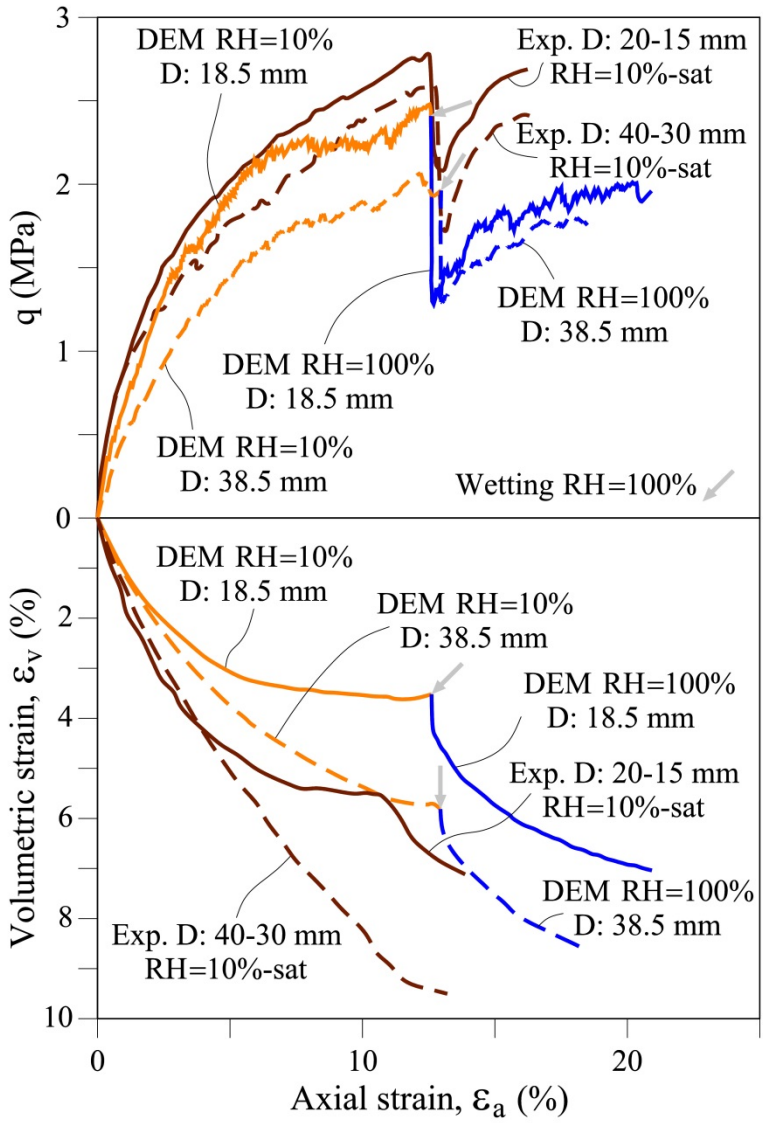

Figure 7-62 Comparison between DEM and experimental results for deviatoric stress and volumetric strain behaviour: Scale effect and influence of Relative Humidity in triaxial tests. DEM properties: μ=0.3; k_n=4 MN/m; K_c=1MPa•m$^{0.5}$. Comparison between two initial macroparticle sizes: 18.5mm and 38.5mm; dry conditions (RH=10%) at the beginning and then wetting (RH=100%) at $\varepsilon_d \approx$ 13%.

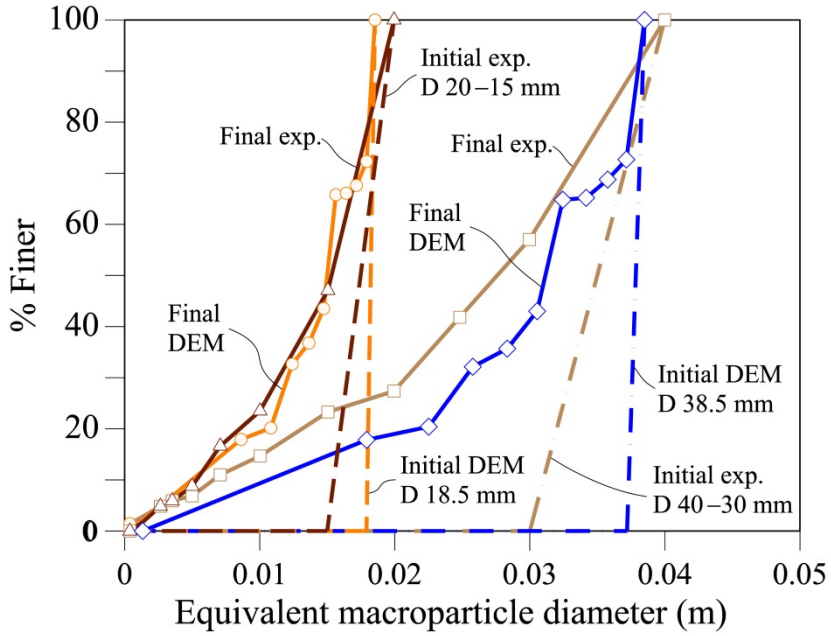

Figure 7-63 Scale effect and influence of Relative Humidity in triaxial tests: Evolution of gsd curves. Comparison between DEM and experimental tests. DEM properties: μ=0.3; k_n=4 MN/m; K_c=1MPa•m$^{0.5}$. Comparison between two initial macroparticles sizes: 18.5mm and 38.5mm; gsd curves in final tests: Dry conditions (RH=10%) at the beginning and then wetting (RH=100%) at ε_a≈ 13%.

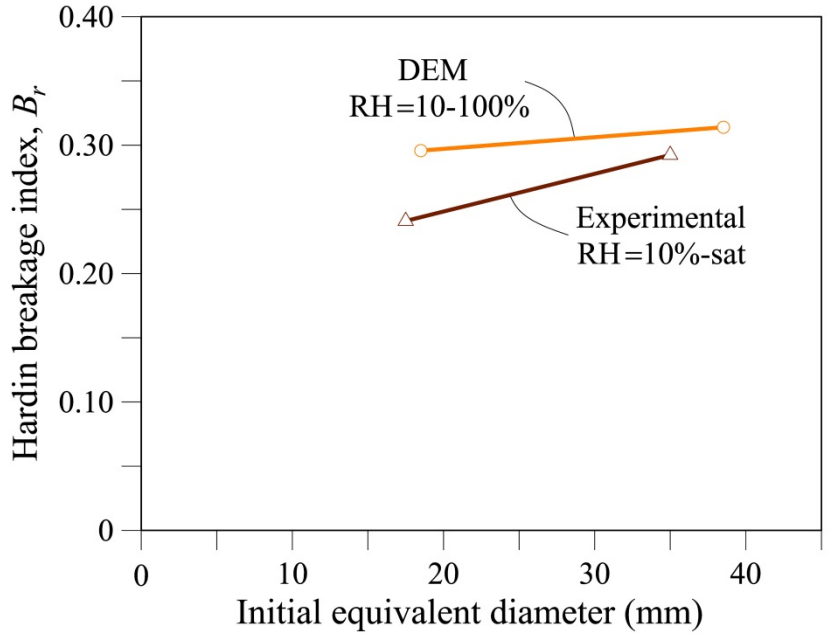

Figure 7-64 Scale effect in triaxial tests: Evolution of Hardin breakage index. Comparison between DEM and experimental tests. DEM properties: μ=0.3; k_n=4 MN/m; K_c=1MPa•m$^{0.5}$. DEM Breakage indexes calculated at ε_a=18%. Comparison between two initial macroparticle sizes: 18.5mm and 38.5mm; Test with dry conditions (RH=10%) at the beginning and then wetting (RH=100%) at ε_a≈ 13%.

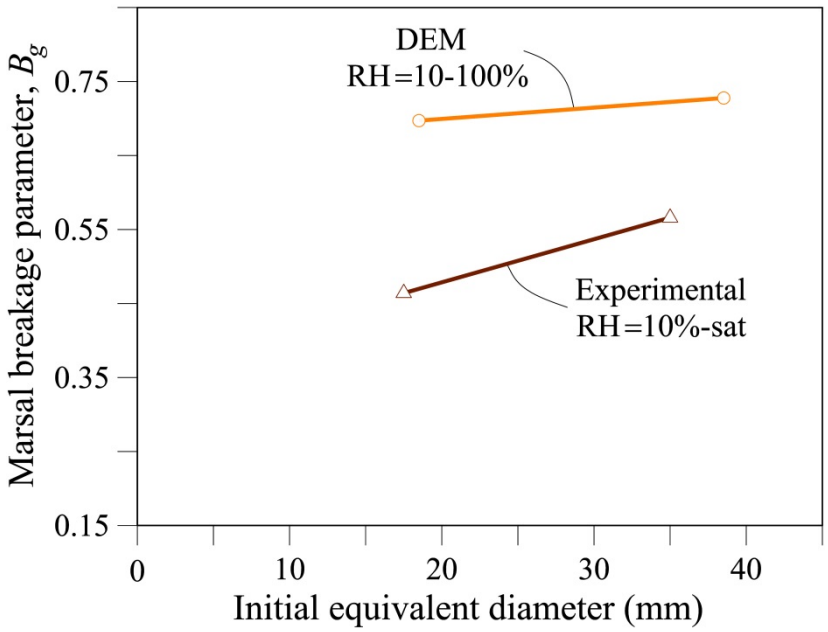

Figure 7-65 Scale effect in triaxial tests: Evolution of Marsal breakage index. Comparison between DEM and experimental tests. DEM properties: μ=0.3; k_n=4 MN/m; K_c=1MPa•m$^{0.5}$. DEM Breakage indexes calculated at ε_a=18%. Comparison between two initial macroparticle sizes: 18.5mm and 38.5mm; Test with dry conditions (RH=10%) at the beginning and then wetting (RH=100%) at ε_a≈ 13%.

7.4 Time effect

7.4.1 Influence of the parameters of the macroparticles

Time is an immersed variable in the model. It is used in the calculation of the crack length inside macroparticles (Eq. (7:6) and (7:7)), defects which propagate with a velocity v depending on the applied load, the stress intensity factor *K*, particle toughness K_c and the relative humidity. This propagation velocity also depends on the length of the defect or crack because this length affects the *K* calculation (Eq. (7:3) and (7:4)).

Following Oldecop and Alonso (2007), the crack propagation is analyzed in a disk with an inner crack subjected to Mode I (Tensile). Eq. (7:3), (7:4), (7:5) and (7:7) were applied for calculating the half length of the crack *a*, the stress intensity factor *K*, and coefficient β in function of the time. The following features were considered: σ=5MPa; K_c=1MPa•m$^{0.5}$; v_0=0.1m/s; *n*=60. Three different initial half lengths of the inner crack were considered: 4mm; 5mm and 6mm.

Figure 7-66 shows the evolution over time of the half crack length – crack growth - inside a macroparticle of a 0.04m equivalent diameter considering the different

initial crack lengths. Similarly, **Figure 7-67** and **Figure 7-68** show the evolution of the stress intensity factor K and the dimensionless coefficient β considering the same initial crack lengths.

Three aspects can be appreciated:

(a) Particles with smaller initial half crack lengths (a_o) break over a longer time.
(b) The crack propagation is slow initially. The propagation velocity is very small.
(c) At a certain time (triggering time), the crack propagation velocity suddenly increases and causes the particle breakage.

Figure 7-66 also illustrates the comparison of the crack growth when coefficient β is considered constant (calculated using the initial crack length a_o) and variable in function of the crack length over time. Triggering time is smaller using a variable β. This DEM model considered variable β.

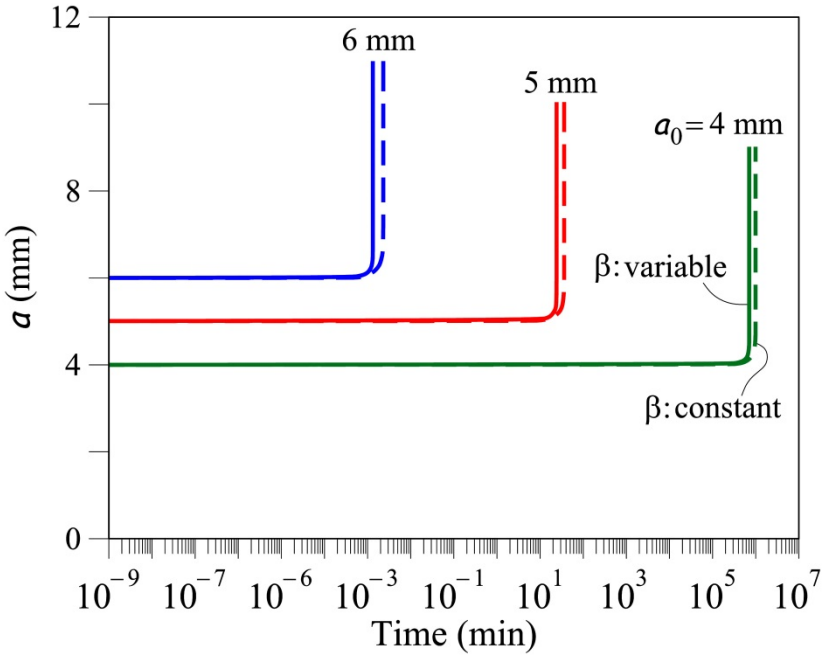

Figure 7-66 Crack growth inside a disk for different initial half crack lengths, a_o: 4mm; 5mm; 6mm. Mode I – Tensile. Disk Diameter=40mm; σ=5MPa; K_c=1MPa•m$^{0.5}$; v_0=0.1m/s; n=60.

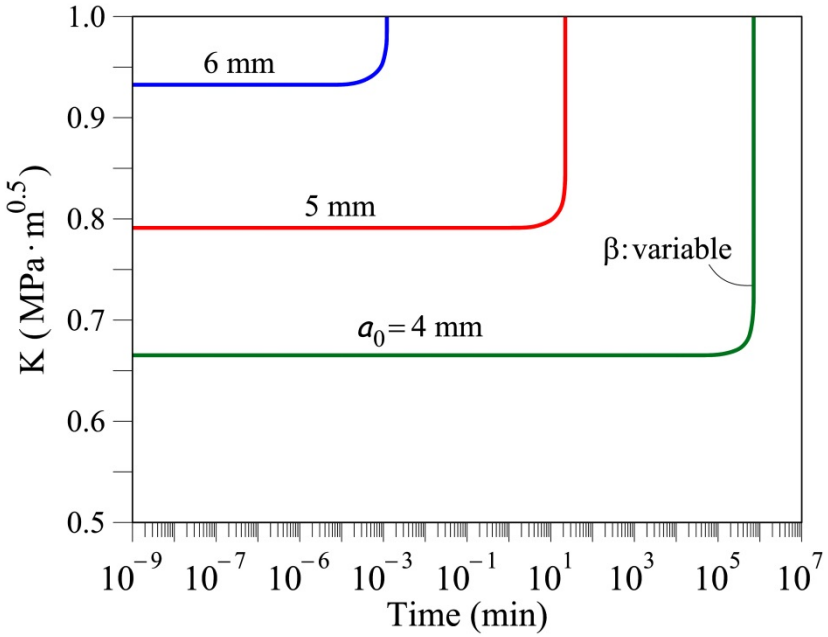

Figure 7-67 Evolution of the stress intensity factor *K* for Mode I (Tensile) over time for a crack growth inside a disk with different initial half crack lengths, a_o: 4mm; 5mm; 6mm. Disk Diameter=40mm; σ=5MPa; K_c=1MPa•m$^{0.5}$; v_0=0.1m/s; n=60.

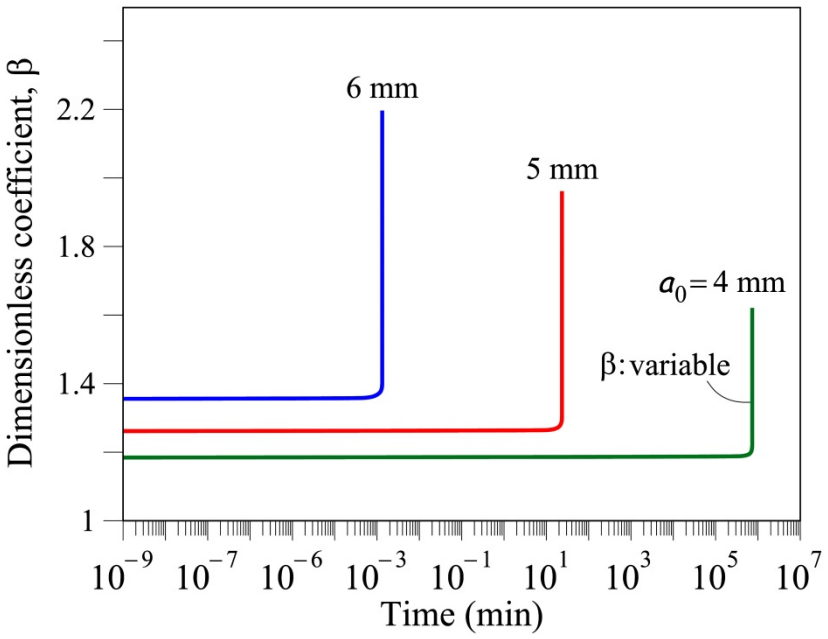

Figure 7-68 Evolution of the dimensionless coefficient β over time for a crack growth inside a disk with different initial half crack lengths,a_o: 4mm; 5mm; 6mm. Mode I – Tensile. Disk Diameter=40mm; σ=5MPa; K_c=1MPa•m$^{0.5}$; v_0=0.1m/s; n=60.

7.4.2 Features of the DEM model

In the DEM model, initial "virtual" crack length is assigned inside each macroparticle randomly using a uniform probability distribution. This type of probability distribution was selected after doing a sensitivity analysis using several probabilistic distributions (see **Appendix 1**). The initial crack length varies between 0.001*D* and 0.5*D*, where *D* is the equivalent diameter of the macroparticle.

In order to study the time-dependent behaviour of coarse aggregates, a numerical simulation of oedometer test on macroparticles with initial uniform size of 28mm (**Figure 7-8**a) is presented and the results are also compared with the experimental data (Ortega, 2008) on limestone fragments (see the initial experimental grain size distribution in **Figure 7-7**).

The parameters of the DEM model are again the same as those used for the previous oedometer tests: μ = 0.3; k_n = 4 MN/m; K_c = 1 MPa.m$^{0.5}$.

The DEM simulations follow the same stress path as the experimental test: 0.1; 0.2; 0.4; 0.6; 0.8; 1.2; 1.6; 2.0; 2.4; 2.8 MPa, for a relative humidity condition of RH=10%. For the maximum vertical stress (2.8MPa), the sample was wetted and therefore RH=100% was imposed. Each vertical stress (required stress) is applied by steps: 100 "small" load increments are done using 50 cycles (time steps) for each one, i.e. 5000 cycles are used to reach the required vertical stress. A certain tolerance (0.01) is allowed between the required stress and the calculated stress:

$$tolerance\ stress = \frac{calculated\ stress - required\ stress}{required\ stress} \tag{7:36}$$

When the required stress is reached, it is maintained during 3333min (200000s): one timestep has been considered as one second. This time is named here as macro time and this is taken into account for the calculation of the crack propagation. The actual test used a time of 1000min in maintaining every applied vertical stress.

Figure 7-69 shows the stress path over macro time for the DEM test. Some alterations in the stresses are present due to particle breakage and rearrangement of particles: for instance, this effect can be observed when the wetting of the specimen is simulated. It should also be noted that 33313min (1998790s) have elapsed from the beginning of the test until the end of the 2.8MPa for dry conditions (RH=10%); and 36647min (2198790s) until the end of the test for wetted conditions (RH=100%).

When breakage of particles occurs, some small extra time (10 timesteps), which is not included in the macro time calculation, is used to relax the macroparticles and avoid instabilities. During these extra timesteps, the translational and rotational velocities of the macroparticles are set to zero. In the process, the required vertical stress is also checked and some extra timesteps are used when required. **Figure 7-70** shows the vertical stress path over all the timesteps for the DEM test: including macro time and the other timesteps. 7686600 timesteps elapse from the

beginning of the test until the end of the 2.8MPa for dry conditions (RH=10%); and 11423600 timesteps elapse until the end of test for wetted conditions (RH=100%).

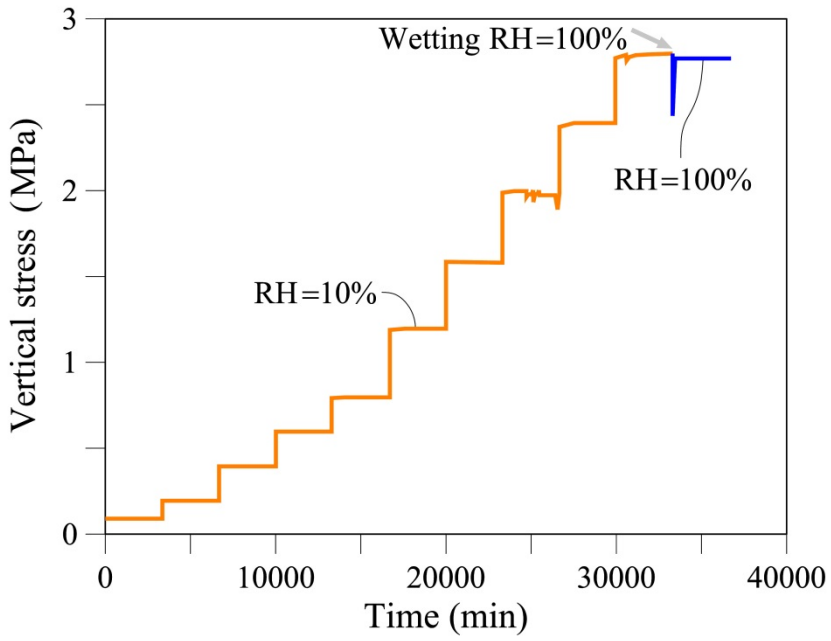

Figure 7-69 Macro time path of applied vertical stress in the oedometer test: DEM simulation.

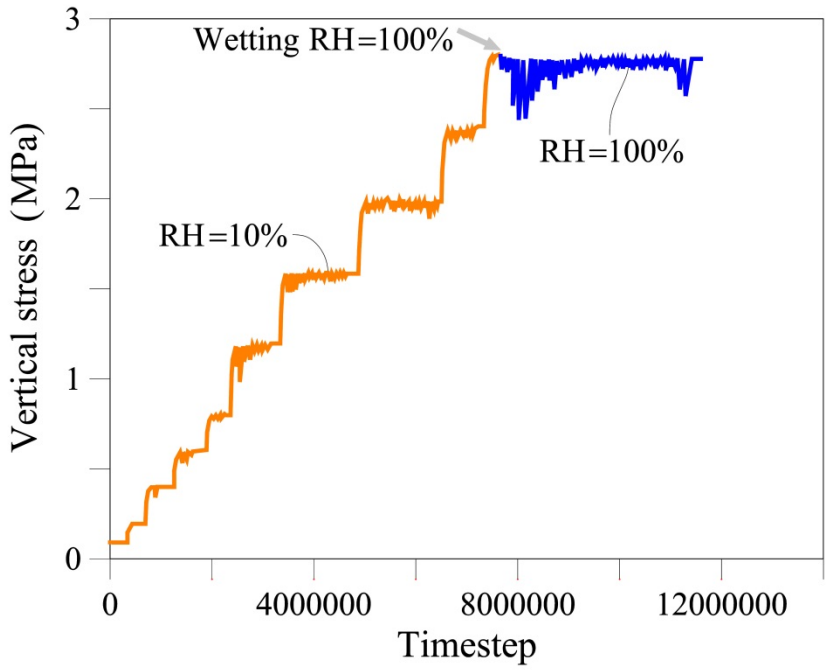

Figure 7-70 Applied vertical stress path over timesteps in the oedometer test: DEM simulation.

7.4.3 Compressibility behaviour

Figure 7-71 presents the experimental results (Ortega, 2008) of deformation behaviour over time for several vertical stresses which are imposed by steps and maintained for 1000min approximately: 0.1; 0.2; 0.4; 0.6; 0.8; 1.2; 1.6; 2.0; 2.4; and 2.8 MPa in dry conditions (RH=10%). For the maximum stress (2.8MPa), the sample was wetted until RH=100%. At the end of the dry conditions under 2.8 MPa, the vertical deformation was 8.76% while at the end of the wetted conditions it was 13.33%.

An almost instantaneous deformation can be observed between the 0.5min point and the first minute after the application of the load. After this main deformation, the sample is deformed in time with a lower velocity. There is a collapse in the vertical deformation between the first and the tenth minute after the wetting of the sample under the higher vertical stress of 2.8 MPa. This collapse can be divided into two main periods: the first occurs between minutes 1 and 2 and the second between minutes 5 and 8. At the end of the test, the vertical deformation has apparently not been stabilized and continued to increase.

Figure 7-72 shows the DEM results of the oedometer test for which the stresses were also imposed by steps and maintained for 3333min. At the end of the dry conditions, under a vertical stress of 2.8 MPa, the vertical deformation was 8.49% while at the end of the wetted conditions it was 12.99%. For dry conditions (RH=10%), the “instantaneous” vertical deformation due to the load application occurs close to minute 0.03 for most of the applied stresses (0.1-2.4MPa) and close to minute 0.05 for the higher stress of 2.8 MPa. Similarly to the actual behaviour, deformations increase in time with a lower velocity. The collapse in vertical deformation occurs close to the seventh minute after wetting. These deformations occur until close to minute 10.

There is a very good fit between the numerical and experimental results, which indicates that the model is accurate.

This time-dependent behaviour can be followed by calculating the long-term compressibility index (or time dependence coefficient) λ_t. This index measures the compressibility of the sample at long elapsed time after loading is applied, and is defined by the following expression:

$$\lambda_t = \frac{d(\varepsilon_a)}{d(\ln t)} \tag{7:37}$$

Figure 7-73 shows the calculated ratio λ_t in function of the vertical load applied load σ_v. The experimental data curve is also shown: experimental results found by (Ortega, 2008) for limestone fragments of 3cm. A very good correlation is observed between DEM and experimental test: λ_t = 0.00023 for DEM model at σ_V=2.8MPa (RH = 10%) and λ_t = 0.00030 for the experimental data in the same stress and environmental condition of RH.

Figure 7-74 illustrates the correlation between the compressibility indexes λ_t and λ at several applied loads σ_v. λ values were calculated using the expression given in

Eq. (7:23) (see **Figure 7-23**). Experimental data which were calculated from the experimental results for RH=10% of Ortega (2008) are also presented in this figure. A very good correlation between the DEM and laboratory data can be seen. The following relationship for the time dependence compressibility behaviour of limestone fragments has been obtained:

$$\frac{\lambda_t}{\lambda} = 0.004 \tag{7:38}$$

This expression coincides with that found in chapter 6, which was obtained from a study of scale effects using this DEM model.

As shown in **Figure 7-74**, both data (DEM and experimental) are placed in the lower range of the proposed ratio by (Oldecop and Alonso, 2007).

7.4.4 Particle breakage

The particle breakage in time is evidenced by plotting the breaking indexes B_r and B_g that occur in time for the different applied loads (**Figure 7-75** and **Figure 7-76**). "Collapses" in breaking index values can be observed and correspond to the collapse also presented in vertical deformation (**Figure 7-72**): For dry conditions, these increments of the breakage occur less than 0.1 minute after the load is applied. However, particle breakage is also prolonged over time. For instance, when 1.2 MPa is applied, B_r increases from 0.03 to 0.06 for a period between 0.03min and 0.12min of elapsed time (see the collapse in **Figure 7-75**) and continues increasing up to a value of 0.07 at 3333min. In the same way, B_g increases from 0.10 to 0.22 for the same period between 0.03min and 0.12min of elapsed time (see the collapse in **Figure 7-76**) and continues increasing up to a value of 0.24 at 3333min. Similarly, for 1.6 MPa, B_r increases from 0.07 to 0.08 for a period between 0.07min and 0.13min of elapsed time (see the collapse in **Figure 7-75**) and continues increasing up to a value of 0.10 at 3333min, while B_g increases from 0.24 to 0.27 for the same period between 0.07min and 0.13min of elapsed time (see the collapse in **Figure 7-76**) and continues increasing up to a value of 0.31 at 3333min.

Particle breakage rate increases fast when the sample is wetted under σ_v = 2.8 MPa for a period between minutes 7 and 10: B_r increases from 0.13 to 0.23 and B_g also increases from 0.40 to 0.61.

Breakage of particles over time is also evident in the evolution in time of the number of macroparticles during the test for each applied load (see **Figure 7-77**) and the number of macroparticles which do not break (see **Figure 7-78**). The number of macroparticles is 471 at the beginning of the test, 11307 at the end of the dry conditions under 2.8MPa, and 21383 at the end of the wetted conditions. The number of macroparticles which have not broken is 202 at the end of the dry conditions under 2.8MPa and 117 at the end of the wetted conditions.

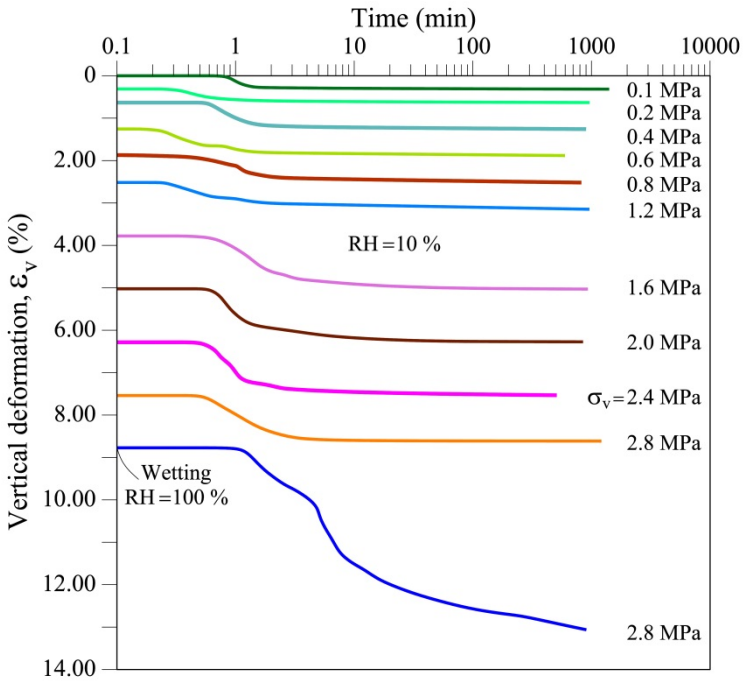

Figure 7-71 Strain behaviour over time for the experimental Oedometer tests (Ortega, 2008).

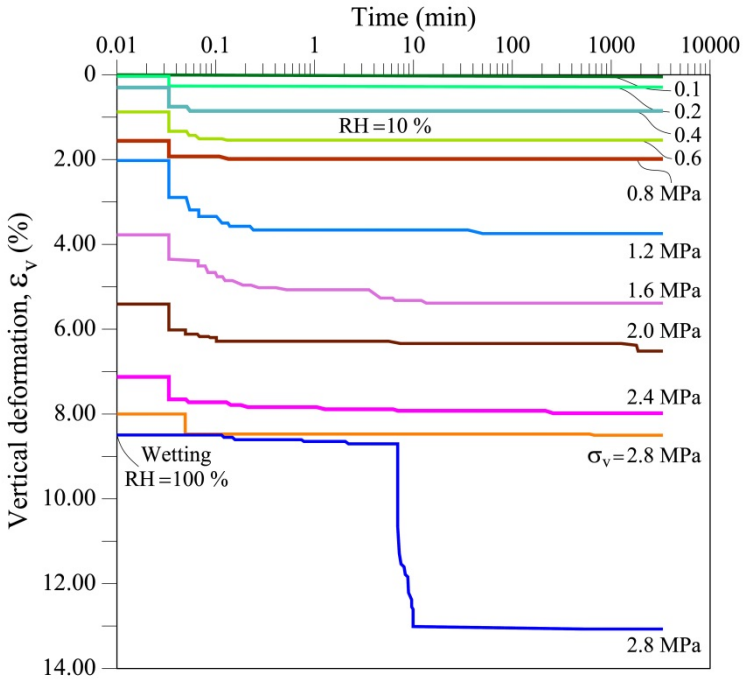

Figure 7-72 Strain behaviour over time of DEM results for the simulation of Oedometer tests.

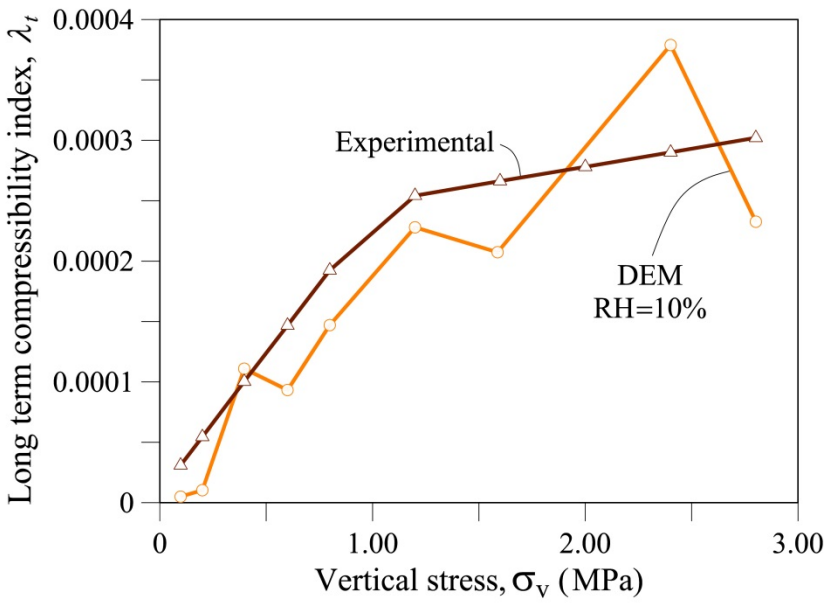

Figure 7-73 DEM results: Evolution of time compressibility index (long-term compressibility index or time dependence coefficient), λ_t. Oedometer tests.

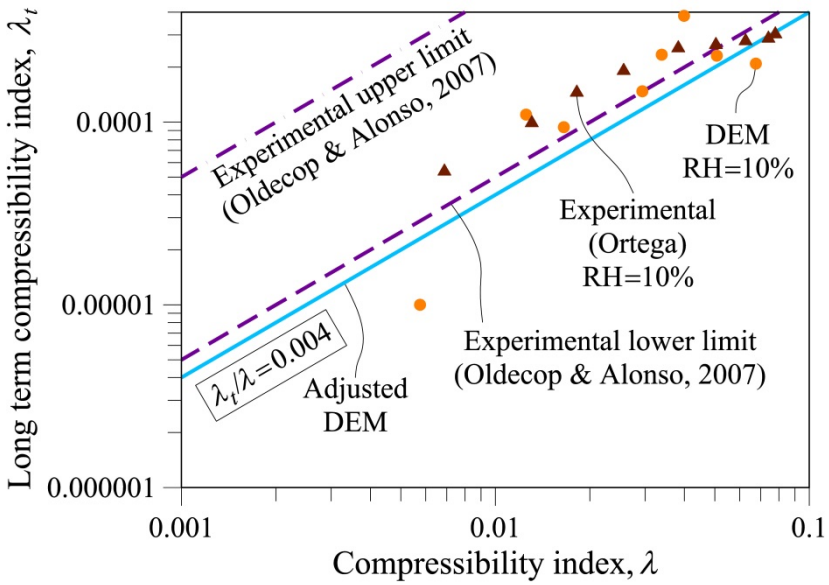

Figure 7-74 Correlation between compressibility coefficient, λ : time compressibility index (long-term compressibility index or time dependence coefficient), λ_t. Oedometer tests. Comparison between DEM and experimental results.

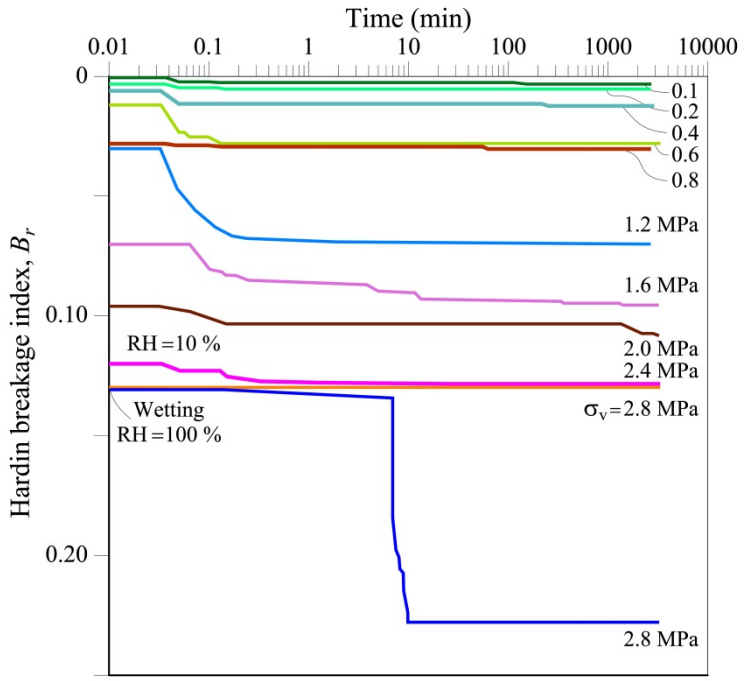

Figure 7-75 Evolution of Hardin breakage index – Time Effect: DEM simulation of oedometer test. DEM properties: μ=0.3; k_n=4 MN/m; K_c=1MPa•m$^{0.5}$.

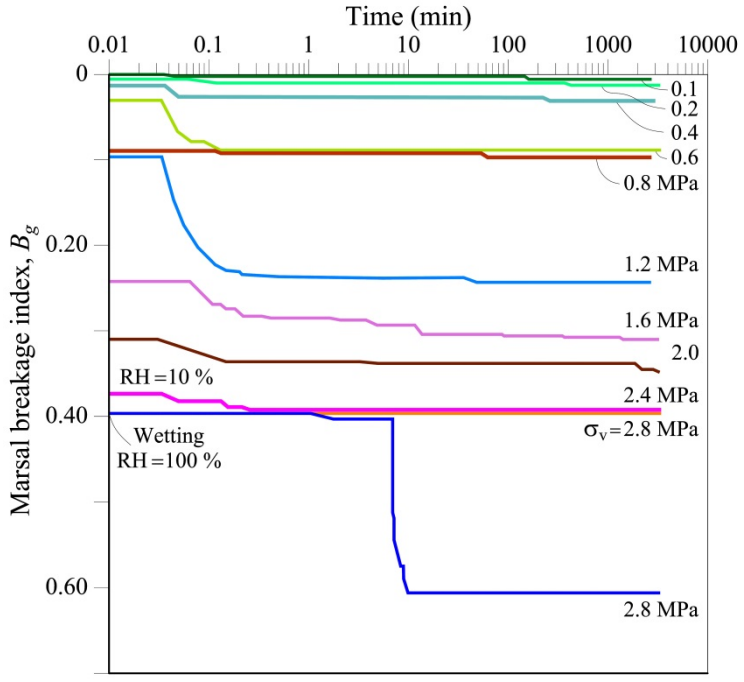

Figure 7-76 Evolution of Marsal breakage index – Time Effect: DEM simulation of oedometer test. DEM properties: μ=0.3; k_n=4 MN/m; K_c=1MPa•m$^{0.5}$.

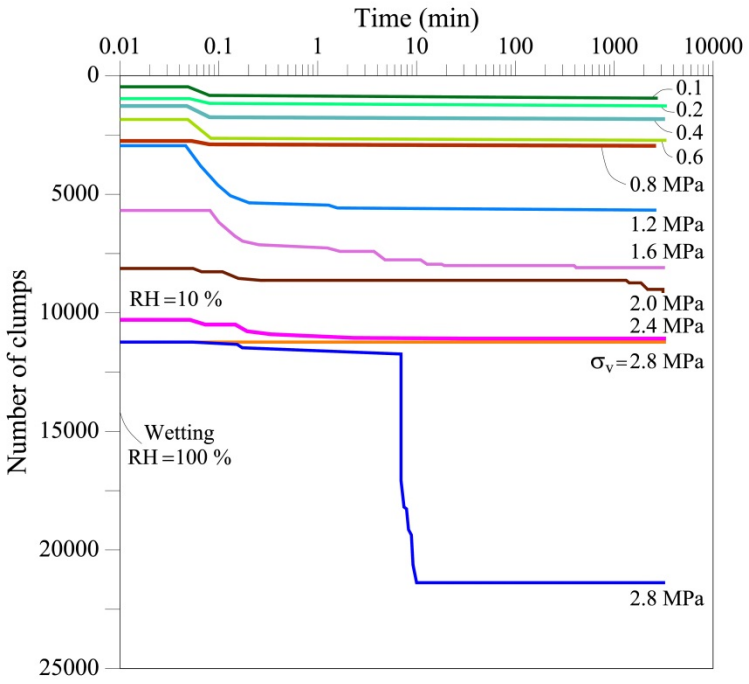

Figure 7-77 Evolution of Number of Macroparticles (Clumps) – Time Effect: DEM simulation of oedometer test. DEM properties: μ=0.3; k_n=4 MN/m; K_c=1MPa•m$^{0.5}$.

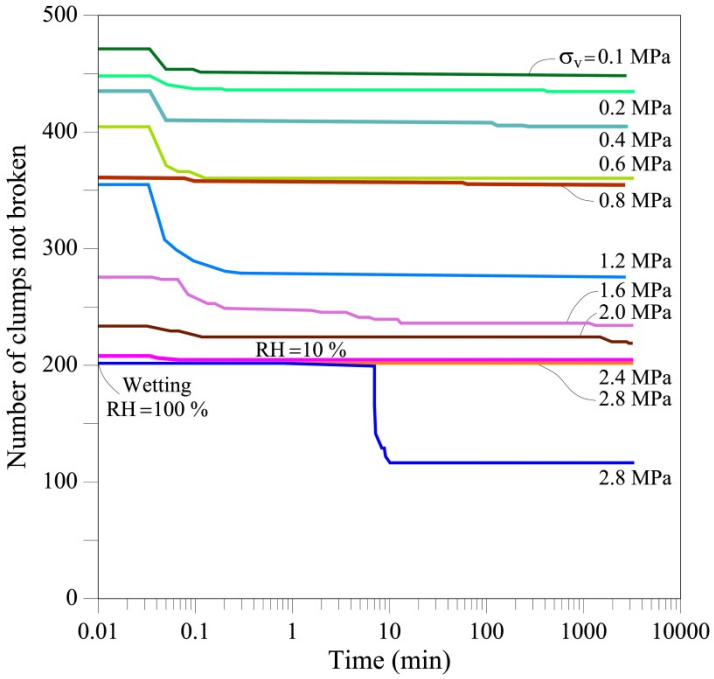

Figure 7-78 Evolution of Number of Macroparticles (Clumps) not broken – Time Effect: DEM simulation of oedometer test. DEM properties: μ=0.3; k_n=4 MN/m; K_c=1MPa•m$^{0.5}$.

7.5 Conclusions

Three models of subcritical crack propagation have been proposed: Generalized model, Model with common region 2, and Simplified model. These models are formulated in a *K*-v space: Stress intensity stress factor – Velocity of crack propagation. Three regions are considered in the *K*-v behaviour. The last two models are based on the first. The models consider the effect of the relative humidity, RH.

The subcritical crack propagation models are supported by experimental data found in the literature from results of subcritical crack propagation tests. Moreover, these models are based on the theory of the stress corrosion for the subcritical crack propagation. The models are formulated based on the Charles's law for the subcritical crack propagation (Charles, 1958a, 1958b) and previous works mainly by Atkinson, (1984) and Oldecop and Alonso, (2007).

Mechanical behaviour of coarse aggregates such as rockfill and gravels is influenced by the relative humidity (environmental conditions). These materials also exhibit a time-dependent behaviour. This behaviour can be explained mainly by the breakage of particles and the subsequent rearrangement of the particles.

The influence of the relative humidity and the effect of the time behaviour are taken into account now by the proposed DEM model.

The DEM model is based on the fracture mechanics and the theory of the crack propagation inside particles. The DEM model for particle breakage incorporates the proposed models of the subcritical crack propagation. The third model (simplified model) was used for the simulation of the tests.

The accuracy of the model is supported by the very good correlation between the simulations of oedometer and triaxial tests and experimental data.

Relative humidity influences the subcritical crack propagation inside the particles. The increase in humidity (decrease in suction) leads to an increase in the crack propagation velocity and can therefore lead to breakage of the particles. This is evidenced by the collapse of deformation that occurs in oedometer tests when suction changes (increasing RH) are applied to a certain applied vertical load, and collapses in both deviatoric stress and volumetric strains for triaxial tests.

The particle breakage depends on the applied loads and also occurs over time. Therefore, delayed deformation behaviour over time occurs in coarse aggregates.

The velocity of crack propagation is small for an initial elapsed time after applying a load and is triggered when a "threshold time" or "rupture time" is reached, causing the breakage of the particle. Moreover, this rupture time is influenced by the magnitude of the load, the relative humidity, and the initial lengths of the defects or cracks inside the particles. These crack lengths are assigned to all the macroparticles randomly using a uniform probability distribution.

The time compressibility index (long term compressibility index) λ_t could be considered a material property: an expression depending on the compressibility index λ has been obtained.

For oedometer tests

In order to analyze the influence of the relative humidity on the compressibility behaviour, a DEM simulation of oedometer test was presented and compared with experimental data from Ortega (2008). Vertical stresses were applied by increments from 0.1MPa until 2.8MPa, for dry conditions (RH=10%). Afterwards, the specimen was subjected to wetting by imposing RH=100%. Two unloading paths were also performed: at the end of the loading path (σ_V=2.8MPa), and at the end of the wetting process (σ_V=2.8MPa). Both unloading processes were performed by steps from 2.8MPa until 0.2MPa.

The DEM results were accordance with the experimental data: The calculated compressibility behaviour was close to the actual behaviour for the loading process. For unloading, there was a greater recovery in the calculated vertical strain than in the experimental results. The evolution of the grain size distributions for DEM results was very close to the actual gsd at the end of the test. The breakage indexes, Hardin and Marsal, for DEM tests at the end of the test were also close to the experimental data.

Likewise, an analysis was done of the evolution of the total external energy of the system in the numerical oedometer test taking into account the work done by the boundaries (walls) on the sample (E_w), kinetic energy (E_k), strain energy (E_s), frictional energy (E_f) and damping energy (E_d). E_s is associated with elastic strain energy. E_f and E_d are associated with plastic dissipation energy. At the end of the loading stage at σ_V=2.8MPa, the plastic dissipation energy corresponded to 55% of the total energy, and 75% at the end of the wetting (for σ_V=2.8MPa). At the end of the unloading processes (for both cases, at σ_V=0.2MPa), the elastic strain energy tended to zero (1-4% of total energy).

The breakage of particles is evaluated through the evolution of the grain (particle) size distribution curves, the breakage indexes (Hardin and Marsal), the number of clumps or macroparticles, and the number of unbroken clumps during the tests. For instance, at the end of the loading in dry conditions, the number of unbroken clumps was 202 and corresponded to 43% of the initial number of macroparticles; at the end of the wetting, this value was 117 and corresponded to 25% of the total initial number of macroparticles.

For triaxial tests

DEM triaxial tests were performed using the same parameters calibrated in previous oedometer tests. These tests simulated experimental tests carried out by Ortega (2008) on limestone fragments with an initial size of about 28mm. A confining pressure of 1 MPa was applied before the deviatoric stage.

One test (Test I) was performed under dry conditions (RH=10%) until an axial

strain of about 10%; then the wetting of the specimen was simulated by imposing a relative humidity of 100%.

A smaller strength was obtained in the DEM test, about 80% of the actual maximum deviatoric stress. By contrast, at the end of the tests, the experimental volumetric strain was smaller than the DEM value and corresponded to 70% of the numerical volumetric strain.

However, the triaxial behaviour (curves q-ε_a; ε_v- ε_a) was similar in both DEM and experimental results.

Collapses in deviatoric stresses and in volumetric strain were very well simulated as they corresponded to what was obtained in the experimental test.

Gsd curves and breakage indexes at the end of the DEM and experimental tests were similar.

A second DEM triaxial test was performed for dry conditions (RH=10%) during the entire test (Test II).

By comparing the two DEM tests which were performed under different relative humidity conditions (Test I and II), it is possible to observe the evolution of the particle breakage due to the deviatoric stresses and the wetting of the sample. A little higher strength was obtained for a dry specimen. However, after the collapse in the deviatoric stress due to the wetting, the strength of the wetted sample tends to reach the strength of the dry sample.

Scale effect in triaxial tests

The scale effect in triaxial tests was analyzed taking into account the influence of the relative humidity: Two additional DEM triaxial tests were performed using two initial sizes: 18.5mm and 38.5mm. The confining stress was 1MPa in both cases. The specimens had the same initial porosity. The DEM tests simulated experimental tests from Ortega (2008) on the same limestone fragments. The DEM parameters were the same as those used previously. Two types of tests were simulated varying the relative humidity conditions: Dry condition (RH=10) during the entire test (Test II) and tests with dry condition at the beginning and wetting at ε_a =13% (Test I) just like in the experimental tests.

The specimen with a smaller size is more rigid and reaches a higher maximum deviatoric stress (peak strength).

The specimen with a greater size is more deformable (compressive).

“Residual” strength tends to be the same in both sizes.

For both sizes, collapses in deviatoric stresses and volumetric strains due to the wetting of the specimens were simulated according to the actual behaviour.

Also for both sizes, after the wetting, the wetted deviatoric curves tend to reach

those representing dry conditions.

Numerical gsd curves at the end of the tests were very similar to the experimental results. Size effect could be noted in the evolution of the gsd curves: this evolution depends on the initial size of the macroparticles.

Based on the evolution of the gsd curves and the breakage indexes (B_r and B_g),it can be observed that greater breakage is obtained for larger sizes.

Time effect

Time is an immersed variable in the model: from the concept of the DEM (interactions of particles and particle motion) to the considerations of crack propagation inside particles that depends on the initial length of the cracks, size of particles, particle toughness, stress intensity factor and environmental conditions (relative humidity).

Crack lengths inside particles are introduced randomly using a uniform probability distribution. This length depends on the equivalent diameter of the macroparticle.

Based on an analysis of crack propagation inside particles with the same size and subjected to the same load (Mode I), but varying the initial crack length, it can be concluded that the smaller the initial crack length, the lower the value of stress intensity factor (K) and also the lower the value of dimensionless coefficient (β), but the greater the value of rupture time. Also, for all the cases, the velocity of crack propagation is much lower at the beginning and increases very fast close to certain "triggering time" (rupture time) and then reaches breakage.

Furthermore, one DEM oedometer tests was performed in order to simulate an experimental test from Ortega (2008) on limestone fragments of 28mm in size. Vertical stresses were applied by steps from 0.1 MPa until 2.8 MPa under dry conditions (RH=10%). For the higher stress (σ_V=2.8 MPa), the particles were subjected to a saturated condition by imposing RH=100%. Each vertical stress increment was maintained for a "macro" time of approximately 3333min (200000s) using timesteps of 1s. The DEM model uses other timesteps in order to stabilize the particles when breakage occurs or due to load application. Macro time is used to calculate the crack propagation.

Calculated compressibility behaviour over time is in accordance with the experimental results for each applied vertical stress: For instance, at the end of the σ_V=2.8MPa for RH=10%, vertical strain is equal to 8.5% and 8.8% for the DEM and experimental tests respectively; and after the wetting, the vertical strain increases to 13.0% and 13.3% for the DEM and experimental tests respectively.

In dry conditions (RH=10%), after the application of the vertical stresses, significant vertical deformation occurs after a small elapsed time between 0.03 and 0.05min for the DEM tests, and between 0.5 and 1min for the experimental data. These "instantaneous" deformations are caused by the application of the load. However, deformations also occur in time. They are associated with particle breakage in time and the rearrangement of the particles.

After the wetting, for σ_v =2.8MPa, a collapse in vertical deformation occurs approximately between minute 7 and 10 for the DEM test. For the experimental data, this collapse occurs over two periods: between minutes 1 and 2 and between minutes 5 and 8. Also, deformations are prolonged in time.

The evolution of the particle breakage in time can also be followed through the evolution of the breakage indexes (B_r and B_g), and the number of clumps or macroparticles.

Breakage of particles can occur suddenly due to the application of loads and/or saturation of the specimen by imposing RH=100%. Likewise, breakage of particles also can occur in time.

7.6 List of Notations

Notation		***Section***
a	Crack half-length; Eq. (7:3); (7:4); (7:7)	7.2.2; 7.4.1
a_0	Crack half-length before a time increment; Eq. (7:7)	7.2.2; 7.4.1
B_g	Marsal breakage index	7.1.1.1; 7.3.3.2; 7.3.4; 7.4.4
B_r	Hardin breakage index	7.1.1.1; 7.3.3.2; 7.3.4; 7.4.4
D	Particle Diameter; Eq. (7:4)	7.2.2; 7.4.2
DEM	Discrete/Distinct Element Method	7
DT	Double Torsion testing method- Subcritical crack propagation test;	7.3.2.4
E	Young's modulus	7.2.4
$E_b^{t+\Delta t}$	Bond energy at time (t+Δt); Eq. (7:31)	7.3.3.3
$E_{bodyforce}^{t+\Delta t}$; $E_{bodyforce}^{t}$	Energy associated with body forces, such as gravity, acting on the particles, at time (t+Δt) and (t) respectively; Eq. (7:25); (7:26)	7.3.3.3
E_d	Damping dissipation energy; Eq. (7:31)	7.3.3.3
$E_d^{t+\Delta t}$	Damping dissipation energy at time (t+Δt); Eq. (7:31)	7.3.3.3
E_e	Elastic strain energy of the system; Eq.	7.3.3.3

	(7:35)	
E_{ext}	External energy of the system; Eq. (7:24); Eq. (7:35)	7.3.3.3
$E_{ext}^{t+\Delta t}$	External energy of the system at time (t+Δt); Eq. (7:25); (7:29)	7.3.3.3
$E_{externalappliedforces}^{t+\Delta t}$; $E_{externalappliedforces}^{t}$	Energy associated with any externally applied loads acting on the particles, at time (t+Δt) and (t) respectively; Eq. (7:25); (7:27)	7.3.3.3
E_f	Total frictional energy; Eq. (7:33)	7.3.3.3; 7.3.4
$E_f^{t+\Delta t}$	Frictional energy at time (t+Δt); Eq. (7:31)	7.3.3.3
E_{int}	Internal energy of the system; Eq. (7:24); (7:31)	7.3.3.3
$E_{\text{int}}^{t+\Delta t}$	Internal energy of the system at time (t+Δt); Eq. (7:31)	7.3.3.3
E_k	Kinetic energy of the system; Eq. (7:24); (7:30)	7.3.3.3
E_p	Plastic dissipation energy of the system; Eq. (7:35)	7.3.3.3
E_s	Total strain energy; Eq. (7:32)	7.3.3.3; 7.3.4
$E_s^{t+\Delta t}$	(Elastic) Strain energy at time (t+Δt); Eq. (7:31); (7:32)	7.3.3.3
E_w	Boundary energy; work done by all walls on the sample (surfaces that confine the sample: cylinder and upper and lower plates)	7.3.3.3; 7.3.4
$E_w^{t+\Delta t}$; E_w^t	Work done on the system by the rigid boundaries, at time (t+Δt) and (t) respectively; Eq. (7:25); (7:28); (7:29)	7.3.3.3
e	Void ratio	7.3.3.1; 7.3.4
F	Normal concentrated force; Normal load; Contact load; Eq. (7:2)	7.2.1
F_i	Resulting force acting on the surface i; Eq. (7:28)	7.3.3.3
$F_i^{applied}$	Applied external force acting on i; Eq. (7:27)	7.3.3.3

$\|F_i^n\|$	Magnitud of the normal component of the contact force at contact *i*; Eq. (7:32)	7.3.3.3
F_i^s	Shear component of the contact force at contact *i*; Eq. (7:33); (7:34)	7.3.3.3
$\|F_i^s\|$	Magnitud of the shear component of the contact force at contact *i*; Eq. (7:32)	7.3.3.3
g_i	Vector of gravitational acceleration acting on *i*; Eq. (7:26)	7.3.3.3
gsd	Grain (particle) size distribution	7.1.1.1; 7.1.2.1; 7.3.3.2; 7.3.4
I_i	Inertia tensor; Eq. (7:30)	7.3.3.3
K	Stress intensity factor; Eq. (7:3); (7:5); (7:8); (7:12); (7:13); (7:17); (7:18)	7.2.2; 7.2.3; 7.3; 7.4.1
$K_{R2}(RH)$	(1) Stress intensity factor for a given RH condition when v= $\nu_{R2}(RH)$; Eq. (7:9) (2) Stress intensity factor for a given RH condition when v= ν_{R2} ; Eq. (7:14)	7.3
K_{R2_dry}	Stress intensity factor for RH=0% when v= ν_{R2} ; Eq. (7:16)	7.3
$K_{R2\_dry}(RH)$	Stress intensity factor for RH=0% when v= $\nu_{R2}(RH)$; Eq. (7:11)	7.3
K_c	Toughness; Eq. (7:5); (7:8); (7:9); (7:11); (7:12); (7:13); (7:14); (7:16); (7:17); (7:18)	7.2.2; 7.2.3; 7.2.4; 7.3; 7.3.3; 7.3.4; 7.4
K_o	Lateral coefficients of earth pressure	7.3.3.1
K_0	Lower limit of the stress intensity factor or threshold stress intensity factor	7.3
k_n	Normal contact stiffness; Eq. (7:32)	7.2.1; 7.2.4; 7.3.3; 7.3.4; 7.4
k_s	Shear contact stiffness; Eq. (7:32)	7.2.1; 7.2.4; 7.3.3
M	*Relationship q/p* at maximum deviatoric stress *q*	7.3.4

M_w	Molecular weight of water; Eq. (7:22)	7.3.2.4
m_i	(1) Mass of the particle *i*; Eq. (7:26); (2) Inertial mass; Eq. (7:30)	7.3.3.3
N_c	Number of contacts; Eq. (7:32); (7:33)	7.3.3.3
N_p	Number of particles; Eq. (7:26); (7:27); (7:30)	7.3.3.3
N_w	Number of walls; Eq. (7:28)	7.3.3.3
n	Parameter for crack propagation; Eq. (7:5)	7.2.2; 7.4.1
n(RH)	Subcritical crack propagation index or stress corrosion index that depends of the relative humidity; Eq. (7:8); (7:9); (7:11); (7:12); (7:13); (7:14); (7:16); (7:17); (7:18); (7:21)	7.3
n(RH=0%)	Subcritical crack propagation index or stress corrosion index when RH=0%; Eq. (7:11); (7:12); (7:16); (7:17)	7.3
n_o	Porosity	7.3.3.1
PFC3D	Particle Flow Code in 3 Dimensions	7.2
p	(1) Contact stress due roughness effect; Eq. (7:1); (7:2)	(1) 7.2.1;
	(2) Mean stress	(2) 7.3.3; 7.3.4
p_v	Partial pressure of water vapour or actual vapour pressure at the temperature *T*; Eq. (7:19)	7.3.2.4
p_{vs}	Equilibrium vapour pressure of water at the same temperature T or the saturation vapour pressure; Eq. (7:19); (7:20)	7.3.2.4
q	Deviatoric stress	7.1.1.1; 7.2.1; 7.3.4
q_{max}	Maximum deviatoric stress	7.3.4
R	(1) Radius of the sphere; Particle Radius; Eq. (7:2)	(1) 7.2.1;
	(2) Gas constant; Eq. (7:22)	(2) 7.3.2.4
RH	Relative Humidity; Eq. (7:19); ; (7:21); (7:22)	7; 7.3; 7.3.2.4
r	Radial distance (spherical-polar coordinate system)	7.2.1
s_ψ	Total suction; Eq. (7:22)	7.3.2.4

T	Temperature; Eq. (7:20); (7:22)	7.3.2.4
t	Time; Macro time; Eq. (7:37)	7.4
V_i	Translational velocity for macroparticle *i*; Eq. (7:30)	7.3.3.3
v	(1) Crack propagation velocity; Eq. (7:5); (7:6); (7:7);	(1) 7.2.2;
	(2) Crack propagation velocity for a given RH condition; Eq. (7:8); (7:10); (7:12); (7:13); (7:15); (7:17); (7:18)	(2) 7.3
v_{R2}	Reference velocity for the material that limits Region 1 and Region; Eq. (7:14); (7:15); (7:16)	7.3
$\mathrm{v}_{R2}(RH)$	Reference velocity that limits Region 1 and Region 2 for a given RH condition; Eq. (7:9); (7:10); (7:11)	7.3
v_0	Reference velocity for crack propagation; Eq. (7:5); (7:8); (7:9); (7:11); (7:12); (7:13); (7:14); (7:16); (7:17); (7:18)	7.2.2; 7.3; 7.4.1
w	Radius of the loaded area or contact stress; Eq. (7:1)	7.2.1
w_i	Rotational velocity for macroparticle *i*; Eq. (7:30)	7.3.3.3
z	Vertical coordinate inside particle under *F* applying; Eq. (7:1)	7.2.1
3PB	Three Point Bend method - Subcritical crack propagation test;	7.3.2.4
α	Dimensionless coefficient used in calculation of stress intensity factor; Eq. (7:4)	7.2.2
β	Dimensionless coefficient used in calculation of stress intensity factor; Eq. (7:3); (7:4)	7.2.2; 7.4.1
Δ_i	Incremental displacement of particle *i*; Eq. (7:26) ; (7:27)	7.3.3.3
Δa	crack half-length increment; Eq. (7:6)	7.2.2
Δu_i	Displacement acting on the surface *i*; Eq.	7.3.3.3

	(7:28)	
Δu_i^s	Increment of shear displacement at contact *i*; Eq. (7:34)	7.3.3.3
$(\Delta u_i^s)^{elast}$	Increment of elastic shear displacement at contact *i*; Eq. (7:34)	7.3.3.3
$(\Delta u_i^s)^{slip}$	Increment of slip displacement at contact *i*; Eq. (7:33); (7:34)	7.3.3.3
Δt	Time increment; timestep; Eq. (7:6); (7:7)	7.2.2; 7.4
ε_a	Axial strain; Eq. (7:23); (7:37)	7.1.1.1; 7.2.1; 7.3.3; 7.3.4; 7.4
ε_p	Volumetric strain	7.1.1.1
ε_v	(1) Vertical deformation; (2) Volumetric strain	(1) 7.3.3; 7.4 (2) 7.3.4
θ	Polar angle (spherical-polar coordinate system)	7.2.1
θ_0	(Half) Solid angle describing contact stresses; Eq. (7:2)	7.2.1
λ	Compressibility index; Eq. (7:23); (7:38)	7.3.3.1; 7.4.3
λ_t	Long-term compressibility index; time dependence coefficient; Eq. (7:37); (7:38)	7.4.3
μ	(Contact) Friction coefficient	7.2.1; 7.2.4; 7.3.3; 7.3.4; 7.4
ν	Poisson ratio; Eq. (7:1)	7.2.1
ρ_l	Density of liquid (water) ; Eq. (7:22)	7.3.2.4
σ	Maximum tensile stress; Eq. (7:1); (7:3)	7.2.1
σ_h	Horizontal stress	7.3.3.1
σ_r	Radial stress (spherical-polar coordinate system)	7.2.1
σ_v	Vertical stress; Eq. (7:23)	7.3.3; 7.4.3; 7.4.4
σ_y	Yield stress	7.2.1; 7.2.3
σ_3	Confining stresses; minor principal stress	7.1.1.1; 7.2.1
σ_θ	(1) Tensile stresses acting on vertical diameter inside macroparticle	7.2.1

	(2) Polar stress; stress in θ direction (spherical-polar coordinate system)	
σ_ψ	Azimuthal stress; stress in ψ direction (spherical-polar coordinate system)	7.2.1
ϕ	Friction angle	7.3.4
ϕ_m	Mineral friction angle	7.2.4
ϕ_b	Basic friction angle	7.2.4
ψ	Azimuth angle (spherical-polar coordinate system)	7.2.1

7.7 References

Alonso, E.E., Olivella, S., Pinyol, N.M., 2005. A review of Beliche Dam. Géotechnique 55, 267–285.

Alonso, E.E., Romero, E.E., Ortega, E., 2016. Yielding of rockfill in relative humidity-controlled triaxial experiments. Acta Geotech. doi:10.1007/s11440-016-0437-9

Atkinson, B.K., 1984. Subcritical crack growth in geological materials. J. Geophys. Res. 89, 4077–4114.

Atkinson, B.K., 1982. Subcritical crack propagation in rock: theory, experimental results and applications. J. Struct. Geol. 4, 41–56.

Atkinson, B.K., 1980. Stress corrosion and the rate-dependent tensile failure of a fine-grained quartz rock. Tectonophysics 65, 281–290.

Atkinson, B.K., 1979a. A fracture mechanics study of subcritical tensile cracking of quartz in wet environments. Pure Appl. Geophys. PAGEOPH 117, 1011–1024. doi:10.1007/BF00876082

Atkinson, B.K., 1979b. Fracture toughness of Tennessee Sandstone and Carrara Marble using the double torsion testing method. Int. J. Rock Mech. Min. Sci. Geomech. Abstr. 16, 49–53.

Atkinson, B.K., Meredith, P.G., 1987. The theory of subcritical crack growth with applications to minerals and rocks, in: Atkinson, B.K. (Ed.), Fracture Mechanics of Rock. Academic Press, London (U.K), pp. 111–166.

Atkinson, B.K., Rawlings, R.D., 1981. Acoustic emission during stress corrosion cracking in rocks, in: Simpson, D.W., Richards, P.G. (Eds.), Earthquake Prediction. American Geophysical Union, Washington, D. C. (USA), pp. 605–616. doi:10.1029/ME004p0605

Barksdale, R.D., Blight, G.E., 1997. Compressibility and settlement of residual soils, in: Mechanics of Residual Soils, Chapter 8. Balkema, Rotterdam, pp. 95–154.

Belytschko, T., Liu, W.K., Moran, B., 2000. Nonlinear Finite Elements for Continua and Structures. Wiley, New York, NY, USA.

Bruner, W.M., 1980. Effects of time-dependent crack growth on the unroofing and unloading behaviour of rock. PhD. thesis. University of California, Los Angeles (USA).

Catalano, E., Chareyre, B., Cortis, A., Barthelemy, E., 2011. A pore-scale hydro-mechanical coupled model for geomaterials, in: Oñate, E., Owen, D.R.J. (Eds.), II International Conference on Particle-Based Methods. Fundamentals and Applications. Barcelona (Spain), pp. 1–12.

Chareyre, B., Scholtès, L., 2011. Discrete Models of Wet Granular Media, in: Radjai, F., Dubois, F. (Eds.), Discrete-Element Modeling of Granular Materials. ISTE Ltd; John Wiley & Sons, Inc., London, UK, pp. 367–392.

Chareyre, B., Scholtès, L., Darve, F., 2009. Micro-statics and micro-kinematics of capillary phenomena in dense granular materials. Powders Grains 2009 (Golden, USA) 1145, 927–930. doi:10.1063/1.3180083

Charles, R.J., 1958a. Static fatigue of glass. I. J. Appl. Phys. 29, 1549–1553. doi:10.1063/1.1722991

Charles, R.J., 1958b. Static fatigue of glass. II. J. Appl. Phys. 29, 1554–1560. doi:10.1063/1.1722992

Charles, R.J., Hilling, W.S., 1962. Kinetics of glass failure of stress corrosion, in: Symposium Sur La Resistance Du Verre et Les Moyens de l'Ameliorer. Union Scientifique Continentale du Verre, Charleroi (Belgium), pp. 511–527.

Chávez, C., 2003. Estudio del comportamiento triaxial de materiales granulares de tamaño medio con énfasis en la influencia de la succión. PhD. Thesis. Technical University of Catalonia. UPC, Barcelona, Spain (in Spanish).

Chávez, C., Alonso, E.E., 2003. A constitutive model for crushed granular aggregates which includes suction effects. Soils Found. 43, 215–227.

Clements, R.P., 1981. The deformation of rockfill: inter-particle behaviour, bulk properties and behaviour in dams. PhD thesis. London University, London, UK.

Cundall, P.A., Strack, O.D.L., 1979. A discrete numerical model for granular assemblies. Géotechnique 29, 47–65.

Evans, A.G., 1972. A method for evaluating the time-dependent failure characteristics of brittle materials - and its application to polycrystalline alumina. Mater. Sci. 7, 1137–1146.

Freiman, S.W., 1984. Effects of Chemical Environments on Slow Crack Growth in Glasses and Ceramics. Geophys. Res. 89, 4072–4076.

Galer, M.M., 1999. A study on the mechanical properties of undisturbed decomposed granite based on in-situ testing and triaxial testing results under elevated confining pressure. PhD. Thesis. Hiroshima University.

Gili, J.A., Alonso, E.E., 2002. Microstructural deformation mechanisms of unsaturated granular soils. Int. J. Numer. Anal. Methods Geomech. 26, 433–468. doi:10.1002/nag.206

Henry, J.-P., Paquet, J., 1976. Mecanique de la rupture de roches calcitiques. Bull.

la Soc. Geol. Fr. Series 7 V, 1573–1582. doi:10.2113/gssgfbull.S7-XVIII.6.1573

Hiramatsu, Y., Oka, Y., 1966. Determination of the tensile strength of rock by a compression test of an irregular test piece. Int. J. Rock Mech. Min. Sci. 3, 89–99.

Itasca, 2008. Manuals of PFC3D v.4.0: Theory and Background, 4th ed. Minneapolis, Minnesota, USA.

Lee, K., Farhoomand, I., 1967. Compressibility and crushing of granular soil in anisotropic tiraxial compression. Can. Geotech. J. 4, 68–86. doi:10.1139/t67-012

Leung, C.F., Lee, F.H., Yet, N.S., 1996. The role of particle breakage in pile creep in sand. Can. Geotech. J. 33, 888–898.

Meredith, P.G., Atkinson, B.K., 1983. Stress corrosion and acoustic emission during tensile crack propagation in Whin Sill dolerite and other basic rocks. Geophys. J. Int. R. Astron. Soc. 75, 1–21. doi:10.1111/j.1365-246X.1983.tb01911.x

Meredith, P.G., Atkinson, B.K., 1982. High-temperature tensile crack propagation in quartz: Experimental results and application to time-dependent earthquake rupture. Earthq. Predict. Res. 1, 377–391.

Michalske, T., Freiman, S.W., 1982. A molecular interpretation of stress corrosion in silica. Nature 295, 511–512.

Nakata, Y., Hyodo, M., Hyde, A.F.L., Kato, Y., Murata, H., 2001. Microscopic particle crushing of sand subjected to high pressure one-dimensional compression. Soils Found. 41, 69–82.

Nara, Y., Hiroyoshi, N., Yoneda, T., Kaneko, K., 2010. Effects of relative humidity and temperature on subcritical crack growth in igneous rock. Int. J. Rock Mech. Min. Sci. 47, 640–646. doi:10.1016/j.ijrmms.2010.04.009

Nara, Y., Morimoto, K., Yoneda, T., Hiroyoshi, N., Kaneko, K., 2011. Effects of humidity and temperature on subcritical crack growth in sandstone. Int. J. Solids Struct. 48, 1130–1140. doi:10.1016/j.ijsolstr.2010.12.019

Nara, Y., Takada, M., Igarashi, T., Hiroyoshi, N., Kaneko, K., 2009. Subcritical crack growth in rocks in an aqueous environment. Explor. Geophys. 40, 163–171.

Nara, Y., Yamanaka, H., Oe, Y., Kaneko, K., 2013. Influence of temperature and water on subcritical crack growth parameters and long-term strength for igneous rocks. Geophys. J. Int. 193, 47–60. doi:10.1093/gji/ggs116

Naylor, D.J., Maranha, J.R., Maranha das Neves, E., Veiga Pinto, A.A., 1997. A back-analysis of Beliche Dam. Géotechnique 47, 221–233.

Naylor, D.J., Maranha Das Neves, E., Mattar, D., Veiga Pinto, A.A., 1986. Prediction of construction performance of Beliche Dam. Géotechnique 36, 359–376.

Nobari, Duncan, 1972. Effect of reservoir filling on stresses and movements in earth and rockfill dams.

O'Sullivan, C., 2011. Particulate Discrete Element Modelling. A Geomechanics

perspective. Spon Press, Taylor & Francis Group, Abingdon, Oxon, Uk.

O'Sullivan, C., Bray, J.D., 2004. Selecting a suitable time step for discrete element simulations that use the central difference time integration scheme. Eng. Comput. 21, 278–303. doi:10.1108/02644400410519794

Oldecop, L.A., 2000. Compresibilidad de escolleras. Influencia de la humedad. PhD. Thesis. Technical University of Catalonia. UPC, Barcelona, Spain (in Spanish).

Oldecop, L.A., Alonso, E.E., 2007. Theoretical investigation of the time-dependent behaviour of rockfill. Géotechnique 57, 289–301.

Oldecop, L.A., Alonso, E.E., 2003. Suction effects on rockfill compressibility. Géotechnique 53, 289–292.

Oldecop, L.A., Alonso, E.E., 2001. A model for rockfill compressibility. Géotechnique 51, 127–139.

Ortega, E., 2008. Comportamiento de materiales granulares gruesos - Efecto de la succión. PhD. Thesis. Technical University of Catalonia. UPC, Barcelona, Spain (in Spanish).

Outwater, J.., Murphy, M.C., Kumble, R.G., Berry, J.T., 1974. Double Torsion Technique as a universal fracture toughness test method, in: Fracture Toughness and Slow-Stable Cracking. ASTM International. Special Tech. Publ. STP 559. pp. 127–138. doi:10.1520/STP38597S

Russell, A.R., Muir Wood, D., 2009. Point load tests and strength measurements for brittle spheres. Int. J. Rock Mech. Min. Sci. 46, 272–280. doi:10.1016/j.ijrmms.2008.04.004

Sano, O., Ogino, S., 1980. Acoustic emission during slow crack growth. Technical Report 2. Yamaguchi , Japan.

Soriano, A., Sánchez, F.J., 1999. Settlements of railroad high embankments, in: Proceedings of XII European Conference on Soil Mechanics and Geotechnical Engineering. Netherlands.

Swanson, P.L., 1984. Subcritical crack growth and other time- and environment-dependent behavior in crustal rocks. J. Geophys. Res. 89, 4137–4152. doi:10.1029/JB089iB06p04137

Swanson, P.L., 1980. Stress corrosion cracking in Westerly granite: An examination by the double torsion technique. MSc. Thesis. Univ. of Colo., Boulder.

Takei, M., Kusakabe, O., Hayashi, T., 2001. Time-dependent behavior of crushable materials in one-dimensional compression tests. Soils Found. 41, 97–121.

Vesic, A.S., Clough, G.W., 1968. Behaviour of granular materials under high stresses. J. Soil Mech. Found. Div. ASCE 94, 661–668.

Wachtman, J.B., Cannon, W.R., Matthewson, M.J., 2009. Subcritical Crack Propagation, in: Mechanical Properties of Ceramics. John Wiley & Sons, Inc., Hoboken, NJ, USA, pp. 151–176. doi:10.1002/9780470451519.ch8

Wang, J., Yan, H., 2012. DEM analysis of energy dissipation in crushable soils. Soils Found. 52, 644–657. doi:10.1016/j.sandf.2012.07.006

Waza, T., Kurita, K., Mizutani, H., 1980. The effect of water on the subcritical crack

growth in silicate rocks. Tectonophysics 67, 25–34. doi:10.1016/0040-1951(80)90162-6

Wiederhorn, S.M., 1978. Mechanisms of subcritical crack growth in glass, in: Bradt, R.C., Hasselman, D.P.H., Lange, F.F. (Eds.), Fracture Mechanics of Ceramics, Vol. 4. Plenum Press, pp. 549–580.

Wiederhorn, S.M., 1974. Subcritical crack growth in ceramics, in: Bradt, R.C., Hasselman, D.P.H., Lange, F.F. (Eds.), Fracture Mechanics of Ceramics, Vol. 2. Plenum Press, New York, pp. 613–646.

Wiederhorn, S.M., Boltz, L.H., 1970. Stress corrosion and static fatigue of glass. J. Am. Ceram. Soc. 53, 543–548.

Wiederhorn, S.M., Freiman, S.W., Fuller, E.R., Simmons, C.J., 1982. Effects of water and other dielectrics on crack growth. Mater. Sci. 17, 3460–3478.

Wilkins, B.J.S., 1980. Slow crack growth and delayed failure of granite. Int. J. Rock Mech. Min. Sci. Geomech. Abstr. 17, 365–369.

Williams, D.P., Evans, A.G., 1973. A simple method for studying slow crack growth. J. Test. Eval. 1, 264–270. doi:http://dx.doi.org/10.1520/JTE10015J

Chapter 8

Summary, conclusions and future work

Finally, the conclusions, a summary of the innovative contributions of this research, and recommendations for future work are presented in this chapter.

The summary and conclusions are essentially related to the seven aspects investigated in this thesis and treated in the previous chapters: the overview of the coarse aggregates behaviour, concepts and features of DEM, particle breakage and the mechanical behaviour of sugar cubes, the (DEM) particle model for rockfill and gravels and crushable coarse aggregate behaviour, the effect of particle size, the influence of the relative humidity and time-dependent behaviour.

8.1 Summary and conclusions

8.1.1 Mechanical behaviour of rockfill and gravels: An overview

Mechanical behaviour of coarse aggregates such as rockfill and gravels is characterized mainly by the following features:

(1) Collapse in deformations occurs when dry aggregates are flooded under confining stress or by imposing a RH=100%.
(2) Deformations (at common engineering stresses) are associated with particle breakage and the subsequent rearrangement of the fragments.
(3) Under an applied load, deformations occur in time, i.e. coarse aggregates display time-dependent behaviour.
(4) The behaviour also depends on the size of the fragments.

These features have been evidenced in field -by large civil structures- and in laboratory –by testing rock fragments in scaled size.

Settlement records of rockfill dams and embankments which have been reported in the literature show collapses during the reservoir impoundment and also after rainfalls. Deformations continue to occur over time from the early stages of the construction until many years after the construction.

Data reports of oedometer and triaxial laboratory tests have registered collapse in both volumetric strain and applied stresses due to flooding or by imposing RH=100%. Furthermore, results of oedometer tests show that higher compressibility is obtained for higher values of Relative Humidity. Time-dependent behaviour has also been observed: delayed vertical strain also occurs when a specimen is subjected to a vertical load over time.

Results of triaxial tests on gravels show that a higher strength is obtained for dry specimens than for saturated. Likewise, the strength enveloped is nonlinear for rockfill and gravels. Critical states are difficult to find because dilatancy is significant at the maximum deviatoric strains of triaxial tests.

In laboratory, breakage of rock fragments is evidenced by the evolution of the curves of the grain size distributions. Both isotropic and deviatoric stresses induce particle breakage.

The breakage of a particle is influenced by the humidity conditions and the particle size. Furthermore, it can be delayed in time.

Regarding size effects, results of laboratory tests of one-directional compression on singular rock fragments show that tensile strength in a particle decreases when the particle size increases. Similarly, analytical solutions from fracture mechanics and the Weibull statistical approach can demonstrate this size effect.

The UPC (Technical University of Catalonia) has done systematic research on the behaviour of unsaturated rockfill/gravels for the last fifteen years. Large equipment for oedometer and triaxial tests with controlled suction has been built, and some constitutive models (compressibility and triaxial behaviour) for a continuum media based on experimental results have been proposed. Some experiments performed in UPC cells were used as benchmark results to validate the models developed in this thesis.

8.1.2 Basic features of DEM

The Discrete (Distinct) Element Method, DEM, is a numerical model capable of describing the mechanical behaviour of assemblies of distinct particles which are generally disks (for 2D analysis) and spheres (for 3D analysis). The particles are infinitely stiff but may overlap at the contacts. The particles can move independently of one another and interact only at contacts or interfaces between them.

A contact law is applied to the contacts and Newton's second law of motion is applied to the particles. The contact law relates the forces and displacements at the contact between two entities (particle-particle; particle-wall). For instance, the following contact laws (or contact models) could be used: (1) Simple contact model: this model considers normal and tangential springs in the contact between two entities (particle-particle; particle-wall) and a "slider mechanism" which controls shear strength. This model takes into account the following parameters: a friction coefficient between particles, and normal and shear stiffness; (2) Contact bond: this model simulates a "glue or cement" behaviour. It can be a simple contact bond

or a parallel contact bond. A simple contact bond can only resist tensile normal and shear forces, and it is defined by normal tensile contact bond strength and shear contact bond strength. The parallel contact bond resists tensile normal and shear forces and moments. It is defined by the normal and shear stiffness per unit area, and the tensile and shear strength; (3) Dashpot elements to consider a damping effect in order to dissipate kinetic energy and avoid instability of the system. Damping can be applied to each ball (local damping) or to each contact (viscous damping).

In the DEM, the interactions between particles are monitored contact by contact and the motion of the particles is modeled particle by particle. The explicit finite difference method is used to solve the equations of motion and therefore to calculate the displacements of the particles.

The commercial code PFC^{3D} (PFC3D- Particle Flow Code for 3 Dimensions) is a discrete element code which makes it possible to model the movement and interaction of stressed assemblies of distinct particles, bodies that occupy a finite amount of space, using Cundall's DEM (Cundall and Strack, 1979). Furthermore, PFC3D also allows introducing new functions through subroutines in FISH programming language in order to include new variables, failure criteria, servo-control systems, specific motion of particles and boundaries, numerical modelling of tests, etc.

PFC3D can employ three entities that comprise the DEM system: balls (spheres), walls (boundaries), and clumps. The balls can be grouped and form clusters using contact bonds. Different types of walls could be used: flat, cylinder, ring, etc. And the clumps are assemblies of balls that behave as rigid bodies and cannot break.

This research uses the PFC3D code to simulate rockfill and gravels and model their behaviour.

A compendium of works that use DEM to model particle breakage was presented, and the techniques used were divided into five types: (1) Breakage of cluster of particles (disks or spheres) which use simple or parallel contact bonds; (2) Replacement of broken particles (disks or spheres) by smaller fragment-particles (disks or spheres); (3) Releasing Clumps (2D); (4) Removing particles from clusters (disks or spheres); and (5) Reducing stiffness in contacts (3D). The first two techniques are the most widely used.

With these particle breakage techniques, special attention needs to be paid to solve certain problem points:

- For the first technique: ensuring the rigidity of the whole cluster that should behave as a rigid macroparticle; avoiding a rolling effect caused by the use of contact bonds, which allows the rolling of one ball relative to another even without breakage. (2D and 3D analysis).
- For the second: ensuring the mass conservation. (2D and 3D analysis).
- For the third: computational cost. (2D analysis).
- For the fourth: mass loss. (2D and 3D analysis).
- The fifth technique does not consider the evolution of the grain size distribution. (3D analysis).

8.1.3 Compressibility, grain breakage and time-dependent behaviour of a gap-graded crushable material: sugar cubes

Particle breakage mechanisms in loaded coarse aggregates can be analyzed by testing regular blocks of a brittle material of relatively low strength in a simple but very informative procedure. Two very different initial porosities (very low and high) can be obtained by two different piling methods (ordered and disordered arrangement) of the regular parallelepiped cubes. The results were surprising: after a loading process at a relatively high confining stress, the gsd curves of these two widely different arrangements converged into a single grain distribution. This confirms that the grain size distribution, irrespective of the initial fabric, evolves into an "attractor" curve during loading.

The gsd curves evolve around two families of grain sizes which are related to the two initial sizes in an apparently independent manner. The final gsd could be defined as a superposition of two limiting "attractors". However, it remains to be shown whether the same conclusion holds if the initial sizes of the gap-graded granular mixture are very close.

In loading processes, the evolution of the grain sizes is explained by the action of the following breakage mechanisms identified: local crushing (comminution), which generates particles significantly smaller than the original particle, and particle splitting (splitting failure), where the particle is divided into roughly two halves. The development of breakage was investigated in more detail using a procedure based on interpreting the mass fractions retained at each particular sieve. It was found that:

- Particle breakage is very limited for stresses below the yield stress
- The intensity of the two breakage mechanisms increase fast in the vicinity of the yield stress

Conventional breakage indexes also increase rapidly at stresses close to the yield stress. In fact, the yield stress is better identified in tests performed by gsd-related criteria than on the basis of the classical interpretation of compression behaviour in e vs. $\log(\sigma)$ plots.

Long-term tests at constant confining stress supported a creep law relating deformations with the logarithm of time. The evolution of breakage was analyzed by examining samples at different creeping times. It was found that the evolution of grain size distributions follows a pattern similar to the pattern observed during a (fast) increase in stress. In particular, creeping was also explained by the emergence of a dominant grain size associated with the crystal size and the reduction of sizes associated with the initial size of cubical particles. No evidence of an asymptotic exhaustion of long-term deformations was found despite the maximum duration of the tests (157.5 days). It appears that the gsd attractor is, in fact, a function of time. Breakage rates evolved from maximum values at early stages towards a progressive reduction in breakage rates as time passes.

The fact that increasing stress and increasing time at constant stress result in

common patterns of gsd suggests that a unified phenomenon explains both phenomena. The subcritical crack propagation within particles was proposed by Oldecop and Alonso (2007, 2001) as a suitable mechanism to explain the response of gravels to confined loading. The present results support this mechanism as well.

The results of this experimental research are useful for a better understanding of the breakage mechanisms taking place in coarse crushable aggregates (gravels and rockfill) subjected to one-dimensional compression conditions. It is believed that some of the findings presented could be of application to generalized stress-strain paths.

The two crushing mechanisms described are associated with the distribution of stresses in particles due to the action of concentrated loads which act around the particle. Splitting failure may be associated with tensile stresses and comminution crushing to shear stresses. The magnitude and distribution of the stresses inside particles depend on the mechanical properties of the particle (e.g. elastic/elasto-plastic parameters), shape of the particle, magnitude and contact area of the applied load, roughness surface, etc. In this regard, a random package of sugar cubes is probably not much different from gravel made of particles with three similar dimensions and sharp edges and vertices. An ordered set of cubes is close to a regular stone fabric in a wall or a variety of masonry structures. The tests on sugar cubes offer an interesting possibility of examining the two extremes of rockfill fabric easily.

8.1.4 Particle model for rockfill and crushable coarse aggregate behaviour

A novel particle model was presented. Some key aspects of the coarse aggregate behaviour such as the breakage of particles, the influence of relative humidity conditions, time-dependent behaviour and size effects have been dealt with by this DEM model.

This model was implemented using the PFC3D code to simulate rockfill and gravel particles and their behaviour.

The rupture of brittle rock particles explains, to a large extent, the stress-strain behaviour of the coarse aggregates. This particle breakage is represented by fracture mechanics and crack propagation concepts. The approach is believed to provide a more accurate description of the real phenomena than other, computationally oriented techniques, which rely on concepts such as particle bonding.

The model requires an estimation of stresses inside the particles and the propagation of existing cracks or defects. They have been described by analytical solutions under a certain set of assumptions. In this way, the calculations associated with the breakage or survival of a given particle may be performed fast within the overall numerical approach.

A particle may break whenever the stress intensity factor (K) reaches the toughness value (K_c) or the crack length reaches the equivalent diameter of the

particle.

The particle shape and its evolution during loading is also a key aspect. It controls the degree of interlocking and the modification of grain size distribution.

Model particles approximate the real shape by aggregating spheres as a rigid body (or clump) in a pyramidal shape. These clumps are known here as macroparticles. The spheres that compose the macroparticles are known as microparticles. An initial macroparticle integrates 14 spheres, an assumption that may be modified in subsequent work.

The initial pyramidal shapes transform into smaller pyramidal and irregular parallelepipedic geometries upon breakage. An interesting feature was the automatic subdivision of smaller particles into a set of elementary particles of even smaller sizes during the calculation process. Mass conservation was enforced. This technique proved to be useful for reproducing observed grain size distributions after oedometric and triaxial testing of gravel aggregates.

The model takes into account the nature of breakage and its evolution under increasing loading. These considerations are based on experiments performed in this research and also in experimental reports from literature. Experiments indicate that contact-related comminution breakage predominates at small contact forces, whereas “equal volume” splitting becomes dominant beyond a given “yielding” stress. The model reproduces these observations.

A protocol for the selection of the breakage mechanisms (comminution or splitting) was implemented based on a probabilistic approach.

Comminution breakage was simulated by relaxing the microparticle that supports the maximum load when the failure criterion is reached.

Splitting breakage was simulated by the division of the macroparticle into two parts following an “equal volume” criterion when the failure is reached.

In terms of material parameters, the model is remarkably simple: it requires the contact stiffness (k_n), the rock toughness (K_c) and the friction coefficients (μ) at particle contacts. K_c and μ may be determined by rock characterization tests.

In this work, K_c was calibrated by the post-test (oedometer) grain size distribution and the comparison of the breakage indexes (from the DEM and actual tests).

Contact friction was experimentally determined for hard limestone: Basic friction angle was proposed to calculate μ.

Although k_n was calibrated by the compressibility behaviour, special experimental tests were also performed to estimate the contact stiffness between particles. It was a comforting finding to realize that the back-analyzed k_n value, interpreting the oedometer compression curve, was within the range of the experimental k_n values.

“Blind” simulation of real triaxial tests, accepting the model parameters, the geometrical characterization of particles and the entire calculation protocol used

previously to interpret an oedometer test, led to a fairly successful prediction which relates to the deviatoric stress-strain behaviour, the volumetric sample response, the grain size distribution and the correct identification of size effects.

8.1.5 Size effect in rockfill behaviour

The LEFM theory (linear elastic fracture mechanics) makes it possible to explain the size effect on the tensile strength which is observed in the experimental results of Point Load tests: Particles with a greater size present lesser strength. In the fracture mechanics, tensile stress which induces the failure (for a certain value of toughness) depends on the crack length. If a given rock mass is assumed to host a distribution of cracks of different lengths, the larger particle under consideration has a higher probability of having large cracks within the particle. Therefore, the breakage of particle is dependent on particle size.

The proposed DEM model uses the concepts of the fracture mechanics. Scale effects on rockfill behaviour can be successfully approached through this proposed DEM, which incorporates a particle breakage criterion based on the mechanics of crack propagation in brittle materials. This opens the possibility of quantifying scale effects in rockfill, a subject of practical interest.

The model parameters have been calibrated using the results of real oedometer tests performed on samples with an average particle diameter of 2.8 cm. Once this is achieved, the model is used as a virtual laboratory to explore size effects in both oedometer and triaxial tests.

Numerical simulations of oedometer tests were then carried out, testing particle sizes in the range 0.28-56 cm (initial particle average size) in order to evaluate the compressibility of the rockfill at different scales. The results were compared with real oedometer tests:

- The compressibility of the aggregates in the numerical oedometer tests increases for the bigger particle sizes.
- Compressibility index (λ) increases with particle size.
- The model also provides information on the evolution of grain size distribution during the loading of specimens for a wide range of particle sizes. This evolution depends on the particle size: The bigger the size, the higher the rupture of particles.
- This size effect is also evidenced in the evolution of the breakage indexes; for instance B_r increases for bigger sizes; however, this index tends to reach an asymptotic value for a size greater than a certain size (14cm for this study).

Using the model parameters of the oedometer tests, “blind” simulations of real triaxial tests on particles of different sizes of the same material were performed and also led to quite a successful prediction of the deviatoric stress-strain behaviour, the volumetric sample response, and the grain size distribution.

Two types of triaxial tests were simulated varying the relative humidity conditions:

Dry condition (RH=10) during the entire test and tests with dry condition at the beginning and wetting (RH=100%) when a certain axial deformation was reached, as was done in the experimental tests.

- The specimens with a smaller particle size have higher rigidity and higher maximum deviatoric stress (peak strength).
- The specimens with a greater particle size have higher compressibility.
- "Residual" strength tends to be the same.
- Collapses in deviatoric stresses and volumetric strains occur due to the wetting of the specimens.
- After wetting, the wetted deviatoric curves tend to reach those obtained from the dry conditions.
- At the end of the tests, the numerical gsd curves were very similar to the experimental results. The size effect could be noted in the evolution of the gsd curves: this evolution depends on the initial size of the macroparticles.
- Based on the evolution of the gsd curves and the breakage indexes (B_r and B_g), it can be observed that greater breakage is obtained for larger sizes.

Rockfill behaviour (compressibility, breakage, strength) is grain size scale dependent in a significant way as demonstrated by the numerical and experimental tests performed on "similar" gsd but varying the mean grain size. Therefore, such assumptions that the mechanical behaviour of actual rockfill is the same as the behaviour of the same material with a scaled gsd are wrong.

8.1.6 Influence of relative humidity in coarse granular aggregates

Mechanical behaviour of coarse aggregates such as rockfill and gravels is influenced by the relative humidity (environmental conditions). Experimental observations in large civil structures and results of laboratory tests have demonstrated that saturation of dry coarse aggregates (by flooding the specimens or imposing RH=100%) causes collapse in volumetric strain. This collapse is associated with the rupture of particles and the subsequent rearrangement of the granular mass.

The breakage of particles can be explained by the crack propagation theory and the subcritical crack propagation theory. This subcritical crack propagation may be due to the stress corrosion phenomenon which can occur at the crack tip. This phenomenon explains the effect of liquid water or vapour that acts as a corrosive agent, and the hydrolysis process in the creation of weak links of hydroxyl groups that cause the decrease in the local toughness and lead to the crack propagation.

Three models of subcritical crack propagation have been proposed taking into account the relative humidity: the Generalized model, the Model with common region 2, and the Simplified model. These models are formulated in a *K*-v space: Stress intensity stress factor – Velocity of crack propagation. Relative humidity influences the subcritical crack propagation inside the particles. The increase in humidity (decrease in suction) increases the crack propagation velocity and can

therefore lead to the breakage of the particles.

These subcritical crack propagation models are supported by experimental data found in the literature of results of subcritical crack propagation tests. Moreover, these models are based on the Charles's law and the theory of the subcritical crack propagation due to stress corrosion.

The DEM model may incorporate the proposed models of the subcritical crack propagation in order to take into account the relative humidity. The third model (simplified model) was used for the simulation of the tests.

The accuracy of the model has been verified by the very good correlation of the oedometer and triaxial test simulations compared with the experimental data. The results of the oedometer and triaxial laboratory tests were taken from Ortega (2008) on limestone gravels.

For the oedometer tests, the DEM results corresponded to the experimental data:

- The calculated compressibility behaviour was close to the actual behaviour for the loading process;
- For the unloading, there was a greater recovery in the calculated vertical strain than in the experimental results;
- The evolution of the grain size distributions for the DEM results was very close to the actual gsd at the end of the test;
- The breakage indexes, Hardin and Marsal, for the DEM tests were also close to the experimental data at the end of the test;
- Collapse in volumetric strain due to wetting was well simulated.

An analysis was done of the evolution of the total external energy of the system in the numerical oedometer test taking into account the work done by the boundaries (walls) on the sample (E_w), kinetic energy (E_k), strain energy (E_s), frictional energy (E_f) and damping energy (E_d). This analysis allowed the stability of the DEM simulation test to be checked: The evolution of the kinetic energy showed energy peaks during the test. These small instabilities were associated with the breakage of macroparticles. However, the magnitude of the kinetic energy peaks was very small compared with the total energy.

The breakage of particles was evaluated through the evolution of the grain (particle) size distribution curves, the breakage indexes (Hardin and Marsal), the number of clumps or macroparticles, and the number of unbroken clumps during the tests.

"Blind" DEM triaxial tests were performed using the parameters calibrated in the previous oedometer tests under two different RH conditions. The following results were obtained:

- The triaxial behaviour (curves q-ε_a; ε_v-ε_a) was similar for the DEM and experimental results;

- Collapses in deviatoric stresses and in volumetric strain, due to the wetting of the specimen, were very well simulated and followed the results obtained in the experimental test.
- Gsd curves and breakage indexes at the end of the DEM and experimental tests were similar.
- A little higher strength was obtained for the dry specimen. However, after collapse in the deviatoric stress due to the wetting, the strength of the wetted sample tends to reach the strength of the dry sample.

8.1.7 Time effect on coarse granular aggregates

Rockfill and gravels exhibit a time-dependent behaviour. This behaviour is evidenced, for instance, by the records of settlements which occur over time in large civil structures such as rockfill dams and railway embankments, and also by the records of deformations from experimental results of oedometer tests on gravels. This behaviour can also be explained mainly by the breakage of particles and the subsequent rearrangement of the particles. Particle breakage depends on the applied loads and also occurs over time. In short, delayed deformation behaviour occurs in coarse aggregates.

Time is an immersed variable in the model due to the very concept of DEM (interactions of particles and particle motion) and also to the considerations of the fracture mechanics and crack propagation inside particles.

The developed model proposes a particular subdivision law of the macroparticles when they reach the failure criteria and break. The subdivision is achieved when a defect or crack propagates through the particle. The time to the final stage of crack propagation is derived from an analysis of the subcritical crack growth under a mode I type of loading, which is accepted as a reasonable mode in granular assemblages in which diametral loading of particles is the dominant mechanism.

This crack propagation depends on the initial length of the cracks, size of the particles, particle toughness, stress intensity factor and environmental conditions (relative humidity).

Crack lengths inside particles are introduced randomly using a uniform probability distribution. This length depends on the equivalent diameter of the macroparticle. The uniform probability distribution was selected after a sensitivity analysis using different probability distributions was done: Exponential (two types), Weibull (three types) and uniform probability distributions were used in the analysis.

Based on an analysis of crack propagation inside particles with the same size and subjected to the same load (Mode I), but varying the initial crack length, it could be concluded that:

- The smaller the initial crack length, the lesser the value of stress intensity factor (K) and also the lesser the value of dimensionless coefficient (β), but the greater the value of rupture time;

- The velocity of crack propagation is much lower at the beginning and increases very fast close to a certain “triggering time” (rupture time) until it reaches the breakage.

One numerical oedometer test was analyzed in order to study the time-dependent behaviour. It was compared with the experimental data from Ortega (2008).

The calculated compressibility behaviour over time is in accordance with the experimental results for each applied vertical stress.

For dry conditions (RH=10%), after the application of each vertical stress, significant vertical deformation occurs after a small elapsed time. This “instantaneous” deformation is caused by the load application. However, deformations also occur in time. They are associated with particle breakage in time and the rearrangement of the particles.

After wetting under the maximum vertical stress, collapse in vertical deformation occurs approximately between minutes 7 and 10 of elapsed time for the DEM test. For the experimental data, this collapse occurs in two periods: between minutes 1 and 2 and between minutes 5 and 8. Furthermore, deformations are prolonged in time.

The evolution of the particle breakage in time can also be followed through the evolution of the breakage indexes (B_r and B_g), and the number of clumps or macroparticles.

Breakage of particles can occur suddenly due to the application of loads and/or the saturation of the specimen by imposing RH=100%. Likewise, breakage of particles can also occur in time.

The model was capable of a precise reproduction of long-term (oedometer) tests considering a wide range of particle sizes. Short-term compressibility (λ) increases with the particle size, as does the creep or secondary coefficient. A ratio λ_t/λ was proposed. This ratio was found to be in reasonable agreement with experimental results derived for different granular materials. The long-term compressibility index, λ_t, may be considered a material property.

8.2 Summary of innovative contributions of this thesis

A novel DEM model was developed. This model takes into account: particle breakage, time-dependent behaviour, Relative Humidity, and effects of particle size. The DEM model and numerical simulations of laboratory tests were programmed in FISH language using the PFC3D code.

Advances and highlights of the research performance are:

1. Laboratory tests were proposed on parent rock of gravels analyzed and performed to find some parameters of the DEM model:
   - Basic (ϕ_b) and mineral (ϕ_m) friction angle determined in shear tests using tilt table tests and direct shear tests in order to find the friction coefficient (μ);
   - Estimation of the mean Roughness R_a by microscope examination to find the contact angle or solid angle describing contact stresses (θ_0);
   - Contact stiffness tests using prismatic specimens in order to calculate the contact stiffness k_n.

   Furthermore, experimental oedometer tests were performed on a brittle and crushable material: sugar cubes. These tests aimed to evaluate breakage mechanisms, the evolution of particle breakage, and the time-dependent behaviour.

   The DEM parameters were also obtained from the sensitivity analysis of numerical oedometer tests which were compared with an actual experimental test. Compressibility, evolution of the grain size distribution, and the calculation of breakage indexes were considered in the calibration of parameters.

2. Two breakage mechanisms were defined and applied to the DEM model: Comminution and Splitting. A protocol for the selection of the breakage mechanisms and the division of the macroparticles when they break was proposed.

   The DEM model considers clumps (macroparticles) of a roughly pyramidal shape to simulate the fragments of rockfill and gravels. Macroparticles can break when they reach a failure criteria based on the fracture mechanics and the subcritical crack propagation theory. Mass conservation is enforced during the breakage process.

3. Three models for the subcritical crack propagation were proposed taking into account the relative humidity. The models were based on the theory of the subcritical crack propagation due to stress corrosion and the experimental data obtained from literature.

   The DEM model developed uses one of the proposed models of the subcritical crack propagation.

4. Blind triaxial tests were simulated using the previous parameters of the oedometer test simulations and compared with the experimental results.

   The DEM simulation of the large scale oedometer and triaxial tests was consistent and accurate. The influence of the relative humidity on the mechanical behaviour, particle size effects, time-dependent behaviour and the evolution of the grain size distribution were well reproduced.

8.3 Recommendations for future work

The following aspects are recommended for future investigations:

- Including not only pyramidal shapes of macroparticles in order to take into account real shapes of the rock fragments. Optical methods could be used to capture images of the fragments to obtain the real shapes and then to build the clumps based on the images.

- Improving the procedure to assign the breakage mechanisms taking into account an additional shear failure criterion, i.e. two failure criteria could be considered:
  - Failure due to shear stresses: Comminution breakage could be associated with this failure;
  - Failure due to tensile stresses. Splitting breakage could be associated with this failure.

- The division of the macroparticle due to the splitting mechanisms could take into account the direction of the critical tensile stress.

- Making a comparison between the use of clumps and clusters of bonded particles and to evaluate computational costs.

- Making an experimental study of crack propagation under different humidity conditions for some rocks in order to validate and/or improve the proposed models for subcritical crack propagations.

- Including the temperature effect on the rupture of particles.

- Including the effect of the pH in an aqueous environment on subcritical crack propagation.

- Including the influence of the relative humidity on fracture toughness.

- Including the humidity flow or liquid water flow inside the granular mass.

- In order to apply the proposed DEM model, performing an analysis of the mechanical behaviour of a large civil structure built with rockfill or gravels, or a study of an interesting geotechnical problem such as landslides, rock falls or debris flows.

References

A compendium of the references used in the thesis is presented below:

Alaei, E., Mahboubi, A., 2012. A discrete model for simulating shear strength and deformation behaviour of rockfill material, considering the particle breakage phenomenon. Granul. Matter 14, 707–717.

Alehossein, H., Boland, J.N., 2004. Strength, toughness, damage and fatigue of rock, in: Proc. Structural Integrity and Fracture International Conference (SIF'04). 26-29/09/2004. Brisbane (Australia).

Alonso, E.E., Oldecop, L., Pinyol, N., 2009. Long term behavior and size effects of coarse granular media, in: Kolymbas, D., Viggiani, G. (Eds.), Mechanics of Natural Solids. Springer-Verlag, Berlin, Germany, pp. 255–281.

Alonso, E.E., Olivella, S., Pinyol, N.M., 2005. A review of Beliche Dam. Géotechnique 55, 267–285.

Alonso, E.E., Romero, E.E., Ortega, E., 2016. Yielding of rockfill in relative humidity-controlled triaxial experiments. Acta Geotech. doi:10.1007/s11440-016-0437-9

Alonso-Marroquín, F., Herrmann, H.J., 2005. The incremental response of soils. An investigation using a discrete-element model. J. Eng. Math. 52, 11–34. doi:10.1007/1-4020-4183-7_2

Alvarado, C., In progress. Chemical loading effects on rockfill behaviour. PhD Thesis. Universitat Politècnica de Catalunya, Barcelona, Spain.

Ashby, M.F., Jones, D.R.H., 1986. Engineering materials 2. Pergamon Press, Oxford.

Astrom, J.A., Herrmann, H.J., 1998. Fragmentation of grains in a two-dimensional packing. Eur. Phys. J. B 5, 551–554.

Atkinson, B.K., 1984. Subcritical crack growth in geological materials. J. Geophys. Res. 89, 4077–4114.

Atkinson, B.K., 1982. Subcritical crack propagation in rock: theory, experimental results and applications. J. Struct. Geol. 4, 41–56.

Atkinson, B.K., 1980. Stress corrosion and the rate-dependent tensile failure of a fine-grained quartz rock. Tectonophysics 65, 281–290.

Atkinson, B.K., 1979a. A fracture mechanics study of subcritical tensile cracking of quartz in wet environments. Pure Appl. Geophys. PAGEOPH 117, 1011–1024. doi:10.1007/BF00876082

Atkinson, B.K., 1979b. Fracture toughness of Tennessee Sandstone and Carrara Marble using the double torsion testing method. Int. J. Rock Mech. Min. Sci. Geomech. Abstr. 16, 49–53.

Atkinson, B.K., Meredith, P.G., 1987. The theory of subcritical crack growth with applications to minerals and rocks, in: Atkinson, B.K. (Ed.), Fracture Mechanics of Rock. Academic Press, London (U.K), pp. 111–166.

Atkinson, B.K., Rawlings, R.D., 1981. Acoustic emission during stress corrosion cracking in rocks, in: Simpson, D.W., Richards, P.G. (Eds.), Earthquake Prediction. American Geophysical Union, Washington, D. C. (USA), pp. 605–616. doi:10.1029/ME004p0605

Ayatollahi, M.R., Aliha, M.R.M., 2008. Mixed mode fracture analysis of polycrystalline graphite-a hite-a modified MTS criterion. Carbon N. Y. 46, 1302–1308.

Backers, T., 2004. Fracture toughness determination and micromechanics of rock under mode I and mode II loading. PhD. Thesis. University of Postdam. Postdam, Germany.

Bahrami, M., Yovanovich, M., Culham, J., 2005. A compact model for spherical rough contacts. ASME, J. Tribol. 127, 884–889.

Bagi, K., 1999. Microstructural stress tensor of granular assemblies with volume forces. J. Appl. Mech. 66, 934–936.

Bagi, K., 1996. Stress and strain in granular assemblies. Mech. Mater. 22, 165–177. doi:10.1016/0167-6636(95)00044-5

Bard, E., 1993. Comportement des materiaux granulaires secs et a liant hydrocarbone. PhD. Thesis. Ecole Centrale de Paris. Châtenay-Malabry, France (in French).

Barksdale, R.D., Blight, G.E., 1997. Compressibility and settlement of residual soils, in: Mechanics of Residual Soils, Chapter 8. Balkema, Rotterdam, pp. 95–154.

Bathe, K.J., Wilson, E.L., 1976. Numerical Methods in Finite Element Analysis. Prentice-Hall, Englewood Cliffs.

Bauer, E., 2009. Hypoplastic modelling of moisture-sensitive weathered rockfill materials. Acta Geotech. 4, 261–272. doi:10.1007/s11440-009-0099-y

Bauer, E., 1996. Calibration of a comprehensive hypoplastic model for granular materials. Soils Found. 36, 13–26.

Bazant, Z.P., 1984. Size effect in Blunt Fracture: Concrete, Rock, Metal. J. Eng. Mech. 110, 518–535. doi:10.1061/(ASCE)0733-9399(1984)110:4(518)

Bazant, Z.P., 1999. Size effect on structural strength: A review. Arch. Appl. Mech. 69, 703–725. doi:10.1007/s004190050252

Been, K., Jefferies, M.G., 1985. A state parameter for sands. Géotechnique 35, 99–112. doi:10.1680/geot.1985.35.2.99

Belytschko, T., Liu, W.K., Moran, B., 2000. Nonlinear Finite Elements for Continua and Structures. Wiley, New York, NY, USA.

Ben-Nun, O., Einav, I., 2010. The role of self-organization during confined comminution of granular materials. Philos. Trans. R. Soc. London A 231–247.

Ben-Nun, O., Einav, I., 2008. A refined DEM study of grain size reduction in uniaxial compression, in: Proocedings of the 12th International Conference of the International Association for Computer Methods and Advances in Geomechanics (IACMAG). Goa, India, pp. 702–708.

Bruce, I.. G., Cruden, D.M., Eaton, T.M., 1989. Use of a tilting table to determine the basic friction angle of hard rock samples. Can. Geotech. J. 26, 474–479.

Bruchmüller, J., Van Wachem, B.G.M., Gu, S., Luo, K.H., 2011. Modelling discrete fragmentation of brittle particles. Powder Technol. 208, 731–739. doi:10.1016/j.powtec.2011.01.017

Bruner, W.M., 1980. Effects of time-dependent crack growth on the unroofing and unloading behaviour of rock. PhD. thesis. University of California, Los Angeles (USA).

Butlanska, J., 2014. Cone penetration tests in a virtual calibration chamber. PhD. Thesis. Universitat Politècnica de Catalunya, Barcelona, Spain.

Cañavate, A., 2011. Influencia de la forma de las partículas en la compresibilidad de las escolleras. Master Thesis. Universitat Politècnica de Catalunya, Barcelona, Spain.

Caproni, N., Armelin, J.L., 1998. Deformabilidade de um enrocamento obtida em ensaios de compressão unidimensional, in: Proceedings of XI Congreso Brasileiro de Mecânica Dos Solos E Engenharia Geotécnica, Brasilia, Brasil, 2. pp. 705–712.

Catalano, E., Chareyre, B., Cortis, A., Barthelemy, E., 2011. A pore-scale hydro-mechanical coupled model for geomaterials, in: Oñate, E., Owen, D.R.J. (Eds.), II International Conference on Particle-Based Methods. Fundamentals and Applications. Barcelona (Spain), pp. 1–12.

Chang, S.H., Lee, C.I., Jeon, S., 2002. Measurement of rock fracture toughness under modes I and II and mixed-mode conditions by using disc-type specimens. Eng. Geol. 66, 79–97. doi:10.1016/S0013-7952(02)00033-9

Chang, S.W., Chen, C.S., 2008. A non-iterative derivation of the common plane for contact detection of polyhedral blocks. Int. J. Numer. Methods Eng. 74, 734–753.

Chareyre, B., Scholtès, L., 2011. Discrete Models of Wet Granular Media, in: Radjai, F., Dubois, F. (Eds.), Discrete-Element Modeling of Granular Materials. ISTE Ltd; John Wiley & Sons, Inc., London, UK, pp. 367–392.

Chareyre, B., Scholtès, L., Darve, F., 2009. Micro-statics and micro-kinematics of capillary phenomena in dense granular materials. Powders Grains 2009 (Golden, USA) 1145, 927–930. doi:10.1063/1.3180083

Charles, J.A., Watts, K.S., 1980. The influence of confining pressure on the shear strength of compacted rockfill. Géotechnique 30, 353–367.

Charles, R.J., 1958a. Static fatigue of glass. I. J. Appl. Phys. 29, 1549–1553. doi:10.1063/1.1722991

Charles, R.J., 1958b. Static fatigue of glass. II. J. Appl. Phys. 29, 1554–1560. doi:10.1063/1.1722992

Charles, R.J., Hilling, W.S., 1962. Kinetics of glass failure of stress corrosion, in: Symposium Sur La Resistance Du Verre et Les Moyens de l'Ameliorer. Union Scientifique Continentale du Verre, Charleroi (Belgium), pp. 511–527.

Chávez, C., 2003. Estudio del comportamiento triaxial de materiales granulares de tamaño medio con énfasis en la influencia de la succión. PhD thesis. Technical University of Catalonia. UPC, Barcelona, Spain.

Chávez, C., Alonso, E.E., 2003. A constitutive model for crushed granular aggregates which includes suction effects. Soils Found. 43, 215–227.

Cheng, Y.., Bolton, M.D., Nakata, Y., 2004. Crushing and plastic deformation of soils simulated using DEM. Géotechnique 54, 131–141. doi:10.1680/geot.2004.54.2.131

Cheng, Y.., Nakata, Y., Bolton, M.D., 2003. Discrete element simulation of crushable soil. Géotechnique 53, 633–641. doi:10.1680/geot.2003.53.7.633

Chrismer, S.M., 1985. Considerations of factors affecting ballast performance. Rep. No. WP-110, Administration of American Railroads, Research and Test

Department, Bulletin 704, American Railway Engineering Association. pp 118-150.

Ciantia, M.O., Arroyo, M., Calvetti, F., Gens, A., 2015. An approach to enhance efficiency of DEM modelling of soils with crushable grains. Géotechnique 65, 91–110.

Clements, R.P., 1981. The deformation of rockfill: inter-particle behaviour, bulk properties and behaviour in dams. PhD thesis. London University, London, UK.

Coop, M.R., Lee, I.K., 1993. The behaviour of granular soils at elevated stresses. Predictive soil mechanics. London.

Coop, M.R., Sorensen, K.K., Bodas Freitas, T., Georgoutsos, G., 2004. Particle breakage during shearing of a carbonate sand. Géotechnique 54, 157–163.

Couroyer, C., Ning, Z., Ghadiri, M., 2000. Distinct element analysis of bulk crushing: effect of particle propertiesand loading rate. Powder Technol. 109, 241–254. doi:10.1016/S0032-5910(99)00240-5

Craig, R.F., 2004. Soil mechanics, Seventh ed. ed. Spon Press, Taylor & Francis Group, London, UK.

Cundall, P.A., 1988a. Formulation of a three-dimensional Distinct Element Model—Part I. A scheme to detect and represent contacts in a system composed of many polyhedral blocks. Int. J. Rock Mech. Min. Sci. 25, 107–116. doi:10.1016/0148-9062(88)92293-0

Cundall, P.A., 1988b. Micromechanics of Granular Materials, in: Satake, M., Jenkins, J.T. (Eds.), . Elsevier, pp. 113–123.

Cundall, P.A., 1971. A computer model for simulating progressive large-scale movements in blocky rock systems, in: Proocedings of the Symposio of the International Society of Rock Mechanics, Nancy 2. p. No. 8.

Cundall, P.A., Strack, O.D.L., 1979a. A discrete numerical model for granular assemblies. Géotechnique 29, 47–65.

Cundall, P.A., Strack, O.D.L., 1979b. The distinct element method as a tool for research in granular media, Part I.

Dantu, P., 1967. Etude expérimentale d'un milieu pulvérulent compris entre deux plans verticaux et parallèle. Ann. des Ponts Chaussées 4, 193–202.

Dantu, P., 1968. Etude statistique des forces intergranulaires dans un milieu pulverulen. Géotechnique 18, 50–55.

De Josselin de Jong, G., Verruijt, A., 1969. Étude photo-élastique d'un empilement de disques. Cah. du Groupe Français Rhéologie 2, 73–86.

Deluzarche, R., Cambou, B., 2006. Discrete numerical modelling of rockfill dams. Int. J. Numer. Anal. Methods Geomech. 30, 1075–1096. doi:10.1002/nag

Dubois, F., 2011. Numerical modeling of granular media composed of polyhedral particles, in: Radjai, F., Dubois, F. (Eds.), Discrete-Element Modeling of Granular Materials. ISTE Ltd; John Wiley & Sons, Inc., London, UK, pp. 233–261.

Dubois, F., Jean, M., 2003. LMGC90 une plateforme de développement dédiée à la modélisation des problèmes d'interaction, in: Sixième Coloque National En Calcul Des Structures, Vol. 1. pp. 111–118.

Duncan, J.M., Chang, C.V., 1970. Nonlinear analysis of stress and strain in soils. J. Soil Mech. Found. Div. ASCE 96, 1629–1654.

Duran, J., 2000. Sands, Powders, and Grains. An introduction to the Physics of Granular Materials. Springer, New York.

Einav, I., 2007a. Breakage mechanics - Part I: Theory. J. Mech. Phys. Solids 55, 1274–1297. doi:10.1016/j.jmps.2006.11.003

Einav, I., 2007b. Breakage mechanics - Part II: Modelling granular materials. J. Mech. Phys. Solids 55, 1298–1320. doi:10.1016/j.jmps.2006.11.004

Einav, I., 2007c. Fracture propagation in brittle granular matter. Proc. R. Soc. A Math. Phys. Eng. Sci. 463, 3021–3035. doi:10.1098/rspa.2007.1898

Evans, A.G., 1972. A method for evaluating the time-dependent failure characteristics of brittle materials - and its application to polycrystalline alumina. Mater. Sci. 7, 1137–1146.

Freiman, S.W., 1984. Effects of Chemical Environments on Slow Crack Growth in Glasses and Ceramics. Geophys. Res. 89, 4072–4076.

Frossard, E., Hu, W., Dano, C., Hicher, P.-Y., 2012. Rockfill shear strength evaluation : a rational method based on size effects. Géotechnique 62, 415–427.

Fumagalli, E., 1969. Tests on cohensionless materials for rockfill dams. J. Soil Mech. Found. Div. ASCE 95, 313–330.

Galer, M.M., 1999. A study on the mechanical properties of undisturbed decomposed granite based on in-situ testing and triaxial testing results under elevated confining pressure. PhD. Thesis. Hiroshima University.

Galindo-Torres, S., Pedroso, D., 2010. Molecular dynamics simulations of complex-shaped particles using Voronoi-based spheropolyhedra. Phys. Rev. E 81, 1–9.

GEOMAR, 2015. Nota técnica del informe de laboratorio L-14-1227 para un análisis de Rugosidad de dos muestras de caliza. Barcelona (Spain).

Gili, J.A., Alonso, E.E., 2002. Microstructural deformation mechanisms of unsaturated granular soils. Int. J. Numer. Anal. Methods Geomech. 26, 433–468. doi:10.1002/nag.206

Golightly, C.R., 1990. Engineering properties of carbonate sands. PhD. thesis. Bradford University.

Gudehus, G., 1996. A comprehensive constitutive equation for granular materials. Soils Found. 36, 1–12.

Hardin, B.O., 1985. Crushing of soil particles. J. Geotech. Eng. ASCE 111, 1177–1192.

Harr, M.E., 1977. Mechanics of particulate media. McGraw-Hill, New York, NY, USA.

Henry, J.-P., Paquet, J., 1976. Mecanique de la rupture de roches calcitiques. Bull. la Soc. Geol. Fr. Series 7 V, 1573–1582. doi:10.2113/gssgfbull.S7-XVIII.6.1573

Hiramatsu, Y., Oka, Y., 1966. Determination of the tensile strength of rock by a compression test of an irregular test piece. Int. J. Rock Mech. Min. Sci. 3, 89–99.

Hogue, C., 1998. Shape representation and contact detection for discrete element simulations of arbitrary geometries. Eng. Comput. 15, 374–390.

Holtz, R.D., Kovacs, W.D., 1981. An introduction to geotechnical engineering. Prentice Hall, Inc, Englewood Cliffs, NJ, USA.

Holtz, W.G., Gibbs, H.J., 1956. Triaxial shear tests on pervious gravelly soils. J. Soil Mech. Found. Div. ASCE 82, 1–22.

Hueso, O., 2003. Compresibilidad de escolleras : Influencia de la humedad relativa. (Final work of undergraduated course). Universitat Politècnica de Catalunya, Escola Tècnica Superior d'Enginyers de Camins Canals i Ports; Universitat de Barcelona, Facultat de Geologia.

Indraratna, B., Ionescu, D., Christie, H.D., 1998. Shear behaviour of railway ballast based on large-scale triaxial tests. J. Geotech. Geoenvironmental Eng. ASCE 439–449.

Indraratna, B., Salim, W., 2002. Modelling of particle breakage of coarse aggregates incorporating strength and dilatancy. Proc. Inst. Civ. Eng. London 155, 243–252.

Indraratna, B., Salim, W., 2001. Shear strength and degradation characteristics of railway ballast, in: Ho, K.K.S., Lo, K.S. (Eds.), Proceedings of the 14th Southeast Asian Geotechnical Conference, Hong Kong. A.A. Balkema, Rotterdam, The Netherlands, pp. Vol. 1, 521–526.

Indraratna, B., Salim, W., Rujikiatkamjorn, C., 2011. Advanced rail geotechnology – ballasted track. Balkema, CRC Press, Taylor & Francis Group, London, UK.

Indraratna, B., Wijewardena, L.S.S., Balasubramaniam, A.S., 1993. Large-scale triaxial testing of greywacke rockfill. Géotechnique 43, 37–51. doi:10.1680/geot.1994.44.3.539

Islam, M.N., Siddika, A., Hossain, M.B., Rahman, A., Asad, M.A., 2011. Effect of particle size on the shear strength behaviour of sands. Aust. Geomech. 46, 75–86.

Itasca, 2008. Manuals of PFC3D v.4.0, 4th ed. USA.

Itasca, 2008. Manuals of PFC3D v.4.0: Theory and Background, 4th ed. Minneapolis, Minnesota, USA.

Jaeger, J.C., 1967. Failure of rocks under tensile conditions. Int. J. Rock Mech. Min. Sci. 4, 219–227.

Jean, M., 2011. Contact Dynamic Method, in: Radjai, F., Dubois, F. (Eds.), Discrete-Element Modeling of Granular Materials. ISTE Ltd; John Wiley & Sons, Inc., London, UK, pp. 27–66.

Kafui, K., Thornton, C., 2000. Numerical simulations of impact breakage of a spherical crystalline agglomerate. Powder Technol. 109, 113–132.

Kjaernsli, B., Sande, A., 1963. Compressibility of some coarse-grained materials, in: Proceedings of the 1st European Conference on Soil Mechanics and Foundation Engineering, Weisbaden, Germany, Vol. 1. pp. 245–251.

Kolbuszewski, J., Frederick, M.R., 1963. The significance of particle shape and size on the mechanical behaviour of granular materials, in: European Conference on Soil Mechanics and Foundation Engineering. Sec. 4, Paper 9. Wiesbaden, Germany, pp. 253–263.

Kolymbas, D., 1985. A generalized hypoplastic constitutive law, in: Proceedings of the Eleventh International Conference on Soil Mechanics and Foundation Engineering, San Francisco, 12-16 August , 1985. Vol. 5. Balkema, 1988, San Francisco, p. 2626.

Kolymbas, D., 1991. An outline of hypoplasticity. Arch. Appl. Mech. 61, 143–151. doi:10.1007/BF00788048

Kondner, R.L., 1963. Hyperbolic stress-strain response: cohesive soils. J. Soil Mech. Found. Div. ASCE 89, 115–143.

Kuhn, M.R., Bagi, K., 2009. Specimen Size Effect in Discrete Element Simulations of Granular Assemblies. J. Eng. Mech. ASCE 135, 485–492.

Lade, P., Yamamuro, J., Bopp, P., 1996. Significance of particle crushing in granular materials. J. Geotech. Eng. ASCE 122, 309–316. doi:10.1061/(ASCE)0733-9410(1996)122:4(309)

Lee, D.M., 1992. The angles of friction of granular. PhD. dissertation. University of Cambridge, Cambridge, UK.

Lee, K., Farhoomand, I., 1967. Compressibility and crushing of granular soil in anisotropic tiraxial compression. Can. Geotech. J. 4, 68–86. doi:10.1139/t67-012

Lee, Y., Yang, C.T., Chien, C.S., 2003. A 3D ellipsoid-based model for packing of granular particles. Int. J. Comput. Appl. Technol. 17, 148–155.

Leung, C.F., Lee, F.H., Yet, N.S., 1996. The role of particle breakage in pile creep in sand. Can. Geotech. J. 33, 888–898.

Lim, W.L., McDowell, G.R., 2005. Discrete element modelling of railway ballast. Granul. Matter 7, 19–29. doi:10.1007/s10035-004-0189-3

Lobo-Guerrero, S., Vallejo, L.E., 2005. Discrete Element Method Evaluation of Granular Crushing Under Direct Shear Test Conditions. J. Geotech. Geoenvironmental Eng. ASCE 131, 1295–1300.

Lu, M., McDowell, G.R., 2006. Discrete element modelling of ballast abrasion. Géotechnique 56, 651–655.

Marachi, N.D., Chan, C.K., Seed, H.B., 1972. Evaluation of properties of rockfill materials. J. Soil Mech. Found. Div. ASCE 98, 95–114.

Marachi, N.D., Chan, C.K., Seed, H.B., Duncan, J.M., 1969. Strength and deformation characteristics of rockfill materials. Berkeley, CA, USA.

Marketos, G., 2007. An investigation of crushing and compaction bands in granular material. PhD. Thesis. Cambridge University, U.K.

Marketos, G., Bolton, M.D., 2009. Compaction bands simulated in discrete element methods. J. Struct. Geol. 31, 479–490.

Marsal, R.J., 1973. Mechanical properties of rockfill, in: Hirschfeld, R.C., Poulos, S.J. (Eds.), Embankment Dam Engineering. Casagrande Volume I. John Wiley & Sons, New York, NY, USA, pp. 110–200.

Marsal, R.J., 1967. Large-scale testing of rockfills materials. J. Soil Mech. Found. Div. ASCE 93, 27–44.

Marsal, R.J., Resendiz, D., 1975. Presas de tierra y enrocamiento, Editorial . ed. Mexico City, Mexico.

McDowell, G.R., 1997. Clastic soil mechanics. PhD. dissertation. University of Cambridge.

McDowell, G.R., Bolton, M.D., 1998. On the micromechanics of crushable aggregates. Géotechnique 48, 667–679.

McDowell, G.R., Bolton, M.D., Robertson, D., 1996. The fractal crushing of granular materials. J. Mech. Phys. Solids 44, 2079–2102.

McDowell, G.R., De Bono, J.P., 2013. On the micro mechanics of one-dimensional normal compression. Géotechnique 63, 895–908. doi:10.1680/geot.12.P.041

McDowell, G.R., Harireche, O., 2002. Discrete element modelling of soil particle fracture. Géotechnique 52, 131–135.

McNamara, S., 2011a. Molecular Dynamics Method, in: Radjai, F., Dubois, F. (Eds.), Discrete-Element Modeling of Granular Materials. ISTE Ltd; John Wiley & Sons, Inc., London, UK, pp. 1–25.

McNamara, S., 2011b. Event-driven Method, in: Radjai, F., Dubois, F. (Eds.), Discrete-Element Modeling of Granular Materials. ISTE Ltd; John Wiley & Sons, Inc., London, UK, pp. 103–121.

Meredith, P.G., Atkinson, B.K., 1983. Stress corrosion and acoustic emission during tensile crack propagation in Whin Sill dolerite and other basic rocks. Geophys. J. Int. R. Astron. Soc. 75, 1–21. doi:10.1111/j.1365-246X.1983.tb01911.x

Meredith, P.G., Atkinson, B.K., 1982. High-temperature tensile crack propagation in quartz: Experimental results and application to time-dependent earthquake rupture. Earthq. Predict. Res. 1, 377–391.

Michalske, T., Freiman, S.W., 1982. A molecular interpretation of stress corrosion in silica. Nature 295, 511–512.

Montobbio, D., 2001. Efecto de la granulometría en la compresibilidad de escolleras. (Final work of undergraduated course). Universitat de Barcelona, Facultat de Geologia; Universitat Politècnica de Catalunya, Escola Tècnica Superior d'Enginyers de Camins, Canals i Ports de Barcelona.

Muir Wood, D., Belkheir, K., Liu, D.F., 1994. Strain softening and state parameter for sand modelling. Géotechnique 44, 335–339. doi:10.1680/geot.1994.44.2.335

Nakata, Y., Hyodo, M., Hyde, A.F.L., Kato, Y., Murata, H., 2001. Microscopic particle crushing of sand subjected to high pressure one-dimensional compression. Soils Found. 41, 69–82.

Nara, Y., Hiroyoshi, N., Yoneda, T., Kaneko, K., 2010. Effects of relative humidity and temperature on subcritical crack growth in igneous rock. Int. J. Rock Mech. Min. Sci. 47, 640–646. doi:10.1016/j.ijrmms.2010.04.009

Nara, Y., Morimoto, K., Yoneda, T., Hiroyoshi, N., Kaneko, K., 2011. Effects of humidity and temperature on subcritical crack growth in sandstone. Int. J. Solids Struct. 48, 1130–1140. doi:10.1016/j.ijsolstr.2010.12.019

Nara, Y., Takada, M., Igarashi, T., Hiroyoshi, N., Kaneko, K., 2009. Subcritical crack growth in rocks in an aqueous environment. Explor. Geophys. 40, 163–171.

Nara, Y., Yamanaka, H., Oe, Y., Kaneko, K., 2013. Influence of temperature and water on subcritical crack growth parameters and long-term strength for igneous rocks. Geophys. J. Int. 193, 47–60. doi:10.1093/gji/ggs116

Naylor, D.J., Maranha Das Neves, E., Mattar, D., Veiga Pinto, A.A., 1986. Prediction of construction performance of Beliche Dam. Géotechnique 36, 359–376.

Naylor, D.J., Maranha, J.R., Maranha das Neves, E., Veiga Pinto, A.A., 1997. A back-analysis of Beliche Dam. Géotechnique 47, 221–233.

Nezami, E.G., Hashash, Y.M.A., Zhao, D., Ghaboussi, J., 2004. A fast contact detection algorithm for 3-D discrete element method. Comput. Geotech. 31, 575–597.

Niemunis, A., Herle, I., 1997. Hypoplastic model for cohesionless soils with elastic strain range. Mech. Cohesive-frictional Mater. 2, 279–299.

Nobari, Duncan, 1972. Effect of reservoir filling on stresses and movements in earth and rockfill dams.

O'Sullivan, C., 2011. Particulate Discrete Element Modelling. A Geomechanics perspective. Spon Press, Taylor & Francis Group, Abingdon, Oxon, Uk.

O'Sullivan, C., Bray, J.D., 2004. Selecting a suitable time step for discrete element simulations that use the central difference time integration scheme. Eng. Comput. 21, 278 – 303. doi:10.1108/02644400410519794

Oldecop, L.A., 2000. Compresibilidad de escolleras. Influencia de la humedad. PhD. Thesis. Technical University of Catalonia. UPC, Barcelona, Spain (in Spanish).

Oldecop, L.A., Alonso, E.E., 2013. Rockfill mechanics, in: (eds), C. et al. (Ed.), Advances in Unsaturated Soils - Proceedings of the 1st Pan-American Conference on Unsaturated Soils. Cartagena de Indias (Colombia), February 20th–22nd, 2013. Taylor & Francis Group, pp. 61–86.

Oldecop, L.A., Alonso, E.E., 2007. Theoretical investigation of the time-dependent behaviour of rockfill. Géotechnique 57, 289–301.

Oldecop, L.A., Alonso, E.E., 2004. Testing rockfill under relative humidity control. Geotech. Test. J. 27, 269–278.

Oldecop, L.A., Alonso, E.E., 2003. Suction effects on rockfill compressibility. Géotechnique 53, 289–292.

Oldecop, L.A., Alonso, E.E., 2001. A model for rockfill compressibility. Géotechnique 51, 127–139.

Ortega, E., 2008. Comportamiento de materiales granulares gruesos - Efecto de la succión. PhD. Thesis. Technical University of Catalonia. UPC, Barcelona, Spain (in Spanish).

Outwater, J.., Murphy, M.C., Kumble, R.G., Berry, J.T., 1974. Double Torsion Technique as a universal fracture toughness test method, in: Fracture Toughness and Slow-Stable Cracking. ASTM International. Special Tech. Publ. STP 559. pp. 127–138. doi:10.1520/STP38597S

Ovalle, C., Frossard, E., Dano, C., Hu, W., Maiolino, S., Hicher, P.-Y., 2014. The effect of size on the strength of coarse rock aggregates and large rockfill samples through experimental data. Acta Mech. 225, 2199–2216. doi:10.1007/s00707-014-1127-z

Parish, O.O., Putnam, T.W., 1977. Equations for the determination of humidity from dewpoint and psychrometric data. Edwards, California (USA).

Parkin, A.K., Adikari, G.S.N., 1981. No Title, in: Proceedings of 10th Int. Conf. Soil Mech. And Found. Engg. (ICSMFE), Stockholm, 4. pp. 727–731.

Pender, M.J., 1978. A model for the behaviour of overconsolidated soil. Géotechnique 28, 1–25. doi:10.1680/geot.1978.28.1.1

Penman, A., Charles, J., 1976. The quality and suitability of rockfill used in dam construction, in: Penman, A.D.M., Charles, J.A., Moore, J.F.A. (Eds.), Dams and Embankments, A.D.M. Penman, J.A. Charles, J.F.A. Moore (Eds.). Edited By: The Building Research Establishment, The Construction Press, Garston, Watford, UK, pp. 72–85.

Perales, R., 2007. Modélisation du comportement mécanique par éléments discrets des ouvrages maçonnés tridimensionnels. Contribution à la définition d'éléments de contacts surfaciques. PhD. Thesis. University of Montpellier 2.

Pöschel, T., Schwager, T., 2005. Computational Granular Dynamics. Models and Algorithms. Springer-Verlag, Berlin, Germany.

Potyondy, D.O., Cundall, P.A., 2004. A bonded-particle model for rock. Int. J. Rock Mech. Min. Sci. 41, 1329–1364. doi:10.1016/j.ijrmms.2004.09.011

Pournin, L., Weber, M., Tsukahara, M., Ferrez, J.A., Ramaioli, M., Liebling, T.M., 2005. Three-dimensional distinct element simulation of spherocylinder crystallization. Granul. Matter 7, 119–126.

Radjai, F., Dubois, F. (Eds.), 2011. Discrete-element Modelling of Granular Materials. ISTE Ltd; John Wiley & Sons, Inc., London, UK.

Ramon, A., 2006. Efecte de la granulometria en el comportament d'esculleres. (Final work of undergraduated course). Universitat Politècnica de Catalunya, Barcelona, Spain.

Ramon, A., Alonso, E.E., Romero, E.E., 2008. Grain size effects on rockfill constitutive behavior, in: Toll, Augarde, Gallipolli, Wheeler (Eds.), In: Unsaturated Soils. Advances in Geo-Engineering: Proceedings of the 1st European Conference on Unsaturated Soils, Durham (U.K.). Taylor and Francis Group, London (U.K), pp. 341–347.

Robertson, D., 2000. Computer simulations of crushable aggregates. PhD. Thesis. Cambridge University.

Robertson, D., Bolton, M.D., 2001. DEM simulations of crushable grains and soils, in: Proceedings of the 4th International Conference on Micromechanics of Powders and Grains. Sendai, Japan, pp. 623–626.

Roscoe, K.H., Schofield, A.N., Thurairajah, A., 1963. Yielding of clays in states wetter than critical. Géotechnique 13, 211–240. doi:10.1680/geot.1963.13.3.211

Russell, A.R., Muir Wood, D., 2009. Point load tests and strength measurements for brittle spheres. Int. J. Rock Mech. Min. Sci. 46, 272–280. doi:10.1016/j.ijrmms.2008.04.004

Salim, W., Indraratna, B., 2004. A new elastoplastic constitutive model for coarse granular aggregates incorporating particle breakage. Can. Geotech. J. 41, 657–671. doi:10.1139/t04-025

Sano, O., Ogino, S., 1980. Acoustic emission during slow crack growth. Technical Report 2. Yamaguchi , Japan.

Santamarina, J.C., Klein, K., Fam, M., 2001. Load deformation behaviour, in: Soils and Waves: Particulate Materials Behaviour, Characterization and Process Monitoring. John Wiley & Sons, Ltd., Chichester (UK), pp. 104–106.

Saouma, V.E., 2007. Lecture notes in fracture mechanics. Barcelona (Spain).

Saussine, G., 2004. Contribution à la modélisation de granulats tridimensionnels: application au ballast. PhD. Thesis. University of Montpellier 2.

Saussine, G., Cholet, C., Dubois, F., Bohatier, C., Gauthier, P., 2004. Modélisation du comportment du ballast par une méthode d'éléments discrets. Reveu Eur. des Eléments Finis 13, 725–736.

Schofield, A.N., Wroth, C.P., 1968. Critical state soil mechanics. McGraw-Hill, London, UK.

Shipway, P.H., Hutchings, I.M., 1993. Fracture of brittle spheres under compression and impact loading. I. Elastic stress distributions. Philos. Mag. A 67, 1389–1404.

Soriano, A., Sánchez, F.J., 1999. Settlements of railroad high embankments, in: Proceedings of XII European Conference on Soil Mechanics and Geotechnical Engineering. Netherlands.

Sowers, G.F., Williams, R.C., Wallace, T.S., 1965. Compressibility of broken rock and settlement of rockfills, in: Proceedings of the 6th ICSMFE, Montreal, Canada, Vol. 2. pp. 561–565.

Swanson, P.L., 1984. Subcritical crack growth and other time- and environment-dependent behavior in crustal rocks. J. Geophys. Res. 89, 4137–4152. doi:10.1029/JB089iB06p04137

Swanson, P.L., 1980. Stress corrosion cracking in Westerly granite: An examination by the double torsion technique. MSc. Thesis. Univ. of Colo., Boulder.

Takei, M., Kusakabe, O., Hayashi, T., 2001. Time-dependent behavior of crushable materials in one-dimensional compression tests. Soils Found. 41, 97–121.

Thom, N.H., Brown, S.F., 1988. The effect of grading and density on the mechanical properties of a crushed dolomitic limestone, in: Proceedings of 14th ARRB Conf., Vol. 14, Part 7. pp. 94–100.

Thom, N.H., Brown, S.F., 1989. The mechanical properties of unbounded aggregates from various sources, in: Jones, R.H., Dawson, A.R. (Eds.), Unbound Aggregates in Roads. pp. 130–142.

Thomas, T.R., 1999. Amplitude Parameters, in: Rough Surfaces. Imperial College Press, London (UK), pp. 133–150.

Thornton, C., 2015. Granular Dynamics, Contact Mechanics and Particle System Simulations. A DEM study, Particle Technology Series. Springer International Publishing. doi:10.1007/978-3-319-18711-2

Thornton, C., Liu, L., 2004. How do agglomerates break? Powder Technol. 143-

144, 110–116.

Tsoungui, O., Vallet, D., Charmet, J.C., 1999. Numerical model of crushing of grains inside two-dimensional granular materials. Powder Technol. 105, 190–198. doi:10.1016/S0032-5910(99)00137-0

Turcotte, D.L., 1986. Fractals and fragmentation. Journal of Geophysical Research- Solid Earth. J. Geophys. Res. Solid Earth 91, 1921–1926.

Vallerga, B.A., Seed, H.B., Monismith, C.L., Cooper, R.S., 1957. Effect of shape, size and surface roughness of aggregate particles on the strength of granular materials, in: Road and Paving Materials. pp. 63–74.

Veiga Pinto, A.A., 1983. Previsao do comportamento estrutural de barragens de enrocamento. PhD thesis. Laboratorio Nacional de Engenharia Civil, Lisbon, Portugal.

Vesic, A.S., Clough, G.W., 1968. Behaviour of granular materials under high stresses. J. Soil Mech. Found. Div. ASCE 94, 661–668.

Wachtman, J.B., Cannon, W.R., Matthewson, M.J., 2009. Subcritical Crack Propagation, in: Mechanical Properties of Ceramics. John Wiley & Sons, Inc., Hoboken, NJ, USA, pp. 151–176. doi:10.1002/9780470451519.ch8

Wan, R.G., Guo, P.J., 1998. A simple constitutive model for granular soils: Modified stress-dilatancy approach. Comput. Geotech. 22, 109–133.

Wang, J., Yan, H., 2012. DEM analysis of energy dissipation in crushable soils. Soils Found. 52, 644–657. doi:10.1016/j.sandf.2012.07.006

Waza, T., Kurita, K., Mizutani, H., 1980. The effect of water on the subcritical crack growth in silicate rocks. Tectonophysics 67, 25–34. doi:10.1016/0040-1951(80)90162-6

Weibull, W., 1951. A statistical distribution function of wide applicability. J. Appl. Mech. 18, 293–297.

Weibull, W., 1939. A statistical theory of the strength of materials, in: Proceedings of the Royal Swedish Institute of Engineering Research, 151.

Wiederhorn, S.M., 1978. Mechanisms of subcritical crack growth in glass, in: Bradt, R.C., Hasselman, D.P.H., Lange, F.F. (Eds.), Fracture Mechanics of Ceramics, Vol. 4. Plenum Press, pp. 549–580.

Wiederhorn, S.M., 1974. Subcritical crack growth in ceramics, in: Bradt, R.C., Hasselman, D.P.H., Lange, F.F. (Eds.), Fracture Mechanics of Ceramics, Vol. 2. Plenum Press, New York, pp. 613–646.

Wiederhorn, S.M., Boltz, L.H., 1970. Stress corrosion and static fatigue of glass. J. Am. Ceram. Soc. 53, 543–548.

Wiederhorn, S.M., Freiman, S.W., Fuller, E.R., Simmons, C.J., 1982. Effects of water and other dielectrics on crack growth. Mater. Sci. 17, 3460–3478.

Wiederhorn, S.M., Fuller, E.R., Thomson, R., 1980. Micromechanisms of crack growth in ceramics and glasses in corrosive environments. Met. Sci. 14, 450–458. doi:http://dx.doi.org/10.1179/msc.1980.14.8-9.450

Wilkins, B.J.S., 1980. Slow crack growth and delayed failure of granite. Int. J. Rock Mech. Min. Sci. Geomech. Abstr. 17, 365–369.

Williams, D.P., Evans, A.G., 1973. A simple method for studying slow crack growth. J. Test. Eval. 1, 264–270. doi:http://dx.doi.org/10.1520/JTE10015J

Wu, W., Bauer, E., Kolymbas, D., 1996. Hypoplastic constitutive model with critical state for granular materials. Mech. Mater. 23, 45–69. doi:10.1016/0167-6636(96)00006-3

Yamamuro, J., Lade, P., 1996. Drained sand behaviour in axisymmetric tests at high pressures. J. Geotech. Eng. ASCE 122, 109–119.

Yasuda, N., Matsumoto, N., 1994. Comparison of deformation characteristics of rockfill materials using monotonic and cycling loading laboratory tests and in situ tests. Can. Geotech. J. 31, 162–174.

Yasuda, N., Matsumoto, N., Yoshioka, R., Takahashi, M., 1997. Undrained monotonic and cyclic strength of compacted rockfill material from triaxial and torsional simple shear tests. Can. Geotech. J. 34, 357–367. doi:10.1139/cgj-34-3-357

Zhang, X., Baudet, B., 2013. Particle breakage in gap-graded soil. Géotechnique Lett. 3, 72–77.

Zhixi, C., Mian, C., Yan, J., Rongzun, H., 1997. Determination of rock fracture toughness and its relationship with acoustic velocity. Int. J. Rock Mech. Min. Sci. 34, 49.e1–49.e11.

Appendix 1

A1. Sensitivity analysis of the probability distribution of the initial-crack length inside the macroparticles

This appendix presents a sensitivity analysis of the manner to insert the length of the cracks inside the macroparticles using different probability distributions. Numerical oedometer tests are performed on specimens of macroparticles of 2.8cm in size which can break.

Six probability distributions are analyzed: a uniform distribution, two types of the exponential distribution and three types of the Weibull distribution.

A novel procedure is proposed to obtain probability distributions based on random values that follow a uniform distribution.

A1.1. Probability distributions

A1.1.1. Defects (crack lengths) inside the macroparticles

After the creation of one macroparticle, a defect is inserted inside it. The defect or flaw is modeled numerically as a virtual crack with a certain initial length. The initial length is chosen randomly according to a probability distribution within a range of values between 0.001D and 0.5D where D is the equivalent diameter of the macroparticle. Therefore, the initial-crack length ($L_{0\text{-crack}}$) is calculated as follows:

$$L_{0-crack} = azarnum * D \tag{A1:1}$$

where "*azarnum"* is the random value according to a probability distribution within a range of values between 0.001and 0.5.

Six types of probability distributions are analyzed (see **Figure A1 - 1**): one of them is the uniform, and the others are five types of the Weibull distributions. Two of these Weibull distributions really correspond to the exponential distributions and another one is similar to the normal distribution.

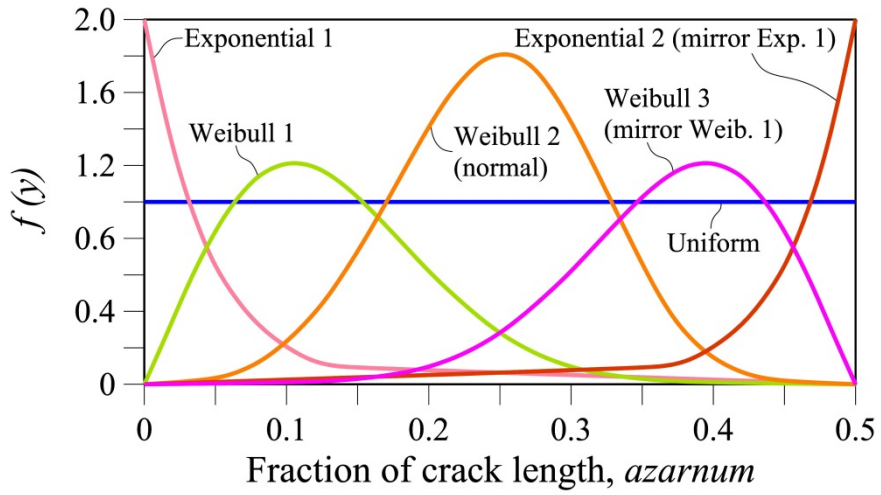

Figure A1 - 1 Probability distributions of the initial-crack length (theoretical density functions). Comparison between six probability distributions: Uniform, exponential 1, exponential 2, Weibull 1, Weibull 2, and Weibull 3.

A1.1.2. Uniform distribution

A uniform probability distribution *f(w)* is shown in **Figure A1 - 1**.

If *w* is a random number between 0.0 and 1.0 according to a uniform probability distribution *f(w)*, which has a mean value of 0.5, then the "*azarnum*" value can be calculated as follows:

$$azarnum = 0.001 + 0.499 * w \qquad \text{(A1:2)}$$

Therefore, *azarnum* is a random value between 0.001 and 0.50 according to a uniform distribution.

A1.1.3. Weibull probability distribution

The Weibull probability distribution *f(y)* has the following values:

$$f(y)=\begin{cases}\dfrac{\alpha}{\beta}y^{\alpha-1}e^{\frac{-y^{\alpha}}{\beta}} & for\quad 0\le y<\infty\ ;\ \alpha>0\ ;\ \beta>0\\ 0 & \text{at any other point}\end{cases} \tag{A1:3}$$

The mean value of *f(y)*, μ, can be calculated by:

$$\mu=\beta^{\frac{1}{\alpha}}\Gamma\left[\frac{\alpha+1}{\alpha}\right] \tag{A1:4}$$

where: α is a shape parameter and β is a scale parameter.

A Weibull probability distribution can be obtained from a uniform density function *f(w)*, by making *w* equal to the function of the cumulative distribution for the range $0\le w\le 1.0$. Therefore,

$$w=F(y)=1-e^{-\frac{y^{\alpha}}{\beta}}\ ;\quad for\quad 0\le w\le 1.0 \tag{A1:5}$$

$$y=\left[-\beta*\ln(1-w)\right]^{\frac{1}{\alpha}}\quad for\quad 0\le w\le 1.0 \tag{A1:6}$$

Different types of Weibull probability distribution can be obtained by varying the values of α and β.

A1.1.3.1. Exponential-1 distribution (Exponential 1)

This probability distribution is obtained when α=1, and has a mean value (μ) of:

$$\mu=\beta \tag{A1:7}$$

Therefore,

$$y=\left[-\beta*\ln(1-w)\right]\quad for\quad 0\le w\le 1.0 \tag{A1:8}$$

A value of β=0.5 is used in this thesis.

If the maximum value of w, w_{max}, is limited to 0.99999, i.e. w_{max}=0.99999, then the maximum value of y, y_{max}, can be calculated as follows:

$$y_{max} = \left[-\beta * \ln\left(1 - w_{max}\right)\right] \tag{A1:9}$$

Consequently,

$$y = \left[-0.5 * \ln\left(1 - w\right)\right] \quad for \quad 0 \le w \le 0.99999;\ 0 \le y \le y_{max} \tag{A1:10}$$

As explained above, *azarnum* is a random value between 0.001 and 0.50, therefore the *azarnum* value according to the exponential distribution can be calculated by:

$$azarnum = 0.001 + \frac{0.499}{y_{max}} * y \tag{A1:11}$$

The mean value of *azarnum* is 0.04 approximately.

In this research, this type of probability distribution is called the *exponential 1* distribution (see **Figure A1 - 1**).

A1.1.3.2. Exponential-2 distribution – Mirror of the Exponential-1 distribution (Exponential 2)

The mirror of the previous function of *azarnum*, about the y=(y_{max})/2 axis, is calculated as follows:

$$azarnum = 0.5 - \frac{0.499}{y_{max}} * y \tag{A1:12}$$

The same values used in the exponential 1 distribution for α and β are applied: α=1, β=0.5.

The mean value of *azarnum* is 0.46 approximately.

In this research, this type of probability distribution is called the *exponential 2* distribution (see **Figure A1 - 1**).

A1.1.3.3. Weibull-1 distribution (Weibull 1)

This probability distribution is obtained when α=1 and β=0.5. The function y is calculated by:

$$y = \left[-0.5*\ln\left(1-w\right)\right]^{\frac{1}{2}} \quad for \quad 0 \le w \le 0.9999 \tag{A1:13}$$

The mean value is:

$$\mu = 0.63 \tag{A1:14}$$

azarnum is calculated by Eq. (A1:11). The mean value of *azarnum* is 0.12.

In this research, this type of probability distribution is called the Weibull 1 distribution (see **Figure A1 - 1**).

A1.1.3.4. Weibull-2 distribution (Weibull 2)

This probability distribution is obtained when α=4 and β=0.5. This type of probability distribution is called the Weibull 2 distribution (see **Figure A1 - 1**). This distribution is similar to the Normal distribution.

The function y is calculated as follows:

$$y = \left[-0.5*\ln\left(1-w\right)\right]^{\frac{1}{4}} \quad for \quad 0 \le w \le 0.99999 \tag{A1:15}$$

The mean value is:

$$\mu = 0.76 \tag{A1:16}$$

azarnum is also calculated by Eq. (A1:11). The mean value of *azarnum* is 0.25.

A1.1.3.5. Weibull-3 distribution – Mirror of the Weibull-1 distribution (Weibull 3)

This probability distribution corresponds to the mirror of the Weibull-1 distribution, about the $y=(y_{max})/2$ axis. The same values used in the Weibull 1 distribution for α and β are applied: α=2, β=0.5.

The function *y* is calculated in the same manner that the Weibull 1:

$$y = \left[-0.5*\ln\left(1-w\right)\right]^{\frac{1}{2}} \quad for \quad 0 \le w \le 0.9999 \tag{A1:17}$$

However, *azarnum* is calculated similarly to the Exponential-2:

$$azarnum = 0.5 - \frac{0.499}{y_{max}} * y \tag{A1:18}$$

The mean value of *azarnum* is 0.37 approximately.

In this research, this type of probability distribution is called the *Weibull 3* distribution (see **Figure A1 - 1**).

A1.2. Numerical simulation of oedometer tests

A1.2.1. The DEM model

The numerical oedometer tests reproduce the dimensions used in the laboratory triaxial tests performed by (Ortega, 2008) at the UPC (see **Figure 5-10b** in chapter 5):

- Sample size: diameter:25cm ; heigth:25cm.
- Size of macroparticles: 2.8 cm. Uniform grain size at the beginning of the test.
- 471 macroparticles at the beginning of the tests.
- Initial porosity of the specimen of macroparticles: 53.14%.

Gravels are modeled as clumps (macroparticles) of 14 microparticles (**Figure 5-10a** in chapter 5). The properties of the macroparticles are presented in **Table A1 - 1**.

Table A1 - 1 Properties of macroparticles in the DEM model.

Normal stiffness, k_n	4 MN/m
Shear stiffness, k_s	4 MN/m
Friction coefficient, μ	0.3
Toughness, K_c	$5x10^6$ Pa•$m^{0.5}$

The failure criteria used in the simulations of the oedometer tests was of the Crack Propagation criterion based on the LEFM -linear elastic fracture mechanics- (see section 5.3 in chapter 5). The stress intensity factor *K* is calculated for the maximum tensile stress that acts inside the macroparticle subjected to a point load condition. As explained in chapter 5, this consideration is according to the loading condition of (Russell and Muir Wood, 2009) for point loading on brittle spheres (see **Fig. 5-6**).

This study only considers the "Splitting failure" mechanisms in the particle breakage process. The simulations have considered dry conditions, i.e. RH=10%. Subparticles of 13 microparticles are not used here to replace the macroparticles of 1 sphere.

A1.2.2. Numerical tests

As explained in section A1.1.1, six probability distributions are used in the DEM model to introduce the initial-crack length inside the macroparticles: Uniform, Exponential 1, Exponential 2, Weibull 1, Weibull 2 and Weibull 3.

Results of numerical oedometer tests are presented in this section in order to make a sensitivity analysis due to the used probability distribution.

Table A1 - 2 Data range of the values of *azarnum* considered in the analysis of the relative frequency of the initial-crack length for all the probability distributions.

azarnum **(Initial-crack length / Half of the equivalent diameter of the macroparticle)**	
Range	**Mean value**
0-0.05	0.025
0.05-0.1	0.075
0.1-0.15	0.125
0.15-0.20	0.175
0.20-0.25	0.225
0.25-0.30	0.275
0.30-0.35	0.325
0.35-0.40	0.375
0.40-0.45	0.425
0.45-0.50	0.475

The numerical tests simulate the experimental oedometer tests performed by (Ortega, 2008) on limestone gravels of sizes between 2.5 and 3.0cm. **Table 5-2**, in chapter 5, provides the properties of the limestone gravels. The vertical stress was applied by steps: 0.1; 0.2; 0.4; 0.6; 0.8; 1.2; 1.6; 2.0; 2.4 and 2.8 MPa. The tests were performed under dry conditions (RH=10%).

Figure A1 - 2 shows the distribution of the relative frequency of the values of *azarnum* –fraction of the initial-crack length- which were assigned in all the macroparticles at the beginning of the tests. For this analysis, ten ranges of the fractions of initial-crack length are taken into account as shown in **Table A1 - 2**. The curves of the **Figure A1 - 2** are similar to the behaviour of the theoretical curves of the probability distributions considered in **Figure A1 - 1**.

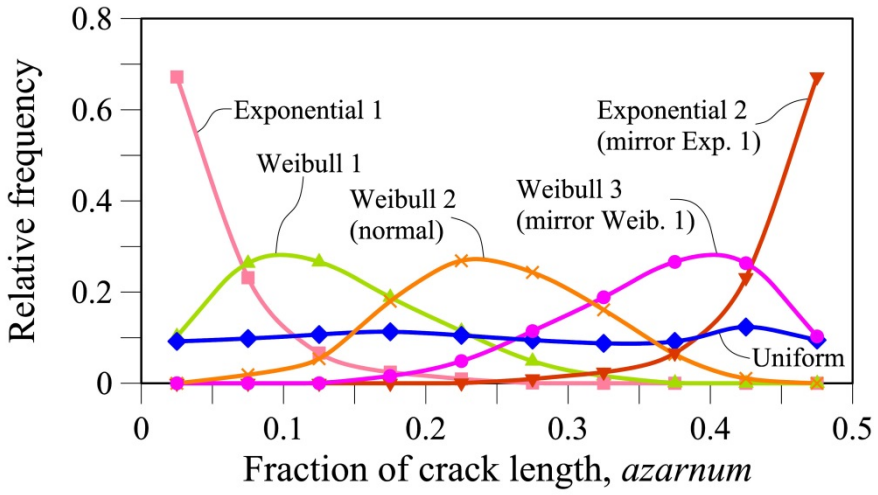

Figure A1 - 2 Relative frequency of the values of *azarnum* –Fraction of the initial-crack length- assigned to all the macroparticles at the beginning of the numerical oedometer tests for the different probability distributions. Comparison between six probability distributions: Uniform, exponential 1, exponential 2, Weibull 1, Weibull 2, and Weibull 3. Ten data ranges of *azarnum* are considered.

A1.2.2.1. Compressibility behaviour

Figure A1 - 3 shows the compressibility curves for all the numerical tests. The probability distributions of Exponential 2 and Weibull 3 present the higher vertical strain at the beginning of the tests. During the tests, the probability distributions of Exponential 2, Weibull 1, Weibull 2 and Weibull 3 present large collapses of vertical strain. Large collapses are related to a considerable particle breakage after the application of certain vertical stresses, for instance, it can be noted the

collapse between the stress σ_v of 0.8 and 1.2 MPa for the Exponential 2 and Weibull 2 distributions, the collapse between the stress σ_v of 1.6 and 2.0 MPa for the Weibull 3 distribution and the collapse between the stress σ_v of 2.0 and 2.4 MPa for the Weibull 1 distribution. The curve of the Exponential 1 presents a small collapse between the stress σ_v of 2.0 and 2.4 MPa. The curve of the uniform distribution presents a similar behaviour to the actual (see the compressibility curve of the limestone gravels in **Figure 5-25**, chapter 5).

The variation of the compressibility index, λ, during the tests is shown in **Figure A1 - 4**. λ curves of experimental results of tests performed by Ortega (2008) on limestone gravels and by Oldecop and Alonso (2007) on slate gravels with similar sizes are also shown in **Figure A1 - 4**. The curves of the Uniform and Exponential 1 are close to the experimental results. Peaks in the values of λ for the other numerical tests are related to large collapses during the tests.

A1.2.2.2. Particle breakage

The curves of grain size distributions at the beginning and the end of the tests are shown in **Figure A1 - 5**. The curves of the Uniform and Exponential-1 distributions tend to present a well-graded behaviour; however the curve of the Uniform is the most similar to the actual gsd shown in **Figure 5-20**, in chapter 5. Exponential 2 and Weibull 3 have a complete breakage at the end of the tests, as it can be also noted in **Figure A1 - 6** where the Hardin breakage indexes (B_r) at the end of the tests are presented.

The breakage can be also seen in the evolution of the number of clumps during the tests (see **Figure A1 - 7**a and **Figure A1 - 7**b). **Figure A1 - 7**a shows the number of clumps in terms of the vertical stress. Similarly, **Figure A1 - 7**b shows the evolution of the number of clumps in terms of the vertical strain during the tests.

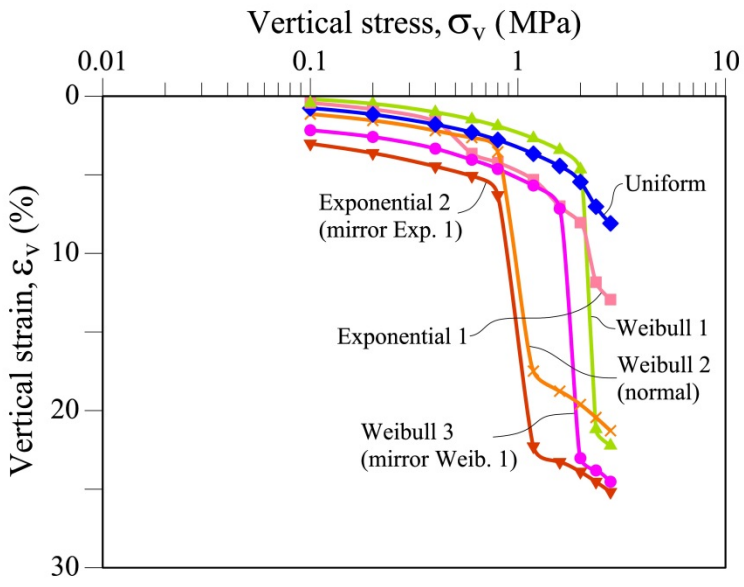

Figure A1 - 3 Effect of the probability distribution of the initial-crack length on the curves of compressibility. Comparison between six probability distributions: Uniform, exponential 1, exponential 2, Weibull 1, Weibull 2, and Weibull 3. Results of numerical simulations of oedometer tests using macroparticles of 14 microparticles. Specimens of 471 macroparticles. Maximum vertical stress: 2.8MPa; RH=10%; Initial porosity: 53%; DEM properties: k_n=4MN/m; K_c=5x10^6 Pa.m$^{0.5}$; μ=0.3.

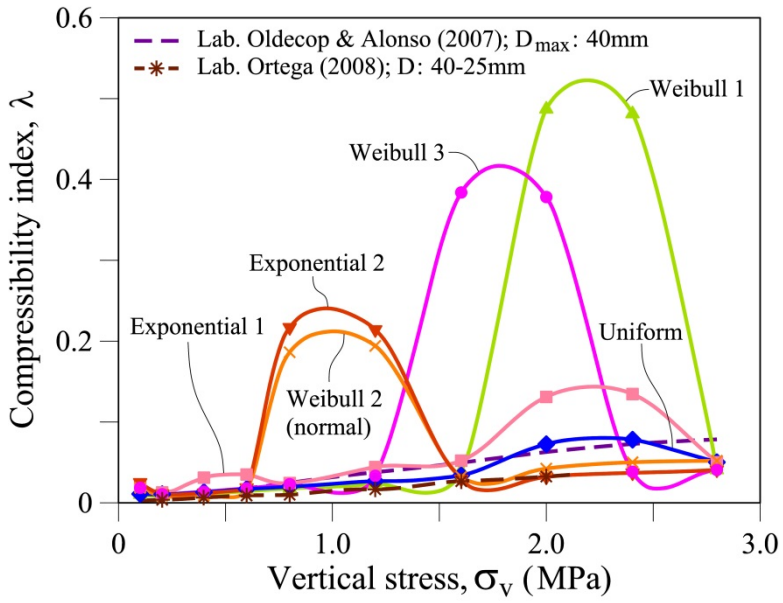

Figure A1 - 4 Effect of the probability distribution of the initial-crack length on the compressibility index. Comparison between six probability distributions (Uniform, exponential 1, exponential 2, Weibull 1, Weibull 2, and Weibull 3) and experimental results. Results of numerical simulations of oedometer tests using macroparticles of 14 microparticles. Specimens of 471 macroparticles. Maximum vertical stress: 2.8MPa; RH=10%; Initial porosity: 53%; DEM properties: k_n=4MN/m; K_c=5x10^6 Pa.m$^{0.5}$; μ=0.3.

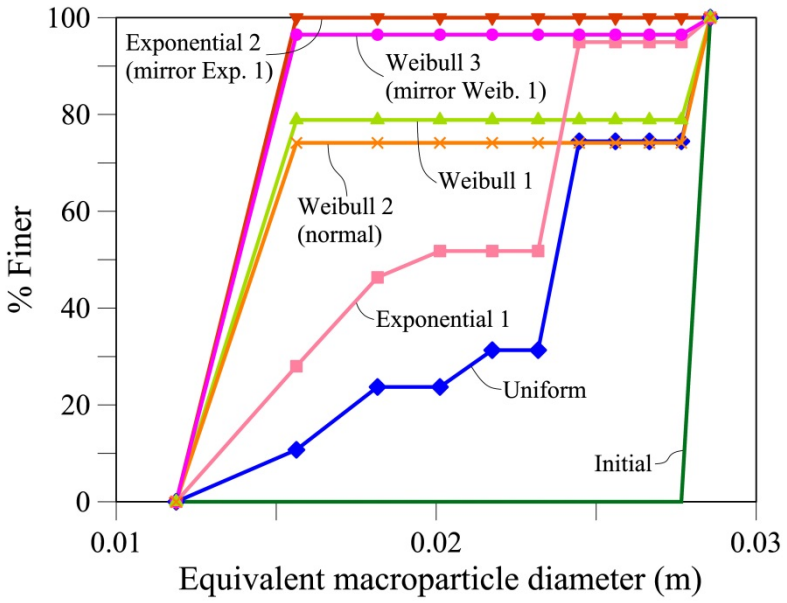

Figure A1 - 5 Effect of the probability distribution of the initial-crack length on the evolution of the grain size distributions at the initial and the end of oedometer tests. Comparison between six probability distributions: Uniform, exponential 1, exponential 2, Weibull 1, Weibull 2, and Weibull 3. Results of numerical simulations of oedometer tests using macroparticles of 14 microparticles. Specimens of 471 macroparticles. Maximum vertical stress: 2.8MPa; RH=10%; Initial porosity: 53%; DEM properties: k_n=4MN/m; K_c=5x10^6 Pa.m$^{0.5}$; μ=0.3.

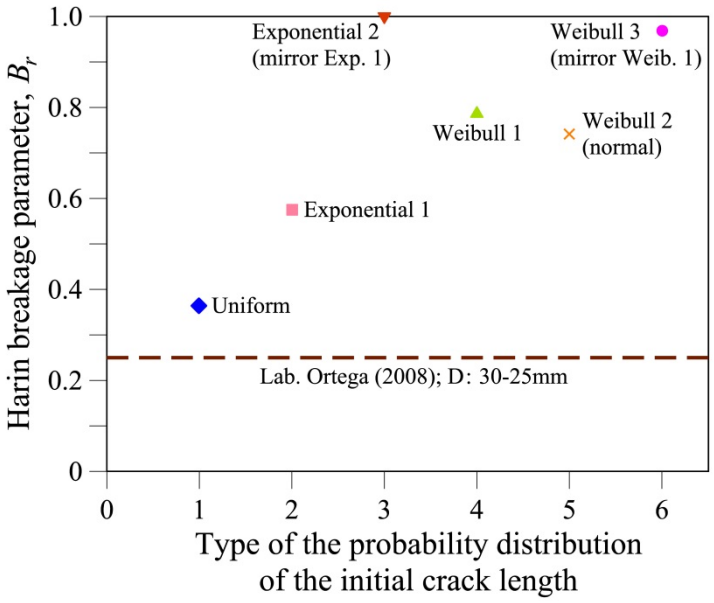

Figure A1 - 6 Effect of the probability distribution of the initial-crack length on the Hardin breakage index B_r at the end of oedometer tests. Comparison between six probability distributions (Uniform, exponential 1, exponential 2, Weibull 1, Weibull 2, and Weibull 3) and experimental results. Results of numerical simulations of oedometer tests using macroparticles of 14 microparticles. Specimens of 471 macroparticles. Maximum vertical stress: 2.8MPa; RH=10%; Initial porosity: 53%; DEM properties: k_n=4MN/m; K_c=5x10^6 Pa.m$^{0.5}$; μ=0.3.

a.

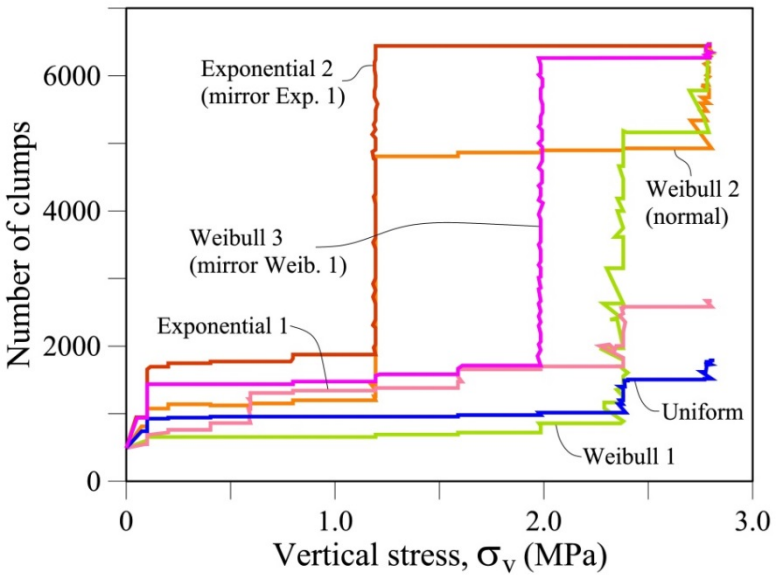

b.

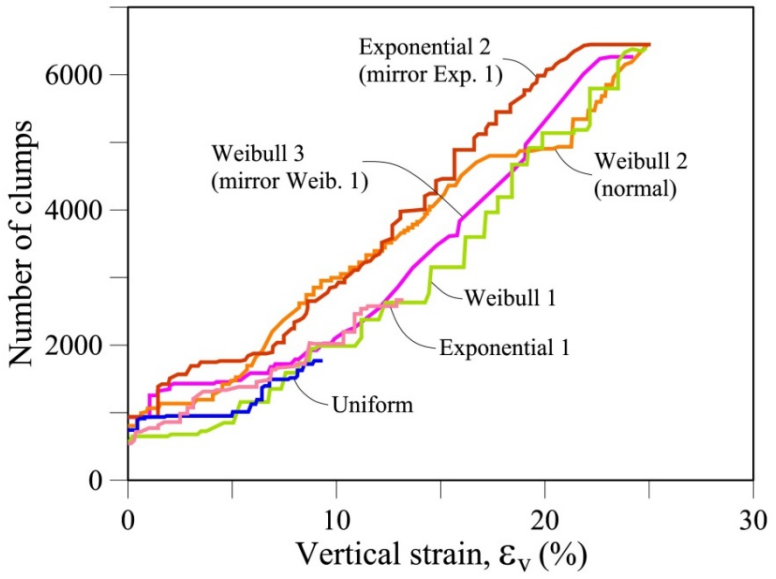

Figure A1 - 7 Effect of the probability distribution of the initial-crack length on the evolution of the number of clumps. Comparison between six probability distributions: Uniform, exponential 1, exponential 2, Weibull 1, Weibull 2, and Weibull 3. Results of numerical simulations of oedometer tests using macroparticles of 14 microparticles. Specimens of 471 macroparticles. Maximum vertical stress: 2.8MPa; RH=10%; Initial porosity: 53%; DEM properties: k_n=4MN/m; K_c=5x10^6 Pa.m$^{0.5}$; μ=0.3. (a) Vertical stress : Number of Clumps; (b) Vertical strain : Number of Clumps.

A1.3. Conclusions

A procedure to obtain different probability distributions based on random values of a uniform distribution was proposed in order to introduce “virtual crack-lengths” inside the macroparticles. Six probability distributions were studied.

The uniform distribution is the probability distribution that presents the most similar behaviour to actual results in comparison with other distributions. Compressibility behaviour and the evolution of the particle breakage was taken into account.

This probability distribution was chosen to assign the initial-crack length inside the macroparticles in the proposed DEM model in this thesis.

A1.4. References

Oldecop, L.A., Alonso, E.E., 2007. Theoretical investigation of the time-dependent behaviour of rockfill. Géotechnique 57, 289–301.

Ortega, E., 2008. Comportamiento de materiales granulares gruesos - Efecto de la succión. PhD. Thesis. Technical University of Catalonia. UPC, Barcelona, Spain (in Spanish).

Russell, A.R., Muir Wood, D., 2009. Point load tests and strength measurements for brittle spheres. Int. J. Rock Mech. Min. Sci. 46, 272–280. doi:10.1016/j.ijrmms.2008.04.004

Appendix 2

A2. Analysis of micro-properties for triaxial behaviour on coarse aggregates using DEM

This appendix describes the results of a work done at the first stage of this research. The results of numerical simulations of triaxial tests using the discrete particle method though the computer code PFC3D are presented.

In this appendix, a sensitivity analysis of some properties on the mechanical behaviour of coarse granular aggregates is performed: failure criteria, macroparticle shape, initial porosity of the aggregate, contact stiffness, toughness, and friction coefficient. A background reference for the conducted study is the set of results of a few large scale triaxial tests performed at the UPC geotechnical laboratory (Ortega, 2008).

The influence of two failure criteria to consider the particle breakage is presented. Additionally, not particle breakage is also considered. For the study of the other influences, the failure criterion based on fracture mechanics has been selected. This study only takes into account the “Splitting failure” mechanisms in the particle breakage process. The simulations have considered dry conditions, i.e. RH=10%.

A2.1. Numerical simulation of triaxial tests

Actual particle shapes are modeled as clumps of 14 microparticles (see **Figure A2 - 1**). Other shapes are considered in the sensitivity analysis presented below. As discussed previously, the clumps are also known as ‘macroparticles’ to distinguish them from the basic spherical particles (microparticles).

The numerical triaxial tests reproduce the dimensions used in the laboratory triaxial tests performed by (Ortega, 2008) at the UPC on limestone gravels (**Figure A2 - 2**):

- Sample size: diameter:25cm ; heigth:50cm.
- Size of macroparticles: 2.8 cm. The results reported here correspond to uniform grain size at the beginning of the test.

Table A2 - 1 shows some properties of the limestone fragments (Ortega, 2008) and **Table A2 - 2** provides some fundamental properties for the DEM simulations.

As explained in chapter 5, an important practical aspect is to ensure that particles do not carry any contact force before applying the real confining stress. Clumps are generated in a random manner and a desired porosity is imposed. A relaxation of internal forces is then necessary before testing.

Table A2 - 1 Rockfill properties: limestone gravels.

Solids density	2.76 Mg/m^3
Young's modulus, E	6800 MPa
Porosity, n_0	0.5
Uniaxial compressive strength, q_u	107.18 MPa

Table A2 - 2 Properties of macroparticles in DEM model.

Normal stiffness, k_n	20 MN/m
Shear stiffness, k_s	20 MN/m
Friction coefficient, μ	0.93 – 0.5 – 0.3
Toughness, K_c	1x10^6 - 1x10^5 - 1x10^4 Pa•m$^{0.5}$

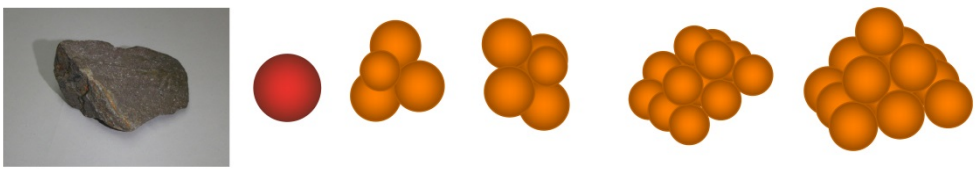

Figure A2 - 1 Rockfill macroparticle. Real and clump models of 1, 4, 5, 13 and 14 microparticles.

A2.2. Influence of the failure criteria of particles

The procedure for the simulation of particle breakage considers the following aspects:

- Calculation of stresses inside the macroparticles
- Application of a failure criterion
- Division of macroparticles (particle breakage) when the failure criterion is reached.

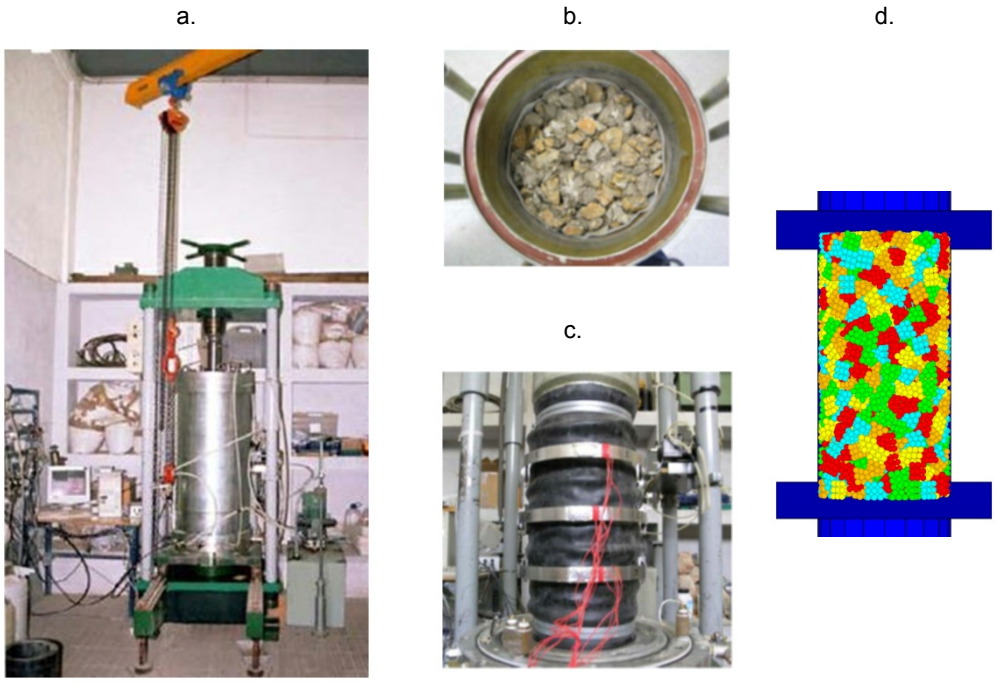

Figure A2 - 2 Triaxial test on rockfill. (a) Large diameter triaxial equipment of UPC geotechnical laboratory (From Chávez (2003)); (b) Limestone gravels about 3cm in size (From Ortega (2008)); (c) Details of sample tested by Ortega (2008); (d) DEM simulation of a sample.

A2.2.1. Calculation of stresses inside the macroparticles

The study presented here considers a calculation of stresses inside the macroparticles that differs of the proposed DEM model presented in chapters 5, 6 and 7.

In this appendix, the concept of stress is defined for a representative elementary volume –REV- (Bagi, 1999, 1996; Itasca, 2008). For this work, the REV is the macroparticle. The following procedure was implemented in the code: a) Identifying the clump; b) Identifying contacts with neighboring clumps; c) Identifying forces in contacts; d) Calculating the mass centroid of the clump; e) Calculating the average stress tensor, $\bar{\bar{\sigma}}_{ij}$, using the following expression (Alonso-Marroquín and Herrmann, 2005):

$$\bar{\bar{\sigma}}_{ij} = \frac{1}{V}\sum_{\alpha\beta} l_i^{\alpha\beta} f_j^{\alpha\beta} \qquad \text{(A2:1)}$$

where: $l_i^{\alpha\beta}$: Position vector between the mass centroid and the contact point where the contact force $f_j^{\alpha\beta}$ acts; α : Particle; β : Contact; V: Volume of macroparticle;

The principal stresses are derived from the stress invariants for each macroparticle.

A2.2.2. Failure criteria for macroparticles

Two failure criteria were compared: a classical Mohr Coulomb criterion and a criterion based on the propagation of cracks inside particles (Oldecop and Alonso, 2007). The second criterion is based on linear elastic fracture mechanics (LEFM).

A2.2.2.1. Mohr-Coulomb criterion

The Mohr-Coulomb criterion requires two parameters for macroparticles: cohesion, c, and internal friction angle, ϕ.

$$\sigma_1^f = \sigma_3 * \frac{1+\sin(\phi)}{1-\sin(\phi)} + 2 * c * \sqrt{\frac{1+\sin(\phi)}{1-\sin(\phi)}} \qquad \text{(A2:2)}$$

A macroparticle breaks when $\sigma_1 \geq \sigma_1^f$. In this case, there were considered the following values of the parameters: c=(c_u=5.36 MPa, and ϕ=0.

A2.2.2.2. Crack propagation criterion

The crack propagation criterion based on the Linear Elastic Fracture Mechanics (LEFM) is particularly useful because if allows the consideration of suction and time effects. The classical result for a mode of failure (say Mode I for failure in tension,σ) specifies that whenever the stress intensity factor K reaches the toughness of the rock (K_c) a fissure will propagate catastrophically and the rock particle will break. K is defined in terms of a characteristic crack length a.

$$K = \beta\sigma\sqrt{(\pi a)} \qquad \text{(A2:3)}$$

where β is a dimensionless coefficient which depends on particle geometry.

However, as explained in chapter 5 and 7, a subcritical propagation of fractures, is also possible when $K<K_c$ (Atkinson, 1984; Oldecop and Alonso, 2001). Oldecop and Alonso (2007) describe a phenomenological model of particle breakage based on subcritical crack growth.

The approach followed here is to assign a randomly distribution of defects (crack lengths) to the macroparticles. Crack length follows a uniform statistical distribution.

The stress intensity factor *K* increases as the crack propagates under a certain tensile stress σ (see Eq. (A2:3)).

In this appendix, the tensile stress σ has been calculated by two different manner:

1. σ is calculated as the maximum tensile stress that acts inside the macroparticle subjected to a point load condition. As explained in chapter 5, this consideration is according to the loading condition of (Russell and Muir Wood, 2009) for point loading on brittle spheres (see **Fig. 5-6**). The calculation of σ is given by the Eq. (5:1).
   This criterion was used in this study of the comparison of the failure criteria (see **Fig. A2-3**). Furthermore, it was used in the analysis of the shape effect which is explained later.
2. σ corresponds to the minor principal stress (σ_3) when σ_3 is a tensile stress. This criterion is used in the analysis of the effects of the contact stiffness, toughness, friction coefficient and confining stress which are discussed later.

For every timestep of calculation, *K* is compared with K_c. Whenever $K \geq K_c$ the particle is broken in two parts. The crack propagation criterion was adopted in all the simulations reported here (study of the effect of different properties of the DEM model).

A2.2.3. Particle division

The particle division follows an arbitrary criterion which takes into account the number of particles integrating a clump and the 'pyramidal' structure of the macroparticle. Clumps are divided following the 'rule': 14→9+5; 9→5+4; 5→3+2; 4→2+2; 3→2+1; 2→1+1.

Subparticles of 13 microparticles are not used here to replace the macroparticles of 1 sphere.

Figure A2 - 3a and **Figure A2 - 3**b provides the results of the deviatoric stress and volumetric strain behaviour and show a comparison of the criteria of Mohr Coulomb and LEFM, and also the consideration of no particle breakage. The simulated triaxial test exhibits the highest strength when no particles break (**Figure A2 - 3**a). Furthermore, the specimen of not rupture presents more dilatancy (**Figure A2 - 3**b). The numerical test using the LEFM criterion is more similar to the actual behaviour (see **Figure 5-33** in chapter 5).

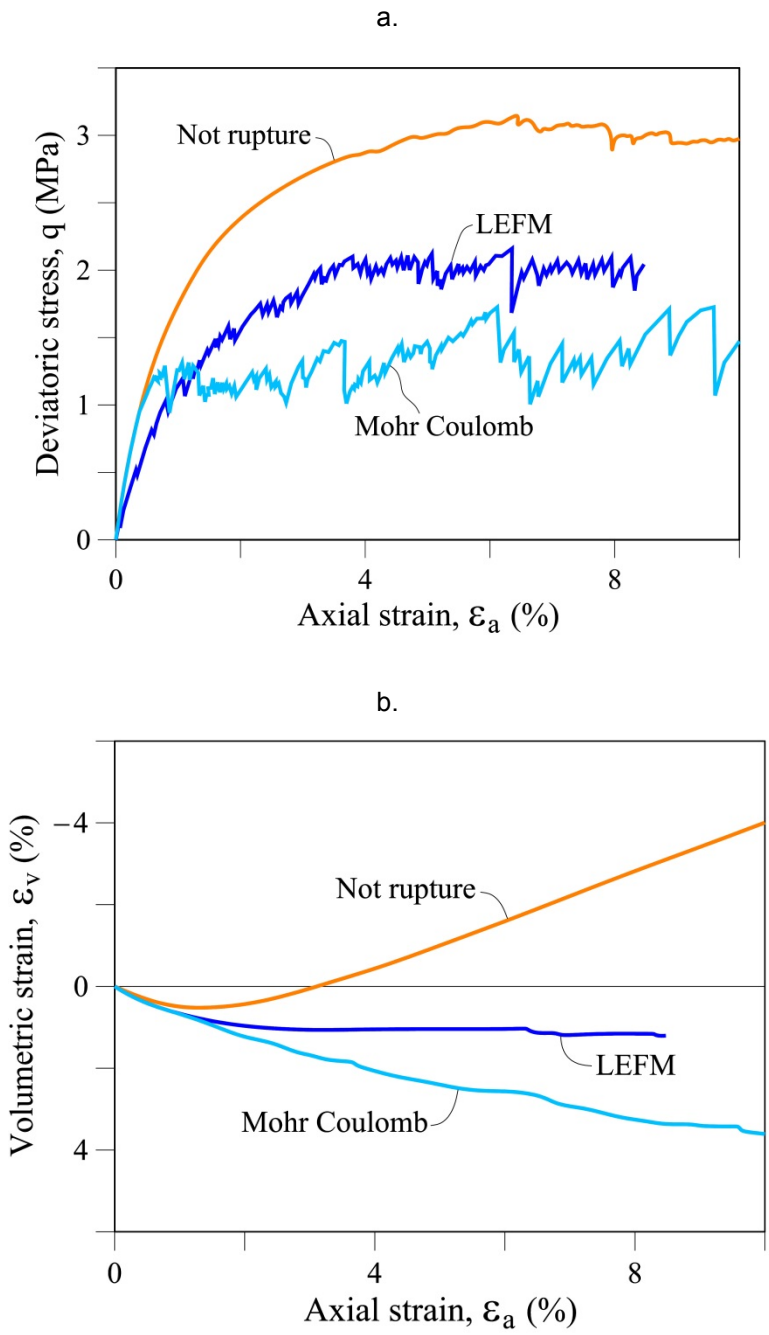

Figure A2 - 3 Failure criteria effect on the triaxial behaviour. Results of numerical simulations of triaxial tests. Comparison among different criteria: No breakage; crack propagation based on LEFM and Mohr Coulomb. Sample of 970 macroparticles using clumps of 14 microparticles. Confining stress: 1.0MPa; Initial porosity:51%. DEM properties: k_n=20MN/m; K_c=5MPa.m$^{0.5}$; μ=0.3; c=5.36MPa; ϕ=0. (a) Deviatoric stress behaviour; (b) Volumetric strain behavior.

A2.3. Influence of the particle shape

Clump sizes of 1, 4(3+1), 5(4+1), 13(9+4), and 14(9+4+1) microparticles, which try always to simulate a pyramidal shape, were tested. Some results are given in **Figure A2 - 4**a and **Figure A2 - 4**b. The highest peak strengths are found for the highest number of particles in a clump. Furthermore, the higher dilatancy is also found for the macroparticles of 14 spheres. The DEM properties were the same for all the numerical triaxial tests: specimens of 970 macroparticles, confining stress of 1.0MPa, initial porosity of the specimens between 51.2% and 53.6%, k_n=k_s=4MN/m, K_c=1x10^{14} MPa.m$^{0.5}$, and μ=0.3. The very high value of the toughness (K_c=1x10^{14} MPa.m$^{0.5}$) was used to avoid particle breakage.

Figure A2 - 5a and **Figure A2 - 5**b also shown a comparison of the shape effect for the results of numerical simulation of triaxial tests using the same type of macroparticles with the same properties except for the values of the contact stiffness: a higher value was used, k_n=k_s=20MN/m. The above conclusions also are applied here. Additionally, the results show that higher values of the contact stiffness of macroparticles cause higher stiffness in the specimen behaviour. The effect of the contact stiffness is discussed below.

A2.4. Influence of the initial porosity of the specimen

The effect of two initial porosities (51% and 61%) on triaxial test results is given in **Figure A2 - 6**. In both cases the initial macroparticle system had no initial contact forces. The following DEM properties were used: specimens of 970 macroparticles, confining stress of 1.0MPa, k_n=k_s=20MN/m, K_c=1 MPa.m$^{0.5}$, and μ=0.93.

The sample exhibiting the lower porosity resulted in the higher stiffness, a consistent result with experimental observations. However, similar peak strength was calculated for the two specimens, a result which is probably explained by particle breakage. The specimen with lower porosity is more compressible at the beginning and then presents more dilatancy, but in general the volumetric strain behaviour is similar for both specimens.

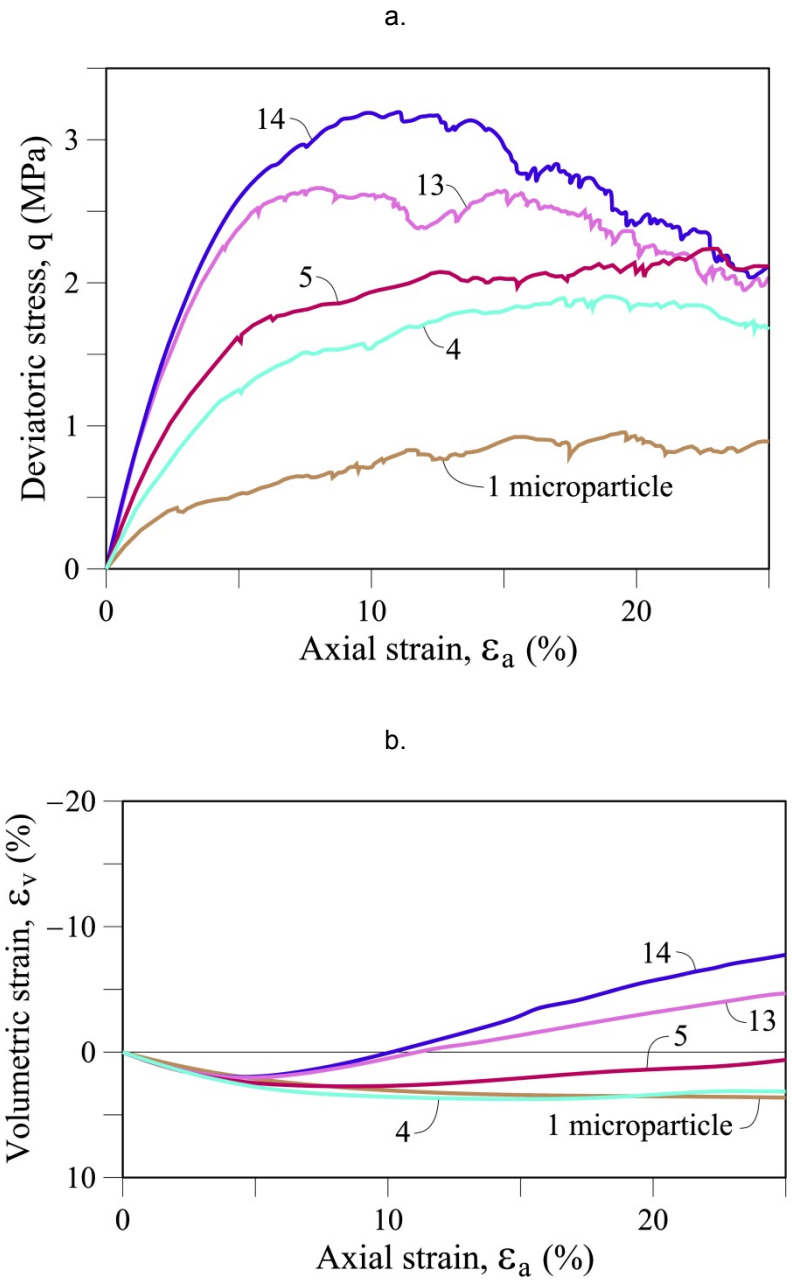

Figure A2 - 4 Shape effects. Results of numerical simulations of triaxial tests using macroparticles of 1, 4, 5, 13 and 14 microparticles. Specimens of 970 macroparticles. Confining stress: 1.0MPa; Initial porosity: 51.2% – 53.6%. DEM properties: k_n=4MN/m; K_c=1x10^{14} MPa.m$^{0.5}$; μ=0.3. (a) Deviatoric stress behaviour; (b) Volumetric strain behavior.

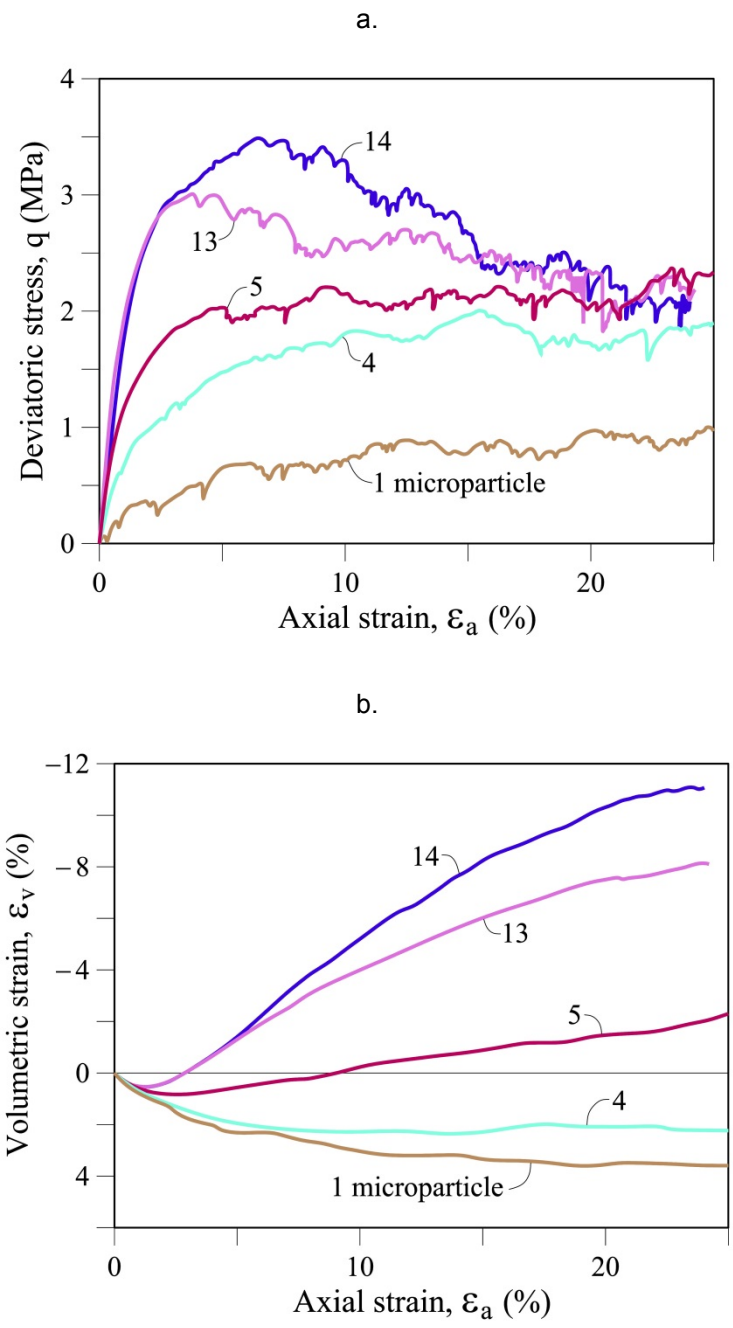

Figure A2 - 5 Shape effects. Results of numerical simulations of triaxial tests using macroparticles of 1, 4, 5, 13 and 14 microparticles. Specimens of 970 macroparticles. Confining stress: 1.0MPa; Initial porosity: 51.2% – 53.6%. DEM properties: k_n=20MN/m; K_c=1x10^{14} MPa.m$^{0.5}$; μ=0.3. (a) Deviatoric stress behaviour; (b) Volumetric strain behavior.

a.

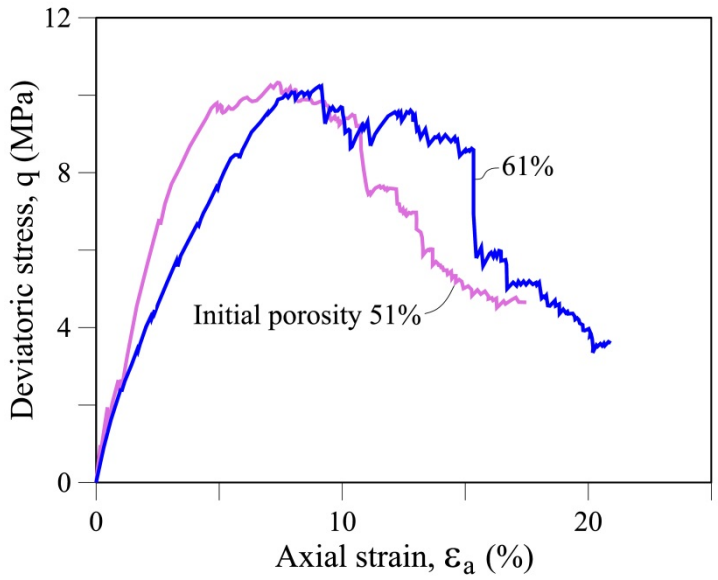

b.

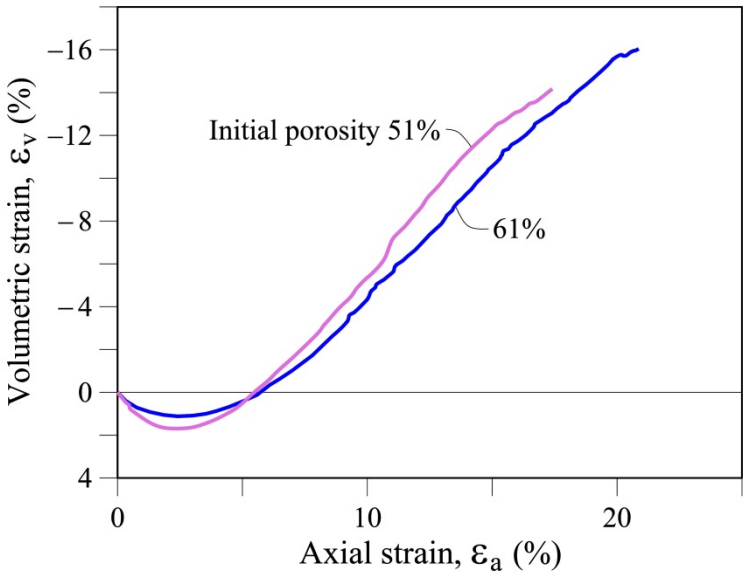

Figure A2 - 6 Initial porosity effect. Comparison between two different initial porosities, 51 % y 61%. Results of numerical simulations of triaxial tests using macroparticles of 14 microparticles. Specimens of 970 macroparticles. Confining stress: 1.0MPa; DEM properties: k_n=20MN/m; K_c=1 MPa.m$^{0.5}$; μ=0.93. (a) Deviatoric stress behaviour; (b) Volumetric strain behavior.

A2.5. Influence of the contact stiffness

The failure criteria used in the simulations was of the Crack Propagation criterion based on the LEFM. The stress intensity factor *K* is calculated for the minor principal stress (σ_3) which corresponds to a tension state, i.e. when σ_3 is a tensile stress.

Three samples having contact normal stiffnesses k_n equal to 2 MN/m, 20 MN/m, and 200 MN/m respectively were tested under triaxial conditions. All the particles had a friction coefficient (μ) equal to 0.3 (ϕ = 17º). The initial porosity of the specimens was 51% and the confining stress was 1 MPa. The toughness of the macroparticles was $1x10^4$ $Pa.m^{0.5}$. The specimen was defined by 970 macroparticles which had an initial equivalent diameter of 2.8cm.

Figure A2 - 7a shows the deviatoric stress-strain relationship. The specimen with the higher contact stiffness in the micro level (particle to particle) has the higher stiffness at the macro level and the higher peak strength.

The volumetric strain behaviour is shown in **Figure A2 - 7**b. As expected, dilatancy increases with the higher contact stiffness. This effect can also be seen in the change in porosity during testing (**Figure A2 - 8**).

The sample having the smallest k_n exhibited a higher number of broken clumps. This sample had the lowest of number of not broken-clumps (**Figure A2 - 9**) and the largest value of the clumps at the end of tests (**Figure A2 - 10**). The evolution of the particle breakage can also be noted on the calculated grain size distribution at the end of the tests (**Figure A2 - 11**). Crushing in these samples results in an increase in particles having equivalent diameters close to 2cm and 2.6cm.

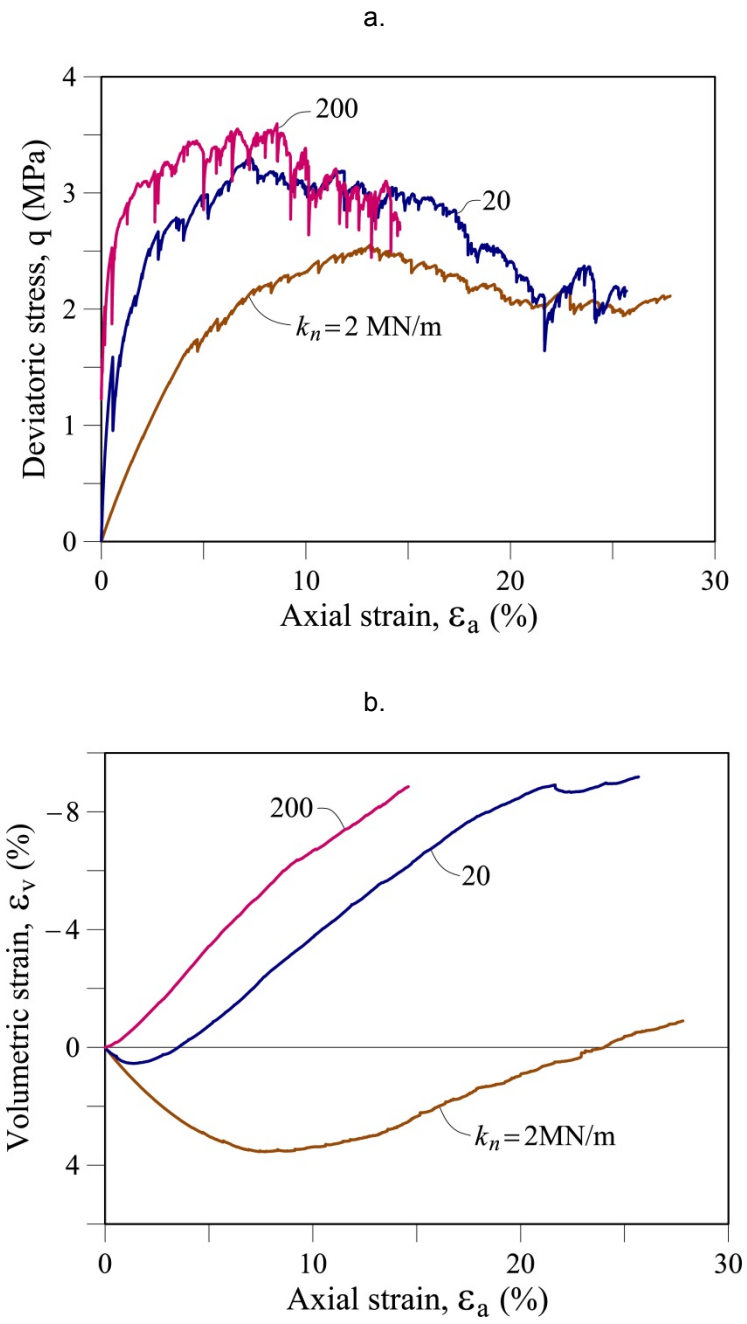

Figure A2 - 7 Effect of the contact stiffness on the triaxial behaviour. Comparison among three different normal stiffnesses (2, 20 and 200 MN/m). Results of numerical simulations of triaxial tests using macroparticles of 14 microparticles. Specimens of 970 macroparticles. Confining stress: 1.0MPa; Initial porosity: 51%; DEM properties: K_c=1x10^4 Pa.m$^{0.5}$; μ=0.3. (a) Deviatoric stress behaviour; (b) Volumetric strain behaviour.

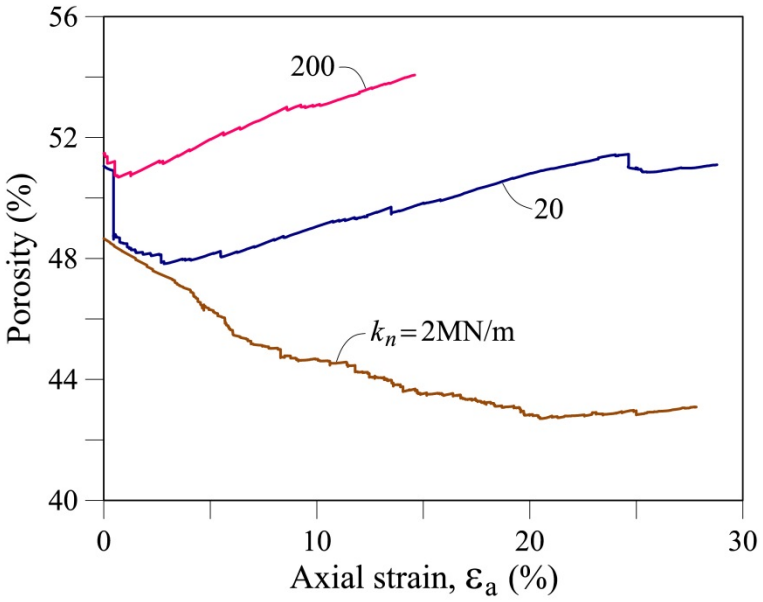

Figure A2 - 8 Effect of the contact stiffness on the porosity. Comparison among three different normal stiffnesses (2, 20 and 200 MN/m). Results of numerical simulations of triaxial tests using macroparticles of 14 microparticles. Specimens of 970 macroparticles. Confining stress: 1.0MPa; Initial porosity: 51%; DEM properties: K_c=1x10^4 Pa.m$^{0.5}$; μ=0.3.

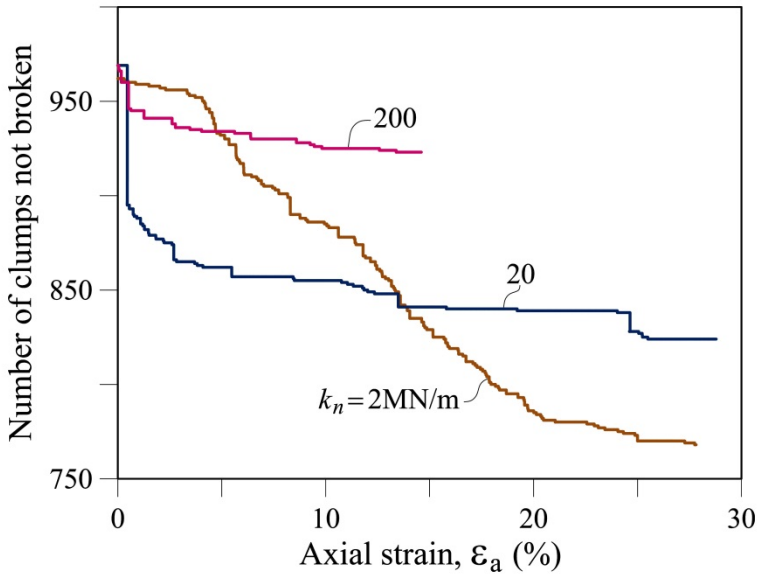

Figure A2 - 9 Effect of the contact stiffness on the number of not broken clumps. Comparison among three different normal stiffnesses (2, 20 and 200 MN/m). Results of numerical simulations of triaxial tests using macroparticles of 14 microparticles. Specimens of 970 macroparticles. Confining stress: 1.0MPa; Initial porosity: 51%; DEM properties: K_c=1x10^4 Pa.m$^{0.5}$; μ=0.3.

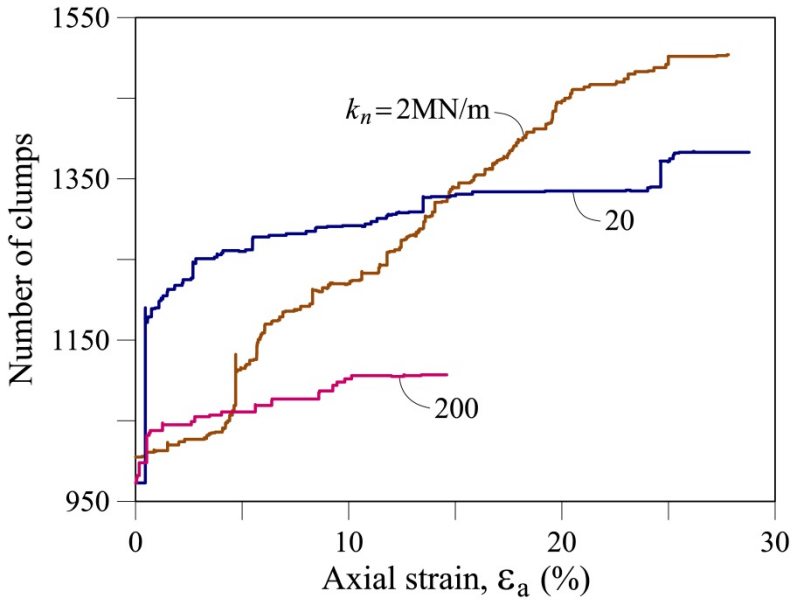

Figure A2 - 10 Effect of the contact stiffness on the evolution of the number of clumps (macroparticles). Comparison among three different normal stiffnesses (2, 20 and 200 MN/m). Results of numerical simulations of triaxial tests using macroparticles of 14 microparticles. Specimens of 970 macroparticles. Confining stress: 1.0MPa; Initial porosity: 51%; DEM properties: K_c=1x10^4 Pa.m$^{0.5}$; μ=0.3.

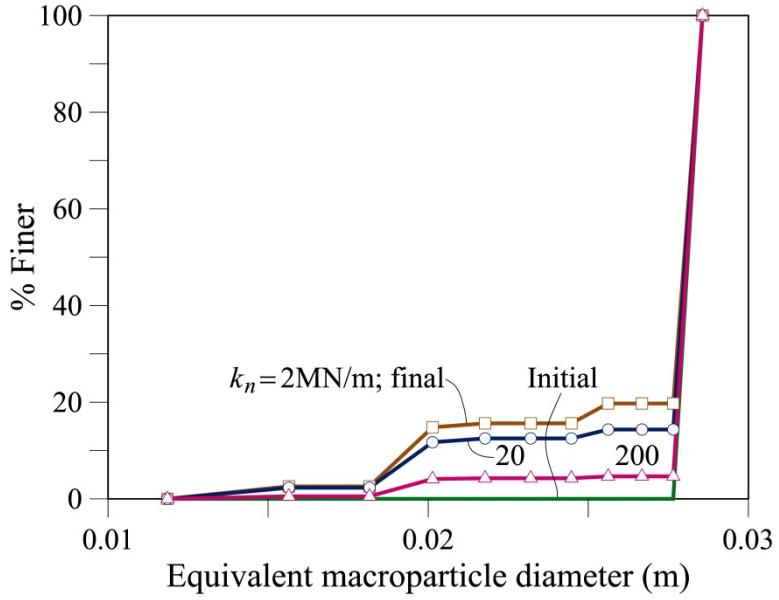

Figure A2 - 11 Effect of the contact stiffness on the evolution of the grain size distributions at the initial and the end of triaxial tests. Comparison among three different normal stiffnesses (2, 20 and 200 MN/m). Results of numerical simulations of triaxial tests using macroparticles of 14 microparticles. Specimens of 970 macroparticles. Confining stress: 1.0MPa; Initial porosity: 51%; DEM properties: K_c=1x10^4 Pa.m$^{0.5}$; μ=0.3.

A2.6. Influence of the toughness, K_c

As explained for the contact stiffness effect, the failure criteria used in the simulations was of the Crack Propagation criterion based on the fracture mechanics. The stress intensity factor K is calculated for the minor principal stress (σ_3) which corresponds to a tension state, i.e. when σ_3 is a tensile stress.

The particle toughness (K_c) is a key property in the selected fracture model or (failure criterion of Crack Propagation). Four values were compared: $1x10^6$ Pa•$m^{0.5}$; $1x10^5$ Pa•$m^{0.5}$; $1x10^4$ Pa•$m^{0.5}$ and $1x10^2$ Pa•$m^{0.5}$. The following DEM properties were the same for all the numerical triaxial tests: specimens of 970 macroparticles at the beginning, confining stress of 1.0MPa, initial porosity of the specimens of 51%, k_n=k_s=20MN/m and μ=0.93 (ϕ = 43º). Some results are given in **Figure A2 - 12** and **Figure A2 - 13**.

Toughness controls the peak strength (**Figure A2 - 12**a) although 'residual' values seem to be less affected. The sample with the highest value of K_c also exhibited the strongest dilatancy (**Figure A2 - 12**b). The lower the K_c value the higher the number of ruptured particles during the test. This is reflected on the calculated grain size distributions at the end of the tests (**Figure A2 - 13**). Crushing in these samples results in an increase in particles having an equivalent diameter close to 2cm. It is clear that much more deformation energy will be required to achieve a stationary grain size distribution.

These are reasonable results which help to increase the confidence on the model.

a.

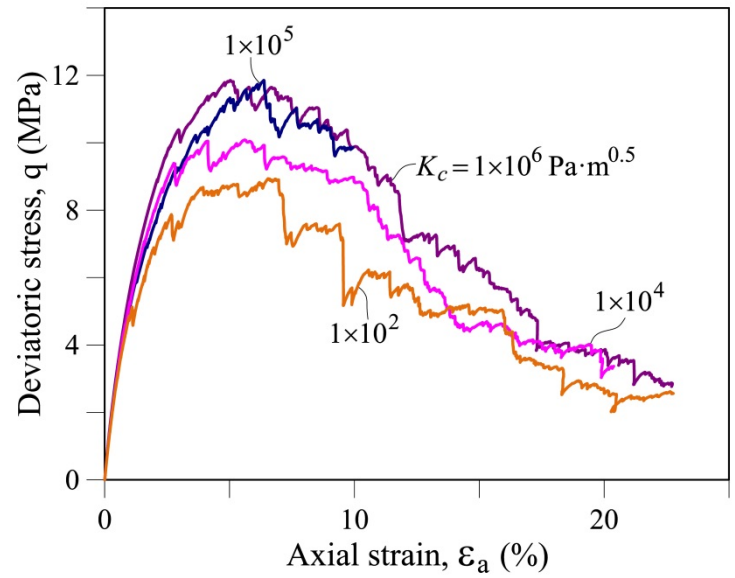

b.

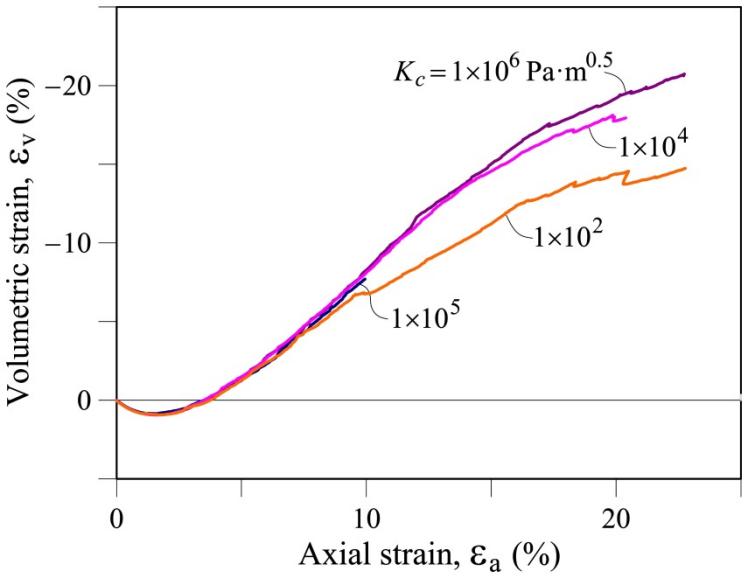

Figure A2 - 12 Effect of the macroparticle toughness on the triaxial behaviour. Comparison among four different toughness ($1x10^6$, $1x10^5$, $1x10^4$ and $1x10^2$ Pa.m$^{0.5}$). Results of numerical simulations of triaxial tests using macroparticles of 14 microparticles. Specimens of 970 macroparticles. Confining stress: 1.0MPa; Initial porosity: 51%; DEM properties: k_n=20MN/m; μ=0.93. (a) Deviatoric stress behaviour; (b) Volumetric strain behaviour.

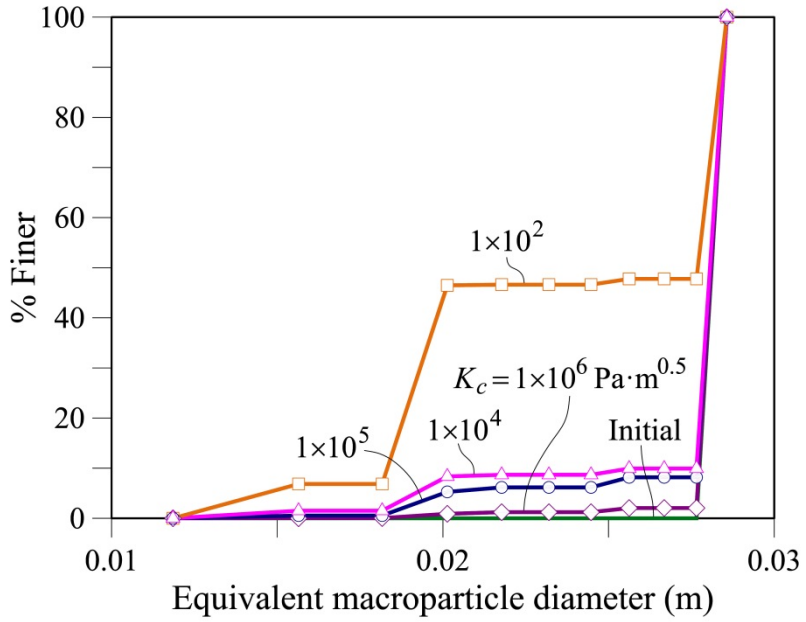

Figure A2 - 13 Effect of the macroparticle toughness on the evolution of the grain size distributions at the initial and the end of triaxial tests. Comparison among four different toughness ($1x10^6$, $1x10^5$, $1x10^4$ and $1x10^2$ Pa.m$^{0.5}$). Results of numerical simulations of triaxial tests using macroparticles of 14 microparticles. Specimens of 970 macroparticles. Confining stress: 1.0MPa; Initial porosity: 51%; DEM properties: k_n=20MN/m; μ=0.93.

A2.6.1. Effect of the reduction of K_c during the triaxial test

In this research, the (fracture) toughness (K_c) has been considered as a property of the particle that does not change under any circumstance. It is always a constant.

However, in order to make a theoretical exercise, an analysis of the effect on the mechanical behaviour of doing a reduction of the toughness during the performance of numerical triaxial tests is presented in this section.

The following DEM properties were used in the numerical simulations of triaxial tests: specimens of 970 macroparticles which had 2.8cm in size and were composed by 14 microparticles; initial porosity of the specimen = 51%; confining stress of 1 MPa; k_n=k_s=20Mn/m; μ=0.93. The toughness was of K_c=$1x10^6$ Pa•m$^{0.5}$; at the beginning of the tests.

Two cases were considered: The first case corresponded to a reduction of the value of K_c from $1x10^6$ Pa•m$^{0.5}$ to $1x10^5$Pa•m$^{0.5}$ when the axial strain approximately

reached the 6% (see **Figure A2 - 14**). Similarly, the second case corresponded to a reduction of the value of K_c from $1x10^6$ Pa•$m^{0.5}$ to $1x10^4$Pa•$m^{0.5}$ for the same value of the axial strain that was reached in the first case (see **Figure A2 - 18**).

The results of the numerical triaxial tests were compared with those previously obtained considering the values of K_c constant during all the tests (see **Figure A2 - 12**), namely, the results of K_c=$1x10^6$ Pa•$m^{0.5}$, $1x10^5$ Pa•$m^{0.5}$ and $1x10^4$ Pa•$m^{0.5}$.

Figure A2 - 14a and **Figure A2 - 14**b show the curves of the deviatoric stress and volumetric strain behaviour for the first case 1: K_c=$1x10^6$ Pa•$m^{0.5}$, K_c=$1x10^5$ Pa•$m^{0.5}$, and the 'K_c *reduction*' effect when K_c is reduced suddenly. The specimen experiences a collapse which is reflected in a sudden reduction of the deviatoric stress. However, further straining results in a recovery of strength.

The effect of the "K_c reduction" on the compressibility of the specimen can be observed more clearly in the curves of the variation of the porosity during the tests (**Figure A2 - 15**). The reduction in porosity associated with this K_c reduction is irreversible.

Porosity increases because of dilatancy in all cases. However, the K_c reduction results in a transient reduction in porosity. The wetted sample falls into the porosity plot for the specimen having initially a reduced K_c value.

Figure A2 - 16 provides additional information on the evolution of broken macroparticles. A value of K_c=$1x10^6$ Pa•$m^{0.5}$ results in a limited breakage of particles. When K_c is decreased to K_c=$1x10^5$ Pa•$m^{0.5}$ the breakage rate increases. The sudden K_c reduction takes the specimen from the K_c=$1x10^6$ Pa•$m^{0.5}$ to K_c=$1x10^5$ Pa•$m^{0.5}$ curve. This result can also be seen in the evolution of the grain size distributions (**Figure A2 - 17**).

Similarly, the results of the numerical triaxial tests of the case 2 (reduction of K_c from $1x10^6$ Pa•$m^{0.5}$ to $1x10^4$Pa•$m^{0.5}$) were compared with the curves for K_c=$1x10^6$ Pa•$m^{0.5}$ and K_c=$1x10^4$ Pa•$m^{0.5}$. **Figure A2 - 18**a and **Figure A2 - 18**b show the deviatoric stress and volumetric strain behaviour: curves q:ε_a and ε_v:ε_a. **Figure A2 - 19** and **Figure A2 - 20** show the variation of the porosity and the not broken-clumps during the tests; and the **Figure A2 - 21** shows the evolution of the grain size distributions. A similar behaviour was obtained for both cases, obviously for the case 2 –where K_c suddenly decreased to a lowest value- the collapse in the deviatoric stress and porosity were higher than the case 1. The breakage of the particles was also higher (**Figure A2 - 20** and **Figure A2 - 21**).

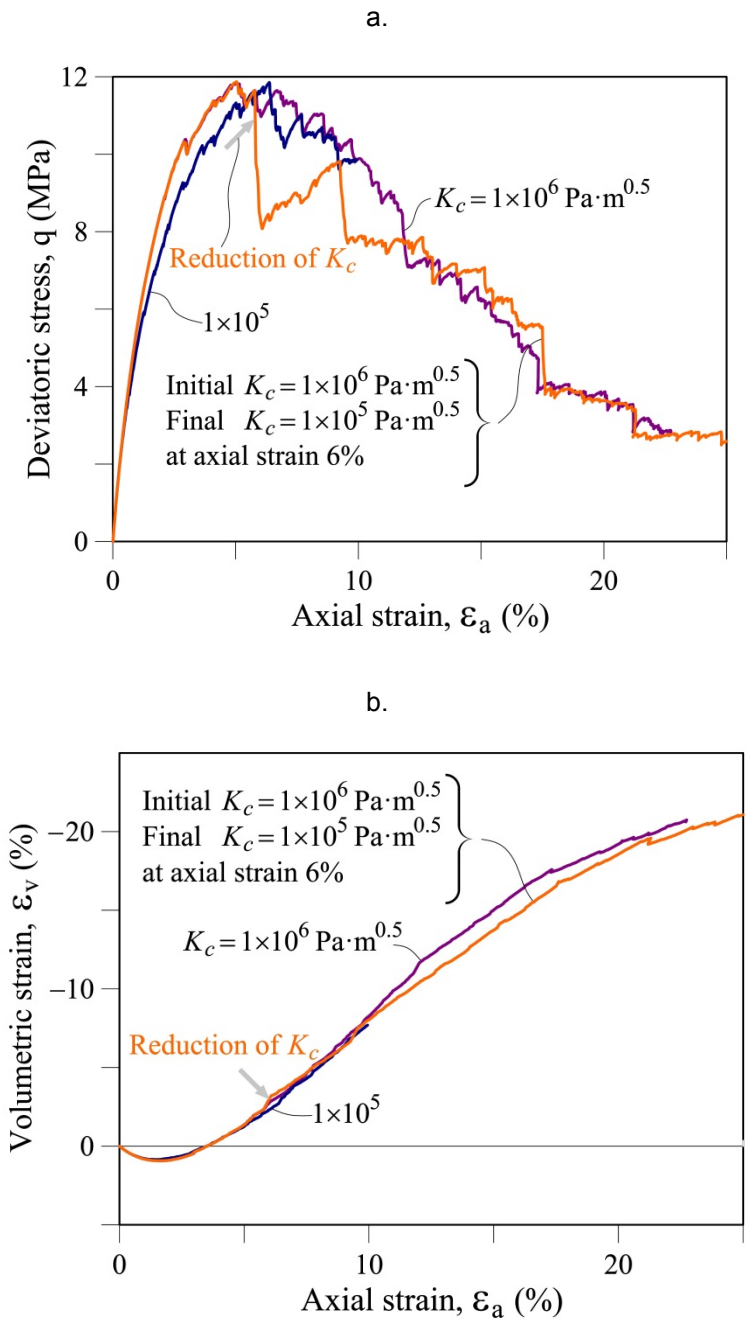

Figure A2 - 14 Effect of the reduction of the macroparticle toughness on the triaxial behaviour. Comparison between K_c of $1x10^6$ and $1x10^5$ Pa.m$^{0.5}$ and the reduction of K_c from $1x10^6$ to $1x10^5$ Pa.m$^{0.5}$ at ε_a=6%. Results of numerical simulations of triaxial tests using macroparticles of 14 microparticles. Specimens of 970 macroparticles. Confining stress: 1.0MPa; Initial porosity: 51%; DEM properties: k_n=20MN/m; μ=0.93. (a) Deviatoric stress behaviour; (b) Volumetric strain behaviour.

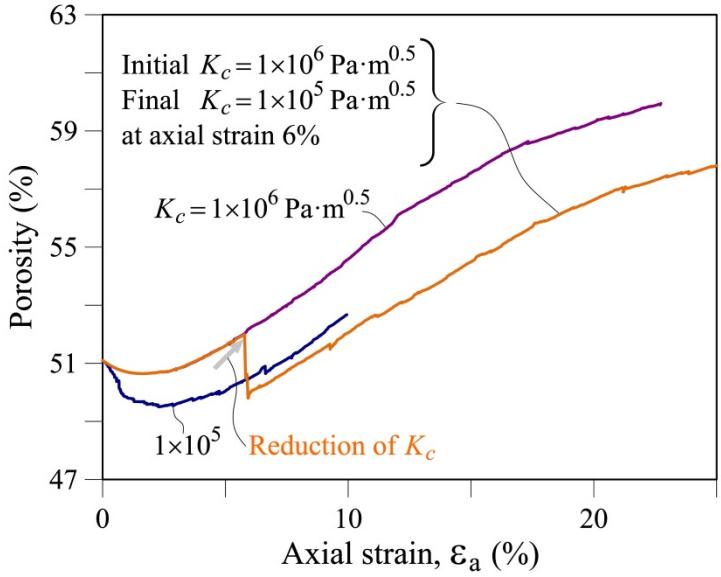

Figure A2 - 15 Effect of the reduction of the macroparticle toughness on the porosity. Comparison between K_c of 1x10^6 and 1x10^5 Pa.m$^{0.5}$ and the reduction of K_c from 1x10^6 to 1x10^5 Pa.m$^{0.5}$ at ε_a=6%. Results of numerical simulations of triaxial tests using macroparticles of 14 microparticles. Specimens of 970 macroparticles. Confining stress: 1.0MPa; Initial porosity: 51%; DEM properties: k_n=20MN/m; μ=0.93.

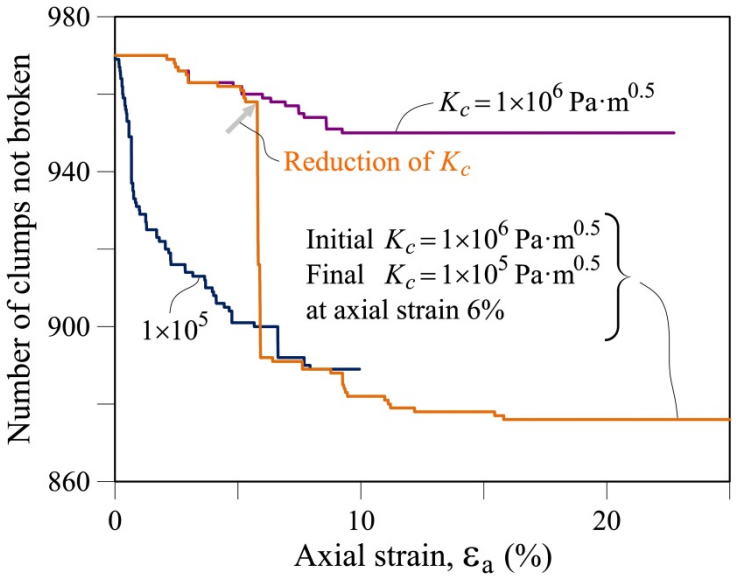

Figure A2 - 16 Effect of the reduction of the macroparticle toughness on the number of not broken clumps. Comparison between K_c of 1x10^6 and 1x10^5 Pa.m$^{0.5}$ and the reduction of K_c from 1x10^6 to 1x10^5 Pa.m$^{0.5}$ at ε_a=6%. Results of numerical simulations of triaxial tests using macroparticles of 14 microparticles. Specimens of 970 macroparticles. Confining stress: 1.0MPa; Initial porosity: 51%; DEM properties: k_n=20MN/m; μ=0.93.

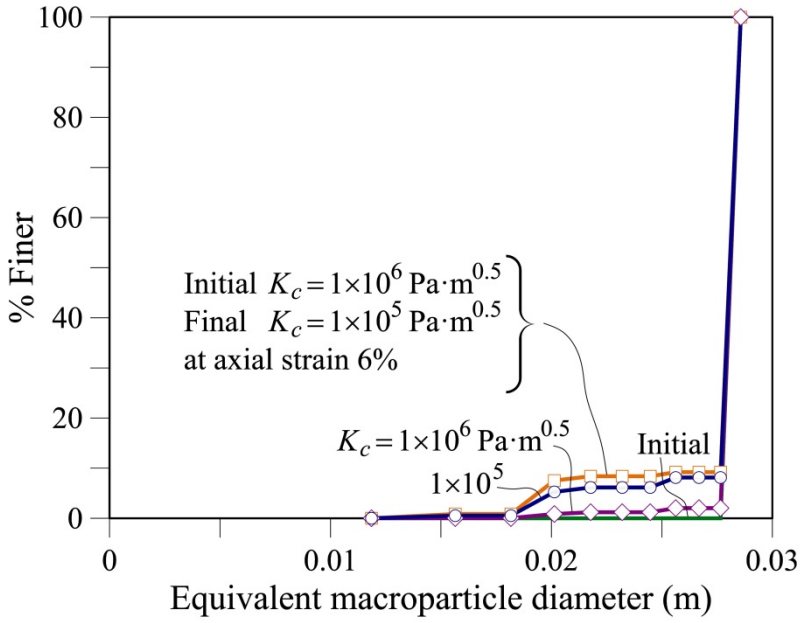

Figure A2 - 17 Effect of the reduction of the macroparticle toughness on the evolution of the grain size distributions at the initial and the end of triaxial tests. Comparison between K_c of 1x10^6 and 1x10^5 Pa.m$^{0.5}$ and the reduction of K_c from 1x10^6 to 1x10^5 Pa.m$^{0.5}$ at ε_a=6%. Results of numerical simulations of triaxial tests using macroparticles of 14 microparticles. Specimens of 970 macroparticles. Confining stress: 1.0MPa; Initial porosity: 51%; DEM properties: k_n=20MN/m; μ=0.93.

a.

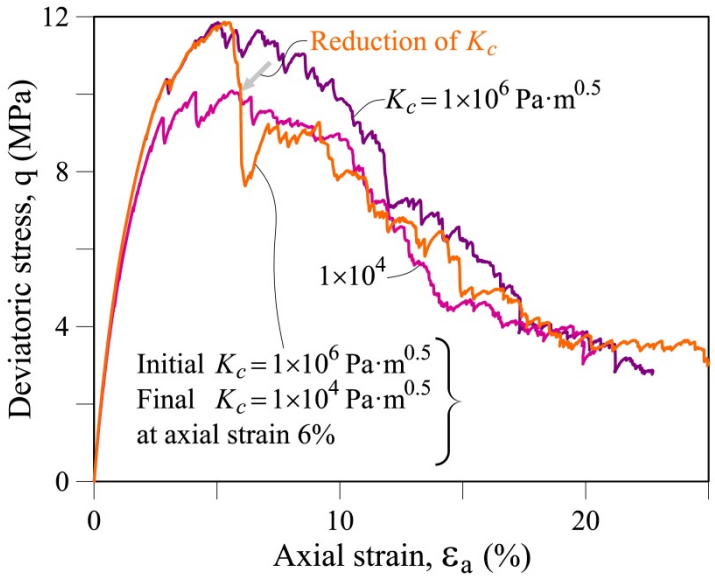

b.

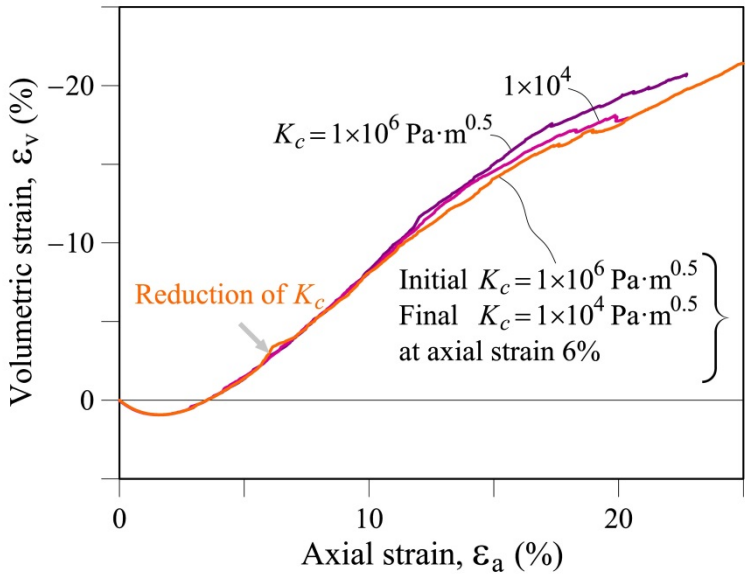

Figure A2 - 18 Effect of the reduction of the macroparticle toughness on the triaxial behaviour. Comparison between K_c of 1x10^6 and 1x10^4 Pa.m$^{0.5}$ and the reduction of K_c from 1x10^6 to 1x10^4 Pa.m$^{0.5}$ at ε_a=6%. Results of numerical simulations of triaxial tests using macroparticles of 14 microparticles. Specimens of 970 macroparticles. Confining stress: 1.0MPa; Initial porosity: 51%; DEM properties: k_n=20MN/m; μ=0.93. (a) Deviatoric stress behaviour; (b) Volumetric strain behaviour.

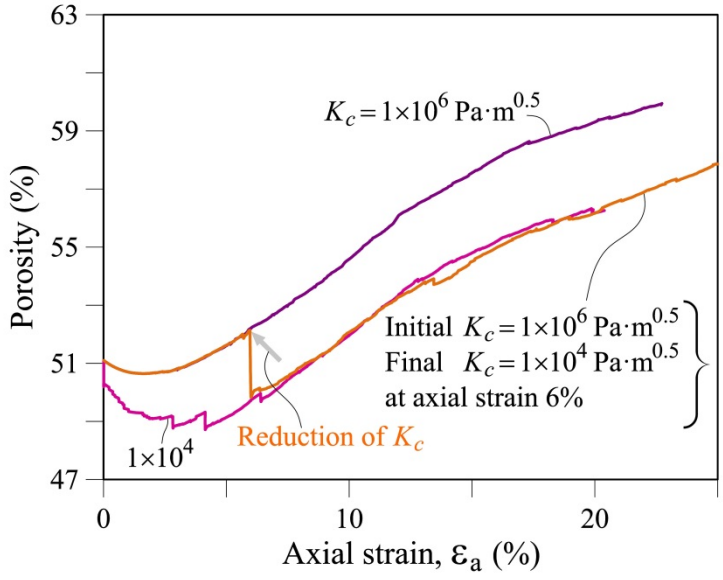

Figure A2 - 19 Effect of the reduction of the macroparticle toughness on the porosity. Comparison between K_c of 1x10^6 and 1x10^4 Pa.m$^{0.5}$ and the reduction of K_c from 1x10^6 to 1x10^4 Pa.m$^{0.5}$ at ε_a=6%. Results of numerical simulations of triaxial tests using macroparticles of 14 microparticles. Specimens of 970 macroparticles. Confining stress: 1.0MPa; Initial porosity: 51%; DEM properties: k_n=20MN/m; μ=0.93.

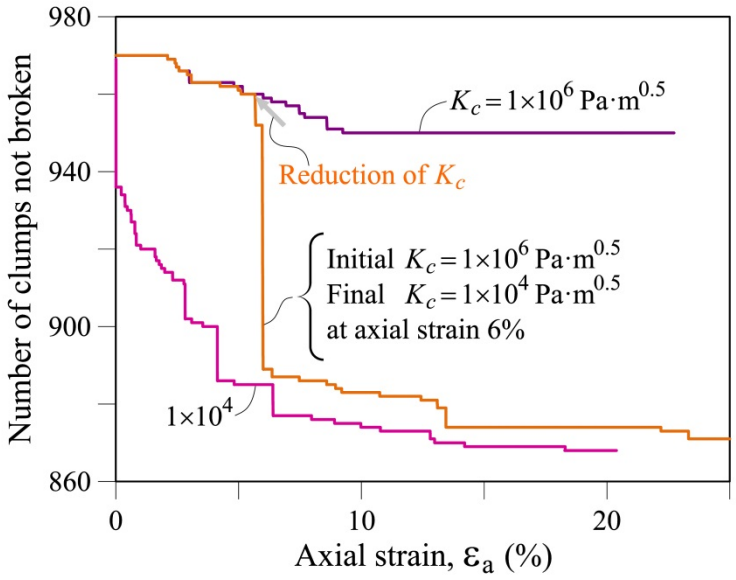

Figure A2 - 20 Effect of the reduction of the macroparticle toughness on the number of not broken clumps. Comparison between K_c of 1x10^6 and 1x10^4 Pa.m$^{0.5}$ and the reduction of K_c from 1x10^6 to 1x10^4 Pa.m$^{0.5}$ at ε_a=6%. Results of numerical simulations of triaxial tests using macroparticles of 14 microparticles. Specimens of 970 macroparticles. Confining stress: 1.0MPa; Initial porosity: 51%; DEM properties: k_n=20MN/m; μ=0.93.

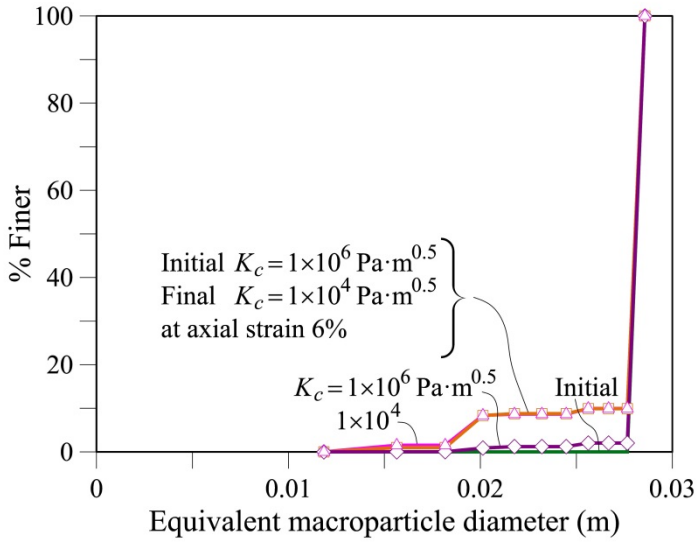

Figure A2 - 21 Effect of the reduction of the macroparticle toughness on the evolution of the grain size distributions at the initial and the end of triaxial tests. Comparison between K_c of 1x10^6 and 1x10^4 Pa.m$^{0.5}$ and the reduction of K_c from 1x10^6 to 1x10^4 Pa.m$^{0.5}$ at ε_a=6%. Results of numerical simulations of triaxial tests using macroparticles of 14 microparticles. Specimens of 970 macroparticles. Confining stress: 1.0MPa; Initial porosity: 51%; DEM properties: k_n=20MN/m; μ=0.93.

A2.7. Influence of the Friction Coefficient, μ

For the study of the effect of the friction coefficient as explained previously, the failure criteria used in the numerical simulations of the triaxial tests was of the Crack Propagation criterion based on the fracture mechanics. The stress intensity factor K is calculated for the minor principal stress (σ_3) which corresponds to a tension state, i.e. when σ_3 is a tensile stress.

Three specimens of macroparticles having friction coefficients (μ) equals to 0.93, 0.50 and 0.30 (ϕ = 43º; 27º; 17º) were tested. The initial porosity of the all samples (specimens) was 51% and the initial confining stress was 1MPa. The toughness of macroparticles (K_c) was 1x10^4 Pa•m$^{0.5}$ and the contact stiffness was k_n=k_s=20MN/m. The specimens were defined by 970 macroparticles which had an initial equivalent diameter of 2.8cm.

Figure A2 - 22a shows the deviatoric stress-strain relationship. The greatest strength was obtained for the highest friction coefficient. A similar residual strength for strains in excess of 20% was found. Dilatancy is shown in **Figure A2 - 22**b. As expected, dilatancy increases with interparticle friction. This behaviour is also evidenced in the variation of the porosity of the specimens during the tests (**Figure A2 - 23**).

The sample having the smallest interparticle friction angle exhibited a higher number of failed clumps (**Figure A2 - 24**). In these tests, most of the broken particles resulted in equivalent particle diameters in the vicinity of 2cm (**Figure A2 - 25**). Only a small percentage of particles broke in these tests.

a.

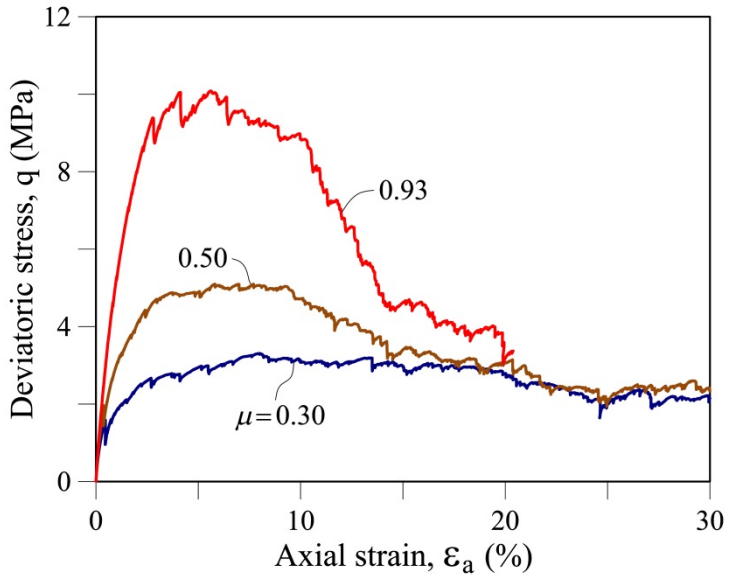

b.

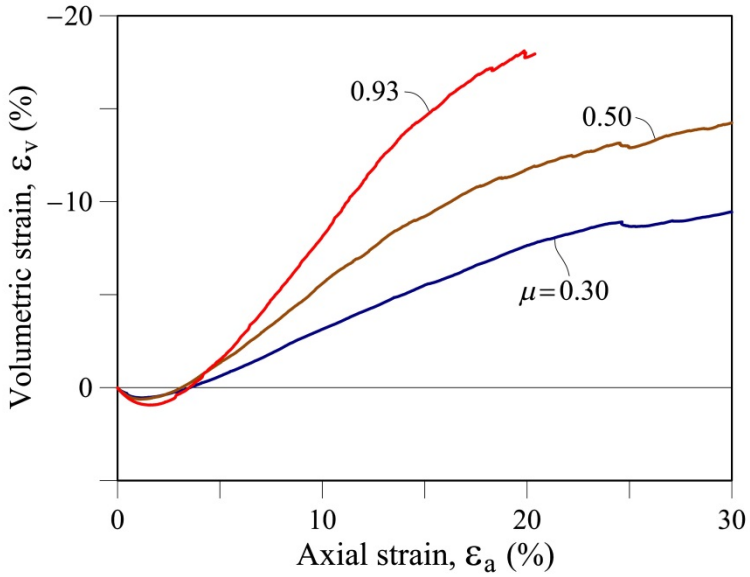

Figure A2 - 22 Influence of the friction coefficient (μ) on the triaxial behaviour. Comparison between three friction coefficients (0.93, 0.50, 0.30). Results of numerical simulations of triaxial tests using macroparticles of 14 microparticles. Specimens of 970 macroparticles. Confining stress: 1.0MPa; Initial porosity: 51%; DEM properties: k_n=20MN/m; K_c=1x10^4 Pa.m$^{0.5}$. (a) Deviatoric stress behaviour; (b) Volumetric strain behaviour.

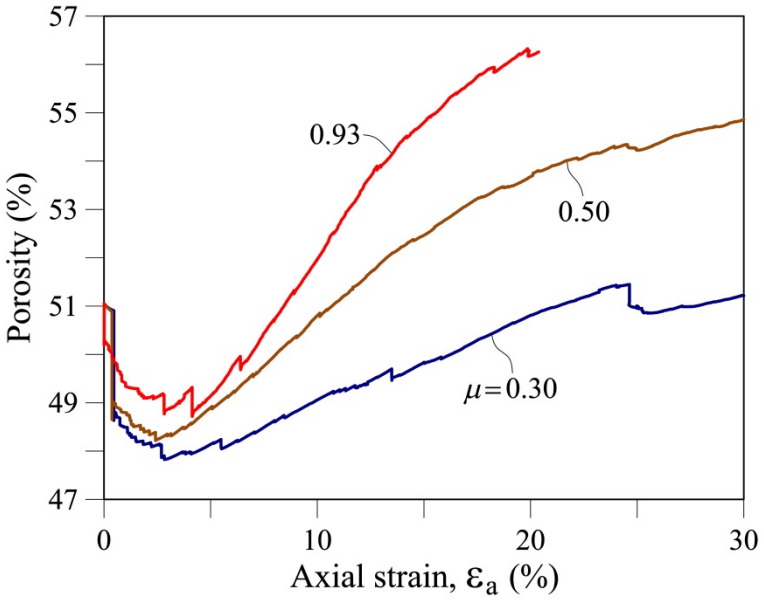

Figure A2 - 23 Influence of the friction coefficient (μ) on the porosity. Comparison between three friction coefficients (0.93, 0.50, 0.30). Results of numerical simulations of triaxial tests using macroparticles of 14 microparticles. Specimens of 970 macroparticles. Confining stress: 1.0MPa; Initial porosity: 51%; DEM properties: k_n=20MN/m; K_c=1x10^4 Pa.m$^{0.5}$.

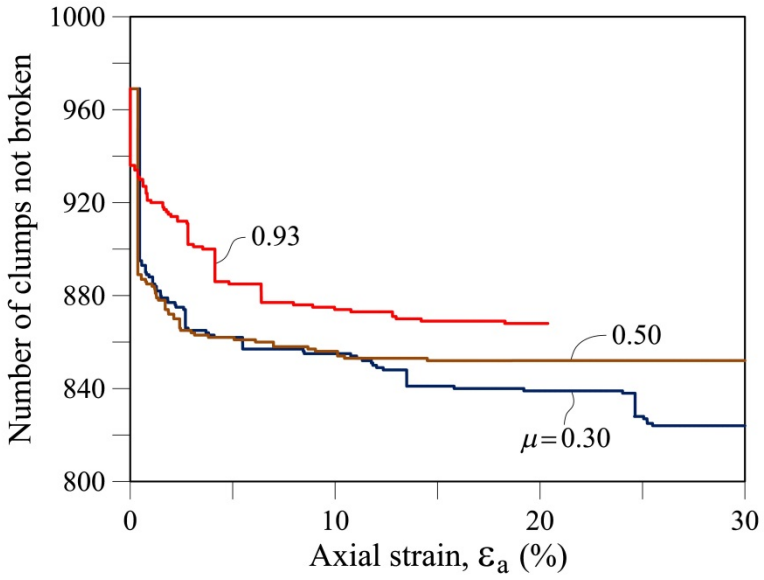

Figure A2 - 24 Influence of the friction coefficient (μ) on the number of not broken clumps. Comparison between three friction coefficients (0.93, 0.50, 0.30). Results of numerical simulations of triaxial tests using macroparticles of 14 microparticles. Specimens of 970 macroparticles. Confining stress: 1.0MPa; Initial porosity: 51%; DEM properties: k_n=20MN/m; K_c=1x10^4 Pa.m$^{0.5}$.

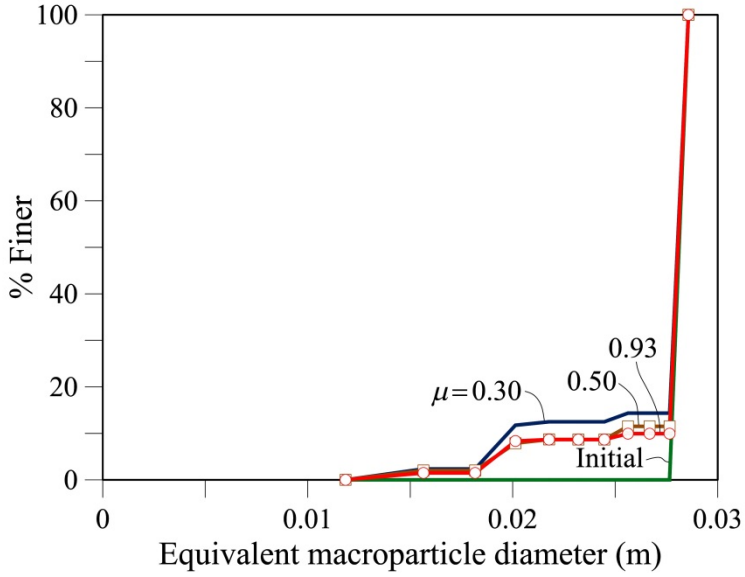

Figure A2 - 25 Influence of the friction coefficient (μ) on the evolution of the grain size distributions at the initial and the end of triaxial tests. Comparison between three friction coefficients (0.93, 0.50, 0.30). Results of numerical simulations of triaxial tests using macroparticles of 14 microparticles. Specimens of 970 macroparticles. Confining stress: 1.0MPa; Initial porosity: 51%; DEM properties: k_n=20MN/m; K_c=1x10^4 Pa.m$^{0.5}$.

A2.8. Influence of the confining stress σ_c

For the analysis of the confining stress effect, the failure criteria used in the numerical simulations of the triaxial tests was of the Crack Propagation criterion based on the fracture mechanics. The stress intensity factor *K* is calculated for the minor principal stress (σ_3) which corresponds to a tension state, i.e. when σ_3 is a tensile stress.

The following DEM properties were used for all the numerical triaxial tests: specimens of 970 macroparticles at the beginning which had an initial equivalent diameter of 2.8cm, initial porosity of the specimens of 51%, K_c=1x10^6 Pa•m$^{0.5}$, k_n=k_s=20MN/m and μ=0.93 (ϕ = 43º).

Three specimens of macroparticles having confining stresses (σ_c) equals to 1, 0.5 and 0.3 MPa were tested.

The results of the tests are shown in the curves of the **Figure A2 - 26** and **Figure A2 - 27**. **Figure A2 - 26**a and **Figure A2 - 26**b show the deviatoric stress and volumetric strain behaviour. Obviously, the greatest strength was obtained for the highest confining stress. The specimen with the lowest confining stress presented more dilatancy.

Figure A2 - 27 presents the stress paths *p*:*q* (mean stress, *p*: deviatoric stress, *q*). A critical state line with a slope M=2.38 was obtained (ϕ = 58º).

a.

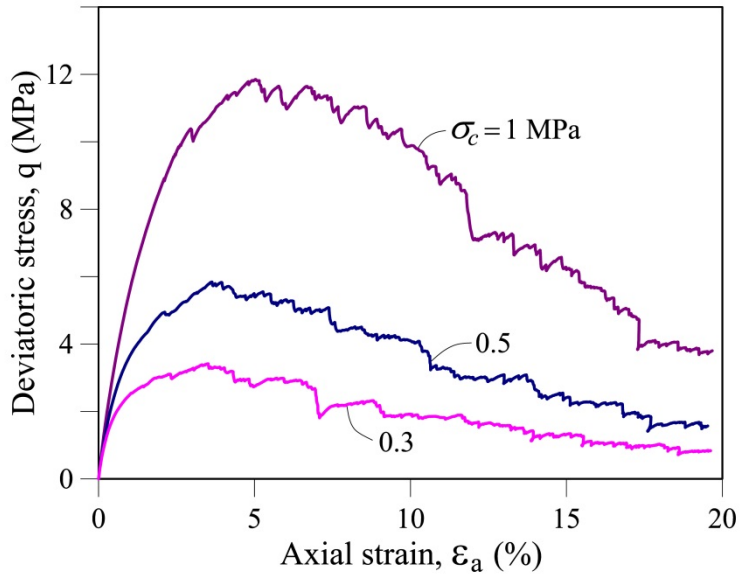

b.

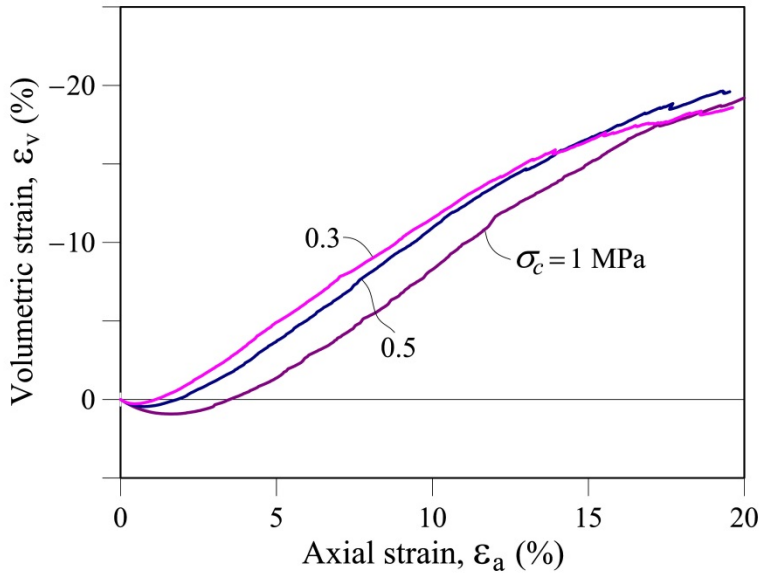

Figure A2 - 26 Influence of the confining stress (σ_c) on the triaxial behaviour. Comparison between three σ_c (1 MPa; 0.5 MPa; 0.3 MPa). Results of numerical simulations of triaxial tests using macroparticles of 14 microparticles. Specimens of 970 macroparticles. Initial porosity: 51%; DEM properties: k_n=20MN/m; K_c=1x10^6 Pa.m$^{0.5}$; μ =0.93. (a) Deviatoric stress behaviour; (b) Volumetric strain behaviour.

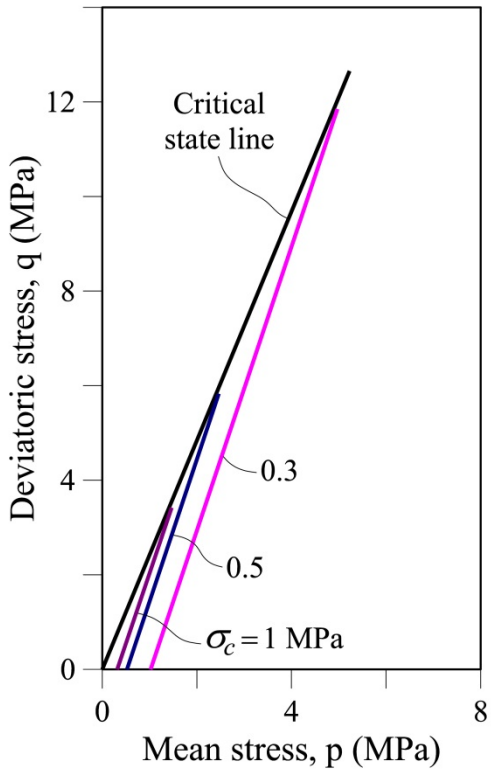

Figure A2 - 27 Stress path p:q . Influence of the confining stress (σ_c) - Comparison between three σ_c (1 MPa; 0.5 MPa; 0.3 MPa). Results of numerical simulations of triaxial tests using macroparticles of 14 microparticles. Specimens of 970 macroparticles. Initial porosity: 51%; DEM properties: k_n=20MN/m; K_c=1x10^6 Pa.m$^{0.5}$; μ =0.93.

A2.9. Conclusions

This appendix presented some results of the influence of some features and properties of a DEM model to simulate the breakage of particles in coarse aggregates. Several numerical triaxial tests were performed. It was analyzed the influence of some failure criteria and the effects of the particle shape, the initial porosity of the specimens of macroparticles and the confining stress. Additionally, the influence of the following properties of the macroparticles was also presented: contact stiffness, toughness and friction coefficient.

The following failure criteria were implemented in the model and compared in the simulations of the triaxial tests: Mohr Coulomb, and Crack Propagation based on the Linear Elastic Fracture Mechanics. Furthermore, Not-breakage was also considered. The results using the Crack propagation criterion were according to actual experiments. This criterion also allows taking into account the time and the influence of the environmental conditions such as the Relative Humidity which was

not considered here in this appendix.

Two different manner to calculate the stress inside the particles were considered: applying the concept of the stresses defined for a Representative Elementary Volume – REV- (Alonso-Marroquín and Herrmann, 2005; Bagi, 1999, 1996; Itasca, 2008), and the analysis of the point loading on brittle spheres (Russell and Muir Wood, 2009).

Regarding the particle shape, the greatest peak strength and the strongest dilatancy were obtained for the largest number of microparticles which compose a macroparticle with pyramidal shape.

With regard to the initial porosity of the specimen, the highest stiffness (macro level/specimen behaviour) was obtained for the lowest porosity.

Regarding the contact stiffness of the macroparticles, a higher stiffness (in the macro level/specimen behaviour), a stronger dilatancy and a lower breakage were obtained for the higher contact stiffness.

Regarding the toughness of the macroparticles, a greater strength and a lower particle breakage were obtained for the higher toughness. Residual values of the strength seemed to be less affected.

A reduction of the value of the toughness causes the collapse in deviatoric stresses due to particle breakage.

With regard to the friction coefficient of the macroparticles, a greater strength and a stronger dilatancy were obtained for the higher friction coefficient. A similar residual strength for strains in excess of 20% was found for all the values of the friction coefficients. A ductile behaviour and a higher breakage were obtained for the lower friction coefficient.

Regarding the confining stress of the specimen, a higher strength was found for a higher confining stress. A stronger dilatancy was obtained for the lower confining stress.

A2.10. References

Alonso-Marroquín, F., Herrmann, H.J., 2005. The incremental response of soils. An investigation using a discrete-element model. J. Eng. Math. 52, 11–34. doi:10.1007/1-4020-4183-7_2

Atkinson, B.K., 1984. Subcritical crack growth in geological materials. J. Geophys. Res. 89, 4077–4114.

Bagi, K., 1999. Microstructural stress tensor of granular assemblies with volume forces. J. Appl. Mech. 66, 934–936.

Bagi, K., 1996. Stress and strain in granular assemblies. Mech. Mater. 22, 165–177. doi:10.1016/0167-6636(95)00044-5

Chávez, C., 2003. Estudio del comportamiento triaxial de materiales granulares de tamaño medio con énfasis en la influencia de la succión. PhD. Thesis. Technical University of Catalonia. UPC, Barcelona, Spain (in Spanish).

Itasca, 2008. Manuals of PFC3D v.4.0: Theory and Background, 4th ed. Minneapolis, Minnesota, USA.

Oldecop, L.A., Alonso, E.E., 2007. Theoretical investigation of the time-dependent behaviour of rockfill. Géotechnique 57, 289–301.

Oldecop, L.A., Alonso, E.E., 2001. A model for rockfill compressibility. Géotechnique 51, 127–139.

Ortega, E., 2008. Comportamiento de materiales granulares gruesos - Efecto de la succión. PhD. Thesis. Technical University of Catalonia. UPC, Barcelona, Spain (in Spanish).

Russell, A.R., Muir Wood, D., 2009. Point load tests and strength measurements for brittle spheres. Int. J. Rock Mech. Min. Sci. 46, 272–280. doi:10.1016/j.ijrmms.2008.04.004

Appendix 3

A3. Analysis of micro-properties for compressibility behaviour on coarse aggregates subjected to numerical oedometer tests using DEM

This appendix presents results of a work done at the first stage of this thesis. Several numerical simulations of oedometer tests have been performed using the discrete element method though the computer code PFC3D. A background reference for the conducted study is the experimental results performed at the UPC geotechnical laboratory (Ortega, 2008).

This appendix describes a sensitivity analysis of some properties of the macroparticles such as the contact stiffness, the toughness and the friction coefficient. The effect of these properties on the compressibility and the particle-breakage behaviour is studied.

A3.1. Numerical simulation of oedometer tests

Several numerical oedometer tests have been performed varying some properties of the DEM model in order to do a sensitivity analysis of the influence of these properties on the compressibility behaviour and the evolution of the breakage of particles. The numerical tests simulate the experimental tests performed by Ortega (2008) on limestone gravels with uniform size between 2.5 and 3.0 cm. The properties of the actual material are shown in **Table 5-2** in chapter 5. A same vertical stress path was applied: 0.1; 0.2; 0.4; 0.6; 0.8; 1.2; 1.6; 2.0; 2.4; 2.8 MPa. The tests were performed considering a relative humidity of 10%.

The numerical tests consider a uniform granular sample, i.e. all macroparticles have the same pyramidal shape and dimensions but their orientation follows a random pattern. Each macroparticle has an initial equivalent diameter of 2.8cm and is composed by 14 spheres or microparticles as considered in the DEM model in chapters 5-7 (see **Figure 5-10a**). The oedometer specimens have the following

dimensions: 25 cm in diameter and 25 cm in height. Each one of the oedometer specimens requires 471 macroparticles. An initial porosity of 53.14% is obtained for all the tests. **Figure 5-10b** in chapter 5 shows an oedometer specimen.

Table A3 - 1 shows the main DEM properties of the macroparticles used in this study.

Table A3 - 1 Properties of the macroparticles.

Normal stiffness, k_n (k_n = Shear stiffness, k_s)	2 – 4 – 8 - 20 MN/m
Friction coefficient, μ	0.93 – 0.4 – 0.3 – 0.2
Toughness, K_c	$5x10^6$ - $1x10^6$ - $1x10^5$ - $1x10^4$ - $1x10^3$- $1x10^2$ Pa•$m^{0.5}$

A3.1.1. Failure criteria for macroparticles

The crack propagation criterion based on the Linear Elastic Fracture Mechanics (LEFM) is used in this study. This criterion was explained in section 5.3 in chapter 5.

For a Mode I condition (tensile stresses), when the stress intensity factor K reaches the toughness of the rock (K_c) a crack will propagate catastrophically and the rock particle will break. K is defined in terms of a characteristic crack length a. The stress intensity factor K is calculated for the maximum tensile stress that acts inside the macroparticle subjected to a point load condition.

A uniform probability distribution was used to assign the random values of crack lengths inside the macroparticles.

This study only considers the “Splitting failure” mechanisms in the particle breakage process as explained in section 5.4 in chapter 5. Subparticles of 13 microparticles are not considered to replace the macroparticles of 1 sphere.

A3.2. Influence of the contact stiffness, k_n

Four samples having contact normal stiffnesses k_n equal to 2, 4, 8, and 20 MN/m respectively were tested. All the particles had a friction coefficient (μ) equal to 0.3 (ϕ = 17º). The toughness of the macroparticles was $5x10^6$ Pa.$m^{0.5}$.

Figure A3 - 1 shows the compressibility curves for all the values of k_n. The highest compressibility is obtained for the lowest stiffness. It can be also seen in the curves of the variation of the compressibility index (λ) in relation to the applied vertical stress (**Figure A3 - 2**). **Figure A3 - 2** also shows the experimental data of Ortega (2008) and Oldecop and Alonso (2007) for gravels with similar sizes. Numerical and experimental tests tend to have a similar behaviour. The experimental values of λ are between the numerical-k_n curves of 2 and 8 MN/m.

The evolution of the particle breakage can be followed through the curves of the grain size distribution (gsd) –**Figure A3 - 3**- and the variation of the Hardin breakage index (B_r) –**Figure A3 - 4**- at the end of the tests. Although in general terms, the curves show the highest particle breakage for the lowest contact stiffness, this tendency is not followed at the intermediate values (k_n equals to 4 and 8 MN/m).

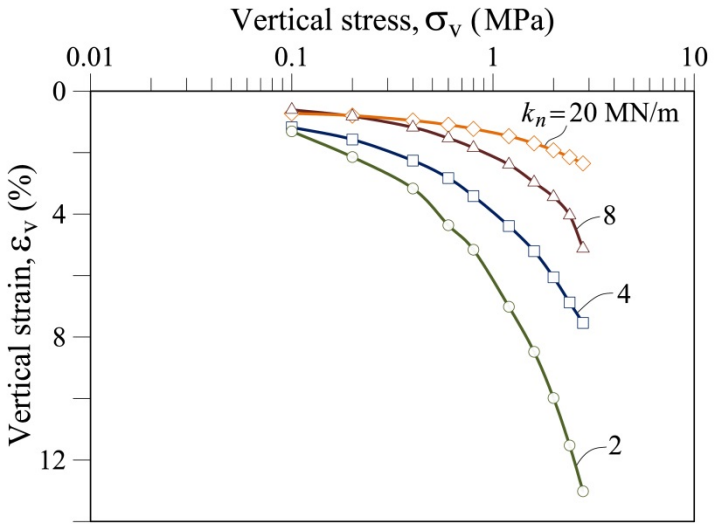

Figure A3 - 1 Effect of the contact stiffness on the curves of compressibility. Comparison between four different normal stiffnesses (2, 4, 8 and 20 MN/m). Results of numerical simulations of oedometer tests using macroparticles of 14 microparticles. Specimens of 471 macroparticles. Maximum vertical stress: 2.8MPa; RH=10%; Initial porosity: 53%; DEM properties: K_c=5x10^6 Pa.m$^{0.5}$; μ=0.3.

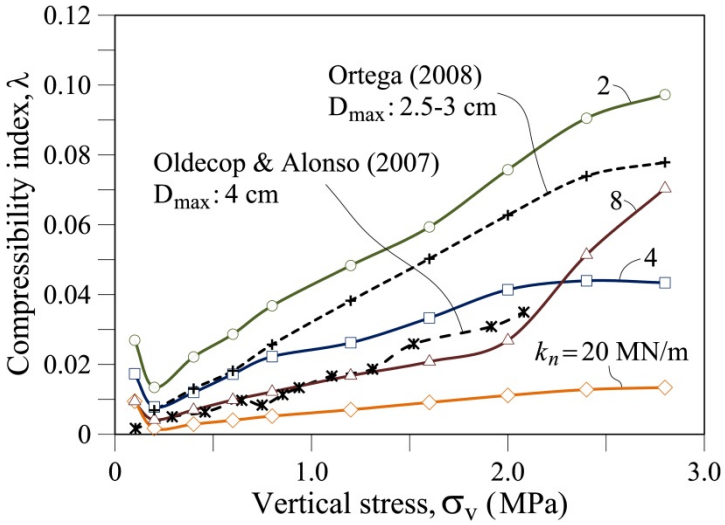

Figure A3 - 2 Effect of the contact stiffness on the compressibility index. Comparison between four different normal stiffnesses (2, 4, 8 and 20 MN/m) and experimental results. Results of numerical simulations of oedometer tests using macroparticles of 14 microparticles. Specimens of 471 macroparticles; RH=10%; Initial porosity: 53%; DEM properties: K_c=5x10^6 Pa.m$^{0.5}$; μ=0.3.

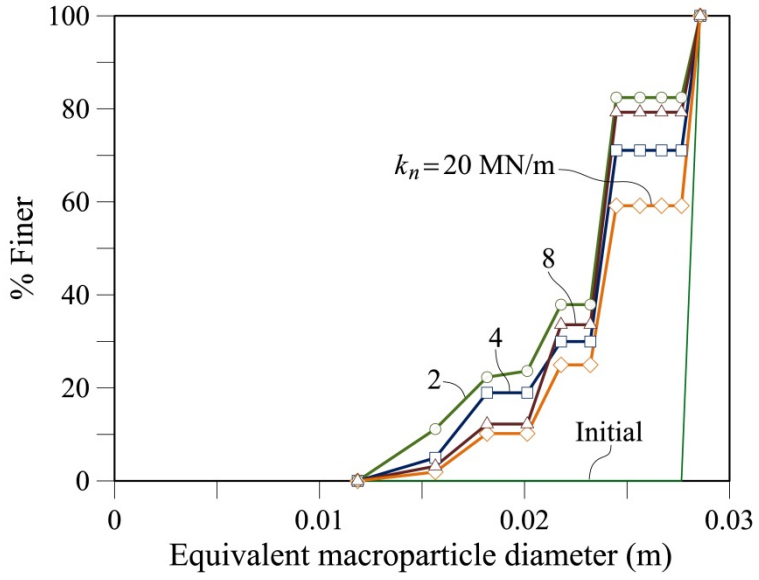

Figure A3 - 3 Effect of the contact stiffness on the evolution of the grain size distributions at the initial and the end of oedometer tests. Comparison between four different normal stiffnesses (2, 4, 8 and 20 MN/m) and experimental results. Results of numerical simulations of oedometer tests using macroparticles of 14 microparticles. Specimens of 471 macroparticles. Maximum vertical stress: 2.8MPa; RH=10%; Initial porosity: 53%; DEM properties: K_c=5x10^6 Pa.m$^{0.5}$; μ=0.3.

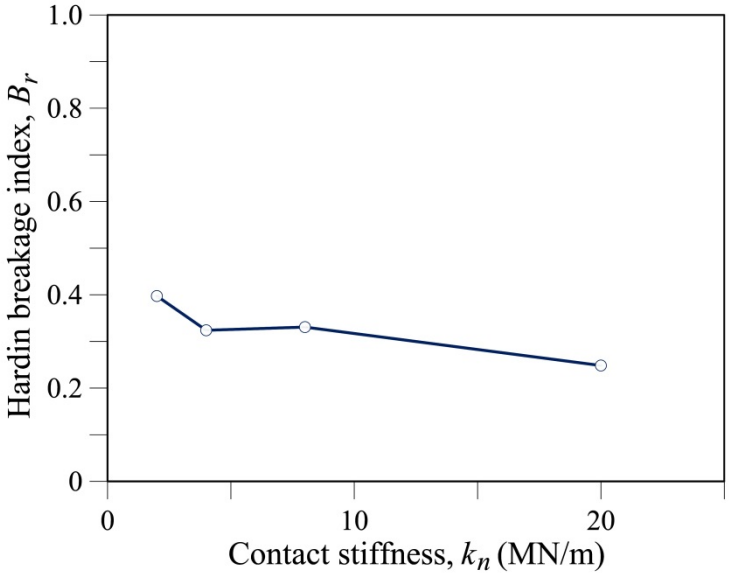

Figure A3 - 4 Effect of the contact stiffness on the Hardin breakage index B_r at the end of oedometer tests. Comparison between four different normal stiffnesses (2, 4, 8 and 20 MN/m) and experimental results. Results of numerical simulations of oedometer tests using macroparticles of 14 microparticles. Specimens of 471 macroparticles. Maximum vertical stress: 2.8MPa; RH=10%; Initial porosity: 53%; DEM properties: K_c=5x10^6 Pa.m$^{0.5}$; μ=0.3.

A3.3. Influence of the toughness, K_c

Five values were compared: 1x10^6 Pa•m$^{0.5}$; 1x10^5 Pa•m$^{0.5}$; 1x10^4 Pa•m$^{0.5}$; 1x10^3 and 1x10^2 Pa•m$^{0.5}$. The following DEM properties were considered for all the numerical oedometer tests: k_n=k_s=20MN/m and μ=0.3 (ϕ = 17º).

The influence of the K_c on the compressibility behaviour can be seen in **Figure A3 - 5** (compressibility curves) and **Figure A3 - 6** (variation of the compressibility indexes, λ). The influence of the K_c on the particle breakage is shown in **Figure A3 - 7** (gsd curves) and **Figure A3 - 8** (variation of the Hardin breakage index, B_r).

The specimens with the lower the toughness present the larger the vertical strain (**Figure A3 - 5**) and the higher the particle breakage (**Figure A3 - 7** and **Figure A3 - 8**).

Regarding the variation of the compressibility index, λ, all the curves in **Figure A3 - 6** present a similar behaviour.

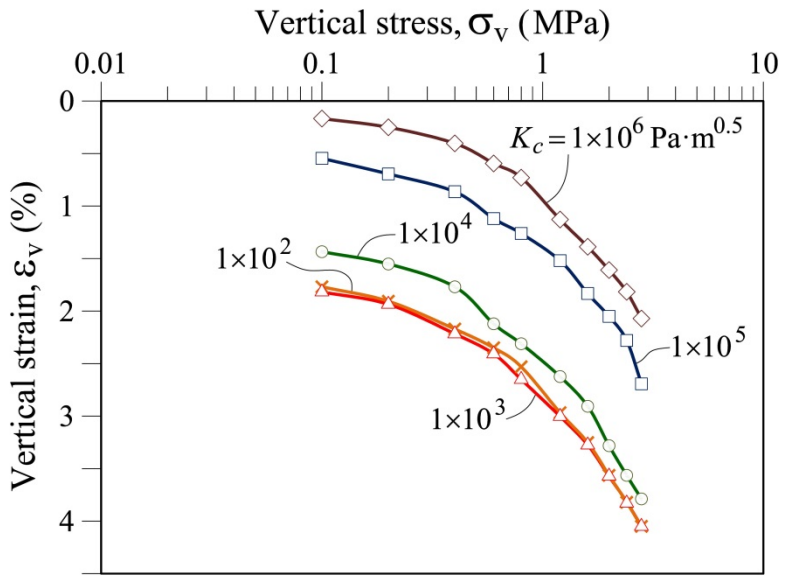

Figure A3 - 5 Effect of the macroparticle toughness on the curves of compressibility. Comparison between five different toughness ($1x10^6$, $1x10^5$, $1x10^4$, $1x10^3$ and $1x10^2$ $Pa.m^{0.5}$). Results of numerical simulations of oedometer tests using macroparticles of 14 microparticles. Specimens of 471 macroparticles. Maximum vertical stress: 2.8MPa; RH=10%; Initial porosity: 53%; DEM properties: k_n=20MN/m; μ=0.3.

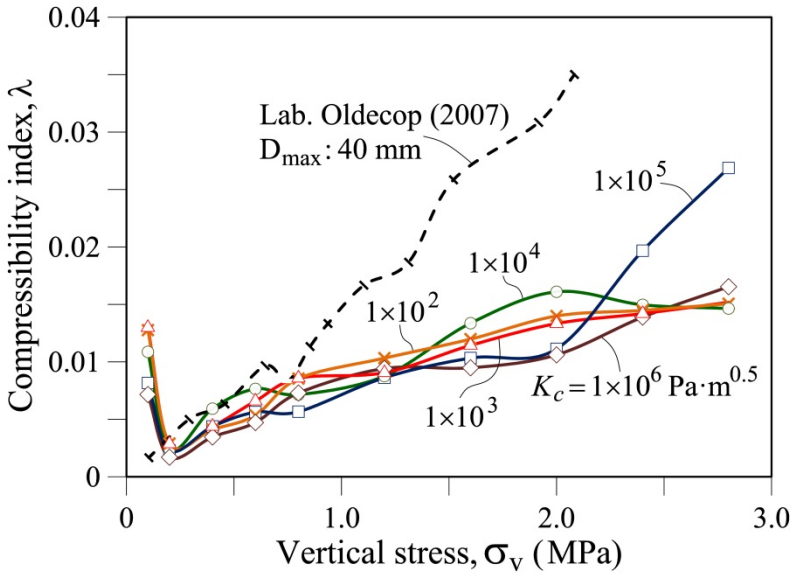

Figure A3 - 6 Effect of the macroparticle toughness on the compressibility index. Comparison between five different toughness ($1x10^6$, $1x10^5$, $1x10^4$, $1x10^3$ and $1x10^2$ $Pa.m^{0.5}$) and experimental results. Results of numerical simulations of oedometer tests using macroparticles of 14 microparticles. Specimens of 471 macroparticles. Maximum vertical stress: 2.8MPa; RH=10%; Initial porosity: 53%; DEM properties: k_n=20MN/m; μ=0.3.

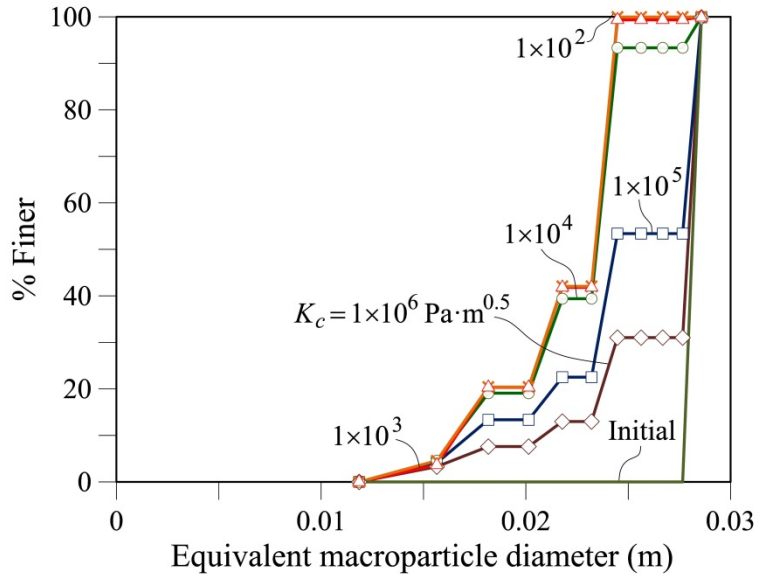

Figure A3 - 7 Effect of the macroparticle toughness on the evolution of the grain size distributions at the initial and the end of oedometer tests. Comparison between five different toughness ($1x10^6$, $1x10^5$, $1x10^4$, $1x10^3$ and $1x10^2$ Pa.m$^{0.5}$). Results of numerical simulations of oedometer tests using macroparticles of 14 microparticles. Specimens of 471 macroparticles. Maximum vertical stress: 2.8MPa; RH=10%; Initial porosity: 53%; DEM properties: k_n=20MN/m; μ=0.3.

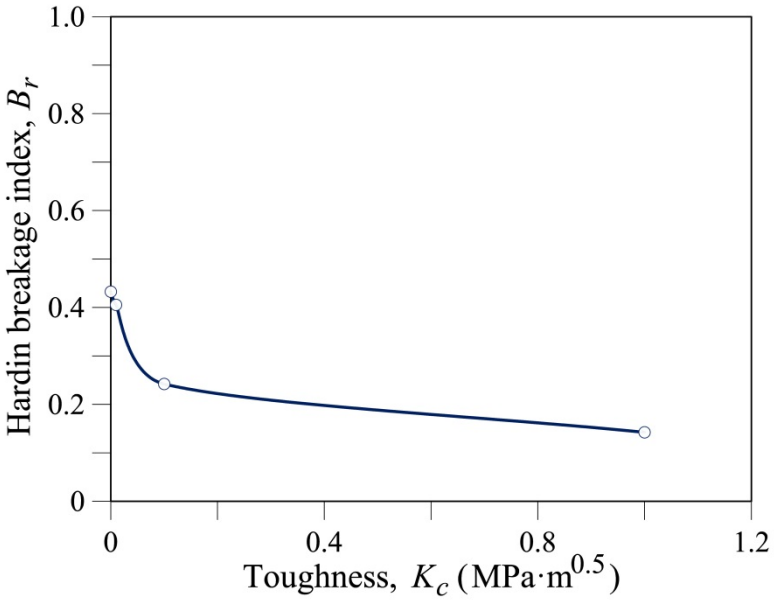

Figure A3 - 8 Effect of the macroparticle toughness on the Hardin breakage index B_r at the end of oedometer tests. Comparison between five different toughness ($1x10^6$, $1x10^5$, $1x10^4$, $1x10^3$ and $1x10^2$ Pa.m$^{0.5}$). Results of numerical simulations of oedometer tests using macroparticles of 14 microparticles. Specimens of 471 macroparticles. Maximum vertical stress: 2.8MPa; RH=10%; Initial porosity: 53%; DEM properties: k_n=20MN/m; μ=0.3.

A3.4. Influence of the Friction Coefficient, μ

Four specimens of macroparticles having friction coefficients (μ) equals to 0.93, 0.40, 0.30 and 0.20 (ϕ = 43º; 27º; 22º; 17º and 11º) were tested. The toughness of macroparticles (K_c) was 5x10^6 Pa•m$^{0.5}$ and the contact stiffness was k_n=k_s=4MN/m.

In the compressibility curves shown in **Figure A3 - 9**, it can be noted that the lower the friction coefficient, the larger the vertical strain.

Furthermore, the specimen with the lowest value of the friction coefficient (μ=0.20) exhibited a considerable collapse of the vertical strain between the applied stresses of 0.6 and 0.8 MPa. It is also shown in the curves of the variation of λ in relation to the applied vertical stress (**Figure A3 - 10**): there is a peak value in λ around these stresses. This specimen also exhibited the highest particle breakage (**Figure A3 - 11** and **Figure A3 - 12**).

Although it is noted in the curves of gsd and the variation of the B_r index (**Figure A3 - 11** and **Figure A3 - 12**) that specimens with the higher the μ present more particle breakage, this effect is not so marked for μ>0.3.

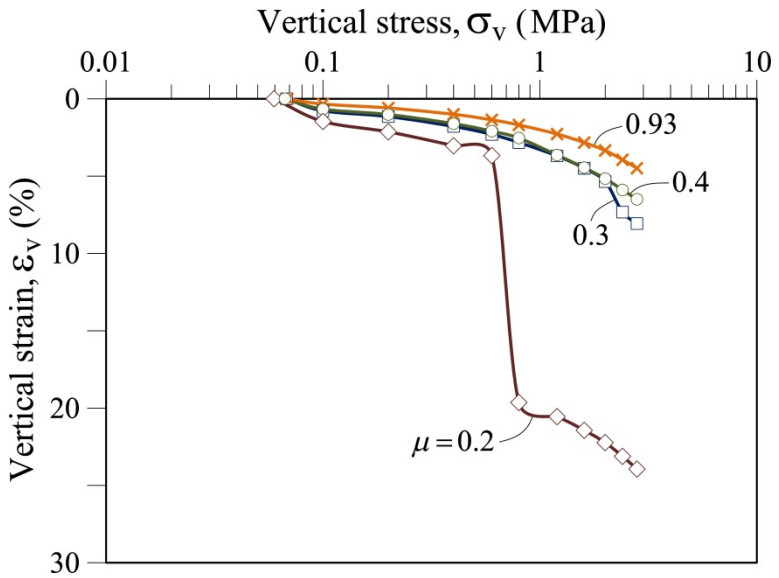

Figure A3 - 9 Influence of the friction coefficient (μ) on the curves of compressibility. Comparison between four friction coefficients (0.93, 0.40, 0.30 and 0.20). Results of numerical simulations of oedometer tests using macroparticles of 14 microparticles. Specimens of 471 macroparticles. Maximum vertical stress: 2.8MPa; RH=10%; Initial porosity: 53%; DEM properties: k_n=4MN/m; K_c=5x10^6 Pa.m$^{0.5}$.

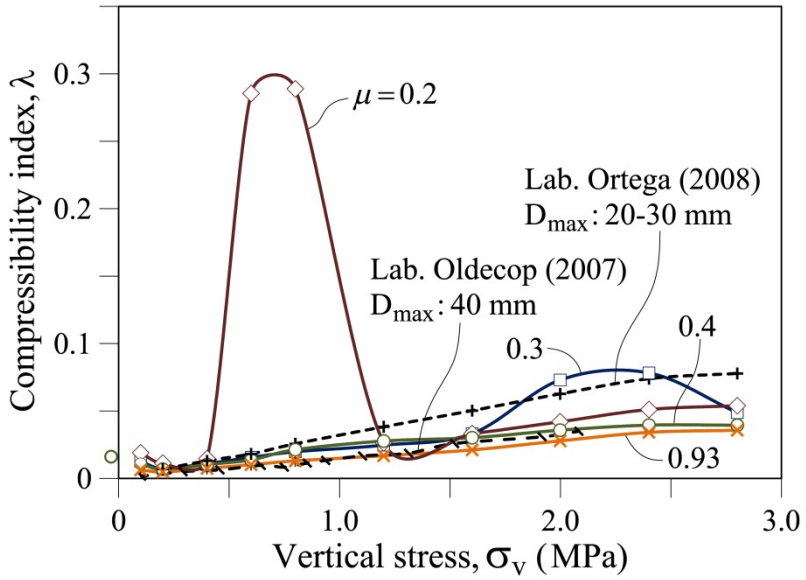

Figure A3 - 10 Influence of the friction coefficient (μ) on the compressibility index. Comparison between four friction coefficients (0.93, 0.40, 0.30 and 0.20) and experimental results. Results of numerical simulations of oedometer tests using macroparticles of 14 microparticles. Specimens of 471 macroparticles. Maximum vertical stress: 2.8MPa; RH=10%; Initial porosity: 53%; DEM properties: k_n=4MN/m; K_c=5x10^6 Pa.m$^{0.5}$.

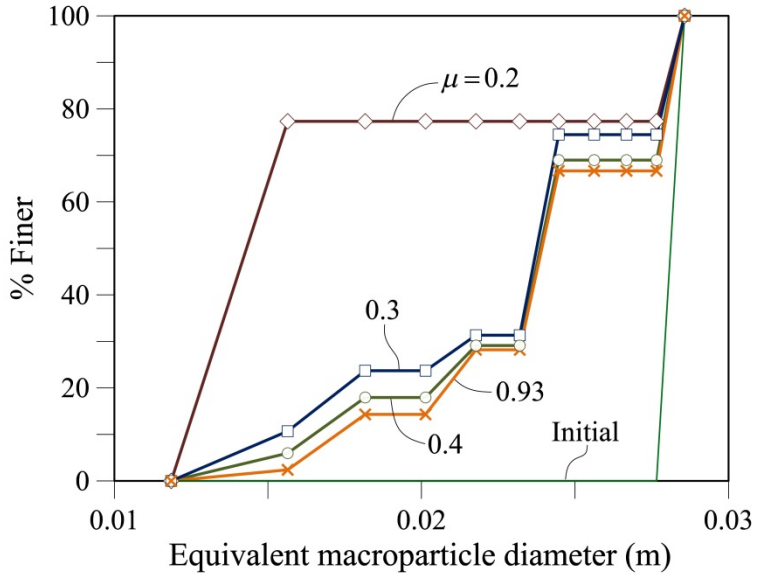

Figure A3 - 11 Influence of the friction coefficient (μ) on the evolution of the grain size distributions at the initial and the end of oedometer tests. Comparison between four friction coefficients (0.93, 0.40, 0.30 and 0.20). Results of numerical simulations of oedometer tests using macroparticles of 14 microparticles. Specimens of 471 macroparticles. Maximum vertical stress: 2.8MPa; RH=10%; Initial porosity: 53%; DEM properties: k_n=4MN/m; K_c=5x10^6 Pa.m$^{0.5}$.

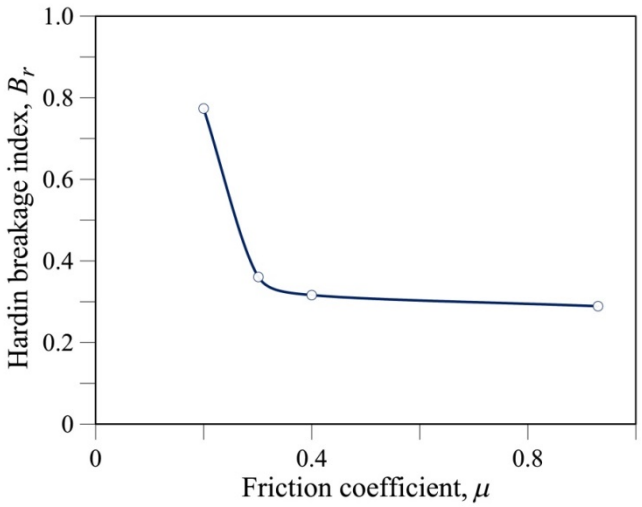

Figure A3 - 12 Influence of the friction coefficient (μ) on the Hardin breakage index B_r at the end of oedometer tests. Comparison between four friction coefficients (0.93, 0.40, 0.30 and 0.20). Results of numerical simulations of oedometer tests using macroparticles of 14 microparticles. Specimens of 471 macroparticles. Maximum vertical stress: 2.8MPa; RH=10%; Initial porosity: 53%; DEM properties: k_n=4MN/m; K_c=5x10^6 Pa.m$^{0.5}$.

A3.5. Conclusions

The influence of different properties of the macroparticles on the compressibility behaviour and particle breakage has been studied. The compressibility behaviour has been studied through the curves of compressibility (vertical stress : vertical strain) and the variation of the compressibility index λ. The particle-breakage behaviour has been studied through the curves of the grain size distribution (gsd) and the variation of the Hardin breakage index B_r.

Specimens with the lower the contact stiffness present the larger the vertical strain and the higher the compressibility index λ.

The toughness K_c is a measurement of the strength of the material.

Specimens with the lower the K_c present the higher the particle breakage.

The higher the particle breakage causes the larger values of the vertical strain of the specimens. The particle breakage is a key mechanism in the deformation of the coarse aggregates.

Specimens with the lower the μ present the larger the vertical strain.

The influence of k_n can be evaluated through the compressibility curves (applied vertical stress : vertical strain) and the variation of the compressibility index λ.

The influence of K_c can be evaluated through the calculation of the particle breakage using the gsd curves and the breakage indexes such as the Hardin breakage index B_r. Furthermore, the compressibility curve (applied vertical stress: vertical strain) is also useful in the analysis.

The influence of μ can be evaluated through the compressibility curves (applied vertical stress: vertical strain).

A3.6. References

Oldecop, L.A., Alonso, E.E., 2007. Theoretical investigation of the time-dependent behaviour of rockfill. Géotechnique 57, 289–301.

Ortega, E., 2008. Comportamiento de materiales granulares gruesos - Efecto de la succión. PhD. Thesis. Technical University of Catalonia. UPC, Barcelona, Spain (in Spanish).

Appendix 4

A4. Laboratory tests on sugar cubes

This appendix contents the experimental results of several tests performed on sugar cubes: unconfined compression strength tests, oedometer tests on ordered and disordered arrangements of sugar cubes in order to study the particle breakage and the behaviour of imposed load, and oedometer tests on disordered arrangements of sugar cubes to analyze the time-dependent behaviour. The analyses of the tests are presented in chapter 4.

A4.1. Unconfined compression strength tests

A4.1.1. Summary of results

Table A4 - 1 Results of Unconfined compression strength tests on sugar cube samples.

Sample	Water content	Density	Simple compression strength	
	(%)	g/cm^3	kg/cm^2	kPa
CS1	0.38	1.01	20.38	1998.88
CS2	0.17	1.01	22.59	2216.53
CS3	0.35	1.01	26.77	2625.79
CS4	0.35	1.02	26.51	2600.61
CS5	0.17	1.02	19.05	1868.40
CS6	0.17	1.06	27.39	2686.63
CS7	0.34	1.04	26.35	2584.99
CS8	0.34	1.04	19.90	1952.25
CS9	0.51	1.02	24.47	2400.38
CS10	0.51	1.03	23.57	2312.19
Mean	0.33	1.03	23.70	2324.67
Standard Deviation	0.13	0.02	3.11	304.81

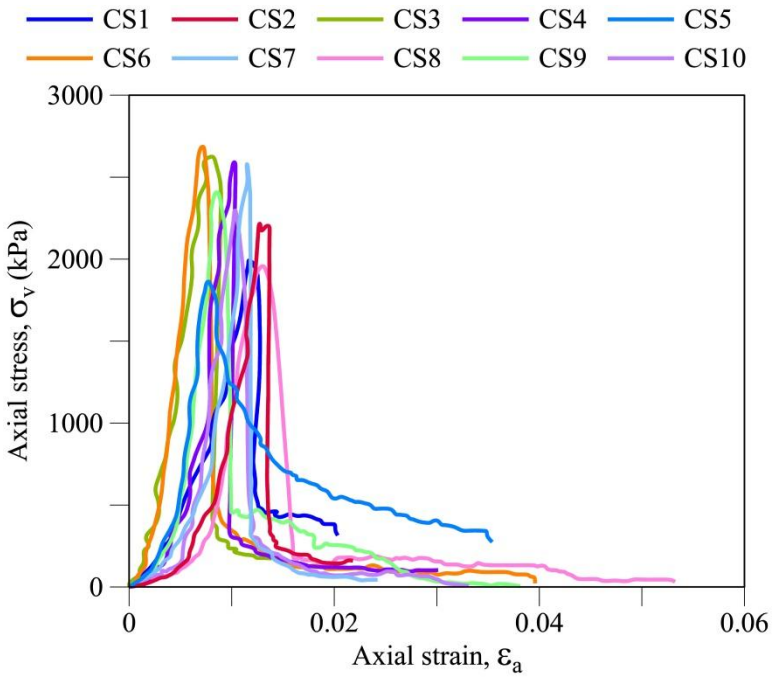

Figure A4 - 1 Results of unconfined compression strength tests on sugar cube samples.

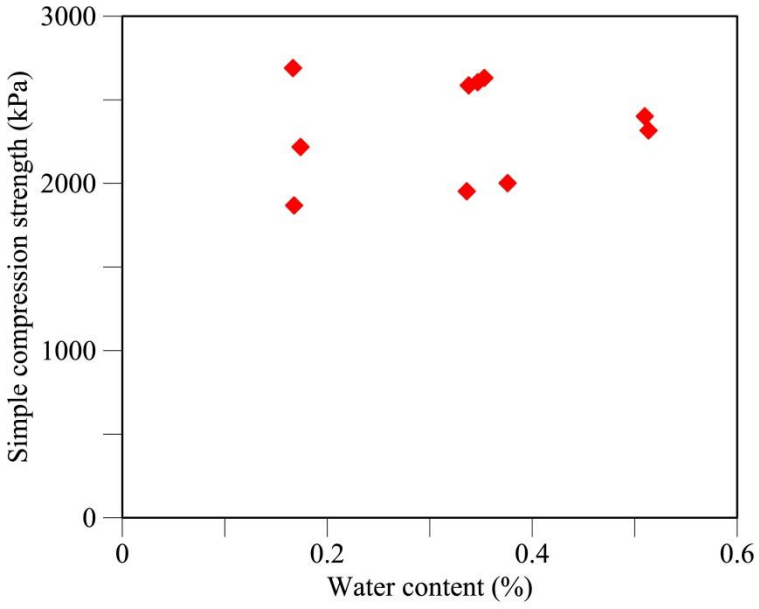

Figure A4 - 2 Relation between the unconfined compression strength and the water content. Results of unconfined compression strength tests on sugar cube samples.

A4.1.2. Test on the CS1 sample

Sample: CS1

Initial length:	**2.745**
Initial length 1 of section (cm):	**1.76**
Initial length 2 of section (cm):	**1.21**
Initial area of section (cm^2):	**2.1296**
Initial volume (cm^3):	**5.845752**
Initial weight (g):	**5.91**
Initial density, (g/cm^3):	**1.010990545**

a. Equipment and sample at the beginning of the test

b. Initial of the test

c. End of the test

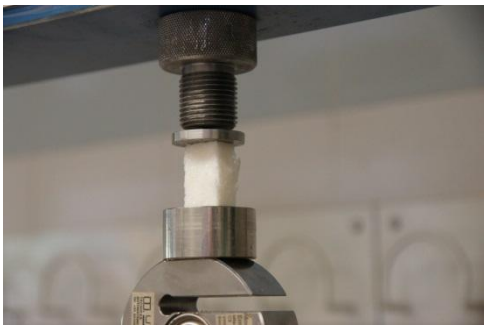

Figure A4 - 3 Simple compression tests on the CS1-sugar cube sample.

Table A4 - 2 Results of Unconfined compression strength tests on the CS1 sample.

Axial stress, σ_v		Axial strain, ε_a
kg/cm^2	kPa	
0.0000	0.0000	0.00000
0.0539	5.2925	0.00095
0.2158	21.1698	0.00095
0.5713	56.0397	0.00120
1.0775	105.7028	0.00189
1.6153	158.4614	0.00262
2.3677	232.2752	0.00310
2.9351	287.9348	0.00404
3.5476	348.0182	0.00423
4.1689	408.9687	0.00470
4.8339	474.2098	0.00499
5.5831	547.6976	0.00546
6.3315	621.1153	0.00594
7.1851	704.8605	0.00659
8.0372	788.4535	0.00736
8.8886	871.9672	0.00801
9.8845	969.6648	0.00801
11.0037	1079.4589	0.00849
12.0839	1185.4309	0.00944
13.2388	1298.7310	0.00944
14.4323	1415.8125	0.00973
15.5975	1530.1182	0.01038
16.8502	1653.0035	0.01086
18.0195	1767.7162	0.01115
19.0835	1872.0941	0.01133
19.9528	1957.3657	0.01162
20.3760	1998.8845	0.01180
19.3476	1897.9956	0.01257
13.6419	1338.2705	0.01275
8.1051	795.1131	0.01209
6.8565	672.6184	0.01228
6.1844	606.6897	0.01228
5.8648	575.3406	0.01228
5.2232	512.4001	0.01257
5.0100	491.4766	0.01257
4.7948	470.3728	0.01304
4.5808	449.3763	0.01322
4.6862	459.7123	0.01348
4.6862	459.7123	0.01348
4.6817	459.2709	0.01443
4.6829	459.3897	0.01417
4.4699	438.5001	0.01417
4.3623	427.9446	0.01443
4.3602	427.7390	0.01490
4.5698	448.2979	0.01559
4.5698	448.2979	0.01559
4.3850	430.1690	0.01650

Axial stress, σ_v		Axial strain, ε_a
kg/cm^2	kPa	
0.0000	0.0000	0.00000
0.0539	5.2925	0.00095
0.2158	21.1698	0.00095
0.5713	56.0397	0.00120
1.0775	105.7028	0.00189
1.6153	158.4614	0.00262
2.3677	232.2752	0.00310
2.9351	287.9348	0.00404
3.5476	348.0182	0.00423
4.1689	408.9687	0.00470
4.8339	474.2098	0.00499
5.5831	547.6976	0.00546
6.3315	621.1153	0.00594
7.1851	704.8605	0.00659
8.0372	788.4535	0.00736
8.8886	871.9672	0.00801
9.8845	969.6648	0.00801
11.0037	1079.4589	0.00849
12.0839	1185.4309	0.00944
13.2388	1298.7310	0.00944
14.4323	1415.8125	0.00973
15.5975	1530.1182	0.01038
16.8502	1653.0035	0.01086
18.0195	1767.7162	0.01115
19.0835	1872.0941	0.01133
19.9528	1957.3657	0.01162
20.3760	1998.8845	0.01180
19.3476	1897.9956	0.01257
13.6419	1338.2705	0.01275
4.4580	437.3334	0.01679
4.4594	437.4631	0.01650
4.4338	434.9597	0.01745
4.3469	426.4260	0.01792
4.2395	415.8975	0.01821
4.1307	405.2247	0.01887
4.0255	394.9030	0.01869
3.9188	384.4347	0.01887
3.9176	384.3205	0.01916
3.9139	383.9494	0.02011
3.9139	383.9494	0.02011
3.4698	340.3906	0.02011
3.2787	321.6434	0.02029

A4.1.3. Test on the CS2 sample

Sample: CS2

Initial length:	**2.745**
Initial length 1 of section (cm):	**1.76**
Initial length 2 of section (cm):	**1.21**
Initial area of section (cm^2):	**2.1296**
Initial volume (cm^3):	**5.845752**
Initial weight (g):	**5.91**
Initial density, (g/cm^3):	**1.010990545**

a. Equipment and sample at the beginning of the test

b. Initial of the test

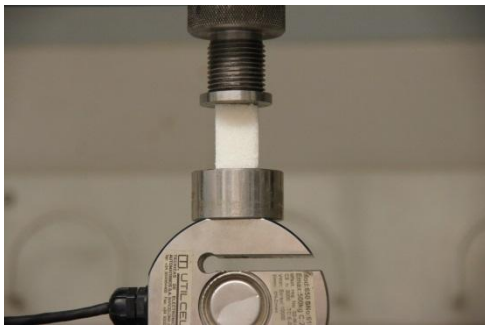

c. End of the test

Figure A4 - 4 Simple compression tests on the CS2-sugar cube sample.

Table A4 - 3 Results of Unconfined compression strength tests on the CS2 sample.

Axial stress, σ_v		Axial strain, ε_a
kg/cm^2	kPa	
0.0000	0.0000	0.00000
0.1080	10.5949	0.00000
0.1079	10.5876	0.00069
0.2157	21.1598	0.00142
0.3234	31.7246	0.00189
0.4310	42.2794	0.00237
0.5380	52.7783	0.00284
0.6454	63.3130	0.00332
0.6453	63.3015	0.00350
0.7525	73.8243	0.00397
0.9672	94.8849	0.00444
1.3107	128.5768	0.00492
1.7173	168.4642	0.00568
2.1464	210.5645	0.00587
2.6820	263.1056	0.00616
3.2181	315.6963	0.00634
3.7524	368.1140	0.00681
4.3939	431.0450	0.00729
5.0329	493.7250	0.00805
5.8867	577.4806	0.00852
6.6350	650.8934	0.00871
7.5423	739.9031	0.00900
8.6599	849.5409	0.00965
9.9430	975.4072	0.00965
11.4340	1121.6766	0.01013
13.0271	1277.9573	0.01089
14.5868	1430.9662	0.01155
16.2227	1591.4445	0.01137
17.8895	1754.9624	0.01184
19.5126	1914.1825	0.01231
21.1078	2070.6769	0.01250
22.5946	2216.5347	0.01275
22.1632	2174.2137	0.01297

Axial stress, σ_v		Axial strain, ε_a
kg/cm^2	kPa	
22.3599	2193.5084	0.01370
6.3902	626.8787	0.01344
3.7264	365.5620	0.01370
3.3221	325.8981	0.01370
3.0863	302.7631	0.01417
3.0551	299.7071	0.01392
2.9806	292.3939	0.01392
2.7662	271.3685	0.01439
2.5544	250.5845	0.01417
2.3930	234.7523	0.01486
2.2313	218.8936	0.01577
2.1250	208.4657	0.01577
2.1250	208.4657	0.01577
2.0925	205.2766	0.01607
2.0168	197.8473	0.01672
2.0152	197.6934	0.01749
1.8027	176.8413	0.01767
1.6958	166.3533	0.01814
1.5889	155.8753	0.01862
1.5892	155.9042	0.01843
1.4830	145.4796	0.01891
1.4830	145.4796	0.01891
1.4820	145.3824	0.01956
1.4815	145.3391	0.01985
1.4813	145.3121	0.02004
1.4808	145.2689	0.02033
1.5846	155.4529	0.02128
1.5851	155.4992	0.02098
1.6903	165.8225	0.02128
1.6895	165.7422	0.02175

A4.1.4. Test on the CS3 sample

Sample: CS3

Initial length:	**2.745**
Initial length 1 of section (cm):	**1.76**
Initial length 2 of section (cm):	**1.21**
Initial area of section (cm^2):	**2.1296**
Initial volume (cm^3):	**5.845752**
Initial weight (g):	**5.91**
Initial density, (g/cm^3):	**1.010990545**

a. Equipment and sample at the beginning of the test

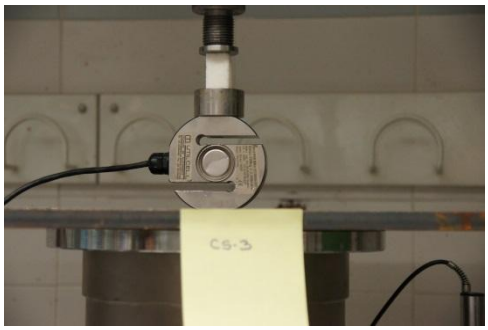

b. Initial of the test

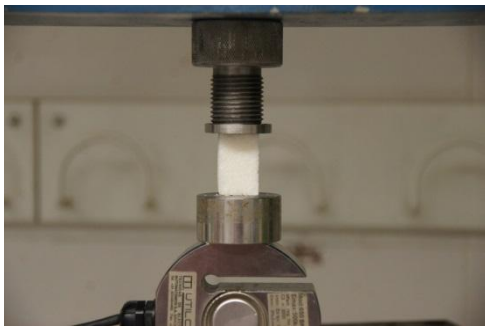

c. End of the test

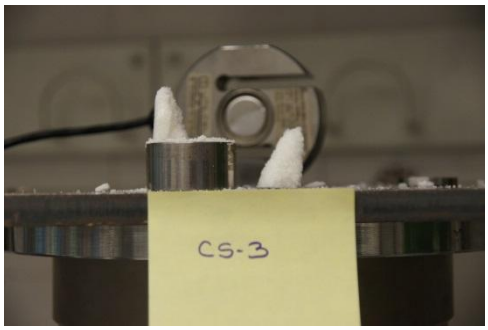

Figure A4 - 5 Simple compression tests on the CS3-sugar cube sample.

Table A4 - 4 Results of Unconfined compression strength tests on the CS3 sample.

Axial stress, σ_v		Axial strain, ε_a
kg/cm^2	kPa	
0.0000	0.0000	0.00000
0.2155	21.1438	0.00000
0.5393	52.9036	0.00047
0.7547	74.0322	0.00117
0.9706	95.2182	0.00095
1.2936	126.8991	0.00117
1.6168	158.6064	0.00142
1.9403	190.3461	0.00142
2.2639	222.0858	0.00142
2.5857	253.6591	0.00189
3.1256	306.6230	0.00160
3.7692	369.7612	0.00237
4.5208	443.4937	0.00284
5.2747	517.4476	0.00284
6.1376	602.0963	0.00255
7.1033	696.8307	0.00302
8.0680	791.4748	0.00350
9.2487	907.3003	0.00379
10.6400	1043.7794	0.00444
12.1408	1191.0090	0.00474
13.8104	1354.8037	0.00444
15.5716	1527.5769	0.00521
17.3889	1705.8485	0.00568
19.2048	1883.9955	0.00616
20.9213	2052.3794	0.00616
22.5160	2208.8210	0.00681
24.1026	2364.4665	0.00681

Axial stress, σ_v		Axial strain, ε_a
kg/cm^2	kPa	
25.3698	2488.7755	0.00758
26.3953	2589.3793	0.00729
26.7664	2625.7873	0.00823
26.2232	2572.4925	0.00852
24.6061	2413.8608	0.00900
4.3905	430.7128	0.00805
3.9613	388.6028	0.00823
3.7246	365.3784	0.00852
3.3181	325.5065	0.00852
2.9963	293.9386	0.00871
2.8870	283.2172	0.00947
2.7795	272.6724	0.00965
2.4587	241.1944	0.00965
2.3495	230.4811	0.01060
2.2441	220.1494	0.01013
2.0274	198.8882	0.01155
1.8966	186.0533	0.01297
1.8125	177.8053	0.01231
1.8108	177.6414	0.01322
1.9183	188.1865	0.01275
1.8104	177.6020	0.01344
1.8091	177.4708	0.01417
1.8091	177.4708	0.01417
1.9156	187.9156	0.01417

A4.1.5. Test on the CS4 sample

Sample: CS4

Initial length:	**2.74**
Initial length 1 of section (cm):	**1.745**
Initial length 2 of section (cm):	**1.2**
Initial area of section (cm^2):	**2.094**
Initial volume (cm^3):	**5.73756**
Initial weight (g):	**5.85**
Initial density, (g/cm^3):	**1.019597181**

a. Equipment and sample at the beginning of the test

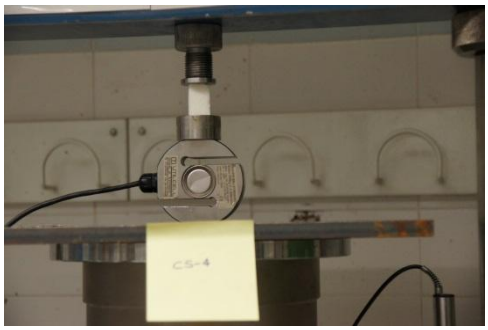

b. Initial of the test

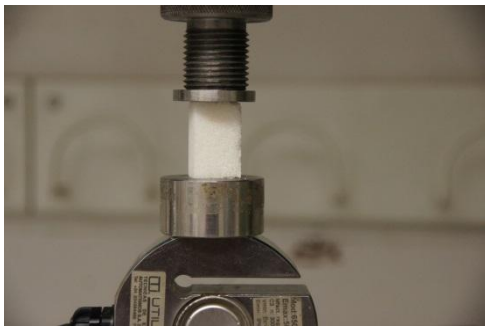

c. End of the test

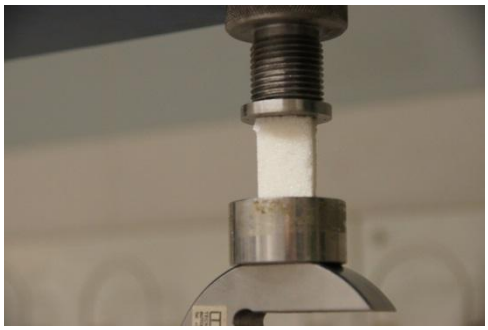

Figure A4 - 6 Simple compression tests on the CS4-sugar cube sample.

Table A4 - 5 Results of Unconfined compression strength tests on the CS4 sample.

Axial stress, σ_v		Axial strain, ε_a
kg/cm^2	kPa	
0.0000	0.0000	0.00000
0.1098	10.7672	0.00073
0.2741	26.8925	0.00168
0.5479	53.7539	0.00139
0.7671	75.2521	0.00168
1.0186	99.9274	0.00234
1.3135	128.8530	0.00310
1.7502	171.6912	0.00358
2.2751	223.1856	0.00376
2.8428	278.8770	0.00405
3.4991	343.2655	0.00405
4.1511	407.2190	0.00500
4.9124	481.9024	0.00566
5.9804	586.6818	0.00595
7.2028	706.5981	0.00595
8.5069	834.5314	0.00661
10.0245	983.3991	0.00755
11.7642	1154.0652	0.00785
13.7030	1344.2635	0.00785
15.6636	1536.6000	0.00785
17.7522	1741.4912	0.00803
19.9150	1953.6587	0.00880
21.9826	2156.4915	0.00880
23.8096	2335.7255	0.00974
25.4355	2495.2239	0.00993
26.5098	2600.6118	0.01040
24.9129	2443.9585	0.01040
3.8593	378.6020	0.00974
3.4791	341.3032	0.00974
3.1523	309.2360	0.00993
3.0420	298.4248	0.01040
2.9319	287.6238	0.01088
2.7147	266.3081	0.01088
2.6048	255.5275	0.01135
2.4954	244.8036	0.01182
2.3858	234.0435	0.01230
2.2778	223.4505	0.01208
2.2773	223.4009	0.01230
2.1688	212.7584	0.01230
2.1688	212.7584	0.01230
2.0593	202.0187	0.01277
2.0588	201.9665	0.01303
2.0036	196.5546	0.01350
1.9491	191.2044	0.01369
1.8402	180.5234	0.01398

Axial stress, σ_v		Axial strain, ε_a
kg/cm^2	kPa	
1.8399	180.4900	0.01416
1.7316	169.8675	0.01416
1.7302	169.7354	0.01493
1.6217	159.0917	0.01511
1.6209	159.0151	0.01558
1.5121	148.3364	0.01606
1.5116	148.2924	0.01635
1.4569	142.9240	0.01682
1.3272	130.1946	0.01730
1.2945	126.9944	0.01748
1.3478	132.2239	0.01796
1.4011	137.4483	0.01843
1.2927	126.8105	0.01891
1.2917	126.7114	0.01967
1.2705	124.6359	0.01938
1.2914	126.6878	0.01985
1.2157	119.2595	0.02015
1.1826	116.0142	0.02080
1.1817	115.9234	0.02157
1.1815	115.9018	0.02175
1.1811	115.8672	0.02204
1.1811	115.8672	0.02204
1.1800	115.7548	0.02299
1.1046	108.3654	0.02318
1.0716	105.1253	0.02394
0.9961	97.7158	0.02442
1.0497	102.9718	0.02442
1.0711	105.0742	0.02442
1.0704	105.0034	0.02507
1.0696	104.9248	0.02580
1.0693	104.9012	0.02602
1.0693	104.9012	0.02602
1.0685	104.8226	0.02675
0.9612	94.2898	0.02723
1.0144	99.5120	0.02741
0.9607	94.2438	0.02770
1.0459	102.6058	0.02788
1.0454	102.5557	0.02836
1.0126	99.3365	0.02912
1.0441	102.4248	0.02960
1.0649	104.4649	0.03007

A4.1.6. Test on the CS5 sample

Sample: CS5

Initial length:	**2.73**
Initial length 1 of section (cm):	**1.77**
Initial length 2 of section (cm):	**1.22**
Initial area of section (cm^2):	**2.1594**
Initial volume (cm^3):	**5.895162**
Initial weight (g):	**6.01**
Initial density, (g/cm^3):	**1.019480041**

a. Equipment and sample at the beginning of the test

b. Initial of the test

c. End of the test

Figure A4 - 7 Simple compression tests on the CS5-sugar cube sample.

Table A4 - 6 Results of Unconfined compression strength tests on the CS5 sample.

Axial stress, σ_v		Axial strain, ε_a
kg/cm^2	kPa	
0.0000	0.0000	0.00000
0.1065	10.4438	0.00048
0.2129	20.8837	0.00066
0.3192	31.3106	0.00114
0.4573	44.8571	0.00161
0.6374	62.5277	0.00190
0.9561	93.7969	0.00209
1.2746	125.0410	0.00238
1.8046	177.0304	0.00286
2.3352	229.0827	0.00304
2.8648	281.0396	0.00333
3.3940	332.9500	0.00381
4.0282	395.1694	0.00429
4.7683	467.7732	0.00476
5.7209	561.2156	0.00495
6.8842	675.3391	0.00524
8.2591	810.2216	0.00542
9.8430	965.5952	0.00590
11.4303	1121.3116	0.00590
13.1984	1294.7674	0.00667
14.9115	1462.8182	0.00667
16.6003	1628.4928	0.00685
18.1779	1783.2497	0.00733
19.0458	1868.3971	0.00780
17.6066	1727.2086	0.00853
15.5166	1522.1794	0.00853
14.4298	1415.5626	0.00923
13.4981	1324.1647	0.00949
12.8627	1261.8320	0.00971
12.3262	1209.2002	0.01044
11.7786	1155.4790	0.01044
11.3726	1115.6512	0.01092
10.8937	1068.6753	0.01139
10.3127	1011.6745	0.01158
9.7791	959.3332	0.01234
9.2487	907.2968	0.01282
8.9337	876.3973	0.01282
8.7192	855.3550	0.01330
8.4549	829.4265	0.01348
8.1163	796.2047	0.01377
7.7663	761.8755	0.01425
7.4477	730.6228	0.01473
7.2344	709.6899	0.01520
7.1247	698.9317	0.01586
7.0199	688.6487	0.01586
6.9117	678.0375	0.01634
6.7026	657.5261	0.01634
6.6994	657.2078	0.01681
6.6450	651.8769	0.01711
6.4848	636.1636	0.01758
6.3759	625.4785	0.01824
6.2695	615.0367	0.01853
6.1115	599.5422	0.01872
6.0354	592.0775	0.01919
5.8248	571.4104	0.01949
5.6362	552.9104	0.01967
5.5301	542.5050	0.01996
5.5796	547.3590	0.02044
5.6307	552.3733	0.02062
5.5223	541.7345	0.02136
5.4168	531.3895	0.02158
5.4154	531.2503	0.02183
5.3100	520.9126	0.02205
5.3074	520.6589	0.02253
5.1994	510.0630	0.02326
5.1982	509.9482	0.02348
4.9889	489.4129	0.02374
4.8840	479.1223	0.02392
4.8802	478.7447	0.02469
4.8585	476.6170	0.02487
4.8769	478.4210	0.02535
4.7716	468.0964	0.02564
4.5623	447.5602	0.02612
4.5614	447.4760	0.02630
4.4542	436.9566	0.02707
4.3497	426.7104	0.02725
4.2449	416.4209	0.02755
4.2441	416.3425	0.02773
4.1393	406.0610	0.02802
4.0330	395.6365	0.02868
4.0310	395.4426	0.02916
4.0298	395.3232	0.02945
4.1324	405.3877	0.02963
4.1304	405.1888	0.03011
3.9226	384.8042	0.03040
3.9012	382.7057	0.03059
3.8683	379.4805	0.03106
3.8148	374.2344	0.03154
3.7106	364.0050	0.03183
3.5855	351.7365	0.03231
3.5024	343.5826	0.03249
3.5013	343.4785	0.03278
3.4996	343.3094	0.03326
3.4972	343.0752	0.03392
3.4961	342.9712	0.03421
3.4945	342.8151	0.03465
3.4938	342.7370	0.03487
3.1854	312.4839	0.03487
2.8756	282.0916	0.03535

A4.1.7. Test on the CS6 sample

Sample: CS6

Initial length:	**2.73**
Initial length 1 of section (cm):	**1.77**
Initial length 2 of section (cm):	**1.185**
Initial area of section (cm^2):	**2.09745**
Initial volume (cm^3):	**5.7260385**
Initial weight (g):	**6.07**
Initial density, (g/cm^3):	**1.060069715**

a. Equipment and sample at the beginning of the test

b. Initial of the test

c. End of the test

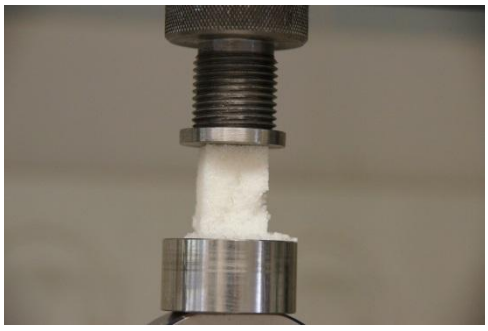

Figure A4 - 8 Simple compression tests on the CS6-sugar cube sample.

Table A4 - 7 Results of Unconfined compression strength tests on the CS6 sample.

Axial stress, σ_v		Axial strain, ε_a
kg/cm^2	kPa	
0.0000	0.0000	0.00000
0.1863	18.2788	0.00048
0.5146	50.4795	0.00066
0.8431	82.7060	0.00095
1.3899	136.3514	0.00161
2.1558	211.4848	0.00161
3.0297	297.2164	0.00209
4.1216	404.3255	0.00256
5.4310	532.7816	0.00304
7.0678	693.3541	0.00333
8.9210	875.1545	0.00381
10.8844	1067.7596	0.00399
12.8433	1259.9229	0.00447
15.0212	1473.5814	0.00476
17.3038	1697.5043	0.00524
19.4809	1911.0793	0.00542
21.6549	2124.3408	0.00571
23.7097	2325.9261	0.00637
25.5545	2506.8954	0.00663
26.9641	2645.1819	0.00685
27.3866	2686.6278	0.00733
23.9803	2352.4676	0.00780
13.6667	1340.6987	0.00806
7.3606	722.0789	0.00806
5.1836	508.5142	0.00853
4.6395	455.1320	0.00875
4.0949	401.7122	0.00901
3.7997	372.7499	0.00949
3.5486	348.1216	0.00996
3.3299	326.6641	0.01044
3.1123	305.3175	0.01062
2.8945	283.9472	0.01092
3.0024	294.5326	0.01110
2.8925	283.7579	0.01158
2.7833	273.0441	0.01187
2.5654	251.6634	0.01234
2.3481	230.3494	0.01282
2.2182	217.6060	0.01282
2.1312	209.0717	0.01300
2.0214	198.2996	0.01377
1.9123	187.5998	0.01425
1.8039	176.9628	0.01443
1.5657	153.5925	0.01473
1.4785	145.0432	0.01520
1.3703	134.4304	0.01568
1.3701	134.4054	0.01586
1.3481	132.2487	0.01615
1.2612	123.7219	0.01663
1.2606	123.6620	0.01711
1.3138	128.8862	0.01758
1.3461	132.0567	0.01758

Axial stress, σ_v		Axial strain, ε_a
kg/cm^2	kPa	
1.3452	131.9680	0.01824
1.2591	123.5191	0.01824
1.2581	123.4224	0.01901
1.1506	112.8695	0.01901
1.1285	110.7052	0.01949
1.1498	112.7936	0.01967
1.1492	112.7389	0.02015
1.1489	112.7094	0.02040
1.1481	112.6293	0.02110
1.1478	112.5998	0.02136
1.1472	112.5450	0.02183
1.2331	120.9630	0.02183
1.1464	112.4649	0.02253
1.1997	117.6915	0.02278
1.2527	122.8878	0.02326
1.3595	133.3699	0.02344
1.3589	133.3048	0.02392
1.2512	122.7449	0.02440
1.1439	112.2163	0.02469
1.0368	101.7054	0.02487
1.0151	99.5775	0.02516
0.9289	91.1265	0.02582
0.9607	94.2420	0.02612
1.0349	101.5258	0.02659
1.0349	101.5258	0.02659
0.9276	90.9929	0.02725
1.0126	99.3343	0.02755
1.0121	99.2856	0.02802
0.9266	90.9038	0.02821
0.9264	90.8764	0.02850
0.8512	83.5041	0.02916
0.9255	90.7873	0.02945
0.8186	80.3073	0.02993
0.7123	69.8719	0.02993
0.8181	80.2527	0.03059
0.8710	85.4411	0.03088
0.8177	80.2133	0.03106
0.8173	80.1739	0.03154
0.7958	78.0667	0.03183
0.8166	80.1102	0.03231
0.9226	90.5029	0.03249
0.9751	95.6597	0.03297
1.0278	100.8305	0.03326
0.9212	90.3693	0.03392
0.9212	90.3693	0.03392
0.9207	90.3247	0.03440
0.9205	90.3007	0.03465
0.9198	90.2356	0.03535
0.9198	90.2356	0.03535
0.9191	90.1671	0.03608
0.9189	90.1465	0.03630

Axial stress, σ_v		Axial strain, ε_a
kg/cm^2	kPa	
0.9504	93.2318	0.03656
0.9182	90.0780	0.03703
0.8439	82.7858	0.03751
0.8122	79.6796	0.03751
0.8117	79.6250	0.03817
0.8114	79.6008	0.03846
0.8110	79.5614	0.03894
0.7056	69.2229	0.03894

Axial stress, σ_v		Axial strain, ε_a
kg/cm^2	kPa	
0.6000	58.8552	0.03941
0.5998	58.8440	0.03960
0.3892	38.1812	0.03960
0.3892	38.1812	0.03960
0.3681	36.1149	0.03960
0.2844	27.8947	0.03960

A4.1.8. Test on the CS7 sample

Sample: CS7

Initial length:	**2.73**
Initial length 1 of section (cm):	**1.77**
Initial length 2 of section (cm):	**1.2**
Initial area of section (cm^2):	**2.124**
Initial volume (cm^3):	**5.79852**
Initial weight (g):	**6.05**
Initial density, (g/cm^3):	**1.043369687**

a. Equipment and sample at the beginning of the test

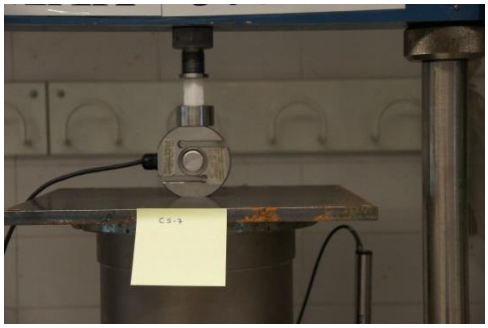

b. Initial of the test

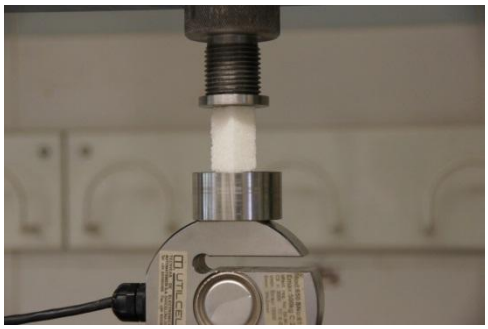

c. End of the test

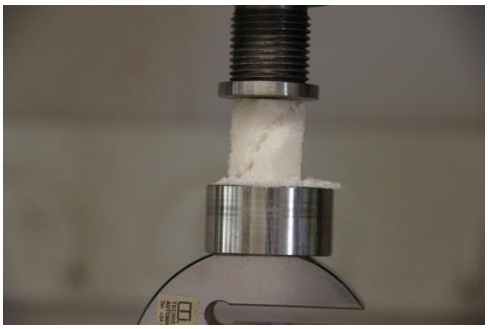

Figure A4 - 9 Simple compression tests on the CS7-sugar cube sample.

Table A4 - 8 Results of Unconfined compression strength tests on the CS7 sample.

Axial stress, σ_v		Axial strain, ε_a
kg/cm^2	kPa	
0.0000	0.0000	0.00000
0.0325	3.1853	0.00048
0.1407	13.8006	0.00066
0.2488	24.4049	0.00114
0.3568	35.0054	0.00143
0.5183	50.8466	0.00190
0.7882	77.3192	0.00234
1.0040	98.4934	0.00256
1.2194	119.6276	0.00304
1.5424	151.3143	0.00330
1.9189	188.2403	0.00399
2.4036	235.7917	0.00425
2.9402	288.4327	0.00495
3.6385	356.9363	0.00538
4.4428	435.8415	0.00615
5.3008	520.0064	0.00663
6.2643	614.5245	0.00729
7.5479	740.4498	0.00806
9.0491	887.7161	0.00824
10.7637	1055.9235	0.00853
12.4723	1223.5331	0.00919
14.5029	1422.7366	0.00967
16.6924	1637.5205	0.01015
18.9011	1854.1991	0.01062
21.2036	2080.0735	0.01062
23.2635	2282.1497	0.01092
25.1415	2466.3857	0.01158
26.3506	2584.9891	0.01158
23.8296	2337.6847	0.01187
4.6313	454.3292	0.01187
3.7753	370.3548	0.01187
3.4547	338.9100	0.01187
3.2407	317.9164	0.01187
3.0262	296.8677	0.01205
2.8114	275.7962	0.01234
2.5970	254.7654	0.01253
2.4905	244.3212	0.01253

Axial stress, σ_v		Axial strain, ε_a
kg/cm^2	kPa	
2.3825	233.7186	0.01300
2.1670	212.5833	0.01377
1.9744	193.6895	0.01396
1.8463	181.1200	0.01396
1.6319	160.0934	0.01443
1.5248	149.5793	0.01473
1.4179	139.0911	0.01520
1.2786	125.4306	0.01568
1.0972	107.6348	0.01586
0.9901	97.1334	0.01634
0.8834	86.6615	0.01659
0.8508	83.4684	0.01729
0.7764	76.1609	0.01729
0.7760	76.1240	0.01777
0.7758	76.1041	0.01802
0.6904	67.7261	0.01850
0.6688	65.6090	0.01897
0.6687	65.5968	0.01916
0.6685	65.5772	0.01945
0.6685	65.5772	0.01945
0.6678	65.5135	0.02040
0.6677	65.5012	0.02059
0.6674	65.4694	0.02106
0.6670	65.4375	0.02154
0.5609	55.0270	0.02183
0.5608	55.0166	0.02201
0.4547	44.6059	0.02249
0.4545	44.5842	0.02297
0.4543	44.5708	0.02326
0.4543	44.5624	0.02344
0.4541	44.5491	0.02374
0.4539	44.5273	0.02421

A4.1.9. Test on the CS8 sample

Sample: CS8

Initial length:	**2.74**
Initial length 1 of section (cm):	**1.77**
Initial length 2 of section (cm):	**1.185**
Initial area of section (cm^2):	**2.09745**
Initial volume (cm^3):	**5.747013**
Initial weight (g):	**5.98**
Initial density, (g/cm^3):	**1.040540538**

a. Equipment and sample at the beginning of the test

b. Initial of the test

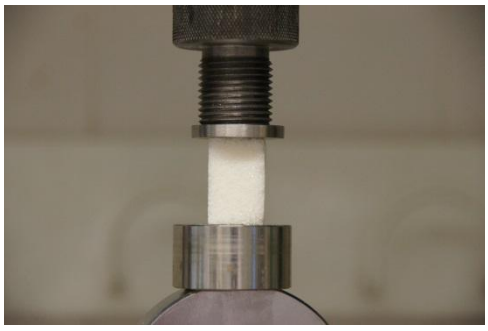

c. End of the test

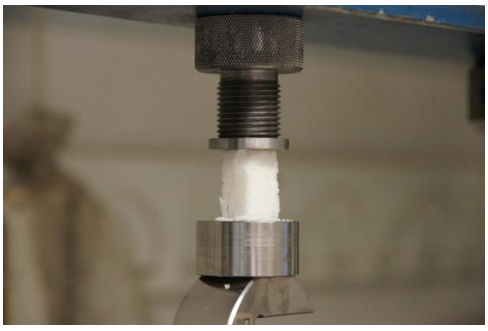

Figure A4 - 10 Simple compression tests on the CS8-sugar cube sample.

Table A4 - 9 Results of Unconfined compression strength tests on the CS8 sample.

Axial stress, σ_v		Axial strain, ε_a
kg/cm^2	kPa	
0.0000	0.0000	0.00000
0.1096	10.7522	0.00047
0.2192	21.5006	0.00066
0.2191	21.4904	0.00113
0.3285	32.2261	0.00142
0.3284	32.2202	0.00161
0.4372	42.8932	0.00208
0.5465	53.6144	0.00234
0.6337	62.1706	0.00281
0.6556	64.3161	0.00281
0.6881	67.5021	0.00328
0.7095	69.5980	0.00398
0.8185	80.2920	0.00423
0.8727	85.6071	0.00471
1.0691	104.8791	0.00471
1.1995	117.6711	0.00518
1.3952	136.8686	0.00566
1.5253	149.6304	0.00584
1.6338	160.2779	0.00613
1.8515	181.6273	0.00631
2.0684	202.9092	0.00679
2.5033	245.5743	0.00708
2.8290	277.5204	0.00726
3.2411	317.9494	0.00774
3.6965	362.6276	0.00803
4.2396	415.9059	0.00821
4.8902	479.7324	0.00850
5.6503	554.2914	0.00869
6.4088	628.7072	0.00898
7.1678	703.1567	0.00916
8.1210	796.6730	0.00945
9.0117	884.0495	0.00945
9.9870	979.7236	0.00964
11.1758	1096.3425	0.01011
12.3652	1213.0266	0.01040
13.6427	1338.3498	0.01058
14.9072	1462.4008	0.01088
16.2331	1592.4666	0.01135
17.3894	1705.9026	0.01153
18.1932	1784.7489	0.01201
18.7293	1837.3467	0.01230
19.4834	1911.3226	0.01248
19.9006	1952.2524	0.01325
17.1588	1683.2768	0.01420
1.6175	158.6770	0.01606
1.7250	169.2239	0.01628
1.8324	179.7595	0.01653
1.7237	169.0984	0.01701
1.7234	169.0607	0.01723
1.6682	163.6530	0.01796
1.6140	158.3356	0.01818

Axial stress, σ_v		Axial strain, ε_a
kg/cm^2	kPa	
1.5060	147.7353	0.01843
1.4299	140.2762	0.01891
1.3974	137.0895	0.01938
1.3972	137.0640	0.01956
1.5038	147.5211	0.01985
1.7184	168.5773	0.02004
1.8253	179.0657	0.02033
1.8245	178.9790	0.02080
1.8236	178.8923	0.02128
1.8769	184.1222	0.02146
1.8223	178.7722	0.02193
1.7143	168.1692	0.02241
1.7143	168.1692	0.02241
1.8200	178.5454	0.02318
1.9262	188.9616	0.02365
1.9039	186.7702	0.02412
1.8174	178.2852	0.02460
1.7957	176.1537	0.02478
1.7630	172.9547	0.02507
1.7088	167.6293	0.02555
1.7084	167.5979	0.02573
1.8147	178.0251	0.02602
1.7605	172.7022	0.02650
1.8135	177.9050	0.02668
1.8126	177.8183	0.02715
1.7054	167.3028	0.02745
1.7046	167.2212	0.02792
1.7051	167.2714	0.02763
1.8109	177.6448	0.02810
1.8100	177.5581	0.02858
1.8094	177.5047	0.02887
1.7878	175.3824	0.02905
1.7021	166.9763	0.02934
1.5949	156.4640	0.02978
1.5946	156.4287	0.03000
1.5725	154.2663	0.03047
1.4127	138.5854	0.03073
1.3806	135.4364	0.03120
1.3803	135.4058	0.03142
1.3796	135.3395	0.03190
1.3792	135.3038	0.03215
1.2725	124.8311	0.03263
1.2722	124.8075	0.03281
1.2716	124.7463	0.03328
1.3770	135.0793	0.03376
1.4820	145.3843	0.03405
1.3759	134.9721	0.03453
1.3756	134.9466	0.03471
1.3538	132.8045	0.03518
1.3745	134.8395	0.03547
1.3738	134.7731	0.03595

Axial stress, σ_v		Axial strain, ε_a
kg/cm^2	kPa	
1.3736	134.7476	0.03613
1.3725	134.6405	0.03690
1.3725	134.6405	0.03690
1.3715	134.5486	0.03755
1.3711	134.5078	0.03785
1.3702	134.4160	0.03850
1.3702	134.4160	0.03850
1.3695	134.3497	0.03898
1.3691	134.3088	0.03927
1.3474	132.1766	0.03974
1.2947	127.0117	0.03974
1.3467	132.1113	0.04022
1.2619	123.7903	0.04069
1.1567	113.4707	0.04069
1.0510	103.1001	0.04117
1.0502	103.0294	0.04182
0.9452	92.7220	0.04182
0.9444	92.6478	0.04259
0.8393	82.3330	0.04277
0.7339	72.0000	0.04325
0.5764	56.5468	0.04350
0.5239	51.3903	0.04372
0.5237	51.3766	0.04398
0.5233	51.3393	0.04467
0.5232	51.3256	0.04493

Axial stress, σ_v		Axial strain, ε_a
kg/cm^2	kPa	
0.5231	51.3138	0.04515
0.5018	49.2218	0.04588
0.4180	41.0029	0.04606
0.4178	40.9904	0.04635
0.4176	40.9700	0.04682
0.4176	40.9621	0.04701
0.4487	44.0157	0.04748
0.4171	40.9213	0.04796
0.4170	40.9088	0.04825
0.4168	40.8884	0.04872
0.4689	45.9962	0.04891
0.5208	51.0863	0.04938
0.5205	51.0608	0.04985
0.5203	51.0451	0.05015
0.5202	51.0353	0.05033
0.5200	51.0098	0.05080
0.5198	50.9941	0.05109
0.5196	50.9686	0.05157
0.5193	50.9431	0.05204
0.5192	50.9333	0.05223
0.5188	50.8921	0.05299
0.4980	48.8547	0.05299
0.3941	38.6599	0.05318

A4.1.10. Test on the CS9 sample

Sample: CS9

Initial length:	**2.73**
Initial length 1 of section (cm):	**1.77**
Initial length 2 of section (cm):	**1.205**
Initial area of section (cm^2):	**2.13285**
Initial volume (cm^3):	**5.8226805**
Initial weight (g):	**5.94**
Initial density, (g/cm^3):	**1.02014871**

a. Equipment and sample at the beginning of the test

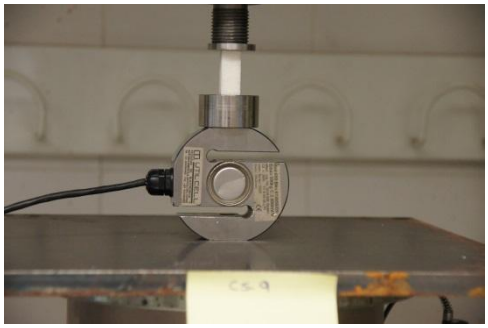

b. Initial of the test

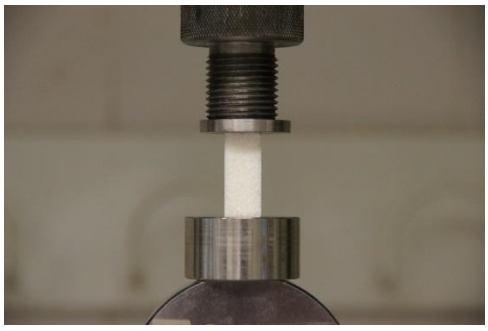

c. End of the test

Figure A4 - 11 Simple compression tests on the CS9-sugar cube sample.

Table A4 - 10 Results of Unconfined compression strength tests on the CS9 sample.

Axial stress, σ_v		Axial strain, ε_a
kg/cm^2	kPa	
0.0000	0.0000	0.00000
0.2156	21.1475	0.00048
0.2155	21.1437	0.00066
0.4305	42.2290	0.00095
0.5379	52.7725	0.00143
0.7532	73.8863	0.00161
0.9678	94.9367	0.00238
1.3440	131.8501	0.00256
1.7518	171.8501	0.00286
2.1487	210.7869	0.00330
2.5769	252.7959	0.00377
3.2200	315.8782	0.00425
4.1839	410.4407	0.00473
5.3092	520.8324	0.00495
6.7541	662.5770	0.00542
8.3062	814.8365	0.00568
10.0696	987.8309	0.00615
11.9961	1176.8150	0.00634
13.9198	1365.5325	0.00663
15.9465	1564.3555	0.00711
17.9499	1760.8874	0.00758
19.8931	1951.5103	0.00777
21.8117	2139.7266	0.00806
23.5227	2307.5778	0.00806
24.4687	2400.3776	0.00872
21.4603	2105.2553	0.00949
4.6952	460.6020	0.00996
4.6205	453.2706	0.00996
4.7775	468.6684	0.01062
4.5325	444.6411	0.01062
4.3478	426.5163	0.01139
4.3683	428.5286	0.01158
4.5801	449.3081	0.01187
4.7904	469.9425	0.01234
4.7896	469.8554	0.01253
4.5748	448.7917	0.01300
4.3607	427.7822	0.01330
4.2522	417.1426	0.01377
4.2502	416.9412	0.01425
4.2502	416.9412	0.01425
4.1431	406.4376	0.01443
4.0337	395.7024	0.01520
4.1391	406.0449	0.01538
4.0317	395.5111	0.01568
3.8176	374.5039	0.01615
3.4981	343.1593	0.01663
3.4753	340.9262	0.01707
3.3685	330.4541	0.01729
3.2829	322.0533	0.01755
3.1542	309.4314	0.01802
2.5401	249.1802	0.01802
2.5383	249.0035	0.01872
2.6434	259.3166	0.01897
2.7486	269.6342	0.01919
2.6416	259.1423	0.01963
2.6403	259.0164	0.02011
2.6395	258.9389	0.02040
2.6179	256.8183	0.02059
2.5314	248.3343	0.02136
2.5310	248.2878	0.02154
2.4247	237.8661	0.02201
2.3193	227.5202	0.02201
2.3186	227.4520	0.02231
2.2116	216.9627	0.02297
2.2110	216.8977	0.02326
2.1046	206.4642	0.02374
1.8937	185.7740	0.02392
1.7879	175.3955	0.02421
1.7660	173.2464	0.02469
1.5759	154.5992	0.02516
1.4701	144.2161	0.02564
1.2602	123.6226	0.02582
1.1546	113.2616	0.02630
1.1546	113.2616	0.02630
0.9443	92.6325	0.02659
0.8389	82.2948	0.02707
0.7338	71.9888	0.02725
0.6286	61.6681	0.02773
0.5235	51.3574	0.02821
0.5234	51.3419	0.02850
0.4184	41.0445	0.02897
0.4183	41.0368	0.02916
0.3974	38.9827	0.02916
0.3657	35.8731	0.02993
0.3138	30.7808	0.03011
0.3137	30.7715	0.03040
0.3135	30.7576	0.03084
0.3134	30.7425	0.03132
0.3133	30.7355	0.03154
0.2088	20.4849	0.03179
0.2087	20.4748	0.03227
0.2087	20.4748	0.03227
0.2086	20.4601	0.03297
0.2085	20.4508	0.03341
0.2397	23.5113	0.03370
0.2084	20.4407	0.03388
0.2083	20.4307	0.03436
0.2082	20.4206	0.03484
0.1353	13.2734	0.03484
0.1040	10.2022	0.03560
0.2080	20.4043	0.03560
0.2079	20.3942	0.03608
0.2078	20.3842	0.03656
0.2078	20.3803	0.03674
0.1557	15.2777	0.03722
0.1038	10.1820	0.03751
0.0830	8.1400	0.03817

A4.1.11. Test on the CS10 sample

Sample: CS10

Initial length:	**2.735**
Initial length 1 of section (cm):	**1.77**
Initial length 2 of section (cm):	**1.185**
Initial area of section (cm^2):	**2.09745**
Initial volume (cm^3):	**5.73652575**
Initial weight (g):	**5.91**
Initial density, (g/cm^3):	**1.030240298**

a. Equipment and sample at the beginning of the test

b. Initial of the test

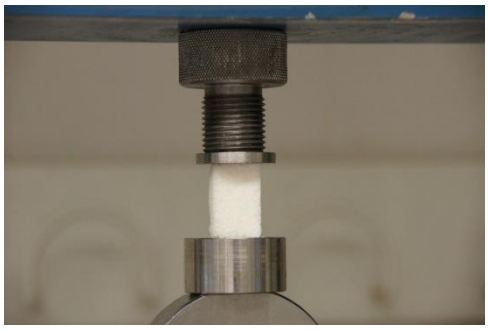

c. End of the test

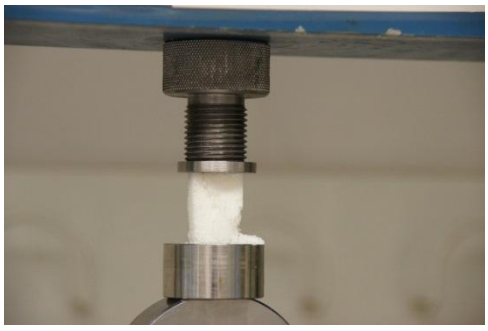

Figure A4 - 12 Simple compression tests on the CS10-sugar cube sample.

Table A4 - 11 Results of Unconfined compression strength tests on the CS10 sample.

Axial stress, σ_v		Axial strain, ε_a
kg/cm^2	kPa	
0.0000	0.0000	0.00000
0.1096	10.7522	0.00048
0.3287	32.2414	0.00095
0.4382	42.9885	0.00095
0.4380	42.9680	0.00143
0.5473	53.6943	0.00172
0.6559	64.3440	0.00238
0.7651	75.0538	0.00267
0.7647	75.0180	0.00314
0.9833	96.4651	0.00314
0.9829	96.4191	0.00362
1.0919	107.1178	0.00380
1.2876	126.3146	0.00453
1.5270	149.8019	0.00501
1.9626	192.5268	0.00523
2.3989	235.3312	0.00523
3.1612	310.1126	0.00548
3.9214	384.6856	0.00618
4.9022	480.9035	0.00618
6.2044	608.6529	0.00691
7.8360	768.7101	0.00709
9.4637	928.3882	0.00757
11.3099	1109.5055	0.00786
13.2649	1301.2830	0.00804
15.3159	1502.4944	0.00899
17.4123	1708.1511	0.00899
19.5428	1917.1521	0.00947
21.5953	2118.4965	0.00995
23.1079	2266.8853	0.01024
23.5698	2312.1949	0.01042
17.3381	1700.8642	0.01137
5.5791	547.3106	0.01166
3.8978	382.3787	0.01214
3.2493	318.7587	0.01185
3.0303	297.2677	0.01261
2.7054	265.3998	0.01280
2.4877	244.0429	0.01327
2.2702	222.7064	0.01375
2.1945	215.2798	0.01375
2.0523	201.3306	0.01452
1.9223	188.5742	0.01470
1.8353	180.0413	0.01499
1.6186	158.7891	0.01565
1.5107	148.2001	0.01565
1.4021	137.5446	0.01612
1.4017	137.5037	0.01642
1.2932	126.8616	0.01689
1.0774	105.6907	0.01707
1.0769	105.6396	0.01755
0.9687	95.0250	0.01803

Axial stress, σ_v		Axial strain, ε_a
kg/cm^2	kPa	
0.9684	95.0003	0.01828
0.8606	84.4207	0.01850
0.8601	84.3798	0.01898
0.8599	84.3578	0.01923
0.7522	73.7908	0.01945
0.7520	73.7716	0.01971
0.7515	73.7221	0.02037
0.7513	73.7000	0.02066
0.7513	73.7000	0.02066
0.7509	73.6643	0.02113
0.8578	84.1534	0.02161
0.8573	84.0968	0.02227
0.8570	84.0716	0.02256
0.9106	89.3290	0.02256
0.8566	84.0308	0.02303
0.7489	73.4717	0.02369
0.7487	73.4497	0.02399
0.7487	73.4497	0.02399
0.8552	83.8924	0.02464
0.9618	94.3563	0.02494
0.9614	94.3103	0.02541
0.9609	94.2643	0.02589
0.7471	73.2928	0.02607
0.7468	73.2570	0.02654
0.7465	73.2350	0.02684
0.7464	73.2213	0.02702
0.7994	78.4163	0.02750
0.7778	76.3010	0.02779
0.7243	71.0584	0.02797
0.6388	62.6626	0.02845
0.6385	62.6320	0.02892
0.6381	62.6013	0.02940
0.5320	52.1899	0.02969
0.4787	46.9620	0.02987
0.4253	41.7236	0.03035
0.2126	20.8555	0.03064
0.2125	20.8453	0.03112
0.2124	20.8358	0.03155
0.2123	20.8311	0.03177
0.2122	20.8209	0.03225
0.1061	10.4077	0.03250
0.1061	10.4053	0.03272
0.1060	10.4002	0.03320
0.0848	8.3180	0.03346

A4.2. Analysis of imposed load in oedometer tests

Table A4 - 12 Results of Oedometer tests performed.

Sample		σ_{vmax} kPa	$e_{o(Initial)}$	$e_{(Final\ \sigma vmax)}$	$e_{(Final\ Unloading)}$
Ordered:	M1	120	0.20	0.20	0.20
	M2	240	0.18	0.17	0.17
	M3	240	0.17	0.16	0.16
	M5	440	0.18	0.16	0.17
	M9	640	0.17	0.16	0.16
Disordered:	M7	30	0.80	0.79	0.79
	M6	60	0.74	0.73	0.73
	M4	120	0.87	0.82	0.82
	M8	440	0.72	0.66	0.66

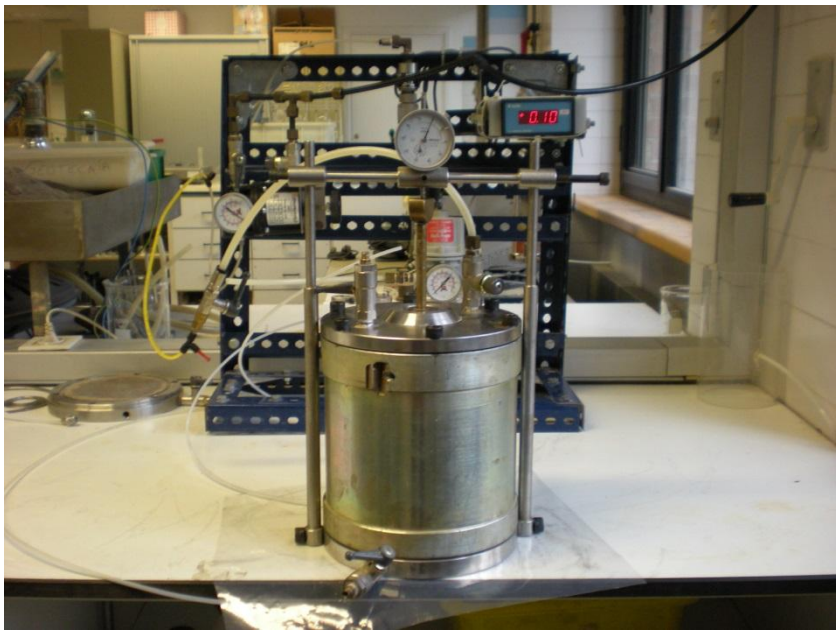

Figure A4 - 13 Oedometer equipment - Rowe cells (Inner diameter 152mm).

A4.2.1. Ordered Arrangements

A4.2.1.1. Sample M1

Sample:	M1
Arrangement of sugar cubes:	Ordered
Maximum vertical stress (kPa):	120
Initial number of sugar cubes:	277

a. Initial: Layer in the upper part

b. End of the test: Layer in the upper part

c. End of the test: Layer 1 in the middle part

d. End of the test: Layer 2 in the middle part

Figure A4 - 14 Sample M1 (Ordered arrangement of sugar cubes, e_o=0.20) inside the oedometer cell (diameter 152mm). (a) Before the test; (b), (c), (d) At the end of the test.

Table A4 - 13 Results of a sieve analysis after the oedometer test on sample M1. Ordered arrangement of sugar cubes.

Sieve			Retained weight on each sieve		% Finer
No.		Opening (mm)	(g)	(%)	
1"		25	0	0.00	100.00
1/2"	Intact original cubes [(a)]	22.37	1569.18	95.03	4.97
	Original cubes damaged locally (local crushing) [(b)]	22.37	0		
	Cubes after a first splitting of the original sugar cubes [(c)]	12.1	36.13	2.19	2.78
3/8"		9.5	16.5	1.00	1.78
No. 4		4.75	3.53	0.21	1.57
No. 10		2.0	1.18	0.07	1.49
No. 16		1.18	0.74	0.04	1.45
No. 40		0.425	14.8	0.90	0.55
No. 100		0.15	8.85	0.54	0.02
No. 200		0.075	1.59	0.10	0.03
Pan			0.57	0.03	

(a), (b), (c): Particles retained on sieve No. 1/2"

Part I of **Figure A4 - 15**

a. Intact particles: Retained in Sieve 1/2”- 12.1mm

null

b. Particles with local crushing: Retained in Sieve 1/2”- 12.1mm

c. Splitting crushing: Retained in Sieve 1/2”- 12.1mm

d. Particles retained in Sieve 3/8”- 9.5mm

e. Particles retained in Sieve # 4 - 4.75mm

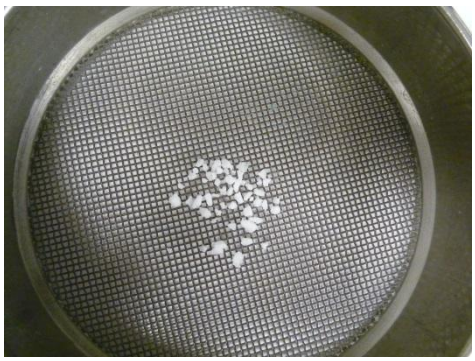

f. Particles retained in Sieve # 10 - 2.0mm

Part II of **Figure A4 - 15**

g. Particles retained in Sieve # 16 - 1.18mm

h. Particles retained in Sieve # 40 - 0.425mm (Sugar Crystals)

i. Particles retained in Sieve # 100 – 0.15mm

j. Particles retained in Sieve # 200 – 0.075mm

Figure A4 - 15 Particle breakage after oedometer test: Retained particles by sieve on sample M1. Ordered arrangement of sugar cubes.

A4.2.1.2. Sample M2

Sample:	M2
Arrangement of sugar cubes:	Ordered
Maximum vertical stress (kPa):	240
Initial number of sugar cubes:	283

a. Initial: Layer in the upper part

b. End of the test: Layer in the upper part

c. End of the test: Layer in the middle part

d. End of the test: Details of Layer in the middle part

Figure A4 - 16 Sample M2 (Ordered arrangement of sugar cubes, e_o=0.18) inside the oedometer cell (diameter 152mm). (a) Before the test; (b), (c), (d) At the end of the test.

Table A4 - 14 Results of a sieve analysis after the oedometer test on sample M2. Ordered arrangement of sugar cubes.

Sieve			Retained weight on each sieve		% Finer
No.		Opening (mm)	(g)	(%)	
1"		25	0	0.00	100.00
1/2"	Intact original cubes [a]	22.37	1428.77	84.61	15.39
	Original cubes damaged locally (local crushing) [b]	22.37	0		
	Cubes after a first splitting of the original sugar cubes [c]	12.1	99.45	5.89	9.50
3/8"		9.5	58.84	3.48	6.02
No. 4		4.75	23.42	1.39	4.63
No. 10		2.0	5.78	0.34	4.29
No. 16		1.18	3.96	0.23	4.05
No. 40		0.425	49.7	2.94	1.11
No. 100		0.15	16.99	1.01	0.11
No. 200		0.075	1.32	0.08	0.03
Pan			0.46	0.03	

(a), (b), (c): Particles retained on sieve No. 1/2"

Part I of **Figure A4 - 17**

a. Intact particles: Retained in Sieve 1/2”- 12.1mm

null

b. Particles with local crushing: Retained in Sieve 1/2”- 12.1mm

c. Splitting crushing: Retained in Sieve 1/2”- 12.1mm

d. Particles retained in Sieve 3/8”- 9.5mm

e. Particles retained in Sieve # 4 - 4.75mm

f. Particles retained in Sieve # 10 - 2.0mm

Part II of **Figure A4 - 17**

g. Particles retained in Sieve # 16 - 1.18mm

h. Particles retained in Sieve # 40 - 0.425mm (Sugar Crystals)

i. Particles retained in Sieve # 100 – 0.15mm

j. Particles retained in Sieve # 200 – 0.075mm

Figure A4 - 17 Particle breakage after oedometer test: Retained particles by sieve on sample M2. Ordered arrangement of sugar cubes.

A4.2.1.3. Sample M3

Sample:	M3
Arrangement of sugar cubes:	Ordered
Maximum vertical stress (kPa):	240
Initial number of sugar cubes:	188

a. Initial: Layer in the upper part

b. End of the test: Layer in the upper part

c. End of the test: Layer in the middle part

d. End of the test: Details of Layer in the middle part

Figure A4 - 18 Sample M3 (Ordered arrangement of sugar cubes, e_o=0.17) inside the oedometer cell (diameter 152mm). (a) Before the test; (b), (c), (d) At the end of the test.

Table A4 - 15 Results of a sieve analysis after the oedometer test on sample M3. Ordered arrangement of sugar cubes.

Sieve			Retained weight on each sieve		% Finer
No.		Opening (mm)	(g)	(%)	
1"		25	0	0.00	100.00
1/2"	Intact original cubes [a]	22.37	1053.26	94.11	5.89
	Original cubes damaged locally (local crushing) [b]	22.37	0		
	Cubes after a first splitting of the original sugar cubes [c]	12.1	37.56	3.36	2.54
3/8"		9.5	15.26	1.36	1.17
No. 4		4.75	1.38	0.12	1.05
No. 10		2.0	0.35	0.03	1.02
No. 16		1.18	0.31	0.03	0.99
No. 40		0.425	2.73	0.24	0.75
No. 100		0.15	0.95	0.08	0.66
No. 200		0.075	0	0.66	0.00
Pan			0	0.00	

(a), (b), (c): Particles retained on sieve No. 1/2"

Part I of **Figure A4 - 19**

null

a. Intact particles: Retained in Sieve 1/2”- 12.1mm

b. Particles with local crushing: Retained in Sieve 1/2”- 12.1mm

c. Splitting crushing: Retained in Sieve 1/2”- 12.1mm

d. Particles retained in Sieve 3/8”- 9.5mm

e. Particles retained in Sieve # 4 - 4.75mm

f. Particles retained in Sieve # 10 - 2.0mm

Part II of **Figure A4 - 19**

g. Particles retained in Sieve # 16 - 1.18mm

h. Particles retained in Sieve # 40 - 0.425mm (Sugar Crystals)

i. Particles retained in Sieve # 100 – 0.15mm

null

j. Particles retained in Sieve # 200 – 0.075mm

Figure A4 - 19 Particle breakage after oedometer test: Retained particles by sieve on sample M3. Ordered arrangement of sugar cubes.

A4.2.1.4. Sample M5

Sample:	M5
Arrangement of sugar cubes:	Ordered
Maximum vertical stress (kPa):	440
Initial number of sugar cubes:	188

a. Initial: Layer in the upper part

b. End of the test: Layer in the upper part

c. End of the test: Layer in the middle part

d. End of the test: Layer in the lower part

Figure A4 - 20 Sample M5 (Ordered arrangement of sugar cubes, e_o=0.18) inside the oedometer cell (diameter 152mm). (a) Before the test; (b), (c), (d) At the end of the test.

Table A4 - 16 Results of a sieve analysis after the oedometer test on sample M5. Ordered arrangement of sugar cubes.

Sieve			Retained weight on each sieve		% Finer
No.		Opening (mm)	(g)	(%)	
1"		25	0	0.00	100.00
1/2"	Intact original cubes [a]	22.37	149.48	17.92	82.08
	Original cubes damaged locally (local crushing) [b]	22.37	51.02		
	Cubes after a first splitting of the original sugar cubes [c]	12.1	221.77	19.82	62.26
3/8"		9.5	131.63	11.76	50.50
No. 4		4.75	110.78	9.90	40.60
No. 10		2.0	28.62	2.56	38.04
No. 16		1.18	23.69	2.12	35.92
No. 40		0.425	323.21	28.88	7.04
No. 100		0.15	73.1	6.53	0.51
No. 200		0.075	4.26	0.51	0.00
Pan			0	0.00	

(a), (b), (c): Particles retained on sieve No. 1/2"

Part I of **Figure A4 - 21**

a. Intact particles: Retained in Sieve 1/2”- 12.1mm

b. Particles with local crushing: Retained in Sieve 1/2”- 12.1mm

c. Splitting crushing: Retained in Sieve 1/2”- 12.1mm

d. Particles retained in Sieve 3/8”- 9.5mm

e. Particles retained in Sieve # 4 - 4.75mm

f. Particles retained in Sieve # 10 - 2.0mm

Part II of **Figure A4 - 21**

g. Particles retained in Sieve # 16 - 1.18mm

h. Particles retained in Sieve # 40 - 0.425mm (Sugar Crystals)

i. Particles retained in Sieve # 100 – 0.15mm

j. Particles retained in Sieve # 200 – 0.075mm

Figure A4 - 21 Particle breakage after oedometer test: Retained particles by sieve on sample M5. Ordered arrangement of sugar cubes.

A4.2.1.5. Sample M9

Sample:	M9
Arrangement of sugar cubes:	Ordered
Maximum vertical stress (kPa):	640
Initial number of sugar cubes:	192

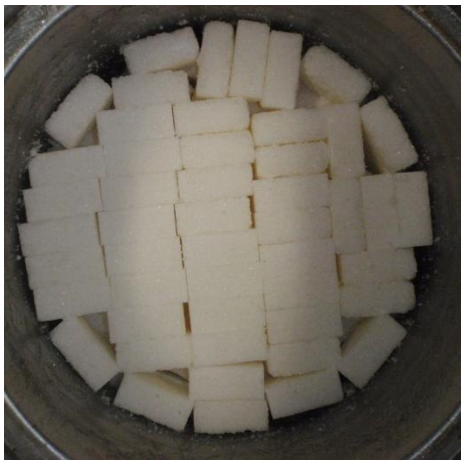

a. Initial: Layer in the upper part

b. End of the test: Layer in the upper part

c. End of the test: Layer in the middle part

d. End of the test: Details of Layer in the middle part

Figure A4 - 22 Sample M9 (Ordered arrangement of sugar cubes, e_o=0.17) inside the oedometer cell (diameter 152mm). (a) Before the test; (b), (c), (d) At the end of the test.

Table A4 - 17 Results of a sieve analysis after the oedometer test on sample M9. Ordered arrangement of sugar cubes.

Sieve			Retained weight on each sieve		% Finer
No.		Opening (mm)	(g)	(%)	
1"		25	0	0.00	100.00
1/2"	Intact original cubes [a]	22.37	114.65	13.30	86.70
	Original cubes damaged locally (local crushing) [b]	22.37	38.09		
	Cubes after a first splitting of the original sugar cubes [c]	12.1	218.06	18.99	67.70
3/8"		9.5	106.99	9.32	58.38
No. 4		4.75	112.39	9.79	48.59
No. 10		2.0	29.95	2.61	45.99
No. 16		1.18	27.24	2.37	43.61
No. 40		0.425	411.54	35.85	7.77
No. 100		0.15	85.4	7.44	0.33
No. 200		0.075	1.76	0.33	0.00
Pan			0	0.00	

(a), (b), (c): Particles retained on sieve No. 1/2"

Part I of **Figure A4 - 23**

a. Intact particles: Retained in Sieve 1/2”- 12.1mm

b. Particles with local crushing: Retained in Sieve 1/2”- 12.1mm

c. Splitting crushing: Retained in Sieve 1/2”- 12.1mm

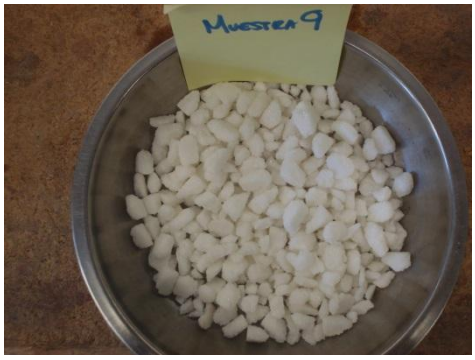

d. Particles retained in Sieve 3/8”- 9.5mm

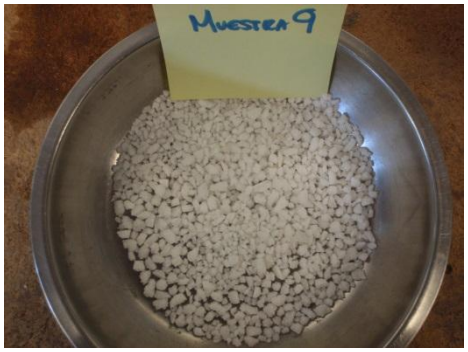

e. Particles retained in Sieve # 10 - 2.0mm

Part II of **Figure A4 - 23**

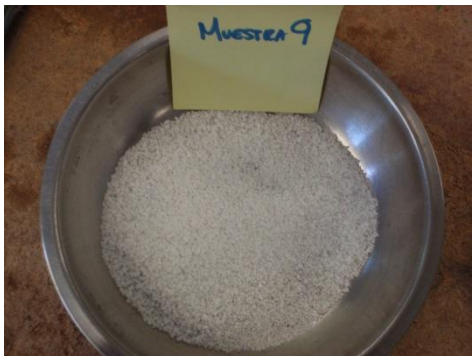

f. Particles retained in Sieve # 16 - 1.18mm

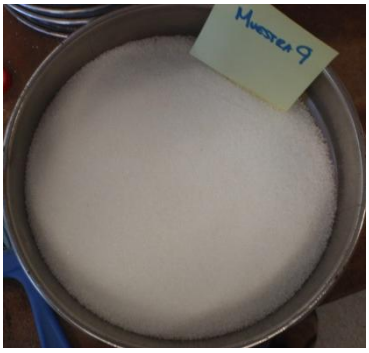

g. Particles retained in Sieve # 40 - 0.425mm (Sugar Crystals)

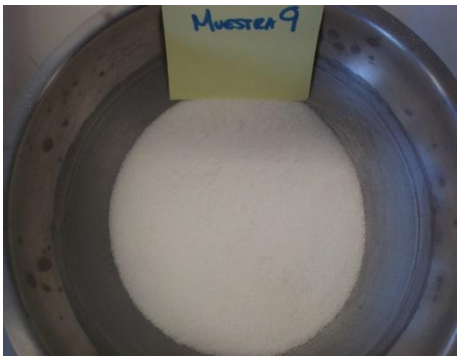

h. Particles retained in Sieve # 100 – 0.15mm

Figure A4 - 23 Particle breakage after oedometer test: Retained particles by sieve on sample M9. Ordered arrangement of sugar cubes.

A4.2.2. Disordered Arrangements

A4.2.2.1. Sample M7

Sample:	M7
Arrangement of sugar cubes:	Disordered
Maximum vertical stress (kPa):	30
Initial number of sugar cubes:	165

a. End of the test: Upper part

b. End of the test: Middle part

c. End of the test: Lower part

Figure A4 - 24 Sample M7 (Disordered arrangement of sugar cubes, e_o=0.80) inside the oedometer cell (diameter 152mm). (a), (b), (c) At the end of the test.

Table A4 - 18 Results of a sieve analysis after the oedometer test on sample M7. Disordered arrangement of sugar cubes.

Sieve			Retained weight on each sieve		% Finer
No.		Opening (mm)	(g)	(%)	
1"		25	0	0.00	100.00
1/2"	Intact original cubes [a]	22.37	946	97.63	2.37
	Original cubes damaged locally (local crushing) [b]	22.37	15.62		
	Cubes after a first splitting of the original sugar cubes [c]	12.1	13.67	1.39	0.98
3/8"		9.5	2.66	0.27	0.71
No. 4		4.75	1.22	0.12	0.58
No. 10		2.0	0.32	0.03	0.55
No. 16		1.18	0.78	0.08	0.47
No. 40		0.425	3.82	0.39	0.09
No. 100		0.15	0.67	0.07	0.02
No. 200		0.075	0	0.02	0.00
Pan			0	0.00	

(a), (b), (c): Particles retained on sieve No. 1/2"

Part I of **Figure A4 - 25**

a. Intact particles: Retained in Sieve 1/2”- 12.1mm

b. Particles with local crushing: Retained in Sieve 1/2”- 12.1mm

c. Splitting crushing: Retained in Sieve 1/2”- 12.1mm

d. Particles retained in Sieve 3/8”- 9.5mm

e. Particles retained in Sieve # 4 - 4.75mm

f. Particles retained in Sieve # 10 - 2.0mm

Part II of **Figure A4 - 29**

g. Particles retained in Sieve # 16 - 1.18mm

h. Particles retained in Sieve # 40 - 0.425mm (Sugar Crystals)

i. Particles retained in Sieve # 100 – 0.15mm

null

j. Particles retained in Sieve # 200 – 0.075mm

Figure A4 - 25 Particle breakage after oedometer test: Retained particles by sieve on sample M7. Disordered arrangement of sugar cubes.

A4.2.2.2. Sample M6

Sample:	M6
Arrangement of sugar cubes:	Disordered
Maximum vertical stress (kPa):	60
Initial number of sugar cubes:	167

Initial: Upper part

Figure A4 - 26 Sample M6 (Disordered arrangement of sugar cubes, e_o=0.74) inside the oedometer cell (diameter 152mm). At the beginning of the test.

Table A4 - 19 Results of a sieve analysis after the oedometer test on sample M6. Disordered arrangement of sugar cubes.

Sieve			Retained weight on each sieve		% Finer
No.		Opening (mm)	(g)	(%)	
1"		25	0	0.00	100.00
1/2"	Intact original cubes [a]	22.37	903.87	95.20	4.80
	Original cubes damaged locally (local crushing) [b]	22.37	45.48		
	Cubes after a first splitting of the original sugar cubes [c]	12.1	22.01	2.21	2.59
3/8"		9.5	4.49	0.45	2.14
No. 4		4.75	2.87	0.29	1.86
No. 10		2.0	1.01	0.10	1.75
No. 16		1.18	4.03	0.40	1.35
No. 40		0.425	8.75	0.88	0.47
No. 100		0.15	2.01	0.20	0.27
No. 200		0.075	0.04	0.27	0.00
Pan			0	0.00	

(a), (b), (c): Particles retained on sieve No. 1/2"

Part I of **Figure A4 - 27**

a. Intact particles: Retained in Sieve 1/2”- 12.1mm

b. Particles with local crushing: Retained in Sieve 1/2”- 12.1mm

c. Splitting crushing: Retained in Sieve 1/2”- 12.1mm

d. Particles retained in Sieve 3/8”- 9.5mm

e. Particles retained in Sieve # 4 - 4.75mm

f. Particles retained in Sieve # 10 - 2.0mm

Part II of **Figure A4 - 27**

g. Particles retained in Sieve # 16 - 1.18mm

h. Particles retained in Sieve # 40 - 0.425mm (Sugar Crystals)

i. Particles retained in Sieve # 100 – 0.15mm

Figure A4 - 27 Particle breakage after oedometer test: Retained particles by sieve on sample M6. Disordered arrangement of sugar cubes.

A4.2.2.3. Sample M4

Sample:	M4
Arrangement of sugar cubes:	Disordered
Maximum vertical stress (kPa):	120
Initial number of sugar cubes:	160

a. End of the test: Upper part

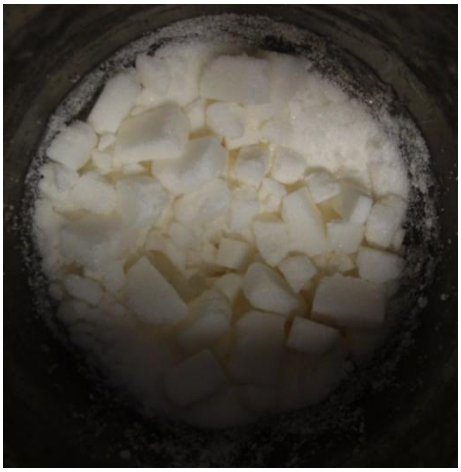

b. End of the test: Middle part

c. End of the test: Lower part

Figure A4 - 28 Sample M4 (Disordered arrangement of sugar cubes, e_o=0.87) inside the oedometer cell (diameter 152mm). (a), (b), (c) At the end of the test.

Table A4 - 20 Results of a sieve analysis after the oedometer test on sample M4. Disordered arrangement of sugar cubes.

Sieve			Retained weight on each sieve		% Finer
No.		Opening (mm)	(g)	(%)	
1"		25	0	0.00	100.00
1/2"	Intact original cubes [(a)]	22.37	177.35	29.20	70.80
	Original cubes damaged locally (local crushing) [(b)]	22.37	102.43		
	Cubes after a first splitting of the original sugar cubes [(c)]	12.1	199.27	20.80	49.99
3/8"		9.5	144.81	15.12	34.88
No. 4		4.75	69.5	7.25	27.62
No. 10		2.0	26.18	2.73	24.89
No. 16		1.18	18.94	1.98	22.91
No. 40		0.425	169.03	17.64	5.27
No. 100		0.15	40.63	4.24	1.03
No. 200		0.075	3.36	1.03	0.00
Pan			0	0.00	

(a), (b), (c): Particles retained on sieve No. 1/2"

Part I of **Figure A4 - 29**

a. Intact particles: Retained in Sieve 1/2”- 12.1mm

b. Particles with local crushing: Retained in Sieve 1/2”- 12.1mm

c. Splitting crushing: Retained in Sieve 1/2”- 12.1mm

d. Particles retained in Sieve 3/8”- 9.5mm

e. Particles retained in Sieve # 4 - 4.75mm

f. Particles retained in Sieve # 10 - 2.0mm

Part II of **Figure A4 - 29**

g. Particles retained in Sieve # 16 - 1.18mm

h. Particles retained in Sieve # 40 - 0.425mm (Sugar Crystals)

i. Particles retained in Sieve # 100 – 0.15mm

j. Particles retained in Sieve # 200 – 0.075mm

Figure A4 - 29 Particle breakage after oedometer test: Retained particles by sieve on sample M4. Disordered arrangement of sugar cubes.

A4.2.2.4. Sample M8

Sample:	M8
Arrangement of sugar cubes:	Disordered
Maximum vertical stress (kPa):	440
Initial number of sugar cubes:	166

a. Initial: Upper part

b. End of the test: Upper part

c. End of the test: Middle part

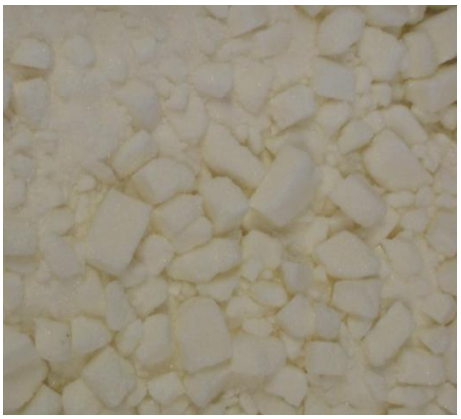

d. End of the test: Lower part

Figure A4 - 30 Sample M8 (Disordered arrangement of sugar cubes, e_o=0.72) inside the oedometer cell (diameter 152mm). (a) Before the test; (b), (c), (d) At the end of the test.

Table A4 - 21 Results of a sieve analysis after the oedometer test on sample M8. Disordered arrangement of sugar cubes.

Sieve			Retained weight on each sieve		% Finer
No.		Opening (mm)	(g)	(%)	
1"		25	0	0.00	100.00
1/2"	Intact original cubes [(a)]	22.37	42.68	13.73	86.27
	Original cubes damaged locally (local crushing) [(b)]	22.37	93.2		
	Cubes after a first splitting of the original sugar cubes [(c)]	12.1	158.92	16.06	70.21
3/8"		9.5	104.59	10.57	59.64
No. 4		4.75	89.35	9.03	50.61
No. 10		2.0	31.22	3.15	47.46
No. 16		1.18	19.68	1.99	45.47
No. 40		0.425	352.66	35.64	9.83
No. 100		0.15	82.96	8.38	1.45
No. 200		0.075	8.58	1.45	0.00
Pan			0	0.00	

(a), (b), (c): Particles retained on sieve No. 1/2"

Part I of **Figure A4 - 31**

a. Intact particles: Retained in Sieve 1/2”- 12.1mm

b. Particles with local crushing: Retained in Sieve 1/2”- 12.1mm

c. Splitting crushing: Retained in Sieve 1/2”- 12.1mm

d. Particles retained in Sieve 3/8”- 9.5mm

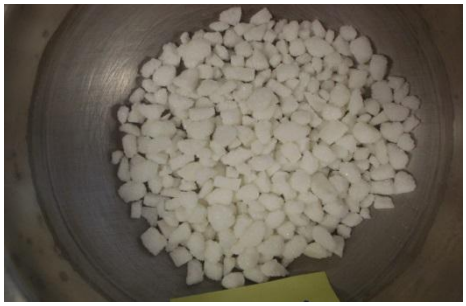

e. Particles retained in Sieve # 4 - 4.75mm

f. Particles retained in Sieve # 10 - 2.0mm

Part II of **Figure A4 - 31**

g. Particles retained in Sieve # 16 - 1.18mm

h. Particles retained in Sieve # 40 - 0.425mm (Sugar Crystals)

i. Particles retained in Sieve # 100 – 0.15mm

j. Particles retained in Sieve # 200 – 0.075mm

Figure A4 - 31 Particle breakage after oedometer test: Retained particles by sieve on sample M8. Disordered arrangement of sugar cubes.

A4.3. Analysis of time-dependent behaviour in oedometer tests

Table A4 - 22 Results of Oedometer tests performed for time-dependent analysis.

Sample (Disordered Arrangements)	σ_{vmax} (1) (kPa)	Elapsed time for imposed stress [Creeping time] (min)	$e_{o(Initial)}$	$e_{(Final\ \sigma vmax)}$	$e_{(Final\ Unloading)}$
T8E	240	10	0.809245705	0.790909666	0.791532895
T2E	240	107	0.759049899	0.739213254	0.739833719
T3E	240	1000	0.807452312	0.779265908	0.779849742
T4E	240	9874	0.844370781	0.80574562	0.80649063
T9E	240	69952	0.831542131	0.788748828	0.789498366
T6E	240	226815	0.798627015	0.736368893	0.736643796

(1) : Imposed load by steps.

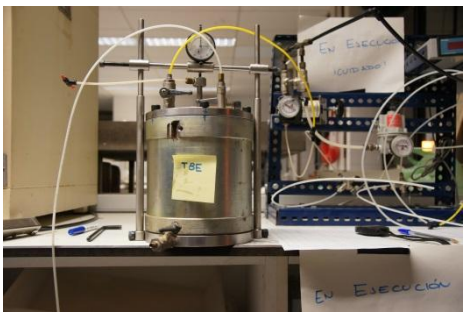

a. Sample T8E

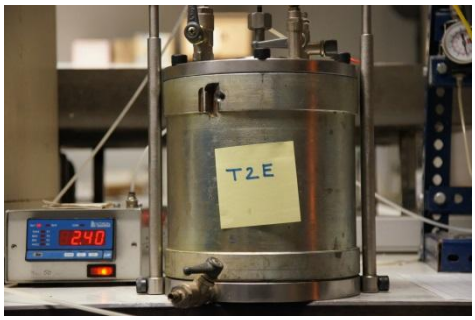

b. Sample T2E

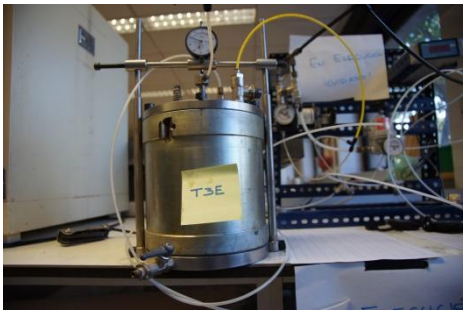

c. Sample T3E

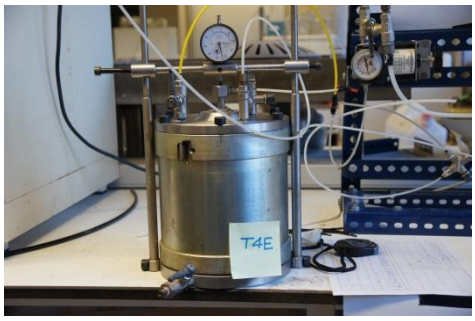

d. Sample T4E

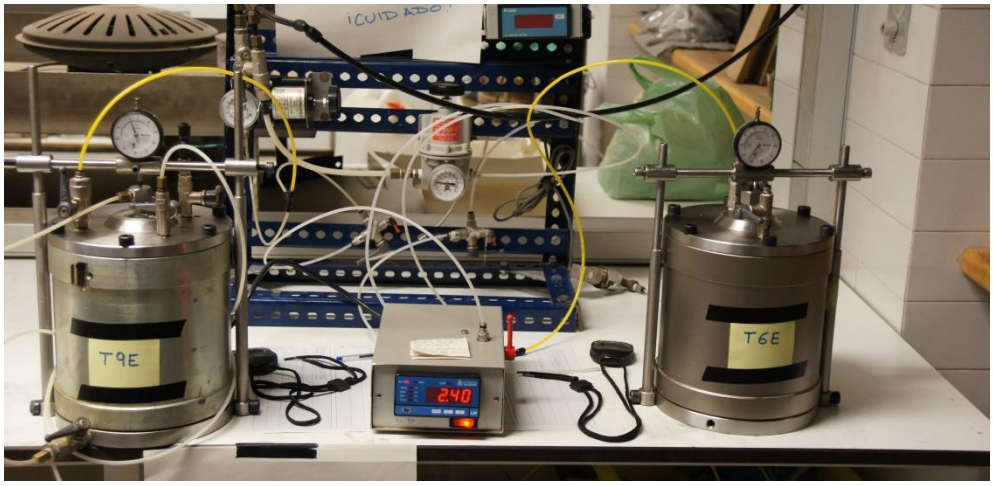

e. Samples T9E y T6E

Figure A4 - 32 Performance of Oedometer tests on disordered arrangements. Rowe cells (inner diameter: 152mm). Analysis of time-dependent behaviour.

A4.3.1. Sample T8E

Sample:	T8E
Arrangement of sugar cubes:	Disordered
Maximum vertical stress (kPa):	240
Initial number of sugar cubes:	169
Creeping time (min):	10

a. Initial: Upper part

b. End of the test: Upper part

c. End of the test: Middle part

d. End of the test: Lower part

Figure A4 - 33 Sample T8E (Disordered arrangement of sugar cubes, e_o=0.81) inside the oedometer cell (diameter 152mm). Analysis of time-dependent behaviour. (a) Before the test; (b), (c), (d) At the end of the test.

Table A4 - 23 Results of a sieve analysis after the oedometer test on sample T8E. Disordered arrangement of sugar cubes - Analysis of time-dependent behaviour.

Sieve			Retained weight on each sieve		% Finer
No.		Opening (mm)	(g)	(%)	
1"		25	0	0.00	100.00
1/2"	Intact original cubes [(a)]	22.37	541.79	84.89	15.11
	Original cubes damaged locally (local crushing) [(b)]	22.37	312.36		
	Cubes after a first splitting of the original sugar cubes [(c)]	12.1	94.05	9.35	5.76
3/8"		9.5	15.8	1.57	4.19
No. 4		4.75	8.97	0.89	3.30
No. 10		2.0	4.41	0.44	2.86
No. 16		1.18	1.34	0.13	2.73
No. 40		0.425	11.29	1.70	1.02
No. 100		0.15	9.52	0.95	0.08
No. 200		0.075	0.78	0.08	0.00
Pan			0	0.00	

(a), (b), (c): Particles retained on sieve No. 1/2"

Part I of **Figure A4 - 34**

a. Intact particles: Retained in Sieve 1/2”- 12.1mm

b. Particles with local crushing: Retained in Sieve 1/2”- 12.1mm

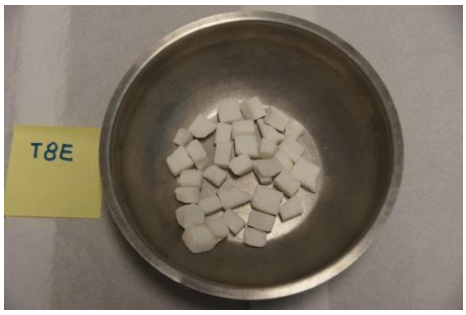

c. Splitting crushing: Retained in Sieve 1/2”- 12.1mm

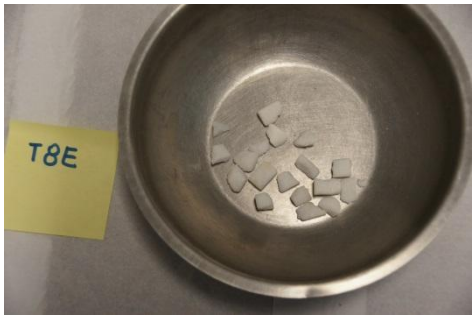

d. Particles retained in Sieve 3/8”- 9.5mm

e. Particles retained in Sieve # 4 - 4.75mm

f. Particles retained in Sieve # 10 - 2.0mm

Part II of **Figure A4 - 34**

g. Particles retained in Sieve # 16 - 1.18mm

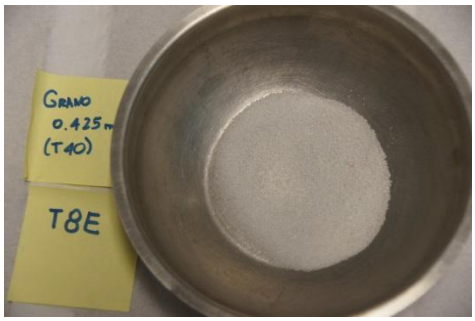

h. Particles retained in Sieve # 40 - 0.425mm (Sugar Crystals)

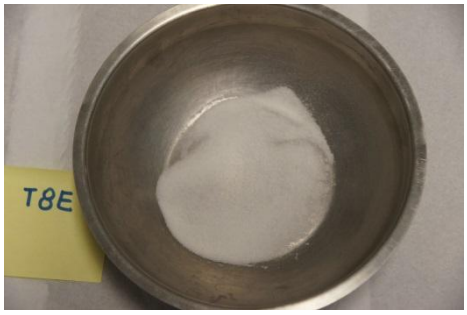

i. Particles retained in Sieve # 100 – 0.15mm

j. Particles retained in Sieve # 200 – 0.075mm

Figure A4 - 34 Particle breakage after oedometer test: Retained particles by sieve on sample T8E. Disordered arrangement of sugar cubes. Analysis of time-dependent behaviour.

A4.3.2. Sample T2E

Sample:	T2E
Arrangement of sugar cubes:	Disordered
Maximum vertical stress (kPa):	240
Initial number of sugar cubes:	168
Creeping time (min):	107

a. Initial: Upper part

b. End of the test: Upper part

c.End of the test: Middle part

d. End of the test: Detail in the middle part

Figure A4 - 35 Sample T2E (Disordered arrangement of sugar cubes, e_o=0.76) inside the oedometer cell (diameter 152mm). Analysis of time-dependent behaviour. (a) Before the test; (b), (c), (d) At the end of the test.

Table A4 - 24 Results of a sieve analysis after the oedometer test on sample T2E. Disordered arrangement of sugar cubes - Analysis of time-dependent behaviour.

Sieve			Retained weight on each sieve		% Finer
No.		Opening (mm)	(g)	(%)	
1"		25	0	0.00	100.00
1/2"	Intact original cubes [(a)]	22.37	546.44	79.20	20.80
	Original cubes damaged locally (local crushing) [(b)]	22.37	249.55		
	Cubes after a first splitting of the original sugar cubes [(c)]	12.1	128.27	12.76	8.03
3/8"		9.5	28.03	2.79	5.24
No. 4		4.75	15.01	1.49	3.75
No. 10		2.0	5.48	0.55	3.20
No. 16		1.18	2.19	0.22	2.99
No. 40		0.425	14.1	1.94	1.05
No. 100		0.15	9.83	0.98	0.07
No. 200		0.075	0.66	0.07	0.00
Pan			0.04	0.00	

(a), (b), (c): Particles retained on sieve No. 1/2"

Part I of **Figure A4 - 36**

a. Intact particles: Retained in Sieve 1/2”- 12.1mm

b. Particles with local crushing: Retained in Sieve 1/2”- 12.1mm

c. Splitting crushing: Retained in Sieve 1/2”- 12.1mm

d. Particles retained in Sieve 3/8”- 9.5mm

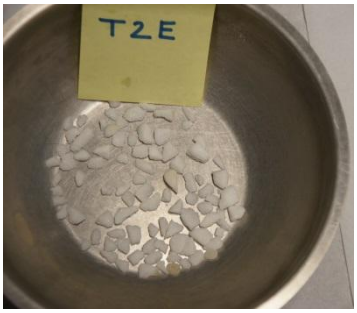

e. Particles retained in Sieve # 4 - 4.75mm

f. Particles retained in Sieve # 10 - 2.0mm

Part II of **Figure A4 - 36**

g. Particles retained in Sieve # 16 - 1.18mm

h. Particles retained in Sieve # 40 - 0.425mm (Sugar Crystals)

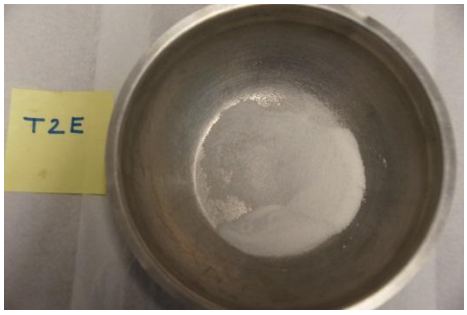

i. Particles retained in Sieve # 100 – 0.15mm

j. Particles retained in Sieve # 200 – 0.075mm

Figure A4 - 36 Particle breakage after oedometer test: Retained particles by sieve on sample T2E. Disordered arrangement of sugar cubes. Analysis of time-dependent behaviour.

A4.3.3. Sample T3E

Sample:	T3E
Arrangement of sugar cubes:	Disordered
Maximum vertical stress (kPa):	240
Initial number of sugar cubes:	168
Creeping time (min):	1000

a. Initial: Upper part

b. End of the test: Upper part

c. End of the test: Middle part

d. End of the test: Lower part

Figure A4 - 37 Sample T3E (Disordered arrangement of sugar cubes, e_o=0.81) inside the oedometer cell (diameter 152mm). Analysis of time-dependent behaviour. (a) Before the test; (b), (c), (d) At the end of the test.

Table A4 - 25 Results of a sieve analysis after the oedometer test on sample T3E. Disordered arrangement of sugar cubes - Analysis of time-dependent behaviour.

Sieve			Retained weight on each sieve		% Finer
No.		Opening (mm)	(g)	(%)	
1"		25	0	0.00	100.00
1/2"	Intact original cubes [(a)]	22.37	481.12	73.37	26.63
	Original cubes damaged locally (local crushing) [(b)]	22.37	256.35		
	Cubes after a first splitting of the original sugar cubes [(c)]	12.1	165.91	16.51	10.12
3/8"		9.5	33.78	3.36	6.76
No. 4		4.75	16.42	1.63	5.13
No. 10		2.0	6.14	0.61	4.52
No. 16		1.18	3.51	0.35	4.17
No. 40		0.425	25.38	3.11	1.06
No. 100		0.15	10.01	1.00	0.06
No. 200		0.075	0.61	0.06	0.00
Pan			0.02	0.00	

(a), (b), (c): Particles retained on sieve No. 1/2"

Part I of **Figure A4 - 38**

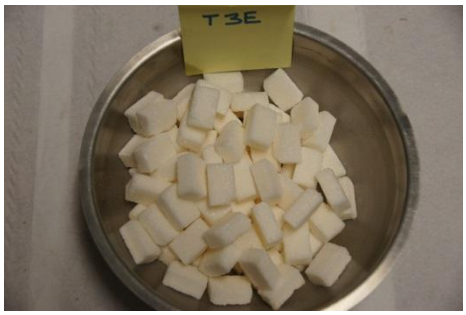

a. Intact particles: Retained in Sieve 1/2”- 12.1mm

b. Particles with local crushing: Retained in Sieve 1/2”- 12.1mm

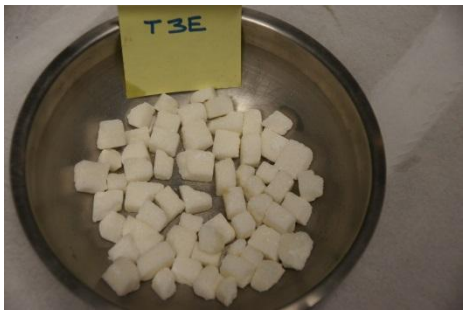

c. Splitting crushing: Retained in Sieve 1/2”- 12.1mm

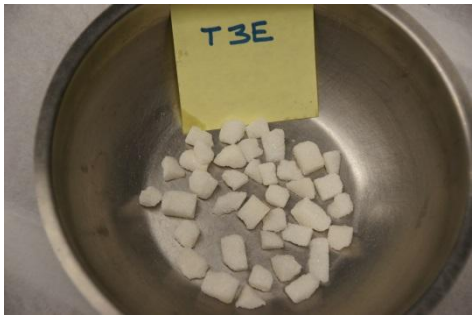

d. Particles retained in Sieve 3/8”- 9.5mm

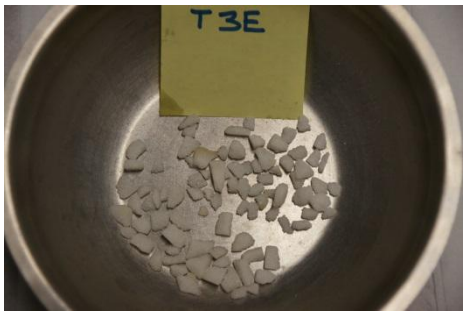

e. Particles retained in Sieve # 4 - 4.75mm

f. Particles retained in Sieve # 10 - 2.0mm

Part II of **Figure A4 - 38**

g. Particles retained in Sieve # 16 - 1.18mm

h. Particles retained in Sieve # 40 - 0.425mm (Sugar Crystals)

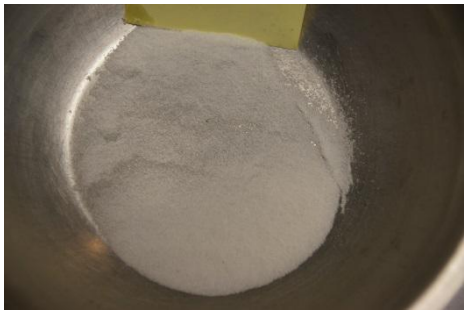

i. Particles retained in Sieve # 100 – 0.15mm

j. Particles retained in Sieve # 200 – 0.075mm

Figure A4 - 38 Particle breakage after oedometer test: Retained particles by sieve on sample T3E. Disordered arrangement of sugar cubes. Analysis of time-dependent behaviour.

A4.3.4. Sample T4E

Sample:	T4E
Arrangement of sugar cubes:	Disordered
Maximum vertical stress (kPa):	240
Initial number of sugar cubes:	168
Creeping time (min):	9874

a. End of the test: Upper part

b. End of the test: Middle part

c. End of the test: Lower part

Figure A4 - 39 Sample T4E (Disordered arrangement of sugar cubes, e_o=0.84) inside the oedometer cell (diameter 152mm). Analysis of time-dependent behaviour. (a), (b), (c) At the end of the test.

Table A4 - 26 Results of a sieve analysis after the oedometer test on sample T4E. Disordered arrangement of sugar cubes - Analysis of time-dependent behaviour.

Sieve			Retained weight on each sieve		% Finer
No.		Opening (mm)	(g)	(%)	
1"		25	0	0.00	100.00
1/2"	Intact original cubes [(a)]	22.37	309.66	61.58	38.42
	Original cubes damaged locally (local crushing) [(b)]	22.37	306.69		
	Cubes after a first splitting of the original sugar cubes [(c)]	12.1	233.43	23.32	15.10
3/8"		9.5	39.87	3.98	11.11
No. 4		4.75	27.87	2.78	8.33
No. 10		2.0	13.22	1.32	7.01
No. 16		1.18	7.49	0.75	6.26
No. 40		0.425	39.87	4.54	1.72
No. 100		0.15	16.11	1.61	0.11
No. 200		0.075	1.12	0.11	0.00
Pan			0	0.00	

(a), (b), (c): Particles retained on sieve No. 1/2"

Part I of **Figure A4 - 40**

a. Intact particles: Retained in Sieve 1/2”- 12.1mm

b. Particles with local crushing: Retained in Sieve 1/2”- 12.1mm

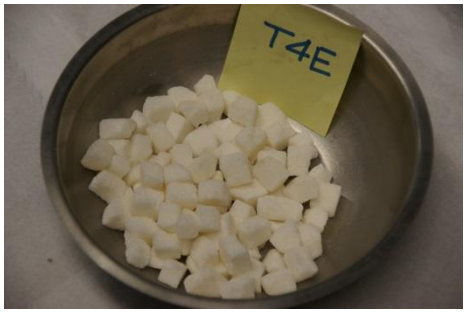

c. Splitting crushing: Retained in Sieve 1/2”- 12.1mm

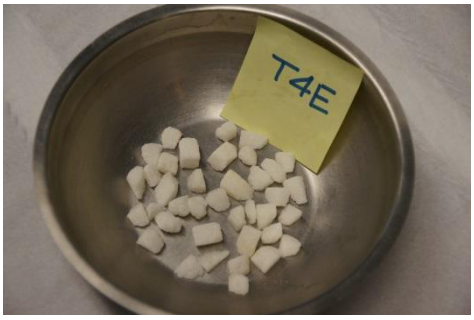

d. Particles retained in Sieve 3/8”- 9.5mm

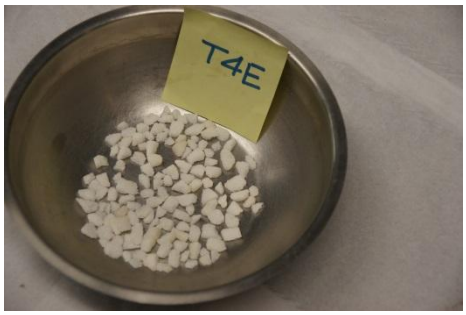

e. Particles retained in Sieve # 4 - 4.75mm

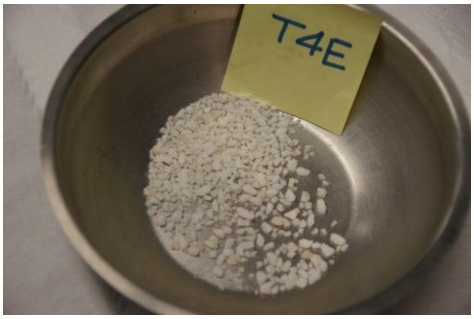

f. Particles retained in Sieve # 10 - 2.0mm

Part II of **Figure A4 - 40**

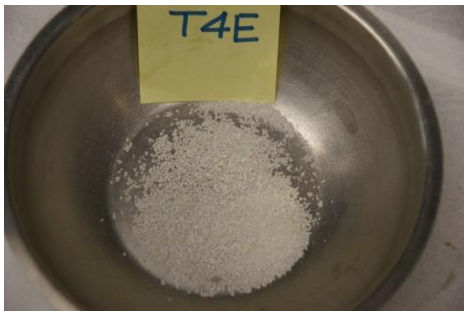

g. Particles retained in Sieve # 16 - 1.18mm

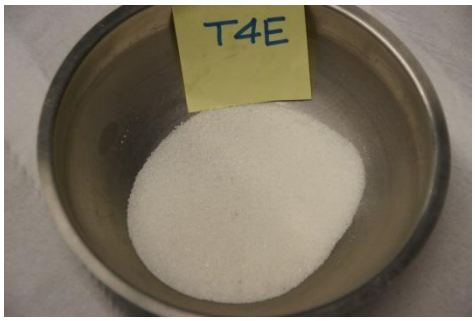

h. Particles retained in Sieve # 40 - 0.425mm (Sugar Crystals)

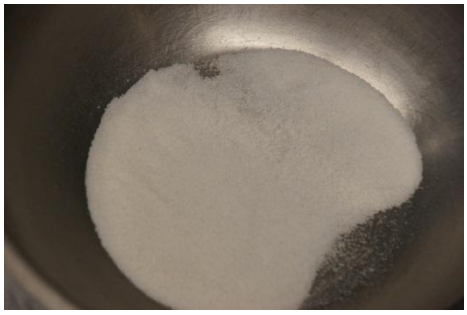

i. Particles retained in Sieve # 100 – 0.15mm

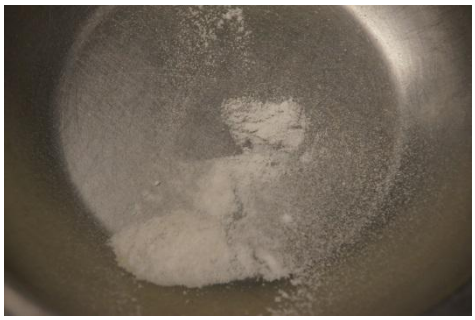

j. Particles retained in Sieve # 200 – 0.075mm

Figure A4 - 40 Particle breakage after oedometer test: Retained particles by sieve on sample T4E. Disordered arrangement of sugar cubes. Analysis of time-dependent behaviour.

A4.3.5. Sample T9E

Sample:	T9E
Arrangement of sugar cubes:	Disordered
Maximum vertical stress (kPa):	240
Initial number of sugar cubes:	168
Creeping time (min):	69952

a. Initial: Upper part

b. End of the test: Upper part

c. End of the test: Middle part

d. End of the test: Lower part

Figure A4 - 41 Sample T9E (Disordered arrangement of sugar cubes, e_o=0.83) inside the oedometer cell (diameter 152mm). Analysis of time-dependent behaviour. (a) Before the test; (b), (c), (d) At the end of the test.

Table A4 - 27 Results of a sieve analysis after the oedometer test on sample T9E. Disordered arrangement of sugar cubes - Analysis of time-dependent behaviour.

Sieve			Retained weight on each sieve		% Finer
No.		Opening (mm)	(g)	(%)	
1"		25	0	0.00	100.00
1/2"	Intact original cubes [(a)]	22.37	143.38	37.91	62.09
	Original cubes damaged locally (local crushing) [(b)]	22.37	235.62		
	Cubes after a first splitting of the original sugar cubes [(c)]	12.1	265.85	26.59	35.50
3/8"		9.5	100.59	10.06	25.43
No. 4		4.75	72.96	7.30	18.14
No. 10		2.0	25.8	2.58	15.55
No. 16		1.18	10.23	1.02	14.53
No. 40		0.425	85.11	9.60	4.93
No. 100		0.15	48.78	4.88	0.05
No. 200		0.075	0.5	0.05	0.00
Pan			0	0.00	

(a), (b), (c): Particles retained on sieve No. 1/2"

Part I of **Figure A4 - 42**

a. Intact particles: Retained in Sieve 1/2”- 12.1mm

b. Particles with local crushing: Retained in Sieve 1/2”- 12.1mm

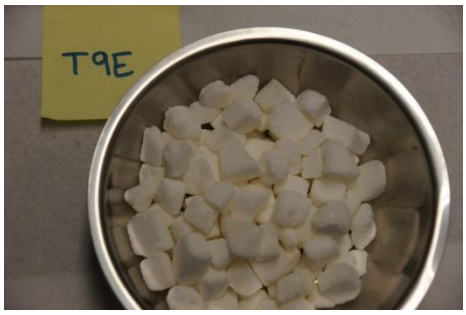

c. Splitting crushing: Retained in Sieve 1/2”- 12.1mm

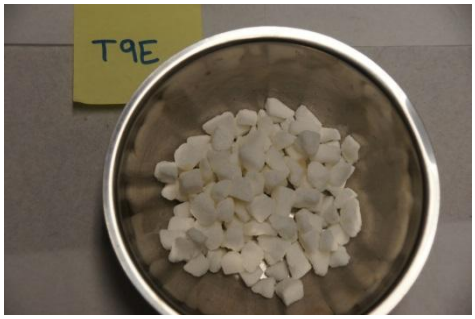

d. Particles retained in Sieve 3/8”- 9.5mm

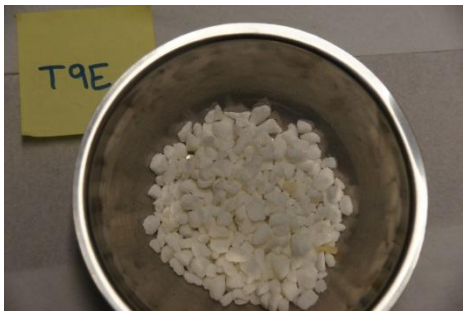

e. Particles retained in Sieve # 4 - 4.75mm

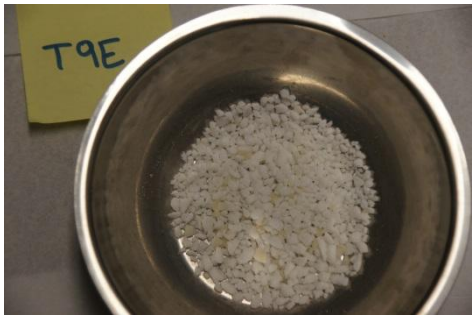

f. Particles retained in Sieve # 10 - 2.0mm

Part II of **Figure A4 - 42**

g. Particles retained in Sieve # 16 - 1.18mm

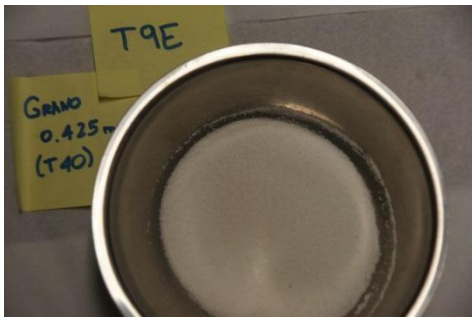

h. Particles retained in Sieve # 40 - 0.425mm (Sugar Crystals)

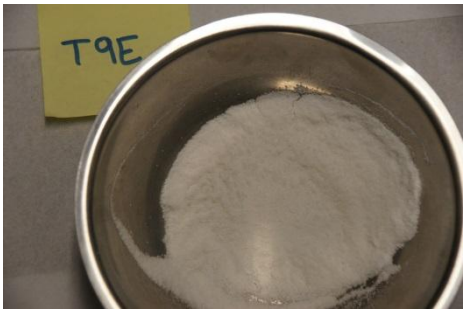

i. Particles retained in Sieve # 100 – 0.15mm

j. Particles retained in Sieve # 200 – 0.075mm

Figure A4 - 42 Particle breakage after oedometer test: Retained particles by sieve on sample T9E. Disordered arrangement of sugar cubes. Analysis of time-dependent behaviour.

A4.3.6. Sample T6E

Sample:	T6E
Arrangement of sugar cubes:	Disordered
Maximum vertical stress (kPa):	240
Initial number of sugar cubes:	168
Creeping time (min):	226815

d. Initial: Upper part

e. End of the test: Upper part

f. End of the test: Middle part

d. End of the test: Lower part

Figure A4 - 43 Sample T6E (Disordered arrangement of sugar cubes, e_o=0.80) inside the oedometer cell (diameter 152mm). Analysis of time-dependent behaviour. (a) Before the test; (b), (c), (d) At the end of the test.

Table A4 - 28 Results of a sieve analysis after the oedometer test on sample T6E. Disordered arrangement of sugar cubes - Analysis of time-dependent behaviour.

Sieve			Retained weight on each sieve		% Finer
No.		Opening (mm)	(g)	(%)	
1"		25	0	0.00	100.00
1/2"	Intact original cubes [(a)]	22.37	22.78	16.62	83.38
	Original cubes damaged locally (local crushing) [(b)]	22.37	143.36		
	Cubes after a first splitting of the original sugar cubes [(c)]	12.1	252.98	25.31	58.07
3/8"		9.5	145.65	14.57	43.50
No. 4		4.75	96.96	9.70	33.79
No. 10		2.0	32.95	3.30	30.50
No. 16		1.18	15.83	1.58	28.91
No. 40		0.425	192.34	20.29	8.62
No. 100		0.15	83.93	8.40	0.23
No. 200		0.075	2.25	0.23	0.00
Pan			0	0.00	

(a), (b), (c): Particles retained on sieve No. 1/2"

Part I of **Figure A4 - 44**

a. Intact particles: Retained in Sieve 1/2”- 12.1mm

b. Particles with local crushing: Retained in Sieve 1/2”- 12.1mm

c. Splitting crushing: Retained in Sieve 1/2”- 12.1mm

d. Particles retained in Sieve 3/8”- 9.5mm

e. Particles retained in Sieve # 4 - 4.75mm

f. Particles retained in Sieve # 10 - 2.0mm

Part II of **Figure A4 - 44**

g. Particles retained in Sieve # 16 - 1.18mm

h. Particles retained in Sieve # 40 - 0.425mm (Sugar Crystals)

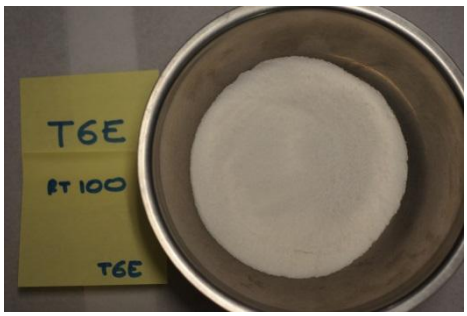

i. Particles retained in Sieve # 100 – 0.15mm

j. Particles retained in Sieve # 200 – 0.075mm

Figure A4 - 44 Particle breakage after oedometer test: Retained particles by sieve on sample T6E. Disordered arrangement of sugar cubes. Analysis of time-dependent behaviour.

A4.4. Ilustration of breakage mechanisms on sugar cubes subjected to oedometer tests

A4.4.1. Splitting failure

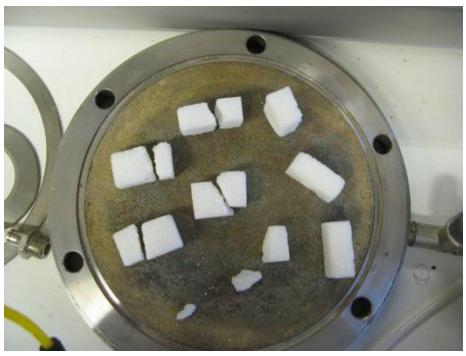

a. Details of broken particles of sample M1

b. Details of broken particles of sample M1

c. Details of broken particles of sample M1

d. Details of broken particles of sample T8E

e. Details of broken particles of sample T8E

f. Details of broken particles of sample T8E: Splitting (center) and Comminution (right)

Figure A4 - 45 Details of splitting failure. Broken particles after oedometer tests.

A4.4.2. Comminution or local crushing

a. Details of broken particles of sample T4E

b. Details of broken particles of sample T8E

c. Details of broken particles of sample T8E: Splitting and Comminution

d. Details of broken particles of sample T8E

Figure A4 - 46 Details of comminution crushing. Broken particles after oedometer tests.

Appendix 5

A5. Laboratory tests on limestone fragments

This appendix contents the experimental results of several tests performed on hard limestone fragments from the quarry FOJ S.A. in Vallirana (Barcelona, Spain): basic and mineral friction angle using the tilt table and direct shear tests, contact stiffness tests and mean roughness tests. These experimental data were used and analyzed in chapter 5: sections 5.6.1 and 5.6.2. Likewise, the results were used by the DEM model in the numerical simulations presented in the thesis.

A5.1. Determination of Basic and Mineral friction angle

A5.1.1. Rock sampling

A5.1.1.1. Source material

a. b.

Figure A5 - 1 Limestone rockfill from the quarry FOJ in Vallirana (Barcelona, Spain): (a) Particle size: 0.1 – 0.5m; (b) Detail of rock fragments.

A5.1.1.2. Rock cutting

Figure A5 - 2 Cutting of rock specimens: (a) Cutting machine – detail of Cut-Off Wheel; (b) Cutting Operation; (c), (d) Rock specimen: before and during the cutting operation.

A5.1.1.3. Rock Samples

Table A5 - 1 Limestone samples for tilt table and direct shear tests.

Sample	Area (cm2)	Description	Roughness
M1R	164	Large. Irregular section	Rough
M2R	42.8	Small. Rectangular section	Rough
M1P	27.8	Small. Rectangular section	Basic
M4G	159.9	Large. Rectangular section	Basic
M5G	163.2	Large. Irregular section	Basic
M2P	24.5	Small. Rectangular section	Mineral
M3P	28.8	Small. Rectangular section	Mineral
M6G	207.2	Large. Rectangular section	Mineral

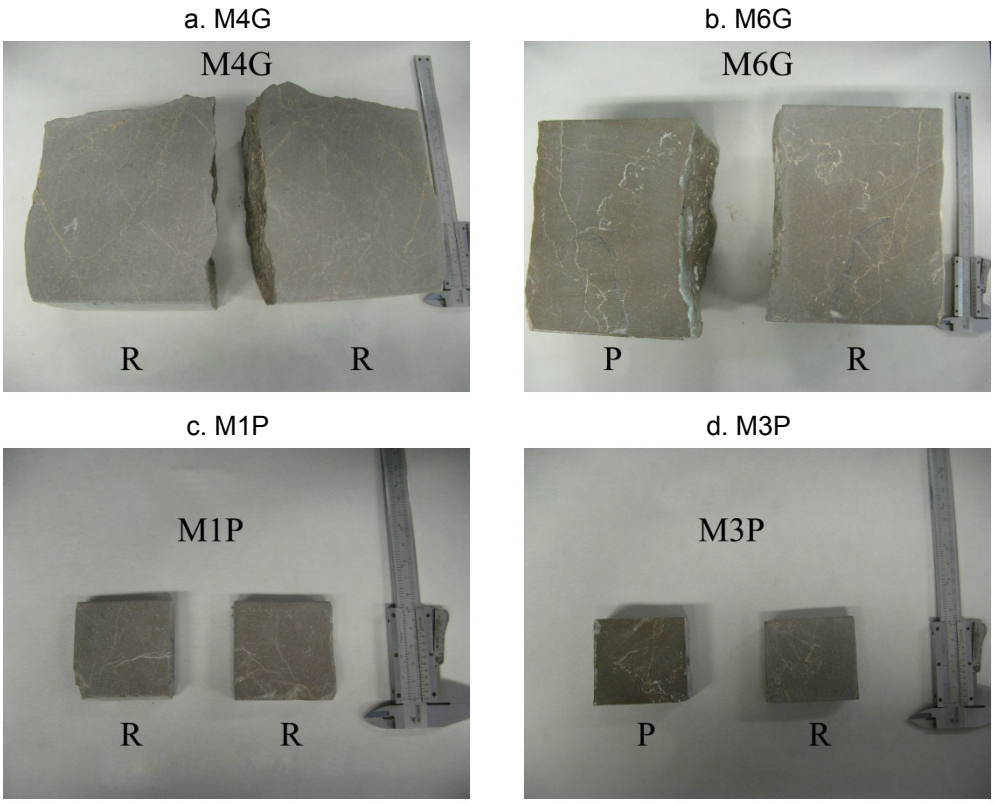

Figure A5 - 3 Limestone samples: R: #80 polished surface; P: #1000 polished surface. (a) M4G sample (12x13cm) – Analysis of basic friction angle; (b) M6G sample (12x17cm) – Analysis of mineral friction angle; (c) M1P sample (5x5cm) – Analysis of basic friction angle; (d) M3P sample (5x5cm) – Analysis of mineral friction angle.

A5.1.2. Tilt table tests

Figure A5 - 4 Tilt table test.

Table A5 - 2 Data results of tilt tests on limestone samples: Part 1.

Sample	Initial Normal Stress	Measurement of Friction angle (°)					Friction angle (°)	Mean Velocity	Comments
	kPa	(1)	(2)	(3)	(4)	(5)	Average	°/min	
M1R	2.0194	31	34	34			33		Test 1_M1R: Direction 1
	2.0194	35	36				35.5		Test 1_M1R: Direction 2
	2.7670	21	23				22		Test 2_M1R: Direction 1
	5.1299	28.5	31				29.8		Test 3_M1R: Direction 1
	8.0011	15.5	13				14.3		Test 4_M1R: Direction 1
M2R	0.4461	33.5	34.5				34		Test 1_M2R: Direction 1
	0.4461	32.5	30	31			31.2		Test 1_M2R: Direction 2
	2.1894	34	33				33.5		Test 2_M2R: Direction 1
	2.1894	29	27				28		Test 2_M2R: Direction 2

Sample	Initial Normal Stress	Measurement of Friction angle (°)					Friction angle (°)	Mean Velocity	Comments
	kPa	(1)	(2)	(3)	(4)	(5)	Average	°/min	
M1P	0.3679	15.5	17.5	18.5	15	15.5	16.4	8.15	Test 1_M1P: Direction 1
	0.3679	20	21				20.5	8.02	Test 2_M1P: Direction 1
	0.7417	16	18				17	8.10	Test 3_M1P: Direction 1
	1.0432	21	17				19	8.10	Test 4_M1P: Direction 1
	1.2312	19	19.5				19.3	8.14	Test 5_M1P: Direction 1
	1.7068	21	22				21.5	8.01	Test 6_M1P: Direction 1
	2.4409	20	22				21	8.03	Test 7_M1P: Direction 1
	3.1740	20	19				19.5	7.92	Test 8_M1P: Direction 1
	5.9079	17.5	16.5				17	8.10	Test 9_M1P: Direction 1
	7.0591	18	16	17.5			17.2	8.15	Test 10_M1P: Direction 1
	10.5154	16.5	14				15.3	7.99	Test 11_M1P: Direction 1
	11.6660	18	15				16.5	8.19	Test 12_M1P: Direction 1
	15.8686	15.5	14.5				15	10.62	Test 13_M1P: Direction 1
M4G	1.8883	20.5	19.5	22.5	25.5	23.5	22.3	8.02	Test 1_M4G: Direction 1
	1.8883	16	16	17.5			16.5	8.19	Test 2_M4G: Direction 2
	1.8883	16	17	17			16.7	8.22	Test 3_M4G: Direction 1
	2.8127	16	19				17.5	8.23	Test 4_M4G: Direction 1
	4.6548	15.5	15.5				15.5	8.30	Test 5_M4G: Direction 1
	8.3359	15	14				14.5	8.25	Test 6_M4G: Direction 1
	14.4709	13	13				13	8.17	Test 7_M4G: Direction 1
	1.8883	17.5					17.5	8.27	Test 8_M4G: Direction 2
	3.4278	16.5	18				17.3	8.15	Test 9_M4G: Direction 2
	4.6548	16.5	16				16.3	8.41	Test 10_M4G: Direction 2

Sample	Initial Normal Stress	Measurement of Friction angle (°)					Friction angle (°)	Mean Velocity	Comments
	kPa	(1)	(2)	(3)	(4)	(5)	Average	°/min	
	8.3359	15.5	17				16.3	7.97	Test 11_M4G: Direction 2
M5G	2.2533	16.5	17	17.5			17	8.03	Test 1_M5G: Direction 1
	2.2533	10	12	13			11.7	8.21	Test 2_M5G: Direction 2
	2.2533	13	15				14	7.93	Test 3_M5G: Direction 1
	3.7619	15	15				15	7.86	Test 4_M5G: Direction 1
	4.9643	16.5	16.5				16.5	7.92	Test 5_M5G: Direction 1
	8.5715	16	17				16.5	8.05	Test 6_M5G: Direction 1
	14.5834	14.5	14				14.3	8.22	Test 7_M5G: Direction 1
	21.7978	12.5	14				13.3	8.17	Test 8_M5G: Direction 1
M2P	0.5832	10	13.5	12	12		11.9	7.97	Test 1_M2P: Direction 1
	0.7840	11	12.5				11.8	8.10	Test 2_M2P: Direction 1
	1.0299	11.5	12				11.8	8.44	Test 3_M2P: Direction 1
	1.3713	11.5					11.5	8.63	Test 4_M2P: Direction 1
	1.5841	12.5	14	13.5			13.3	7.94	Test 5_M2P: Direction 1
	2.1225	15	15.5				15.3	7.99	Test 6_M2P: Direction 1
	2.9536	14.5	14				14.3	7.92	Test 7_M2P: Direction 1
	3.7835	14	12.5				13.3	8.08	Test 8_M2P: Direction 1
	6.8785	11	12.5				11.8	7.92	Test 9_M2P: Direction 1
	8.1818	11	10.5				10.8	8.22	Test 10_M2P: Direction 1
	12.0946	10	11				10.5	8.54	Test 11_M2P: Direction 1
	18.1549	10	10				10	7.69	Test 12_M2P: Direction 1
M3P	0.3837	19	22	19			20	8.32	Test 1_M3P: Direction 1
	0.7093	14	10.5	14.5			13	8.10	Test 2_M3P: Direction 1

Sample	Initial Normal Stress	Measurement of Friction angle (°)					Friction angle (°)	Mean Velocity	Comments
	kPa	(1)	(2)	(3)	(4)	(5)	Average	°/min	
	0.9999	14	14.5				14.3	7.84	Test 3_M3P: Direction 1
	1.1810	14	13				13.5	8.26	Test 4_M3P: Direction 1
	1.6393	13	13				13	8.00	Test 5_M3P: Direction 1
	2.3467	13.5	10	11			11.5	8.09	Test 6_M3P: Direction 1
	3.0530	10	12				11	7.85	Test 7_M3P: Direction 1
	5.6873	12.5	9	12.5			11.3	8.24	Test 8_M3P: Direction 1
	6.7966	10	11.5				10.8	8.18	Test 9_M3P: Direction 1
M6G	1.9323	15.5	17	17	20		17.4	7.98	Test 1_M6G: Direction 1
	1.9323	19	19	18			18.7	8.16	Test 2_M6G: Direction 2
	1.9323	17	17				17	8.06	Test 3_M6G: Direction 1
	3.1202	17	19				18	8.18	Test 4_M6G: Direction 1
	4.0670	18.5	21				19.8	8.12	Test 5_M6G: Direction 1
	6.9073	17.5	16				16.8	7.94	Test 6_M6G: Direction 1
	11.6411	15.5	17				16.3	7.77	Test 7_M6G: Direction 1
	16.3748	19	17				18	8.58	Test 8_M6G: Direction 1

Table A5 - 3 Data results of tilt tests on limestone samples: Part 2.

Sample	Friction angle	Initial Normal Stress	Friction angle (°)		Friction Coefficient	Normal stress	Shear stress	Comments
		kPa	Average			kPa	kPa	
M1R	ROUGH SURFACE	2.0194	33	29	0.65	1.6936	1.0999	Test 1_M1R: Direction 1
		2.0194	35.5		0.71	1.6440	1.1727	Test 1_M1R: Direction 2
		2.7670	22		0.40	2.5655	1.0365	Test 2_M1R: Direction 1
		5.1299	29.8		0.57	4.4538	2.5455	Test 3_M1R: Direction 1
		8.0011	14.3		0.25	7.7549	1.9695	Test 4_M1R: Direction 1
M2R	ROUGH SURFACE	0.4461	34		0.67	0.3698	0.2494	Test 1_M2R: Direction 1
		0.4461	31.2		0.60	0.3817	0.2308	Test 1_M2R: Direction 2
		2.1894	33.5		0.66	1.8257	1.2084	Test 2_M2R: Direction 1
		2.1894	28		0.53	1.9331	1.0279	Test 2_M2R: Direction 2
M1P	BASIC	0.3679	16.4	17	0.29	0.3529	0.1039	Test 1_M1P: Direction 1
		0.3679	20.5		0.37	0.3446	0.1288	Test 2_M1P: Direction 1
		0.7417	17		0.31	0.7093	0.2168	Test 3_M1P: Direction 1
		1.0432	19		0.34	0.9864	0.3396	Test 4_M1P: Direction 1
		1.2312	19.3		0.35	1.1624	0.4059	Test 5_M1P: Direction 1
		1.7068	21.5		0.39	1.5880	0.6255	Test 6_M1P: Direction 1
		2.4409	21		0.38	2.2788	0.8748	Test 7_M1P: Direction 1
		3.1740	19.5		0.35	2.9919	1.0595	Test 8_M1P: Direction 1
		5.9079	17		0.31	5.6498	1.7273	Test 9_M1P: Direction 1
		7.0591	17.2		0.31	6.7446	2.0835	Test 10_M1P: Direction 1
		10.5154	15.3		0.27	10.1451	2.7659	Test 11_M1P: Direction 1
		11.6660	16.5		0.30	11.1855	3.3133	Test 12_M1P: Direction 1
		15.8686	15		0.27	15.3279	4.1071	Test 13_M1P: Direction 1

Sample	Friction angle	Initial Normal Stress	Friction angle (°)		Friction Coefficient	Normal stress	Shear stress	Comments
		kPa	Average			kPa	kPa	
M4G	BASIC	1.8883	22.3	17	0.41	1.7470	0.7165	Test 1_M4G: Direction 1
		1.8883	16.5		0.30	1.8105	0.5363	Test 2_M4G: Direction 2
		1.8883	16.7		0.30	1.8089	0.5416	Test 3_M4G: Direction 1
		2.8127	17.5		0.32	2.6825	0.8458	Test 4_M4G: Direction 1
		4.6548	15.5		0.28	4.4855	1.2439	Test 5_M4G: Direction 1
		8.3359	14.5		0.26	8.0703	2.0871	Test 6_M4G: Direction 1
		14.4709	13		0.23	14.1001	3.2553	Test 7_M4G: Direction 1
		1.8883	17.5		0.32	1.8009	0.5678	Test 8_M4G: Direction 2
		3.4278	17.3		0.31	3.2736	1.0165	Test 9_M4G: Direction 2
		4.6548	16.3		0.29	4.4688	1.3025	Test 10_M4G: Direction 2
		8.3359	16.3		0.29	8.0028	2.3326	Test 11_M4G: Direction 2
M5G	BASIC	2.2533	17		0.31	2.1548	0.6588	Test 1_M5G: Direction 1
		2.2533	11.7		0.21	2.2067	0.4557	Test 2_M5G: Direction 2
		2.2533	14		0.25	2.1863	0.5451	Test 3_M5G: Direction 1
		3.7619	15		0.27	3.6337	0.9737	Test 4_M5G: Direction 1
		4.9643	16.5		0.30	4.7599	1.4099	Test 5_M5G: Direction 1
		8.5715	16.5		0.30	8.2185	2.4344	Test 6_M5G: Direction 1
		14.5834	14.3		0.25	14.1347	3.5898	Test 7_M5G: Direction 1
		21.7978	13.3		0.24	21.2175	4.9961	Test 8_M5G: Direction 1
M2P	MINERAL	0.5832	11.9		0.21	0.5708	0.1200	Test 1_M2P: Direction 1
		0.7840	11.8		0.21	0.7676	0.1597	Test 2_M2P: Direction 1
		1.0299	11.8		0.21	1.0083	0.2097	Test 3_M2P: Direction 1
		1.3713	11.5		0.20	1.3438	0.2734	Test 4_M2P: Direction 1
		1.5841	13.3		0.24	1.5414	0.3653	Test 5_M2P: Direction 1

Sample	Friction angle	Initial Normal Stress	Friction angle (°)		Friction Coefficient	Normal stress	Shear stress	Comments
		kPa	Average			kPa	kPa	
		2.1225	15.3		0.27	2.0478	0.5583	Test 6_M2P: Direction 1
		2.9536	14.3		0.25	2.8628	0.7270	Test 7_M2P: Direction 1
		3.7835	13.3		0.24	3.6827	0.8672	Test 8_M2P: Direction 1
		6.8785	11.8		0.21	6.7344	1.4008	Test 9_M2P: Direction 1
		8.1818	10.8		0.19	8.0382	1.5261	Test 10_M2P: Direction 1
		12.0946	10.5		0.19	11.8921	2.2041	Test 11_M2P: Direction 1
		18.1549	10		0.18	17.8790	3.1526	Test 12_M2P: Direction 1
M3P	MINERAL	0.3837	20		0.36	0.3605	0.1312	Test 1_M3P: Direction 1
		0.7093	13		0.23	0.6912	0.1596	Test 2_M3P: Direction 1
		0.9999	14.3		0.25	0.9692	0.2461	Test 3_M3P: Direction 1
		1.1810	13.5		0.24	1.1484	0.2757	Test 4_M3P: Direction 1
		1.6393	13	14.0	0.23	1.5973	0.3688	Test 5_M3P: Direction 1
		2.3467	11.5		0.20	2.2996	0.4679	Test 6_M3P: Direction 1
		3.0530	11		0.19	2.9969	0.5825	Test 7_M3P: Direction 1
		5.6873	11.3		0.20	5.5764	1.1177	Test 8_M3P: Direction 1
		6.7966	10.8		0.19	6.6773	1.2677	Test 9_M3P: Direction 1
M6G	MINERAL	1.9323	17.4		0.31	1.8442	0.5770	Test 1_M6G: Direction 1
		1.9323	18.7		0.34	1.8307	0.6185	Test 2_M6G: Direction 2
		1.9323	17		0.31	1.8479	0.5650	Test 3_M6G: Direction 1
		3.1202	18		0.32	2.9675	0.9642	Test 4_M6G: Direction 1
		4.0670	19.8		0.36	3.8277	1.3743	Test 5_M6G: Direction 1
		6.9073	16.8		0.30	6.6142	1.9906	Test 6_M6G: Direction 1
		11.6411	16.3		0.29	11.1760	3.2575	Test 7_M6G: Direction 1
		16.3748	18		0.32	15.5734	5.0601	Test 8_M6G: Direction 1

A5.1.3. Direct Shear tests

A5.1.3.1. Large-Direct Shear test

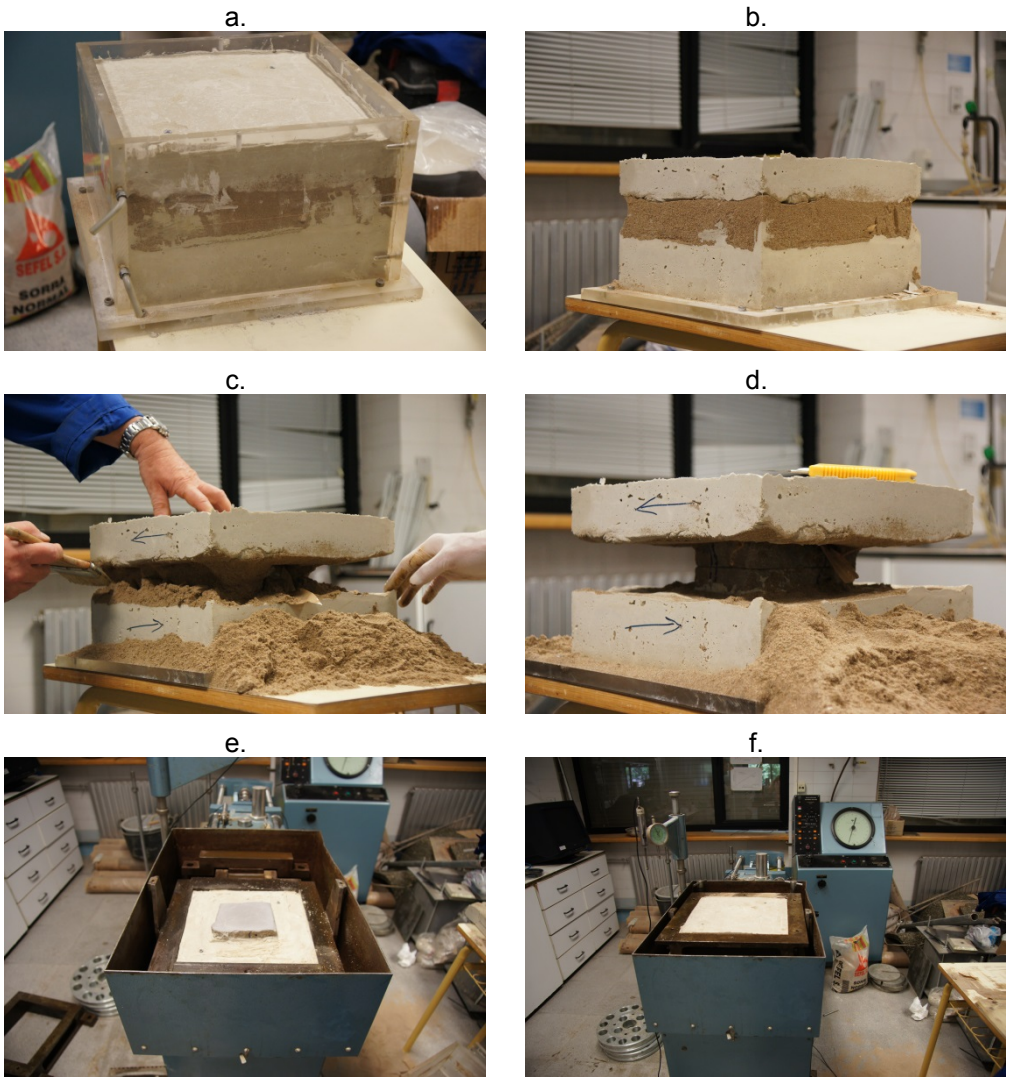

Figure A5 - 5 Preparation of the M4G sample in the large-Direct Shear equipment: (a), (b), (c), (d) Sequence of preparation of the upper and lower-support blocks; (e) Lower block inside the Direct Shear box; (f) Upper block inside the Direct Shear box.

Figure A5 - 6 Large-Direct Shear equipment.

A5.1.3.1.1. Sample M4G – Test 1

Large-Direct Shear test	
Sample:	M4G
Objective:	Basic Friction Angle
Initial Normal stress (kPa):	637.37
Initial Normal stress (kg/cm2):	6.50
Initial Contact Area, (cm^2):	159.9

Table A5 - 4 Data results of Direct Shear tests on the sample M4G: Test 1.

Normal stress (kPa)	Shear stress (kPa)	Normal stress (kPa)	Shear stress (kPa)	Normal stress (kPa)	Shear stress (kPa)	Normal stress (kPa)	Shear stress (kPa)	Normal stress (kPa)	Shear stress (kPa)
637.37	0.00	638.79	20.66	640.26	62.63	641.75	100.89	643.23	138.93
637.65	6.87	639.08	29.82	640.55	70.59	642.04	108.81	643.53	145.95
637.94	8.01	639.38	37.18	640.85	78.99	642.34	115.00	643.84	154.15
638.22	8.00	639.67	44.88	641.15	87.44	642.64	122.08	644.15	163.27
638.51	10.71	639.96	52.45	641.45	94.18	642.93	128.88	644.45	172.62

Normal stress (kPa)	Shear stress (kPa)
644.76	182.60
645.06	150.02
645.36	146.14
645.67	174.56
645.96	169.84
646.27	168.21
646.57	164.98
646.88	164.22
647.18	162.23
647.49	158.66
647.80	157.44
648.10	154.14
648.40	151.46
648.71	150.15
649.01	144.50
649.32	140.20
649.63	170.47
649.94	166.47
650.24	162.62
650.56	157.80
650.86	151.84
651.17	148.93
651.48	142.46
651.78	171.37

Normal stress (kPa)	Shear stress (kPa)
652.09	165.12
652.40	159.87
652.71	153.13
653.01	144.78
653.32	174.51
653.63	166.72
653.95	161.02
654.26	150.81
654.55	142.00
654.87	171.98
655.19	163.43
655.50	158.17
655.81	150.52
656.12	141.53
656.44	171.50
656.75	162.36
657.07	152.67
657.38	142.46
657.70	171.83
658.00	160.44
658.32	150.03
658.63	139.32
658.95	168.49
659.27	156.67

Normal stress (kPa)	Shear stress (kPa)
659.59	147.34
659.90	176.62
660.22	166.16
660.54	154.56
660.84	143.49
661.16	172.43
661.47	160.14
661.79	149.23
662.10	177.36
662.42	165.81
662.74	153.21
663.07	138.47
663.38	168.16
663.70	152.47
664.03	137.75
664.35	167.87
664.67	152.26
664.99	137.70
665.31	166.84
665.64	152.25
665.97	139.04
666.29	168.32
666.61	151.86
666.94	139.80

Normal stress (kPa)	Shear stress (kPa)
667.26	169.17
667.59	151.25
667.92	135.93
668.24	165.44
668.57	151.20
668.90	180.47
669.22	163.39
669.55	148.44
669.87	178.16
670.19	161.72
670.52	142.50
670.86	173.67
671.18	155.95
671.51	135.41
671.84	168.42
672.17	149.00
672.50	178.19
672.84	158.46
673.15	141.95
673.51	170.23
673.82	152.71
674.14	180.72
674.50	160.05
674.78	138.66

Normal stress (kPa)	Shear stress (kPa)
675.11	168.44
675.46	149.04
675.78	177.91
676.11	160.40
676.40	141.38
676.74	166.34
677.07	143.93
677.40	171.97
677.75	198.42
678.04	155.95
678.38	189.54
678.66	161.53
679.03	192.01
679.33	159.48
679.63	189.51
680.00	161.75
680.29	192.49
680.62	165.12
680.96	194.01
681.26	170.29
681.58	196.93
681.89	169.88
682.22	197.15
682.56	171.57

A5.1.3.1.2. Sample M4G – Test 2

Large-Direct Shear test

Sample:	M4G
Objective:	Basic Friction Angle
Initial Normal stress (kPa):	1262.76
Initial Normal stress (kg/cm2):	12.87
Initial Contact Area, (cm^2):	159.9

Table A5 - 5 Data results of Direct Shear tests on the sample M4G: Test 2.

Normal stress (kPa)	Shear stress (kPa)
1262.76	0.00
1263.29	2.55
1263.81	2.92
1264.35	4.29
1264.92	4.62
1265.48	5.14
1266.05	5.87
1266.60	4.75
1267.19	5.34
1267.78	5.96
1268.34	6.96
1268.93	5.69
1269.52	9.20
1270.07	10.83
1270.65	11.69
1271.23	15.39
1271.81	20.09
1272.40	30.17
1272.99	39.11
1273.58	48.20
1274.17	56.35
1274.76	66.59
1275.33	76.90
1275.94	85.39
1276.53	94.60
1277.13	103.24
1277.73	110.44
1278.33	118.23
1278.93	126.26
1279.51	133.61
1280.11	138.87
1280.70	148.12
1281.31	157.08
1281.91	167.50

Normal stress (kPa)	Shear stress (kPa)
1282.51	175.60
1283.13	182.40
1283.72	192.30
1284.35	200.71
1284.96	207.38
1285.56	214.83
1286.18	222.57
1286.79	230.47
1287.38	239.89
1287.98	246.76
1288.59	256.26
1289.22	263.21
1289.82	271.57
1290.47	279.17
1291.09	287.29
1291.68	291.72
1292.29	298.38
1292.90	302.20
1293.51	306.78
1294.16	313.61
1294.76	318.00
1295.37	276.67
1296.01	273.26
1296.63	285.02
1297.27	278.67
1297.90	274.33
1298.51	285.49
1299.13	281.13
1299.75	274.97
1300.39	275.20
1301.00	278.05
1301.62	277.15
1302.25	285.70
1302.89	281.91

Normal stress (kPa)	Shear stress (kPa)
1303.51	276.76
1304.13	284.41
1304.75	281.71
1305.38	276.46
1306.01	285.32
1306.64	278.40
1307.28	284.13
1307.92	280.78
1308.58	279.14
1309.19	284.30
1309.84	280.78
1310.47	282.98
1311.09	282.24
1311.72	283.83
1312.36	283.06
1312.99	285.66
1313.63	283.71
1314.30	287.94
1314.94	283.83
1315.58	292.57
1316.22	291.42
1316.85	310.86
1317.49	302.24
1318.12	331.95
1318.76	310.05
1319.40	343.28
1320.07	316.24
1320.72	344.95
1321.39	324.35
1322.03	349.68
1322.68	321.59
1323.29	339.85
1323.97	321.02
1324.61	334.93

Normal stress (kPa)	Shear stress (kPa)
1325.27	321.35
1325.92	334.16
1326.61	322.28
1327.25	329.40
1327.90	358.93
1328.55	329.35
1329.22	356.59
1329.87	324.38
1330.54	344.58
1331.20	322.87
1331.85	340.61
1332.53	325.13
1333.18	335.58
1333.86	359.48
1334.52	327.28
1335.18	347.22
1335.86	325.46
1336.52	343.62
1337.17	364.72
1337.85	330.78
1338.53	353.27
1339.22	326.89
1339.89	343.25
1340.57	325.80
1341.24	334.07
1341.89	360.73
1342.59	333.58
1343.26	362.56
1343.94	328.30
1344.61	342.93
1345.30	375.43
1346.00	331.67
1346.67	362.11
1347.37	326.27

Normal stress (kPa)	Shear stress (kPa)
1348.02	345.29
1348.70	378.86
1349.39	332.98
1350.05	361.27
1350.73	328.52
1351.41	342.51
1352.09	374.78
1352.81	329.68
1353.49	358.70
1354.18	327.58
1354.86	340.46
1355.53	375.21
1356.23	330.41
1356.90	354.12
1357.60	386.56
1358.28	331.99
1358.98	365.34
1359.70	331.29
1360.40	345.08
1361.05	375.76
1361.77	331.95
1362.43	355.26
1363.13	389.41
1363.83	336.96
1364.53	370.02
1365.24	330.22
1365.94	347.26
1366.62	380.76
1367.34	330.62
1368.02	351.57
1368.71	385.38
1369.42	333.77
1370.09	362.83
1370.77	394.66

Normal stress (kPa)	Shear stress (kPa)
1371.47	342.52
1372.19	376.12
1372.89	332.66
1373.60	351.40
1374.29	385.32
1374.99	332.93
1375.70	362.12
1376.39	395.50
1377.09	339.08
1377.80	370.33
1378.52	333.57
1379.22	346.76
1379.91	380.62

Normal stress (kPa)	Shear stress (kPa)
1380.64	333.72
1381.34	353.11
1382.05	387.45
1382.77	335.77
1383.47	365.33
1384.15	396.04
1384.91	340.68
1385.61	371.05
1386.31	402.89
1387.02	345.62
1387.74	380.35
1388.46	337.98
1389.17	356.94

Normal stress (kPa)	Shear stress (kPa)
1389.88	386.89
1390.61	337.59
1391.33	359.15
1392.05	393.71
1392.78	338.12
1393.51	365.22
1394.20	397.80
1394.93	340.99
1395.66	371.36
1396.36	400.67
1397.11	344.10
1397.83	378.53
1398.58	338.41

Normal stress (kPa)	Shear stress (kPa)
1399.32	353.03
1400.04	392.36
1400.77	338.81
1401.47	360.65
1402.20	397.81
1402.97	340.08
1403.69	367.14
1404.42	400.32
1405.16	340.94
1405.89	374.50
1406.63	403.53
1407.38	351.86
1408.11	384.53

Normal stress (kPa)	Shear stress (kPa)
1408.85	340.43
1409.59	353.45
1410.33	383.33
1411.07	339.00
1411.82	351.85
1412.55	385.24
1413.32	338.44
1414.08	352.58
1414.80	386.09
1415.54	409.51
1416.29	348.09
1417.05	381.44

A5.1.3.1.3. Sample M4G – Test 3

Large-Direct Shear test

Sample:	M4G
Objective:	Basic Friction Angle
Initial Normal stress (kPa):	2513.55
Initial Normal stress (kg/cm2):	25.62
Initial Contact Area, (cm^2):	159.9

Table A5 - 6 Data results of Direct Shear tests on the sample M4G: Test 3.

Normal stress (kPa)	Shear stress (kPa)
2513.55	0.00
2514.47	0.41
2515.54	1.55
2516.58	1.90
2517.57	5.75
2518.64	6.97
2519.66	7.95
2520.69	8.72

Normal stress (kPa)	Shear stress (kPa)
2521.81	10.41
2522.83	11.89
2523.89	12.47
2525.02	14.68
2526.01	16.23
2527.12	18.54
2528.20	20.60
2529.29	22.88

Normal stress (kPa)	Shear stress (kPa)
2530.36	25.80
2531.42	28.04
2532.51	30.71
2533.64	33.02
2534.71	35.39
2535.76	38.96
2536.85	42.52
2537.93	47.92

Normal stress (kPa)	Shear stress (kPa)
2539.04	51.25
2540.16	56.25
2541.23	61.13
2542.31	65.83
2543.39	71.43
2544.51	77.60
2545.58	84.18
2546.69	91.37

Normal stress (kPa)	Shear stress (kPa)
2547.77	98.40
2548.87	105.32
2549.95	112.30
2551.08	119.88
2552.23	127.63
2553.31	135.61
2554.40	142.76
2555.51	150.00

Normal stress (kPa)	Shear stress (kPa)
2556.64	157.69
2557.75	165.76
2558.82	173.67
2559.93	181.83
2561.04	190.02
2562.18	198.18
2563.30	206.19
2564.43	214.32
2565.53	221.20
2566.67	229.16
2567.83	236.96
2568.95	244.21
2570.12	251.92
2571.27	260.10
2572.46	268.32
2573.63	275.47
2574.82	282.92
2575.99	290.56
2577.19	298.37
2578.34	306.07
2579.51	314.11
2580.71	322.72
2581.96	331.26
2583.09	340.73
2584.31	350.57
2585.52	360.34
2586.74	371.68
2587.95	383.86
2589.15	394.66
2590.34	406.20
2591.53	417.80
2592.76	431.25
2593.95	444.79
2595.18	458.62
2596.39	473.14
2597.63	488.00

Normal stress (kPa)	Shear stress (kPa)
2598.85	503.33
2600.06	518.17
2601.30	533.48
2602.50	548.14
2603.79	563.30
2604.96	578.13
2606.21	594.27
2607.46	609.70
2608.70	624.74
2609.95	639.79
2611.18	654.30
2612.43	669.63
2613.71	684.25
2614.94	699.01
2616.17	713.78
2617.43	727.94
2618.71	742.82
2619.94	757.16
2621.25	770.94
2622.51	783.04
2623.75	794.92
2625.01	807.03
2626.23	819.10
2627.52	831.39
2628.78	842.35
2630.05	853.16
2631.35	865.59
2632.66	877.56
2633.91	887.25
2635.21	896.27
2636.46	904.28
2637.74	912.69
2639.01	921.73
2640.29	928.71
2641.59	935.73
2642.85	941.18

Normal stress (kPa)	Shear stress (kPa)
2644.16	946.94
2645.49	949.68
2646.77	951.01
2648.06	952.72
2649.34	956.58
2650.61	959.34
2651.90	962.55
2653.21	963.50
2654.50	964.65
2655.77	965.65
2657.14	966.08
2658.44	966.21
2659.73	967.12
2661.01	966.91
2662.33	967.76
2663.58	968.39
2664.96	968.75
2666.24	969.25
2667.54	969.70
2668.90	970.31
2670.20	970.79
2671.54	971.16
2672.85	971.84
2674.18	972.01
2675.52	972.98
2676.78	973.73
2678.15	974.73
2679.46	975.06
2680.81	975.70
2682.15	976.64
2683.52	978.67
2684.84	980.13
2686.14	982.13
2687.44	983.59
2688.71	985.27
2690.04	988.55

Normal stress (kPa)	Shear stress (kPa)
2691.39	992.28
2692.72	996.33
2694.08	997.73
2695.44	997.27
2696.77	993.26
2698.13	989.66
2699.46	981.78
2700.80	975.95
2702.09	971.80
2703.46	963.33
2704.85	953.10
2706.24	945.77
2707.53	940.66
2708.93	935.35
2710.30	926.18
2711.62	919.97
2713.00	915.77
2714.35	910.61
2715.73	907.68
2717.11	905.66
2718.41	904.57
2719.82	902.52
2721.20	901.21
2722.58	899.47
2723.94	887.24
2725.33	873.46
2726.72	871.71
2728.06	871.80
2729.40	871.45
2730.82	870.80
2732.16	871.12
2733.56	871.83
2734.95	871.93
2736.35	872.52
2737.75	873.15
2739.10	873.70

Normal stress (kPa)	Shear stress (kPa)
2740.50	874.79
2741.86	875.70
2743.24	876.22
2744.64	877.31
2746.03	879.63
2747.49	884.69
2748.92	888.22
2750.34	890.97
2751.70	894.08
2753.11	898.40
2754.48	901.66
2755.87	904.24
2757.29	904.68
2758.69	904.89
2760.11	904.55
2761.53	905.53
2763.01	905.48
2764.39	905.62
2765.81	905.61
2767.22	906.05
2768.65	906.38
2770.11	906.39
2771.52	906.85
2772.95	906.93
2774.39	907.56
2775.88	907.71
2777.30	908.87
2778.82	909.87
2780.23	911.69
2781.70	914.87
2783.15	919.91
2784.68	924.73
2786.15	929.64

A5.1.3.2. Conventional Direct Shear test

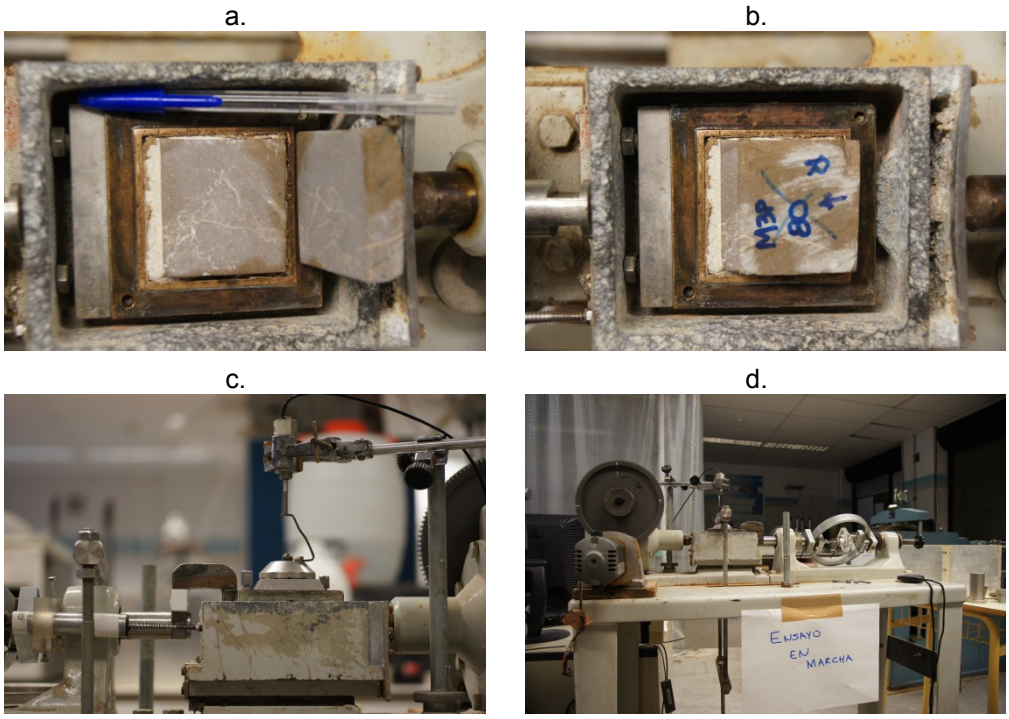

Figure A5 - 7 Conventional Direct Shear test: (a), (b) M3P sample in the Direct Shear box); (c) Direct Shear box; (d) Direct Shear equipment.

A5.1.3.2.1. Sample M3P – Test 1

Conventional Direct Shear test	
Sample:	M3P
Objective:	Mineral Friction Angle
Initial Normal stress (kPa):	14.53
Initial Normal stress (kg/cm2):	0.15
Initial Contact Area, (cm^2):	28.82

Table A5 - 7 Data results of Direct Shear tests on the sample M3P: Test 1.

Normal stress (kPa)	Shear stress (kPa)	Normal stress (kPa)	Shear stress (kPa)	Normal stress (kPa)	Shear stress (kPa)	Normal stress (kPa)	Shear stress (kPa)	Normal stress (kPa)	Shear stress (kPa)
14.53	0.00	14.80	5.03	15.04	5.71	15.33	7.87	15.61	8.34
14.53	0.92	14.80	4.89	15.05	5.61	15.34	7.19	15.63	8.20
14.53	2.83	14.81	4.96	15.06	5.68	15.35	7.05	15.64	8.13
14.54	4.84	14.82	4.96	15.07	5.75	15.35	7.01	15.65	8.14
14.55	4.26	14.82	5.14	15.07	5.90	15.36	7.31	15.66	8.11
14.56	4.71	14.83	4.93	15.08	5.69	15.37	7.06	15.66	8.07
14.57	4.40	14.84	4.90	15.09	5.76	15.38	7.31	15.67	8.19
14.58	4.92	14.84	4.97	15.10	5.87	15.38	7.24	15.68	7.68
14.59	4.89	14.85	5.15	15.11	5.84	15.39	7.57	15.69	7.90
14.60	4.65	14.86	5.19	15.12	5.91	15.40	7.50	15.70	7.83
14.62	4.93	14.87	5.26	15.13	5.99	15.41	7.54	15.71	7.91
14.62	5.14	14.87	5.05	15.14	6.06	15.42	7.80	15.72	7.95
14.63	4.56	14.88	5.12	15.15	6.14	15.42	7.70	15.72	8.11
14.64	4.22	14.89	5.27	15.16	6.32	15.43	7.74	15.73	7.96
14.65	4.94	14.89	5.51	15.17	5.86	15.44	4.74	15.74	8.11
14.65	5.01	14.90	5.41	15.18	6.40	15.45	7.60	15.75	8.12
14.66	4.95	14.91	5.45	15.19	6.40	15.46	7.71	15.76	8.16
14.67	4.98	14.92	5.59	15.19	6.55	15.47	7.46	15.77	8.24
14.67	5.02	14.92	5.52	15.20	6.66	15.48	7.69	15.78	8.32
14.68	4.78	14.93	5.46	15.21	6.59	15.48	7.47	15.79	8.29
14.69	4.82	14.94	5.35	15.22	6.63	15.49	7.91	15.80	8.22
14.70	5.10	14.94	5.46	15.23	6.78	15.50	8.03	15.81	8.37
14.70	5.10	14.95	5.43	15.24	6.71	15.51	7.89	15.81	8.41
14.71	5.14	14.96	5.57	15.25	6.89	15.52	8.00	15.82	8.53
14.72	4.97	14.97	5.58	15.26	6.79	15.53	8.11	15.83	8.64
14.73	4.80	14.98	5.68	15.26	6.72	15.54	8.08	15.84	8.50
14.74	4.87	14.98	5.79	15.27	6.80	15.55	8.12	15.85	8.39
14.75	5.01	14.99	5.69	15.28	6.66	15.56	8.31	15.85	8.47
14.75	4.87	15.00	5.83	15.29	6.81	15.57	8.21	15.86	8.51
14.76	4.74	15.01	5.84	15.30	6.77	15.58	8.14	15.87	8.55
14.77	5.02	15.01	5.98	15.30	6.96	15.58	8.25	15.88	8.56
14.78	4.99	15.02	5.95	15.31	6.82	15.59	8.18	15.89	8.49
14.79	4.92	15.03	5.81	15.32	7.00	15.60	8.19	15.89	8.53

Normal stress (kPa)	Shear stress (kPa)	Normal stress (kPa)	Shear stress (kPa)	Normal stress (kPa)	Shear stress (kPa)	Normal stress (kPa)	Shear stress (kPa)	Normal stress (kPa)	Shear stress (kPa)
15.90	8.42	15.96	8.75	16.03	8.75	16.09	8.52	16.17	8.14
15.91	8.46	15.97	8.64	16.04	8.75	16.10	8.34	16.18	8.11
15.92	8.43	15.98	8.72	16.04	8.80	16.11	8.57	16.19	7.97
15.93	8.40	15.99	8.65	16.05	8.69	16.12	8.39		
15.94	8.59	16.00	8.55	16.06	8.58	16.13	8.32		
15.94	8.59	16.01	8.59	16.07	8.62	16.15	8.32		
15.95	8.93	16.02	8.52	16.08	8.44	16.16	8.37		

A5.1.3.2.2. Sample M3P – Test 2

Conventional Direct Shear test

Sample:	M3P
Objective:	Mineral Friction Angle
Initial Normal stress (kPa):	36.35
Initial Normal stress (kg/cm2):	0.37
Initial Contact Area, (cm^2):	28.82

Table A5 - 8 Data results of Direct Shear tests on the sample M3P: Test 2.

Normal stress (kPa)	Shear stress (kPa)	Normal stress (kPa)	Shear stress (kPa)	Normal stress (kPa)	Shear stress (kPa)	Normal stress (kPa)	Shear stress (kPa)	Normal stress (kPa)	Shear stress (kPa)
36.35	0.00	36.53	7.01	36.85	7.18	37.19	6.76	37.57	7.35
36.36	1.80	36.55	6.98	36.88	7.18	37.22	6.48	37.60	7.53
36.36	2.01	36.57	7.05	36.91	7.08	37.24	6.45	37.62	7.68
36.36	2.11	36.60	7.02	36.93	7.02	37.26	6.45	37.65	7.75
36.36	1.84	36.62	6.99	36.96	6.92	37.29	6.46	37.67	7.83
36.36	1.97	36.64	7.10	36.98	6.82	37.32	6.43	37.70	8.01
36.36	1.80	36.66	7.07	37.01	6.90	37.35	6.29	37.72	8.12
36.37	3.61	36.68	6.87	37.03	6.73	37.38	6.33	37.75	8.27
36.38	6.40	36.71	7.01	37.05	6.77	37.41	6.30	37.77	8.28
36.40	6.82	36.73	7.08	37.08	6.70	37.43	6.24	37.80	8.81
36.43	6.82	36.75	7.09	37.11	6.57	37.46	6.31	37.83	8.25
36.45	6.86	36.78	7.16	37.13	6.85	37.49	6.67	37.85	8.36
36.48	6.80	36.80	7.13	37.15	6.64	37.52	6.92	37.88	8.30
36.50	6.97	36.83	7.17	37.17	6.54	37.55	7.14	37.91	8.52

Normal stress (kPa)	Shear stress (kPa)
37.93	8.20
37.96	8.35
37.99	8.22
38.02	8.47
38.05	8.48
38.08	8.49
38.11	8.56
38.13	8.61
38.16	8.65
38.19	8.62
38.22	8.70
38.25	8.67
38.28	8.67
38.30	8.75
38.33	8.72
38.36	8.80
38.39	8.73
38.41	8.74
38.44	8.78
38.48	8.61
38.51	8.73
38.55	8.73
38.58	8.71
38.62	8.71
38.65	8.79
38.69	8.84
38.72	8.85

Normal stress (kPa)	Shear stress (kPa)
38.75	8.89
38.77	8.79
38.80	8.79
38.83	8.73
38.86	8.81
38.89	8.81
38.92	8.96
38.95	8.75
38.97	8.94
39.00	8.87
39.03	8.66
39.06	9.07
39.09	8.82
39.13	8.90
39.16	8.98
39.19	9.36
39.22	9.00
39.25	8.97
39.28	9.05
39.32	8.98
39.35	9.03
39.38	9.00
39.42	9.01
39.45	8.87
39.48	8.98
39.51	8.99
39.54	8.63

Normal stress (kPa)	Shear stress (kPa)
39.57	8.89
39.60	8.94
39.64	8.80
39.68	8.73
39.71	9.33
39.75	8.82
39.79	8.90
39.83	8.80
39.86	8.51
39.90	8.89
39.93	8.94
39.97	8.94
40.00	8.95
40.03	8.92
40.06	9.04
40.09	9.05
40.12	9.05
40.16	9.10
40.19	9.07
40.22	9.15
40.25	9.12
40.28	9.24
40.31	9.13
40.34	9.18
40.37	8.96
40.41	9.27
40.44	9.16

Normal stress (kPa)	Shear stress (kPa)
40.48	9.25
40.51	9.22
40.54	9.41
40.58	9.23
40.61	9.13
40.65	9.21
40.68	9.10
40.71	9.11
40.74	9.19
40.78	9.09
40.81	9.09
40.84	9.10
40.88	8.99
40.92	9.16
40.95	9.85
40.99	9.06
41.03	8.95
41.06	9.00
41.10	8.97
41.14	8.86
41.17	9.17
41.20	8.83
41.24	9.00
41.27	8.89
41.30	9.05
41.33	8.98
41.36	9.02

Normal stress (kPa)	Shear stress (kPa)
41.39	9.07
41.42	9.00
41.45	8.77
41.48	8.93
41.51	9.06
41.54	9.06
41.57	9.07
41.60	9.07
41.63	9.00
41.66	9.05
41.69	9.06
41.73	9.03
41.76	8.45
41.79	9.04
41.83	9.09
41.86	9.13
41.90	9.02
41.93	9.15
41.97	9.12
42.00	9.12

A5.1.3.2.3. Sample M3P – Test 3

Conventional Direct Shear test

Sample:	M3P
Objective:	Mineral Friction Angle
Initial Normal stress (kPa):	70.39
Initial Normal stress (kg/cm2):	0.72

Initial Contact Area, (cm^2): 28.82

Table A5 - 9 Data results of Direct Shear tests on the sample M3P: Test 3.

Normal stress (kPa)	Shear stress (kPa)	Normal stress (kPa)	Shear stress (kPa)	Normal stress (kPa)	Shear stress (kPa)	Normal stress (kPa)	Shear stress (kPa)	Normal stress (kPa)	Shear stress (kPa)
70.39	0.00	70.40	6.16	70.41	10.35	70.41	15.15	70.45	15.19
70.40	2.79	70.40	6.33	70.40	10.69	70.41	15.25	70.45	15.23
70.40	2.76	70.40	6.47	70.41	10.79	70.38	15.42	70.45	15.36
70.40	2.69	70.40	6.64	70.41	10.83	70.41	15.66	70.45	15.33
70.40	2.66	70.40	6.71	70.41	11.13	70.41	16.04	70.45	15.47
70.40	2.72	70.40	6.88	70.41	11.40	70.42	13.66	70.45	15.36
70.40	3.44	70.40	6.98	70.41	11.51	70.42	14.00	70.46	15.50
70.40	2.72	70.40	7.12	70.41	11.64	70.42	14.20	70.46	15.33
70.40	2.76	70.40	7.29	70.41	11.92	70.42	14.37	70.46	15.37
70.40	2.79	70.40	7.39	70.41	11.92	70.42	14.47	70.46	15.40
70.40	3.00	70.40	7.52	70.41	11.98	70.42	14.58	70.46	15.43
70.40	3.06	70.40	7.66	70.41	12.36	70.41	14.57	70.47	15.40
70.40	3.40	70.40	7.83	70.41	12.46	70.43	14.54	70.46	15.47
70.40	3.34	70.40	7.90	70.41	12.43	70.43	14.88	70.47	15.40
70.40	3.57	70.40	8.17	70.41	12.73	70.43	14.64	70.47	15.44
70.40	3.81	70.40	8.17	70.41	12.87	70.43	14.71	70.47	15.44
70.40	3.98	70.40	8.41	70.41	12.53	70.43	14.75	70.47	15.91
70.40	4.19	70.40	8.44	70.41	13.11	70.43	14.51	70.47	15.33
70.40	4.39	70.41	8.65	70.41	13.28	70.43	14.95	70.47	15.40
70.40	4.43	70.40	8.65	70.41	13.24	70.44	14.61	70.47	15.44
70.40	4.70	70.41	8.82	70.41	13.07	70.44	14.95	70.47	15.40
70.40	4.87	70.41	9.02	70.41	13.72	70.44	15.02	70.48	15.34
70.40	4.83	70.41	9.09	70.41	13.86	70.44	14.89	70.48	15.17
70.40	5.07	70.41	9.29	70.41	13.89	70.44	15.02	70.48	15.44
70.40	5.17	70.41	9.36	70.41	14.16	70.44	15.09	70.49	15.37
70.40	5.38	70.41	9.60	70.41	14.27	70.44	15.09	70.49	15.44
70.40	5.48	70.41	9.36	70.41	14.44	70.44	15.23	70.49	15.27
70.40	5.62	70.40	9.80	70.41	14.71	70.44	15.23	70.49	15.47
70.41	5.69	70.41	9.94	70.41	14.13	70.44	15.23	70.49	15.44
70.40	5.58	70.41	10.11	70.41	13.79	70.45	15.26	70.48	15.54
70.40	6.09	70.41	10.18	70.41	14.50	70.45	15.19	70.49	15.54

Normal stress (kPa)	Shear stress (kPa)
70.49	15.58
70.49	15.44
70.49	15.58
70.50	15.65
70.50	15.58
70.50	15.54
70.50	15.44
70.50	15.65
70.50	15.75
70.50	15.65
70.50	15.48
70.50	15.61
70.51	15.51
70.51	15.75
70.51	15.58
70.51	15.68
70.51	15.58
70.51	15.79
70.52	15.72
70.52	15.65
70.52	15.69
70.50	15.68
70.52	15.79
70.52	15.72
70.53	15.69
70.53	15.65
70.53	15.72
70.53	15.76
70.53	19.17
70.53	15.65
70.53	15.79
70.53	15.72
70.53	15.72
70.53	15.76
70.53	15.86
70.54	15.66

Normal stress (kPa)	Shear stress (kPa)
70.54	15.83
70.54	15.79
70.54	15.83
70.54	15.79
70.54	15.79
70.55	15.86
70.55	15.83
70.55	15.80
70.55	15.80
70.53	15.41
70.55	15.80
70.56	15.80
70.56	15.69
70.56	15.73
70.56	15.66
70.56	15.63
70.56	16.41
70.57	15.56
70.57	15.66
70.56	15.59
70.57	15.53
70.56	15.63
70.57	15.53
70.57	15.63
70.57	15.60
70.58	15.56
70.58	15.56
70.58	15.67
70.58	15.67
70.58	15.80
70.58	15.73
70.58	15.73
70.59	15.70
70.59	15.53
70.59	15.50
70.59	15.57

Normal stress (kPa)	Shear stress (kPa)
70.59	15.63
70.60	15.57
70.60	15.57
70.60	15.57
70.60	15.57
70.60	15.64
70.60	15.70
70.60	15.64
70.60	15.67
70.60	15.67
70.61	15.67
70.61	15.74
70.61	15.64
70.61	15.64
70.61	15.60
70.62	15.61
70.62	15.13
70.62	15.61
70.62	15.43
70.62	15.37
70.62	15.44
70.62	15.54
70.62	15.74
70.62	15.68
70.63	15.71
70.63	15.47
70.63	15.71
70.63	15.71
70.63	15.78
70.63	16.09
70.64	15.78
70.64	15.71
70.64	15.78
70.64	15.71
70.64	15.75
70.64	15.75

Normal stress (kPa)	Shear stress (kPa)
70.64	15.78
70.65	15.75
70.66	15.72
70.65	15.71
70.65	15.82
70.65	15.85
70.65	15.85
70.65	15.82
70.65	15.82
70.66	15.78
70.66	15.89
70.66	15.89
70.66	15.99
70.66	15.96
70.66	15.85
70.66	15.92
70.67	15.86
70.70	16.03
70.67	15.75
70.67	16.03
70.67	15.99
70.67	16.03
70.67	16.06
70.67	16.06
70.68	16.16
70.68	16.16
70.68	16.06
70.68	16.06
70.68	16.06
70.68	15.82
70.68	16.10
70.68	16.10
70.69	16.00
70.69	16.00
70.69	15.83
70.69	16.03

Normal stress (kPa)	Shear stress (kPa)
70.69	15.79
70.69	15.31
70.69	16.00
70.70	16.10
70.70	16.17
70.70	16.03
70.70	16.03
70.70	16.00
70.70	16.03
70.71	15.97
70.71	16.31
70.71	16.07
70.71	16.04
70.71	15.97
70.71	16.04
70.72	16.00
70.72	15.73
70.72	16.17
70.72	15.97
70.72	16.04
70.72	15.97
70.72	16.00
70.72	15.90
70.73	16.01
70.73	15.94
70.73	15.94
70.73	15.94
70.73	16.38
70.73	15.87
70.74	15.87
70.74	15.84
70.74	15.80
70.74	15.84
70.74	15.67
70.74	15.74
70.75	15.74

Normal stress (kPa)	Shear stress (kPa)
70.74	15.91
70.75	15.77
70.75	15.81
70.75	15.91
70.75	15.98
70.75	15.91
70.75	15.74
70.76	15.94
70.76	15.98
70.76	16.01
70.76	16.05
70.76	16.01
70.76	15.98
70.76	15.98
70.77	15.98
70.77	16.05
70.77	16.02
70.77	16.08
70.77	16.05
70.77	16.08
70.78	16.02
70.78	16.09
70.78	16.19
70.78	16.15
70.78	16.16
70.78	16.09
70.79	16.19
70.78	16.16
70.79	16.19
70.79	16.19
70.79	16.26
70.79	16.09
70.79	16.16
70.79	16.81
70.79	16.26
70.80	16.43

Normal stress (kPa)	Shear stress (kPa)
70.80	16.36
70.80	16.37
70.80	16.54
70.80	16.43
70.80	16.40
70.81	16.37
70.81	16.44
70.81	16.43
70.81	16.37
70.81	16.33
70.81	16.09
70.82	16.44
70.82	16.37
70.82	16.20
70.82	16.33
70.82	16.37
70.82	16.30
70.82	16.23
70.82	16.20
70.83	16.17
70.83	16.13
70.83	16.13
70.83	16.23
70.83	16.06
70.83	16.03
70.84	16.06
70.84	15.96
70.84	16.03
70.84	16.00
70.84	16.00
70.84	15.45
70.85	16.03
70.85	16.03
70.85	16.86
70.85	15.97
70.85	15.79

Normal stress (kPa)	Shear stress (kPa)
70.86	15.93
70.86	15.90
70.86	15.93
70.86	16.00
70.86	16.00
70.86	16.04
70.86	15.97
70.86	16.00
70.87	16.11
70.89	16.83
70.93	16.81
70.97	16.54
71.01	16.79
71.05	16.73
71.09	16.77
71.13	17.09
71.17	17.04
71.21	17.29
71.26	17.30
71.30	17.62
71.34	17.56
71.37	17.57
71.42	17.72
71.47	17.59
71.51	17.95
71.55	17.99
71.59	18.14
71.63	18.29
71.67	18.26
71.72	18.38
71.76	18.25
71.80	18.37
71.85	18.52
71.89	18.63
71.93	18.78
71.97	18.93

Normal stress (kPa)	Shear stress (kPa)
72.02	19.05
72.06	19.30
72.10	18.86
72.14	19.26
72.18	18.88
72.23	19.35
72.28	19.36
72.32	19.23
72.37	19.74
72.41	19.85
72.46	20.25
72.51	20.16
72.55	19.93
72.61	19.70
72.65	20.73
72.70	20.81
72.75	21.21
72.79	21.05
72.84	21.13
72.89	21.11
72.93	21.30
72.98	21.14
73.02	20.97
73.06	21.23
73.11	21.18
73.16	21.19
73.21	21.38
73.25	21.54
73.29	21.48
73.34	21.67
73.38	21.61
73.43	22.01
73.47	22.17
73.51	22.15
73.56	22.16
73.61	22.32

Normal stress (kPa)	Shear stress (kPa)
73.65	22.47
73.70	22.56
73.75	22.72
73.79	22.77
73.84	23.21
73.89	22.83
73.94	22.99
73.98	23.18
74.00	23.62
74.07	23.64
74.11	23.51
74.16	23.81
74.20	23.86
74.24	23.91
74.29	24.28
74.34	24.30
74.38	24.46
74.43	23.54
74.47	23.98
74.52	23.68
74.57	24.23
74.62	24.21
74.66	24.15
74.71	24.20
74.75	24.36
74.81	23.84
74.85	24.32
74.90	24.34
74.95	23.12
75.00	23.54
75.04	24.71
75.09	24.62
75.13	24.78
75.20	24.58
75.22	24.01
75.27	23.33

Normal stress (kPa)	Shear stress (kPa)
75.31	24.36
75.35	23.79
75.40	24.21
75.44	24.26
75.49	24.38
75.53	25.46
75.58	24.41
75.63	23.96
75.68	24.70
75.73	23.95
75.77	24.22
75.83	23.72
75.87	24.51
75.92	25.18
75.97	25.27
76.02	25.55
76.06	26.08
76.11	25.73
76.16	26.18
76.21	25.13

Normal stress (kPa)	Shear stress (kPa)
76.26	26.22
76.31	24.80
76.36	25.48
76.40	26.12
76.45	26.50
76.51	24.97
76.55	26.21
76.60	26.59
76.65	25.65
76.70	25.44
76.75	26.27
76.80	26.03
76.85	26.16
76.90	25.99
76.97	23.08
77.01	26.21
77.06	25.53
77.11	25.99
77.16	26.19
77.21	26.06

Normal stress (kPa)	Shear stress (kPa)
77.26	26.41
77.31	25.87
77.37	25.74
77.42	24.82
77.47	24.50
77.52	25.19
77.57	25.47
77.63	23.54
77.67	25.73
77.72	24.54
77.76	26.66
77.81	25.43
77.85	26.20
77.90	26.71
77.95	25.71
78.00	24.93
78.04	25.47
78.09	25.83
78.14	25.88
78.19	25.41

Normal stress (kPa)	Shear stress (kPa)
78.24	26.14
78.28	26.69
78.34	26.44
78.39	26.57
78.45	25.98
78.50	26.57
78.56	25.30
78.61	26.42
78.66	26.62
78.70	26.91
78.75	26.50
78.80	27.05
78.86	25.59
78.90	27.43
78.96	27.72
79.01	26.55
79.07	26.08
79.12	27.20
79.17	27.41
79.23	26.05

Normal stress (kPa)	Shear stress (kPa)
79.28	27.18
79.33	27.39
79.39	25.34
79.44	27.16
79.49	27.17
79.55	26.04
79.60	25.94
79.65	26.50
79.72	25.63
79.77	27.46
79.84	25.40
79.89	26.73
79.94	26.94
80.00	25.34
80.05	26.44
80.10	27.07
80.16	26.94
80.22	26.42
80.26	27.59
80.32	27.85

A5.1.3.2.4. Sample M3P – Test 4

Conventional Direct Shear test	
Sample:	M3P
Objective:	Mineral Friction Angle
Initial Normal stress (kPa):	138.47
Initial Normal stress (kg/cm2):	1.41
Initial Contact Area, (cm^2):	28.82

Table A5 - 10 Data results of Direct Shear tests on the sample M3P: Test 4.

Normal stress (kPa)	Shear stress (kPa)
138.47	0.00
138.54	7.56
138.60	11.18
138.67	12.95
138.75	14.29
138.83	15.15
138.89	17.96
139.01	12.95
139.09	13.30
139.16	13.17
139.23	13.66
139.31	13.73
139.39	13.57
139.47	13.71
139.55	13.34
139.64	13.39
139.72	13.70
139.79	13.71
139.88	13.93
139.95	14.28
140.04	14.29
140.12	14.19
140.21	14.27
140.29	14.35
140.39	14.32
140.48	14.40
140.57	14.10
140.65	14.52
140.73	14.70
140.82	14.68
140.91	14.76
140.99	14.76
141.08	15.05

Normal stress (kPa)	Shear stress (kPa)
141.15	15.37
141.24	15.45
141.33	15.50
141.40	15.95
141.49	16.03
141.57	16.15
141.65	16.12
141.73	16.62
141.81	16.94
141.89	17.20
141.97	17.55
142.06	17.77
142.14	17.92
142.23	18.29
142.31	18.61
142.41	18.52
142.49	18.81
142.58	18.75
142.67	18.80
142.76	19.16
142.86	19.45
142.94	19.43
143.02	19.62
143.12	20.16
143.20	20.24
143.30	20.50
143.39	20.69
143.50	20.81
143.58	21.11
143.68	21.02
143.77	21.13
143.87	21.11
143.96	21.52

Normal stress (kPa)	Shear stress (kPa)
144.05	21.60
144.14	21.69
144.24	21.77
144.34	21.61
144.43	21.91
144.53	21.99
144.62	22.50
144.71	23.12
144.81	23.21
144.91	23.12
145.01	23.24
145.11	23.36
145.20	23.42
145.30	23.97
145.39	24.73
145.50	23.18
145.58	23.91
145.69	21.85
145.77	23.86
145.86	23.92
145.94	24.04
146.03	23.94
146.14	23.96
146.22	24.91
146.31	24.71
146.41	24.37
146.52	23.95
146.61	24.94
146.71	25.39
146.83	24.54
146.92	25.57
147.01	26.02
147.19	19.76

Normal stress (kPa)	Shear stress (kPa)
147.23	24.57
147.33	25.28
147.41	25.76
147.56	22.49
147.63	25.91
147.79	18.89
147.83	25.11
147.92	26.80
148.02	25.98
148.11	26.51
148.23	24.45
148.30	26.72
148.41	26.23
148.54	23.26
148.61	26.38
148.71	25.92
148.83	25.06
148.91	26.61
149.01	27.25
149.11	27.38
149.25	25.53
149.39	22.33
149.45	26.86
149.57	26.18
149.66	27.56
149.81	23.61
149.90	26.13
150.01	26.14
150.11	27.16
150.23	25.70
150.40	18.89
150.43	25.96
150.54	26.68

Normal stress (kPa)	Shear stress (kPa)
150.64	26.85
150.75	26.68
150.83	28.25
150.97	26.46
151.10	23.59
151.17	27.28
151.34	21.50
151.41	26.83
151.52	27.15
151.62	27.92
151.75	26.37
151.94	18.04
151.98	25.93
152.08	27.96
152.21	26.75
152.30	28.15
152.45	24.70
152.53	28.01
152.67	25.93
152.76	28.05
152.89	25.63
152.97	28.58
153.12	24.73
153.21	28.32
153.37	22.77
153.44	27.72
153.59	24.69
153.74	20.03
153.78	27.18
153.88	28.94
154.02	25.44
154.10	28.79
154.25	25.78

Normal stress (kPa)	Shear stress (kPa)
154.34	28.23
154.49	25.98
154.57	28.65
154.73	24.80
154.80	28.35
154.96	24.07
155.03	28.43
155.17	25.52
155.25	28.20
155.42	22.54
155.49	27.02
155.67	20.74
155.72	27.22
155.82	28.84
155.98	24.66

Normal stress (kPa)	Shear stress (kPa)
156.06	28.12
156.23	23.77
156.31	27.74
156.49	22.43
156.56	27.52
156.68	28.69
156.79	28.60
156.96	26.08
157.07	27.88
157.19	28.32
157.35	25.37
157.46	27.75
157.63	24.26
157.72	28.11
157.93	20.92

Normal stress (kPa)	Shear stress (kPa)
157.98	28.16
158.21	17.89
158.25	26.80
158.47	18.23
158.51	26.46
158.62	28.31
158.79	25.26
158.88	28.71
159.05	26.27
159.16	27.86
159.32	25.30
159.42	28.45
159.59	25.89
159.80	18.82
159.84	26.05

Normal stress (kPa)	Shear stress (kPa)
159.95	28.35
160.11	25.62
160.21	28.24
160.39	22.55
160.46	28.48
160.57	30.19
160.74	26.47
160.85	27.40
161.01	26.48
161.11	29.43
161.28	26.76
161.40	29.04
161.57	26.25
161.79	18.85
161.86	27.33

Normal stress (kPa)	Shear stress (kPa)
161.98	29.27
162.13	29.93
162.32	24.78
162.42	29.70
162.60	26.42
162.72	28.96
162.90	26.35
163.12	19.01
163.17	28.04
163.29	29.82
163.42	31.09

A5.1.3.2.5. Sample M3P – Test 5

Conventional Direct Shear test

Sample:	M3P
Objective:	Mineral Friction Angle
Initial Normal stress (kPa):	274.63
Initial Normal stress (kg/cm2):	2.80
Initial Contact Area, (cm^2):	28.82

Table A5 - 11 Data results of Direct Shear tests on the sample M3P: Test 5.

Normal stress (kPa)	Shear stress (kPa)
274.63	0.00
274.64	4.63
274.65	10.21
274.68	16.44
274.73	24.35

Normal stress (kPa)	Shear stress (kPa)
274.82	30.32
274.98	34.87
275.18	38.47
275.39	41.54
275.57	45.60

Normal stress (kPa)	Shear stress (kPa)
275.65	54.67
275.71	63.94
275.79	73.19
276.44	50.16
276.58	51.90

Normal stress (kPa)	Shear stress (kPa)
276.74	52.00
276.93	51.42
277.08	51.17
277.25	50.41
277.44	49.17

Normal stress (kPa)	Shear stress (kPa)
277.61	48.41
277.62	56.84
277.80	57.33
277.97	56.16
278.16	56.06

Normal stress (kPa)	Shear stress (kPa)
278.32	54.78
278.49	55.47
278.69	54.16
278.89	52.82
279.07	51.33
279.25	49.98
279.45	48.35
279.48	56.88
279.67	54.94
279.89	52.18
280.10	51.59
280.32	50.00
280.33	58.72
280.54	57.62
280.73	56.51
280.92	55.88
281.12	54.63
281.31	53.63
281.51	52.27
281.70	51.43
281.89	49.86
281.93	59.02
282.12	58.43
282.31	57.77
282.53	55.85
282.75	53.13
282.95	51.69
283.16	50.54

Normal stress (kPa)	Shear stress (kPa)
283.19	60.30
283.40	58.59
283.62	57.55
283.84	56.15
284.06	54.64
284.28	53.10
284.49	52.36
284.52	61.22
284.74	59.43
284.96	57.92
285.18	55.50
285.41	53.81
285.68	49.86
285.69	59.74
285.91	58.58
286.15	57.00
286.38	55.51
286.60	53.32
286.82	51.65
286.84	61.61
287.09	58.50
287.35	55.81
287.38	64.90
287.72	56.99
287.96	54.11
288.19	51.76
288.23	61.66
288.46	58.17

Normal stress (kPa)	Shear stress (kPa)
288.71	56.15
288.95	53.26
288.97	62.97
289.21	59.76
289.48	56.51
289.72	53.47
289.97	51.00
290.00	61.25
290.20	60.79
290.46	58.07
290.70	56.17
290.99	52.55
291.01	63.05
291.36	54.57
291.41	64.80
291.71	59.91
292.08	51.04
292.10	61.77
292.43	55.64
292.68	53.40
292.72	63.60
293.01	58.76
293.28	55.73
293.52	52.97
293.56	63.27
293.82	61.40
294.14	54.83
294.18	65.01

Normal stress (kPa)	Shear stress (kPa)
294.48	60.70
294.74	57.68
294.78	67.81
295.16	58.31
295.44	54.30
295.48	64.60
295.77	60.19
296.09	53.76
296.14	64.12
296.55	52.89
296.57	63.34
296.89	57.99
297.21	52.13
297.23	62.70
297.68	49.55
297.71	59.37
298.01	53.63
298.06	63.80
298.36	58.69
298.67	53.83
298.71	64.31
299.03	58.52
299.34	53.39
299.37	64.08
299.69	59.06
300.00	54.88
300.03	66.04
300.49	53.41

Normal stress (kPa)	Shear stress (kPa)
300.52	64.10
300.84	59.18
301.19	52.75
301.21	63.47
301.56	57.00
301.59	67.06
302.02	56.30
302.05	66.56
302.36	61.50
302.69	54.96
302.73	65.14
303.04	59.95
303.36	54.07
303.40	64.83
303.73	58.09
304.06	52.08
304.10	62.15
304.41	56.26
304.45	66.64
304.80	58.56
304.85	68.54
305.22	59.96
305.58	52.95
305.61	63.37
305.93	57.75
305.99	67.93
306.32	61.85
306.66	55.80

A5.1.4. Summary of results

Table A5 - 12 Friction angles on limestone samples obtained from tilt tests and Direct Shear tests.

Friction Angle	Tilt tests	Direct Shear tests
Rough surfaces, ϕ_r	29°	
Basic friction angle, ϕ_b	17°	18°
Mineral friction angle, ϕ_m	13° - 14°	12°

A5.2. Contact stiffness tests

a. Before the tests

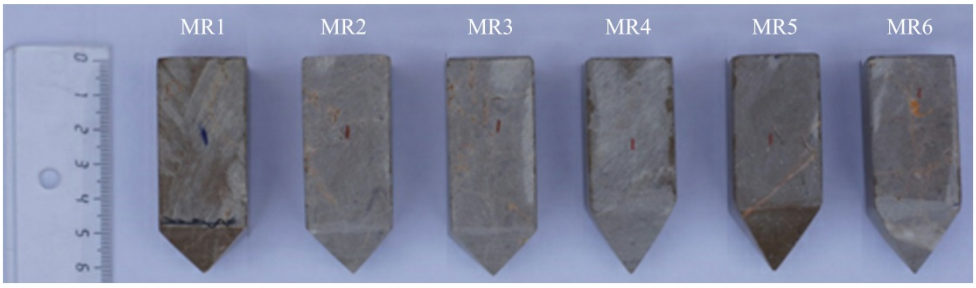

b. At the end of the tests

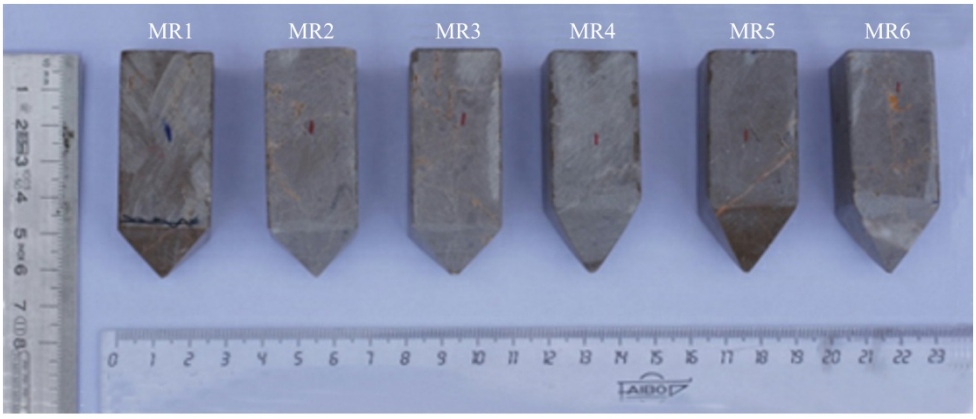

Figure A5 - 8 Limestone pyramidal samples used in the Contact Stiffness tests: MR1, MR2, and MR3 (90º apex angle); MR4, MR5 and MR6 (70º apex angle). Height of samples: 6 cm; Cross section: 2.5 cm x 2.5 cm.

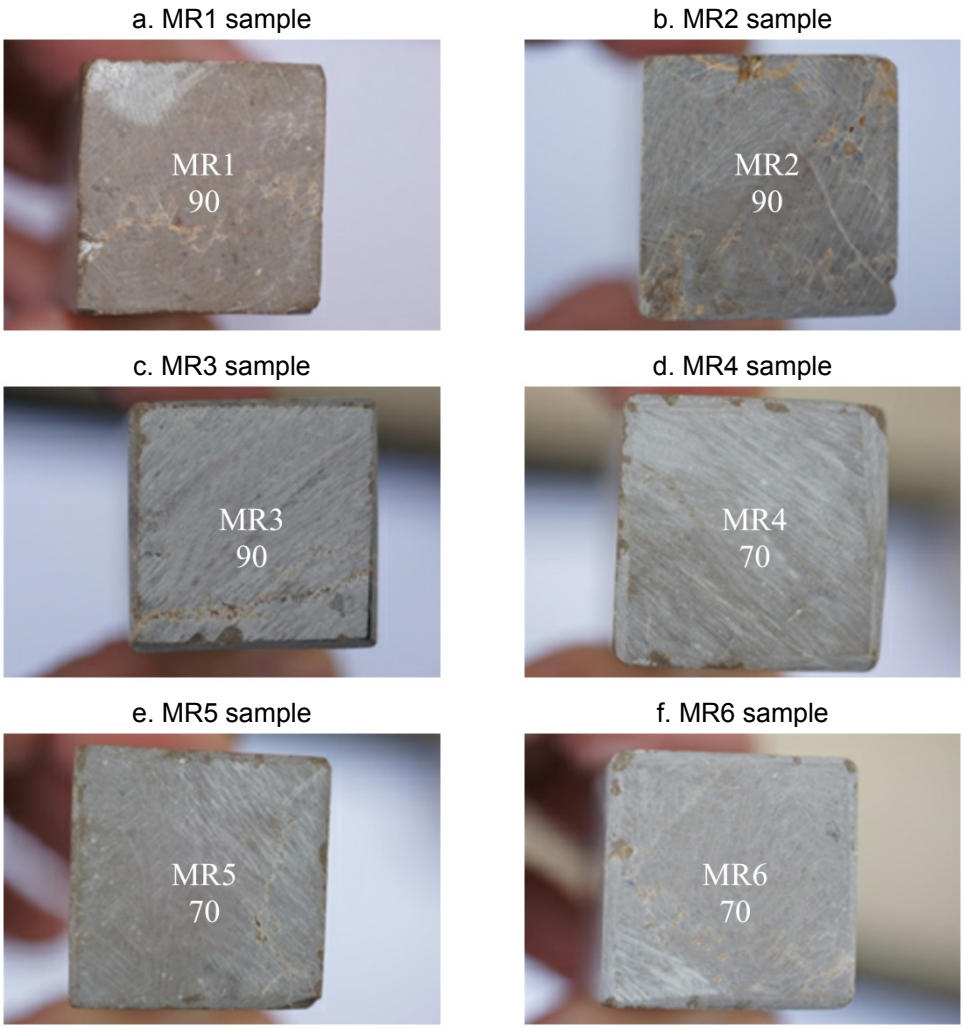

Figure A5 - 9 Detail of square cross-section (2.5x2.5cm) of the Limestone pyramidal samples used in the Contact Stiffness tests.

a. MR1 sample: 90º apex angle

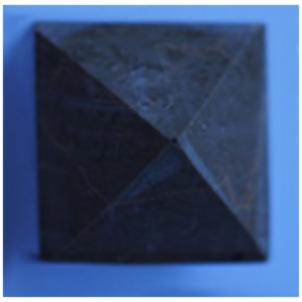

b. MR2 sample: 90º apex angle

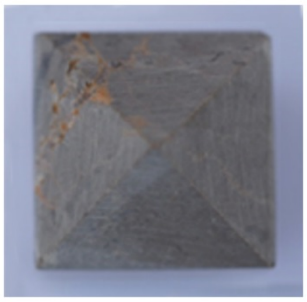

c. MR3 sample: 90º apex angle

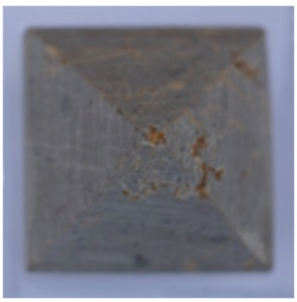

d. MR4 sample: 70º apex angle

e. MR5 sample: 70º apex angle

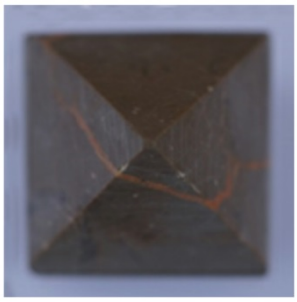

f. MR6 sample: 70º apex angle

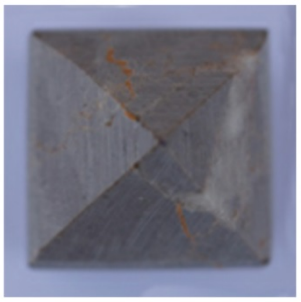

Figure A5 - 10 Detail of pyramidal shape in one of the edge of the Limestone samples used in the Contact Stiffness tests. Cross section: 2.5x2.5 cm.

a.

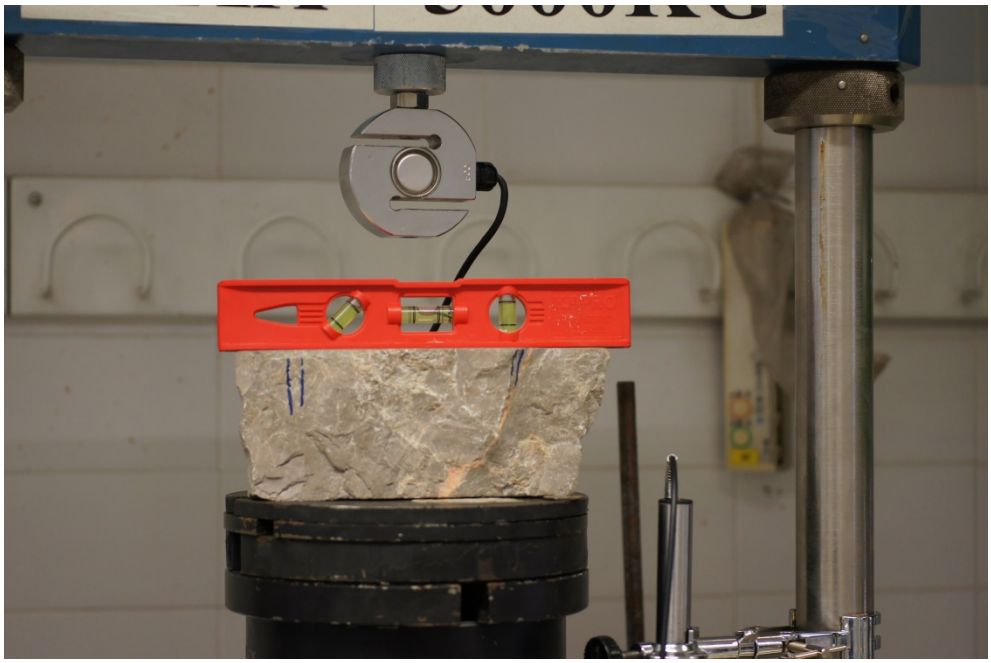

b.

Figure A5 - 11 Equipment of the Contact Stiffness tests: (a) Detail of the load cell and the limestone block that supports the pressure of the apex of limestone pyramidal sample; (b) Detail of the polished surface of limestone block.

A5.2.1. Sample MR1

A5.2.1.1. Details of the test

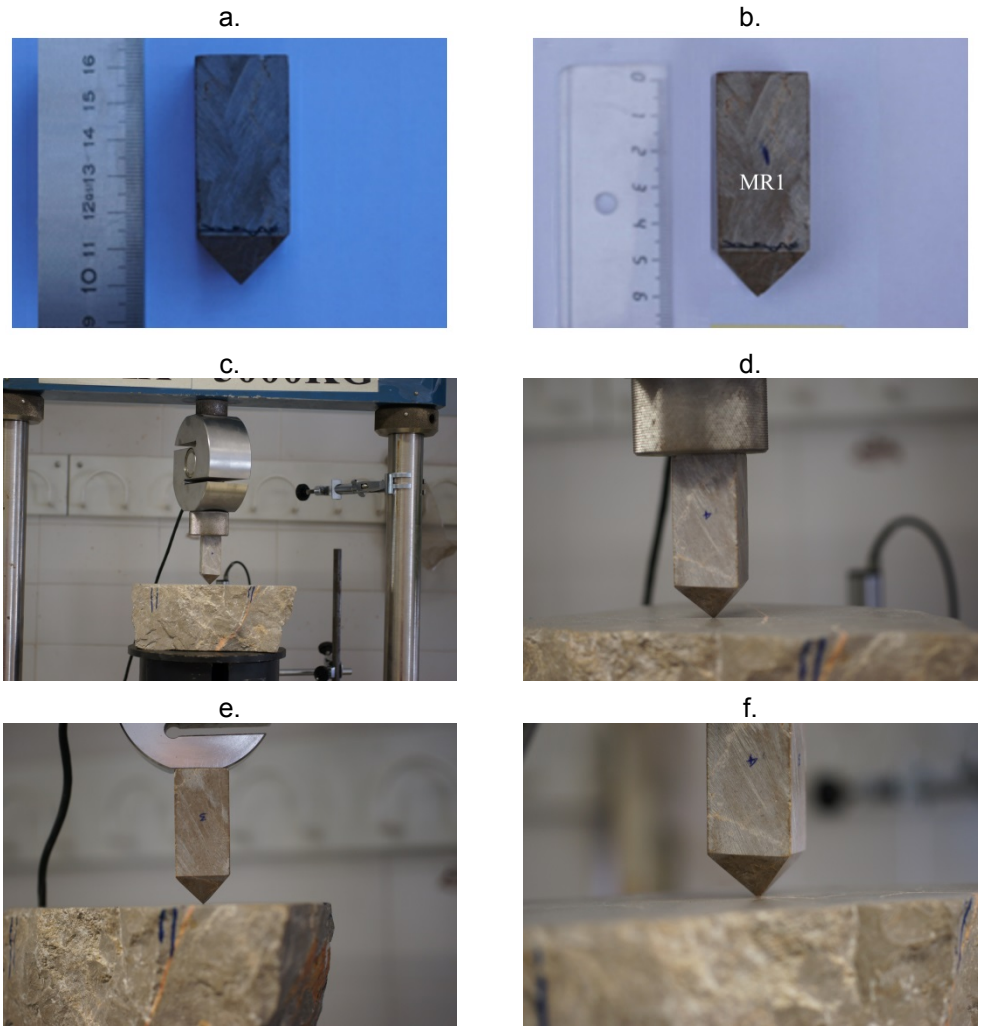

Figure A5 - 12 Details of the Contact Stiffness test on the Limestone MR1-sample (90º apex angle; Height of sample: 6 cm; Cross section: 2.5 cm x 2.5 cm): (a) Before the test; (b) At the end of the test; (c) Detail of testing arrangement; (d), (e), (f) Details of the contact (apex sample-support block) during the test.

A5.2.1.2. Data results

Sample: MR1

Description: Limestone from Vallirana (Barcelona, Spain). 90° apex angle; Height of sample: 6 cm; Cross section: 2.5 cm x 2.5 cm

Velocity of test, mm/min: 0.02

Table A5 - 13 Experimental data of the contact stiffness test on the sample MR1.

Time (s)	Force		Deformation (mm)
	(kg)	(N)	
0	5.06	49.6	0.0000
10	6.21	60.9	0.0040
20	7.59	74.5	0.0110
30	8.74	85.7	0.0150
40	10.12	99.3	0.0210
50	11.50	112.8	0.0290
60	12.88	126.4	0.0300
70	14.26	139.9	0.0320
80	15.82	155.2	0.0350
90	17.25	169.2	0.0370
100	18.63	182.8	0.0380
110	20.01	196.3	0.0390
120	21.39	209.8	0.0460

Time (s)	Force		Deformation (mm)
	(kg)	(N)	
130	22.84	224.1	0.0460
140	24.15	236.9	0.0470
150	25.53	250.4	0.0490
160	26.91	264.0	0.0510
170	28.29	277.5	0.0540
180	29.44	288.8	0.0600
190	30.59	300.1	0.0630
200	31.74	311.4	0.0660
210	32.89	322.7	0.0680
220	33.58	329.4	0.0710
230	34.27	336.2	0.0740
240	24.15	236.9	0.0790
250	24.15	236.9	0.0860

Table A5 - 14 Calculated values of contact stiffness for the sample MR1 based on experimental data: Load stage.

Force (N)	Contact stiffness (MN/m)
50 - 110	2.26
110 - 300	6.55
300 - 350	3.69

A5.2.2. Sample MR2

A5.2.2.1. Details of the test

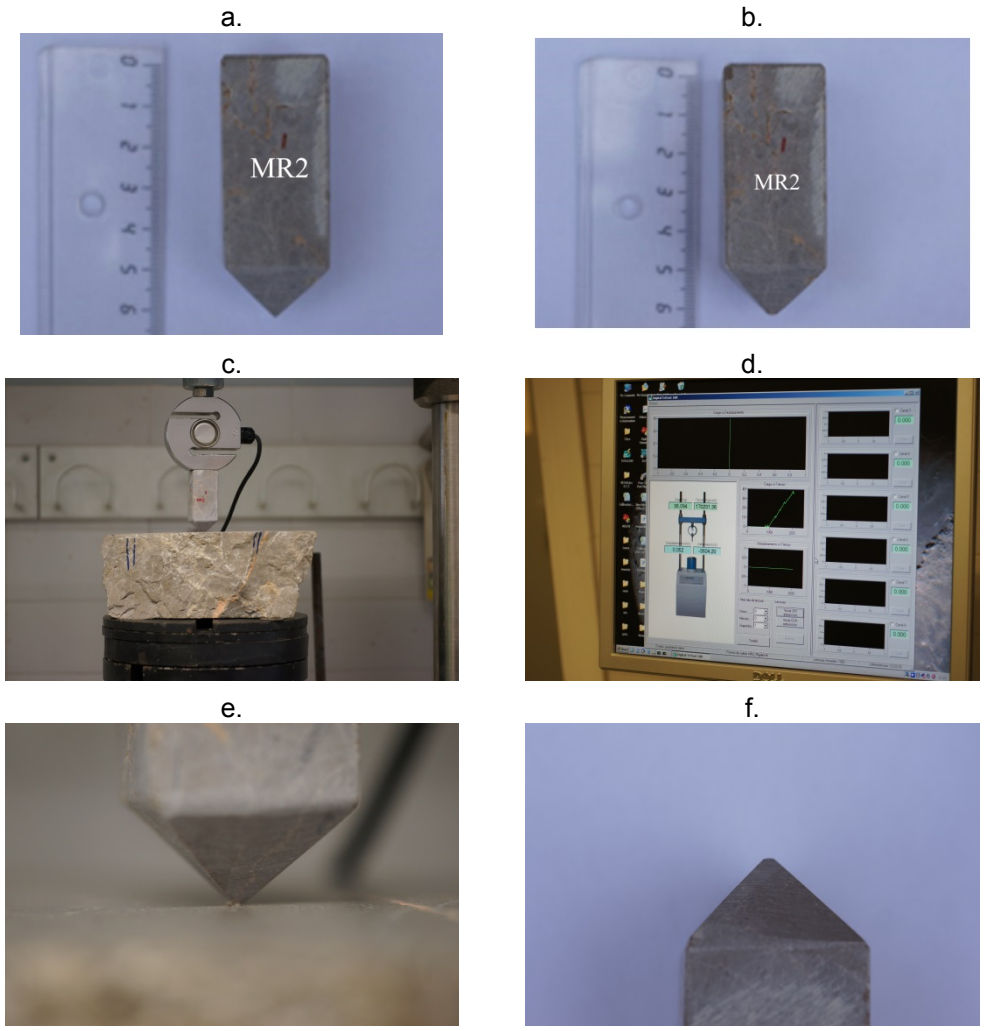

Figure A5 - 13 Details of the Contact Stiffness test on the Limestone MR2-sample (90º apex angle; Height of sample: 6 cm; Cross section: 2.5 cm x 2.5 cm): (a) Before the test; (b) At the end of the test; (c) Detail of testing arrangement; (d) Data acquisition system; (e), (f) Details of the contact (apex sample-support block) during the test.

A5.2.2.2. Data results

Sample: MR2

Description: Limestone from Vallirana (Barcelona, Spain). 90° apex angle; Height of sample: 6 cm; Cross section: 2.5 cm x 2.5 cm

Velocity of test, mm/min: 0.02

Table A5 - 15 Experimental data of the contact stiffness test on the sample MR2.

Time (s)	Force		Deformation (mm)
	(kg)	(N)	
0	9.43	92.5	0.0000
10	9.43	92.5	0.0060
20	10.12	99.2	0.0160
30	10.58	103.7	0.0200
40	11.04	108.3	0.0240
50	11.73	115.0	0.0260
60	12.19	119.5	0.0280
70	12.65	124.0	0.0320
80	12.87	126.3	0.0350
90	10.81	106.0	0.0380
100	11.04	108.3	0.0390
110	11.50	112.8	0.0410
120	11.96	117.3	0.0480
130	12.42	121.8	0.0520
140	13.10	128.6	0.0550
150	13.56	133.1	0.0580
160	14.21	139.4	0.0590
170	14.71	144.3	0.0600
180	15.17	148.8	0.0650
190	15.63	153.4	0.0660
200	16.09	157.9	0.0680
210	16.55	162.4	0.0750
220	16.51	161.9	0.0800
230	17.01	166.9	0.0870
240	17.47	171.4	0.0920
250	17.93	175.9	0.0970
260	18.39	180.4	0.1000
270	19.04	186.7	0.1050
280	19.31	189.5	0.1070
290	19.08	187.2	0.1100
300	19.54	191.7	0.1160
310	20.19	198.0	0.1190
320	20.69	203.0	0.1250
330	21.15	207.5	0.1270
340	21.73	213.1	0.1310
350	22.07	216.5	0.1370
360	22.30	218.8	0.1400
370	22.07	216.5	0.1430
380	22.53	221.0	0.1450
390	22.99	225.5	0.1470
400	23.45	230.0	0.1530
410	24.14	236.8	0.1560
420	24.60	241.3	0.1580
430	25.06	245.8	0.1640
440	25.75	252.6	0.1670
450	26.21	257.1	0.1700
460	26.67	261.6	0.1770
470	26.90	263.9	0.1820
480	27.13	266.1	0.1880
490	25.98	254.9	0.1920

Time (s)	Force		Deformation (mm)
	(kg)	(N)	
500	26.16	256.7	0.1950
510	26.21	257.1	0.1960
520	26.39	258.9	0.1980
530	26.90	263.9	0.1990
540	27.36	268.4	0.2040
550	27.82	272.9	0.2070
560	28.51	279.7	0.2080
570	28.97	284.2	0.2120
580	29.43	288.7	0.2140
590	29.89	293.2	0.2150
600	29.66	290.9	0.2160
610	29.66	290.9	0.2180
620	30.19	296.1	0.2230
630	30.81	302.2	0.2260
640	31.27	306.7	0.2290
650	31.73	311.2	0.2330
660	31.96	313.5	0.2350
670	31.50	309.0	0.2370
680	31.73	311.2	0.2390

Time (s)	Force		Deformation (mm)
	(kg)	(N)	
690	32.19	315.7	0.2430
700	32.83	322.1	0.2470
710	33.29	326.6	0.2520
720	33.80	331.5	0.2560
730	34.26	336.0	0.2570
740	34.26	336.0	0.2600
750	34.49	338.3	0.2640
760	34.95	342.8	0.2680
770	35.41	347.3	0.2740
780	35.64	349.6	0.2760
790	36.09	354.1	0.2780
800	36.55	358.6	0.2800
810	37.01	363.1	0.2820
820	37.70	369.9	0.2860
830	38.39	376.6	0.2900
840	39.08	383.4	0.2940
850	37.24	365.4	0.2960
860	36.78	360.9	0.2980

Table A5 - 16 Calculated value of contact stiffness for the sample MR2 based on experimental data: Load stage.

Force (N)	Contact stiffness (MN/m)
90 - 380	0.96

A5.2.3. Sample MR3

A5.2.3.1. Details of the test

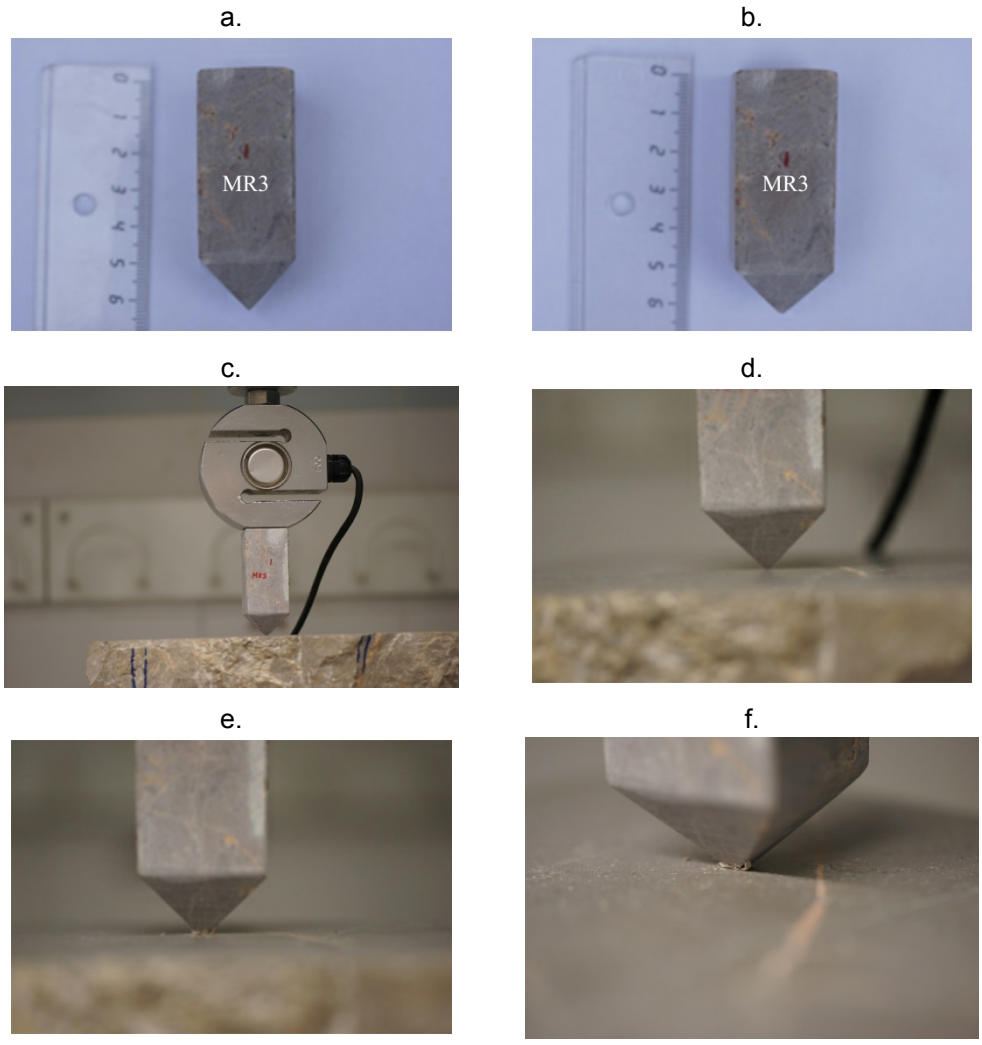

Figure A5 - 14 Details of the Contact Stiffness test on the Limestone MR3-sample (90º apex angle; Height of sample: 6 cm; Cross section: 2.5 cm x 2.5 cm): (a) Before the test; (b) At the end of the test; (c) Detail of testing arrangement; (d), (e), (f) Details of the contact (apex sample-support block) during the test.

A5.2.3.2. Data results

Sample: MR3

Description: Limestone from Vallirana (Barcelona, Spain). 90° apex angle; Height of sample: 6 cm; Cross section: 2.5 cm x 2.5 cm

Velocity of test, mm/min: 0.02

Table A5 - 17 Experimental data of the contact stiffness test on the sample MR3.

Time (s)	Force		Deformation (mm)
	(kg)	(N)	
0	1.61	15.8	0.0000
5	2.07	20.3	0.0060
15	2.71	26.6	0.0060
25	3.22	31.6	0.0130
35	3.91	38.3	0.0130
45	4.60	45.1	0.0190
55	5.29	51.9	0.0260
65	6.09	59.8	0.0260
75	6.85	67.2	0.0260
85	7.59	74.4	0.0260
95	8.28	81.2	0.0320
105	8.97	88.0	0.0320
115	9.89	97.0	0.0450
125	10.81	106.0	0.0450
135	11.56	113.4	0.0390
145	12.60	123.6	0.0520
155	13.52	132.6	0.0520
165	14.44	141.6	0.0450
175	15.40	151.1	0.0580
185	16.32	160.1	0.0580
195	17.24	169.2	0.0650
205	18.16	178.2	0.0710
215	19.15	187.9	0.0650
225	20.23	198.5	0.0710
235	21.15	207.5	0.0710
245	22.07	216.5	0.0780
255	22.99	225.5	0.0780
265	23.91	234.6	0.0780
275	24.83	243.6	0.0830
285	25.75	252.6	0.0910
295	26.67	261.6	0.0910
305	27.59	270.6	0.0910
315	28.51	279.7	0.0960
325	29.43	288.7	0.0960
335	30.35	297.7	0.1040
345	31.27	306.7	0.1090
355	32.19	315.7	0.1040
365	33.11	324.8	0.1090
375	33.80	331.5	0.1090
385	33.98	333.3	0.1170
395	32.88	322.5	0.1170
405	31.73	311.2	0.1090
415	29.66	290.9	0.1090

Time (s)	Force		Deformation (mm)
	(kg)	(N)	
425	28.05	275.2	0.1040
435	26.21	257.1	0.1040
445	24.60	241.3	0.0960
455	22.99	225.5	0.0960
465	21.38	209.7	0.0960
475	19.77	194.0	0.0960
485	18.39	180.4	0.0830
495	17.01	166.9	0.0910
505	15.63	153.4	0.0830
515	14.48	142.1	0.0830
525	13.79	135.3	0.0830
535	14.02	137.6	0.0780
545	14.25	139.8	0.0780
555	15.63	153.4	0.0830
565	17.01	166.9	0.0830
575	18.62	182.7	0.0910
585	20.00	196.2	0.0910
595	21.38	209.7	0.0960
605	22.99	225.5	0.1040
615	24.60	241.3	0.0960
625	26.21	257.1	0.1040
635	27.82	272.9	0.1040
645	29.43	288.7	0.1090
655	31.04	304.5	0.1090
665	32.65	320.3	0.1220
675	34.03	333.8	0.1170
685	35.18	345.1	0.1220
695	36.09	354.1	0.1220
705	37.01	363.1	0.1220
715	38.05	373.3	0.1300
725	39.04	383.0	0.1300
735	40.00	392.4	0.1300
745	40.92	401.4	0.1350
755	41.91	411.1	0.1350
765	42.99	421.7	0.1480

Time (s)	Force		Deformation (mm)
	(kg)	(N)	
775	43.75	429.2	0.1480
785	44.67	438.2	0.1480
795	45.59	447.2	0.1480
805	46.62	457.4	0.1560
815	47.36	464.6	0.1560
825	48.51	475.9	0.1610
835	49.20	482.6	0.1610
845	49.89	489.4	0.1610
855	50.35	493.9	0.1740
865	51.27	502.9	0.1740
875	52.19	512.0	0.1740
885	53.34	523.2	0.1820
895	54.26	532.3	0.1820
905	55.41	543.5	0.1820
915	56.44	553.7	0.1820
925	57.48	563.8	0.1870
935	58.46	573.5	0.1870
945	59.54	584.1	0.1950
955	60.46	593.2	0.1950
965	61.38	602.2	0.2000
975	62.30	611.2	0.1950
985	63.22	620.2	0.2000
995	63.91	627.0	0.2080
1005	64.83	636.0	0.2080
1015	65.52	642.8	0.2130
1025	66.21	649.5	0.2130
1035	67.13	658.6	0.2130
1045	67.89	666.0	0.2130
1055	68.74	674.3	0.2260
1065	69.66	683.4	0.2260
1075	70.76	694.2	0.2340
1085	71.73	703.7	0.2340
1095	72.42	710.4	0.2340
1105	73.29	719.0	0.2340
1115	74.03	726.2	0.2390

Time (s)	Force		Deformation (mm)
	(kg)	(N)	
1125	74.72	733.0	0.2390
1135	75.25	738.2	0.2470
1145	75.87	744.3	0.2470
1155	76.33	748.8	0.2520
1165	76.56	751.0	0.2520

Time (s)	Force		Deformation (mm)
	(kg)	(N)	
1175	77.02	755.5	0.2520
1185	72.88	714.9	0.2600

Table A5 - 18 Calculated values of contact stiffness for the sample MR3 based on experimental data: Load stage.

Force (N)	Contact stiffness (MN/m)
15 - 50	1.39
50 -750	3.12

Table A5 - 19 Calculated value of contact stiffness for the sample MR3 based on experimental data: Unload/Reload stage.

Force (N)	Contact stiffness (MN/m)
100 - 300	5.51

A5.2.4. Sample MR4

A5.2.4.1. Details of the test

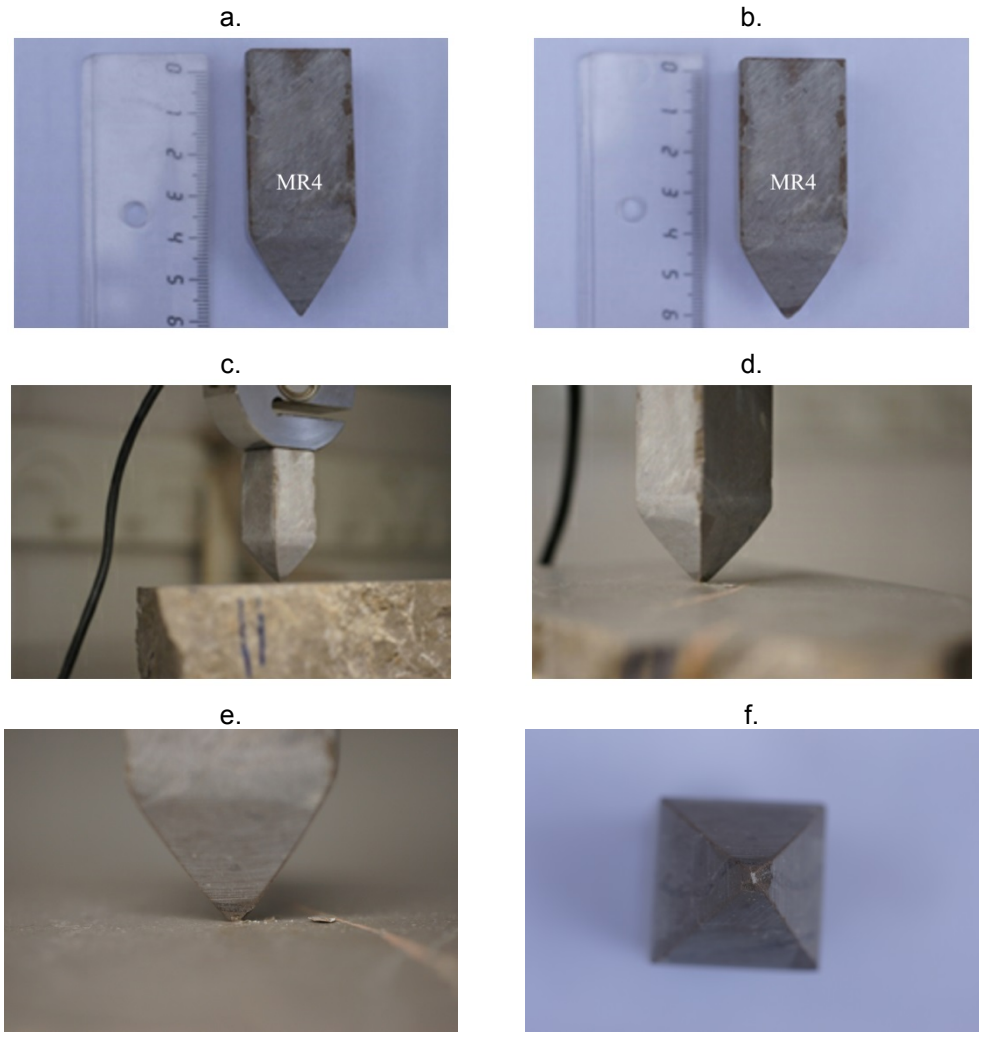

Figure A5 - 15 Details of the Contact Stiffness test on the Limestone MR4-sample (70º apex angle; Height of sample: 6 cm; Cross section: 2.5 cm x 2.5 cm): (a) Before the test; (b) At the end of the test; (c) Detail of testing arrangement; (d), (e) Details of the contact (apex sample-support block) during the test; (f) Detail of the apex after the test.

A5.2.4.2. Data results

Sample: MR4

Description: Limestone from Vallirana (Barcelona, Spain). 70° apex angle; Height of sample: 6 cm; Cross section: 2.5 cm x 2.5 cm

Velocity of test, mm/min: 0.02

Table A5 - 20 Experimental data of the contact stiffness test on the sample MR4.

Time (s)	Force		Deformation (mm)
	(kg)	(N)	
0	0.00	0.0	0.0000
5	0.23	2.3	0.0000
15	0.69	6.8	0.0080
25	1.15	11.3	0.0080
35	1.84	18.0	0.0080
45	2.30	22.6	0.0130
55	2.99	29.3	0.0210
65	3.68	36.1	0.0210
75	4.14	40.6	0.0260
85	4.83	47.4	0.0210
95	5.52	54.1	0.0260
105	6.21	60.9	0.0340
115	6.90	67.7	0.0390
125	7.59	74.4	0.0390
135	8.28	81.2	0.0390
145	8.97	88.0	0.0390
155	9.66	94.7	0.0470
165	10.58	103.7	0.0520
175	11.33	111.2	0.0520
185	12.19	119.5	0.0520
195	13.10	128.6	0.0520
205	14.02	137.6	0.0600
215	14.94	146.6	0.0650
225	15.86	155.6	0.0650

Time (s)	Force		Deformation (mm)
	(kg)	(N)	
235	16.78	164.6	0.0650
245	17.70	173.7	0.0730
255	18.46	181.1	0.0730
265	19.31	189.5	0.0780
275	19.77	194.0	0.0780
285	20.00	196.2	0.0780
295	19.66	192.8	0.0860
305	20.12	197.3	0.0860
315	20.81	204.1	0.0910
325	21.61	212.0	0.0860
335	22.07	216.5	0.0990
345	22.99	225.5	0.0990
355	23.68	232.3	0.1040
365	24.37	239.1	0.0990
375	25.29	248.1	0.1040
385	26.16	256.7	0.1040
395	24.37	239.1	0.1170
405	24.83	243.6	0.1240
415	25.36	248.8	0.1240
425	25.98	254.9	0.1240
435	26.21	257.1	0.1240
445	26.55	260.5	0.1300
455	26.90	263.9	0.1300
465	27.36	268.4	0.1370

Time (s)	Force		Deformation (mm)
	(kg)	(N)	
475	28.05	275.2	0.1370
485	28.97	284.2	0.1370
495	29.43	288.7	0.1370
505	29.89	293.2	0.1430
515	30.58	300.0	0.1500
525	30.53	299.5	0.1500
535	29.89	293.2	0.1500
545	28.74	281.9	0.1500
555	27.13	266.1	0.1500
565	25.52	250.3	0.1500
575	23.91	234.6	0.1430
585	22.53	221.0	0.1370
595	20.92	205.2	0.1370
605	19.54	191.7	0.1300
615	18.16	178.2	0.1370
625	16.78	164.6	0.1300
635	16.32	160.1	0.1240
645	16.55	162.4	0.1300
655	17.89	175.5	0.1300
665	19.31	189.5	0.1300
675	20.69	203.0	0.1240
685	22.30	218.8	0.1370
695	23.68	232.3	0.1300
705	25.17	247.0	0.1370
715	26.67	261.6	0.1370
725	28.05	275.2	0.1430
735	29.43	288.7	0.1500
745	30.58	300.0	0.1500
755	31.50	309.0	0.1500
765	32.42	318.0	0.1560
775	33.11	324.8	0.1560
785	34.03	333.8	0.1630
795	34.14	334.9	0.1630
805	34.90	342.4	0.1690
815	35.64	349.6	0.1690
825	36.32	356.3	0.1820

Time (s)	Force		Deformation (mm)
	(kg)	(N)	
835	37.01	363.1	0.1760
845	37.89	371.7	0.1820
855	38.62	378.9	0.1820
865	39.50	387.5	0.1820
875	40.23	394.7	0.1890
885	40.69	399.2	0.1890
895	40.92	401.4	0.1890
905	36.32	356.3	0.1940
915	37.24	365.4	0.1940
925	38.39	376.6	0.2070
935	38.62	378.9	0.2020
945	37.47	367.6	0.2020
955	36.78	360.9	0.2070
965	35.18	345.1	0.2020
975	33.34	327.0	0.2020
985	31.73	311.2	0.2020
995	30.00	294.3	0.2020
1005	28.46	279.2	0.1890
1015	26.90	263.9	0.1940
1025	25.29	248.1	0.1820
1035	23.75	233.0	0.1820
1045	23.22	227.8	0.1820
1055	23.29	228.5	0.1820
1065	24.83	243.6	0.1760
1075	26.44	259.4	0.1820
1085	28.05	275.2	0.1890
1095	29.66	290.9	0.1890
1105	31.27	306.7	0.1890
1115	32.88	322.5	0.2020
1125	34.49	338.3	0.1940
1135	36.09	354.1	0.2020
1145	37.70	369.9	0.2020
1155	39.08	383.4	0.2070
1165	40.23	394.7	0.2070
1175	41.38	406.0	0.2150
1185	42.53	417.2	0.2150

Time (s)	Force		Deformation (mm)
	(kg)	(N)	
1195	43.68	428.5	0.2150
1205	44.60	437.5	0.2200
1215	45.75	448.8	0.2280
1225	46.67	457.8	0.2280

Time (s)	Force		Deformation (mm)
	(kg)	(N)	
1235	47.36	464.6	0.2280
1245	37.89	371.7	0.2330

Table A5 - 21 Calculated values of contact stiffness for the sample MR4 based on experimental data: Load stage.

Force (N)	Contact stiffness (MN/m)
0 - 10	0.99
10 - 100	2.12
100 - 200	2.82
200 - 300	1.50
300 - 400	1.97
400 - 463	2.86

Table A5 - 22 Calculated values of contact stiffness for the sample MR4 based on experimental data: Unload/Reload stage.

Force (N)	Contact stiffness (MN/m)
150 -250	5.55
250 - 400	6.41

A5.2.5. Sample MR5

A5.2.5.1. Details of the test

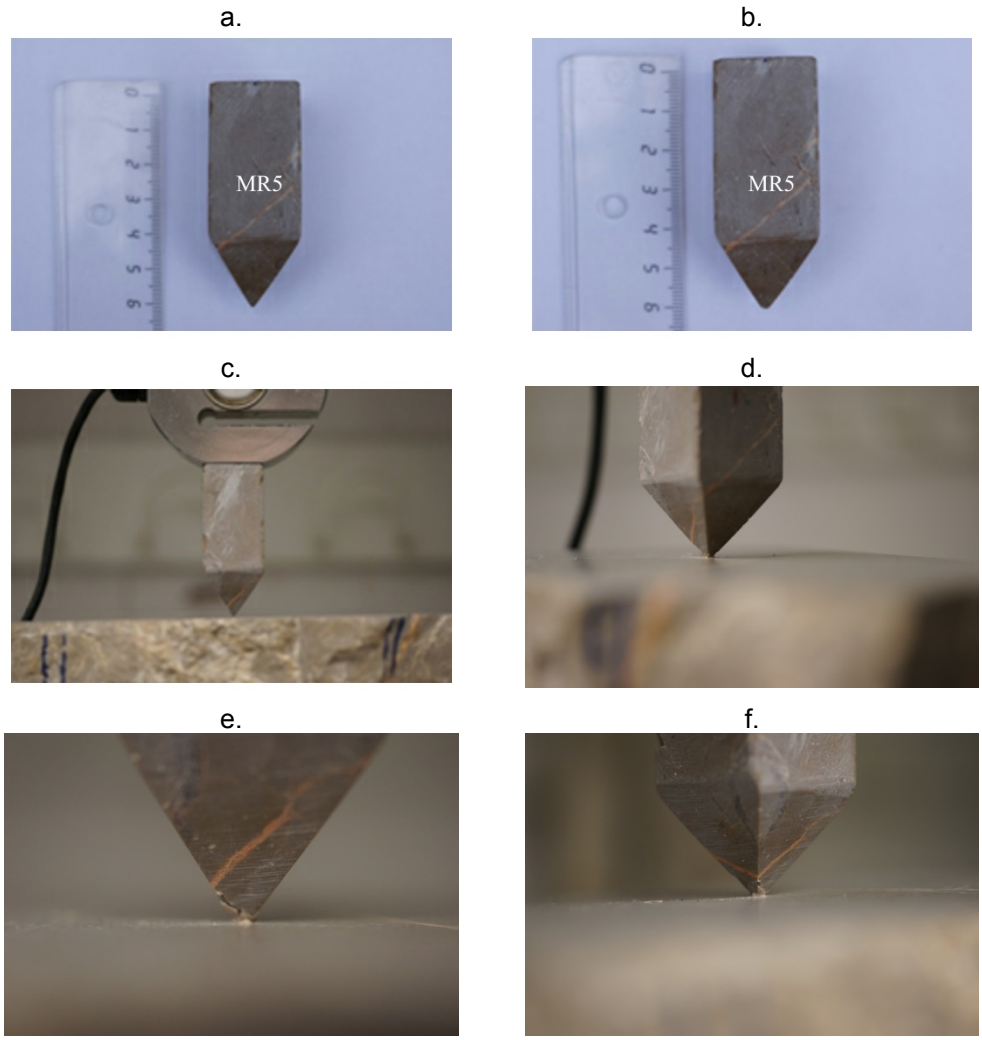

Figure A5 - 16 Details of the Contact Stiffness test on the Limestone MR5-sample (70º apex angle; Height of sample: 6 cm; Cross section: 2.5 cm x 2.5 cm): (a) Before the test; (b) At the end of the test; (c) Detail of testing arrangement (see also Fig. 5.23b in chapter 5); (d), (e), (f) Details of the contact (apex sample-support block) during the test.

A5.2.5.2. Data results

Sample: MR5

Description: Limestone from Vallirana (Barcelona, Spain). 70° apex angle; Height of sample: 6 cm; Cross section: 2.5 cm x 2.5 cm

Velocity of test, mm/min: 0.02

Table A5 - 23 Experimental data of the contact stiffness test on the sample MR5.

Time (s)	Force		Deformation (mm)
	(kg)	(N)	
0	0.92	9.0	0.0000
5	1.10	10.8	0.0130
15	1.38	13.5	0.0050
25	1.84	18.0	0.0050
35	2.30	22.6	0.0180
45	2.76	27.1	0.0180
55	3.22	31.6	0.0260
65	3.68	36.1	0.0260
75	4.25	41.7	0.0260
85	4.60	45.1	0.0310
95	5.06	49.6	0.0310
105	5.59	54.8	0.0390
115	5.98	58.6	0.0390
125	6.44	63.1	0.0390
135	6.90	67.7	0.0440
145	7.36	72.2	0.0440
155	7.82	76.7	0.0510
165	8.23	80.7	0.0510
175	8.51	83.4	0.0640
185	8.97	88.0	0.0570
195	9.43	92.5	0.0640
205	8.35	81.9	0.0640
215	7.82	76.7	0.0640
225	7.82	76.7	0.0700
235	8.28	81.2	0.0700
245	8.74	85.7	0.0770
255	9.43	92.5	0.0830
265	9.89	97.0	0.0830
275	10.35	101.5	0.0900
285	10.87	106.7	0.0900
295	11.27	110.5	0.0960
305	10.35	101.5	0.1030
315	10.58	103.7	0.0960
325	10.92	107.1	0.1030
335	11.45	112.3	0.1090
345	11.96	117.3	0.1090
355	12.19	119.5	0.1160
365	12.83	125.8	0.1160
375	13.10	128.6	0.1160
385	13.10	128.6	0.1220
395	13.56	133.1	0.1220
405	14.25	139.8	0.1290
415	14.21	139.4	0.1340
425	14.71	144.3	0.1290
435	15.36	150.7	0.1340
445	15.86	155.6	0.1420
455	16.32	160.1	0.1420
465	16.78	164.6	0.1420
475	17.66	173.2	0.1470
485	18.39	180.4	0.1470

Time (s)	Force		Deformation (mm)
	(kg)	(N)	
495	19.31	189.5	0.1550
505	20.00	196.2	0.1550
515	20.88	204.8	0.1550
525	21.38	209.7	0.1600
535	22.07	216.5	0.1680
545	22.53	221.0	0.1680
555	22.48	220.6	0.1600
565	22.76	223.3	0.1730
575	23.68	232.3	0.1730
585	24.37	239.1	0.1810
595	25.29	248.1	0.1730
605	26.21	257.1	0.1860
615	26.90	263.9	0.1860
625	27.13	266.1	0.1940
635	27.82	272.9	0.1940
645	28.69	281.5	0.1990
655	29.15	286.0	0.1990
665	29.50	289.4	0.1990
675	30.35	297.7	0.1990
685	31.04	304.5	0.2070
695	30.81	302.2	0.2200
705	31.04	304.5	0.2120
715	31.50	309.0	0.2200
725	31.96	313.5	0.2200
735	29.66	290.9	0.2250
745	29.89	293.2	0.2200
755	30.58	300.0	0.2250
765	31.27	306.7	0.2330
775	32.19	315.7	0.2380

Time (s)	Force		Deformation (mm)
	(kg)	(N)	
785	32.88	322.5	0.2380
795	33.57	329.3	0.2460
805	33.80	331.5	0.2460
815	34.26	336.0	0.2460
825	34.49	338.3	0.2460
835	34.95	342.8	0.2510
845	35.64	349.6	0.2590
855	36.32	356.3	0.2590
865	36.74	360.4	0.2640
875	37.24	365.4	0.2640
885	38.16	374.4	0.2640
895	39.08	383.4	0.2720
905	39.96	392.0	0.2720
915	40.92	401.4	0.2770
925	41.84	410.5	0.2770
935	42.72	419.0	0.2770
945	43.45	426.3	0.2850
955	44.03	431.9	0.2900
965	44.60	437.5	0.2900
975	44.83	439.8	0.2980
985	44.60	437.5	0.2980
995	44.60	437.5	0.3030
1005	44.10	432.6	0.3030
1015	44.60	437.5	0.3110
1025	45.29	444.3	0.3160
1035	45.98	451.1	0.3160
1045	45.75	448.8	0.3240

Table A5 - 24 Calculated values of contact stiffness for the sample MR5 based on experimental data: Load stage.

Force (N)	Contact stiffness (MN/m)
9 - 22	0.75
22 -92	1.64
75 -160	1.10
150 - 300	2.13
300 - 440	2.03

A5.2.6. Sample MR6

A5.2.6.1. Details of the test

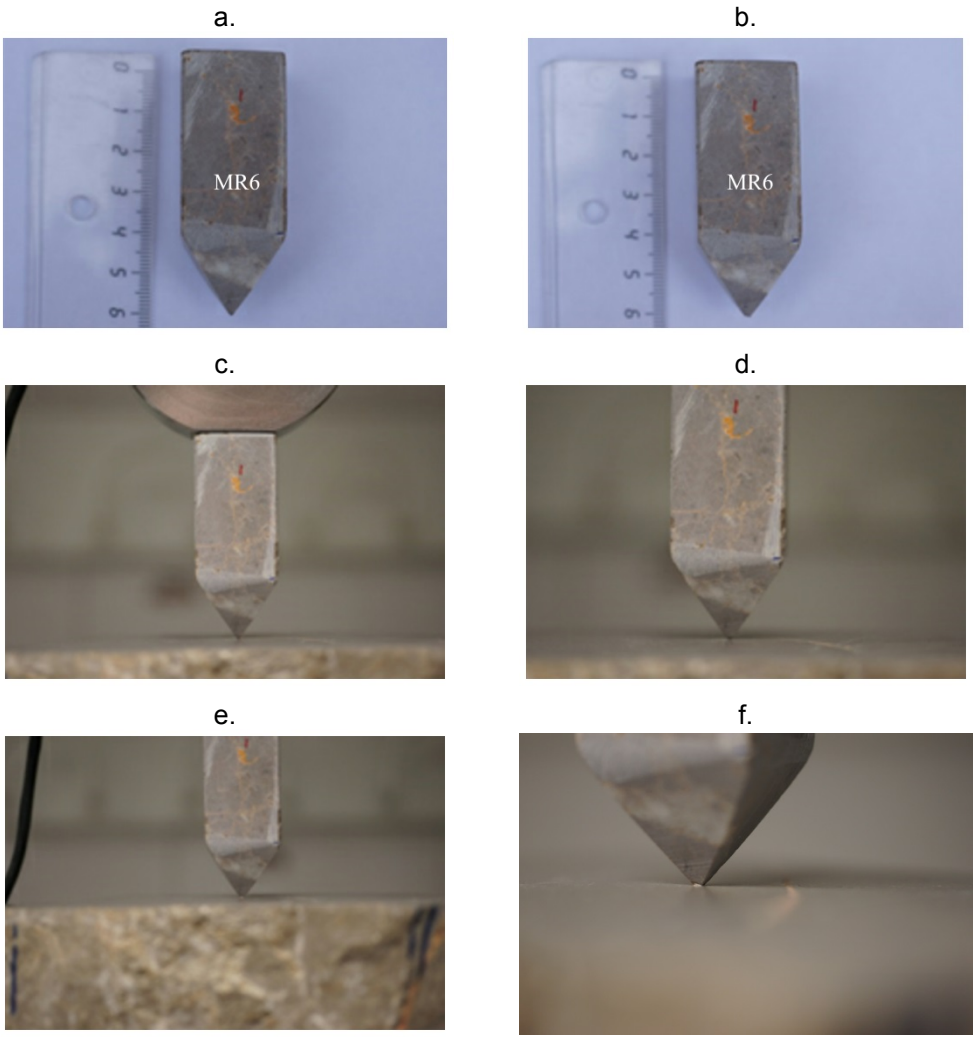

Figure A5 - 17 Details of the Contact Stiffness test on the Limestone MR6-sample (70º apex angle; Height of sample: 6 cm; Cross section: 2.5 cm x 2.5 cm): (a) Before the test; (b) At the end of the test; (c) Detail of testing arrangement; (d), (e), (f) Details of the contact (apex sample-support block) during the test.

A5.2.6.2. Data results

Sample:	**MR6**
Description:	Limestone from Vallirana (Barcelona, Spain). 70° apex angle; Height of sample: 6 cm; Cross section: 2.5 cm x 2.5 cm
Velocity of test, mm/min:	**0.02**

Table A5 - 25 Experimental data of the contact stiffness test on the sample MR6.

Time (s)	Force		Deformation (mm)
	(kg)	(N)	
0	0.00	0.0	0.0000
4	0.23	2.3	0.0080
14	0.69	6.8	0.0080
24	0.92	9.0	0.0080
34	1.38	13.5	0.0080
44	1.61	15.8	0.0210
54	2.07	20.3	0.0210
64	2.53	24.8	0.0210
74	2.99	29.3	0.0210
84	3.45	33.8	0.0260
94	3.91	38.3	0.0340
104	4.21	41.3	0.0340
114	4.60	45.1	0.0260
124	5.06	49.6	0.0340
134	5.29	51.9	0.0390
144	5.52	54.1	0.0470
154	5.98	58.6	0.0470
164	5.13	50.3	0.0470
174	5.40	53.0	0.0520
184	5.52	54.1	0.0600
194	5.75	56.4	0.0520
204	6.05	59.3	0.0600
214	6.44	63.1	0.0650
224	5.98	58.6	0.0650
234	6.21	60.9	0.0730

Time (s)	Force		Deformation (mm)
	(kg)	(N)	
244	6.67	65.4	0.0730
254	6.97	68.3	0.0730
264	7.36	72.2	0.0780
274	7.59	74.4	0.0860
284	7.82	76.7	0.0860
294	8.28	81.2	0.0860
304	8.51	83.4	0.0860
314	7.13	69.9	0.0910
324	7.36	72.2	0.0990
334	7.82	76.7	0.1040
344	7.36	72.2	0.1040
354	7.36	72.2	0.1110
364	7.59	74.4	0.1040
374	7.59	74.4	0.1110
384	7.59	74.4	0.1170
394	7.82	76.7	0.1170
404	8.05	78.9	0.1240
414	8.28	81.2	0.1240
424	8.28	81.2	0.1300
434	8.74	85.7	0.1300
444	8.97	88.0	0.1300
454	9.43	92.5	0.1370
464	9.66	94.7	0.1370
474	10.12	99.2	0.1370
484	10.35	101.5	0.1430

Time (s)	Force		Deformation (mm)
	(kg)	(N)	
494	10.81	106.0	0.1430
504	11.04	108.3	0.1560
514	11.50	112.8	0.1560
524	11.96	117.3	0.1560
534	12.19	119.5	0.1560
544	12.42	121.8	0.1630
554	12.42	121.8	0.1630
564	12.65	124.0	0.1690
574	12.87	126.3	0.1760
584	13.33	130.8	0.1760
594	13.79	135.3	0.1760
604	14.25	139.8	0.1820
614	14.71	144.3	0.1760
624	15.29	150.0	0.1820
634	15.86	155.6	0.1890
644	16.51	161.9	0.1890
654	16.74	164.2	0.1890
664	15.40	151.1	0.1940
674	15.29	150.0	0.2020
684	15.86	155.6	0.2020
694	16.32	160.1	0.2020
704	16.97	166.4	0.2070
714	17.47	171.4	0.2070
724	18.12	177.7	0.2150
734	18.62	182.7	0.2150
744	19.31	189.5	0.2200
754	20.00	196.2	0.2200
764	20.46	200.7	0.2200
774	21.15	207.5	0.2280
784	21.84	214.3	0.2330
794	22.53	221.0	0.2330
804	22.99	225.5	0.2410
814	23.68	232.3	0.2410
824	24.37	239.1	0.2410
834	24.83	243.6	0.2410
844	25.52	250.3	0.2410
854	25.98	254.9	0.2460
864	26.44	259.4	0.2460
874	26.90	263.9	0.2540
884	26.44	259.4	0.2590
894	13.33	130.8	0.2670
904	13.79	135.3	0.2670

Table A5 - 26 Calculated values of contact stiffness for the sample MR6 based on experimental data: Load stage.

Force (N)	Contact stiffness (MN/m)
4 - 50	1.47
50 - 90	0.35
90 - 150	0.94
150 - 265	2.13

A5.3. Calculation of normal stiffness following the Hertz's theory

Table A5 - 28 shows the results predicted by Hertz's theory (Santamarina et al., 2001) for the contact between elastic spheres (E = 6800 MPa, ν = 0.25; sphere diameter: 2.8 cm). These properties are in accordance with the properties of the limestone gravels (see **Table A5 - 27**). **Figure 5-24a** in chapter 5 illustrates these results.

Table A5 - 29 shows some average values of calculated normal stiffness for some ranges of normal force: the analysis was derived from the Hertzian curve (see **Figure 5-24b** in chapter 5).

These results are analyzed in the section 5.6.2 (chapter 5).

Table A5 - 27 Properties of limestone gravels of Vallirana (Barcelona) (From Ortega (2008)):.

Young's modulus, E (MPa)	6800
Poisson ratio, ν	0.25
Equivalent diameter of particles, (cm)	2.8

Table A5 - 28 Theoretical relationship between Force and Deformation for two elastic spheres in contact (E=6800 MPa, ν=0.25; sphere diameter: 2.8 cm). Analysis from Hertz`s theory.

Normal Force (N)	Deformation (mm)	Contact radius (mm)	Normal Stiffness MN/m
0	0	0	0.0000
0.1	0.00039	0.05251	0.3809
0.2	0.00063	0.06615	0.4798
0.4	0.00099	0.08335	0.6046
0.6	0.00130	0.09541	0.6921
0.8	0.00158	0.10501	0.7617
1	0.00183	0.11312	0.8205
1.2	0.00206	0.12021	0.8719
1.5	0.00240	0.12949	0.9393
2	0.00290	0.14253	1.0338
4	0.00461	0.17957	1.3025
5	0.00535	0.19344	1.4031
8	0.00731	0.22625	1.6410
10	0.00849	0.24372	1.7678

Normal Force (N)	Deformation (mm)	Contact radius (mm)	Normal Stiffness MN/m
20	0.01347	0.30706	2.2272
30	0.01765	0.35150	2.5495
40	0.02138	0.38687	2.8061
50	0.02481	0.41675	3.0228
100	0.03939	0.52507	3.8085
500	0.11516	0.89786	6.5125
1000	0.18281	1.13123	8.2052
2000	0.29019	1.42526	10.3379
3000	0.38026	1.63151	11.8339
4000	0.46066	1.79571	13.0249
5000	0.53454	1.93437	14.0307

(Continuation of **Table A5 - 28**)

Table A5 - 29 Calculated values of contact stiffness for two elastic spheres in contact (E=6800 MPa, ν=0.25; sphere diameter: 2.8 cm). Analysis from Hertz`s theory.

Normal Force (N)	Average of Normal Stiffness (MN/m)
0.1 - 1.5	0.6938
1.5 -100	2.0456
100 - 1000	6.1754
2000 - 4000	11.4865

A5.4. Roughness tests

Results of roughness tests performed in the laboratory of GEOMAR-Enginyeria del Terreny SLP (GEOMAR, 2015), on limestone blocks polished to #80 and #1000 grades are presented below. The #80 and #1000-polished surfaces correspond to those tested for basic and mineral frictions (see section A5.1 above).

As explained in chapter 5 (section 5.6.1), thin sections were cut from the polished limestone-blocks. Ten micro photographed profiles were analyzed per section. **Figure A5 - 19** and **Figure A5 - 20** show the analyzed profiles for #80 and #1000 polished surfaces respectively.

Five representative points per each profile were selected for measuring deviations (a) of the curved profile with respect to the midline of the profile (see **Figure A5 - 19** and **Figure A5 - 20**). **Figure A5 - 18** shows a scheme to calculate the deviations.

R_a roughness is calculated as the arithmetic average of the deviations (Thomas, 1999), and is obtained as follows:

Equation Chapter (Next) Section 1

$$R_a = \frac{|a_1| + |a_2| + \ldots + |a_n|}{n} \quad \text{(A5:1)}$$

where:

a_1, a_2, a_n: deviations of the curved profile with respect to the midline of the profile at the points 1, 2 and n respectively;

n: number of measurements of the deviations.

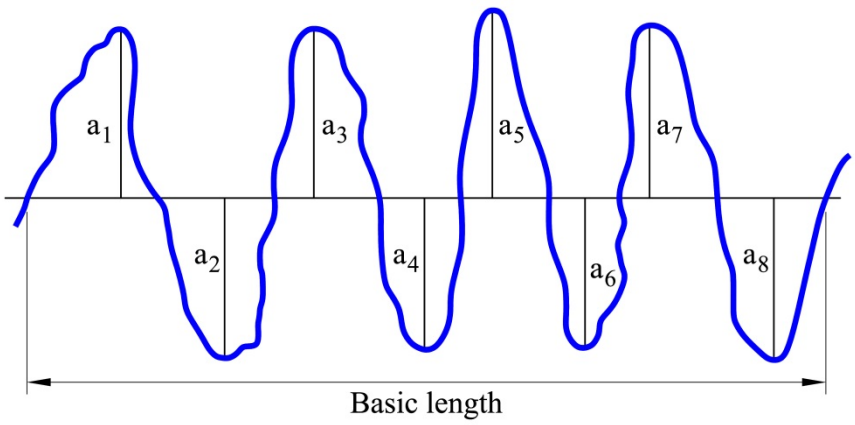

Figure A5 - 18 Scheme of a rough surface and measurement of roughness: a_i is the deviation of the curved profile with respect to the midline of the profile at the point i . (From GEOMAR (2015))

Table A5 - 30 shows the calculated values of R_a for each analyzed section considering the two types of polished surfaces: #80 and #1000.

Table A5 - 30 Measurements of roughness taken using rock-section images from microscope.

	Measurements of Roughness (μm)	
	#80	**#1000**
	4.7 μm	2.5 μm
	4.5 μm	2.4 μm
	5.1 μm	1.3 μm
	2.8 μm	1.9 μm
	3.3 μm	0.7 μm
	2.2 μm	0.5 μm
	2.5 μm	0.9 μm
	2.9 μm	0.5 μm
	2.8 μm	2.9 μm
	6.0 μm	3.7 μm
Mean value, R_a	3.7 μm	1.7 μm

Part I of **Figure A5 - 19**

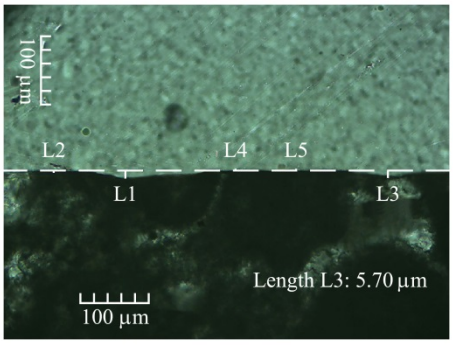

a. Measurement 1.

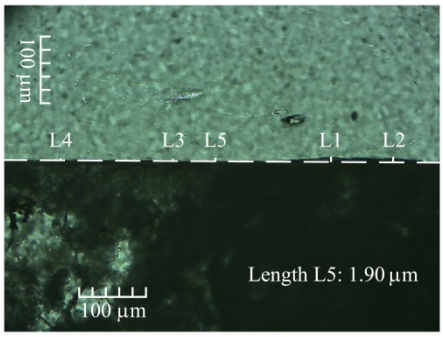

b. Measurement 2.

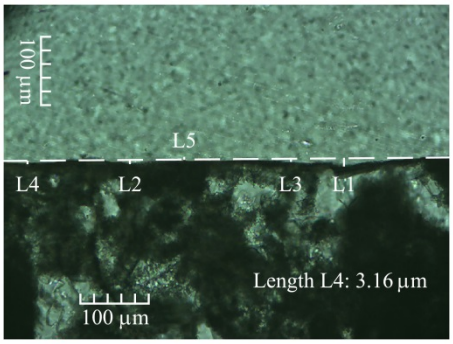

c. Measurement 3.

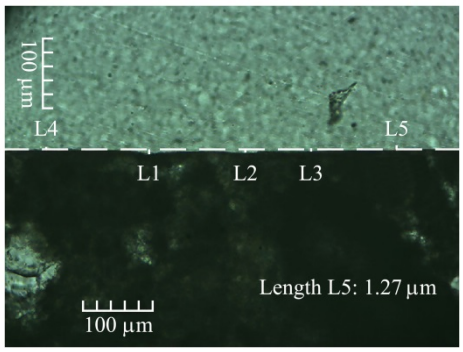

d. Measurement 4.

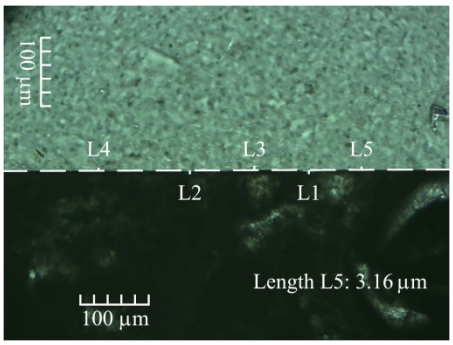

e. Measurement 5.

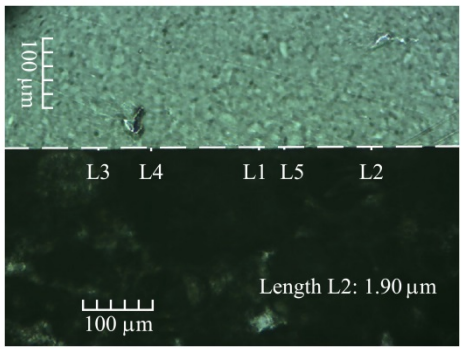

f. Measurement 6.

Part II of **Figure A5 - 19**

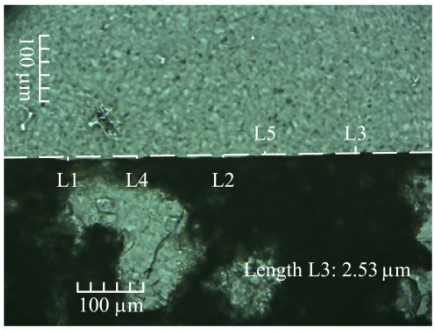

g. Measurement 7.

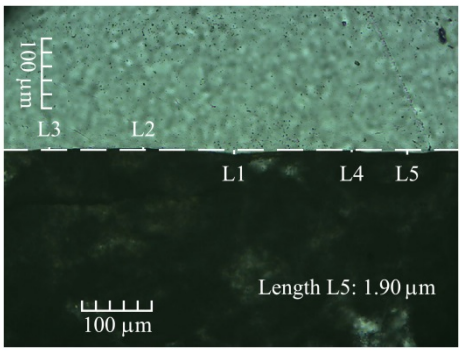

h. Measurement 8.

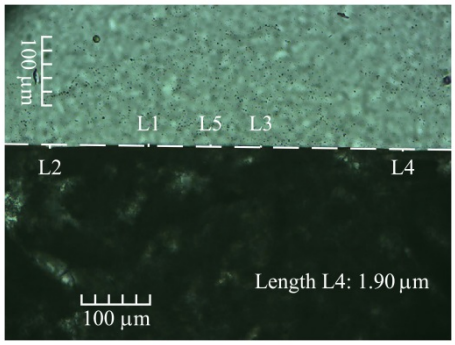

i. Measurement 9.

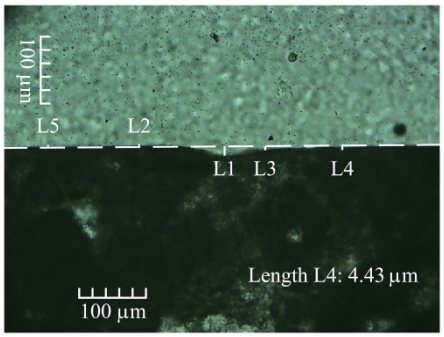

j. Measurement 10.

Figure A5 - 19 Roughness measurement on #80 polished surface of limestone blocks: Profiles of thin sections of limestone by microscope examination. (Limestone in dark color in the lower part. Epoxy resin –upper part- covers the rock).

Part I of **Figure A5 - 20**

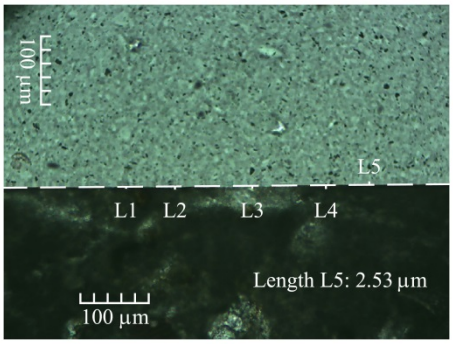

a. Measurement 1.

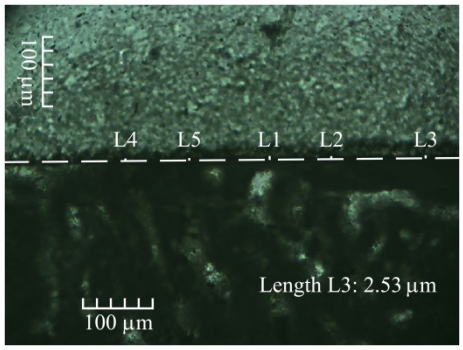

b. Measurement 2.

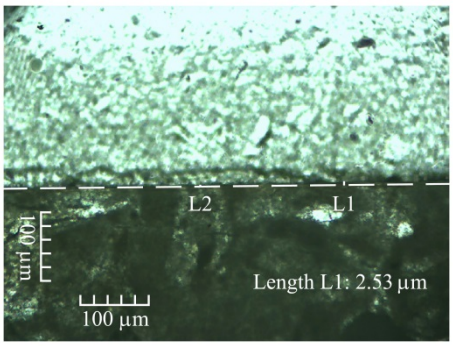

c. Measurement 3.

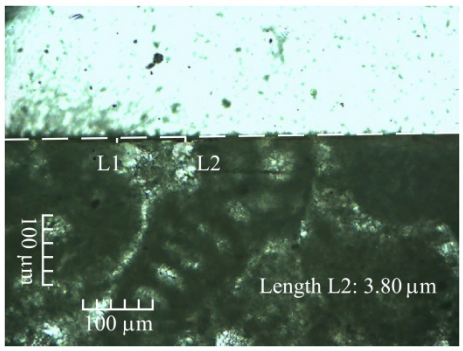

d. Measurement 4.

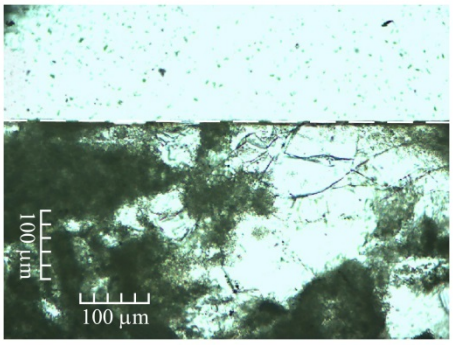

e. Measurement 5.

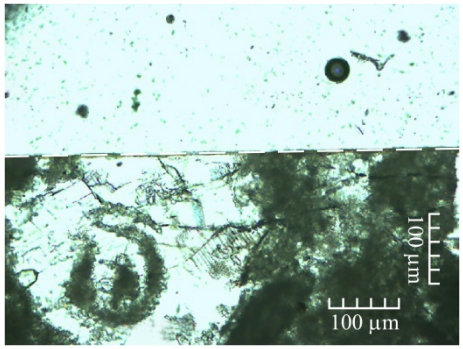

f. Measurement 6.

Part II of **Figure A5 - 20**

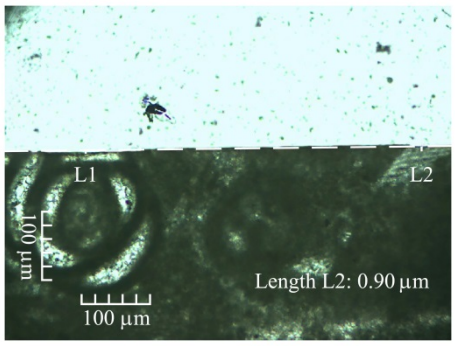

g. Measurement 7.

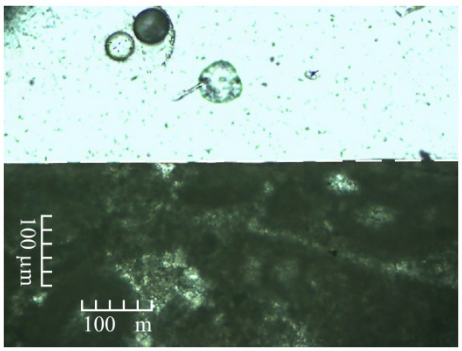

h. Measurement 8.

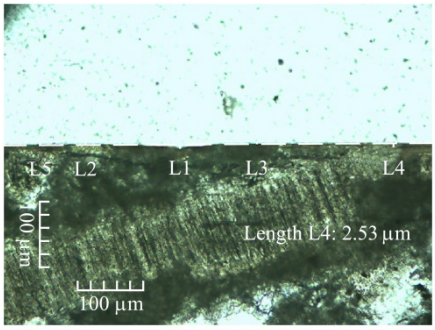

i. Measurement 9.

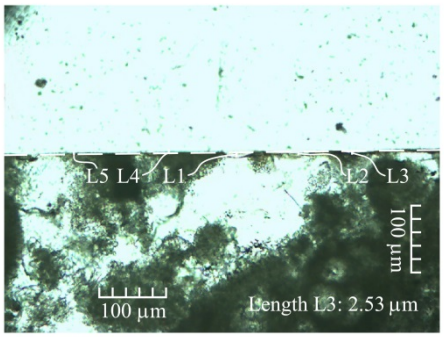

j. Measurement 10.

Figure A5 - 20 Roughness measurement on #1000 polished surface of limestone blocks: Profiles of thin sections of limestone by microscope examination. (Limestone in dark color in the lower part. Epoxy resin –upper part- covers the rock).

A5.5. References

GEOMAR, 2015. Nota técnica del informe de laboratorio L-14-1227 para un análisis de Rugosidad de dos muestras de caliza. Barcelona (Spain).

Ortega, E., 2008. Comportamiento de materiales granulares gruesos - Efecto de la succión. PhD. Thesis. Technical University of Catalonia. UPC, Barcelona, Spain (in Spanish).

Santamarina, J.C., Klein, K., Fam, M., 2001. Load deformation behaviour, in: Soils and Waves: Particulate Materials Behaviour, Characterization and Process Monitoring. John Wiley & Sons, Ltd., Chichester (UK), pp. 104–106.

Thomas, T.R., 1999. Amplitude Parameters, in: Rough Surfaces. Imperial College Press, London (UK), pp. 133–150.

Appendix 6

A6. DEM code

This appendix presents the main functions that compose the DEM code developed in the thesis. This code was written in FISH language for PFC3D v4.0 (see section 3.7 in chapter 3).

The execution of the code is explained in the first part (section A6.1). Subsequently, the functions of the code are presented.

A6.1. Execution of tests using the PFC3D

A6.1.1. Parameters of the DEM model

; A. **Failure Criteria::**
; 1.) Proposed Criterion based on the Fracture Mechanics (LEFM) and the subcritical crack propagation: Tensile stress calculated from Russell and Muir Wood (2009): set IndicadorRompe=10.0
; 2.) Criterion based on LEFM: Calculation of Principal stresses; SIGMA3 - Tensile stress: set IndicadorRompe=20.0
; 3.) Mohr Coulomb Criterion: set IndicadorRompe=30.0
; 4.) No breakage: set IndicadorRompe=0.0

set IndicadorRompe=10.0 ; For this example

; B. **Division Criteria:**
; 1.) Only Equal volumen crushing: set IndiCriterioDivision=10.0
; 2.) Pure Commintuion crushing: set IndiCriterioDivision=20.0
; 3.) Mix criterion: Equal volumen crushing and Commintuion crushing – Not use subparticles of 13P to replacement clumps of 1P: set IndiCriterioDivision=80.0
; 4.) Mix criterion (Proposed Criterion): Equal volumen crushing and Commintuion crushing – Using subparticles of 13P to replacement clumps of 1P and considering mass conservation: set IndiCriterioDivision=90.0

; 5.) Mix criterion: Equal volumen crushing and Commintuion crushing – Using subparticles of 13P to replacement clumps of 1P and not considering mass conservation: set IndiCriterioDivision=100.0

set IndiCriterioDivision=90.0 ; Criterion used in the simulations

; SET z_servo=0 ; To fix the horizontal stresses applied to the cell (For triaxial tests)
; SET z_servo=1 ; To fix the vertical stresses applied (szzreq) to the cell (For Oedometer tests)

SET z_servo=1 ; For this exercise

macro zero 'ini xvel 0 yvel 0 zvel 0 xspin 0 yspin 0 zspin 0'
macro clzero 'clump property xvel 0 yvel 0 zvel 0 xspin 0 yspin 0 zspin 0'

zero ;
clzero;

; C. Properties of the particles

; (1) **Assignment of contact properties of the particles**:
; Normal and shear contact stiffness (kn and ks): Given in (N/m)
; Friction coefficient (fric)

macro BolasPropiedades 'prop kn=4.0e6 ks=4.0e6 fric 0.3' ; For this exercise
BolasPropiedades

; (2) **Parameters of the criterion based on Fracture mechanics and subcritical crack propagation**:
; (2.1) Reference velocity for crack propagation v_o= VoCharles: Given in (m/s)
; (2.2) Fracture Toughness, K_c: Given in Pa*m$^{0.5}$.
; (a) For macroparticles of clumps:
; Before Wetting: Kc2
; After Wetting: Kc2f
; (b) For microparticles:
; Before Wetting: Kc1
; After Wetting: Kc1f
; Breakage of macroparticles will be considered only
; (2.3) Poisson ratio: poisson
; (2.4) Soild angle: tetaCarga: Given in radians
; (2.5) Time: tr: Given in (s)

; For this exercise:
set VoCharles=0.1 Kc2=1.0e6 Kc1=100000000000000000000. poisson=0.25

tetaCarga=0.08727 tr=1.
set Kc2f=1.0e6 Kc1f=100000000000000000000. ;

; (3) **Relative Humidity**: HR: Given in porcentaje (%):

set HR=10.0 ; For example (Relative Humidity = 10%)

; (4) **Parameters of strength of Mohr Coulomb criterion**:
; cohesion: Given in Pa.
; angulofiGrados: Given in degrees

SET cohesion=53590000.0 angulofiGrados=0.0 ;;; For this exercise

; (5) **Yield stress:**
; Yield stress: Parameter of the model. Given in Pa
;; Compresion (-).

set ESFFLUENCIA=-600000. ; For this exercise

set comminution1=0.90 ;; Percent of Comminution crushing (90%) before to reach the yield stress;
set comminution2=0.60 ;; Percent of Comminution crushing (60%) after to reach the yield stress;

; (6) **Damping coefficient**:

DAMP default local 0.7

; **D. Other parameters**:

set alpha=0.001 ;;Parameter to control the velocity of the walls when a required stress is applied;

;set dt=0.00000001 ; Timestep: Given in (s)
set dt auto ; For this exercise

SET RC_CLM=500; Number of timesteps to check if the clumps are inside the sample

set NBOLASCLUMPTIPO1=14 ; Number of balls of the clump type 1: In our case is 14

set NBOLASCLUMPTIPO2=28 ; ; Number of balls of the clump type 2: It is not considered in the performed simulations;

; TiempoSigmaV=Macro time: It is a number of timesteps used to maintain the vertical stress during this period in the oedometer tests.

SET TiempoSigmaV=200000. ; For this exercise

```
set_ini                 ; Call Function
conf                    ; Call Function
Trace energy on         ; FISH Function
arraysMP                ; Call Function
make_array              ; Call Function
setupMEsferas           ; Call Function
setupDefectoIn          ; Call Function
TextoPrimeraLinea       ; Call Function
NUEVO_CREACLUMPS        ; Call Function
CreaMEsferasMuestra     ; Call Function
Rutina_volumenBolas     ; Call Function
```

```
set m_nsteps= 5000  m_nchunks= 100
set numbolanew=100000
```

set rminimoCM=0.0005 ;;; Lowest value of radius to generate balls in the criterion of mass conservation; It is used in "CREABOLAS1P_FINOS" and "DefectoInicio"; It is given in m.

set R1P_14P=0.005927 ;;; Radius of a ball (1P) (microparticle) of the original clump 14P

set gen_error off ;;;;

SET hist_rep=200 ; Sampling interval

A6.1.2. Selection of variables to be stored during the DEM simulations

a. Using the History command

b. Using the Plot command

c. Using output files

A6.1.3. Numerical simulation of tests

A6.1.3.1. Introduction of defects inside the macroparticles

```
DefectoInicial ;            Call Function
```

A6.1.3.2. Measurement of properties inside the Virtual Spheres MP

```
Esfpropiedades;             Call Function
```

A6.1.3.3. Calculation of particle breakage

```
; MAIN AND KEY FUNCTION: Rompeclump (Inside of the Function RompimientoMaestro). Calculation of particle breakage.
;          It is called at the start of each calculation cycle.

set fishcall FC_CYC_TOP RompimientoMaestro  ;       Call Function

set fishcall FC_CYC_XMOT VelocidadCeroBolas  ;      Call Function
```

A6.1.3.4. Performance of tests

```
; Application of the required vertical stress (szzreq) for the Oedometer test (z_servo=1):

;Example 1:
set szzreq= -1.0e5 sig_tol=0.05 z_servo=1
set HR=10.0  ;

EJECUCION;                  Call Function
Esfpropiedades              Call Function
save File.SAV

;Example 2:
set szzreq= -2.8e6 sig_tol=0.05 z_servo=1
set HR=100.0  ; Saturation of the specimen

EJECUCION;                  Call Function
Esfpropiedades              Call Function
save File.SAV

return
```

A6.2. Initialization of variables type array

A6.2.1. Function make_array

```
;           Introduction of arrays;

def make_array

  array nx(30);                                  array V_SIGMA1_ROTURA(400000);
  array ny(30);                                  array V_Desviador(400000);
  array nz(30);                                  array V_SIGMA_PRINCIPAL1(400000);
  array normaPosicion(30);                       array V_SIGMA_PRINCIPAL2(400000);
  array unitarionx(30);                          array V_SIGMA_PRINCIPAL3(400000);
  array unitariony(30);                          array MaxfuerzanormalContactoV(400000);
  array unitarionz(30);                          array SIGMATETAV(400000);
  array Dif_unitarionx(30) ;                     array    id_clump(400000);
  array Dif_unitariony(30);                      array    num_clump(400000);
  array Dif_unitarionz(30);                      array K02(400000);
  array bola(30) ;                               array K01(400000);
  array Xc(30);                                  array BETAT2(400000);
  array Yc(30) ;                                 array BETAT1(400000);
  array Zc(30);                                  array AlturaHClump(400000);
  array n12n1sx(30);                             array TiempoRotura1(400000);
  array n12n1sy(30);                             array TiempoRotura2(400000);
  array n12n1sz(30);                             array Voi2_Vector(400000);
  array Norman12n1s(30);                         array id_clumpInicio(400000);
  array unitarion12n1sx(30);                     array num_clumpInicio(400000);
  array unitarion12n1sy(30);                     array a01(400000);
  array unitarion12n1sz(30);                     array a02(400000);
  array Dif_unitarion12n1sx(30);                 array IntactoClump(400000);
  array Dif_unitarion12n1sy(30);                 array w_Uniforme_inicio(400000)  ;
  array Dif_unitarion12n1sz(30);                 array Y_Dist_inicio(400000);
  array Dif_neg_unitarion12n1sx(30);             array AzarNum_inicio(400000);
  array Dif_neg_unitarion12n1sy(30);             array aio2_inicio(400000);
  array Dif_neg_unitarion12n1sz(30);             array AlturaHClump_Inicio(400000);
  array otrabola(30);                            array s_w_Uniforme_inicio(400000);
  array Xcentroclump_cl(400000);                 array s_Y_Dist_inicio(400000);
  array Ycentroclump_cl(400000);                 array s_AzarNum_inicio(400000)  ;
  array Zcentroclump_cl(400000);                 array s_aio2_inicio(400000);
  array tensionesClump(3,3);                     array s_AlturaHClump_Inicio(400000);
  array V_SIGMA1(400000);                        array s_id_clumpInicio(400000);
  array V_SIGMA3(400000);                        array s_num_clumpInicio(400000);
  array Ppromedio_Array(400000);                 array poly(3,4);

end
```

A6.2.2. Function arraysMP

```
 def arraysMP

          array infomp1(100)  ;
```

```
        array infomp2(100)  ;
        array infomp3(100)  ;
        array infomp4(100)  ;
        array infomp5(100)  ;
        array infomp6(100)  ;
        array infomp7(100)  ;
        array infomp8(100)  ;
        array infomp9(100)  ;
        array infomp10(100)  ;
        array infclumpMP1(100000)  ;
        array infclumpMP2(100000)  ;
        array infclumpMP3(100000)  ;
        array infclumpMP4(100000)  ;
        array infclumpMP5(100000)  ;
        array infcontactosMP1(1000000)  ;
        array infcontactosMP2(1000000)  ;
        array infcontactosMP3(1000000)  ;
        array infcontactosMP4(1000000)  ;
        array infcontactosMP5(1000000)  ;
        array infclump1(100000)  ;
        array infclump2(100000)  ;
        array infclump3(100000)  ;
        array infclump4(100000)  ;
        array infclump5(10)          ;
        array infcontactos1(1000000)  ;
        array infcontactos2(1000000)  ;
        array infcontactos3(1000000)  ;
        array infcontactos4(1000000)  ;
        array infcontactos5(1000000)  ;

end
```

A6.3. Initialization of other variables and parameters

A6.3.1. Function set_ini

```
;  Initial strain

def set_ini
  wezz_0  = wezz             ; Axial strain
  wevol_0 = wevol                    ; Volumetric strain
end
```

A6.3.2. Function conf

```
; Variables: Stresses and strain

def conf

        Sz=wszz; Vertical stress
        Sr=wsrr; Radial stress
        devi  = wszz - wsrr          ;  Deviatoric stress
        deax  = wezz - wezz_0        ; Axial strain
        devol = wevol - wevol_0    ; Volumetric strain
        conf  = wsrr                 ; Confining stress, p'
end
```

A6.3.3. Function setupMEsferas

```
def setupMEsferas

        IO_WRITE = 1
        IO_ASCII = 1
        esferaradio=0.07  ; To select. This value is an exaple. The value depends of the
diameter of the clumps: Diameter of MP sphere = 2*esferaradio = 5*Diameter of the original
clump of 14P(2.8cm) = 14cm
        esferaradio1=0.025
        esferaradio2=0.050
        esferaradio3=0.075
        esferaradio4=0.100
        esferaradio5=0.125
        ContadorFile = 1  ;
        ContadorFileMP = 1  ;
end
```

A6.3.4. Function setupDefectoIn

```
; Type of Probabilistic distribution of crack length

def setupDefectoIn
```

```
IO_WRITE = 1
IO_FISH  = 0
IO_ASCII = 1
w_Max=0.99999   ;
Beta_Weibull=0.5

;;;;alfa_Weibull=1.0 ; Exponential distribution
;;;;alfa_Weibull=2.0 ; Weibull_1 distribution
;;;;alfa_Weibull=4.0 ; Weibull_2 distribution
;;;;Dist_inv=0 ; Exponential and/or Weibull distributions
;;;;Dist_inv=1 ; Mirror of Exponential and/or Weibull distributions
;;;;Dist_inv=2   ; Uniform distribution


; Example:

alfa_Weibull=2.0 ; Weibull_1
Dist_inv=2 ; Uniform distribution

end
```

A6.3.5. Function TextoPrimeraLinea

```
; Text in output file

def TextoPrimeraLinea

        infomp1 (1) = 'emindex'+'  '+'idmp'+'          '+'mpradio'+'       '+'mxcentro'+'
        '+'mycentro'+'      '+'mzcentro'+'      '+'NCoordinacion'
        infomp2 (1) = 'emindex'+'  '+'mporosidad'+'  '+'mslidingfraction'          +          '
        '+'ContadorClumpMP' + '   '+'totalclumpESFERAMP'
        infomp3 (1) = 'emindex'+'  '+'MSIGMA1'+'    '+'MSIGMA2' + '   '+'MSIGMA3'+        '
        '+'mtension11'+ '  '+'mtension12'+ '  '+'mtension13'
        infomp4 (1) = 'emindex'+'  '+'mtension21'+'  '+'mtension22' + ' '+'mtension23'+      '
        '+'mtension31'+ '  '+'mtension32'+ '  '+'mtension33'
        infomp5 (1) = 'emindex'+'  '+'mvdef11'+'      '+'mvdef12' + '     '+'mvdef13'+          '
        '+'mvdef21'+ '      '+'mvdef22'+ '      '+'mvdef23'
        infomp6 (1) = 'emindex'+'  '+'cont_step'+'    '+'mvdef31' + '     '+'mvdef32'+          '
        '+'mvdef33'
        infomp7 (1) = 'emindex'+'  '+'pponderado_volclump'+''+'pponderado_diamclump' + '
        '+'pponderado_totalbolas'+ '          '+'prom_volclump'+ '          '+'prom_diamclump'+
'       '+'prom_totalbolas'
        infomp8 (1) = 'emindex'+'  '+'cPRINCIPALES_r1'+'    '+'cPRINCIPALES_r2'    +    '
        '+'c_r1'+ '           '+'c_r2'
        infomp9 (1) = 'emindex'+'  '+'c_r1modif'+ '    '+'c_r2modif' + '   '+'c_r3modif'
        infomp10 (1) = 'emindex'+''+'numClumpTotalMP'+ '   '+'numClumpVaciosMP'+      '
        '+'numClumpSinContactoMP'+'      '+'numClumpBuenosMP'+'
        '+'numClumpSinFCyBuenosMP'

        infcontactosMP1 (1) = 'ContadorContactomuestra'+'  '+'idbcl'+'          '+'idcl'   +   '
        '+'         '+'XContacto'+ '   '+'YContacto'+ '   '+'ZContacto'+ '   '+'idmp'
        infcontactosMP2 (1) = 'ContadorContactomuestra'+'  '+'idbcl'+'          '+'radiobola'
+ '       '+'totalbolas'+ '    '+'DequivalenteClump'+ '   '+'VolumenClump'
```

```
        infcontactosMP3 (1) = 'ContadorContactomuestra'+'  '+'fuerzanormalContacto'+'
        '+'XVectorunitarioContacto' + '       '+'YVectorunitarioContacto'+                '
        '+'ZVectorunitarioContacto'
        infcontactosMP4 (1) = 'ContadorContactomuestra'+'  '+'XFuerzacorteContacto'  +  '
        '+'YFuerzacorteContacto'+ '          '+'ZFuerzacorteContacto'+                   '
        '+'IncrEnergiaContacto'
        infcontactosMP5 (1) = 'ContadorContactomuestra'+'  '+'ContadorContactoclump'+'
        '+'ab'+'   '+'cont_step'

        infclumpMP1 (1) = 'ContadorClumpMP'+'     '+'idcl'+'  '+'Xcentroclump'       +       '
        '+'Ycentroclump'+ '          '+'Zcentroclump'+ '          '+'totalbolas'+ '    '+'cont_step'
        infclumpMP2 (1) = 'ContadorClumpMP'+'     '+'ccc'+'  '+'RequivalenteClump'+'
        '+'DequivalenteClump' + '  '+'VolumenClump'+ '        '+'Fnmax'+                  '
        '+'SIGMATETA'
        infclumpMP3 (1) = 'ContadorClumpMP'+'     '+'sigma11'+'      '+'sigma12'      +     '
        '+'sigma13'+ '      '+'sigma21'+ '      '+'sigma22'+ '      '+'sigma23'
        infclumpMP4 (1) = 'ContadorClumpMP'+'     '+'sigma31'+'      '+'sigma32'      +     '
        '+'sigma33'+ '      '+'SIGMA1'+ '       '+'SIGMA2'+ '       '+'SIGMA3'
        infclumpMP5 (1) = 'ContadorClumpMP'+'     '+'ccc'+'  '+'idcl'+'  '+'idmp'

        infcontactos1 (1) = 'ContadorContactomuestra'+'       '+'idbcl'+'          '+'idcl'   +  '
        '+'XContacto'+ '   '+'YContacto'+ '   '+'ZContacto'+ '   '+'cont_step'
        infcontactos2 (1) = 'ContadorContactomuestra'+'       '+'idbcl'+'          '+'radiobola'
+ '     '+'totalbolas'+ '    '+'DequivalenteClump'+ '   '+'VolumenClump'
        infcontactos3 (1) = 'ContadorContactomuestra'+'       '+'fuerzanormalContacto'+'
        '+'XVectorunitarioContacto' + '       '+'YVectorunitarioContacto'+                '
        '+'ZVectorunitarioContacto'
        infcontactos4 (1) = 'ContadorContactomuestra'+'       '+'XFuerzacorteContacto'  +  '
        '+'YFuerzacorteContacto'+ '          '+'ZFuerzacorteContacto'+                   '
        '+'IncrEnergiaContacto'
        infcontactos5 (1) = 'ContadorContactomuestra'+'       '+'ContadorContactoclump'+'
        '+'ab'+'   '+'cont_step'

        infclump1 (1) = 'numClumpBuenos'+'          '+'idcl'+'  '+'Xcentroclump'       +       '
        '+'Ycentroclump'+ '          '+'Zcentroclump'+ '          '+'totalbolas'+ '    '+'cont_step'
        infclump2 (1) = 'numClumpBuenos'+'          '+'ccc'+'  '+'RequivalenteClump'+'
        '+'DequivalenteClump' + '  '+'VolumenClump'+ '        '+'Fnmax'+                  '
        '+'SIGMATETA'
        infclump3 (1) = 'numClumpBuenos'+'          '+'sigma11'+'      '+'sigma12'      +     '
        '+'sigma13'+ '      '+'sigma21'+ '      '+'sigma22'+ '      '+'sigma23'
        infclump4 (1) = 'numClumpBuenos'+'          '+'sigma31'+'      '+'sigma32'      +     '
        '+'sigma33'+ '      '+'SIGMA1'+ '       '+'SIGMA2'+ '       '+'SIGMA3'

        infclump5 (1) = 'cont_step'+'          '+'numClumpBuenos'+'     '+'numClumpTotal'+'
        '+'numClumpVacios'+'       '+'numClumpSinContacto'+'
        '+'numClumpSinFCyBuenos'

end
```

A6.3.6. Function NUEVO_CREACLUMPS

```
; Generation of Clumps:    Clump of 13P (subparticle); Clumps of 14P; 28P ;

def NUEVO_CREACLUMPS
```

```
COMMAND
        clump template make nuevocl13HEXd40 13          &
      radii 0.020 0.020 0.020 0.020 0.020 0.020 0.020 0.020 0.020 0.020 0.020
0.020 0.020 &
      pos (-0.02,-0.011547,0.03266) &
                  (0.0, 0.02309401, 0.03266) &
                  (0.0, 0.0, 0.0) &
                  (-0.02,-0.034641016151378,0.0) &
                  (-0.04,0.0,0.0) &
                  (-0.02,0.034641016151378,0.0) &
                  (-0.02,0.011547,-0.03266) &
                  (0.0,-0.02309401, -0.03266) &
                  (0.02,0.011547,-0.03266) &
                  (0.02,0.034641016151378,0.0) &
                  (0.04,0.0,0.0) &
                  (0.02,-0.034641016151378,0.0) &
                  (0.02, -0.011547, 0.03266)

        clump template make nuevocl14d40 14          &
      radii 0.020 0.020 0.020 0.020 0.020 0.020 0.020 0.020 0.020 0.020 0.020
0.020 0.020 0.020 &
      pos (0.02,0.02,0.028284271247) &
                  (0.0, 0.0, 0.0) &
                  (-0.02,-0.02,-0.028284271247) &
                  (0.02,-0.02,-0.028284271247) &
                  (0.02,0.02,-0.028284271247) &
                  (-0.02,0.02,-0.028284271247) &
                  (-0.02,0.06,-0.028284271247) &
                  (0.0, 0.04, 0.0) &
                  (0.04,0.04,0.0) &
                  (0.02,0.06,-0.028284271247) &
                  (0.06,0.06,-0.028284271247) &
                  (0.06,0.02,-0.028284271247) &
                  (0.06,-0.02,-0.028284271247) &
                  (0.04, 0.0, 0.0)

        clump template make nuevocl28d40 28          &
      radii 0.020 0.020 0.020 0.020 0.020 0.020 0.020 0.020 0.020 0.020 0.020
0.020 0.020 0.020 &
            0.020 0.020 0.020 0.020 0.020 0.020 0.020 0.020 0.020 0.020 0.020 0.020
0.020 0.020 &
      pos (0.02,0.02,0.028284271247) &
                  (0.0, 0.0, 0.0) &
                  (-0.02,-0.02,-0.028284271247) &
                  (0.02,-0.02,-0.028284271247) &
                  (0.02,0.02,-0.028284271247) &
                  (-0.02,0.02,-0.028284271247) &
                  (-0.02,0.06,-0.028284271247) &
                  (0.0, 0.04, 0.0) &
                  (0.04,0.04,0.0) &
                  (0.02,0.06,-0.028284271247) &
                  (0.06,0.06,-0.028284271247) &
                  (0.06,0.02,-0.028284271247) &
                  (0.06,-0.02,-0.028284271247) &
                  (0.04, 0.0, 0.0) &
                  (0.0, 0.0, -0.096568542494) &
                  (-0.02,-0.02,-0.068284271247) &
```

```
                    (-0.02,0.02,-0.068284271247) &
                    (-0.02,0.06,-0.068284271247) &
                    (0.02,0.06,-0.068284271247) &
                    (0.0, 0.04, -0.096568542494) &
                    (0.04,0.04,-0.096568542494) &
                    (0.06,0.06,-0.068284271247) &
                    (0.06,0.02,-0.068284271247) &
                    (0.02,0.02,-0.068284271247) &
                    (0.02,-0.02,-0.068284271247) &
                    (0.06,-0.02,-0.068284271247) &
                    (0.04, 0.0, -0.096568542494) &
                    (0.02,0.02,-0.124852813741)
        END_COMMAND
end
```

A6.3.7. Function CreaMEsferasMuestra

```
; Creation of virtual spheres (MP#) for doing measuments: Five levels; Five spheres MP per
level
; Diameter of MP =  5 * diameter of original clump of 14P(2.8cm) = 14cm

def CreaMEsferasMuestra

        command
                ;;; Level 1: Upper Part I (considering εa=15%)
            MEASURE ID=1 X=0.0 Y=0.0 Z=0.16125 radius=esferaradio
            MEASURE ID=2 X=-0.052 Y=0.0 Z=0.16125 radius=esferaradio
            MEASURE ID=3 X=0.052 Y=0.0 Z=0.16125 radius=esferaradio
            MEASURE ID=4 X=0.0 Y=0.052 Z=0.16125 radius=esferaradio
            MEASURE ID=5 X=0.0 Y=-0.052 Z=0.16125 radius=esferaradio

                ;;; Level 2: Upper Part 2 (considering εa=30%)
            MEASURE ID=6 X=0.0 Y=0.0 Z=0.1425 radius=esferaradio
            MEASURE ID=7 X=-0.052 Y=0.0 Z=0.1425 radius=esferaradio
            MEASURE ID=8 X=0.052 Y=0.0 Z=0.1425 radius=esferaradio
            MEASURE ID=9 X=0.0 Y=0.052 Z=0.1425 radius=esferaradio
            MEASURE ID=10 X=0.0 Y=-0.052 Z=0.1425 radius=esferaradio

                ;;; Level 3: Central Part I
            MEASURE ID=11 X=0.0 Y=0.0 Z=0.125 radius=esferaradio
            MEASURE ID=12 X=-0.052 Y=0.0 Z=0.125 radius=esferaradio
            MEASURE ID=13 X=0.052 Y=0.0 Z=0.125 radius=esferaradio
            MEASURE ID=14 X=0.0 Y=0.052 Z=0.125 radius=esferaradio
            MEASURE ID=15 X=0.0 Y=-0.052 Z=0.125 radius=esferaradio

                ;;; Level 4: Lower Part 2 (considering εa=30%)
            MEASURE ID=16 X=0.0 Y=0.0 Z=0.1075 radius=esferaradio
            MEASURE ID=17 X=-0.052 Y=0.0 Z=0.1075 radius=esferaradio
            MEASURE ID=18 X=0.052 Y=0.0 Z=0.1075 radius=esferaradio
            MEASURE ID=19 X=0.0 Y=0.052 Z=0.1075 radius=esferaradio
            MEASURE ID=20 X=0.0 Y=-0.052 Z=0.1075 radius=esferaradio

                ;;; Level 5: Lower Part 1 (considering εa=15%)
            MEASURE ID=21 X=0.0 Y=0.0 Z=0.08875 radius=esferaradio
            MEASURE ID=22 X=-0.052 Y=0.0 Z=0.08875 radius=esferaradio
```

```
                MEASURE ID=23 X=0.052 Y=0.0 Z=0.08875 radius=esferaradio
                MEASURE ID=24 X=0.0 Y=0.052 Z=0.08875 radius=esferaradio
                MEASURE ID=25 X=0.0 Y=-0.052 Z=0.08875 radius=esferaradio
        end_command

end
```

A6.3.8. Function Rutina_volumenBolas

```
; Volume of balls

def Rutina_volumenBolas

  Vol_Bolas = 0.0 ; get actual porosity
  bp = ball_head

  loop while bp # null
    Vol_Bolas = Vol_Bolas + 4.0 / 3.0 * pi * b_rad(bp)^3
    bp  = b_next(bp)
  end_loop

end
```

A6.4. Introduction of defects (cracks) inside the macroparticles

A6.4.1. Function DefectoInicial

```
; Introduction of defects at the beginning of the test

def DefectoInicial

cl= clump_head   ; pointer de lista de clumps
ddd=1; numeracion de clump
RADIOMAYOR=0.
RADIOMENOR=10.
VolumenTotalClumpMuestraInicio=0.
TipoRango1=0.
TipoRango2=0.
TipoRango3=0.
TipoRango4=0.
TipoRango5=0.
TipoRango6=0.
TipoRango7=0.
TipoRango8=0.
TipoRango9=0.
TipoRango10=0.
VolumenRango1=0.
VolumenRango2=0.
VolumenRango3=0.
VolumenRango4=0.
VolumenRango5=0.
VolumenRango6=0.
VolumenRango7=0.
VolumenRango8=0.
VolumenRango9=0.
VolumenRango10=0.

        loop while cl # null

                idclInicio=cl_id(cl);
                id_clumpInicio(ddd)=idclInicio        ;
                num_clumpInicio(ddd)=ddd              ;
                IntactoClump(idclInicio)=10                     ;
                bcl=cl_list(cl)       ;
                jK=1 ;
                SUMradiobolaInicio=0 ;

                loop while bcl # null
                        idbclInicio=b_id(bcl)         ;
                        radiobolaInicio=b_rad(bcl) ;
                        totalbolasinicio=jK
                        SUMradiobolaInicio=(SUMradiobolaInicio+radiobolaInicio) ;

                        Distribucion_Probable

                        aio1=AzarNum*2*radiobolaInicio ;
```

```
                    a01(idbclInicio)=aio1                    ;
                    jk=jk+1
                    bcl=b_cllist(bcl)   ;
                end_loop;

                promradiobolaInicio=(SUMradiobolaInicio)/totalbolasinicio ;

        VolumenClumpInicio=((4* pi *(promradiobolaInicio)^3 )/ 3)*totalbolasinicio  ;
        VolumenClump=VolumenClumpInicio
        VolumenTotalClumpMuestraInicio=VolumenTotalClumpMuestraInicio+VolumenClu
mpInicio
        VolumenTotalClumpMuestra=VolumenTotalClumpMuestraInicio

        If promradiobolaInicio>=RADIOMAYOR
                RADIOMAYOR=promradiobolaInicio
                VOLUMENMAYORinicio=VolumenClumpInicio
        end_if

        If promradiobolaInicio<=RADIOMENOR
                RADIOMENOR=promradiobolaInicio
                VOLUMENMENORinicio=VolumenClumpInicio
        end_if

        Distribucion_Probable

        AlturaClump=2.0*((totalbolasinicio)^(1.0/3.0))*promradiobolaInicio
        AlturaHClump(idclInicio)=AlturaClump
        aio2=AzarNum*AlturaClump ;
        a02(idclInicio)=aio2                    ;

        w_Uniforme_inicio(ddd)=w_Uniforme
        Y_Dist_inicio(ddd)=Y_Dist
        AzarNum_inicio(ddd)=AzarNum
        aio2_inicio(ddd)=aio2
        AlturaHClump_Inicio(ddd)=AlturaClump
        s_w_Uniforme_inicio(ddd)=string(w_Uniforme_inicio(ddd))
        s_Y_Dist_inicio(ddd)=string(Y_Dist_inicio(ddd))
        s_AzarNum_inicio(ddd)=string(AzarNum_inicio(ddd))
        s_aio2_inicio(ddd)=string(aio2_inicio(ddd))
        s_AlturaHClump_Inicio(ddd)=string(AlturaHClump_Inicio(ddd))
        s_id_clumpInicio(ddd)=string(id_clumpInicio(ddd))
        s_num_clumpInicio(ddd)=string(num_clumpInicio(ddd))

        Totalddd_Inicio=ddd   ;;;;Numero de Clumps al inicio
        ddd=ddd+1 ; Numeracion de clumps dentro del loop
        cl=cl_next(cl)      ; Busca siguiente clump

        end_loop ;

VOLUMENMAYORCLUMPinicio=VOLUMENMAYORinicio
VOLUMENMENORCLUMPinicio=VOLUMENMENORinicio

VOLUMENMENORPOSIBLEinicio=((4.* pi *(RADIOMENOR)^3 )/ 3.)    ;

        If IndiCriterioDivision=50.0 ;
                VOLUMENMENORPOSIBLEinicio=((4.* pi *(rminimoCM)^3 )/ 3.)  ;
        END_IF  ;
```

```
        If IndiCriterioDivision=60.0 ;
                VOLUMENMENORPOSIBLEinicio=((4.* pi *(rminimoCM)^3 )/ 3.)  ;
        END_IF  ;;;; Final del If IndiCriterioDivision=60.0 ;


        If IndiCriterioDivision=70.0 ;
                VOLUMENMENORPOSIBLEinicio=((4.* pi *(rminimoCM)^3 )/ 3.)  ;
        END_IF  ;;;; Final del If IndiCriterioDivision=70.0 ;

        If IndiCriterioDivision=90.0 ;
                VOLUMENMENORPOSIBLEinicio=((4.* pi *(rminimoCM)^3 )/ 3.)  ;
        END_IF  ;

        If IndiCriterioDivision=100.0 ;
                R1escalado_14P=R1P_14P*0.78377822924            ;
                R1P_13P=(R1escalado_14P)*((1/13)^(1/3))
                VOLUMENMENORPOSIBLEinicio=((4.* pi *(R1P_13P)^3 )/ 3.)  ;
        END_IF  ;

VOLUMENRANGO=((VOLUMENMAYORCLUMPinicio-
VOLUMENMENORPOSIBLEinicio)/NGRUPOS)

Limite0=VOLUMENMENORPOSIBLEinicio
Limite1=Limite0+VOLUMENRANGO
Limite2=Limite1+VOLUMENRANGO
Limite3=Limite2+VOLUMENRANGO
Limite4=Limite3+VOLUMENRANGO
Limite5=Limite4+VOLUMENRANGO
Limite6=Limite5+VOLUMENRANGO
Limite7=Limite6+VOLUMENRANGO
Limite8=Limite7+VOLUMENRANGO
Limite9=Limite8+VOLUMENRANGO
Limite10=Limite9+VOLUMENRANGO          ;

salidaDefectoInicial_test

end
```

A6.4.2. Function DefectoTiempo

```
; Introduction of defects in time

def DefectoTiempo

If IntactoClump(idcl) # 10
        Distribucion_Probable
        AlturaClump=2.0*((totalbolas)^(1.0/3.0))*promradiobola          ;
        AlturaHClump(idcl)=AlturaClump
        aio2=AzarNum*AlturaClump ;
        a02(idcl)=aio2                          ;
end_if  ;

        IntactoClump(idcl)=10                   ;
end
```

A6.4.3. Function Distribucion_Probable

```
; Probabilistic distribution of crack length
; Parameters have been introduced in the Function setupDefectoIn

def Distribucion_Probable

        w_Uniforme=urand

if Dist_inv<2

        if w_Uniforme>w_Max
                w_Uniforme=w_Max
        end_if

        Y_Dist=((-Beta_Weibull)*(ln(1-w_Uniforme)))^(1/alfa_Weibull)
        YMAX_Dist=((-Beta_Weibull)*(ln(1-w_Max)))^(1/alfa_Weibull)

        if Dist_inv=0 ;;;; (Caso 3.1; 3.2; o 3.3)
                AzarNum=0.001+(0.499/(YMAX_Dist))*Y_Dist;
        else  ;
                AzarNum=0.5-(0.499/(YMAX_Dist))*Y_Dist;
        end_if
else  ;
        AzarNum=0.001+0.499*w_Uniforme ;
end_if

end
```

A6.4.4. Function salidaDefectoInicial_test

```
; Generation of files with information about the defects

def salidaDefectoInicial_test

  status = open('Ms_w_Uniforme_inicio.dat', IO_WRITE, IO_ASCII)
  status = write(s_w_Uniforme_inicio,Totalddd_Inicio)
  status = close

  status = open('s_Y_Dist_inicio.dat', IO_WRITE, IO_ASCII)
  status = write(s_Y_Dist_inicio,Totalddd_Inicio)
  status = close

  status = open('s_AzarNum_inicio.dat', IO_WRITE, IO_ASCII)
  status = write(s_AzarNum_inicio,Totalddd_Inicio)
  status = close

  status = open('s_aio2_inicio.dat', IO_WRITE, IO_ASCII)
  status = write(s_aio2_inicio,Totalddd_Inicio)
  status = close
```

```
  status = open('s_AlturaHClump_Inicio.dat', IO_WRITE, IO_ASCII)
  status = write(s_AlturaHClump_Inicio,Totalddd_Inicio)
  status = close

  status = open('s_id_clumpInicio.dat', IO_WRITE, IO_ASCII)
  status = write(s_id_clumpInicio,Totalddd_Inicio)
  status = close

  status = open('s_num_clumpInicio.dat', IO_WRITE, IO_ASCII)
  status = write(s_num_clumpInicio,Totalddd_Inicio)
  status = close

end
```

A6.5. Particle breakage

A6.5.1. Failure criteria

A6.5.1.1. Function RompimientoMaestro

```
def RompimientoMaestro
        Rompeclump  ;           Call Function
        RompeTiempo ;           Call Function
end
```

A6.5.1.2. Function Rompeclump

```
def Rompeclump

ContadorGranDivision=0

If Cont_Carga=1
        exit  ;
end_if

MACROTIEMPO=MACROTIEMPO+tr
MACROTIEMPO_I=MACROTIEMPO_I+1.
MACROTIEMPO_F=MACROTIEMPO_F+tr
;
controltime= time

IndicadorNumClumpS3Neg=0 ;
EliminaClumpM   ;               Call Function
totalclump=0
totalbolas=0
promradiobola=0.0
VolClumpInicioM=0.0
NumClumpsOriginal=0 ;
ContadorUnaBola=0.0 ;;;

section  ; SECCION 1
        cl= clump_head   ; pointer de lista de clumps
        GGG=1; numeracion de clump
        VolumenTotalClumpMuestra=0.
        TipoRango1=0.
        TipoRango2=0.
        TipoRango3=0.
        TipoRango4=0.
        TipoRango5=0.
        TipoRango6=0.
```

```
TipoRango7=0.
TipoRango8=0.
TipoRango9=0.
TipoRango10=0.
VolumenRango1=0.
VolumenRango2=0.
VolumenRango3=0.
VolumenRango4=0.
VolumenRango5=0.
VolumenRango6=0.
VolumenRango7=0.
VolumenRango8=0.
VolumenRango9=0.
VolumenRango10=0.

loop while cl # null
        idcl=cl_id(cl)       ;
        totalclump=GGG
        VolClM=cl_vol(cl);
        VolClumpInicioM=VolClumpInicioM+VolClM ;
        SUMradiobola=0.0 ;
        radiobola=0.0    ;
        bcl=cl_list(cl)      ;
        j=1 ;

        loop while bcl # null
                idbcl=b_id(bcl)     ;
                radiobola=b_rad(bcl) ;
                totalbolas=j
                SUMradiobola=(SUMradiobola+radiobola) ;
                j=j+1
                bcl=b_cllist(bcl)   ; Siguiente bola de la lista del clump "cl"
        end_loop;

        If totalbolas >0  ;
                promradiobola=(SUMradiobola)/totalbolas ;
        end_if

VolumenClump=((4* pi *(promradiobola)^3 )/ 3)*totalbolas  ;
VolumenTotalClumpMuestra=VolumenTotalClumpMuestra+VolumenClump

        GRANULOMETRIA ;                 Call Function

        AsignaColorClump  ;             Call Function

        If totalbolas = 14 ;
        PorcpromradiobolaInicio=promradiobolaInicio*0.005
        liminfpromradiobolaInicio=promradiobolaInicio-PorcpromradiobolaInicio

                If promradiobola >= liminfpromradiobolaInicio
                        NumClumpsOriginal=NumClumpsOriginal+1
                end_if
        end_if
        GGG=GGG+1

        cl=cl_next(cl)      ;
```

```
        end_loop ;

        POROSIDADInicial ;              Call Function

end_section

RevisaClumps_FINOS ;            Call Function

cl= clump_head   ; pointer de lista de clumps

ccc=1; numeracion de clump
maxDesviador=0.;
maxSig1Rotura=0.                ;
numclumpdividido=0.     ;
maxSig1=0.              ;
maxSIGMATETA=0.                 ;
MINSig3=10000000000.    ;
IndicadorNumClumpS3Neg_2=0 ;

loop while cl # null
        idcl=cl_id(cl)      ;
        id_clump(ccc)=idcl      ;
        num_clump(ccc)=ccc      ;

        if ccc>totalclump

                exit        ;
        end_if

        Xcentroclump= cl_x( cl )
        Ycentroclump= cl_y( cl )
        Zcentroclump= cl_z( cl )

        Xmenorbola= Xcentroclump
        Xmayorbola= Xcentroclump
        Ymenorbola= Ycentroclump
        Ymayorbola= Ycentroclump
        Zmenorbola= Zcentroclump
        Zmayorbola= Zcentroclump

        Xcentroclump_cl(idcl)=Xcentroclump
        Ycentroclump_cl(idcl)=Ycentroclump
        Zcentroclump_cl(idcl)=Zcentroclump

        section
                SUMradiobola=0.0 ;
                totalbolas=0 ;
                radiobola=0.0
                promradiobola=0.0
                MaxfuerzanormalContacto=0.0      ;

                bcl=cl_list(cl)      ;
                j=1 ; numeración de bolas dentro de clump

                loop while bcl # null
                        idbcl=b_id(bcl)    ;
                        radiobola=b_rad(bcl) ;
```

```
                totalbolas=j
                SUMradiobola=(SUMradiobola+radiobola) ;

                cpbcl=b_clist(bcl) ;
                ab=1 ;

                loop while cpbcl # null
                        cpbola1=c_ball1(cpbcl)
                        cpbola2=c_ball2(cpbcl)
                        fuerzanormalContacto=c_nforce(cpbcl)
                if abs(fuerzanormalContacto)>MaxfuerzanormalContacto
                        MaxfuerzanormalContacto=fuerzanormalContacto ;
                        IDBolaMaxContactoNormal=idbcl ;
                        radiobolaMaxContactoNormal=radiobola ;
                end_if

                        if c_ball1(cpbcl)=bcl then
                                cpbcl=c_b1clist(cpbcl)
                        else
                                cpbcl=c_b2clist(cpbcl)
                        end_if

                        ab=ab+1
                end_loop;

                        j=j+1
                        bcl=b_cllist(bcl)   ;
        end_loop;

        IF totalbolas > 0
                promradiobola=(SUMradiobola)/totalbolas ;

        END_IF

end_section

section
        If totalbolas <= 1  ;
                exit section  ;
        end_if


        DefectoTiempo ;             Call Function


        ;;;;;;;;;   Calculation of SIGMATETA  ;;;;;;;;;;;;;;;;;;;;;;;;;;;;;;;;

        Senotetaareacargada=sin(tetaCarga)
        Fnmax=abs(MaxfuerzanormalContacto)
        AlturaClump=AlturaHClump(idcl)
        radioClump=AlturaClump/2
        cargaP=(Fnmax)/(PI * radioClump^2 * (Senotetaareacargada)^2)
        wcarga=radioClump*tan(tetaCarga)
        zcarga=radioClump*(1-0.8075)        ;
        SIGMATETA=(0.5+poisson-
((1+poisson)/((1+(wcarga/zcarga)^2)^(0.5)))+(1/(2*((1+(wcarga/zcarga)^2)^(1.5)))))*cargaP
        MaxfuerzanormalContactoV(idcl)=MaxfuerzanormalContacto
```

```
SIGMATETAV(idcl)=SIGMATETA

;Calculation of the highest value of the tensile stress of SIGMATETA
if abs(SIGMATETAV(idcl))>maxSIGMATETA
    maxSIGMATETA=SIGMATETAV(idcl)
    maxSIGMATETAccc=ccc
    maxidclumpSIGMATETA=idcl
end_if

TensorTensiones= cl_stress (cl,tensionesClump)

sigma11=tensionesClump(1,1)
sigma12=tensionesClump(1,2)
sigma13=tensionesClump(1,3)
sigma21=tensionesClump(2,1)
sigma22=tensionesClump(2,2)
sigma23=tensionesClump(2,3)
sigma31=tensionesClump(3,1)
sigma32=tensionesClump(3,2)
sigma33=tensionesClump(3,3)

sigma12_prom=(sigma12+sigma21)/2
sigma13_prom=(sigma13+sigma31)/2
sigma23_prom=(sigma23+sigma32)/2

if ccc=50
    sigma11_Clump1=tensionesClump(1,1)
    sigma12_Clump1=tensionesClump(1,2)
    sigma13_Clump1=tensionesClump(1,3)
    sigma21_Clump1=tensionesClump(2,1)
    sigma22_Clump1=tensionesClump(2,2)
    sigma23_Clump1=tensionesClump(2,3)
    sigma31_Clump1=tensionesClump(3,1)
    sigma32_Clump1=tensionesClump(3,2)
    sigma33_Clump1=tensionesClump(3,3)

    sigma12_prom_Clump1=(sigma12+sigma21)/2
    sigma13_prom_Clump1=(sigma13+sigma31)/2
    sigma23_prom_Clump1=(sigma23+sigma32)/2

    Xcentroclump_50=Xcentroclump
    Ycentroclump_50=Ycentroclump
    Zcentroclump_50=Zcentroclump
END_iF

; Calculation of principal stresses

I1=sigma11+sigma22+sigma33
I2=(sigma11*sigma22+sigma22*sigma33+sigma33*sigma11)-((sigma12_prom)^2+(sigma13_prom)^2+(sigma23_prom)^2)
I3=sigma11*sigma22*sigma33+2*sigma12_prom*sigma13_prom*sigma23_prom-sigma11*(sigma23_prom)^2-sigma22*(sigma13_prom)^2-sigma33*(sigma12_prom)^2
Ppromedio=I1/3
I1_Cuadrado=(I1)^2
I2_por3=3*(I2)
```

```
                if I1_Cuadrado <= I2_por3
                        exit ;
                end_if

                QQ=((I1)^2-3*(I2))^3
                Q_modificado=2*(SQRT(abs(QQ)))
                R_modificado=(2*(I1)^3-9*I1*I2+27*I3)
                R_mod_cuadrado=(R_modificado)^2
                Q_mod_cuadrado=(Q_modificado)^2

                if R_mod_cuadrado >= Q_mod_cuadrado
                        exit ; Sale de la función
                end_if

                COEFIC_A=(R_modificado/Q_modificado)
                COEFIC_B=sqrt(abs((1./((COEFIC_A)^2))-1))
                TETA=atan(COEFIC_B)
                if COEFIC_A<0
                        TETA=(TETA*(-1.0))+PI
                end_if

                TETA3=TETA/3
                TETAMAS=(TETA+2*pi)/3
                TETAMENOS=(TETA-2*pi)/3

SIGMA_PRINCIPAL1=((I1)/3.)+(2.0/3.)*(SQRT(ABS((I1)^2-3.*(I2))))*cos(TETA3)
SIGMA_PRINCIPAL2=((I1)/3)+(2.0/3.)*(SQRT(ABS((I1)^2-3.*(I2))))*cos(TETAMAS)       ;
SIGMA_PRINCIPAL3=((I1)/3)+(2.0/3.)*(SQRT(ABS((I1)^2-3.*(I2))))*cos(TETAMENOS)   ;

; PFC considers that tensile stresses are positive; and compression stresses are negative

                SIGMA_PRINCIPAL1=-SIGMA_PRINCIPAL1
                SIGMA_PRINCIPAL2=-SIGMA_PRINCIPAL2
                SIGMA_PRINCIPAL3=-SIGMA_PRINCIPAL3

                if SIGMA_PRINCIPAL1>=SIGMA_PRINCIPAL2
                        if SIGMA_PRINCIPAL1>=SIGMA_PRINCIPAL3
                                SIGMA1=SIGMA_PRINCIPAL1
                                IF SIGMA_PRINCIPAL2>=SIGMA_PRINCIPAL3
                                        SIGMA2=SIGMA_PRINCIPAL2
                                        SIGMA3=SIGMA_PRINCIPAL3
                                else
                                        SIGMA2=SIGMA_PRINCIPAL3
                                        SIGMA3=SIGMA_PRINCIPAL2
                                end_if
                        else
                                SIGMA1=SIGMA_PRINCIPAL3
                                SIGMA2=SIGMA_PRINCIPAL1
                                SIGMA3=SIGMA_PRINCIPAL2
                        end_if
                else
                        if SIGMA_PRINCIPAL2>=SIGMA_PRINCIPAL3
                                SIGMA1=SIGMA_PRINCIPAL2
                                if SIGMA_PRINCIPAL1>=SIGMA_PRINCIPAL3
                                        SIGMA2=SIGMA_PRINCIPAL1
                                        SIGMA3=SIGMA_PRINCIPAL3
                                else
```

```
                        SIGMA2=SIGMA_PRINCIPAL3
                        SIGMA3=SIGMA_PRINCIPAL1
                end_if
        else
                SIGMA1=SIGMA_PRINCIPAL3
                SIGMA2=SIGMA_PRINCIPAL2
                SIGMA3=SIGMA_PRINCIPAL1
        end_if
end_if

; Failure criterion of Mohr Coulomb

angulofi=angulofiGrados*PI/180.  ;
Kp=(1.+sin(angulofi))/(1.-sin(angulofi));
SIGMA1_ROTURA=SIGMA3*Kp+2.0*cohesion*sqrt(ABS(Kp))

V_SIGMA1(idcl)= SIGMA1                          ;
V_SIGMA3(idcl)= SIGMA3                          ;
Ppromedio_Array(idcl)=Ppromedio
V_SIGMA1_ROTURA(idcl)=SIGMA1_ROTURA     ;
V_Desviador(idcl)=V_SIGMA1(idcl)-V_SIGMA3(idcl) ;
V_SIGMA_PRINCIPAL1(idcl)=SIGMA_PRINCIPAL1
V_SIGMA_PRINCIPAL2(idcl)=SIGMA_PRINCIPAL2
V_SIGMA_PRINCIPAL3(idcl)=SIGMA_PRINCIPAL3
V_SIGMA_PRINCIPAL1(idcl)=V_SIGMA1(idcl);
V_SIGMA_PRINCIPAL3(idcl)=V_SIGMA3(idcl);.

        if V_Desviador(idcl)>maxDesviador
                maxDesviador=V_Desviador(idcl)
                maxDESVccc=ccc
                maxidclumpDESV=idcl
        end_if

        if V_SIGMA1_ROTURA(idcl)>maxSig1Rotura
                maxSig1Rotura=V_SIGMA1_ROTURA(idcl)
                maxRoturaccc=ccc
                maxidclumpRotura=idcl
        end_if

        if V_SIGMA1(idcl)>maxSig1
                maxSig1=V_SIGMA1(idcl)
                maxSig1ccc=ccc
                maxidclumpSig1=idcl
        end_if

        if V_SIGMA3(idcl)<MINSig3
                MINSig3=V_SIGMA3(idcl)
                MINSig3ccc=ccc
                MINidclumpSig3=idcl
        end_if

; Failure Criteria

If IndicadorRompe=10.0 ;
        sigmai_inicial2=abs(SIGMATETA)
        TiempoRotura  ;
END_IF ;
```

```
                If IndicadorRompe=20.0 ;
                        if  SIGMA3 < 0.0  ;
                                sigmai_inicial2=abs(SIGMA3)
                                TiempoRotura ;              Call Function
                        end_if   ;
                end_if ;


                If IndicadorRompe=30.0 ; MOHR COULOMB

                        if  SIGMA1 >= SIGMA1_ROTURA  ;

                                GranDivision      ;                    Call Function
                                NumClumpDivididos=NumClumpDivididos+1          ;

                                command
                                        clump add range group Otroclump_group
                                        group delete Otroclump_group
                                        print ccc
                                        print controltime
                                end_command

                        end_if  ;

                end_if ;

                if  SIGMA3 < 0.0  ; Tensile stress: sigma 3

                        IndicadorNumClumpS3Neg=IndicadorNumClumpS3Neg+1
        IndicadorNumClumpS3Neg_2=IndicadorNumClumpS3Neg_2+1 ;
        IndicadorNumClumpS3Neg_3=IndicadorNumClumpS3Neg_3+1 ;

                end_if ; Final de if y else de ( SIGMA3 < 0 )

        end_section  ;

        ccc=ccc+1 ; Numeracion de clumps dentro del loop

        cl=cl_next(cl)      ;
end_loop ;

end
```

A6.5.1.3. Function RompeTiempo

```
; Execution after Function Rompeclump: variables

def RompeTiempo

abcdefg=1

If Cont_Carga=1
        exit  ;
end_if

SIGMA1_1000=V_SIGMA1(50)                        ;
SIGMA3_1000=V_SIGMA3(50)                        ;
SIG1_ROTURA_1000=V_SIGMA1_ROTURA(50)    ;
Ppromedio_Array_1000=Ppromedio_Array(50)
V_IdClump1000=id_clump(50)
MaxfuerzanormalContacto_1000=MaxfuerzanormalContactoV(50)
SIGMATETA_1000=SIGMATETAV(50)

SIGMA1_MAXDESV=V_SIGMA1(maxidclumpDESV)
SIGMA3_MAXDESV=V_SIGMA3(maxidclumpDESV)
SIGMA1_ROTURA_MAXDESV=V_SIGMA1_ROTURA(maxidclumpDESV)
MaxfuerzanormalContacto_MAXDESV=MaxfuerzanormalContactoV(maxidclumpDESV)
SIGMATETA_MAXDESV=SIGMATETAV(maxidclumpDESV)

SIGMA1_MAXROTURA=V_SIGMA1(maxidclumpRotura)
SIGMA3_MAXROTURA=V_SIGMA3(maxidclumpRotura)
SIGMA1_ROTURA_MAXROTURA=V_SIGMA1_ROTURA(maxidclumpRotura)
Ppromedio_Array_MAXROTURA=Ppromedio_Array(maxidclumpRotura)
MaxfuerzanormalContacto_MAXROTURA=MaxfuerzanormalContactoV(maxidclumpRotura)
SIGMATETA_MAXROTURA=SIGMATETAV(maxidclumpRotura)

Xcentroclump_maxRotura=Xcentroclump_cl(maxidclumpRotura)
Ycentroclump_maxRotura=Ycentroclump_cl(maxidclumpRotura)
Zcentroclump_maxRotura=Zcentroclump_cl(maxidclumpRotura)

V_SIGMA_PRINCIPAL1_1000=V_SIGMA_PRINCIPAL1(50)
V_SIGMA_PRINCIPAL2_1000=V_SIGMA_PRINCIPAL2(50)
V_SIGMA_PRINCIPAL3_1000=V_SIGMA_PRINCIPAL3(50)

V_SIGMA_PRINCIPAL1_MaxRotura=V_SIGMA_PRINCIPAL1(maxidclumpRotura)
V_SIGMA_PRINCIPAL2_MaxRotura=V_SIGMA_PRINCIPAL2(maxidclumpRotura)
V_SIGMA_PRINCIPAL3_MaxRotura=V_SIGMA_PRINCIPAL3(maxidclumpRotura)

SIGMA1_MAXSIG1=V_SIGMA1(maxidclumpSig1)                 ;
SIGMA3_MAXSIG1=V_SIGMA3(maxidclumpSig1)                 ;
SIG1_ROTURA_MAXSIG1=V_SIGMA1_ROTURA(maxidclumpSig1)     ;
Ppromedio_Array_MAXSIG1=Ppromedio_Array(maxidclumpSig1)
V_IdClumpMAXSIG1=id_clump(maxidclumpSig1)
MaxfuerzanormalContacto_MAXSIG1=MaxfuerzanormalContactoV(maxidclumpSig1)
SIGMATETA_MAXSIG1=SIGMATETAV(maxidclumpSig1)

SIGMA1_MINSIG3=V_SIGMA1(MINidclumpSig3)                 ;
SIGMA3_MINSIG3=V_SIGMA3(MINidclumpSig3)                 ;
```

```
MaxfuerzanormalContacto_MINSIG3=MaxfuerzanormalContactoV(MINidclumpSig3)
SIGMATETA_MINSIG3=SIGMATETAV(MINidclumpSig3)

SIGMA1_maxTETA=V_SIGMA1(maxidclumpSIGMATETA)
SIGMA3_maxTETA=V_SIGMA3(maxidclumpSIGMATETA)
MaxfuerzanormalContacto_maxTETA=MaxfuerzanormalContactoV(maxidclumpSIGMATET
A)
SIGMATETA_maxTETA=SIGMATETAV(maxidclumpSIGMATETA)

K02_MAXSIG1=K02(maxidclumpSig1)                         ;
K01_MAXSIG1=K01(maxidclumpSig1)                         ;
BETAT2_MAXSIG1=BETAT2(maxidclumpSig1)                           ;
BETAT1_MAXSIG1=BETAT1(maxidclumpSig1)                           ;
a02_MAXSIG1=a02(maxidclumpSig1)                         ;
a01_MAXSIG1=a01(maxidclumpSig1)                         ;
TR1_MAXSIG1=TiempoRotura1(maxidclumpSig1)                       ;
TR2_MAXSIG1=TiempoRotura2(maxidclumpSig1)                       ;

K02_MAXDESV=K02(maxidclumpDESV)                         ;
K01_MAXDESV=K01(maxidclumpDESV)                         ;
BETAT2_MAXDESV=BETAT2(maxidclumpDESV)                           ;
BETAT1_MAXDESV=BETAT1(maxidclumpDESV)                           ;
a02_MAXDESV=a02(maxidclumpDESV)                         ;
a01_MAXDESV=a01(maxidclumpDESV)                         ;
TR1_MAXDESV=TiempoRotura1(maxidclumpDESV)               ;
TR2_MAXDESV=TiempoRotura2(maxidclumpDESV)               ;

K02_MAXROTURA=K02(maxidclumpRotura)                             ;
K01_MAXROTURA=K01(maxidclumpRotura)                             ;
BETAT2_MAXROTURA=BETAT2(maxidclumpRotura)                               ;
BETAT1_MAXROTURA=BETAT1(maxidclumpRotura)                               ;
a02_MAXROTURA=a02(maxidclumpRotura)                             ;
a01_MAXROTURA=a01(maxidclumpRotura)                             ;
TR1_MAXROTURA=TiempoRotura1(maxidclumpRotura)                           ;
TR2_MAXROTURA=TiempoRotura2(maxidclumpRotura)                           ;

K02_50=K02(50)                  ;
K01_50=K01(50)                  ;
BETAT2_50=BETAT2(50)            ;
BETAT1_50=BETAT1(50)            ;
a02_50=a02(50)                  ;
a01_50=a01(50)                  ;
TR1_50=TiempoRotura1(50)        ;
TR2_50=TiempoRotura2(50)        ;

K02_MINSIG3=K02(MINidclumpSig3)                 ;
K01_MINSIG3=K01(MINidclumpSig3)                 ;
BETAT2_MINSIG3=BETAT2(MINidclumpSig3)           ;
BETAT1_MINSIG3=BETAT1(MINidclumpSig3)           ;
a02_MINSIG3=a02(MINidclumpSig3)                 ;
a01_MINSIG3=a01(MINidclumpSig3)                 ;
TR1_MINSIG3=TiempoRotura1(MINidclumpSig3)       ;
TR2_MINSIG3=TiempoRotura2(MINidclumpSig3)       ;

K02_maxTETA=K02(maxidclumpSIGMATETA)                    ;
K01_maxTETA=K01(maxidclumpSIGMATETA)                    ;
BETAT2_maxTETA=BETAT2(maxidclumpSIGMATETA)              ;
```

```
BETAT1_maxTETA=BETAT1(maxidclumpSIGMATETA)                ;
a02_maxTETA=a02(maxidclumpSIGMATETA)                      ;
a01_maxTETA=a01(maxidclumpSIGMATETA)                      ;
TR1_maxTETA=TiempoRotura1(maxidclumpSIGMATETA)            ;
TR2_maxTETA=TiempoRotura2(maxidclumpSIGMATETA)            ;

TotalClumpsOriginal=NumClumpsOriginal

end
```

A6.5.1.4. Function VelocidadCeroBolas

```
def VelocidadCeroBolas

if ContadorGranDivision=1 ; Breakage has occurred
        command
        ini xvel 0.0 yvel 0.0 zvel 0.0 xspin 0.0 yspin 0.0 zspin 0.0
        clump property xvelocity=0.0 yvelocity=0.0 zvelocity=0.0 xspin=0.0 yspin=0.0
zspin=0.0
        end_command

NumCiclosSeparacion=NumCiclosSeparacion+1 ;

end_if

end
```

A6.5.1.5. Function EliminaClumpM

```
; Verification of clumps inside the sample

def EliminaClumpM

contador1M=contador1M+1
if contador1M > RC_CLM  ;
        contador1M=0
          wadd1_1M = find_wall(1)
          wadd5_5M = find_wall(5)
          wadd6_6M = find_wall(7)
         new_radM = w_radend1(wadd1_1M) ;
          rdifM  = new_radM - rad_cy          ;
          zdifM  = w_z(wadd6_6M) - w_z(wadd5_5M)  ;
          new_heightM = height + zdifM          ;
        cl= clump_head   ; pointer de lista de clumps

        loop while cl # null
                idcl=cl_id( cl )
                next=cl_next(cl)
                Pos_x = cl_x( cl ) ;
                Pos_y = cl_y( cl ) ;
                Pos_z = cl_z( cl ) ;
                Dist_xy = sqrt(((abs(Pos_x))^2 + (abs(Pos_y))^2))
                Permitido_xy  =new_radM
                Permitido_z1  =height + zdifM/2.0 ;
                Permitido_z2  =0.0 - zdifM/2.0        ;
```

```
                If abs(Dist_xy) > Permitido_xy
                command
                        delete clump range id=idcl
                        EliminadoCL=EliminadoCL+1       ;
                end_command
                else
                If (Pos_z) < Permitido_z2
                        command
                                delete clump range id=idcl
                                EliminadoCL=EliminadoCL+1       ;
                        end_command
                else
                        If (Pos_z) > Permitido_z1
                                command
                                        delete clump range id=idcl
                                        EliminadoCL=EliminadoCL+1       ;
                                end_command
                        end_if
                end_if
                end_if
                cl=next
        end_loop ;
end_if

EliminadoCL_M=EliminadoCL

end
```

A6.5.1.6. Function GRANULOMETRIA

```
def GRANULOMETRIA

        If VolumenClump<Limite1
                TipoRango1=TipoRango1+1
                VolumenRango1=VolumenRango1+VolumenClump
        Else
                If VolumenClump<Limite2
                        TipoRango2=TipoRango2+1
                        VolumenRango2=VolumenRango2+VolumenClump
                Else
                        If VolumenClump<Limite3
                                TipoRango3=TipoRango3+1
                                VolumenRango3=VolumenRango3+VolumenClump
                        Else
                                If VolumenClump<Limite4
                                        TipoRango4=TipoRango4+1

        VolumenRango4=VolumenRango4+VolumenClump
                                Else
                                        If VolumenClump<Limite5
                                                TipoRango5=TipoRango5+1

        VolumenRango5=VolumenRango5+VolumenClump
                                        Else
                                                If VolumenClump<Limite6
```

```
                                                    TipoRango6=TipoRango6+1

        VolumenRango6=VolumenRango6+VolumenClump
                                                Else
                                                    If VolumenClump<Limite7

        TipoRango7=TipoRango7+1

        VolumenRango7=VolumenRango7+VolumenClump
                                                    Else
                                                    If VolumenClump<Limite8

        TipoRango8=TipoRango8+1

        VolumenRango8=VolumenRango8+VolumenClump
                                                        Else
                                                    If VolumenClump<Limite9

        TipoRango9=TipoRango9+1

        VolumenRango9=VolumenRango9+VolumenClump
                                                            Else

        TipoRango10=TipoRango10+1

        VolumenRango10=VolumenRango10+VolumenClump
                                                            End_if
                                                        End_if
                                                    End_if
                                                End_if
                                            End_if
                                        End_if
                                    End_if
                                End_if
                            End_if
                        End_if
                    End_if
                End_if
        End_if

end
```

A6.5.1.7. Function AsignaColorClump

```
; Assignment of colors according to the number of microparticles

Def AsignaColorClump
        If totalbolas = NBOLASCLUMPTIPO2   ;
                cl_color(cl)=15
        Else
                If totalbolas = NBOLASCLUMPTIPO1   ;
                        cl_color(cl)=0
                Else
                        If totalbolas = 13   ;
                                cl_color(cl)=1
                        Else
                                If totalbolas = 12   ;;
                                        cl_color(cl)=2
                                Else
                                        If totalbolas = 11   ;
```

```
                                        cl_color(cl)=3
                                Else
                                        If totalbolas = 10   ;
                                                cl_color(cl)=4
                                        Else
                                                If totalbolas = 9   ;
                                                        cl_color(cl)=5
                                                Else
                                                        If totalbolas = 8   ;
                                                        cl_color(cl)=6
                                                        Else
                                                        If totalbolas = 7
                                                        cl_color(cl)=7
Else
If totalbolas = 6   ;
        cl_color(cl)=8
        Else
                If totalbolas = 5   ;
                cl_color(cl)=9
                Else
                If totalbolas = 4   ;
                        cl_color(cl)=10
                Else
                        If totalbolas = 3   ;
                                cl_color(cl)=11
                        Else
                                If totalbolas = 2   ;
                                        cl_color(cl)=12
                                Else
                                        If totalbolas = 1
                                                cl_color(cl)=13
                                        end_If;
                                end_If;
                        end_If;
                end_If;
        end_If;
        end_If;
        end_if;
                                                                end_If;
                                                        end_If;
                                                end_If;
                                        end_If;
                                end_If;
                        end_If;
                end_If;
        end_If ;

end
```

A6.5.1.8. Function POROSIDADInicial

```
def POROSIDADInicial ;

  wadd1_i = find_wall(1)
  wadd5_i = find_wall(5)
  wadd6_i = find_wall(7)
```

```
 new_rad = w_radend1(wadd1_i) ;
 rdif  = new_rad - rad_cy         ;
 zdif  = w_z(wadd6_i) - w_z(wadd5_i)  ;
 new_height = height + zdif          ;

New_vOL=(new_height * pi * (new_rad)^2.0)
Vol_Clump=1000*((4* pi *(rlo30)^3 )/ 3)  ;
PorosidadIC=(New_vOL-VolumenTotalClumpMuestra)/New_vOL;
PorosidadIB=(New_vOL-Vol_Bolas)/New_vOL;
Porosidad_iM=(New_vOL-VolClumpInicioM)/New_vOL ;
e_RelacionVacios_iM=(New_vOL-VolClumpInicioM)/VolClumpInicioM ;

end
```

A6.5.1.9. Function RevisaClumps_FINOS

```
; Replacement of Clumps of 1P by Clumps of 13P
; Criterion of Mass conservation: Addition of subparticles of 1P

def RevisaClumps_FINOS

        totalbolas=0
        promradiobola=0.0
        ContadorUnaBola=0.0 ;
        cl= clump_head   ; pointer de lista de clumps
        TGGG=1; numeracion de clump
        section
                loop while cl # null
                        idcl=cl_id(cl)       ;
                        if TGGG>totalclump
                                exit section         ;
                        end_if
                        Xcentroclump_b1p= cl_x( cl )
                        Ycentroclump_b1p= cl_y( cl )
                        Zcentroclump_b1p= cl_z( cl )
                        SUMradiobola=0.0 ;
                        radiobola=0.0    ;
                        bcl=cl_list(cl)      ;
                        j=1 ;
                        loop while bcl # null
                                idbcl=b_id(bcl)     ;
                                radiobola=b_rad(bcl) ;
                                totalbolas=j
                                SUMradiobola=(SUMradiobola+radiobola) ;
                                j=j+1
                                bcl=b_cllist(bcl)    ;
                        end_loop;
                        If totalbolas >0  ;
                                promradiobola=(SUMradiobola)/totalbolas ;
                        end_if
                        If totalbolas = 1    ;
                                If IndiCriterioDivision=50.0 ;
                                        LIBERABOLA1P;            Call Function
                                END_IF  ;
                                If IndiCriterioDivision=60.0 ;
                                        LIBERABOLA1P;            Call Function
```

```
                                END_IF  ;
                                If IndiCriterioDivision=70.0 ;
                                        LIBERABOLA1P;           Call Function
                                END_IF  ;
                                If IndiCriterioDivision=90.0 ;
                                        LIBERABOLA1P;           Call Function
                                END_IF  ;
                                If IndiCriterioDivision=100.0 ;
                                        LIBERABOLA1P;           Call Function
                                END_IF  ;
                        end_if ;
                        TGGG=TGGG+1
                        cl=cl_next(cl)      ;
                end_loop ;
        end_section
        HACECLUMP1P   ;                 Call Function
        NumClumpInicio=totalclump
        NumClumpInicioVerdad=NumClumpInicio-NumClumps1P  ;
        if ContadorGranDivision=1
                exit  ;
        end_if
        ContLiberabola1P=0

end
```

A6.5.1.10. Function TiempoRotura

```
; Time effect

def TiempoRotura

IndicadorMICROROTURAPROGRESIVA=0
IndicadorMACROROTURAPROGRESIVA=0

If deax <= DeformaxialSaturacion
        Kc2= Kc2f
        Kc1= Kc1f
end_if

FIJOSTIEMPOROTURA;          Call Function
PreAnalisisTiempoRoturaMACRO;           Call Function

If aio2 >= MitadAlturaHClump        ;
        GranDivision      ;         Call Function
                NumClumpDivididos=NumClumpDivididos+1           ;
                command
                        clump add range group Otroclump_group
                        group delete Otroclump_group
                        print controltime
                end_command
        TiempoRotura2(idcl)= 0. ;
Else
        If Kio2 >= Kc2 ;
                GranDivision      ;                     Call Function
                NumClumpDivididos=NumClumpDivididos+1           ;
                TiempoRotura2(idcl)= 0. ;
```

```
                command
                        clump add range group Otroclump_group
                        group delete Otroclump_group
                        print ccc
                        print controltime
                end_command
        Else    ;
                IF tib2 <= tr;
                        GranDivision    ;               Call Function
                        NumClumpDivididos=NumClumpDivididos+1           ;
                numclumpDividoTiempoM=numclumpDividoTiempoM+1 ;
                numclumpDividoTiempoM2=numclumpDividoTiempoM2+1 ;
                TiempoRotura2(idcl)= 0. ;
                 command
                  clump add range group Otroclump_group
                  group delete Otroclump_group
                  print controltime
                 end_command

                Else
                        IndicadorMACROROTURAPROGRESIVA=20
                        ROTURAPROGRESIVA;               Call Function
                End_if  ;
        End_if;
end_if;

end
```

A6.5.1.11. Function FIJOSTIEMPOROTURA

```
; Calculation of variables for each load increment

def FIJOSTIEMPOROTURA
                Ko1=0.3*Kc1
                Ko2=0.3*Kc2
end
```

A6.5.1.12. Function PreAnalisisTiempoRoturaMACRO

```
; Time effect in macroparticles

def PreAnalisisTiempoRoturaMACRO

aio2=a02(idcl)
MitadAlturaHClump= (AlturaHClump(idcl))/2.

if aio2 < MitadAlturaHClump
        alfaT2=2.*aio2/(AlturaHClump(idcl))             ;
        BBetaT2=(1./(1.-alfaT2))*(1.-0.4964*alfaT2+1.5582*alfaT2^2-
3.1818*alfaT2^3+10.0962*alfaT2^4-20.7782*alfaT2^5+20.1342*alfaT2^6-7.5067*alfaT2^7)

        BETAT2(idcl)=BBetaT2                            ;
        Kio2=abs(BBetaT2*(sqrt(abs(PI*aio2)))*sigmai_inicial2)          ;
        K02(idcl)=Kio2    ; Kio2 en el clump ccc en el tiempo
```

```
        NCHARLES_M=((100.)*(exp(-0.015*HR)));

        Voi2=VoCharles*(Kio2/Kc2)^(NCHARLES_M)
        Voi2_Vector(idcl)=Voi2

        if Voi2 # 0.0
                tib2=(2./(NCHARLES_M-2.))*aio2/Voi2        ;
        else
                tib2=0.;
        end_if;
        TiempoRotura2(idcl)=tib2                ;

end_if ;

end
```

A6.5.1.13. Function ROTURAPROGRESIVA

```
; Propagation of cracks in time

def ROTURAPROGRESIVA

deltatr=tr
IF IndicadorMACROROTURAPROGRESIVA=20
                Voi2=Voi2_Vector(idcl)
                aio2=a02(idcl)
                daio2=Voi2*deltatr ;
                aio2=aio2+daio2
                a02(idcl)=aio2
                MitadAlturaHClump= (AlturaHClump(idcl))/2.

        If aio2 >= MitadAlturaHClump        ;
                ContadorRotProg1=contadorRotProg1+1
                GranDivision       ;
                NumClumpDivididos=NumClumpDivididos+1             ;
                numclumpDividoTiempoM=numclumpDividoTiempoM+1 ;
                command
                        clump add range group Otroclump_group
                        group delete Otroclump_group
                        print ccc
                        print controltime
                end_command
                TiempoRotura2(idcl)= 0. ;
        End_if ;

End_if ;

end
```

A6.5.1.14. Function LIBERABOLA1P

```
; Releasing of ball of cump of 1P (from the original clump of 14P)

Def  LIBERABOLA1P
```

```
        If totalbolas = 1   ;
                Porcpromradiobolalnicio=promradiobolalnicio*0.005
                liminfpromradiobolalnicio=promradiobolalnicio-Porcpromradiobolalnicio
                If promradiobola >= liminfpromradiobolalnicio
                        ContadorUnaBola=1.0 ;
                        NumClumps1P=NumClumps1P+1 ;
                        ContLiberabola1P=ContLiberabola1P+1  ;
                        command
                                clump scale 0.78377822924 range id=idcl   ;
                                clump release id=idcl
                        end_command
                                If IndiCriterioDivision=100.0 ;
                                        b12345=1  ;
                                Else
                                        CREABOLAS1P_FINOS;     Call Function
                                END_IF  ;
                end_if ;
        end_if  ;
END
```

A6.5.1.15. Function HACECLUMP1P

; Creation of clumps of 13P (Subparticle)

```
Def  HACECLUMP1P
        if ContadorUnaBola=1.0
                COMMAND   ;
                        clump replace 1 nuevocl13HEXd40 1.0  ;
                END_COMMAND
                ContadorUnaBola=0.0
        end_if
        numbolanew=numbolanew+(13*ContLiberabola1P)
END
```

A6.5.1.16. Function CREABOLAS1P_FINOS

```
def CREABOLAS1P_FINOS

        ContadorGranDivision=1
        R1DR1P_14P=1.0*(2.0*R1P_14P)
        R2DR1P_14P=2.0*(2.0*R1P_14P)
        R3DR1P_14P=3.0*(2.0*R1P_14P)
        R5DR1P_14P=5.0*(2.0*R1P_14P)
        R7DR1P_14P=7.0*(2.0*R1P_14P)
        R10DR1P_14P=10.0*(2.0*R1P_14P)

        R2Final=R1DR1P_14P ;
        V1P_14P=((4.*PI)/3.)*((R1P_14P)^3)
        VRR=(1.-(13./27.))*V1P_14P
        VRG_ACUMULADO=0.0
        VRESTANTE=VRR-VRG_ACUMULADO
        RRESTANTE=((3.0/(4.0*PI))*(VRESTANTE))^(1./3.)
        nrmax=RRESTANTE
          waddn1_1 = find_wall(1)
```

```
            waddn5_5 = find_wall(5)
            waddn7_7 = find_wall(7)
            nnew_radM = w_radend1(waddn1_1) ;
            nzdifM  = w_z(waddn7_7) - w_z(waddn5_5)  ;
            nnew_heightM = height + nzdifM          ;
            nnew_Permitido_z1  =height + nzdifM/2.0 ;
            nnew_Permitido_z2  =0.0 - nzdifM/2.0        ;
            nrad_cy = nnew_radM
            _xnlo = -nnew_radM
            _xnhi = nnew_radM
            _ynlo = -nnew_radM
            _ynhi = nnew_radM
            _znlo = nnew_Permitido_z2
            _znhi = nnew_Permitido_z1

          LOOP while VRG_ACUMULADO <= 0.90*VRR ;
                    RRESTANTE=((3.0/(4.0*PI))*(VRESTANTE))^(1./3.)
                    nrmax=RRESTANTE*0.70
                    command
gen  tries=2000000  id=numbolanew,numbolanew  rad=rminimoCM,nrmax  x=(_xnlo,  _xnhi)
y=(_ynlo, _ynhi) z=(_znlo, _znhi)  &
annulus Xcentroclump_b1p Ycentroclump_b1p Zcentroclump_b1p R1P_14P R2Final  &
filter newff_cylinder_Edom

range name NuevaBola1P_Fino id=numbolanew
group NuevaBola1P_Fino_group range NuevaBola1P_Fino ;
prop dens=2760 kn=4.0e6 ks=4.0e6 fric 0.05 range group NuevaBola1P_Fino_group ;
clump add range group NuevaBola1P_Fino_group
group delete NuevaBola1P_Fino_group
                    end_command
                    VRG_I=((4.*PI)/3.)*((_nbrad)^3)
                    VRG_ACUMULADO=VRG_ACUMULADO+VRG_I
                    VRESTANTE=VRR-VRG_ACUMULADO
                    numbolanew=numbolanew+1
          END_LOOP

end
```

A6.5.1.17. Function newff_cylinder_Edom

```
def newff_cylinder_Edom

  newff_cylinder_Edom = 0
  _nbrad = fc_arg(0)
  _nbx   = fc_arg(1)
  _nby   = fc_arg(2)
  _nbz   = fc_arg(3)
  _nrad  = sqrt(_nbx^2 + _nby^2)
  if _nrad + _nbrad > 0.8*nrad_cy then
    newff_cylinder_Edom = 1
  end_if

end
```

A6.5.2. Division criteria

A6.5.2.1. Function GranDivision

```
Def GranDivision

IntactoClump(idcl)=0        ;
ContadorGranDivision=1
If IndiCriterioDivision=10.0 ;
        Division_EqualVolumen;   Call Function
end_if ;
If IndiCriterioDivision=20.0  ;
        Separa1Bola_clump
end_if ;
If IndiCriterioDivision=30.0 ;
        NumAzar=urand
        If NumAzar <= 0.50
                Separa1Bola_clump;       Call Function
        Else
                Division_EqualVolumen;   Call Function
        end_if
end_if;
If IndiCriterioDivision=50.0 ;
        Division_EqualVolumen;   Call Function
end_if ;
If IndiCriterioDivision=60.0  ;
        Separa1Bola_clump;       Call Function
end_if ;
If IndiCriterioDivision=70.0 ;
        NumAzar=urand
        If NumAzar <= 0.50
                Separa1Bola_clump;       Call Function
        Else
                Division_EqualVolumen;   Call Function
        end_if
end_if ;
If IndiCriterioDivision=90.0 ;
        NumAzar=urand
        If szzreq > ESFFLUENCIA   ;
                If NumAzar <= comminution1
                        Separa1Bola_clump;       Call Function
                Else
                        Division_EqualVolumen;   Call Function
                end_if
        Else
                If NumAzar <= comminution2
                        Separa1Bola_clump;       Call Function
                Else
                        Division_EqualVolumen;   Call Function
                end_if
        end_if  ;
end_if ;
If IndiCriterioDivision=80.0 ;
```

```
        NumAzar=urand
        If szzreq > ESFFLUENCIA   ;
                If NumAzar <= comminution1
                        Separa1Bola_clump;        Call Function
                Else
                        Division_EqualVolumen;    Call Function
                end_if
        Else
                If NumAzar <= comminution2
                        Separa1Bola_clump;        Call Function
                Else
                        Division_EqualVolumen;    Call Function
                end_if
        end_if  ;
end_if ;
If IndiCriterioDivision=100.0 ;
        NumAzar=urand
        If szzreq > ESFFLUENCIA   ;
                If NumAzar <= comminution1
                        Separa1Bola_clump;        Call Function
                Else
                        Division_EqualVolumen;    Call Function
                end_if
        Else
                If NumAzar <= comminution2
                        Separa1Bola_clump;        Call Function
                Else
                        Division_EqualVolumen;    Call Function
                end_if
        end_if  ;
end_if ;

end
```

A6.5.2.2. Function Division_EqualVolumen

```
Def Division_EqualVolumen

NumMacroClump=NumMacroClump+1;

If totalbolas = NBOLASCLUMPTIPO2   ;
  Divisionclump28P;          Call Function
  Else
  If totalbolas = NBOLASCLUMPTIPO1   ;
    Divisionclump; Call Function
    Else
    If totalbolas = 13   ;
      Divisionclump;          Call Function
      Else
      If totalbolas = 12   ;
        Divisionclump;          Call Function
        Else
            If totalbolas = 11   ;
              Divisionclump;   Call Function
              Else
              If totalbolas = 10   ;
```

```
            Division10clump;          Call Function
            Else
            If totalbolas = 9   ;
              Division8Clump;         Call Function
              Else
              If totalbolas = 8   ;
                    Division8Clump;   Call Function
                    Else
                    If totalbolas = 7   ;
                      Division8Clump;           Call Function
                      Else
                      If totalbolas = 6   ;
                        Division6Clump;         Call Function
                        Else
                        If totalbolas = 5   ;
                          Division6Clump;       Call Function
                          Else
                          If totalbolas = 4   ;
                                Division4Clump;   Call Function
                                Else
                                If totalbolas = 3   ;
                                  Division3_2Clump;         Call Function
                                  Else
                                  If totalbolas = 2   ;
                                    Division3_2Clump;       Call Function
                                  end_If;
                                end_If;
                           end_If;
                        end_If;
                    end_If;
               end_If;
            end_If;
          end_If;
        end_If;
      end_If;
    end_If;
  end_If;
end_If ;

end
```

A6.5.2.3. Function Separa1Bola_clump

```
; Releasing a microparticle with the máximum contact load; Comminution crushing

def Separa1Bola_clump

bcl=cl_list(cl)       ;
loop while bcl # null
            idbcl=b_id(bcl)     ; Identifica la bola del clump, su id
            if idbcl=IDBolaMaxContactoNormal
                        NumBolassolasseparadas=NumBolassolasseparadas+1;
                        command
                                    range name Otroclump id=idbcl
                                    group Otroclump_group range Otroclump ;
```

```
                print controltime
            end_command
                exit
        end_if ;
        bcl=b_cllist(bcl)   ;
end_loop;

end
```

A6.5.2.4. Function Divisionclump28P

```
; Division of 28P clump  in two clumps of 14P+14P
; This type of clump is still not used in the proposed DEM model

def Divisionclump28P
        idclM=cl_id(cl)     ;
        bcl=cl_list(cl)     ;
        idbcl=b_id(bcl)     ;
        s=1;
            command
                print idbcl                 ;
                print s
            end_command

        loop while bcl # null
            idbcl=b_id(bcl)     ;
            bola(s)=idbcl
                command
                    print idbcl                 ;
                    print s
                    print bola(s)
                end_command
            if s<=14
                command
                    print idbcl                 ;
                    print s
                    print bola(s)
                    range name Otroclump id=idbcl
                    group Otroclump_group range Otroclump ;
                    print group
                end_command
            end_if ;
            bcl=b_cllist(bcl)   ;
            s=s+1
                command
                    print s
                    print bola(s)
                end_command
            bola(s)=idbcl
                command
                    print bola(s)
                end_command
        end_loop;
end
```

A6.5.2.5. Function Divisionclump

```
; Division of 14P clump  in two clumps of 8P+6P
; Division of 13P clump  in two clumps of 7P+6P
; Division of 12P clump  in two clumps of 6P+6P
; Division of 11P clump  in two clumps of 5P+6P

def Divisionclump
	idclM=cl_id(cl)	;
	bcl=cl_list(cl)	;
	idbcl=b_id(bcl)	;
	s=1;
		command
			print idbcl			;
			print s
		end_command
	loop while bcl # null
		idbcl=b_id(bcl)	;
		bola(s)=idbcl
			command
				print idbcl			;
				print s
				print bola(s)
			end_command
		if s>=7
			command
				print idbcl			;
				print s
				print bola(s)
				range name Otroclump id=idbcl
				group Otroclump_group range Otroclump ;
				print group
			end_command
		end_if ;
		bcl=b_cllist(bcl)	;
		s=s+1
			command
				print s
				print bola(s)
			end_command
		bola(s)=idbcl
			command
				print bola(s)
			end_command
	end_loop;
end
```

A6.5.2.6. Function Division10Clump

```
; Division of 10P clump  in two clumps of 5P+5P

def Division10Clump
	idclM=cl_id(cl)	;
	bcl=cl_list(cl)	;
```

```
        idbcl=b_id(bcl)    ;
        s=1;
                command
                        print idbcl                     ;
                        print s
                end_command

        loop while bcl # null
                idbcl=b_id(bcl)    ;
                bola(s)=idbcl
                        command
                        print idbcl                     ;
                        print s
                        print bola(s)
                        end_command
                if s<=5
                        command
                        print idbcl                     ;
                        print s
                        print bola(s)
                        range name Otroclump id=idbcl
                        group Otroclump_group range Otroclump ;
                        print group
                        end_command
                end_if ;

                bcl=b_cllist(bcl)   ;
                s=s+1
                        command
                        print s
                        print bola(s)
                        end_command
                bola(s)=idbcl
                        command
                        print bola(s)
                        end_command
        end_loop;
end
```

A6.5.2.7. Function Division8Clump

```
; Division of 8P clump  in two clumps of 4P+4P
; Division of 9P clump  in two clumps of 5P+4P
; Division of 7P clump  in two clumps of 3P+4P

def Division8Clump
        idclM=cl_id(cl)    ;
        bcl=cl_list(cl)    ;
        idbcl=b_id(bcl)    ;
        s=1;
                command
                        print idbcl                     ;
                        print s
                end_command
        loop while bcl # null
                idbcl=b_id(bcl)    ;
```

```
                bola(s)=idbcl
                        command
                                print idbcl                     ;
                                print s
                                print bola(s)
                        end_command
                if s<=4
                        command
                                print idbcl                     ;
                                print s
                                print bola(s)
                                range name Otroclump id=idbcl
                                group Otroclump_group range Otroclump ;
                                print group
                        end_command
                end_if ;(final del if de s<=4)

                bcl=b_cllist(bcl)   ;
                s=s+1
                        command
                                print s
                                print bola(s)
                        end_command
                bola(s)=idbcl
                        command
                                print bola(s)
                        end_command
        end_loop;
end
```

A6.5.2.8. Function Division6Clump

```
; Division of 6P clump  in two clumps of 3P+3P;
; Division of 5P clump  in two clumps of 3P+2P;

def Division6Clump
        idclM=cl_id(cl)     ;
        bcl=cl_list(cl)     ;
        idbcl=b_id(bcl)     ; Identifica la bola del clump, su id
        s=1; numeracion de bolas dentro de clump
                command
                        print idbcl                     ;
                        print s
                end_command

        loop while bcl # null
                idbcl=b_id(bcl)     ;
                bola(s)=idbcl
                        command
                                print idbcl                     ;
                                print s
                                print bola(s)
                        end_command
                if s<=3
                        command
                                print idbcl                     ;
```

```
                                        print s
                                        print bola(s)
                                        range name Otroclump id=idbcl
                                        group Otroclump_group range Otroclump ;
                                        print group
                                end_command
                        end_if ;
                        bcl=b_cllist(bcl)   ;
                        s=s+1
                                command
                                        print s
                                        print bola(s)
                                end_command
                        bola(s)=idbcl
                                command
                                print bola(s)
                                end_command
        end_loop;
end
```

A6.5.2.9. Function Division4Clump

```
; Division of 4P clump  in two clumps of 2P+2P

def Division4Clump
        idclM=cl_id(cl)     ;
        bcl=cl_list(cl)     ;
        idbcl=b_id(bcl)     ;
        s=1;
                command
                        print idbcl                     ;
                        print s
                end_command

        loop while bcl # null
                idbcl=b_id(bcl)     ;
                bola(s)=idbcl
                        command
                                print idbcl                     ;
                                print s
                                print bola(s)
                        end_command
                if s<=2
                        command
                                print idbcl                     ;
                                print s
                                print bola(s)
                                range name Otroclump id=idbcl
                                group Otroclump_group range Otroclump ;
                                print group
                        end_command
                end_if ;
                bcl=b_cllist(bcl)   ;
                s=s+1
                        command
                                print s
```

```
                                print bola(s)
                        end_command
                bola(s)=idbcl
                        command
                        print bola(s)
                        end_command
        end_loop;
end
```

A6.5.2.10. Function Division3_2Clump

```
; Division of 3P clump  in two clumps of 2P+1P
; Division of 2P clump  in two clumps of 1P+1P

def Division3_2Clump
        bcl=cl_list(cl)       ;
        idbcl=b_id(bcl)     ;
        s=1;
        loop while bcl # null
                idbcl=b_id(bcl)     ;
                bola(s)=idbcl
                        command
                                print idbcl                     ;
                                print s
                                print bola(s)
                                range name Tipoclump2 id=idbcl
                                group Tipoclump2_group range Tipoclump2 ;
                        end_command
                if s=1
                        command
                                print idbcl                     ;
                                print s
                                print bola(s)
                                range name Otroclump id=idbcl
                                group Otroclump_group range Otroclump ;
                                print group
                        end_command
                end_if ;
                bcl=b_cllist(bcl)    ;
                s=s+1
                        command
                                print s
                                print bola(s)
                        end_command
                bola(s)=idbcl
                        command
                                print bola(s)
                        end_command
        end_loop;
end
```

A6.6. Measurement of properties inside the virtual spheres

A6.6.1.1. Function Esfpropiedades

```
; Measurement of properties inside the Spheres MP

def Esfpropiedades

        cont_step=cycle  ;
        section ;
                mp = circ_head
                emindex = 1
                ContadorClumpMP = 1;
                ContadorContactomuestra_MP = 1  ;
                totalclumpESFERAMP=0
                loop while mp # null
                        prom_volclump = 0.
                        prom_diamclump = 0.
                        prom_totalbolas = 0.
                        prom2_volclumpvolcl = 0.
                        prom2_diamclumpvolcl = 0.
                        prom2_totalbolasvolcl = 0.
                        idmp = m_id(mp)             ;
                mpradio = m_rad(mp)       ;
                        mxcentro = m_x(mp)        ;
                        mycentro = m_y(mp)        ;
                        mzcentro = m_z(mp)        ;
                        NCoordinacion = m_coord(mp)
                        mporosidad = m_poros(mp)
                        mslidingfraction = m_sfrac(mp)
                        cstress_call = measure(mp,1)  ;
                        mtension11 = m_s11(mp)
                        mtension12 = m_s12(mp)
                        mtension13 = m_s13(mp)
                        mtension21 = m_s21(mp)
                        mtension22 = m_s22(mp)
                        mtension23 = m_s23(mp)
                        mtension31 = m_s31(mp)
                        mtension32 = m_s32(mp)
                        mtension33 = m_s33(mp)
                        if mtension11 < mtension22 then
                                c_s1 = mtension11
                                c_s2 = mtension22
                        else
                                c_s1 = mtension22
                                c_s2 = mtension11
                        end_if
                        if c_s2 < mtension33 then
                                c_s3 = mtension33
                        else
                                if c_s1 < mtension33 then
                                c_s3 = c_s2
                                c_s2 = mtension33
```

```
            else
            c_s3 = c_s2
            c_s2 = c_s1
            c_s1 = mtension33
            end_if
end_if
c_r1 = 0.
if c_s3 # 0. then
            c_r1 = c_s1 / c_s3
end_if
c_r2 = 0.
if c_s3 # 0. then
            c_r2 = c_s2 / c_s3
end_if
c_r1modif = 0.
if mtension11 # 0. then
            c_r1modif = mtension33 / mtension11
end_if
c_r2modif = 0.
if mtension11 # 0. then
            c_r2modif = mtension22 / mtension11
end_if
c_r3modif = 0.
if mtension22 # 0. then
            c_r3modif = mtension33 / mtension22
end_if
cstrain_call = measure(mp,2)  ; compute stress
mvdef11 = m_ed11(mp)
mvdef12 = m_ed12(mp)
mvdef13 = m_ed13(mp)
mvdef21 = m_ed21(mp)
mvdef22 = m_ed22(mp)
mvdef23 = m_ed23(mp)
mvdef31 = m_ed31(mp)
mvdef32 = m_ed32(mp)
mvdef33 = m_ed33(mp)
sigma11=mtension11
sigma12=mtension12
sigma13=mtension13
sigma21=mtension21
sigma22=mtension22
sigma23=mtension23
sigma31=mtension31
sigma32=mtension32
sigma33=mtension33
sigma12_prom=(mtension12+mtension21)/2
sigma13_prom=(mtension13+mtension31)/2
sigma23_prom=(mtension23+mtension32)/2

TENSIONESPRINCIPALES;          Call Function

if I1_Cuadrado <= I2_por3 ;
            exit section ;
end_if
MSIGMA1=SIGMA1
MSIGMA2=SIGMA2
MSIGMA3=SIGMA3
```

```
                        cPRINCIPALES_r1 = 0.
                        if MSIGMA3 # 0. then
                                cPRINCIPALES_r1 = MSIGMA1 / MSIGMA3
                        end_if
                        cPRINCIPALES_r2 = 0.
                        if c_s3 # 0. then
                                cPRINCIPALES_r2 = MSIGMA2 / MSIGMA3
                        end_if

                        REVISACLUMPS_MP ;     Call Function

VolclumpTotalEsfera=prom_volclump ;
prom_volclump = prom_volclump / totalclumpESFERAMP
prom_diamclump = prom_diamclump / totalclumpESFERAMP
prom_totalbolas = prom_totalbolas / totalclumpESFERAMP

pponderado_volclump = prom2_volclumpvolcl / VolclumpTotalEsfera
pponderado_diamclump = prom2_diamclumpvolcl / VolclumpTotalEsfera
pponderado_totalbolas = prom2_totalbolasvolcl / VolclumpTotalEsfera

infomp1 (emindex+1) = string (emindex)+'   '+string(idmp)+'   '+string(mpradio)       +       '
        '+string(mxcentro)+ '       '+string(mycentro)+ '       '+string(mzcentro)+             '
        '+string(NCoordinacion)
infomp2 (emindex+1) = string (emindex)+'   '+string(mporosidad)+'
        '+string(mslidingfraction) + '          '+string(ContadorClumpMP)           +           '
        '+string(totalclumpESFERAMP)
infomp3 (emindex+1) = string (emindex)+'   '+string(MSIGMA1)+'       '+string(MSIGMA2) +
'       '+string(MSIGMA3)+ '       '+string(mtension11)+ '     '+string(mtension12)+           '
        '+string(mtension13)
infomp4 (emindex+1) = string (emindex)+'   '+string(mtension21)+'       '+string(mtension22)
+ '       '+string(mtension23)+ '     '+string(mtension31)+ '     '+string(mtension32)+           '
        '+string(mtension33)
infomp5 (emindex+1) = string (emindex)+'   '+string(mvdef11)+'          '+string(mvdef12) + '
        '+string(mvdef13)+ '       '+string(mvdef21)+ '       '+string(mvdef22)+              '
        '+string(mvdef23)
infomp6 (emindex+1) = string (emindex)+'   '+string(cont_step)+'        '+string(mvdef31) + '
        '+string(mvdef32)+ '       '+string(mvdef33)
infomp7 (emindex+1) = string (emindex)+'   '+string(pponderado_volclump)+'
        '+string(pponderado_diamclump) + '          '+string(pponderado_totalbolas)+        '
        '+string(prom_volclump)+ ''+string(prom_diamclump)+                                 '
        '+string(prom_totalbolas)
infomp8 (emindex+1) = string (emindex)+'   '+string(cPRINCIPALES_r1)+'
        '+string(cPRINCIPALES_r2) + '      '+string(c_r1)+ '   '+string(c_r2)
infomp9 (emindex+1) = string (emindex)+'   '+string(c_r1modif)+ '       '+string(c_r2modif)+ '
        '+string(c_r3modif)
infomp10 (emindex+1) = string (emindex)+'  '+string(numClumpTotalMP)+                          '
        '+string(numClumpVaciosMP)+ '     '+string(numClumpSinContactoMP)+'
        '+string(numClumpBuenosMP)+'      '+string(numClumpSinFCyBuenosMP)

        end_section ;

                        emindex = emindex+1
                        mp = m_next(mp)

                end_loop

empropiedades1='13E22I112D_empropiedades1_'+string(ContadorFileMP)+'.dat'
```

```
empropiedades2='13E22I112D_empropiedades2_'+string(ContadorFileMP)+'.dat'
empropiedades3='13E22I112D_empropiedades3_'+string(ContadorFileMP)+'.dat'
empropiedades4='13E22I112D_empropiedades4_'+string(ContadorFileMP)+'.dat'
empropiedades5='13E22I112D_empropiedades5_'+string(ContadorFileMP)+'.dat'
empropiedades6='13E22I112D_empropiedades6_'+string(ContadorFileMP)+'.dat'
empropiedades7='13E22I112D_empropiedades7_'+string(ContadorFileMP)+'.dat'
empropiedades8='13E22I112D_empropiedades8_'+string(ContadorFileMP)+'.dat'
empropiedades9='13E22I112D_empropiedades9_'+string(ContadorFileMP)+'.dat'
empropiedades10='13E22I112D_empropiedades10_'+string(ContadorFileMP)+'.dat'

Info_ClumpsMP1='13E22I112D_Info_ClumpsMP1_'+string(ContadorFileMP)+'.dat'
Info_ClumpsMP2='13E22I112D_Info_ClumpsMP2_'+string(ContadorFileMP)+'.dat'
Info_ClumpsMP3='13E22I112D_Info_ClumpsMP3_'+string(ContadorFileMP)+'.dat'
Info_ClumpsMP4='13E22I112D_Info_ClumpsMP4_'+string(ContadorFileMP)+'.dat'
Info_ClumpsMP5='13E22I112D_Info_ClumpsMP5_'+string(ContadorFileMP)+'.dat'

Info_ContactosMP1='13E22I112D_Info_ContactosMP1_'+string(ContadorFileMP)+'.dat'
Info_ContactosMP2='13E22I112D_Info_ContactosMP2_'+string(ContadorFileMP)+'.dat'
Info_ContactosMP3='13E22I112D_Info_ContactosMP3_'+string(ContadorFileMP)+'.dat'
Info_ContactosMP4='13E22I112D_Info_ContactosMP4_'+string(ContadorFileMP)+'.dat'
Info_ContactosMP5='13E22I112D_Info_ContactosMP5_'+string(ContadorFileMP)+'.dat'

        ;;;; Data files of the spheres MP

        status = open(empropiedades1,IO_WRITE,IO_ASCII)
        status = write(infomp1,emindex)
        status = close

        status = open(empropiedades2,IO_WRITE,IO_ASCII)
        status = write(infomp2,emindex)
        status = close

        status = open(empropiedades3,IO_WRITE,IO_ASCII)
        status = write(infomp3,emindex)
        status = close

        status = open(empropiedades4,IO_WRITE,IO_ASCII)
        status = write(infomp4,emindex)
        status = close

        status = open(empropiedades5,IO_WRITE,IO_ASCII)
        status = write(infomp5,emindex)
        status = close

        status = open(empropiedades6,IO_WRITE,IO_ASCII)
        status = write(infomp6,emindex)
        status = close

        status = open(empropiedades7,IO_WRITE,IO_ASCII)
        status = write(infomp7,emindex)
        status = close

        status = open(empropiedades8,IO_WRITE,IO_ASCII)
        status = write(infomp8,emindex)
        status = close

        status = open(empropiedades9,IO_WRITE,IO_ASCII)
```

```
        status = write(infomp9,emindex)
        status = close

        status = open(empropiedades10,IO_WRITE,IO_ASCII)
        status = write(infomp10,emindex)
        status = close

        ;;;; Data files of clumps inside the spheres MP

        status = open(Info_ClumpsMP1,IO_WRITE,IO_ASCII)
        status = write(infclumpMP1,ContadorClumpMP)
        status = close

        status = open(Info_ClumpsMP2,IO_WRITE,IO_ASCII)
        status = write(infclumpMP2,ContadorClumpMP)
        status = close

        status = open(Info_ClumpsMP3,IO_WRITE,IO_ASCII)
        status = write(infclumpMP3,ContadorClumpMP)
        status = close

        status = open(Info_ClumpsMP4,IO_WRITE,IO_ASCII)
        status = write(infclumpMP4,ContadorClumpMP)
        status = close

        status = open(Info_ClumpsMP5,IO_WRITE,IO_ASCII)
        status = write(infclumpMP5,ContadorClumpMP)
        status = close

        ;;;; Data files of contacts inside the spheres MP

        status = open(Info_ContactosMP1,IO_WRITE,IO_ASCII)
        status = write(infcontactosMP1,ContadorContactomuestra_MP)
        status = close

        status = open(Info_ContactosMP2,IO_WRITE,IO_ASCII)
        status = write(infcontactosMP2,ContadorContactomuestra_MP)
        status = close

        status = open(Info_ContactosMP3,IO_WRITE,IO_ASCII)
        status = write(infcontactosMP3,ContadorContactomuestra_MP)
        status = close

        status = open(Info_ContactosMP4,IO_WRITE,IO_ASCII)
        status = write(infcontactosMP4,ContadorContactomuestra_MP)
        status = close

        status = open(Info_ContactosMP5,IO_WRITE,IO_ASCII)
        status = write(infcontactosMP5,ContadorContactomuestra_MP)
        status = close

        ContadorFileMP = ContadorFileMP + 1  ;

End
```

A6.6.1.2. Function TENSIONESPRINCIPALES

```
def TENSIONESPRINCIPALES

                    I1=sigma11+sigma22+sigma33;
                    I2=(sigma11*sigma22+sigma22*sigma33+sigma33*sigma11)-
((sigma12_prom)^2+(sigma13_prom)^2+(sigma23_prom)^2);
          I3=sigma11*sigma22*sigma33+2*sigma12_prom*sigma13_prom*sigma23_prom-
sigma11*(sigma23_prom)^2-sigma22*(sigma13_prom)^2-sigma33*(sigma12_prom)^2;
                    Ppromedio=I1/3;
                    I1_Cuadrado=(I1)^2;
                    I2_por3=3*(I2);
                    if I1_Cuadrado <= I2_por3 ;
                              exit ;
                    end_if
                    QQ=((I1)^2-3*(I2))^3
                    Q_modificado=2*(SQRT(abs(QQ)));
                    R_modificado=(2*(I1)^3-9*I1*I2+27*I3)
                    R_mod_cuadrado=(R_modificado)^2
                    Q_mod_cuadrado=(Q_modificado)^2
                    if R_mod_cuadrado >= Q_mod_cuadrado
                              exit ; Sale de la función
                    end_if
                    COEFIC_A=(R_modificado/Q_modificado)
                    COEFIC_B=sqrt(abs((1./((COEFIC_A)^2))-1));
                    TETA=atan(COEFIC_B)
                    if COEFIC_A<0
                              TETA=(TETA*(-1.0))+PI
                    end_if
                    TETA3=TETA/3; Igual al Fi que tengo en la libreta de apuntes
                    TETAMAS=(TETA+2*pi)/3
                    TETAMENOS=(TETA-2*pi)/3 ; Esto es igual=(TETA+4*pi)/3

SIGMA_PRINCIPAL1=((I1)/3.)+(2.0/3.)*(SQRT(ABS((I1)^2-3.*(I2))))*cos(TETA3)          ;
SIGMA_PRINCIPAL2=((I1)/3)+(2.0/3.)*(SQRT(ABS((I1)^2-3.*(I2))))*cos(TETAMAS)        ;
SIGMA_PRINCIPAL3=((I1)/3)+(2.0/3.)*(SQRT(ABS((I1)^2-3.*(I2))))*cos(TETAMENOS)   ;

                    SIGMA_PRINCIPAL1=-SIGMA_PRINCIPAL1
                    SIGMA_PRINCIPAL2=-SIGMA_PRINCIPAL2
                    SIGMA_PRINCIPAL3=-SIGMA_PRINCIPAL3

                    if SIGMA_PRINCIPAL1>=SIGMA_PRINCIPAL2
                              if SIGMA_PRINCIPAL1>=SIGMA_PRINCIPAL3
                                        SIGMA1=SIGMA_PRINCIPAL1
                                        IF SIGMA_PRINCIPAL2>=SIGMA_PRINCIPAL3
                                                  SIGMA2=SIGMA_PRINCIPAL2
                                                  SIGMA3=SIGMA_PRINCIPAL3
                                        else
                                                  SIGMA2=SIGMA_PRINCIPAL3
                                                  SIGMA3=SIGMA_PRINCIPAL2
                                        end_if
                              else
                                        SIGMA1=SIGMA_PRINCIPAL3
                                        SIGMA2=SIGMA_PRINCIPAL1
                                        SIGMA3=SIGMA_PRINCIPAL2
```

```
                    end_if
                else
                    if SIGMA_PRINCIPAL2>=SIGMA_PRINCIPAL3
                        SIGMA1=SIGMA_PRINCIPAL2
                        if SIGMA_PRINCIPAL1>=SIGMA_PRINCIPAL3
                            SIGMA2=SIGMA_PRINCIPAL1
                            SIGMA3=SIGMA_PRINCIPAL3
                        else
                            SIGMA2=SIGMA_PRINCIPAL3
                            SIGMA3=SIGMA_PRINCIPAL1
                        end_if
                    else
                        SIGMA1=SIGMA_PRINCIPAL3
                        SIGMA2=SIGMA_PRINCIPAL2
                        SIGMA3=SIGMA_PRINCIPAL1
                    end_if
                end_if

end
```

A6.6.1.3. Function REVISACLUMPS_MP

```
def REVISACLUMPS_MP
        cl= clump_head   ; pointer de lista de clumps
        ccc=1; numeracion de clump
        ContadorContactomuestra=1;
        numClumpTotalMP=0 ;
        numClumpVaciosMP=0 ;
        numClumpSinContactoMP=0 ;
        numClumpBuenosMP=0 ;
        numClumpSinFCyBuenosMP=0 ;
        maxDesviador=0.;
        maxSig1Rotura=0.                ;
        numclumpdividido=0.     ;
        maxSig1=0.              ;
        maxSIGMATETA=0.                 ;
        MINSig3=10000000000.    ;
        IndicadorNumClumpS3Neg_2=0 ;
        VolumenTotalClumpMuestra=0.
loop while cl # null
        idcl=cl_id(cl)      ;
        id_clump(ccc)=idcl      ;
        num_clump(ccc)=ccc      ;
        totalcontactosmuestra = ContadorContactomuestra ;

        Xcentroclump= cl_x( cl )
        Ycentroclump= cl_y( cl )
        Zcentroclump= cl_z( cl )
        Xmenorbola= Xcentroclump
        Xmayorbola= Xcentroclump
        Ymenorbola= Ycentroclump
        Ymayorbola= Ycentroclump
        Zmenorbola= Zcentroclump
        Zmayorbola= Zcentroclump
        Xcentroclump_cl(idcl)=Xcentroclump
        Ycentroclump_cl(idcl)=Ycentroclump
```

```
        Zcentroclump_cl(idcl)=Zcentroclump
        XDistanciaClump_MP = Xcentroclump-mxcentro
        YDistanciaClump_MP = Ycentroclump-mycentro
        ZDistanciaClump_MP = Zcentroclump-mzcentro
        DistanciaClump_MP                                                    =
((((XDistanciaClump_MP)^2)+((YDistanciaClump_MP)^2)+((ZDistanciaClump_MP)^2))^(0.5)
)

If DistanciaClump_MP < mpradio   ;
        section
                SUMradiobola=0.0 ;
                totalbolas=0 ;
                radiobola=0.0
                promradiobola=0.0
                MaxfuerzanormalContacto=0.0       ;
                bcl=cl_list(cl)       ;
                j=1 ;
                ContadorContactoclump=1 ;

                loop while bcl # null
                        idbcl=b_id(bcl)     ;
                        radiobola=b_rad(bcl) ;
                        totalbolas=j
                        SUMradiobola=(SUMradiobola+radiobola) ;
                        totalcontactosclump = ContadorContactoclump ;
                        cpbcl=b_clist(bcl) ;
                        ab=1 ;

                        loop while cpbcl # null
                                cpbola1=c_ball1(cpbcl)
                                cpbola2=c_ball2(cpbcl)
                                fuerzanormalContacto=c_nforce(cpbcl)
                        if abs(fuerzanormalContacto)>MaxfuerzanormalContacto

                                MaxfuerzanormalContacto=fuerzanormalContacto;
                                IDBolaMaxContactoNormal=idbcl ;
                                radiobolaMaxContactoNormal=radiobola ;
                        end_if
                                totalcontactosbola = ab     ;
                                XContacto=c_x(cpbcl)
                                YContacto=c_y(cpbcl)
                                ZContacto=c_z(cpbcl)
                                XVectorunitarioContacto=c_xun(cpbcl)
                                YVectorunitarioContacto=c_yun(cpbcl)
                                ZVectorunitarioContacto=c_zun(cpbcl)
                                ;;FuerzacorteContacto=c_sforce(cpbcl)
                                XFuerzacorteContacto=c_xsforce(cpbcl)
                                YFuerzacorteContacto=c_ysforce(cpbcl)
                                ZFuerzacorteContacto=c_zsforce(cpbcl)
                                IncrEnergiaContacto=c_slipwork(cpbcl) ;

        infcontactosMP1          (ContadorContactomuestra_MP+1)          =          string
(ContadorContactomuestra)+'       '+string(idbcl)+'    '+string(idcl) + '    '+'
        '+string(XContacto)+ '       '+string(YContacto)+ '       '+string(ZContacto)+             '
        '+string(idmp)
        infcontactosMP2          (ContadorContactomuestra_MP+1)          =          string
(ContadorContactomuestra)+'       '+string(idbcl)+'    '+string(radiobola)           +            '
```

```
        '+string(totalbolas)+ '        '+string(DequivalenteClump)+                    '
        '+string(VolumenClump)
        infcontactosMP3         (ContadorContactomuestra_MP+1)          =          string
(ContadorContactomuestra)+'        '+string(fuerzanormalContacto)+'
        '+string(XVectorunitarioContacto) + '          '+string(YVectorunitarioContacto)+      '
        '+string(ZVectorunitarioContacto)
        infcontactosMP4         (ContadorContactomuestra_MP+1)          =          string
(ContadorContactomuestra)+'        '+string(XFuerzacorteContacto)              +          '
        '+string(YFuerzacorteContacto)+ '   '+string(ZFuerzacorteContacto)+                '
        '+string(IncrEnergiaContacto)
        infcontactosMP5         (ContadorContactomuestra_MP+1)          =          string
(ContadorContactomuestra)+'        '+string(ContadorContactoclump)+' '+string(ab)+'
        '+string(cont_step)

                                if c_ball1(cpbcl)=bcl then
                                        cpbcl=c_b1clist(cpbcl)
                                else
                                        cpbcl=c_b2clist(cpbcl)
                                end_if

        ab=ab+1 ;;; Listado de contactos por bola
        ContadorContactoclump = ContadorContactoclump+1   ;
        ContadorContactomuestra = ContadorContactomuestra+1;
        ContadorContactomuestra_MP = ContadorContactomuestra_MP + 1;

                                end_loop;
                                j=j+1
                                bcl=b_cllist(bcl)   ;
                        end_loop;
                        IF totalbolas > 0
                                promradiobola=(SUMradiobola)/totalbolas ;
                        END_IF
        end_section
        section
                        IF totalbolas = 0
                                numClumpVaciosMP=numClumpVaciosMP+1                     ;
                                exit section  ;
                        END_IF
numClumpSinFCyBuenosMP=numClumpSinFCyBuenosMP+1 ;
VolumenClump=((4.* pi *(promradiobola)^3. )/ 3.)*totalbolas  ;
VolumenTotalClumpMuestra=VolumenTotalClumpMuestra+VolumenClump
                        RequivalenteClump=((VolumenClump*3./(4.*pi))^(1./3.))
                        DequivalenteClump=2.*RequivalenteClump
                        totalclumpESFERAMP = numClumpSinFCyBuenosMP  ;
prom_volclump = prom_volclump + VolumenClump
prom_diamclump = prom_diamclump + DequivalenteClump
prom_totalbolas = prom_totalbolas + totalbolas
prom2_volclumpvolcl = prom2_volclumpvolcl + VolumenClump*VolumenClump
prom2_diamclumpvolcl=prom2_diamclumpvolcl+DequivalenteClump*VolumenClump
prom2_totalbolasvolcl = prom2_totalbolasvolcl + totalbolas*VolumenClump
Senotetaareacargada=sin(tetaCarga)
Fnmax=abs(MaxfuerzanormalContacto)
                        IF Fnmax = 0.
                                numClumpSinContactoMP=numClumpSinContactoMP+1;
                                exit section  ; Que de paso al siguiente clump
                        END_IF
                        radioClump=RequivalenteClump
```

```
                cargaP=(Fnmax)/(PI * radioClump^2 * (Senotetaareacargada)^2.)
                wcarga=radioClump*tan(tetaCarga)
                zcarga=radioClump*(1-0.8075)        ;
                SIGMATETA=(0.5+poisson-
((1+poisson)/((1+(wcarga/zcarga)^2)^(0.5)))+(1/(2*((1+(wcarga/zcarga)^2)^(1.5)))))*cargaP
                MaxfuerzanormalContactoV(idcl)=MaxfuerzanormalContacto
                SIGMATETAV(idcl)=SIGMATETA
                        if abs(SIGMATETAV(idcl))>maxSIGMATETA
                                maxSIGMATETA=SIGMATETAV(idcl)
                                maxSIGMATETAccc=ccc
                                maxidclumpSIGMATETA=idcl
                        end_if

                TensorTensiones= cl_stress (cl,tensionesClump)
                sigma11=tensionesClump(1,1)
                sigma12=tensionesClump(1,2)
                sigma13=tensionesClump(1,3)
                sigma21=tensionesClump(2,1)
                sigma22=tensionesClump(2,2)
                sigma23=tensionesClump(2,3)
                sigma31=tensionesClump(3,1)
                sigma32=tensionesClump(3,2)
                sigma33=tensionesClump(3,3)
                sigma12_prom=(sigma12+sigma21)/2
                sigma13_prom=(sigma13+sigma31)/2
                sigma23_prom=(sigma23+sigma32)/2
                if ccc=50 ;
                        sigma11_Clump1=tensionesClump(1,1)
                        sigma12_Clump1=tensionesClump(1,2)
                        sigma13_Clump1=tensionesClump(1,3)
                        sigma21_Clump1=tensionesClump(2,1)
                        sigma22_Clump1=tensionesClump(2,2)
                        sigma23_Clump1=tensionesClump(2,3)
                        sigma31_Clump1=tensionesClump(3,1)
                        sigma32_Clump1=tensionesClump(3,2)
                        sigma33_Clump1=tensionesClump(3,3)

                        sigma12_prom_Clump1=(sigma12+sigma21)/2
                        sigma13_prom_Clump1=(sigma13+sigma31)/2
                        sigma23_prom_Clump1=(sigma23+sigma32)/2
                        Xcentroclump_50=Xcentroclump
                        Ycentroclump_50=Ycentroclump
                        Zcentroclump_50=Zcentroclump
                END_iF
                TENSIONESPRINCIPALES;          Call Function
                if I1_Cuadrado <= I2_por3 ;
                        exit section ;
                end_if

        numClumpBuenosMP=numClumpBuenosMP+1                    ;

        infclumpMP1      (ContadorClumpMP+1)      =      string      (ContadorClumpMP)+'
        '+string(idcl)+'     '+string(Xcentroclump) + '  '+string(Ycentroclump)+                    '
        '+string(Zcentroclump)+ '   '+string(totalbolas)+ '        '+string(cont_step)
        infclumpMP2 (ContadorClumpMP+1) = string (ContadorClumpMP)+'    '+string
(ccc)+'   '+string(RequivalenteClump)+'       '+string(DequivalenteClump)           +           '
        '+string(VolumenClump)+ ''+string(Fnmax)+ '            '+string(SIGMATETA)
```

```
        infclumpMP3 (ContadorClumpMP+1) = string (ContadorClumpMP)+'
        '+string(sigma11)+' '+string(sigma12) + ' '+string(sigma13)+ '
        '+string(sigma21)+ ' '+string(sigma22)+ ' '+string(sigma23)
        infclumpMP4 (ContadorClumpMP+1) = string (ContadorClumpMP)+'
        '+string(sigma31)+' '+string(sigma32) + ' '+string(sigma33)+ '
        '+string(SIGMA1)+ ' '+string(SIGMA2)+ ' '+string(SIGMA3)
        infclumpMP5 (ContadorClumpMP+1) = string (ContadorClumpMP)+' '+string
(ccc)+' '+string(idcl)+' '+string(idmp)

        ContadorClumpMP = ContadorClumpMP+1 ;

        end_section ;

        numClumpTotalMP=numClumpTotalMP+1 ;

        END_IF ;
        ccc=ccc+1 ;
        cl=cl_next(cl) ;
end_loop ;

end
```

A6.7. Performance of tests

A6.7.1.1. Function EJECUCION

```
def EJECUCION

Ensayoiterate ; Control of Stresses;            Call Function

DELTAMACROTIEMPO=1
DELTAMACROTIEMPO_10=1

loop while DELTAMACROTIEMPO<=TiempoSigmaV
        if ContadorGranDivision=1
                RelajaRompimiento;                  Call Function
        end_if ;
        if abs((wszz - szzreq)/szzreq) >= sig_tol then
                M_Ensayoiterate ;                   Call Function
        end_if  ;;; Fin de if abs((wszz - szzreq)/szzreq) >= sig_tol
        Cont_Carga=0

        IF DELTAMACROTIEMPO_10=10
                command
                ini xvel 0.0 yvel 0.0 zvel 0.0 xspin 0.0 yspin 0.0 zspin 0.0
                clump  property  xvelocity=0.0  yvelocity=0.0  zvelocity=0.0  xspin=0.0
        yspin=0.0 zspin=0.0
                end_command

                DELTAMACROTIEMPO_10=0
          END_IF
                command
                        cyc 1
                end_command

        DELTAMACROTIEMPO=DELTAMACROTIEMPO+1
        DELTAMACROTIEMPO_10=DELTAMACROTIEMPO_10+1
end_loop

DELTAMACROTIEMPO=TiempoSigmaV
szzreq_anterior=szzreq

end
```

A6.7.1.2. Function Ensayoiterate

```
; Application of the stresses

def Ensayoiterate

Cont_Carga=1 ; No breakage

  loop while 1 # 0
    get_gain
```

```
      exit
    end_if
if szzreq_anterior # szzreq ;
          M_accel_platens  ; Applying of  szzreq by steps ;                Call Function
end_if
  command
    cycle 100 calm 5
  end_command
 end_loop
Cont_Carga=0 ; Considering breakage

end
```

A6.7.1.3. Function M_Ensayoiterate

```
def M_Ensayoiterate

Cont_Carga=1 ; No breakage
command
gz=0  ;
cyc 5000 calm 10
end_command
 loop while 1 # 0
  get_gain
    if abs((wszz - szzreq)/szzreq) < sig_tol then
      exit
    end_if
  command
    cycle 100 calm 5
  end_command
 end_loop
Cont_Carga=0 ;

end
```

A6.7.1.4. Function RelajaRompimiento

```
; Assignation of velocities of clumps and balls=0

def RelajaRompimiento

NumCiclosSeparacion=NumCiclosSeparacion+1 ;
Cont_Carga=1 ; No breakage
gz=0  ;
command
          ini xvel 0.0 yvel 0.0 zvel 0.0 xspin 0.0 yspin 0.0 zspin 0.0
          clump  property  xvelocity=0.0  yvelocity=0.0  zvelocity=0.0  xspin=0.0  yspin=0.0
zspin=0.0
          cyc 10 calm 10 ;;; (13E15)
end_command

ContadorGranDivision=0
Cont_Carga=0 ;

end
```

A6.7.1.5. Function M_accel_platens

```
def M_accel_platens

  m_niter = m_nsteps / m_nchunks
  loop m_chnk (1,m_nchunks)
delta_szzreq=(szzreq-szzreq_anterior)
szzreq_intermedio=szzreq_anterior+m_chnk*(delta_szzreq/m_nchunks)
    command
      cycle m_niter calm 10
    end_command
  end_loop
szzreq = szzreq_intermedio
szzreq_anterior=szzreq  ;

end
```

A6.7.1.6. Function NewColorclump

```
; Counter of clumps and assignation of colours

def NewColorclump

        cl= clump_head   ; pointer de lista de clumps
        VolClumpInicio=0.0
        loop while cl # null
                SUMradiobola=0.0 ;
                radiobola=0.0    ;
                bcl=cl_list(cl)       ;
                j=1 ;
                loop while bcl # null
                        idbcl=b_id(bcl)     ;
                        radiobola=b_rad(bcl) ;
                        totalbolas=j
                        SUMradiobola=(SUMradiobola+radiobola) ;
                        j=j+1
                        bcl=b_cllist(bcl)   ;
                end_loop;

                AsignaColorClump;                   Call Function

                cl=cl_next(cl)       ;
        end_loop ;
        command
                plot add clump orange yellow lblue lred dgray white blue lgreen red lgray
cyan green brown magenta black lorange
        end_command

end
```